



**University of
Nottingham**

UK | CHINA | MALAYSIA

Multiscale aeroelastic modelling in porous composite structures

Submitted August 2021, in partial fulfillment of
the conditions for the award of the degree **PhD Mechanical Engineering**.

Abhilash Sreekumar

20119029

Supervised by
Dr. Savvas Triantafyllou
Dr. Jelena Ninic
Dr. Matteo Icardi

School of Mechanical, Materials and Manufacturing Engineering
University of Nottingham

I hereby declare that this dissertation is all my own work, except as indicated in the text:

Signature 

Date 19 / 11 / 2021

I hereby declare that I have all necessary rights and consents to publicly distribute this dissertation via the University of Nottingham's e-dissertation archive.

Public access to this dissertation is restricted until: DD/MM/YYYY

Abstract

Driven by economic, environmental and ergonomic concerns, porous composites are increasingly being adopted by the aeronautical and structural engineering communities for their improved physical and mechanical properties. Such materials often possess highly heterogeneous material descriptions and tessellated/complex geometries. Deploying commercially viable porous composite structures necessitates numerical methods that are capable of accurately and efficiently handling these complexities within the prescribed design iterations. Classical numerical methods, such as the Finite Element Method (FEM), while extremely versatile, incur large computational costs when accounting for heterogeneous inclusions and high frequency waves. This often renders the problem prohibitively expensive, even with the advent of modern high performance computing facilities.

Multiscale Finite Element Methods (MsFEM) is an order reduction strategy specifically developed to address such issues. This is done by introducing meshes at different scales. All underlying physics and material descriptions are explicitly resolved at the fine scale. This information is then mapped onto the coarse scale through a set of numerically evaluated multiscale basis functions. The problems are then solved at the coarse scale at a significantly reduced cost and mapped back to the fine scale using the same multiscale shape functions. To this point, the MsFEM has been developed exclusively with quadrilateral/hexahedral coarse and fine elements. This proves highly inefficient when encountering complex coarse scale geometries and fine scale inclusions. A more flexible meshing scheme at all scales is essential for ensuring optimal simulation runtimes.

The Virtual Element Method (VEM) is a relatively recent development within the computational mechanics community aimed at handling arbitrary polygonal (potentially non-convex) elements. In this thesis, novel VEM formulations for poromechanical problems (consolidation and vibroacoustics) are developed. This is then integrated at the fine scale into the multiscale procedure to enable versatile meshing possibilities. Further, this enhanced capability is also extended to the coarse scale to allow for efficient macroscale discretizations of complex structures.

The resulting Multiscale Virtual Element Method (MsVEM) is originally applied to problems in elastostatics, consolidation and vibroacoustics in porous media to successfully drive down computational run times without significantly affecting accuracy. Following this, a parametric Model Order Reduction scheme for coupled problems is introduced for the first time at the fine scale to obtain a Reduced Basis Multiscale Virtual Element Method. This is used to augment the rate of multiscale basis function evaluation in spectral acoustics problems. The accuracy of all the above novel contributions are investigated in relation to standard numerical methods, i.e., the FEM and MsFEM, analytical solutions and experimental data. The associated efficiency is quantified in terms of computational run-times, complexity analyses and speed-up metrics.

Several extended applications of the VEM and the MsVEM are briefly visited, e.g., VEM phase field Methods for brittle fracture, structural and acoustical topology optimization, random vibrations and stochastic dynamics, and structural vibroacoustics.

Acknowledgements

I would like to express my heartfelt gratitude to Dr. Savvas Triantafyllou, for being very patient with my tendencies to ramble, helping me to resolve research roadblocks that seemed insurmountable at the time, constantly providing invaluable guidance on multiple fronts, and encouraging me to pursue a wide range of open questions. I would certainly have not been able to get very far in this work, without him.

I am very thankful to Dr. Jelena Ninic for her consistent inputs into my work, very insightful comments on the thesis, support with administrative tasks and helping me ground my research aspirations in a mature fashion. Thanks are also due to Dr. Matteo Icardi, for reading my thesis in detail, providing me with several useful resources and many interesting discussions over the course of my work.

I am deeply indebted to Matelys Research Lab, France, more specifically to Fabien Chevillotte, Dr. François-Xavier Bécot and Dr. Luc Jaouen, for providing an enormous wealth of resources such as proprietary software, data, literature and highly focused expertise in several critical points of the thesis. I sincerely appreciate the wholesome research environment they provided during my industrial secondment at the lab.

I would like to acknowledge that this work has been carried out under the auspices of the grant: “European industrial doctorate for advanced, lightweight and silent, multi-functional composite structures—N2N.” The No2Noise (N2N) project is funded under the European Union’s Horizon 2020 Research and Innovation Programme under the Marie Skłodowska-Curie Actions Grant: 765472.

I am also very grateful to Dr. Dimitrios Chronopoulos, Sarah Fletcher, Paul Wysocki and Manuela Cabrera for managing all the administrative aspects of the project in a timely and efficient way. They have put in a lot of effort to make all Early Stage Researchers feel welcome.

I extend my thanks to the thesis examiners, Professor René de Borst and Dr. Tao Liu for taking the time to read the work in great detail, and for providing invaluable feedback to improve the manuscript.

This list of acknowledgements would not be complete without recognizing the contributions of my peers, Arasan Uthayasuriyan, Vivek Thaminni Ramamoorthy and Dr. Udit Pillai. In addition to having memorable impromptu conversations on a wide variety of topics, I had also been fortunate to foster fruitful collaborations with them.

Finally, I would like to thank my mother Malini Sreekumar, and my father Thyagarajapuram Swaminathan Sreekumar for continuously being a pillar of love and support throughout my PhD.

Contents

Abstract	i
Acknowledgements	iii
I Theoretical Background	5
1 Introduction	6
1.1 Motivation and Problem Statement	6
1.2 Project Scope	8
1.3 Aim and Research Objectives	8
1.4 Methodology	10
1.5 Original Contributions	11
1.6 Publications	12
1.6.1 Articles published in International Peer Reviewed Journals	12
1.6.2 Articles submitted and under review	12
1.6.3 Peer Reviewed Conference Papers	12
1.6.4 Presentations at International Conferences	13
1.7 Layout	14
2 Computational Poroelasticity	15
2.1 Overview on Poroelasticity Formulations	15
2.2 Constitutive Relations	17
2.3 Continuity Relations	20
2.4 Computing Biot coefficients	21
2.5 Consolidation	23
2.6 Vibroacoustics	24
2.7 Finite Element Formulation	28
2.7.1 Elastostatics	28
2.7.2 Consolidation	31

2.7.3	Vibroacoustics	37
2.7.4	Computing acoustic indicators	49
2.8	Summary	50

II Fine scale Methods 52

3 Virtual Element Methods 53

3.1	Overview on Element Formulations	53
3.2	Virtual Element Spaces	55
3.3	Elastostatics	57
3.3.1	Virtual approximants at the element level	57
3.3.2	Computing the projectors	60
3.3.3	Computing the projector Π_k^ε	61
3.3.4	Consistency terms	62
3.3.5	Stability terms	63
3.3.6	State matrices	64
3.4	Consolidation	65
3.4.1	Virtual approximants at the element level	65
3.4.2	Computing the projectors	66
3.4.3	Computing the projector $\Pi_k^{\nabla p}$	67
3.4.4	Computing the projector Π_k^{0p}	68
3.4.5	Consistency terms	70
3.4.6	Stability terms	71
3.4.7	State matrices	72
3.5	Vibro-acoustics	73
3.5.1	Virtual approximants at the element level	73
3.5.2	Computing the projectors	75
3.5.3	Computing the projectors $\Pi_k^{\nabla u}$	76
3.5.4	Computing the projectors Π_k^{0u}	77
3.5.5	Consistency terms	78
3.5.6	Stability terms	79
3.5.7	State matrices	81
3.6	Numerical examples	81
3.6.1	Square poroelastic domain	82

3.6.2	Multilayer systems	87
3.6.3	Porous composite with tortuous inclusion	94
3.6.4	Mesoscale inclusions	96
3.7	Summary	99

III Multiscale Methods 102

4 Multiscale Finite Element Methods 103

4.1	Overview on Multiscale Methods	103
4.2	Elastostatics	105
4.2.1	Constructing multiscale basis functions	108
4.2.2	Governing multiscale equilibrium equations	110
4.2.3	Solution at the coarse scale and downscaling	111
4.3	Consolidation	112
4.3.1	Constructing multiscale basis functions	113
4.3.2	Governing multiscale equilibrium equations	113
4.3.3	Downscaling	117
4.4	Vibro-acoustics	117
4.4.1	Evaluation of multiscale basis functions	117
4.4.2	Upscaling procedure	118
4.5	Numerical examples	119
4.5.1	Melamine Foam	121
4.5.2	Highly dissipative material: 2437-9B	126
4.5.3	Porous composites	129
4.6	Summary	132

5 Multiscale Virtual Element Methods 133

5.1	Overview	133
5.2	Elastostatics	135
5.3	Numerical examples	137
5.3.1	Square plate under tension	138
5.3.2	Cantilever beam subjected to parabolic traction	139
5.3.3	Cantilever beam with a periodic microstructure	142
5.3.4	Cantilever beam with a highly heterogeneous material distribution subjected to parabolic traction	145

5.4	Consolidation	152
5.4.1	Oscillatory boundary conditions	152
5.5	Numerical examples	155
5.5.1	Porous domain with cavity	156
5.5.2	Heterogeneous Soil Domain	162
5.5.3	Honeycomb structure	171
5.6	Vibroacoustics	176
5.7	Parametric Model Order Reduction	177
5.7.1	Affine representations	179
5.7.2	Computing the reduced optimal basis	182
5.7.3	Reduced order model	184
5.8	Coupled Reduced Basis Multiscale Methods	185
5.9	Numerical examples	185
5.9.1	Reduced basis pMOR for a poroelastic square domain	185
5.9.2	Convergence behaviour of the MsVEM for vibroacoustics	190
5.9.3	Periodically repeating inclusions	192
5.9.4	Highly heterogeneous poroelastic domain	197
5.10	Summary	200

IV Summary 202

6 Conclusions and Future Research 203

6.1	Conclusions	203
6.2	Limitations and extensions	204
6.3	Future applications	206
6.3.1	Topology Optimization	206
6.3.2	Condensed models for vibroacoustics of multi-layered structures	208
6.3.3	Random vibroacoustics in porous media	208
6.3.4	Fractures in composite materials with mesoscale inclusions	209
6.3.5	Data driven modelling	210

Bibliography 210

List of Tables

2.1	Volumetric response of a poroelastic material when subjected to a change in isotropic compression dP_c	19
2.2	Boundary integrals.	42
2.3	Interface coupling integrals.	45
3.1	Generalized scalar and vector valued monomials for $\mathbb{M}_k(\mathcal{K})$ and $[\mathbb{M}_k(\mathcal{K})]^2$, respectively.	56
3.2	Degrees of Freedom for $\mathcal{V}_h^u(\mathcal{K})$. For Area moment, the monomials belong to $[\mathbb{M}_{k-2}(\mathcal{K})]^2$	57
3.3	Degrees of Freedom for $\mathcal{V}_h^p(\mathcal{K})$. For Area moment, the monomials belong to $\mathbb{M}_{k-2}(\mathcal{K})$	58
3.4	Definition of operator kernels.	59
3.5	Discretization used for the error-based mesh sensitivity analysis.	84
3.6	Alternate parametrization of higher order elements using a first order VEM.	86
3.7	Macroscopic material parameters corresponding to the relevant material ID.	90
3.8	Macroscopic material parameters corresponding to the relevant material ID.	94
3.9	Macroscopic material parameters corresponding to the relevant material ID.	97
3.10	Discretizations for the four inclusion-types used in Section 3.6.4.	100
4.1	Macroscopic material parameters corresponding to the relevant material ID.	120
4.2	Material names.	120
4.3	Computation time taken (in seconds) and speedup offered by the MsFEM over FEM for a melamine foam with rigid backing.	123
4.4	Computation time taken (in seconds) and speedup offered by the MsFEM over FEM for a melamine foam with air backing.	124
4.5	Legend Labels used in Fig. 4.13.	125
4.6	Computation time taken (in seconds) and speedup offered by the MsFEM over FEM for a melamine foam with mesoscale perforation.	126
5.1	Convergence behaviour of EMsFEM and EMsVEM are studied with respect to different element types.	140
5.2	Convergence rates of the \mathcal{L}_2 relative error norm.	141
5.3	Convergence rates of the \mathcal{H}_1 relative error norm.	142

5.4	Arbitrarily chosen micro-structural definition assigned periodically to each unit-cell.	143
5.5	Neutral axis free end displacements in the y-direction computed using EMsVEM and analytical solution.	143
5.6	Meshes used to discretize the micro-structure.	144
5.7	\mathcal{L}_2 and \mathcal{H}_1 error norms for Mesh 2 and Mesh 3 using Mesh 1 as a reference solution and computational times.	144
5.8	Multiscale method labeling based on the boundary conditions used to evaluate the multiscale basis functions.	146
5.9	Number of elements considered in each run. The discretization scheme B is illustrated in Fig. 5.16.	147
5.10	Relative \mathcal{L}_2 errors between standard solutions and multiscale solutions computed at coarse-nodes.	149
5.11	Opposite and adjacent boundary edges and nodes used for computing multiscale basis functions	154
5.12	Homogeneous material parameters used	157
5.13	Discretization scheme specifications.	158
5.14	Rates of error convergence.	161
5.15	Discretization schemes	164
5.16	Homogeneous material parameters of the soil domain.	165
5.17	Methods investigated.	165
5.18	Fine-scale $\ \mathbf{u}\ $ (in [mm]) and $\epsilon_{yy}(\times 10^{-3})$ along interface for coarse element 16. . .	170
5.19	Fine-scale $\ \mathbf{u}\ $ (in [mm]) and $\epsilon_{yy}(\times 10^{-3})$ along interface for coarse element 31. . .	170
5.20	Material parameters used.	173
5.21	Coarse scale discretizations for QUAD and CVT meshes.	191
5.22	Number of QUAD/CVT elements contained in each micro-structure.	191
5.23	Unit cell configurations.	194
5.24	Global mesh information for the six unit cell configurations.	194
5.25	Homogeneous macroscopic material parameters	198
5.26	Number of elements and nodes contained in each mesh.	198

List of Figures

1.1	Propagation of acoustic and elastic waves through a multilayer composite system with a poroelastic core	7
1.2	A wedge with solid inclusions	8
1.3	Original applications of the novel Multiscale Virtual Element Method	9
1.4	Methodology and Work Flow.	10
2.1	A poro-elastic domain Ω subjected to acoustic and mechanical excitations.	15
2.3	Arbitrary two dimensional domain for elastostatics	28
2.4	Discretized domain Ω_h decomposed into n_{el} quadrilateral elements.	30
2.5	Two dimensional porous domain Ω with boundary $\partial\Omega$	32
2.6	Schematic for Terzaghi's uniaxial consolidation test.	37
2.9	Medium subject to a plane wave acoustic excitation at an angle of incidence θ	39
2.10	A poro-elastic domain Ω subjected to acoustic and mechanical excitations.	40
2.11	Different kinds of interfaces encountered in Biot poroelasticity	43
2.12	Discretized domain Ω_h decomposed into n_{el} quadrilateral elements.	45
2.13	Anechoic wedge placed within an impedance tube	50
2.14	Sound Absorption Coefficients calculated for a poroelastic anechoic wedge with air backing.	51
3.1	Discretized domain Ω_h decomposed into n_{el} arbitrary potentially non-convex polygonal elements.	55
3.2	VEM DoFs illustrated for a $k = 2$ element with $N_v = 7$	57
3.3	VEM basis functions	59
3.4	A discretized solution field and its polynomial components visualized over a polygonal element.	60
3.5	A poroelastic domain in impedance tube configuration subject to plane-wave acoustical excitation \bar{p} at normal incidence.	82
3.12	Multilayer configuration with roller supports on lateral edges	88
3.13	Resolving non-conforming interfaces	89
3.14	Influence of different stabilization choices	89

3.17	SAC computed by VEM, FEM and TMM for the multilayer absorption problem.	91
3.23	Thick rigid skeleton porous material with second rigid porous material as a tortuous inclusion.	95
3.24	Discretization of porous composite with tortuous inclusion	95
3.26	SAC computed by the VEM, axisymmetric FEM and TMM for the rigid porous composite material.	97
3.27	Domain with a single infinitely rigid circular inclusion per unit cell	98
3.28	SAC computed by the VEM for the domain with and without inclusion	98
3.30	A 3.5 cm thick domain with two infinitely rigid circular inclusions per unit cell	99
3.31	SAC computed by the VEM for the domain with and without inclusions.	100
4.1	Motivation for multiscale approaches.	104
4.2	Multiscale mesh with 9 coarse quadrilateral elements and 81 quadrilateral fine-elements.	105
4.3	MsFEM upscaling procedure	106
4.4	Visualizing multiscale basis functions for a heterogeneous domain.	107
4.5	RVE with 9 quadrilateral elements	109
4.6	Schematic of a melamine foam placed against a rigid backing with coarse mesh.	121
4.9	Schematic of a melamine foam backed with a 40 mm air activity with coarse mesh.	123
4.14	Schematic of a dissipative material with rigid backing.	127
4.16	Schematic of a dissipative material with air backing.	127
4.18	Schematic of a dissipative material with mesoscale perforation.	128
4.20	Schematic of a rigid frame double porosity medium.	130
4.22	Schematic of a rigid frame porous material with porous inclusion.	131
4.24	Schematic of a rigid frame porous material with tortuous porous inclusion.	131
5.1	Multiscale mesh with 9 coarse quadrilateral elements and 81 polygonal (possibly non-convex) fine-elements.	135
5.2	RVE with 9 generalized (possibly non-convex) polygonal elements	135
5.3	MsVEM upscaling procedure for elastostatics	136
5.4	Process flow of the Multiscale Virtual Element procedure.	137
5.7	Relative error plots: EMsFEM and EMsVEM displacements compared against FEM and VEM	139
5.8	Schematic diagram of a cantilever beam subject to parabolic tractions.	140
5.12	Cantilever with a periodic micro-structure: Geometry and boundary conditions.	144
5.21	Multiscale mesh with $n_M = 22$ coarse nodes and $n_{Me_l} = 9$ polygonal coarse elements	152

5.22	An example 6-noded coarse element	153
5.23	Process flow of the Coupled Multiscale Virtual Element procedure.	155
5.24	Geometry and boundary conditions of a porous domain with circular cavity.	156
5.25	Compressive loading history.	157
5.39	Loading history.	164
5.49	Microstructures of adjacent coarse elements 16 and 31. The interface joins coarse nodes M_{47} and M_{50}	173
5.54	Schematic of a honeycomb structure.	176
5.63	Decay of the first $n_s = 15$ singular values computed for the snapshot matrix \mathbf{S}	187
5.68	Sound Absorption Coefficients as computed by the FOM, ROM and the Lo-Fi model.	190
5.73	Coarse elements chosen and proposed as future extensions.	195
5.76	A poroelastic domain with an anechoic backing subject to plane-wave acoustical excitation \bar{p} at normal incidence.	197
5.80	Sound Transmission Loss coefficient as calculated with the VEM, MsVEM and RBMsVEM for the heterogeneous realization shown in Fig. 5.77.	200
6.1	A fidget-spinner shaped poroelastic domain with a highly heterogeneous material definition	203

List of Algorithms

1	Elastic stiffness matrix evaluation schema.	65
2	Consolidation state matrices evaluation schema.	73
3	Upscaling procedure performed for solid and fluid phases	116
4	Multiscale basis function evaluation schema.	136
5	Multiscale basis function evaluation schema using the pMOR.	186

Glossary

Abbreviation	Expansion
BEM	Boundary Element Method
CMA-ES	Covariance Matrix Adaptation Evolution Strategy
CMsFEM	Coupled Multiscale Finite Element Method
CMsRBVEM	Coupled Multiscale Reduced Basis Virtual Element Method
CVT	Centroidal Voronoi Tesselations
DBM	Delany - Bazley - Miki model
DoF	Degree of Freedom
EMsFEM	Extended Multiscale Finite Element Method
EMsVEM	Extended Multiscale Virtual Element Method
FEM	Finite Element Method
FOM	Full Order Model
GFEM	Generalized Finite Element Method
GMRES	Generalized Minimal Residual method
HPC	High Performance Computing
IEM	Infinite Element Method
IGA	Isogeometric Analysis
JCAL	Johson Champoux Allard Lafarge model
LSM	Level Set Method
MFD	Mimetic Finite Difference method
MITC	Mixed Interpolation of Tensorial Components
ML	Mixing Law
MMA	Method of Moving Asymptotes
MOR	Model Order Reduction
MsFEM	Multiscale Finite Element Method
MsRBM	Multiscale Reduced Basis Method
MsVEM	Multiscale Virtual Element Method
NURBS	Non-Uniform Rational B-Splines
PC	Porous Composite
PCA	Principal Component Analysis
PCG	Preconditioned Conjugate Gradient method
PFEM	Polygonal Finite Element Method
PML	Perfectly Matched Layer
POD	Proper Orthogonal Decomposition
PSD	Power Spectral Density
PUFEM	Partition of Unity Finite Element Method

PUM	Partition of Unity Method
QUAD	Quadrilateral
RAND	Random
ROM	Reduced Order Model
RVE	Representative Volume Element
SAC	Sound Absorption Coefficient
SBFEM	Scaled Boundary Finite Element Method
SEM	Spectral Element Method
SIMP	Solid Isotropic Material with Penalization
STL	Sound Transmission Loss coefficient
SVD	Singular Value Decomposition
TMM	Transfer Matrix Method
VEM	Virtual Element Method
XFEM	eXtended Finite Element Method

Nomenclature

Parameter	Description	Value	Units
\mathbf{u}	solid-skeleton displacement		m
\mathbf{U}	fluid displacement		m
p	fluid pressure		Pa
$\boldsymbol{\sigma}_s$	in-vacuo stress tensor		$\text{N} \cdot \text{m}^{-2}$
$\boldsymbol{\varepsilon}_s$	infinitesimal strain tensor		-
E	Young's modulus		$\text{N} \cdot \text{m}^{-2}$
ν	Poisson's ratio		-
$\eta_s(\omega)$	structural loss factor		-
$\tilde{\mathbb{D}}$	elastic constitutive tensor		$\text{N} \cdot \text{m}^{-2}$
$\tilde{\rho}$	modified Biot density		$\text{kg} \cdot \text{m}^{-3}$
$\tilde{\rho}_{\text{eq}}$	dynamic mass density		$\text{kg} \cdot \text{m}^{-3}$
\tilde{k}_{eq}	dynamic bulk modulus		$\text{N} \cdot \text{m}^{-2}$
$\tilde{\gamma}$	coupling factor		-
ω	angular frequency		$\text{rad} \cdot \text{s}^{-1}$
ϕ	porosity		-
ρ_0	air density at rest	1.2042	$\text{kg} \cdot \text{m}^{-3}$
ρ_s	solid skeleton-material density		$\text{kg} \cdot \text{m}^{-3}$
ρ_1	solid skeleton-frame density		$\text{kg} \cdot \text{m}^{-3}$
ρ_f	fluid density		$\text{kg} \cdot \text{m}^{-3}$
K_b	porous skeleton bulk modulus at constant pressure		$\text{N} \cdot \text{m}^{-2}$
K_s	solid skeleton-material bulk modulus		$\text{N} \cdot \text{m}^{-2}$
K_f	fluid bulk modulus		$\text{N} \cdot \text{m}^{-2}$
σ	static airflow resistivity		$\text{N} \cdot \text{s} \cdot \text{m}^{-4}$
α_∞	high frequency limit of dynamic tortuosity		-
Λ	viscous characteristic length		m
Λ'	thermal characteristic length		m
k'_0	static thermal permeability		m^2
c_{air}	speed of sound in air	343.377	$\text{m} \cdot \text{s}^{-1}$
z_{air}	impedance of air	413.4807	$\text{kg} \cdot \text{m}^{-2} \cdot \text{s}^{-1}$
P_0	atmospheric pressure	101,325	$\text{N} \cdot \text{m}^{-2}$
C_p	specific heat of fluid at constant pressure	1.0024×10^3	$\text{J} \cdot \text{kg}^{-1}$
η	dynamic viscosity	1.8214×10^{-5}	$\text{N} \cdot \text{s} \cdot \text{m}^{-2}$

γ	adiabatic index	1.4012	—
α	sound absorption coefficient		-
\mathcal{T}	sound transmission loss coefficient		-
κ	thermal conductivity	0.0257	$\text{W} \cdot \text{m}^{-1} \cdot \text{K}^{-1}$
k	wave number of acoustic excitation		m^{-1}
α_B	Biot coefficient		-
S_ε	storativity coefficient		$\text{N}^{-1} \cdot \text{m}^2$
γ_f	specific weight of pore-fluid		$\text{kg} \cdot \text{m}^{-2} \cdot \text{s}^{-2}$
G	Shear modulus		$\text{N} \cdot \text{m}^{-2}$
A, Q, R, S	Biot coefficients		$\text{N} \cdot \text{m}^{-2}$
\mathbf{k}	permeability		m^2

Part I

Theoretical Background

Chapter 1

Introduction

1.1 Motivation and Problem Statement

The aeronautical industry is driven by a major societal challenge, i.e., that of reducing emissions by minimizing or even eliminating oil dependency while increasing the safety of passengers and cargo, see, e.g., [1]. The Strategic Research and Innovation Agenda (SRIA) stipulates a 50% reduction in fuel consumption within the transport sector through the upcoming years [2]. A reduction in structural weight can address these concerns by minimizing engine load; thereby bringing down fuel consumption, reducing resulting emissions and significantly driving down operating costs.

Composite materials are a well studied alternative to conventional metallic ones as they exhibit superior structural characteristics, e.g., high stiffness and strength to weight ratios. Hence, the aerospace industry finds itself steadily employing an increasing percentage of such composite materials in its structures. Unfortunately, composites also come with mechanical limitations that, to this point, prevent their widespread uptake in the aerospace industry.

Due to their greater thickness and reduced weight, such composite structures allow for an increased number of acoustic waves to propagate within them. Consequently, poorer vibration and acoustic isolation are offered, at least when compared against their metallic counterparts [3,4]. This is undesirable as such isolation is essential for the safety and comfort of passengers and cargo. Furthermore, this is critical in reducing fatigue damage in sensitive equipment and load bearing structures.

These shortcomings are often overcome by adding appropriate mechanical damping/dissipation and acoustic noise cancellation technologies collectively known as sound packages [5]. The sound packages if non-optimally designed, can add significant weight to the structure, thereby compromising the weight saving benefits gained by employing composite structures in the first place. There is thus an urgent need to design optimal lightweight sound packages for commercial deployment.

The study of multifunctional composites is a discipline aimed at developing composite materials that exhibit optimal structural properties while at the same time offering good vibroacoustic isolation characteristics. Sandwich materials are not a new concept to material science. These are multilayered composites developed specifically to augment certain desirable traits and minimize undesirable ones (see Fig. 1.1). It has been shown in [6] that having metallic foams as an inclu-

poroelastic domains in general and porous composite structures in particular.

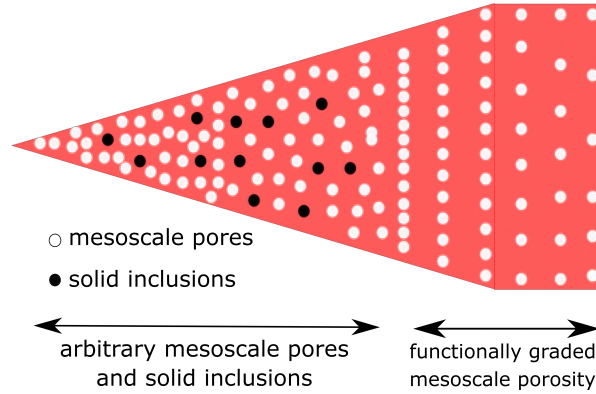


Figure 1.2: A wedge (modeled using double porosity theory) with solid inclusions. The talon-base contains functionally graded definitions for mesoscale pores. The triangular segment contains arbitrarily distributed mesoscale pores and solid inclusions. Inspired by [7].

1.2 Project Scope

Multiscale Finite Element Methods (MsFEM) [8] have been recently introduced in composite modelling by means of optimizing the trade-off between simulation accuracy and computational efficiency. Unlike FE^2 [9] and computational homogenization [10] approaches, these methods do not rely on periodicity or scale separation. Hence, they lend themselves naturally to the description of complex mechanical and vibroacoustic behaviour of highly heterogeneous domains. Representative Volume Elements (RVEs) along with a corresponding fine-mesh are defined to account for the constituents of the composite material. Fine-scale morphologies and RVE shapes can often be quite complex, necessitating the use of optimal flexible meshing capabilities at the fine scale to ensure efficiency and accuracy. This motivates the investigation of numerical schemes that can handle such flexible element shapes, within a multiscale context. The Virtual Element Method (VEM) [11] is a relatively new development in the computational mechanics community; and has been specifically designed to address polygonal (potentially non-convex) discretizations and non-conforming interfaces.

The scope of this work involves developing a novel computational theory incorporating these methods explicitly with a purpose to efficiently and accurately resolve elastostatic and poromechanical behaviour (consolidation and vibroacoustics) over complex and highly heterogeneous material domains.

1.3 Aim and Research Objectives

Given this aim, the following research objectives (ROs) are identified.

- **RO.1:** To deliver a novel numerical approach for poromechanics and vibroacoustics harnessing the meshing power of the virtual element method.

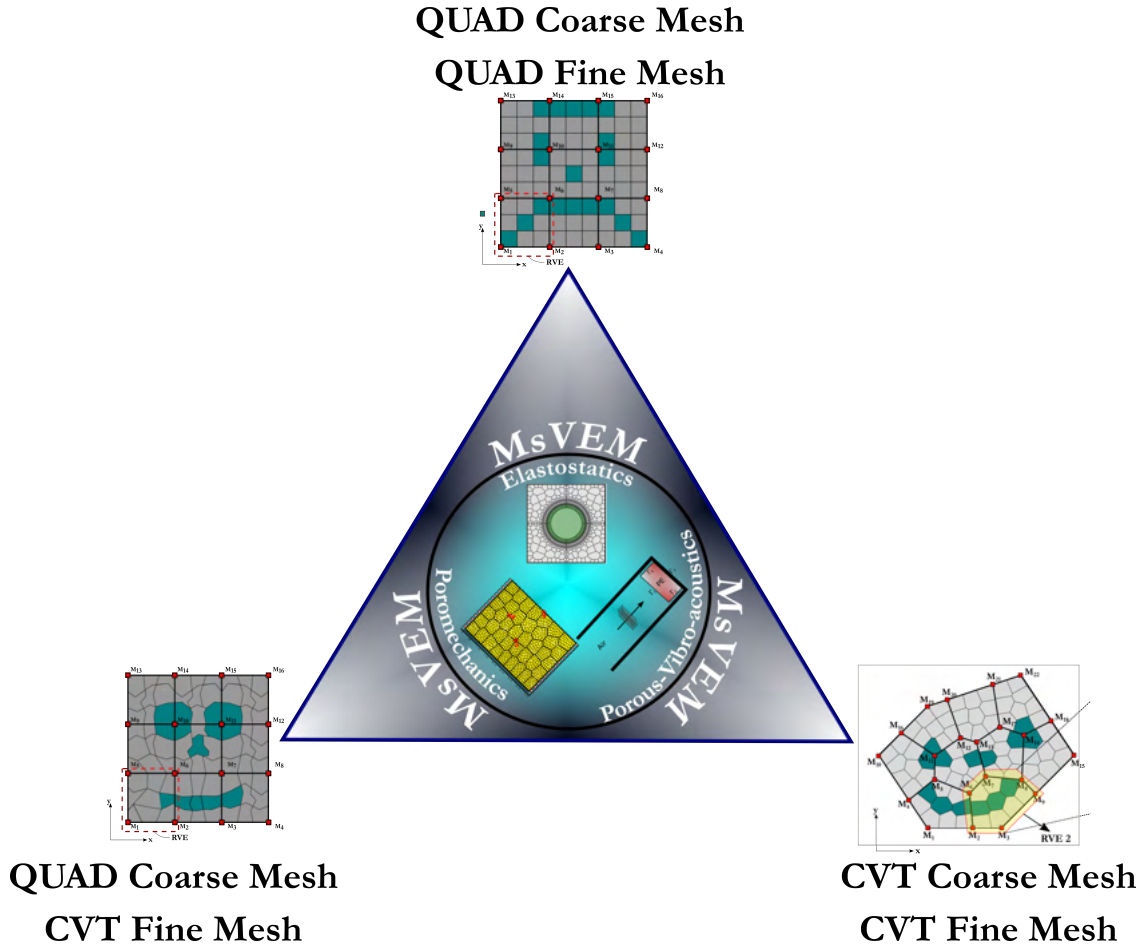


Figure 1.3: Original applications of the novel Multiscale Virtual Element method developed in this work.

- **RO.2:** To deploy a generalized multiscale scheme for elastostatic problems harnessing the the meshing flexibility of the VEM. Point of departure is the MsFEM that is also originally introduced in this research within the context of porous vibroacoustics.
- **RO.3:** To extend the VEM inspired multiscale method into the time domain, to account for coupled poroelastic consolidation.
- **RO.4:** To provide a procedure by which flexible polygonal (possibly non-convex shapes) are employed at all scales.
- **RO.5:** To implement a multiscale scheme using the FEM and VEM at the fine scale to describe the vibroacoustics of poroelastic materials in the frequency regime.
- **RO.6:** To further accelerate the frequency domain multiscale method at the fine scale using Proper Orthogonal Decomposition, to yield a reduced basis formulation.

The resulting Multiscale Virtual Element Method (MsVEM) is custom fit to applications in elastostatics, poromechanics and porous vibroacoustics as described in Fig. 1.3.

1.4 Methodology

To achieve these Research Objectives, the methodology adopted has been organized into seven Work Packages (WPs) as illustrated in Fig. 1.4. All implementations were initially developed in Matlab. A portion of this code has been translated into Fortran to benefit from computational acceleration. These Work Packages are elaborated below:

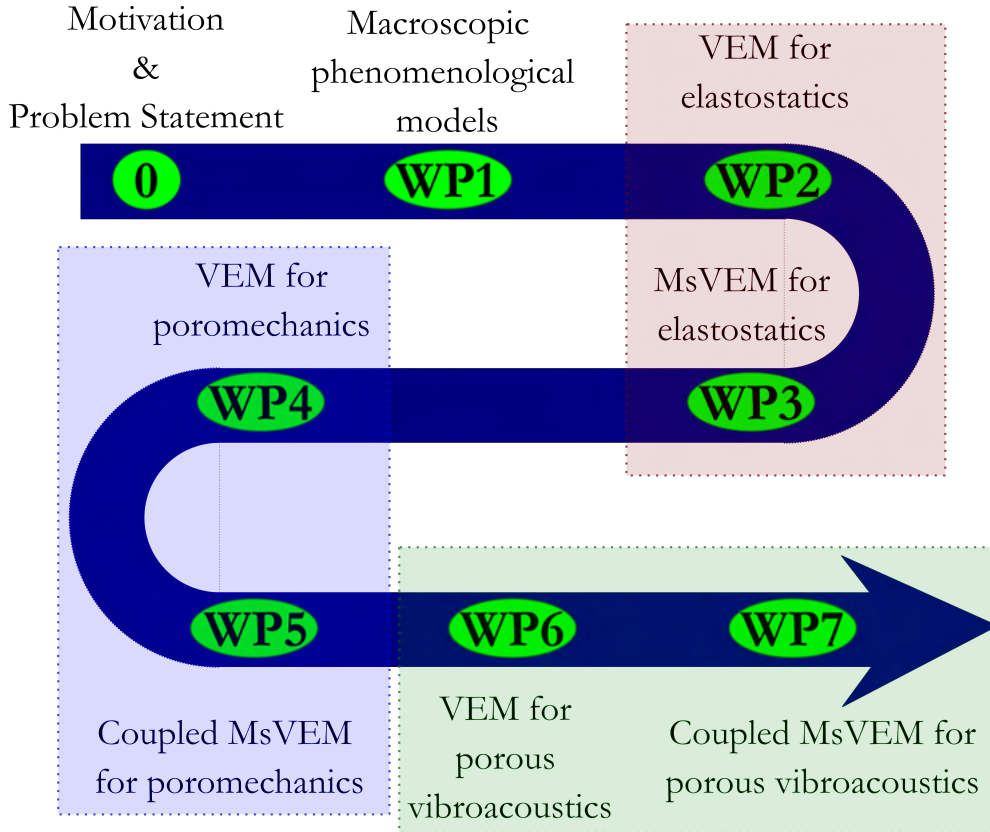


Figure 1.4: Methodology and Work Flow.

1. **WP.1 Macroscopic phenomenological models:** A review of Terzaghi and Biot poroelasticity within a consolidation and vibroacoustics framework is conducted. This includes an overview of semi-phenomenological models popularly used in these equations.
2. **WP.2 VEM for elastostatics:** Points of departure from the classical FEM is observed. A suitable polygonal mesher is incorporated into the solver. A VEM for Laplace/Poisson equations and linear elasticity is implemented.
3. **WP.3 MsVEM for elastostatics:** Points of departure of the MsFEM from classical FE^2 and computational homogenization methods is discussed. The VEM is incorporated into the method, with flexible meshing at the fine scale to resolve heterogeneities. Convergence, acceleration and accuracy of the MsVEM are demonstrated.
4. **WP.4 VEM for poromechanics:** Nuances involving mixed formulations necessary in coupled field problems are studied. An arbitrary order VEM discretization for Biot consolidation is developed. The numerical behaviour of this method is investigated.

5. **WP.5 Coupled MsVEM for poromechanics:** The VEM for poromechanics above is integrated within a coupled multiscale framework. Extensions to account for flexible RVE shapes are made. Influence of different boundary conditions on the accuracy of the method are shown.
6. **WP.6 VEM for porous vibroacoustics:** A VEM formulation for the fully dynamic Biot mixed displacement pressure formulation in the frequency domain, is proposed. Ability to accommodate different fluid structure couplings and non-conforming discretizations are provided.
7. **WP.7 Coupled MsFEM and MsVEM for porous vibroacoustics:** The ability of the method to resolve high frequency waves is investigated. Further computational gains pertaining to computing multiscale properties, using a reduced basis method is proposed.

1.5 Original Contributions

The novel contributions in this work are summarized below

1. The VEM schema derived for elastic wave propagation in poroelastic media (see Section 3.5). The Biot mixed $\mathbf{u} - p$ formulation for wave-propagation is discretized using implicitly defined basis functions. Projection operators are derived from first principles and used to formulate the state matrices. Different stabilisation strategies are explored. Novel advantages concerning convergence rates and resolving non-conforming interfaces are highlighted in Examples 3.6.1-3.6.2, respectively.
2. The multiscale virtual element method for elastostatics as developed in Section 5.2. Multiscale basis functions are calculated using the VEM at the fine scale. Original applications demonstrating the need for flexible meshing at the RVE scale are shown in Example 5.3.4.
3. The coupled multiscale virtual element method for Biot consolidation explained in Section 5.4. Multiscale basis functions are separately calculated for the solid and fluid phase by solving decoupled cell-problems with the VEM. Significant computational gains over a standard approach without upscaling are established in Example 5.5.2.
4. Flexible polygonal (potentially non-convex) elements at all scales as developed in Section 5.4.1. Benefits achieved using this approach in resolving complex global domains is illustrated in Example 5.5.3.
5. Oscillatory boundary conditions for polygonal RVEs as an alternative to linear or periodic boundary conditions (see Section 5.4.1). Instead of imposing a displacement or pressure profile over an RVE boundary, these profiles are numerically obtained through a reduced form of the cell-problem, over the relevant RVE edge. Improvements in accuracy within a highly heterogeneous material description are given in Example 5.5.2.
6. The multiscale finite element method for vibroacoustics of poroelastic media, as derived in Section 4.4. The governing equations are upscaled and solved at the coarse scale for all desired frequency steps. Novel applications to tortuous porous composite structures are provided in Examples 4.5.3.

7. The multiscale virtual element method for vibroacoustics of poroelastic media given in Section 5.6. Advantages of flexible meshing capabilities are provided in Example 5.9.3.
8. A reduced basis multiscale method using Proper Orthogonal decomposition at the fine scale (see Section 5.7). A POD basis is obtained using the Singular Value Decomposition of a snapshot matrix. The cell-problems are then projected onto the POD basis and solved over the frequency spectra at an accelerated pace. Accelerations in spectral computations of multiscale basis functions are discussed in Example 5.9.4.

1.6 Publications

1.6.1 Articles published in International Peer Reviewed Journals

- [1] **A. Sreekumar**, S. P. Triantafyllou, F. Chevillotte, "Virtual Elements for sound propagation in complex poroelastic media", *Computational Mechanics*, (2021) pp.1-36,.
- [2] **A. Sreekumar**, S. P. Triantafyllou, F.-X. Bécot, F. Chevillotte, "Multiscale VEM for Biot consolidation analysis of complex and highly heterogeneous domains", *Computer Methods in Applied Mechanics and Engineering* 375: 113543.
- [3] **A. Sreekumar**, S. P. Triantafyllou, F.-X. Bécot, F. Chevillotte, "A multiscale virtual element method for the analysis of heterogeneous media", *International Journal for Numerical Methods in Engineering*, (Dec. 2019) 121(8), pp.1791-1821.
- [4] V. T. Ramamoorthy, E. Özcan, A. J. Parkes, **A. Sreekumar**, L. Jaouen, F.-X. Bécot, "Comparison of heuristics and metaheuristics for topology optimisation in acoustic porous materials", *The Journal of the Acoustical Society of America*, 150(4), pp.3164-3175.

1.6.2 Articles submitted and under review

- [1] U. Arasan, **A. Sreekumar**, F. Chevillotte, S. P. Triantafyllou, D. Chronopoulos, E. Gourdon, "Condensed finite element scheme for symmetric multi-layer structures including dilatational motion", *Journal of Sound and Vibration*, (submitted, under review).

1.6.3 Peer Reviewed Conference Papers

- [1] **A. Sreekumar**, S. P. Triantafyllou, F.-X. Bécot, F. Chevillotte, "Accelerated vibro-acoustics of porous domains via a novel coupled multiscale virtual element method", *International Conference on Noise and Vibration Prediction, September 7-9 2020, Leuven, Belgium (virtual conference)*.
- [2] V. T. Ramamoorthy, E. Özcan, A. J. Parkes, **A. Sreekumar**, L. Jaouen, F.-X. Bécot, "Acoustic topology optimisation using CMA-ES", *International Conference on Noise and Vibration Prediction, September 7-9 2020, Leuven, Belgium (virtual conference)*.

1.6.4 Presentations at International Conferences

This research has also been disseminated at the following international conferences

- [1] S. P. Triantafyllou, **A. Sreekumar**, "Phase field fractures in composite materials with meso-scale inclusions using polygonal element technologies", *10th GRACM International Congress on Computational Mechanics, 5-7 July 2021, Athens, Greece (virtual conference)*.
- [2] **A. Sreekumar**, S. P. Triantafyllou, F.-X. Bécot, F. Chevillotte, L. Jaouen, "A novel Coupled Multiscale Virtual Element method for vibro-acoustics of porous domains across multiple length scales", *EMI/PMC International Conference, May 25-28 2021, NY, US (virtual conference)*.
- [3] **A. Sreekumar**, I. Kougiumtzoglou, S. P. Triantafyllou, "Filter Approximations for Random Vibro-Acoustics of Porous Media", *EMI/PMC International Conference, May 25-28 2021, NY, US (virtual conference)*.
- [4] **A. Sreekumar**, S. P. Triantafyllou, F.-X. Bécot, F. Chevillotte, L. Jaouen, "Resolving vibro-acoustics in double porosity materials via a coupled multiscale finite element method", *UKACM Conference on Computational Mechanics, April 14-16 2021, Loughborough, UK (virtual conference)*.
- [5] **A. Sreekumar**, S. P. Triantafyllou, F.-X. Bécot, F. Chevillotte, "Virtual Elements for Sound Propagation in Poroelastic Media", *14th World Congress on Computational Mechanics / ECCOMAS Congress, January 11-15 2021, Paris, France (virtual conference)*.
- [6] **A. Sreekumar**, S. P. Triantafyllou, F.-X. Bécot, F. Chevillotte, L. Jaouen, "Coupled Multiscale Finite Element methods for double porosity materials", *Forum Acusticum, International Congress on Acoustics, December 7-11 2020, Lyon, France (virtual conference)*.
- [7] S. P. Triantafyllou, **A. Sreekumar**, F.-X. Bécot, F. Chevillotte, "Accelerated vibro-acoustics of porous domains via a novel coupled multiscale virtual element method", *Eurodyn, 11th International Conference on Structural Dynamics, November 23-26 2020, Athens, Greece (virtual conference)*.
- [8] **A. Sreekumar**, S. P. Triantafyllou, F.-X. Bécot, F. Chevillotte, L. Jaouen, "Multiscale Virtual Element Methods for analysis of heterogeneous media", *HSTAM, 12th International Conference on Mechanics, September 22-25 2019, Thessaloniki, Greece*.
- [9] **A. Sreekumar**, S. P. Triantafyllou, F.-X. Bécot, F. Chevillotte, L. Jaouen, "Multiscale Virtual Element Methods for analysis of heterogeneous poroelastic media", *Coupled Problems, 8th International Conference on Coupled Problems in Science and Engineering, June 3-5 2019, Sitges (Barcelona), Spain*.
- [10] **A. Sreekumar**, S. P. Triantafyllou, F.-X. Bécot, F. Chevillotte, L. Jaouen, "Multiscale Virtual Element methods for heterogeneous media", *EMI International Conference, June 18-21 2019, CA, US*.

1.7 Layout

This thesis is divided into four parts. Part I contains the theoretical background. This comprises an overview discussing the state of the art physical modelling strategies used in poromechanics (Chapter 2). This chapter also covers the relevant finite element method solution procedures. Part II describes fine-scale methods. Here, Chapter 3 discusses the fundamental postulates underlying the Virtual Element Method. This is applied to elastostatics and coupled-field porous phenomena. Part III concerns Multiscale methodologies. The Multiscale Finite Element Method is developed from first principles for elastostatic problems in Chapter 4. This is then extended to the coupled porous media problems as well. The VEM is incorporated at the fine scale to obtain the MsVEM in Chapter 5. Alternate complexity reduction strategies are also discussed here. In Part IV, Chapter 6 summarizes the work with concluding remarks, limitations and future stakes.

Chapter 2

Computational Poroelasticity

In this Chapter, the mixed displacement-pressure formulations for Biot poromechanics, i.e., consolidation and vibroacoustics are derived from first principles. This is then discretized using a coupled finite element method procedure, with additional focus on Robin boundary conditions and different interface coupling constraints. The resulting numerical schemes are then verified against analytical solutions in the case of consolidation, i.e., the Terzaghi consolidation test, and experimental solutions in the case of wave propagation, i.e., the Sound Absorption Coefficient curve (SAC) for an anechoic wedge.

2.1 Overview on Poroelasticity Formulations

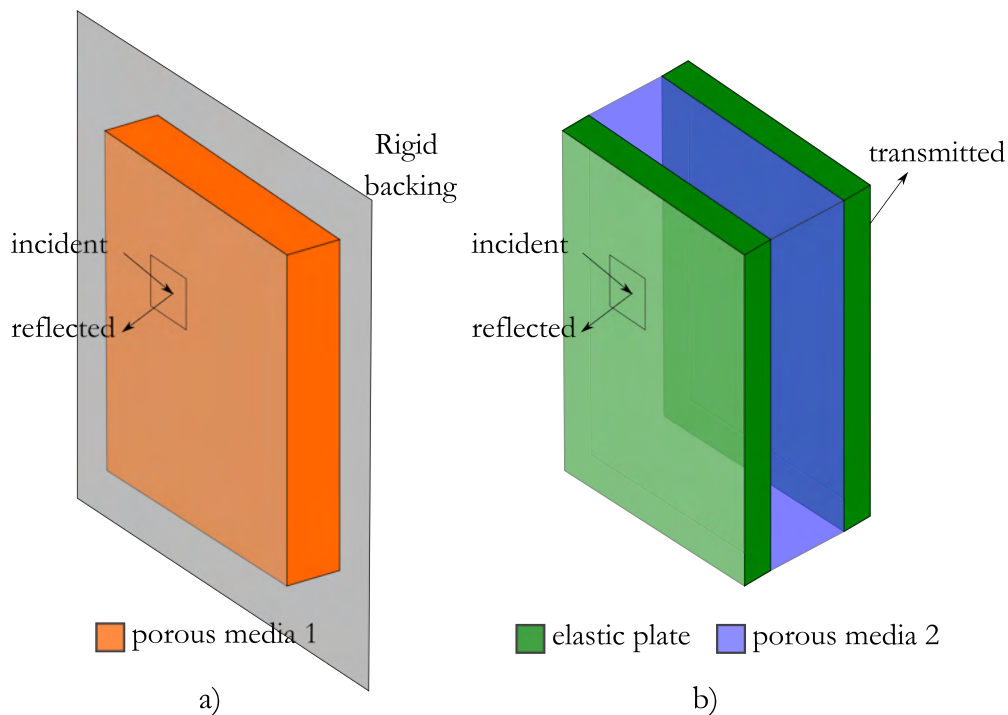


Figure 2.1: A poro-elastic domain Ω subjected to acoustic and mechanical excitations.

Within the context of porous materials with elastic frames, the skeleton deformations are negligible for large acoustical frequency bandwidths. This is often the case when rigid backing

supports are used (see Fig. 2.1a). In such situations, one can safely employ the equivalent fluid descriptions for porous media with rigid and motionless skeletons shown in [12]. However, there are certain resonance effects manifesting due to the elastic deformability of the skeleton, that cannot be captured with this model. This is especially true for elastic sandwich materials with poroelastic cores, where the elastic vibrations of the plate excite the skeleton, and vice-versa [13] (see Fig. 2.1b). In such cases, waves propagate in a coupled fashion through both the solid skeleton and pore-fluid phases.

A theory describing poroelasticity was first developed within a consolidation environment by Terzaghi in [14,15]. In this approach, the solid and fluid phases were assumed to be incompressible. Further, the model was valid solely for uniaxial environments. These assumptions were relaxed by Biot in [16] and further extended to anisotropic elastic skeletons in [17]. A dynamic model governing wave propagation in poroelastic materials was derived in [18,19].

The classical Biot theory provides a phenomenological description based on the following physical assumptions.

1. The characteristic size of the micro-scale, e.g., pore radius, is significantly smaller in comparison to the wavelengths of the propagating waves. This is necessary for a macroscopic continuum description to be valid.
2. The medium is a two phase system. The porous network is interconnected, continuous and fully saturated by a single Newtonian fluid. The solid skeleton comprises solid grain from a single material.
3. All phases undergo small deformations. This ensures that **no geometric non-linearities are encountered**.
4. Waves are dissipated exclusively due to viscous effects in the pore-fluid. Thermal dissipation is ignored. The skeleton is assumed to be homogeneous and isotropic. Structural dissipation is ignored.

Several attempts have successfully been made to relax some of these assumptions. The modified Biot formulation [20] adapts the formalism for anisotropic materials as well. This is further extended to inhomogeneous media in [21]. The model has been generalized to partially saturated porous media in [22] and to multi-phase problems in [23]. Further improvements and generalizations expanding the description to soil mechanics, geometric and material non-linearities etc. were developed in [24–30]. The ability to introduce different visco-thermal dissipation mechanisms into the governing equations, such as the three-parameter Delany-Bazley-Miki model [31], or the six-parameter Johnson-Champoux-Allard-Lafarge model [32–34], was developed in [35].

There exist multiple formalisms of Biot poroelasticity. The original, as developed for consolidation in [16] and wave propagation in [18,19] is a $\mathbf{u} - \mathbf{U}$ formulation, where \mathbf{u} and \mathbf{U} denote macroscopic solid skeleton and pore-fluid displacements, respectively. The modified Biot formulation for anisotropic materials in [20] is a $\mathbf{u} - \mathbf{w}$ formulation, where $\mathbf{w} = \phi(\mathbf{U} - \mathbf{u})$ denotes the fluid flow relative to the skeleton. The effective porosity is represented by ϕ . This is further extended to inhomogeneous poroelastic media through a $\mathbf{u} - \mathbf{u}_w$ in [21], where \mathbf{u}_w corresponds to the volume averaged microscopic pore fluid displacements. A $\mathbf{u} - p$ formulation was developed in [36] where p denotes pore-fluid pressures. This is restricted to isotropic materials, but offers

the advantage of requiring only 3 DoFs (4 DoFs in 3-D) when compared with 4 DoFs (6 DoFs in 3-D) required by the other formalisms. The merits and bottlenecks of each formulation is studied within a consolidation context in [37].

The transfer matrix method (TMM) [38–41] is a semi analytical approach used to solve these governing equations. It is especially used widely to predict the vibroacoustic behaviour of multilayered panels. Matrices are used to describe the wave propagation through each medium; and coupling constraints are introduced at the interfaces. Each layer is assumed to be homogeneous with planar surfaces and infinite lateral dimensions. The lateral dimension requirement is removed in [42]. The planar face requirement is relaxed in [7] by applying dual porosity theory [43–46]. However, this is still limited to periodically repeating structures. Heterogeneities are incorporated by considering inclusions in [47] and tortuous porous composites in [48]. However, all these approaches are custom fit to particular applications. Obtaining a generalized model that takes these extensions into consideration remains an open question. To this end, it is instructive to adopt numerical techniques like the FEM, which are not bound by any such physical considerations.

In this Chapter, the $\mathbf{u} - p$ formulation is derived from the $\mathbf{u} - \mathbf{U}$. Constitutive and continuity relations are defined and developed in Sections 2.2-2.3. The Biot coefficients are derived in Section 2.4. The $\mathbf{u} - p$ formulation for consolidation is presented in Section 2.5. Finally the $\mathbf{u} - p$ formulation for wave-propagation is provided in Section 2.6. The finite element discretization for these equations are described in detail in Section 2.7.

2.2 Constitutive Relations

The ensuing derivations are a summary of [49]. The bulk volume V_b of a poroelastic sample can be expressed in terms of its constituent phases

$$V_b = V_f + V_s, \quad (2.1)$$

where the volume of the saturating fluid V_f and elastic frame V_s are

$$V_f = \phi V_b, \quad V_s = (1 - \phi)V_b, \quad (2.2)$$

and the effective porosity ϕ is defined as

$$\phi = \frac{V_\phi}{V_b}. \quad (2.3)$$

The symbol V_ϕ denotes the volume of the interconnected pore network contained within the representative domain. Since the original Biot theory ([18, 19]) requires that the porous network be fully saturated with a single fluid, one has $V_\phi = V_f$.

Under the assumption of small deformation, the infinitesimal strain tensors $\boldsymbol{\varepsilon}_s$ and $\boldsymbol{\varepsilon}_f$ for the solid and fluid phases respectively, are provided

$$\boldsymbol{\varepsilon}_s = \frac{1}{2}(\nabla \mathbf{u} + \nabla^T \mathbf{u}), \quad (2.4)$$

$$\boldsymbol{\varepsilon}_f = \frac{1}{2}(\nabla\mathbf{U} + \nabla^T\mathbf{U}). \quad (2.5)$$

The symbol $\nabla(\cdot)$ denotes the gradient operator and read $\nabla_j = \frac{\partial}{\partial x_j}$. The tensors $\boldsymbol{\varepsilon}_s$ and $\boldsymbol{\varepsilon}_f$ are symmetric, i.e., $\varepsilon_{s,ij} = \varepsilon_{s,ji}$ and $\varepsilon_{f,ij} = \varepsilon_{f,ji}$. The total stress tensor over a bulk cubic element, $\boldsymbol{\sigma}_t$ is defined as

$$\boldsymbol{\sigma}_t = \boldsymbol{\sigma}_s + \sigma_f\mathbb{I}, \quad (2.6)$$

where $\boldsymbol{\sigma}_t$ is a **symmetric tensor**. The quantity σ_f denotes the contribution of $\boldsymbol{\sigma}_t$ to the fluid phase,

$$\sigma_f = -\phi p, \quad (2.7)$$

where the pore-fluid pressure p is positive under compression. Since this is assumed to be a Newtonian fluid, it does not accommodate shear stresses. The term $\boldsymbol{\sigma}_s$ represents the contribution of $\boldsymbol{\sigma}_t$ to the solid frame,

$$\boldsymbol{\sigma}_s = -\bar{\boldsymbol{\sigma}} - (1 - \phi)p\mathbb{I}. \quad (2.8)$$

The intergranular stresses $\bar{\boldsymbol{\sigma}}$ are also positive under compression. Inserting Eqs. (2.7) and (2.8) into Eq. (2.6) yields

$$\boldsymbol{\sigma}_t = -\bar{\boldsymbol{\sigma}} - p\mathbb{I}. \quad (2.9)$$

Within the isotropic limit, four unique coefficients A, Q, R and G are sufficient to describe the constitutive relations between stresses and strains for both phases of the porous medium

$$\sigma_{s,ij} = 2G\varepsilon_{s,ij} + (A\varepsilon_s + Q\varepsilon_f)\delta_{ij}, \quad (2.10)$$

$$\sigma_f = Q\varepsilon_s + R\varepsilon_f, \quad (2.11)$$

where ε_s and ε_f denote volumetric strains, $\varepsilon_s = \varepsilon_{s,kk}$ and $\varepsilon_f = \varepsilon_{f,kk}$, respectively. The corresponding volumetric stress for the solid frame is $\bar{\sigma} = \frac{1}{3}\bar{\sigma}_{kk}$. The constants A, Q and R are related to physical parameters like the shear modulus G , bulk modulus of the porous medium K_b , bulk modulus of the solid grain K_s , bulk modulus of the fluid K_f and porosity ϕ . This is done in [50] through gendanken experiments that investigate volume effects induced by pore-fluid pressure and solid-grain stresses. These effects include the bulk compressibility and solid compressibility.

Unjacketed tests (see Fig. 2.2a) isolate the influence of fluid pressure by fully saturating a porous sample with water and imposing a change in confining pressure dP_c . The pore-fluid pressure p also changes by the same amount $dp = dP_c$, whereas the intergranular stresses remain constant $d\bar{\sigma}_{ii} = 0, ii = 1, 2, 3$. Since the variation in fluid pressure is uniform everywhere, the porosity remains unchanged as well $d\phi = 0$. As a result, the compressibility of the bulk medium and solid grain at constant solid-grain stress, are equal

$$\frac{dV_b/V_b}{dp} = \frac{dV_s/V_s}{dp} = -\frac{1}{K_s}. \quad (2.12)$$

Jacketed tests (see Fig. 2.2b) isolate the influence of intergranular stresses. This is done by jacketing a fully drained sample and submerging it in water subject to a confining pressure dP_c . The porous network is connected to external air and maintains constant pressure $dp = 0$. In this case, solid grain stresses change by the same amount $d\bar{\sigma}_{ii} = dP_c, ii = 1, 2, 3$. Consequently, there

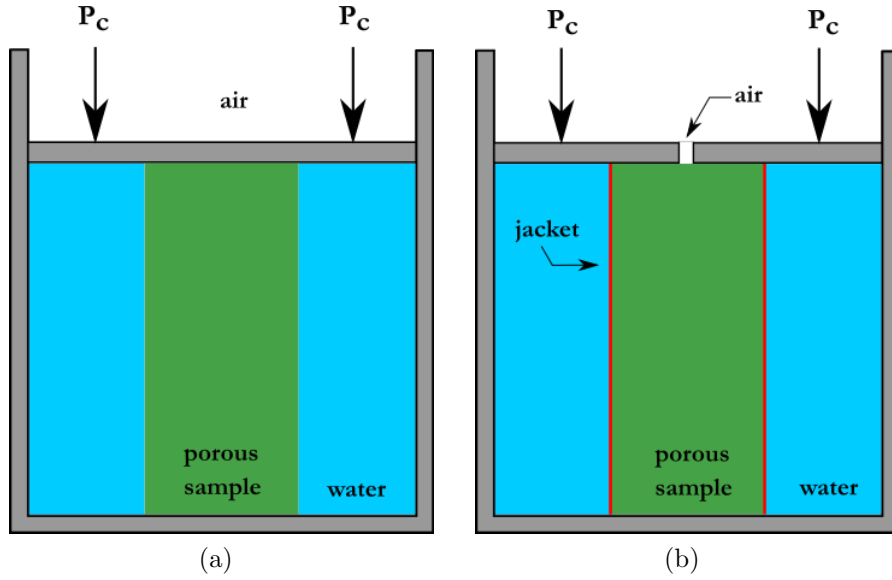


Figure 2.2: (a) Unjacketed and (b) jacketed compressibility tests.

	Unjacketed configuration	Jacketed configuration
Effect	Pore-fluid pressure	Solid-grain stress
Pore-fluid pressure	$dp = dP_c$	$dp = 0$
Solid-grain stress	$d\bar{\sigma}_{ii} = 0,$ $i = 1, 2, 3$	$d\bar{\sigma}_{ii} = dP_c,$ $i = 1, 2, 3$
Bulk compressibility	$\frac{dV_b/V_b}{dp} = -\frac{1}{K_s}$	$\frac{dV_b/V_b}{d\bar{\sigma}} = -\frac{1}{K_b}$
Porosity	$\frac{d\phi}{dp} = 0$	$\frac{d\phi}{d\bar{\sigma}} = -\left(\frac{1-\phi}{K_b} - \frac{1}{K_s}\right)$
Solid compressibility	$\frac{dV_s/V_s}{dp} = -\frac{1}{K_s}$	$\frac{dV_s/V_s}{d\bar{\sigma}} = -\frac{1}{(1-\phi)K_s}$

Table 2.1: Volumetric response of a poroelastic material when subjected to a change in isotropic compression dP_c .

is also a change in porosity. The compressibility of the bulk medium and solid grain at constant pore-fluid pressure read

$$\frac{dV_b/V_b}{d\bar{\sigma}} = -\frac{1}{K_b}, \quad (2.13)$$

$$\frac{dV_s/V_s}{d\bar{\sigma}} = -\frac{1}{(1-\phi)K_s}. \quad (2.14)$$

These relations are summarized in Table 2.1.

The total relative change in bulk volume $\frac{dV_b}{V_b}$ is now expressed using a combination of both effects, i.e., the pore-fluid pressure and solid-grain stress

$$\frac{dV_b}{V_b} = -\frac{1}{K_s}dp - \frac{1}{K_b}d\bar{\sigma}. \quad (2.15)$$

Observing that $d\varepsilon_s = d\varepsilon_{s,kk} = \frac{dV_b}{V_b}$, Eq. (2.15) is integrated to obtain

$$-\bar{\sigma} = K_b \varepsilon_s + \frac{K_b}{K_s} p. \quad (2.16)$$

Eq. (2.16) does not yet include shear deformation. This is incorporated using classical linear elasticity constitutive theory since the pore-fluid exhibits zero shear restoring force.

$$\bar{\sigma}_{ij} = \underbrace{\left(K_b - \frac{2}{3}G\right)\varepsilon_s \delta_{ij}}_{\text{volumetric}} + \underbrace{2G\varepsilon_{s,ij}}_{\text{deviatoric}} + \frac{K_b}{K_s} p \delta_{ij}. \quad (2.17)$$

2.3 Continuity Relations

Further derivations are now necessary to obtain the coefficients A, Q and R . To this end, the Euler continuity equation is used to describe fluid mass balance

$$\frac{\partial(\phi\rho_f)}{\partial t} + \text{div}(\phi\rho_f\dot{\mathbf{U}}) = 0, \quad (2.18)$$

where $m_f = \rho_f V_f = \phi\rho_f V_b$ represents the fluid mass saturating the porous network, and ρ_f contains the fluid density. This is simplified to read

$$\phi \frac{\partial\rho_f}{\partial t} + \rho_f \frac{\partial\phi}{\partial t} + \phi\rho_f \text{div}(\dot{\mathbf{U}}) = 0. \quad (2.19)$$

Given that the fluid compressibility K_f can be expressed as follows

$$\frac{\partial V_f/V_f}{\partial p} = -\frac{1}{K_f}, \quad (2.20)$$

one can exploit the conservation of fluid mass $\dot{m}_f = \frac{\partial(\rho_f V_f)}{\partial t} = 0$ to obtain the relation

$$\frac{\partial V_f}{V_f} = -\frac{\partial\rho_f}{\rho_f}. \quad (2.21)$$

Inserting Eq. (2.21) into Eq. (2.20) and differentiating with respect to time, the following constitutive relation is derived for the fluid phase

$$K_f \frac{\partial\rho_f}{\partial t} = \rho_f \frac{\partial p}{\partial t}. \quad (2.22)$$

Now, the simplified form of the Euler continuity equation for the solid phase is given

$$(1 - \phi) \frac{\partial\rho_s}{\partial t} - \rho_s \frac{\partial\phi}{\partial t} + (1 - \phi)\rho_s \text{div}(\dot{\mathbf{u}}) = 0. \quad (2.23)$$

Following a similar argument as shown for the fluid phase, the final form of the constitutive

relation is provided

$$K_s \frac{\partial \rho_s}{\partial t} = \rho_s \frac{\partial p}{\partial t} + \frac{\rho_s}{1 - \phi} \frac{\partial \bar{\sigma}}{\partial t}. \quad (2.24)$$

Substituting the constitutive relations Eqs. (2.22) and (2.24) into the relevant continuity equations Eqs. (2.19) and (2.23) yields

$$\frac{\phi}{K_f} \frac{\partial p}{\partial t} + \frac{\partial \phi}{\partial t} + \phi \operatorname{div}(\dot{\mathbf{U}}) = 0, \quad (2.25)$$

$$\frac{1 - \phi}{K_s} \frac{\partial p}{\partial t} + \frac{1}{K_s} \frac{\partial \bar{\sigma}}{\partial t} - \frac{\partial \phi}{\partial t} + (1 - \phi) \operatorname{div}(\dot{\mathbf{u}}) = 0. \quad (2.26)$$

Adding Eqs. (2.25) and (2.26) yields

$$\left(\frac{1 - \phi}{K_s} + \frac{\phi}{K_f} \right) \frac{dp}{dt} + \frac{1}{K_s} \frac{d\bar{\sigma}}{dt} + (1 - \phi) \operatorname{div}(\dot{\mathbf{u}}) + \phi \operatorname{div}(\dot{\mathbf{U}}) = 0. \quad (2.27)$$

Eq. (2.27) is the storage equation and denotes the conservation of fluid mass in a fully saturated porous media [24]. This will be used in Section 2.5 to develop governing equations for consolidation problems.

2.4 Computing Biot coefficients

Using Eqs. (2.16) and (2.27), the term $\bar{\sigma}$ is eliminated. Further, recalling the relation $\dot{\varepsilon}_s = \operatorname{div}(\dot{\mathbf{u}})$, one obtains

$$\left(\phi + \frac{K_f}{K_s} \left(1 - \phi - \frac{K_b}{K_s} \right) \right) \frac{\partial \sigma}{\partial t} + \phi K_b \operatorname{div}(\dot{\mathbf{u}}) - \phi K_f \frac{K_b}{K_s} \operatorname{div}(\dot{\mathbf{U}}) = 0, \quad (2.28)$$

and

$$\left(\phi + \frac{K_f}{K_s} \left(1 - \phi - \frac{K_b}{K_s} \right) \right) \frac{\partial p}{\partial t} + K_f \left(1 - \phi - \frac{K_b}{K_s} \right) \operatorname{div}(\dot{\mathbf{u}}) + \phi K_f \operatorname{div}(\dot{\mathbf{U}}) = 0. \quad (2.29)$$

Finally, combining Eqs. (2.16) and (2.28), Eqs. (2.17) and (2.29), and comparing with Eqs. (2.10) and (2.11), the Biot coefficients can now be written out

$$A = K_b - \frac{2}{3}G + \frac{K_f \left(1 - \phi - \frac{K_b}{K_s} \right)^2}{\phi + \frac{K_f}{K_s} \left(1 - \phi - \frac{K_b}{K_s} \right)}, \quad (2.30)$$

$$Q = \frac{\phi K_f \left(1 - \phi - \frac{K_b}{K_s} \right)}{\phi + \frac{K_f}{K_s} \left(1 - \phi - \frac{K_b}{K_s} \right)}, \quad (2.31)$$

$$R = \frac{\phi^2 K_f}{\phi + \frac{K_f}{K_s} \left(1 - \phi - \frac{K_b}{K_s} \right)}. \quad (2.32)$$

The solid skeleton stresses $\boldsymbol{\sigma}_s$ in Eq. (2.10) is a function of both the solid skeleton and pore-fluid displacements, i.e., $\boldsymbol{\sigma}_s(\mathbf{u}, \mathbf{U})$. For Sections 2.5 and 2.6, it is useful to decouple these effects. To this end, Eqs. (2.10) and (2.11) are combined to read

$$\boldsymbol{\sigma}_s(\mathbf{u}, \mathbf{U}) = \left(A - \frac{Q^2}{R} \right) \text{div}(\mathbf{u})\mathbb{I} + 2G\boldsymbol{\varepsilon}_s - \phi \frac{Q}{R} p\mathbb{I}. \quad (2.33)$$

An effective stress tensor $\hat{\boldsymbol{\sigma}}_s(\mathbf{u})$ dependent only on solid skeleton displacements is introduced such that

$$\hat{\boldsymbol{\sigma}}_s(\mathbf{u}) = \left(A - \frac{Q^2}{R} \right) \text{div}(\mathbf{u})\mathbb{I} + 2G\boldsymbol{\varepsilon}_s. \quad (2.34)$$

The quantity Eq. (2.34) is more explicitly defined using the expressions for A, Q, R as provided in Eqs. (2.30), (2.31), (2.32) [51]

$$-\hat{\sigma}_{s,ij} = \left(K_b - \frac{2}{3}G \right) \varepsilon_s \delta_{ij} + 2G\varepsilon_{s,ij}. \quad (2.35)$$

Exploiting the symmetries in Eq. (2.35), one can re-express this in convenient Voigt notation

$$-\hat{\boldsymbol{\sigma}}_s = \mathbb{D}\boldsymbol{\varepsilon}_s, \quad (2.36)$$

where \mathbb{D} denotes the linear elastic constitutive tensor. The bulk and shear moduli K_b and G are expressed in terms of the more familiar quantities, i.e., the Young's modulus E and Poisson's ratio ν

$$K_b = \frac{E}{3(1-2\nu)}, \quad G = \frac{E}{2(1+\nu)}. \quad (2.37)$$

Using the above relation, the tensor \mathbb{D} assumes the form

$$\mathbb{D} = \frac{E}{(1+\nu)(1-2\nu)} \begin{bmatrix} 1-\nu & \nu & 0 \\ \nu & 1-\nu & 0 \\ 0 & 0 & \frac{1-2\nu}{2} \end{bmatrix}. \quad (2.38)$$

Eq. (2.33) now simplifies to

$$\boldsymbol{\sigma}_s(\mathbf{u}, \mathbf{U}) = \hat{\boldsymbol{\sigma}}_s(\mathbf{u}) - \phi \frac{Q}{R} p\mathbb{I}. \quad (2.39)$$

Inserting this expression for $\boldsymbol{\sigma}_s$ into Eq. (2.6) yields

$$\boldsymbol{\sigma}_t = \hat{\boldsymbol{\sigma}}_s - \underbrace{\phi \left(1 + \frac{Q}{R} \right)}_c p\mathbb{I}, \quad (2.40)$$

where c is a constant parameter (not to be confused with the speed of sound in a medium). Inserting the expressions for Q, R into Eq. (2.40) yields

$$\boldsymbol{\sigma}_t = \hat{\boldsymbol{\sigma}}_s - \alpha_B p\mathbb{I}, \quad (2.41)$$

where the Biot coefficient α_B has the form

$$\alpha_B = 1 - \frac{K_b}{K_s}. \quad (2.42)$$

This is called the principle of effective stress [52].

2.5 Consolidation

The consolidation phenomena described by the Biot theory is a slow process. The pore-fluid transport is described by the static Darcy law

$$\mathbf{q} = -\frac{\mathbf{k}}{\gamma_f} \nabla p, \quad (2.43)$$

where \mathbf{k} and $\gamma_f = \rho_f g$ denote the permeability and specific weight of the pore-fluid, respectively. The specific discharge \mathbf{q} describes the amount of fluid content entering or exiting the bulk volume

$$\mathbf{q} = \phi(\dot{\mathbf{U}} - \dot{\mathbf{u}}). \quad (2.44)$$

It is now recalled that $\dot{\mathbf{u}} = \frac{\partial \varepsilon_s}{\partial t}$. Further, using the expression for σ_s derived in Eq. (2.16), and the discharge in Eq. (2.44), the storage expression in Eq. (2.27) is simplified

$$\left(1 - \frac{K_b}{K_s}\right) \frac{\partial \varepsilon_s}{\partial t} + \left(\frac{1}{K_s} \left(1 - \frac{K_b}{K_s}\right) + \phi \left(\frac{1}{K_f} - \frac{1}{K_s}\right)\right) \frac{\partial p}{\partial t} = -\text{div}(\mathbf{q}). \quad (2.45)$$

To be consistent with soil mechanics literature [53], the storativity coefficient S_ϵ is defined

$$S_\epsilon = \frac{\alpha_B}{K_s} + \phi \left(\frac{1}{K_f} - \frac{1}{K_s}\right). \quad (2.46)$$

Eqs. (2.42) and (2.46) are inserted into Eq. (2.45) along with the Darcy law (Eq. (2.43)) to yield the following form for the storage equation

$$\alpha_B \frac{\partial \varepsilon_s}{\partial t} + S_\epsilon \frac{\partial p}{\partial t} = \text{div} \left(\frac{\mathbf{k}}{\gamma_f} \nabla p \right). \quad (2.47)$$

The equilibrium equation for the solid phase is written out in a straightforward way

$$\text{div}(\boldsymbol{\sigma}_t) + \mathbf{b} = 0, \quad (2.48)$$

where \mathbf{b} contains a generalized body force. Using the principle of effective stress (Eq. (2.41)), this is recast as

$$\text{div}(\hat{\boldsymbol{\sigma}}_s) + \mathbf{b} = \text{div}(\alpha_B p \mathbb{I}), \quad (2.49)$$

where the linear-elastic constitutive relation in Eq. (2.36) holds for $\hat{\boldsymbol{\sigma}}_s$.

Eqs. (2.49) and (2.47) are collected and summarized below as the coupled strong form for the Biot $\mathbf{u} - p$ formulation for consolidation

$$\operatorname{div}(\hat{\boldsymbol{\sigma}}_s) + \mathbf{b} = \operatorname{div}(\alpha_B \mathbb{p} \mathbb{I}), \quad (2.50)$$

$$\alpha_B \frac{\partial \varepsilon_s}{\partial t} + S_\epsilon \frac{\partial \mathbb{p}}{\partial t} = \operatorname{div} \left(\frac{\mathbf{k}}{\gamma_f} \nabla \mathbb{p} \right). \quad (2.51)$$

2.6 Vibroacoustics

While the consolidation phenomena discussed in Section 2.5 is a slow process, the Lagrangian formalism originally introduced in [18, 19] adopts a more generalized approach by accommodating acceleration effects as well. These effects are significant at large acoustical frequencies and cannot be reasonably neglected. This introduces inertial forces arising due to the relative motion between the solid-skeleton and pore-fluid. The associated kinetic energy of the system is

$$E_K = \frac{1}{2} \rho_{11} |\dot{\mathbf{u}}|^2 + \rho_{12} \dot{\mathbf{u}} \cdot \dot{\mathbf{U}} + \frac{1}{2} \rho_{22} |\dot{\mathbf{U}}|^2, \quad (2.52)$$

where ρ_{12} , ρ_{11} and ρ_{22} are apparent densities accounting for the geometry of the frame and porous network, which assume the following form [13]

$$\rho_{12} = -\phi \rho_f (\alpha_\infty - 1), \quad (2.53)$$

$$\rho_{11} = (1 - \phi) \rho_s - \rho_{12}, \quad (2.54)$$

and

$$\rho_{22} = \phi \rho_f - \rho_{12}, \quad (2.55)$$

respectively. The inertial force components of the solid and fluid phases, respectively, are obtained by applying the Euler-Lagrange equations

$$\mathbf{F}_s^I = \frac{\partial}{\partial t} \left(\frac{\partial E_K}{\partial \dot{\mathbf{u}}} \right) = \rho_{11} \ddot{\mathbf{u}} + \rho_{12} \ddot{\mathbf{U}}, \quad (2.56)$$

and

$$\mathbf{F}_f^I = \frac{\partial}{\partial t} \left(\frac{\partial E_K}{\partial \dot{\mathbf{U}}} \right) = \rho_{12} \ddot{\mathbf{u}} + \rho_{22} \ddot{\mathbf{U}}. \quad (2.57)$$

These inertial forces occur even in the presence of a non-viscous fluid. However, for the material to truly be dissipative, the following dissipated energy is introduced

$$E_D = \frac{1}{2} \tilde{\mathbf{b}}(\dot{\mathbf{u}} - \dot{\mathbf{U}}) \cdot (\dot{\mathbf{u}} - \dot{\mathbf{U}}), \quad (2.58)$$

where $\tilde{\mathbf{b}}$ is a dissipation parameter, accounting for viscous interaction. The (\cdot) denotes the complex-valued nature of its argument, and its dependence on the excitation angular frequency ω . The corresponding forces on either phase are

$$\mathbf{F}_s^D = \tilde{\mathbf{b}}(\dot{\mathbf{u}} - \dot{\mathbf{U}}), \quad (2.59)$$

and

$$\mathbf{F}_f^D = -\tilde{b}(\dot{\mathbf{u}} - \dot{\mathbf{U}}). \quad (2.60)$$

The inertial forces \mathbf{F}_s^I and \mathbf{F}_f^I from Eqs. (2.56), (2.57) and the dissipative forces \mathbf{F}_s^D and \mathbf{F}_f^D from Eqs. (2.59) and (2.60) are used to derive the equilibrium equations for Biot wave propagation

$$\operatorname{div}(\boldsymbol{\sigma}_s) = \rho_{11}\ddot{\mathbf{u}} + \rho_{12}\ddot{\mathbf{U}} + \tilde{b}(\dot{\mathbf{u}} - \dot{\mathbf{U}}), \quad (2.61)$$

and

$$\operatorname{div}(\boldsymbol{\sigma}_f) = \rho_{12}\ddot{\mathbf{u}} + \rho_{22}\ddot{\mathbf{U}} - \tilde{b}(\dot{\mathbf{u}} - \dot{\mathbf{U}}). \quad (2.62)$$

Eqs. (2.61) and (2.62) are the Biot $\mathbf{u} - \mathbf{U}$ formulation for wave propagation in poroelastic media. Applying the Fourier transform, this is expressed in the frequency domain

$$\operatorname{div}(\boldsymbol{\sigma}_s) = -\omega^2\rho_{11}\mathbf{u} - \omega^2\rho_{12}\mathbf{U} + (j\omega)\tilde{b}(\mathbf{u} - \mathbf{U}), \quad (2.63)$$

and

$$\operatorname{div}(\boldsymbol{\sigma}_f) = -\omega^2\rho_{12}\mathbf{u} - \omega^2\rho_{22}\mathbf{U} - (j\omega)\tilde{b}(\mathbf{u} - \mathbf{U}). \quad (2.64)$$

There are two significant drawbacks of the $\mathbf{u} - \mathbf{U}$ formulation from a computational perspective. The first is that for a three-dimensional problem, there are six degrees of freedom associated with each discretized node in a standard FE mesh. These include three displacement components for the solid and fluid phases, respectively. The second is that the stress tensor $\boldsymbol{\sigma}_s$ is frequency dependent. These features create major bottlenecks during the assembly and solution of detailed FE models in spectral analysis. These difficulties are addressed in [36] by developing a mixed displacement-pressure formalism ($\mathbf{u} - p$).

To this end, the effective densities $\tilde{\rho}_{11}$, $\tilde{\rho}_{22}$ and $\tilde{\rho}_{12}$ are introduced such that

$$\tilde{\rho}_{11} = \rho_{11} + \frac{\tilde{b}}{j\omega}, \quad (2.65)$$

$$\tilde{\rho}_{22} = \rho_{22} + \frac{\tilde{b}}{j\omega}, \quad (2.66)$$

$$\tilde{\rho}_{12} = \rho_{12} + \frac{\tilde{b}}{j\omega}. \quad (2.67)$$

Recalling Eq. (2.7), Eqs. (2.63) and (2.64) are now provided in a simplified form

$$\operatorname{div}(\boldsymbol{\sigma})_s - \omega^2\tilde{\rho}_{11}\mathbf{u} + \omega^2\tilde{\rho}_{12}\mathbf{U} = 0, \quad (2.68)$$

and

$$-\phi\nabla p + \omega^2\tilde{\rho}_{12}\mathbf{u} + \omega^2\tilde{\rho}_{22}\mathbf{U} = 0. \quad (2.69)$$

The fluid displacement \mathbf{U} can be expressed in terms of the pore-fluid pressure p and solid-skeleton displacements \mathbf{u} by rearranging Eq. (2.69)

$$\mathbf{U} = \frac{1}{\omega^2\phi\tilde{\rho}_{\text{eq}}}\nabla p - \frac{\tilde{\rho}_{12}}{\tilde{\rho}_{22}}\mathbf{u}. \quad (2.70)$$

Eliminating \mathbf{U} from Eqs. (2.68) and (2.69), the following equation is derived

$$\operatorname{div}(\boldsymbol{\sigma}_s) + \omega^2 \tilde{\rho} \mathbf{u} + \phi \frac{\tilde{\rho}_{12}}{\tilde{\rho}_{22}} \nabla p = 0, \quad (2.71)$$

where the solid-skeleton effective density $\tilde{\rho}$ has the form

$$\tilde{\rho} = \tilde{\rho}_{11} - \frac{(\tilde{\rho}_{12})^2}{\tilde{\rho}_{22}}. \quad (2.72)$$

Recalling $\boldsymbol{\sigma}_s \equiv \boldsymbol{\sigma}_s(\mathbf{u}, \mathbf{U})$, a frequency dependent analogue of Eq. (2.39) is employed

$$\boldsymbol{\sigma}_s(\mathbf{u}, \mathbf{U}) = \hat{\boldsymbol{\sigma}}_s(\mathbf{u}) - \phi \frac{\tilde{Q}}{\tilde{R}} p \mathbb{I}. \quad (2.73)$$

where the solid skeleton constitutive relation reads

$$\hat{\boldsymbol{\sigma}}_s = \tilde{\mathbb{D}} \boldsymbol{\varepsilon}_s(\mathbf{u}). \quad (2.74)$$

The elastic constitutive tensor $\tilde{\mathbb{D}}$ depends on the modified Young's modulus \tilde{E} and the Poisson's ratio ν ,

$$\tilde{\mathbb{D}} \equiv \tilde{\mathbb{D}}(\tilde{E}, \nu). \quad (2.75)$$

The modified Young's modulus \tilde{E} in Eq. (2.75) is expressed as

$$\tilde{E} = E(1 + j\eta_s(\omega)), \quad (2.76)$$

where E and $\eta_s(\omega)$ are the Young's modulus and the structural loss factor, respectively.

The Biot coefficients A , Q , R and G are replaced with frequency-dependent counterparts \tilde{A} , \tilde{Q} , \tilde{R} and \tilde{G} . The complex shear modulus \tilde{G} accounts for structural dissipation. The fluid bulk modulus K_f in Eqs. (2.30)-(2.32) is replaced by

$$\tilde{K}_f = \frac{\tilde{K}_{\text{eq}}}{\phi}, \quad (2.77)$$

where \tilde{K}_{eq} is the equivalent bulk modulus characterizing thermal dissipation.

Inserting Eq. (2.73) into Eq. (2.71) reads

$$\operatorname{div}(\hat{\boldsymbol{\sigma}}_s(\mathbf{u})) + \tilde{\rho} \omega^2 \mathbf{u} = -\tilde{\gamma} \nabla p, \quad (2.78)$$

where the coupling coefficient $\tilde{\gamma}$ is

$$\tilde{\gamma} = \phi \left(\frac{\tilde{\rho}_{12}}{\tilde{\rho}_{22}} - \frac{\tilde{Q}}{\tilde{R}} \right). \quad (2.79)$$

The corresponding equilibrium equation is derived by considering the divergence of Eq. (2.69) and re-arranging into the following expression

$$-\phi \Delta p + \omega^2 \tilde{\rho}_{12} \operatorname{div}(\mathbf{u}) + \omega^2 \tilde{\rho}_{22} \operatorname{div}(\mathbf{U}) = 0. \quad (2.80)$$

Using the constitutive relation in Eq. (2.11), the term $\operatorname{div}(\mathbf{U})$ is eliminated from Eq. (2.80) to

yield

$$\frac{\phi^2}{\tilde{\rho}_{22}} \Delta \mathbf{p} + \frac{\phi^2}{\tilde{R}} \omega^2 \mathbf{p} = -\omega^2 \tilde{\gamma} \operatorname{div}(\mathbf{u}). \quad (2.81)$$

For most acoustical poroelastic materials $\phi \rightarrow 1$ and $\tilde{K}_f \ll K_s$. Under these assumptions, the following relations hold [35]

$$\tilde{\rho}_{\text{eq}} = \frac{\tilde{\rho}_{22}}{\phi^2}, \quad (2.82)$$

$$\tilde{K}_{\text{eq}} = \frac{\tilde{R}}{\phi^2}, \quad (2.83)$$

Using these relations, Eq. (2.81) is finally written as

$$\frac{\Delta \mathbf{p}}{\tilde{\rho}_{\text{eq}}} + \omega^2 \frac{\mathbf{p}}{\tilde{K}_{\text{eq}}} = \omega^2 \tilde{\gamma} \operatorname{div}(\mathbf{u}). \quad (2.84)$$

The coefficients $\tilde{\rho}_{\text{eq}}$ and \tilde{K}_{eq} are the dynamic mass density and bulk modulus. They encode visco-inertial and thermal effects, respectively, at the micro-scale. These coefficients are computed through semi-phenomenological models, such as the six-parameter Johnson-Champoux-Allard-Lafarge (JCAL) model [32–34]

$$\tilde{\rho}_{\text{eq}}(\omega) = \frac{\alpha_\infty \rho_0}{\phi} \left[1 + \frac{\sigma \phi}{j \omega \rho_0 \alpha_\infty} \sqrt{1 + j \frac{4 \alpha_\infty^2 \eta \rho_0 \omega}{\sigma^2 \Lambda^2 \phi^2}} \right], \quad (2.85)$$

and

$$\tilde{K}_{\text{eq}}(\omega) = \frac{\gamma P_0 / \phi}{\gamma - (\gamma - 1) \left[1 - j \frac{\phi \kappa}{k'_0 C_p \rho_0 \omega} \sqrt{1 + j \frac{4 k'^2_0 C_p \rho_0 \omega}{\kappa \Lambda^2 \phi^2}} \right]^{-1}}. \quad (2.86)$$

The macroscopic material parameters α_∞ , σ , η , Λ , Λ' , γ , P_0 , k'_0 , C_p and κ denote the high frequency limit of dynamic tortuosity, static airflow resistivity, dynamic viscosity, viscous and thermal characteristic lengths, adiabatic index, atmospheric pressure, static thermal permeability, specific heat at constant pressure and thermal conductivity. A concise list of the expressions for all semi-phenomenological models is provided in [12].

The mixed $\mathbf{u} - \mathbf{p}$ formulation, Eqs. (2.78), (2.84) is collected and summarized below

$$\operatorname{div}(\hat{\boldsymbol{\sigma}}_s(\mathbf{u})) + \tilde{\rho} \omega^2 \mathbf{u} = -\tilde{\gamma} \nabla \mathbf{p}, \quad (2.87)$$

$$\frac{\Delta \mathbf{p}}{\tilde{\rho}_{\text{eq}}} + \omega^2 \frac{\mathbf{p}}{\tilde{K}_{\text{eq}}} = \omega^2 \tilde{\gamma} \operatorname{div}(\mathbf{u}). \quad (2.88)$$

This formalism alleviates the difficulties associated with the $\mathbf{u} - \mathbf{U}$ formulation, by requiring only four degrees of freedom per FE node. These include three displacement components for the solid phase and a pressure field for the fluid phase. Further, recall from Eq. (2.73) that unlike $\boldsymbol{\sigma}_s$, $\hat{\boldsymbol{\sigma}}_s$ is frequency independent. Consequently, the corresponding state matrices do not require repeated assembly during spectral analyses.

2.7 Finite Element Formulation

2.7.1 Elastostatics

Strong form

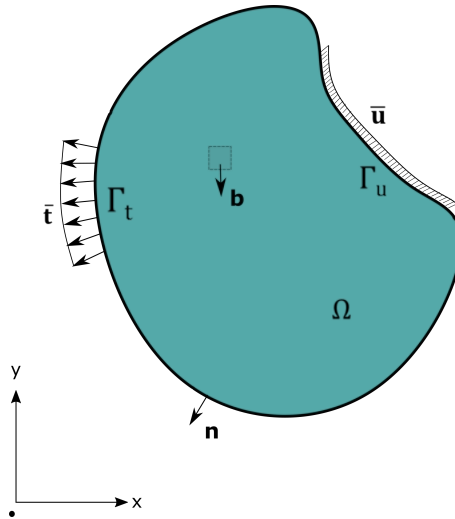


Figure 2.3: Schematic representation of a two dimensional domain Ω with boundary Γ . Essential and natural boundaries $\bar{\mathbf{u}}$ and $\bar{\mathbf{t}}$ are prescribed on Γ_u and Γ_t respectively.

The case of a domain $\Omega \subset \mathbb{R}^2$ is considered herein, subjected to plane stress or plane strain conditions. The domain is subjected to a body force \mathbf{b} , and is prescribed a displacement and traction $\bar{\mathbf{u}}$ and $\bar{\mathbf{t}}$ over the boundaries Γ_u and Γ_t respectively. The displacement and traction boundaries are defined to be non-intersecting, i.e., $\Gamma_u \cap \Gamma_t = \emptyset$. This is illustrated in Fig. 2.3. The corresponding equilibrium, constitutive, and compatibility equations are defined in Eqs. (2.89a), (2.89b), and (2.89c), respectively as

$$\operatorname{div}(\boldsymbol{\sigma}) + \mathbf{b} = 0, \quad (2.89a)$$

$$\boldsymbol{\sigma} = \mathbb{D}\boldsymbol{\varepsilon}(\mathbf{u}), \quad (2.89b)$$

$$\boldsymbol{\varepsilon}(\mathbf{u}) = \frac{\nabla \mathbf{u} + (\nabla \mathbf{u})^T}{2}, \quad (2.89c)$$

subject to generalized inhomogeneous displacement and traction boundaries defined as follows

$$\mathbf{u} = \bar{\mathbf{u}} \text{ on } \Gamma_u, \quad \text{--enforced boundary conditions,} \quad (2.90a)$$

$$\boldsymbol{\sigma} \cdot \mathbf{n} = \mathbf{t} = \bar{\mathbf{t}} \text{ on } \Gamma_t \quad \text{-- natural boundary conditions,} \quad (2.90b)$$

where the displacement and traction boundary values are specified by $\bar{\mathbf{u}}$ and $\bar{\mathbf{t}}$, respectively.

Weak form

Eq. (2.89) is cast into its appropriate weak form

$$\begin{cases} \text{Find } \mathbf{u} \in \mathcal{V}^u := [\mathcal{H}^1(\Omega)]^2 \text{ such that} \\ \mathbf{a}^\varepsilon(\mathbf{u}, \delta\mathbf{u})_{\mathbb{D}} = \mathbf{f}^u(\delta\mathbf{u}) \quad \forall \delta\mathbf{u} \in \mathcal{V}^u, \end{cases} \quad (2.91)$$

where $\mathbf{a}^\varepsilon(\cdot, \cdot)_{\mathbb{D}}$ and $\mathbf{f}^u(\cdot)$ are bilinear and linear functionals, respectively defined as

$$\mathbf{a}^\varepsilon(\mathbf{u}, \delta\mathbf{u})_{\mathbb{D}} = \int_{\Omega} \boldsymbol{\varepsilon}(\mathbf{u}) \mathbb{D} \boldsymbol{\varepsilon}(\delta\mathbf{u}) \, d\Omega, \quad (2.92a)$$

$$\mathbf{f}^u(\delta\mathbf{u}) = \int_{\Gamma_t} \bar{\mathbf{t}} \cdot \delta\mathbf{u} \, d\Gamma + \int_{\Omega} \mathbf{b} \cdot \delta\mathbf{u} \, d\Omega. \quad (2.92b)$$

Discretization

The displacement field is approximated through the following finite dimensional approximation, i.e.,

$$\mathbf{u}_h, \delta\mathbf{u}_h \in \mathcal{V}_h^u \subset \mathcal{V}^u, \quad (2.93)$$

where \mathbf{u}_h and $\delta\mathbf{u}_h$ are the discretized trial and test functions, respectively; these are defined over a finite-dimensional subspace \mathcal{V}_h^u .

Inserting the discretized form in Eq. (2.93) into Eq. (2.91) yields the discretized abstract weak form

$$\begin{cases} \text{Find } \mathbf{u}_h \in \mathcal{V}_h^u \text{ such that} \\ \mathbf{a}^\varepsilon(\mathbf{u}_h, \delta\mathbf{u}_h)_{\mathbb{D}} = \mathbf{f}^u(\delta\mathbf{u}_h) \quad \forall \delta\mathbf{u}_h \in \mathcal{V}_h^u. \end{cases} \quad (2.94)$$

The domain Ω_h is the discretized approximation of the original domain geometry, i.e.,

$$\Omega_h = \bigcup_{\mathcal{K}_i \in \Omega_h} \mathcal{K}_i \approx \Omega, \quad (2.95)$$

where the terms \mathcal{K}_i , $i = 1, \dots, n_{el}$ denote non-intersecting quadrilateral sub-domains as shown in Fig. 2.4. This corresponds with standard element discretizations as used in conventional FEM. The parameter h is understood as the maximum diameter of all elements contained in Ω_h . The discretized boundaries Γ_{hu} , Γ_{ht} , Γ_{hp} and Γ_{hq} are also obtained in the same fashion.

The bilinear and linear functional forms used in Eq. (2.112) can now be computed through additively assembling local element-wise operators as shown below

$$\mathbf{a}^\varepsilon(\mathbf{u}_h, \delta\mathbf{u}_h)_{\mathbb{D}} = \sum_{i=1}^{n_{el}} \mathbf{a}_{\mathcal{K}_i}^\varepsilon(\mathbf{u}_h, \delta\mathbf{u}_h)_{\mathbb{D}}, \quad (2.96a)$$

$$\mathbf{f}^u(\delta\mathbf{u}_h) = \sum_{i=1}^{n_{el}} \mathbf{f}_{\mathcal{K}_i}^u(\delta\mathbf{u}_h). \quad (2.96b)$$

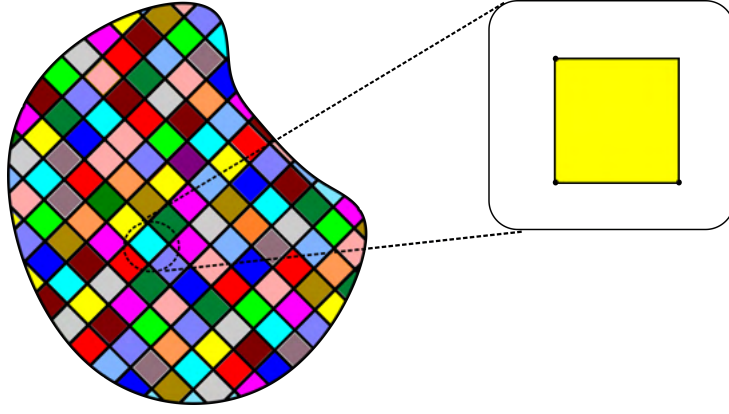


Figure 2.4: Discretized domain Ω_h decomposed into n_{el} quadrilateral elements.

The element-wise components in Eq. (2.96) are expressed

$$a_{\mathcal{K}_i}^{\boldsymbol{\varepsilon}}(\mathbf{u}_h, \delta \mathbf{u}_h)_{\mathbb{D}} = \int_{\mathcal{K}_i} \boldsymbol{\varepsilon}(\mathbf{u}_h) \mathbb{D} \boldsymbol{\varepsilon}(\delta \mathbf{u}_h) \, d\Omega, \quad (2.97a)$$

$$f_{\mathcal{K}_i}^u(\delta \mathbf{u}_h) = \int_{\Gamma_{ht}^{\mathcal{K}_i}} \bar{\mathbf{t}} \cdot \delta \mathbf{u}_h \, d\Gamma + \int_{\mathcal{K}_i} \mathbf{b} \cdot \delta \mathbf{u}_h \, d\Omega. \quad (2.97b)$$

In the FEM, the globally continuous displacement \mathbf{u}_h field and its corresponding weight function $\delta \mathbf{u}_h$ are discretized into piece-wise continuous functions over each element \mathcal{K}_i according to the following expressions

$$\mathbf{u}_h = \underbrace{[\boldsymbol{\Phi}^u]}_{(n_{\text{dof}}^u \times 2)}^T \hat{\mathbf{u}}, \quad \delta \mathbf{u}_h = \underbrace{[\boldsymbol{\Phi}^u]}_{(n_{\text{dof}}^u \times 2)}^T \hat{\delta \mathbf{u}}, \quad (2.98)$$

where $\hat{\mathbf{u}}$ and $\hat{\delta \mathbf{u}}$ denote vectors containing element-wise trial and test nodal displacement values, respectively. The quantity n_{dof}^u denote the number of DoFs for $\mathcal{V}_h^u(\mathcal{K})$.

The arrays $[\boldsymbol{\Phi}^u]$ contain the canonical basis functions that span \mathcal{V}_h^u . The conventional Bubnov-Galerkin FEM definition for these spaces for a k_{th} order method is provided below

$$\mathcal{V}_h^u = [\mathcal{W}_h]^d, \quad d = 2, \quad (2.99a)$$

$$\mathcal{W}_h = \{v \in [\mathcal{H}^1(\Omega) \cap C^0(\Omega_h)], \quad v|_{\mathcal{K}} \in \mathcal{V}_h^{\mathcal{K}}(\mathcal{K}), \quad \forall \mathcal{K} \in \Omega_h\}, \quad (2.99b)$$

where $\mathcal{V}_h^{\mathcal{K}}(\mathcal{K})$ has the following definition

$$\mathcal{V}_h^{\mathcal{K}}(\mathcal{K}) = \{v \in [\mathcal{H}^1(\mathcal{K}) \cap C^0(\mathcal{K})] : v_{,i}|_{\mathcal{K}} \in \mathbb{L}_k(\mathcal{K}), \quad \text{for } i = 1, \dots, d\}. \quad (2.100)$$

The canonical basis function possess the classical properties

$$\Phi_i^u(\mathbf{x}_j) = \delta_{ij}, \quad i = 1, \dots, n_{\text{dof}}^u, \quad (2.101)$$

and partition of unity properties

$$\sum_{i=1}^{n_{\text{dof}}^u} \Phi_i^u(\mathbf{x}_j) = 1, \quad (2.102)$$

over $\mathcal{V}_h^u(\mathcal{K})$. The term $\mathbb{L}_k(\mathcal{K})$ in Eq. (2.100) denotes k_{th} order Lagrange interpolating polynomials defined over an element domain \mathcal{K} . These polynomials spanning the FEM space are explicitly defined and fully dependent on the element geometry.

Substituting Eqs. (2.98) into the element-wise integrals for the solid phase in Eqs. (2.97), yields an elastic stiffness term

$$a_{\mathcal{K}_i}^\varepsilon(\mathbf{u}_h, \delta \mathbf{u}_h) = \delta \hat{\mathbf{u}}^T \underbrace{\left[\int_{\mathcal{K}_i} \mathbf{B}^{uT} \tilde{\mathbb{D}} \mathbf{B}^u \, d\Omega \right]}_{\mathbf{K}_{\mathcal{K}_i}} \hat{\mathbf{u}}, \quad (2.103)$$

where $\mathbf{B}^u = \boldsymbol{\varepsilon}_s(\boldsymbol{\Phi}^u)$. An elastic load is also obtained

$$\mathbf{f}_{\mathcal{K}_i}^u(\delta \mathbf{u}_h) = \delta \hat{\mathbf{u}}^T \underbrace{\left[\int_{\Gamma_{ht}^{\mathcal{K}_i}} \boldsymbol{\Phi}^{uT} \bar{\mathbf{t}} \, d\Gamma + \int_{\mathcal{K}_i} \boldsymbol{\Phi}^{uT} \mathbf{b} \, d\Omega \right]}_{\mathbf{f}_{\mathcal{K}_i}^u}. \quad (2.104)$$

The local state matrices and vectors are assembled, over the entire domain Ω_h using a direct approach to obtain their global counterparts

$$\mathbf{K} = \mathop{\text{A}}_{i=1}^{n_{\text{el}}} \mathbf{K}_{\mathcal{K}_i}, \quad \mathbf{f}^u = \mathop{\text{A}}_{i=1}^{n_{\text{el}}} \mathbf{f}_{\mathcal{K}_i}^u. \quad (2.105)$$

One now obtains the global matrix form for Eq. (2.94)

$$\mathbf{K} \hat{\mathbf{u}} = \mathbf{f}^u. \quad (2.106)$$

Eq. (2.106) is solved in a straightforward way using classical procedures like Preconditioned Conjugate Gradients (PCG) or Generalized Minimal Residual Method (GMRES).

2.7.2 Consolidation

Strong form

The case of an arbitrary continuous two-dimensional porous domain $\Omega \subset \mathbb{R}^2$ with a domain boundary Γ is considered as shown in Fig. 2.5. In addition to the constraints specified in Fig. 2.3, the domain is further subjected to a set of enforced pressures \bar{p} on Γ_p , applied volume fluxes $\bar{\mathbf{q}}$ on Γ_q such that $\Gamma_u \cap \Gamma_t = \emptyset$ and $\Gamma_p \cap \Gamma_q = \emptyset$. The domain is also subjected to a source/sink term Q . The strong form of the governing equations as provided in Eqs. (2.50)-(2.51) are supplemented by the following set of initial and boundary conditions

$$\mathbf{u} = \mathbf{u}_0, \quad p = p_0, \quad \text{in } \Omega \quad - \text{ initial conditions}, \quad (2.107a)$$

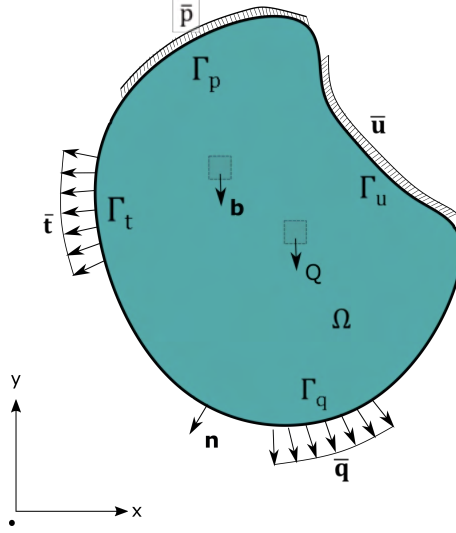


Figure 2.5: Schematic representation of a two dimensional domain Ω with boundary $\partial\Omega$. Essential and natural boundaries for the solid phase $\bar{\mathbf{u}}$ and $\bar{\mathbf{t}}$ are prescribed on Γ_u and Γ_t respectively. Similarly, the relevant boundaries for the fluid phase \bar{p} and $\bar{\mathbf{q}}$ are applied on Γ_p and Γ_q respectively.

$$\mathbf{u} = \bar{\mathbf{u}} \text{ on } \Gamma_u, \quad p = \bar{p}, \text{ on } \Gamma_p \quad - \text{enforced boundary conditions,} \quad (2.107b)$$

$$\mathbf{t} = \bar{\mathbf{t}} \text{ on } \Gamma_t, \quad \mathbf{q} = \bar{\mathbf{q}}, \text{ on } \Gamma_q \quad - \text{natural boundary conditions,} \quad (2.107c)$$

where \mathbf{u}_0 and p_0 denote the initial displacement and pressure distributions over the domain at time $t = 0$. The Dirichlet boundary values for the fluid phase is represented by \bar{p} . The Neumann flux boundary values are contained in $\bar{\mathbf{q}}$.

Weak form

The weak form of the governing Eqs. (2.50)-(2.51) is derived accordingly as

$$\left\{ \begin{array}{l} \text{Find } (\mathbf{u}, p) \in \mathcal{V}^u \times \mathcal{V}^p := [\mathcal{H}^1(\Omega)]^2 \times [\mathcal{H}^1(\Omega)] \text{ such that} \\ a^\varepsilon(\mathbf{u}, \delta\mathbf{u})_{\mathbb{D}} - a^{(\varepsilon, 0)}(p, \delta\mathbf{u})_{\alpha_B \mathbf{m}} = f^u(\delta\mathbf{u}) \quad \forall \delta\mathbf{u} \in \mathcal{V}^u \\ a^{(\varepsilon, 0)}(\dot{\mathbf{u}}, \delta p)_{\alpha_B \mathbf{m}^T} + b^0(\dot{p}, \delta p)_{S_\varepsilon} + b^\nabla(p, \delta p)_{\mathbf{k}/\gamma_f} = f^p(\delta p) \quad \forall \delta p \in \mathcal{V}^p, \end{array} \right. \quad (2.108)$$

where $a^{(\cdot)}$, $b^{(\cdot)}$ and $f^{(\cdot)}$ are bilinear and linear functional operators and δp denotes test functions such that $p, \delta p \in \mathcal{V}^p$. The space \mathcal{V}^p denote the space of admissible pressures. This assumes a standard one-dimensional $\mathcal{H}^1(\Omega)$ Hilbert Space. The individual operators are defined as follows for the fluid phase

$$b^\nabla(p, \delta p)_{\mathbf{k}/\gamma_f} = \int_{\Omega} \nabla(p) \frac{\mathbf{k}}{\gamma_f} \nabla(\delta p) \, d\Omega, \quad (2.109a)$$

$$b^0(\dot{p}, \delta p)_{S_\varepsilon} = \frac{d}{dt} \int_{\Omega} p S_\varepsilon \delta p \, d\Omega, \quad (2.109b)$$

$$f^p(\delta p) = - \int_{\Gamma_q} \bar{\mathbf{q}} \cdot \delta p \, d\Gamma + \int_{\Omega} Q \delta p \, d\Omega, \quad (2.109c)$$

and coupling phase

$$\mathbf{a}^{\boldsymbol{\varepsilon},0}(\mathbf{p}, \delta \mathbf{u})_{\alpha_B \mathbf{m}} = \int_{\Omega} \boldsymbol{\varepsilon}(\delta \mathbf{u}) \alpha_B \mathbf{m} \mathbf{p} \, d\Omega, \quad (2.110a)$$

$$\mathbf{a}^{\boldsymbol{\varepsilon},0}(\dot{\mathbf{u}}, \delta \mathbf{p})_{\alpha_B \mathbf{m}^T} = \frac{d}{dt} \int_{\Omega} \boldsymbol{\varepsilon}(\mathbf{u}) \alpha_B \mathbf{m}^T \delta \mathbf{p} \, d\Omega. \quad (2.110b)$$

Discretization

Similar to Eq. (2.93), the discretized pressure field trial \mathbf{p}_h and test $\delta \mathbf{p}_h$ functions are defined accordingly as

$$\mathbf{p}_h, \delta \mathbf{p}_h \in \mathcal{V}_h^p \subset \mathcal{V}^p, \quad (2.111)$$

over the finite-dimensional subspace \mathcal{V}_h^p .

Using the discrete approximations introduced in Eqs. (2.93) and (2.111), the abstract formulation of the discretized weak form is expressed

$$\left\{ \begin{array}{l} \text{Find } (\mathbf{u}_h, \mathbf{p}_h) \in \mathcal{V}_h^u \times \mathcal{V}_h^p \text{ such that :} \\ \mathbf{a}^{\boldsymbol{\varepsilon}}(\mathbf{u}_h, \delta \mathbf{u}_h)_{\mathbb{D}} - \mathbf{a}^{(\boldsymbol{\varepsilon},0)}(\mathbf{p}_h, \delta \mathbf{u}_h)_{\alpha_B \mathbf{m}} = \mathbf{f}^u(\delta \mathbf{u}_h) \quad \forall \delta \mathbf{u}_h \in \mathcal{V}_h^u \\ \mathbf{a}^{(\boldsymbol{\varepsilon},0)}(\dot{\mathbf{u}}_h, \delta \mathbf{p}_h)_{\alpha_B \mathbf{m}^T} + \mathbf{b}^0(\dot{\mathbf{p}}_h, \delta \mathbf{p}_h)_{S_\varepsilon} + \mathbf{b}^\nabla(\mathbf{p}_h, \delta \mathbf{p}_h)_{\mathbf{k}/\gamma_f} = \mathbf{f}^p(\delta \mathbf{p}_h) \quad \forall \delta \mathbf{p}_h \in \mathcal{V}_h^p. \end{array} \right. \quad (2.112)$$

The functional forms used in Eq. (2.94) for the solid phase have already been additively assembled from local contributions in Eq. (2.96). The operators corresponding to the fluid phase assume the following form

$$\mathbf{b}^\nabla(\mathbf{p}_h, \delta \mathbf{p}_h)_{\mathbf{k}/\gamma_f} = \sum_{i=1}^{n_{el}} \mathbf{b}_{\mathcal{K}_i}^\nabla(\mathbf{p}_h, \delta \mathbf{p}_h)_{\mathbf{k}/\gamma_f}, \quad (2.113a)$$

$$\mathbf{b}^0(\mathbf{p}_h, \delta \mathbf{p}_h)_{S_\varepsilon} = \sum_{i=1}^{n_{el}} \mathbf{b}_{\mathcal{K}_i}^0(\mathbf{p}_h, \delta \mathbf{p}_h)_{S_\varepsilon}, \quad (2.113b)$$

$$\mathbf{f}^p(\delta \mathbf{p}_h) = \sum_{i=1}^{n_{el}} \mathbf{f}_{\mathcal{K}_i}^p(\delta \mathbf{p}_h). \quad (2.113c)$$

Finally, the operators corresponding to phase coupling become

$$\mathbf{a}^{(\boldsymbol{\varepsilon},0)}(\mathbf{p}_h, \delta \mathbf{u}_h)_{\alpha_B \mathbf{m}} = \sum_{i=1}^{n_{el}} \mathbf{a}_{\mathcal{K}_i}^{(\boldsymbol{\varepsilon},0)}(\mathbf{p}_h, \delta \mathbf{u}_h)_{\alpha_B \mathbf{m}}, \quad (2.114a)$$

$$\mathbf{a}^{(\boldsymbol{\varepsilon},0)}(\dot{\mathbf{u}}_h, \delta \mathbf{p}_h)_{\alpha_B \mathbf{m}^T} = \sum_{i=1}^{n_{el}} \mathbf{a}_{\mathcal{K}_i}^{(\boldsymbol{\varepsilon},0)}(\dot{\mathbf{u}}_h, \delta \mathbf{p}_h)_{\alpha_B \mathbf{m}^T}. \quad (2.114b)$$

The element-wise components in Eqs. (2.113) - (2.114) are expressed for the fluid phase

$$b^{\nabla}(\mathbf{p}_h, \delta \mathbf{p}_h)_{\mathbf{k}/\gamma_f} = \int_{\mathcal{K}_i} \nabla(\mathbf{p}_h) \frac{\mathbf{k}}{\gamma_f} \nabla(\delta \mathbf{p}_h) \, d\Omega, \quad (2.115a)$$

$$b^0(\dot{\mathbf{p}}_h, \delta \mathbf{p}_h)_{S_\varepsilon} = \frac{d}{dt} \int_{\mathcal{K}_i} \mathbf{p}_h S_\varepsilon \delta \mathbf{p}_h \, d\Omega, \quad (2.115b)$$

$$f^p(\delta \mathbf{p}_h) = - \int_{\Gamma_{hq}^{\mathcal{K}_i}} \bar{\mathbf{q}}_h \cdot \delta \mathbf{p}_h \, d\Gamma + \int_{\mathcal{K}_i} Q \delta \mathbf{p}_h \, d\Omega, \quad (2.115c)$$

and coupling terms

$$\mathbf{a}^{\varepsilon,0}(\mathbf{p}_h, \delta \mathbf{u}_h)_{\alpha_B \mathbf{m}} = \int_{\mathcal{K}_i} \boldsymbol{\varepsilon}(\delta \mathbf{u}_h) \alpha_B \mathbf{m} \, p_h \, d\Omega, \quad (2.116a)$$

$$\mathbf{a}^{\varepsilon,0}(\dot{\mathbf{u}}_h, \delta \mathbf{p}_h)_{\alpha_B \mathbf{m}^T} = \frac{d}{dt} \int_{\mathcal{K}_i} \boldsymbol{\varepsilon}(\mathbf{u}_h) \alpha_B \mathbf{m}^T \delta \mathbf{p}_h \, d\Omega. \quad (2.116b)$$

The fields p_h and δp_h are discretized into piecewise continuous functions analogous to Eq. (2.98)

$$p_h = \underbrace{[\boldsymbol{\Phi}^p]^T}_{(n_{\text{dof}}^p \times 1)} \hat{\mathbf{p}}, \quad \delta p_h = \underbrace{[\boldsymbol{\Phi}^p]^T}_{(n_{\text{dof}}^p \times 1)} \hat{\delta \mathbf{p}}, \quad (2.117)$$

where $\hat{\mathbf{p}}$ and $\hat{\delta \mathbf{p}}$ are vectors containing element-wise trial and test nodal pressure values, respectively. The number of DoFs pertaining to $\mathcal{V}_h^p(\mathcal{K})$ is contained within n_{dof}^p . The array $[\boldsymbol{\Phi}^p]$ represents canonical basis functions spanning \mathcal{V}_h^p . This space is defined as follows

$$\mathcal{V}_h^p = [\mathcal{W}_h]^d, \quad d = 1, \quad (2.118)$$

where in \mathcal{W}_h is defined in Eq. (2.99b). $[\boldsymbol{\Phi}^p]$ also possesses the properties shown in Eqs. (2.101)-(2.102)

$$\Phi_i^p(\mathbf{x}_j) = \delta_{ij}, \quad i = 1, \dots, n_{\text{dof}}^p, \quad (2.119)$$

and

$$\sum_{i=1}^{n_{\text{dof}}^p} \Phi_i^p(\mathbf{x}_j) = 1, \quad (2.120)$$

over $\mathcal{V}_h^p(\mathcal{K})$.

Inserting Eqs. (2.117) into Eqs. (2.115) yields the fluid kinetic term

$$b_{\mathcal{K}_i}^{\nabla}(\mathbf{p}_h, \delta \mathbf{p}_h)_{\mathbf{k}/\gamma_f} = \delta \hat{\mathbf{p}}^T \underbrace{\left[\int_{\mathcal{K}_i} \nabla \boldsymbol{\Phi}^{pT} \frac{\mathbf{k}}{\gamma_f} \nabla \boldsymbol{\Phi}^p \, d\Omega \right]}_{\mathbf{H}_{\mathcal{K}_i}} \hat{\mathbf{p}}, \quad (2.121)$$

where $\mathbf{B}^{\nabla} = \nabla \boldsymbol{\Phi}^p$ is often used as a convenient shorthand. Next, one obtains the compressibility

term

$$b_{\mathcal{K}_i}^0(\dot{\mathbf{p}}_h, \delta \mathbf{p}_h)_{S_\varepsilon} = \frac{d}{dt} \delta \hat{\mathbf{p}}^T \underbrace{\left[\int_{\mathcal{K}_i} \Phi^{pT} S_\varepsilon \Phi^p d\Omega \right]}_{\mathbf{S}_{\mathcal{K}_i}} \hat{\mathbf{p}}, \quad (2.122)$$

and the fluid phase forcing term

$$\mathbf{f}_{\mathcal{K}_i}^p(\delta \mathbf{p}_h) = \delta \hat{\mathbf{p}}^T \underbrace{\left[- \int_{\Gamma_{hq}^{\mathcal{K}_i}} \Phi^{pT} \bar{\mathbf{q}}_h d\Gamma + \int_{\mathcal{K}_i} \Phi^{pT} Q d\Omega \right]}_{\mathbf{f}_{\mathcal{K}_i}^p}. \quad (2.123)$$

The discretized coupling terms are derived by substituting Eqs. (2.98) and (2.117) into Eqs. (2.116)

$$a_{\mathcal{K}_i}^{(\varepsilon,0)}(\mathbf{p}_h, \delta \mathbf{u}_h)_{\alpha_B \mathbf{m}} = \delta \hat{\mathbf{p}}^T \underbrace{\left[\int_{\mathcal{K}_i} \mathbf{B}^{uT} \alpha_B \mathbf{m} \Phi^p d\Omega \right]}_{\mathbf{Q}_{\mathcal{K}_i}} \hat{\mathbf{u}}, \quad (2.124)$$

and

$$a_{\mathcal{K}_i}^{(\varepsilon,0)}(\dot{\mathbf{u}}_h, \delta \mathbf{p}_h)_{\alpha_B \mathbf{m}} = \frac{d}{dt} \delta \hat{\mathbf{p}}^T \underbrace{\left[\int_{\mathcal{K}_i} \Phi^{pT} \alpha_B \mathbf{m}^T \mathbf{B}^u d\Omega \right]}_{\mathbf{Q}_{\mathcal{K}_i}^T} \hat{\mathbf{u}}. \quad (2.125)$$

The local state matrices and vectors are assembled, over the entire domain Ω_h in a similar manner to Eq. (2.105)

$$\mathbf{H} = \mathop{\text{A}}_{i=1}^{n_{el}} \mathbf{H}_{\mathcal{K}_i}, \quad \mathbf{S} = \mathop{\text{A}}_{i=1}^{n_{el}} \mathbf{S}_{\mathcal{K}_i}, \quad \mathbf{Q} = \mathop{\text{A}}_{i=1}^{n_{el}} \mathbf{Q}_{\mathcal{K}_i}, \quad \mathbf{f}^p = \mathop{\text{A}}_{i=1}^{n_{el}} \mathbf{f}_{\mathcal{K}_i}^p. \quad (2.126)$$

The global matrix form of the governing equations are now elaborated in accordance with Eqs. (2.112)

$$\begin{bmatrix} \mathbf{K} & -\mathbf{Q} \\ \mathbf{0} & \mathbf{H} \end{bmatrix} \begin{Bmatrix} \hat{\mathbf{u}} \\ \hat{\mathbf{p}} \end{Bmatrix} + \begin{bmatrix} \mathbf{0} & \mathbf{0} \\ \mathbf{Q}^T & \mathbf{S} \end{bmatrix} \begin{Bmatrix} \dot{\hat{\mathbf{u}}} \\ \dot{\hat{\mathbf{p}}} \end{Bmatrix} = \begin{bmatrix} \mathbf{f}^u \\ \mathbf{f}^p \end{bmatrix}. \quad (2.127)$$

Solution procedure

Eq. (2.127) is a system of first order differential/ algebraic equations with respect to time of the following generic form

$$\mathbf{A} \dot{\mathbf{X}} + \mathbf{B} \mathbf{X} = \mathbf{F}, \quad (2.128)$$

where $\mathbf{X} = \{\hat{\mathbf{u}} \ \hat{\mathbf{p}}\}^T$. The quantities \mathbf{A} , \mathbf{B} and \mathbf{F} can be obtained from Eq. (2.127) by inspection.

In this Chapter, a theta rule time discretization scheme is employed to obtain solution states at each time step. Assuming that the time domain is discretized into a finite number of $N_t + 1$ points, i.e., $t_0 < t_1 \cdots < t_n < t_{n+1} < \cdots < t_{N_t}$ the solution vector \mathbf{X} and its time derivative $\dot{\mathbf{X}}$

are defined as

$$\mathbf{X}_{n+\theta} = (1 - \theta)\mathbf{X}_n + \theta\mathbf{X}_{n+1}, \quad (2.129)$$

and

$$\dot{\mathbf{X}}_{n+\theta} = \frac{\mathbf{X}_{n+1} - \mathbf{X}_n}{\Delta t}, \quad (2.130)$$

respectively, where Δt is the time increment and θ is the implicitness parameter $0 \leq \theta \leq 1$. The vectors \mathbf{X}_n and \mathbf{X}_{n+1} denote the state vectors at time t_n and t_{n+1} , respectively.

Substituting Eqs. (2.129) and (2.130) into Eq. (2.128) gives rise to the following time marching scheme

$$\tilde{\mathbf{A}}\mathbf{X}_{n+1} = \tilde{\mathbf{B}}\mathbf{X}_n + \Delta t\mathbf{F}_{n+\theta}, \quad (2.131)$$

where $\tilde{\mathbf{A}}$ and $\tilde{\mathbf{B}}$ are the effective state matrices, which after the necessary algebraic manipulation assume the following form, i.e.,

$$\tilde{\mathbf{A}} = \begin{bmatrix} \theta\mathbf{K} & -\theta\mathbf{Q} \\ \mathbf{Q}^T & \mathbf{S} + \Delta t\theta\mathbf{H} \end{bmatrix}_{n+\theta}, \quad (2.132)$$

and

$$\tilde{\mathbf{B}} = \begin{bmatrix} (\theta - 1)\mathbf{K} & (1 - \theta)\mathbf{Q} \\ \mathbf{Q}^T & \mathbf{S} - (1 - \theta)\Delta t\mathbf{H} \end{bmatrix}_{n+\theta}, \quad (2.133)$$

respectively and the discretized forcing vector $\mathbf{F}_{n+\theta} = \{\mathbf{f}^u \quad \mathbf{f}^p\}^T$.

A central difference scheme, $\theta = \frac{1}{2}$ is adopted. Since such a scheme is conditionally stable, one should exercise caution in choosing appropriate spatial and temporal time discretization steps. **Alternatively, an unconditionally stable implicit scheme may be chosen.**

Validation

The numerical schemes proposed above are verified using the Terzaghi consolidation test [15]. A soil column of height $h = 7$ m and width $D = 1$ m is fully saturated with water and subjected to a uniaxial compressional load $q = 1$ kPa at the top. The top is exposed to air and consequently has a pore-fluid pressure $p = 0$ Pa. The lateral sides are provided with roller supports and the bottom is fully clamped. No-flow conditions are imposed over all boundaries, i.e., $\nabla p \cdot \mathbf{n} = 0$, where \mathbf{n} denotes the corresponding outward facing surface normal. These conditions are illustrated in Fig. 2.6.

Further, initial conditions $\mathbf{u}(t = 0) = 0$ and $p(t = 0) = q$ are given. The soil has a Young's modulus $E = 8$ MPa, Poisson's Ratio $\nu = 0.3$ and permeability $10^{-6} \text{ m} \cdot \text{s}^{-1}$. The specific weight of the pore-fluid (water) is $\gamma_f = 9.81 \times 10^3 \text{ kg} \cdot \text{m}^{-2} \cdot \text{s}^{-2}$.

The time evolution of pore-fluid pressure is obtained by solving the equation

$$\frac{\partial p}{\partial t} = c_v \frac{\partial^2 p}{\partial z^2}, \quad (2.134)$$

where z denotes the elevation in the soil column. The consolidation coefficient c_v has the form

$$c_v = \frac{k}{\gamma_w m_v}, \quad m_v = \frac{1}{K + \frac{4}{3}G} = \frac{(1 + \nu)(1 - 2\nu)}{E(1 - \nu)}. \quad (2.135)$$

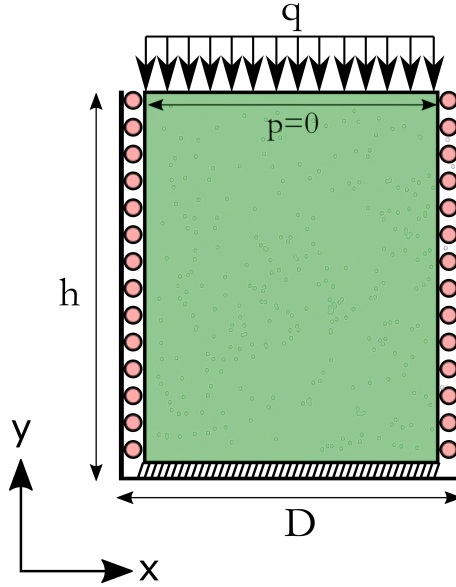


Figure 2.6: Schematic for Terzaghi's uniaxial consolidation test.

The term m_v indicated the Terzaghi compressibility coefficient. This equation is solved analytically in [54]

$$\frac{p(z, t)}{p_0} = \frac{4}{\pi} \sum_{j=1}^{\infty} \frac{(-1)^{j-1}}{2j-1} \cos \left[(2j-1) \frac{\pi z}{2h} \right] e^{-(2j-1)^2 \frac{\pi^2}{4} \frac{c_v t}{h^2}}. \quad (2.136)$$

The deformation of the soil column is evaluated by integrating the corresponding strains

$$\Delta h_t = \int_0^h \varepsilon dz = -m_v h q + m_v \int_0^h p_w dz. \quad (2.137)$$

The numerical solution is calculated by solving Eq. (2.127) with 700 quadrilateral finite elements. The analytical and numerical distribution of pressures within the soil column at time instants $t_1 = 100$ s, $t_2 = 1,300$ s, $t_3 = 4,300$ s, $t_4 = 13,300$ s, $t_5 = 23,300$ s, $t_6 = 43,300$ s are provided in Fig. 2.7a. The deformations at the top surface $z = h$ are compared in Fig. 2.7b. Near perfect agreements are observed in all cases.

The pore-fluid pressure contours are provided at these six time instants in Fig. 2.8 for completeness. This example demonstrates the ability of the FE model described above to accurately simulate consolidation behaviour in poroelastic media.

2.7.3 Vibroacoustics

Transfer Matrix Method

The Transfer Matrix Method (TMM) is a semi-analytical approach used to forecast acoustical indicators such as the Sound Absorption Coefficient (SAC) and Sound Transmission Loss Coefficient (STL) in flat multi-layered systems. The method is used as a verification tool for several vibroacoustic applications presented in this thesis.

A medium of thickness H is subject to an acoustical plane-wave excitation impinging at an

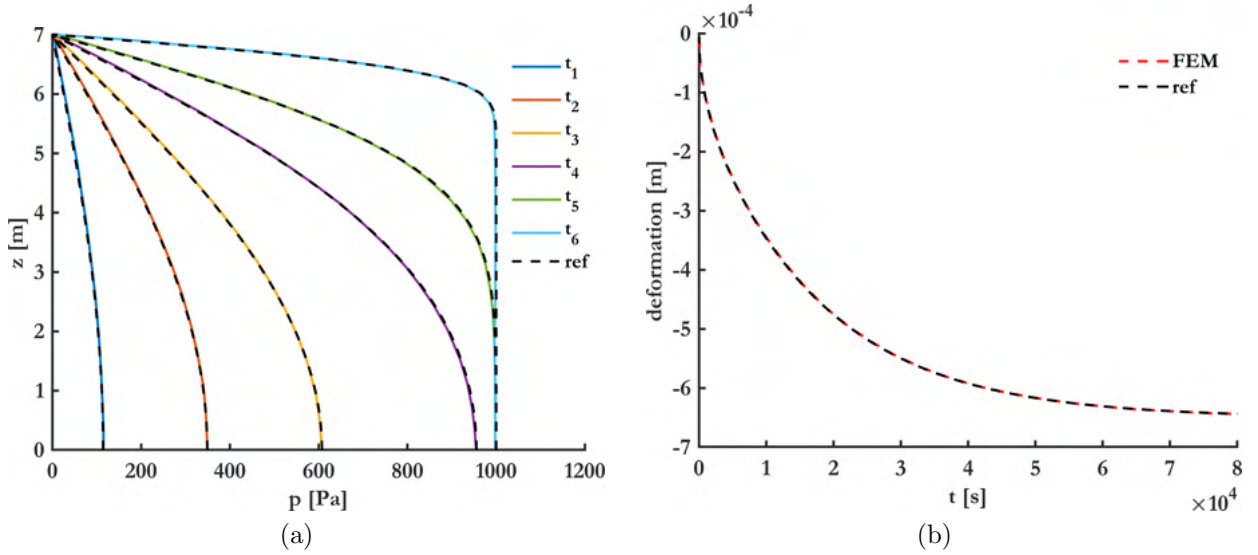


Figure 2.7: (a) Distribution of pore water pressures in the soil column at six different time instances, (b) Evolution of soil settlement at the top surface $z = h$ with time. Analytical solutions are provided in dotted black lines.

angle of incidence θ . Two points, A and B are arbitrarily chosen close to the incidence and rear faces, respectively. This is illustrated in Fig. 2.9.

A matrix \mathbf{T} can be formulated to describe wave propagation in the medium, such that

$$\mathbf{V}(A) = \mathbf{T} \mathbf{V}(B), \quad (2.138)$$

where the vector $\mathbf{V}(A)$ contains quantities describing the acoustic field at A in the medium. The transfer matrix \mathbf{T} depends on the thickness H and the material parameters characterizing the medium.

For a fluid, $\mathbf{V}(A)$ has the form

$$\mathbf{V}^f(A) = [p(A), v_x(A)]^T, \quad (2.139)$$

where $p(A)$ and $v_x(A)$ denote the fluid pressure and velocity in the x-direction at point A. In the case of a solid (elastic) medium, it is to be noted that the variables constituting $\mathbf{V}(\cdot)$ need not be unique. Following [13, 39], four independent quantities are chosen

$$\mathbf{V}^s(A) = [v_x^s(A), v_y^s(A), \sigma_{xx}^s(A), \sigma_{xy}^s(A)]^T, \quad (2.140)$$

where $v_x^s(A)$ and $v_y^s(A)$ denote x and y-direction velocities at point A, respectively. Normal and shear stresses are respectively indicated by the terms $\sigma_{xx}^s(A)$ and $\sigma_{xy}^s(A)$. In a poroelastic medium, the vectors for both phases are combined to yield

$$\mathbf{V}^p(A) = [v_x^s(A), v_y^s(A), v_x^f(A), \sigma_{xx}^s(A), \sigma_{xy}^s(A), \sigma_{xx}^f(A)]^T. \quad (2.141)$$

For a detailed derivation of the expression for the relevant transfer matrix operators \mathbf{T}^f , \mathbf{T}^s and \mathbf{T}^p , the reader is referred to [13].

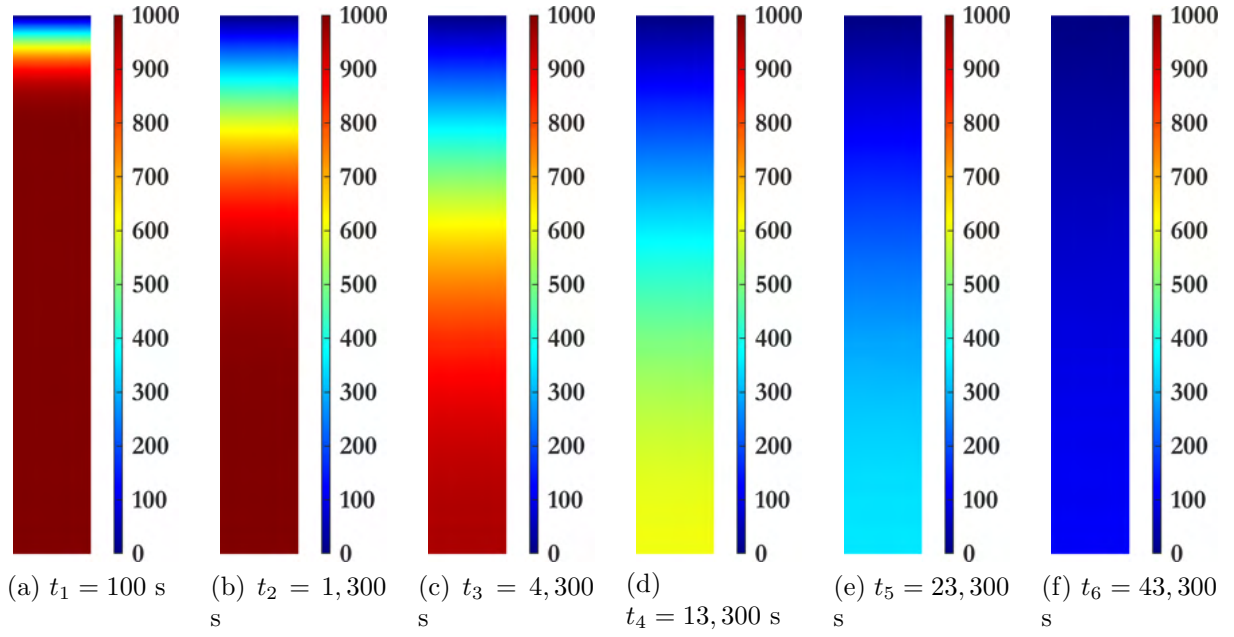


Figure 2.8: Water pressure contours at six different time instances.

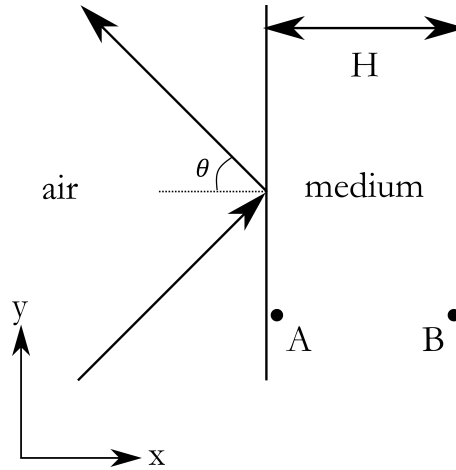


Figure 2.9: A medium of thickness H subject to a plane wave acoustic excitation at an angle of incidence θ .

Strong form

A generalized continuous two-dimensional poroelastic domain $\Omega \in \mathbb{R}^d$, $d = 2$ with a boundary Γ is shown in Fig. 2.10. The domain Ω is surrounded by arbitrary neighbours Ω_1^e and Ω_2^e . These neighbouring domains may be elastic (solid), acoustic (fluid) or porous domains. Similar Dirichlet and Neumann boundary conditions to Section 2.7.2 are considered. Additionally, an impedance-type Robin boundary is also provided over Γ_r .

The mixed displacement-pressure $\mathbf{u} - p$ formulation, Eqs. (2.87)-(2.88) is subjected to the following set of essential

$$\mathbf{u} = \bar{\mathbf{u}} \text{ on } \Gamma_u, \quad p = \bar{p}e^{-j\mathbf{k}\cdot\mathbf{x}} \text{ on } \Gamma_p, \quad (2.142)$$

natural

$$\mathbf{t} = \bar{\mathbf{t}} \text{ on } \Gamma_t, \quad \mathbf{q} = \bar{\mathbf{q}} \text{ on } \Gamma_q, \quad (2.143)$$

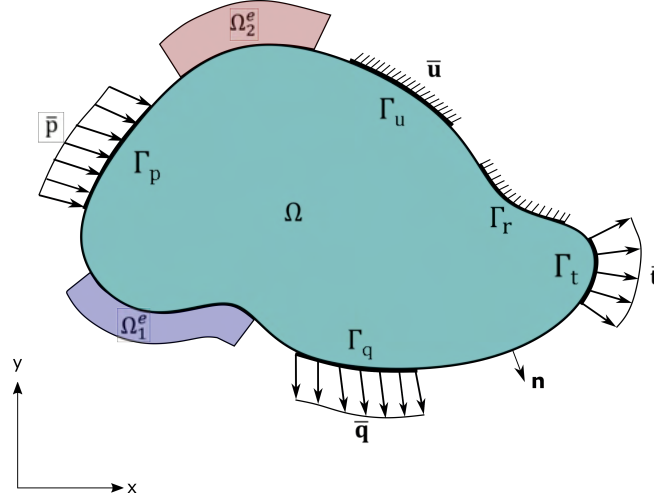


Figure 2.10: A poro-elastic domain Ω subjected to acoustic and mechanical excitations.

and impedance boundary conditions

$$z(\theta)\nabla p \cdot \mathbf{n} + j\omega\tilde{\rho}_{\text{eq}}p = \bar{g} \text{ on } \Gamma_r, \quad (2.144)$$

respectively. For a time-harmonic acoustic excitation of amplitude \bar{p} incident at an angle θ , the vector valued wave number is represented by $\mathbf{k} = [k\cos(\theta), k\sin(\theta)]$, where $k = \omega/c_{\text{air}}$. The vector $\mathbf{x} = [x, y]^T$ denotes the coordinates of a point on the incident face Γ_p . A Robin-type boundary value \bar{g} is specified over Γ_r where z denotes an impedance constant $z(\theta) = z_{\text{air}}/\cos(\theta)$. The parameters c_{air} and $z_{\text{air}} = \rho_0 c_{\text{air}}$ denote the speed of sound in air and impedance of air, respectively. For our purposes, we take $\bar{g} = 0$ [55].

Weak form

The weak form of Eqs. (2.87)-(2.88) is derived by multiplying each expression with the relevant test functions $\delta\mathbf{u}$ and δp and integrating over the entire domain

Find $(\mathbf{u}, p) \in \mathcal{V}^u \times \mathcal{V}^p := [\mathcal{H}^1(\Omega)]^d \times [\mathcal{H}^1(\Omega)]$, $d = 2$, such that

Solid phase

$$\begin{aligned} & \int_{\Omega} \boldsymbol{\sigma}_s(\mathbf{u}) : \boldsymbol{\varepsilon}_s(\delta\mathbf{u}) \, d\Omega - \omega^2 \int_{\Omega} \tilde{\rho} \mathbf{u} \cdot \delta\mathbf{u} \, d\Omega - \int_{\Omega} \tilde{\gamma} \nabla p \cdot \delta\mathbf{u} \, d\Omega \\ & - \underbrace{\int_{\Gamma_t} (\boldsymbol{\sigma}_s \cdot \mathbf{n}) \cdot \delta\mathbf{u} \, d\Gamma}_{I_1} = 0 \quad \forall \delta\mathbf{u} \in \mathcal{V}^u, \end{aligned} \quad (2.145)$$

and

$$\begin{aligned}
 & \text{Fluid phase} \\
 & \int_{\Omega} \frac{1}{\tilde{\rho}_{\text{eq}}} \nabla \mathbf{p} \cdot \nabla \delta \mathbf{p} \, d\Omega - \omega^2 \int_{\Omega} \frac{1}{\tilde{K}_{\text{eq}}} \mathbf{p} \, \delta \mathbf{p} \, d\Omega - \omega^2 \int_{\Omega} \tilde{\gamma} \nabla \delta \mathbf{p} \cdot \mathbf{u} \, d\Omega \\
 & + \omega^2 \underbrace{\int_{\Gamma} \left(\tilde{\gamma} \mathbf{u} \cdot \mathbf{n} - \frac{1}{\omega^2 \tilde{\rho}_{\text{eq}}} \nabla \mathbf{p} \cdot \mathbf{n} \right) \delta \mathbf{p} \, d\Gamma}_{I_2} = 0 \quad \forall \delta \mathbf{p} \in \mathcal{V}^p.
 \end{aligned} \tag{2.146}$$

Using Eq. (2.40), the boundary integral I_1 in Eq. (2.145) is modified to

$$I_1 = \int_{\Gamma_t} \left(\boldsymbol{\sigma}_t \cdot \mathbf{n} + c \mathbb{I} \cdot \mathbf{n} \right) \cdot \delta \mathbf{u} \, d\Gamma. \tag{2.147}$$

Similarly, the boundary integral I_2 in Eq. (2.146) is decomposed into the relevant Neumann and Robin contributions according to the identity $\Gamma \equiv \Gamma_q \cup \Gamma_r$: $I_2 = I_2^{\Gamma_q} + I_2^{\Gamma_r}$, where, employing Eq. (2.70) the following expression is eventually established

$$I_2^{\Gamma_q} = -\omega^2 \int_{\Gamma_q} \left(c \mathbf{u} \cdot \mathbf{n} + \mathbf{w}_n \right) \delta \mathbf{p} \, d\Gamma, \tag{2.148}$$

where $\mathbf{w}_n = \phi(\mathbf{U} - \mathbf{u}) \cdot \mathbf{n}$ is the normal component of the fluid displacement relative to the solid skeleton. This is measured in volume per unit area of the bulk medium [20,21]. Using Eq. (2.144), a simplified expression for $I_2^{\Gamma_r}$ is obtained

$$I_2^{\Gamma_r} = \frac{j\omega}{z(\theta)} \int_{\Gamma_r} \mathbf{p} \, \delta \mathbf{p} \, d\Gamma. \tag{2.149}$$

Is it to be noted that the solid skeleton normal displacements are not defined over Γ_r .

When subject to acoustic excitation, variations in $\delta \mathbf{p}$ are zero. To ensure continuities, one requires $\boldsymbol{\sigma}_t \cdot \mathbf{n} = -p \mathbb{I} \cdot \mathbf{n}$. Using the result for classical sound absorbing materials, i.e., $c \approx 1$ [56], $I_1 = I_2 = 0$. The acoustic wave is simply imposed on the incident face as a pressure Dirichlet boundary (Eq. (2.142)). Considering roller or fully clamped supports, variations in $\delta \mathbf{u}$ are zero. Further, $\mathbf{u} \cdot \mathbf{n}$ and \mathbf{w}_n are zero as well. Consequently, once again, $I_1 = I_2 = 0$. Given an impedance-type anechoic termination, $I_1 = 0$, $I_2 = I_2^{\Gamma_r}$. These integral conditions are tabulated in Table 2.2.

The coupling conditions encountered at the interface between Ω and Ω_e^1 , Ω_e^2 etc. need to be taken into account. They are critical to generating accurate predictive models of porous composites. This is illustrated in Fig. 2.11.

1. Poroelastic-elastic coupling: The traction obtained at the interface Γ of the elastic medium $\mathbf{t} = \boldsymbol{\sigma}_e \cdot (-\mathbf{n})$ is incorporated into the boundary integral I_1

$$I_1 = \int_{\Gamma} \left(\boldsymbol{\sigma}_t \cdot \mathbf{n} + c \mathbb{I} \cdot \mathbf{n} - \boldsymbol{\sigma}_e \cdot \mathbf{n} \right) \cdot \delta \mathbf{u} \, d\Gamma. \tag{2.150}$$

Boundary Condition	Boundary Integrals
Acoustic	$I_1 = 0$
Excitation	$I_2 = 0$
Roller	$I_1 = 0$
Support	$I_2 = 0$
Clamped	$I_1 = 0$
Support	$I_2 = 0$
Anechoic	$I_1 = 0$
Termination	$I_2 = \frac{j\omega}{z(\theta)} \int_{\Gamma_r} p \delta p \, d\Gamma$

Table 2.2: Boundary integrals.

The fluid phase term I_2 remains the same

$$I_2 = -\omega^2 \int_{\Gamma} (\mathbf{c}\mathbf{u} \cdot \mathbf{n} + \mathbf{w}_n) \delta p \, d\Gamma. \quad (2.151)$$

The coupling conditions are now specified over Γ according to [56]

$$\begin{cases} \boldsymbol{\sigma}_t \cdot \mathbf{n} = \boldsymbol{\sigma}_e \cdot \mathbf{n}, \\ \mathbf{w}_n = 0, \\ \mathbf{u} = \mathbf{u}_e, \end{cases} \quad (2.152)$$

where the first condition introduces continuity of traction. The second equation ensures zero relative mass flux across the interface by requiring that no relative motion exists between the the solid and fluid phase of the poroelastic material. The third equation enforces continuity of solid displacements for both media. Inserting Eqs. (2.152) into Eqs. (2.150) and (2.151) yields

$$I_1 = \int_{\Gamma} (cp\mathbb{I} \cdot \mathbf{n}) \cdot \delta \mathbf{u} \, d\Gamma, \quad (2.153)$$

and

$$I_2 = -\omega^2 \int_{\Gamma} (\mathbf{c}\mathbf{u} \cdot \mathbf{n}) \delta p \, d\Gamma. \quad (2.154)$$

Eqs. (2.153) and (2.154) resemble classical fluid-structure coupling matrices and naturally couple poroelastic fluid pressures with elastic solid displacements. Finally the kinematic constraint $\mathbf{u} = \mathbf{u}_e$ is explicitly imposed.

2. Poroelastic-acoustic coupling condition

The weak formulations of the poroelastic and acoustic media are combined

$$I_1 = \int_{\Gamma} (\boldsymbol{\sigma}_t \cdot \mathbf{n} + cp\mathbb{I} \cdot \mathbf{n}) \cdot \delta \mathbf{u} \, d\Gamma, \quad (2.155)$$

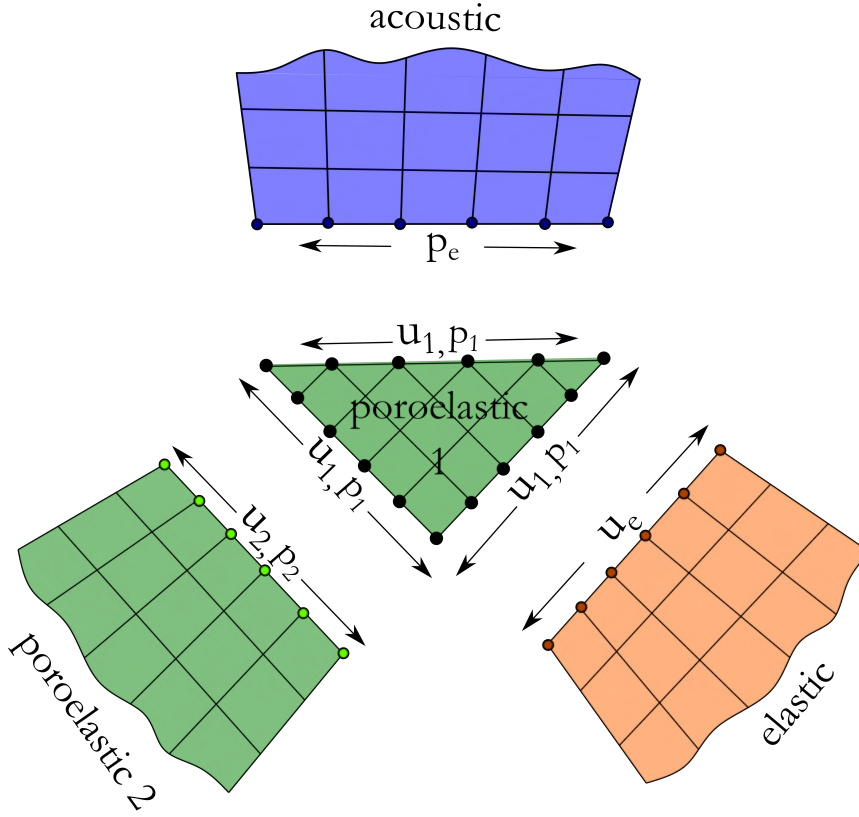


Figure 2.11: A schematic illustrating the different kinds of interfaces encountered in Biot poroelasticity.

and

$$I_2 = -\omega^2 \int_{\Gamma} \left(c\mathbf{u} \cdot \mathbf{n} + \mathbf{w}_n - \frac{1}{\omega^2 \rho_0} \nabla p_a \cdot \mathbf{n} \right) \delta p \, d\Gamma. \quad (2.156)$$

Here, the coupling conditions over Γ are provided

$$\begin{cases} \boldsymbol{\sigma}_t \cdot \mathbf{n} = -p_a \mathbb{I} \cdot \mathbf{n} \\ ((1 - \phi)\mathbf{u} + \phi\mathbf{U}) \cdot \mathbf{n} = \frac{1}{\omega^2 \rho_0} \nabla p_a \cdot \mathbf{n} = \mathbf{u} \cdot \mathbf{n} + \mathbf{w}_n \\ p = p_a, \end{cases} \quad (2.157)$$

where, as in the previous case, the relations express the continuity of traction, relative mass fluxes and pressures, respectively. Substituting Eqs. (2.157) into Eqs. (2.155) and (2.156) read

$$I_1 = \int_{\Gamma} (c - 1) p_a \mathbb{I} \cdot \mathbf{n} \cdot \delta \mathbf{u} \, d\Gamma, \quad (2.158)$$

and

$$I_2 = -\omega^2 \int_{\Gamma} (c - 1) \delta \mathbf{u} \cdot \mathbf{n} \delta p_a \, d\Gamma. \quad (2.159)$$

Within the context of classical sound absorbing materials, since $c \approx 1$, the resulting integrals I_1 and I_2 are zero. Consequently, only the kinematic relation $p = p_a$ need be explicitly imposed.

3. Poroelastic-poroelastic coupling The weak form for two poroelastic materials, labelled 1 and 2 are combined below

$$I_1 = \int_{\Gamma} \left(\boldsymbol{\sigma}_{t,1} \cdot \mathbf{n} + c p_1 \mathbb{I} \cdot \mathbf{n} \right) \cdot \delta \mathbf{u}_1 \, d\Gamma - \int_{\Gamma} \left(\boldsymbol{\sigma}_{t,2} \cdot \mathbf{n} + c p_2 \mathbb{I} \cdot \mathbf{n} \right) \cdot \delta \mathbf{u}_2 \, d\Gamma, \quad (2.160)$$

and

$$I_2 = -\omega^2 \left[\int_{\Gamma} \left(c \mathbf{u}_1 \cdot \mathbf{n} + \mathbf{w}_{n,1} \right) \delta p_1 \, d\Gamma - \int_{\Gamma} \left(c \mathbf{u}_2 \cdot \mathbf{n} + \mathbf{w}_{n,2} \right) \delta p_2 \, d\Gamma \right]. \quad (2.161)$$

Continuity conditions on traction, mass flux, displacement and pressure are established across the interface as follows

$$\begin{cases} \boldsymbol{\sigma}_{t,1} \cdot \mathbf{n} = \boldsymbol{\sigma}_{t,2} \cdot \mathbf{n} \\ \mathbf{w}_{n,1} = \mathbf{w}_{n,2} \\ \mathbf{u}_1 = \mathbf{u}_2 \\ p_1 = p_2. \end{cases} \quad (2.162)$$

Inserting Eqs. (2.162) into Eqs. (2.160) - (2.161) and using the relation $c \approx 1$, once again, the integrals $I_1 = I_2 = 0$. In this case, the displacement and pressure continuity conditions are explicitly imposed at the boundary.

4. Acoustic-Elastic coupling

The coupling matrices involved at the interface of an acoustic and elastic domain resemble Eqs. (2.158)-(2.159)

$$I_1 = \int_{\Gamma} (p_a \mathbb{I} \cdot \mathbf{n}) \cdot \delta \mathbf{u}_e \, d\Gamma, \quad (2.163)$$

$$I_2 = -\omega^2 \int_{\Gamma} (\mathbf{u}_e \cdot \mathbf{n}) \delta p_a \, d\Gamma. \quad (2.164)$$

The above considerations illustrate the potential advantages offered by the $\mathbf{u} - p$ formulation over the $\mathbf{u} - \mathbf{U}$ in terms of simplicity of boundary and interface conditions. The boundary integrals I_1 and I_2 are either zero, or assume familiar fluid-structure coupling forms. Normal components of solid displacements and acoustic pressures are naturally coupled. Kinematic relations concerning displacements and pressures are easily imposed. These conditions are summarized in Table 2.3. For a more detailed discussion of the boundary conditions involved, see [56].

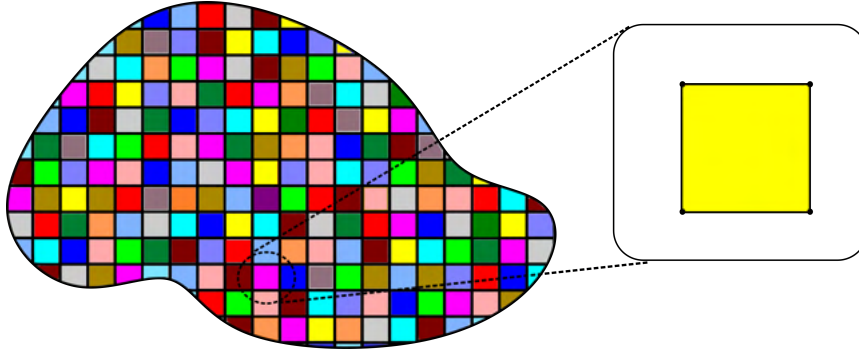
Discretization

Substituting the discrete approximations introduced in Eqs. (2.93) and (2.111) in the weak form and collecting terms gives rise to the following abstract weak formulation, i.e.,

$$\begin{cases} \text{Find } (\mathbf{u}_h, p_h) \in \mathcal{V}_h^u \times \mathcal{V}_h^p \text{ such that} \\ a^\varepsilon(\mathbf{u}_h, \delta \mathbf{u}_h) - \omega^2 a^0(\mathbf{u}_h, \delta \mathbf{u}_h)_{\bar{\rho}} - a^{(\nabla,0)}(p, \delta \mathbf{u})_{\bar{\gamma}} - a^{0\Gamma}(p_h, \delta \mathbf{u}_h)_c = 0 \quad \forall \delta \mathbf{u}_h \in \mathcal{V}_h^u, \\ b^\nabla(p_h, \delta p_h)_{1/\bar{\rho}_{\text{eq}}} - \omega^2 b^0(p_h, \delta p_h)_{1/\bar{K}_{\text{eq}}} - \omega^2 a^{(\nabla,0)}(\delta p_h, \mathbf{u}_h)_{\bar{\gamma}} - a^{0\Gamma}(\mathbf{u}_h, \delta p_h)_c + \\ j\omega b^{0\Gamma}(p_h, \delta p_h)_{\frac{1}{z(\theta)}} = 0, \quad \forall \delta p_h \in \mathcal{V}_h^p, \end{cases} \quad (2.165)$$

Primary Domain	Neighbour Domain	Boundary Integrals
Poroelastic	Acoustic	$I_1 = 0$ $I_2 = 0$ $I_1 = - \int c(\mathbf{p}\mathbb{I} \cdot \mathbf{n}) \cdot \delta \mathbf{u} \, d\Gamma$
Poroelastic	Elastic	$I_2 = -\omega^2 \int_{\Gamma_t} \mathbf{c} \mathbf{u} \cdot \mathbf{n} \, \delta p \, d\Gamma$
Poroelastic	Poroelastic	$I_1 = 0$ $I_2 = 0$

Table 2.3: Interface coupling integrals.

Figure 2.12: Discretized domain Ω_h decomposed into n_{el} quadrilateral elements.

where $a^{(\cdot)}(\cdot, \cdot)_{(\cdot)}$ and $b^{(\cdot)}(\cdot, \cdot)_{(\cdot)}$ represent bilinear functional operators, which assume the following for the solid phase

$$a^\varepsilon(\mathbf{u}_h, \delta \mathbf{u}_h) = \int_{\Omega_h} \boldsymbol{\sigma}_s(\mathbf{u}_h) : \boldsymbol{\varepsilon}_s(\delta \mathbf{u}_h) \, d\Omega, \quad (2.166a)$$

$$a^0(\mathbf{u}_h, \delta \mathbf{u}_h)_{\tilde{\rho}} = \int_{\Omega_h} \tilde{\rho} \mathbf{u}_h \cdot \delta \mathbf{u}_h \, d\Omega, \quad (2.166b)$$

and the fluid phase

$$b^\nabla(p_h, \delta p)_{\frac{1}{\tilde{\rho}_{eq}}} = \int_{\Omega_h} \frac{1}{\tilde{\rho}_{eq}} \nabla p_h \cdot \nabla \delta p_h \, d\Omega, \quad (2.167a)$$

$$b^0(p_h, \delta p_h)_{\frac{1}{\tilde{K}_{eq}}} = \int_{\Omega_h} \frac{1}{\tilde{K}_{eq}} p_h \delta p_h \, d\Omega, \quad (2.167b)$$

$$b^{0\Gamma}(p_h, \delta p_h)_{\frac{1}{z(\theta)}} = \int_{\Gamma_{hr}} \frac{1}{z(\theta)} p_h \delta p_h \, d\Gamma, \quad (2.167c)$$

and for phase coupling

$$a^{(\nabla, 0)}(p_h, \delta \mathbf{u}_h)_{\tilde{\gamma}} = \int_{\Omega_h} \tilde{\gamma} \nabla p_h \cdot \delta \mathbf{u}_h \, d\Omega, \quad (2.168a)$$

$$a^{0\Gamma}(\mathbf{p}_h, \delta \mathbf{u}_h)_c = \int_{\Gamma_{ht}} c(\mathbf{p}_h \mathbb{I} \cdot \mathbf{n}) \cdot \delta \mathbf{u}_h \, d\Gamma. \quad (2.168b)$$

The fluid phase contribution $a^{0\Gamma}(\mathbf{u}_h, \delta \mathbf{p}_h)_c$ from Eq. (2.165) is evaluated as shown in Eq. (2.168b). However, the integration is performed over Γ_{hq} . Additionally, it is to be noted that the boundary forms $a^{0\Gamma}(\mathbf{p}_h, \delta \mathbf{u}_h)_c$ and $b^{0\Gamma}(\mathbf{p}_h, \delta \mathbf{p}_h)$ are obtained as generalizations of the boundary and interface conditions provided in Tables 2.2-2.3.

In Eqs. (2.166)-(2.168), the domain Ω_h is the discretized approximation of the original domain geometry, with non-intersecting quadrilateral sub-domains as shown in Fig. 2.12. As before, the discretized boundaries Γ_{hu} , Γ_{ht} , Γ_{hp} , Γ_{hq} and Γ_{hr} are also obtained in a similar way.

Using Eq. (2.95), the bilinear forms of Eqs. (2.166a)-(2.168b) can be additively assembled from elemental contributions for the solid phase, i.e.,

$$a^\varepsilon(\mathbf{u}_h, \delta \mathbf{u}_h) = \sum_{i=1}^{n_{el}} a_{\mathcal{K}_i}^\varepsilon(\mathbf{u}_h, \delta \mathbf{u}_h), \quad (2.169a)$$

$$a^0(\mathbf{u}_h, \delta \mathbf{u}_h)_{\bar{\rho}} = \sum_{i=1}^{n_{el}} a_{\mathcal{K}_i}^0(\mathbf{u}_h, \delta \mathbf{u}_h)_{\bar{\rho}}, \quad (2.169b)$$

for the fluid phase

$$b^\nabla(\mathbf{p}_h, \delta \mathbf{p}_h)_{\frac{1}{\bar{\rho}_{eq}}} = \sum_{i=1}^{n_{el}} b_{\mathcal{K}_i}^\nabla(\mathbf{p}_h, \delta \mathbf{p}_h)_{\frac{1}{\bar{\rho}_{eq}}}, \quad (2.170a)$$

$$b^0(\mathbf{p}_h, \delta \mathbf{p}_h)_{\frac{1}{\bar{K}_{eq}}} = \sum_{i=1}^{n_{el}} b_{\mathcal{K}_i}^0(\mathbf{p}_h, \delta \mathbf{p}_h)_{\frac{1}{\bar{K}_{eq}}}, \quad (2.170b)$$

$$b^{0\Gamma}(\mathbf{p}_h, \delta \mathbf{p}_h)_{\frac{1}{z}} = \sum_{i=1}^{n_{el}} b_{\mathcal{K}_i}^{0\Gamma}(\mathbf{p}_h, \delta \mathbf{p}_h)_{\frac{1}{z}}, \quad (2.170c)$$

and for phase coupling

$$a^{(\nabla,0)}(\mathbf{p}_h, \delta \mathbf{u}_h)_{\bar{\gamma}} = \sum_{i=1}^{n_{el}} a_{\mathcal{K}_i}^{(\nabla,0)}(\mathbf{p}_h, \delta \mathbf{u}_h)_{\bar{\gamma}}, \quad (2.171a)$$

$$a^{0\Gamma}(\mathbf{p}_h, \delta \mathbf{u}_h)_c = \sum_{i=1}^{n_{el}} a_{\mathcal{K}_i}^{0\Gamma}(\mathbf{p}_h, \delta \mathbf{u}_h)_c. \quad (2.171b)$$

The elemental contributions in Eqs. (2.169) - (2.171) assume the following forms for the solid phase

$$a_{\mathcal{K}_i}^\varepsilon(\mathbf{u}_h, \delta \mathbf{u}_h) = \int_{\mathcal{K}_i} \boldsymbol{\sigma}_s(\mathbf{u}_h) : \boldsymbol{\varepsilon}_s(\delta \mathbf{u}_h) \, d\Omega, \quad (2.172a)$$

$$a_{\mathcal{K}_i}^0(\mathbf{u}_h, \delta \mathbf{u}_h)_{\bar{\rho}} = \int_{\mathcal{K}_i} \tilde{\rho} \mathbf{u}_h \cdot \delta \mathbf{u}_h \, d\Omega, \quad (2.172b)$$

fluid phase

$$b_{\mathcal{K}_i}^{\nabla}(\mathbf{p}_h, \delta \mathbf{p}_h)_{\frac{1}{\tilde{\rho}_{\text{eq}}}} = \int_{\mathcal{K}_i} \frac{1}{\tilde{\rho}_{\text{eq}}} \nabla \mathbf{p}_h \cdot \nabla \delta \mathbf{p}_h \, d\Omega, \quad (2.173a)$$

$$b_{\mathcal{K}_i}^0(\mathbf{p}_h, \delta \mathbf{p}_h)_{\frac{1}{\tilde{K}_{\text{eq}}}} = \int_{\mathcal{K}_i} \frac{1}{\tilde{K}_{\text{eq}}} \mathbf{p}_h \delta \mathbf{p}_h \, d\Omega, \quad (2.173b)$$

$$b_{\mathcal{K}_i}^{0\Gamma}(\mathbf{p}_h, \delta \mathbf{p}_h)_{\frac{1}{z(\theta)}} = \int_{\Gamma_{hr}^{\mathcal{K}_i}} \frac{1}{z(\theta)} \mathbf{p}_h \delta \mathbf{p}_h \, d\Gamma, \quad (2.173c)$$

and coupling terms

$$a_{\mathcal{K}_i}^{(\nabla,0)}(\mathbf{p}_h, \delta \mathbf{u}_h)_{\tilde{\gamma}} = \int_{\mathcal{K}_i} \tilde{\gamma} \nabla \mathbf{p}_h \cdot \delta \mathbf{u}_h \, d\Omega, \quad (2.174a)$$

$$a_{\mathcal{K}_i}^{0\Gamma}(\mathbf{p}_h, \delta \mathbf{u}_h)_c = \int_{\Gamma_{ht}^{\mathcal{K}_i}} c(\mathbf{p}_h \mathbb{I} \cdot \mathbf{n}) \cdot \delta \mathbf{u}_h \, d\Gamma. \quad (2.174b)$$

The discretized field variables in Eq. (2.98) are now inserted into the elemental integral forms for the solid phase in Eqs. (2.169) to yield an elastic stiffness term

$$a_{\mathcal{K}_i}^{\varepsilon}(\mathbf{u}_h, \delta \mathbf{u}_h) = \delta \hat{\mathbf{u}}^T \underbrace{\left[\int_{\mathcal{K}_i} \mathbf{B}^{uT} \tilde{\mathbb{D}} \mathbf{B}^u \, d\Omega \right]}_{\tilde{\mathbf{K}}_{\mathcal{K}_i}} \hat{\mathbf{u}}. \quad (2.175)$$

An elastic mass term is also retrieved

$$a_{\mathcal{K}_i}^0(\mathbf{u}_h, \delta \mathbf{u}_h)_{\tilde{\rho}} = \delta \hat{\mathbf{u}}^T \underbrace{\left[\int_{\mathcal{K}_i} \Phi^{uT} \tilde{\rho} \Phi^u \, d\Omega \right]}_{\tilde{\mathbf{M}}_{\mathcal{K}_i}} \hat{\mathbf{u}}. \quad (2.176)$$

Similarly, expressions for the fluid phase are established by substituting Eq. (2.117) into Eqs. (2.170). The fluid kinetic terms assumes the form

$$b_{\mathcal{K}_i}^{\nabla}(\mathbf{p}_h, \delta \mathbf{p}_h)_{\frac{1}{\tilde{\rho}_{\text{eq}}}} = \delta \hat{\mathbf{p}}^T \underbrace{\left[\int_{\mathcal{K}_i} \nabla \Phi^{pT} \frac{1}{\tilde{\rho}_{\text{eq}}} \nabla \Phi^p \, d\Omega \right]}_{\tilde{\mathbf{H}}_{\mathcal{K}_i}} \hat{\mathbf{p}}, \quad (2.177)$$

and the fluid compressibility term

$$b_{\mathcal{K}_i}^0(\mathbf{p}_h, \delta \mathbf{p}_h)_{\frac{1}{\tilde{K}_{\text{eq}}}} = \delta \hat{\mathbf{p}}^T \underbrace{\left[\int_{\mathcal{K}_i} \Phi^{pT} \frac{1}{\tilde{K}_{\text{eq}}} \Phi^p \, d\Omega \right]}_{\tilde{\mathbf{Q}}_{\mathcal{K}_i}} \hat{\mathbf{p}}. \quad (2.178)$$

Finally, following the same procedure, the phase coupling term Eq. (2.171) reads

$$a_{\mathcal{K}_i}^{(\nabla,0)}(\mathbf{p}_h, \delta \mathbf{u}_h)_{\tilde{\gamma}} = \delta \hat{\mathbf{p}}^T \underbrace{\left[\int_{\mathcal{K}_i} \nabla \Phi^p T \tilde{\gamma} \Phi^u d\Omega \right]}_{\tilde{\mathbf{C}}_{\mathcal{K}_i}} \hat{\mathbf{u}}. \quad (2.179)$$

The local state matrices are assembled into their global forms as before, using a direct approach as done in earlier sections

$$\tilde{\mathbf{K}} = \underset{i=1}{\overset{n_{el}}{\mathbf{A}}} \tilde{\mathbf{K}}_{\mathcal{K}_i}, \quad \tilde{\mathbf{M}} = \underset{i=1}{\overset{n_{el}}{\mathbf{A}}} \tilde{\mathbf{M}}_{\mathcal{K}_i}, \quad \tilde{\mathbf{H}} = \underset{i=1}{\overset{n_{el}}{\mathbf{A}}} \tilde{\mathbf{H}}_{\mathcal{K}_i}, \quad \tilde{\mathbf{Q}} = \underset{i=1}{\overset{n_{el}}{\mathbf{A}}} \tilde{\mathbf{Q}}_{\mathcal{K}_i}, \quad \tilde{\mathbf{C}} = \underset{i=1}{\overset{n_{el}}{\mathbf{A}}} \tilde{\mathbf{C}}_{\mathcal{K}_i}. \quad (2.180)$$

The boundary terms in Eqs. (2.173c) and (2.174b) are also computed in a similar fashion to yield the following matrices

$$\tilde{\mathbf{A}}_{\mathcal{K}} = \int_{\Gamma_{hr}^{\mathcal{K}}} \frac{1}{z(\theta)} \Phi^p \cdot \Phi^p d\Gamma, \quad (2.181a)$$

$$\tilde{\mathbf{S}}_{\mathcal{K}} = \int_{\Gamma_{ht}^{\mathcal{K}}} c(\Phi^p \cdot \mathbf{n}) \cdot \Phi^u d\Gamma, \quad (2.181b)$$

where $\tilde{\mathbf{A}}_{\mathcal{K}}$ denotes a local admittance matrix encountered over Robin boundary $\Gamma_{hr}^{\mathcal{K}}$ (see Eq. (2.173c)). Matrix $\tilde{\mathbf{S}}_{\mathcal{K}}$ denotes a local fluid-structure coupling matrix encountered at an interface (see Eq. (2.174b)). Similar to Eq. (2.180), these integrals are assembled over the relevant boundaries Γ_{hr} , Γ_{ht} , Γ_{hq} to yield global boundary matrices

$$\tilde{\mathbf{A}} = \underset{i}{\mathbf{A}} \tilde{\mathbf{A}}_{\mathcal{K}(i)}, \quad \tilde{\mathbf{S}} = \underset{i}{\mathbf{A}} \tilde{\mathbf{S}}_{\mathcal{K}(i)}. \quad (2.182)$$

The discretized version of the weak form in Eqs. (2.145)-(2.146) is written as a coupled system of linear equations in matrix form

$$\underbrace{\begin{bmatrix} \tilde{\mathbf{K}} - \omega^2 \tilde{\mathbf{M}} & -(\tilde{\mathbf{C}} + \tilde{\mathbf{S}}) \\ -\omega^2 (\tilde{\mathbf{C}}^T + \tilde{\mathbf{S}}^T) & \tilde{\mathbf{H}} + j\omega \tilde{\mathbf{A}} - \omega^2 \tilde{\mathbf{Q}} \end{bmatrix}}_{\tilde{\mathbf{Z}}} \underbrace{\begin{Bmatrix} \hat{\mathbf{u}} \\ \hat{\mathbf{p}} \end{Bmatrix}}_{\tilde{\mathbf{X}}} = \underbrace{\begin{bmatrix} \mathbf{f}^u \\ \mathbf{f}^p \end{bmatrix}}_{\tilde{\mathbf{F}}}, \quad (2.183)$$

where \mathbf{f}^u and \mathbf{f}^p are load terms for either phase. It has already been shown in Section 2.7.3 that all coupling and support conditions yield either zero-value boundary integrals or forms that are bilinear in nature, (see Tables 2.2-2.3). Furthermore, since only acoustic excitations are considered for this work, it is reasonable to allow $\mathbf{f}^u = \mathbf{0}$ and $\mathbf{f}^p = \mathbf{0}$. These excitations are imposed as Dirichlet pressures.

It is worth noting that despite Eq. (2.183) being linear in $\hat{\mathbf{u}}$ and $\hat{\mathbf{p}}$, it exhibits an explicit parametric non-linearity with respect to ω . Implicit material non-linearities are encountered in the global state matrices through their complex frequency-dependent material parameters, see, e.g, Eqs. (2.85)-(2.86) for the JCAL model.

Owing to the spectral nature of the problem, multiple solutions to Eq. (2.183) are required

over a desired frequency bandwidth to sufficiently characterize the vibroacoustic behaviour of the system. It is possible to significantly reduce the assembly time by exploiting the affine nature of the governing equations. This is done by assembling the global state matrices only once without the implicit frequency-dependent content; this can be post-multiplied during the solution stage.

2.7.4 Computing acoustic indicators

The complex valued surface impedance at the incident face normalized with respect to the impedance of air $z(\theta)$ is computed

$$Z_{\text{sn}\mathcal{K}}(\omega, \theta) = \left(\frac{p_{\mathcal{K}}^{\text{in}}}{v_{n\mathcal{K}}^{\text{in}}} \right)_{\Gamma_{hI}^{\mathcal{K}}} / z(\theta) \quad (2.184)$$

where $p_{\mathcal{K}}^{\text{in}}$ and $v_{n\mathcal{K}}^{\text{in}}$ denote inlet pressures and normal component of fluid velocities over the elementary incident face $\Gamma_{hI}^{\mathcal{K}}$. This quantity is now used to obtain the elementary coefficient of reflection

$$R_{\mathcal{K}}(\omega, \theta) = \frac{Z_{\text{sn}\mathcal{K}}(\omega, \theta) - 1}{Z_{\text{sn}\mathcal{K}}(\omega, \theta) + 1} \quad (2.185)$$

As the FEM computes only resultant quantities (the net incident and reflected waves), one requires $R_{\mathcal{K}}(\omega, \theta)$ to obtain purely incident pressures and normal fluid velocities over $\Gamma_{hI}^{\mathcal{K}}$

$$p_{\mathcal{K}}^{\text{inc}} = \left| \frac{p_{\mathcal{K}}^{\text{in}}}{1 + R_{\mathcal{K}}(\omega, \theta)} \right|_{\Gamma_{hI}^{\mathcal{K}}}, \quad v_{n\mathcal{K}}^{\text{inc}} = \frac{p_{\mathcal{K}}^{\text{inc}}}{z(\theta)}. \quad (2.186)$$

The time averaged powers are evaluated according to Eqs. (2.187) below

$$\mathbb{W}^{\text{in}}(\omega, \theta) = \frac{1}{2} \Re \left(\int_{\Gamma_{hI}} p^{\text{in}} \cdot v_n^{\text{in}*} d\Gamma \right) = \frac{1}{2} \Re \left(\sum_i \int_{\Gamma_{hI}^{\mathcal{K}(i)}} p_{\mathcal{K}(i)}^{\text{in}} \cdot v_{n\mathcal{K}(i)}^{\text{in}*} d\Gamma \right), \quad (2.187a)$$

$$\mathbb{W}^{\text{inc}}(\omega, \theta) = \frac{1}{2} \int_{\Gamma_{hI}} p^{\text{inc}} \cdot v_n^{\text{inc}} d\Gamma = \frac{1}{2} \sum_i \int_{\Gamma_{hI}^{\mathcal{K}(i)}} p_{\mathcal{K}(i)}^{\text{inc}} \cdot v_{n\mathcal{K}(i)}^{\text{inc}} * d\Gamma, \quad (2.187b)$$

$$\mathbb{W}^{\text{ref}}(\omega, \theta) = \mathbb{W}^{\text{inc}}(\omega, \theta) - \mathbb{W}^{\text{in}}(\omega, \theta), \quad (2.187c)$$

$$\mathbb{W}^{\text{trans}}(\omega, \theta) = \frac{1}{2} \Re \left(\int_{\Gamma_{hO}} p^{\text{out}} \cdot v_n^{\text{out}*} d\Gamma \right) = \frac{1}{2} \Re \left(\sum_i \int_{\Gamma_{hO}^{\mathcal{K}(i)}} p_{\mathcal{K}(i)}^{\text{out}} \cdot v_{n\mathcal{K}(i)}^{\text{out}*} d\Gamma \right), \quad (2.187d)$$

where \mathbb{W}^{in} , \mathbb{W}^{inc} , \mathbb{W}^{ref} and $\mathbb{W}^{\text{trans}}$ represent inlet, incident, reflected and transmitted powers, respectively. The operator $\Re(\cdot)$ extracts real valued data, Complex conjugation is denoted by $(*)$. Outlet fluid pressures and normal components of fluid velocity $p_{\mathcal{K}(i)}^{\text{out}}$ and $v_{n\mathcal{K}(i)}^{\text{out}}$ are evaluated over an elementary outlet face $\Gamma_{hO}^{\mathcal{K}(i)}$. The SAC and STL are finally derived for a plane wave incident at an angle θ with a driving angular frequency of ω

$$\alpha(\omega, \theta) = 1 - \frac{\mathbb{W}^{\text{ref}}(\omega, \theta)}{\mathbb{W}^{\text{inc}}(\omega, \theta)}, \quad \mathcal{T}(\omega, \theta) = 10 \log \frac{\mathbb{W}^{\text{inc}}(\omega, \theta)}{\mathbb{W}^{\text{trans}}(\omega, \theta)}. \quad (2.188)$$

For a detailed report investigating the post-processing procedures involved in structural and porous vibroacoustics, see, e.g., [57], [13].

Experimental validation

The following example is provided to validate the implementation of the numerical models detailed in this chapter. An anechoic wedge constituted of melamine foam is placed within an impedance tube. The macroscopic material parameters are provided as Material ID III in Table 3.7. The JCAL model (see Eqs. (2.85)-(2.86)) is used to obtain the equivalent dynamic bulk modulus and mass density.

The geometry is parametrised by the length of the wedge proper $L = 630$ mm, the heel $H = 380$ mm, and a width of $D = 300$ mm. The wedge is backed by an air plenum of thickness $P = 100$ mm. This configuration is illustrated in Fig. 2.13.

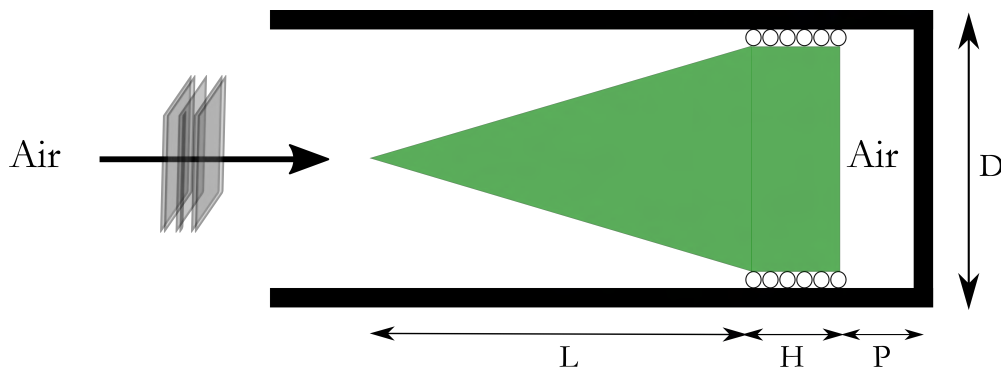


Figure 2.13: A schematic of an anechoic wedge placed within an impedance tube with air backing. $L = 630$ mm, $H = 380$ m, $P = 100$ mm, $D = 300$ mm.

The lateral edges are provided with roller supports. The setup is subject to a plane wave acoustical excitation impinging at normal incidence. The frequency bandwidth of the excitation is $f = [20, 500]$ Hz.

The entire geometry is modelled using 5000 quadrilateral plane strain elements. Assuming a deformable elastic skeleton, Eqs. (2.183) is solved to obtain displacements and pressures at 50 frequency steps. These steps are equally spaced between 20 and 500 Hz. Next, the SAC is evaluated as shown in Section 2.7.4. The resulting curve is compared against an experimentally measured result (obtained from [7]) in Fig. 2.14.

The curves obtained agree very well across the entire bandwidth. This shows that the FE model described in this Chapter can describe the vibroacoustic behaviour of poroelastic materials with sufficient accuracy.

2.8 Summary

In this Chapter, a motivation to study poroelasticity was established along with a review of different physical and mathematical models. The governing equations for porous consolidation and wave propagation were developed from first principles. Finally, the FEM procedure was provided in detail for elastostatics, consolidation and vibroacoustics. Caveats with respect to boundary

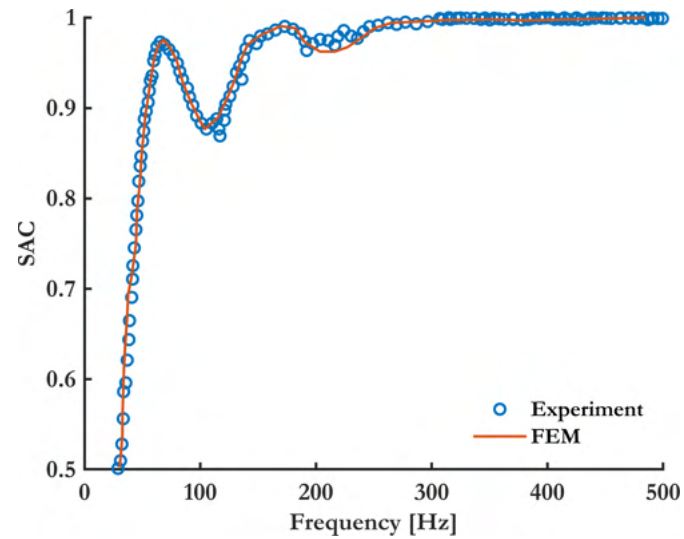


Figure 2.14: Sound Absorption Coefficients calculated for a poroelastic anechoic wedge with air backing.

conditions and interface coupling constraints were discussed. In the next chapter, the limitations of the FEM will be discussed. Several competing element formulations will be reviewed and the Virtual Element Method procedure will be applied to the governing equations derived herein.

Part II

Fine scale Methods

Chapter 3

Virtual Element Methods

In this Chapter, a novel Virtual Element Method (VEM) is developed to resolve the mixed Biot displacement pressure formulation governing wave propagation in porous media. Within this setting, the weak form of the governing equations is discretized using implicitly defined canonical basis functions and the resulting integral forms are computed using appropriate polynomial projections. The projection operator accounting for the solid, fluid, and coupling phases of the problem are presented. Different boundary, interface and excitation conditions are accounted for. The convergence behaviour, accuracy, and efficiency of the method is examined through a set of illustrative examples. A node insertion strategy is proposed to resolve non-conforming interfaces that naturally arise in multilayered systems. Finally the power of the VEM is exploited to examine the acoustic response of composite materials with periodic and non-periodic inclusions of complex geometries.

3.1 Overview on Element Formulations

Solving the aforementioned equations using classical finite-element techniques involves meshing the domain with quadrilateral or triangular elements. Using such elements to resolve complex shaped mesoscale heterogeneous morphologies necessitate fine resolutions, thus rendering the problem expensive. Optimal mesh discretizations would aid in augmenting the efficiency of the method. This motivates the investigation of numerical techniques that can handle flexible element geometries.

Polygonal finite elements PFEM [58–60] are used in a wide range of applications where one encounters complicated interface and inclusion geometries as in the case of e.g., topology and shape optimization [61, 62], fracture and damage modelling [63–65], contact mechanics [66], and fluid-structure interaction problems [67]. Defining shape functions over arbitrary polygonal domains is an active field of research and encompasses a large family of approaches. These include Wachspress [68, 69], natural neighbour [70, 71], mean-value coordinate [72, 73] and maximum entropy [74, 75] shape functions. A detailed summary collating advances in these polygonal shape functions is provided in [76]. The method involves treating these typically non-polynomial functions with special numerical schemes [77], or standard quadrature rules over sub-triangulated domains. Sub-optimal convergence rates are observed due to the errors arising from numerical integration of complicated non-polynomial functions. Employing higher quadrature rules to minimize this error

can significantly drive up computational costs, especially in problems where iterative solutions are necessary, e.g., spectral problems, time domain analysis, topology optimization etc. The Virtual Element Method (VEM) [11, 78–83] is a relatively recent technique introduced into the computational mechanics community to specifically address these shortcomings.

The method naturally emerged from advances in Mimetic Finite Difference (MFD) methods [84–89]. MFDs, when used in conjunction with the Finite Element Method, seek to model trial and test functions spaces without resorting to explicit representations of basis functions over the element interior. When extended to non-standard element geometries, the accuracy of the method is improved by enriching the function spaces with possibly non-polynomial expressions. The basis functions, which are allowed to assume complex non-polynomial forms, are implicitly defined through carefully chosen degrees of freedom. This implicit representation does away with the problem of analytically or numerically deriving basis functions over complex element domains. A significant point of departure of the VEM from MFDs lies in VEM’s attempt to preserve polynomial accuracy over element boundaries [11]. This allows for extension to more generalized inter-element continuity and conformity requirements [90]. Extensions to curved geometries is a new development [91–93]. This method is being applied extensively in fracture mechanics [94–96], modelling of structures [97–99], topology and shape optimization [62], different problems in elasticity [100–104], contact and micro-mechanics [105, 106], composite materials [107], sound propagation in solid or fluid, i.e., uncoupled, domains [108, 109] and very recently in electromagneto-mechanical couplings [110]. The VEM has been used in [111] to treat solid domains for reservoir modelling, considering also the case of fracture propagation [112] using a combined Discrete Element-Virtual Element approach. With regards to fluid domains, the case of Darcy and Brinkman flow has been addressed using the VEM in [113, 114]. Other miscellaneous applications have been addressed in [115–122].

Mixed VEM formulations have emerged over the past years to address elliptic problems [79, 123, 124]. This paved the way for extended applications in poromechanics such as mixed finite-volume discretizations [125] and three field formulations for the Biot consolidation equations [126, 127]. Very recently, multiphase problems pertaining to miscible fluids have been treated in [128]. A hybridised MFD-VEM has been developed for a similar application in [129] considering the case of Darcy flow in elastic domains under quasi-static loading conditions. Further to the current state-of-the-art, in this work the power of the VEM is harnessed vis-à-vis its ability to resolve complex geometries and examine the case of wave propagation in poroelastic domains considering all the pertinent inertial and viscous terms arising from the solid to fluid couplings; this is a direction not yet explored in the literature.

Several competing approaches exist, such as the Scaled Boundary Finite Element Method (SBFEM) [130–135], where a local polar coordinate system is introduced. The field under consideration is only discretized along the tangential boundary; an analytical expression is provided over the radial direction. This reduces the dimensionality of the problem by one. The method imposes a star-convexity constraint on the element. It has found several applications in crack propagation [136–140] and acoustics [141, 142].

The advent of Partition of Unity methods (PUM) [143–146] allows for an enrichment of the solution space, to induce higher convergence rates. This has found significant application in acoustics in the form the Partition of Unity Finite Element Method (PUFEM) [147–150], where each standard Lagrange polynomial shape function is expanded into a linear combination of plane waves.

Conversely, the ability to use the PU functions for local enrichment has driven its applications in fracture in the form of eXtended Finite Element Methods (XFEM) [151–156] and Generalised Finite Element Methods (GFEM) [143, 157, 158]. For a more detailed review on the PUFEM, XFEM and GFEM, the reader is referred to the review publications [138, 159–163] .

Within the context of exterior acoustic problems, the Boundary Element Method (BEM) [164–168] is used almost ubiquitously within the vibroacoustics community to obtain efficient solution procedures. The weak form of the governing equations are moved to the domain boundary, as the name suggests, with the help of fundamental solutions, also known as Green’s functions. This helps reduce the physical dimensionality of the problem by one, thereby reducing the complexity of the problem. However, when dealing with geometries that move beyond classical shapes, a larger number of boundary elements are required to achieve accurate representations, e.g., a curved exterior.

Modern techniques like Isogeometric Analysis (IGA) [169–171] have paved the way for exact boundary representations by replacing traditional polynomial shape functions with flexible alternatives derived from Computer Aided Design, such as Bézier curves, Non Uniform Rational B-Splines, T-Splines etc. Mesh dependent and mesh-free techniques, such as the Galerkin [172–174] and Collocation [175–177] IGA have been successfully coupled with the BEM to achieve efficient discretizations in complex structures. The IGA-BEM has found applications in other fields such as transport and flow problems [178–181] and shape optimization [182–185] as well.

In this Chapter, the fundamentals of the VEM are laid out in Section 3.2. This is then applied as a first step to elastostatics in Section 3.3. Details concerning projectors, consistency and stability matrices etc. are discussed here. This is further extended to consolidation in Section 3.4. Distinctions between computing \mathcal{H}_1 and \mathcal{L}_2 projectors are made here. Next, the VEM discretization is originally formulated for vibroacoustics in Section 3.5. Finally, this is applied to industry relevant numerical examples in Section 3.6.

3.2 Virtual Element Spaces

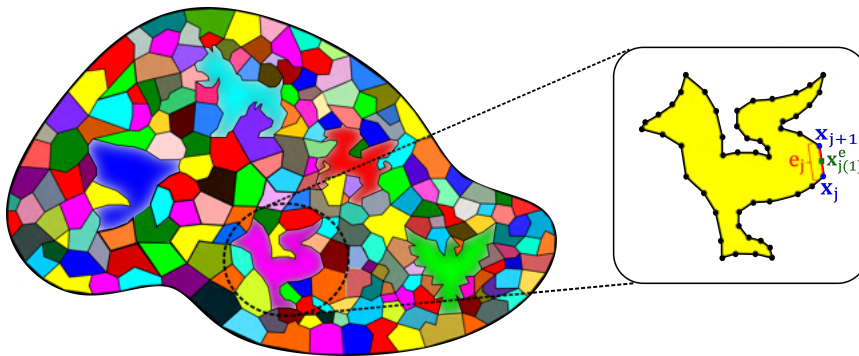


Figure 3.1: Discretized domain Ω_h decomposed into n_{el} arbitrary potentially non-convex polygonal elements. An example chicken element with $N_v = 51$ edges adapted from [62] is shown. The j th edge e_j connects vertex nodes \mathbf{x}_j and \mathbf{x}_{j+1} . A single edge node $\mathbf{x}_{j(1)}^e$ is also illustrated.

Contrary to the discretization provided in Eq. (2.95), here, \mathcal{K}_i , $i = 1, \dots, n_{el}$ correspond to non-intersecting polygonal sub-domains, i.e., virtual elements as shown in Fig. 3.1. An arbitrary element is also shown in Fig. 3.1 with polynomial order $k \geq 1$. The vertex coordinates are given

by \mathbf{x}_j , $j = 1, \dots, N_v$, where N_v is the number of edges; this equals the number of vertices. Each edge e_j , $j = 1, \dots, N_v$ connects vertices \mathbf{x}_j and \mathbf{x}_{j+1} and contains $k - 1$ internal nodes per edge. These internal nodes are labelled \mathbf{x}^e .

To accommodate element domains \mathcal{K}_i of arbitrary shapes, the VEM seeks to avoid explicit definitions of these basis functions. To facilitate this, certain restricting assumptions on the approximating subspace $\mathcal{V}_h^{\mathcal{K}}(\mathcal{K})$ need to be relaxed. This is done by enlarging the space to allow for potentially non-polynomial function definitions over the element interior. The associated enrichments provide desirable stabilisation properties and correctly capture the relevant kinematic modes of the element. Within this setting, the space $\mathcal{V}_h^{\mathcal{K}}(\mathcal{K})$ is defined as

$$\mathcal{V}_h^{\mathcal{K}}(\mathcal{K}) = \{v \in [\mathcal{H}^1(\mathcal{K}) \cap C^0(\mathcal{K})] : v_{,i}|_e \in \mathbb{P}_k(e) \forall e \in \partial\mathcal{K} ; \Delta v_{,i}|_{\mathcal{K}} \in \mathbb{P}_{k-2}(\mathcal{K}), \text{ for } i = 1, \dots, d\}, \quad (3.1)$$

where $\mathbb{P}_k(\mathcal{K})$ denotes a k_{th} order polynomial space, which is spanned by appropriately defined monomials, and d denotes the physical dimensionality of the problem. The subspaces $[\mathbb{P}_k(\mathcal{K})]^2$ and $[\mathbb{P}_k(\mathcal{K})]$ are spanned by vector and scalar valued scaled monomials belonging to $[\mathbb{M}_k(\mathcal{K})]^2$ and $[\mathbb{M}_k(\mathcal{K})]$, respectively. The members of these monomial spaces are provided in Table 3.1.

Polynomial order	$\mathbb{M}_k(\mathcal{K})$	$[\mathbb{M}_k(\mathcal{K})]^2$
$k = 0$	$\mathbb{M}_0(\mathcal{K}) = \{1\}$	$[\mathbb{M}_0(\mathcal{K})]^2 = \left\{ \begin{Bmatrix} 1 \\ 0 \end{Bmatrix}, \begin{Bmatrix} 0 \\ 1 \end{Bmatrix} \right\}$
arbitrary order k	$\mathbb{M}_k(\mathcal{K}) = \left\{ \begin{array}{l} \mathbb{M}_{k-1}(\mathcal{K}), \\ \xi^{k-1}\eta, \dots, \eta^k \end{array} \right\}$	$[\mathbb{M}_k(\mathcal{K})]^2 = \left\{ \begin{array}{l} [\mathbb{M}_{k-1}(\mathcal{K})]^2, \begin{Bmatrix} \xi^k \\ 0 \end{Bmatrix}, \\ \begin{Bmatrix} 0 \\ \xi^k \end{Bmatrix}, \begin{Bmatrix} \xi^{k-1}\eta \\ 0 \end{Bmatrix}, \begin{Bmatrix} 0 \\ \xi^{k-1}\eta \end{Bmatrix}, \\ \dots, \begin{Bmatrix} \eta^k \\ 0 \end{Bmatrix}, \begin{Bmatrix} 0 \\ \eta^k \end{Bmatrix} \end{array} \right\}$

Table 3.1: Generalized scalar and vector valued monomials for $\mathbb{M}_k(\mathcal{K})$ and $[\mathbb{M}_k(\mathcal{K})]^2$, respectively.

Here, $\xi = \frac{x-x_{\mathcal{K}}}{h_{\mathcal{K}}}$ and $\eta = \frac{y-y_{\mathcal{K}}}{h_{\mathcal{K}}}$ denote scaled monomials in each parametric direction. The number of terms in $[\mathbb{M}_k(\mathcal{K})]^2$ and $[\mathbb{M}_k(\mathcal{K})]$ are $n_k^u = (k+1)(k+2)$ and $n_k^p = \frac{(k+1)(k+2)}{2}$, respectively.

A significant point of departure from the FEM consists in a two-fold observation of Eq. (3.1). First, the VEM space $\mathcal{V}_h^{\mathcal{K}}(\mathcal{K})$ no longer requires its members to have exclusively polynomial definitions over the element interior. Second, the members are implicitly defined through carefully chosen DoFs, as defined in Table 3.2-3.3. The total number of DoFs for each VEM space is $n_{\text{dof}}^u = 2N_vk + k(k-1)$ and $n_{\text{dof}}^p = N_vk + k(k-1)/2$, respectively. This is illustrated in Fig. 3.2 for an element with $N_v = 7$ edges.

From Eq. (3.1), it is to be noted that these generalized non-polynomial functions assume continuous k_{th} order polynomial expressions over the element boundary. These polynomials can be uniquely determined through the corner and edge DoFs. This behaviour is consistent with the classical FEM definition provided in Eq. (2.100). The behaviour of the functions remain unknown within the element interior, except through a condition on its Laplacian, as defined in the area moment DoFs. Owing to the C^0 conforming nature of the method induced by the governing equations, it is sufficient to retain the Laplacian operator, as originally defined for elliptic problems

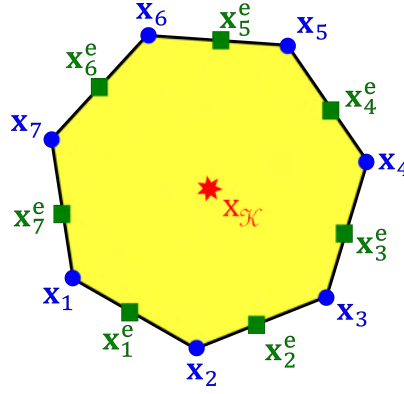


Figure 3.2: VEM DoFs illustrated for a $k = 2$ element with $N_v = 7$. The centroid and element diameter are denoted by \mathbf{x}_K and h_K , respectively. This element contains $n_{\text{dof}}^u = 30$ and $n_{\text{dof}}^p = 15$ displacement and pressure DoFs, respectively.

DoF Type	Location		\mathcal{V}_h^u
		Number of DoFs	Description
Corner	vertices of \mathcal{K}	$N_C^u = 2N_v$	$\mathbf{u}_h(\mathbf{x}_j)$, $j = 1, \dots, N_v$
Edge	internal boundary points on each edge of \mathcal{K}	$N_E^u = 2N_v(k-1)$	$\mathbf{u}_h(\mathbf{x}_j^e)$, $j = 1, \dots, k-1$ for each edge
Area Moment	point lying in interior of domain \mathcal{K}	$N_A^u = 2^{\frac{k(k-1)}{2}}$	$\frac{1}{ \mathcal{K} } \int_{\mathcal{K}} \mathbf{u}_h \cdot \mathbf{m} d\mathcal{K}$ $\forall \mathbf{m} \in [\mathbb{M}_{k-2}(\mathcal{K})]^2$

Table 3.2: Degrees of Freedom for $\mathcal{V}_h^u(\mathcal{K})$. For Area moment, the monomials belong to $[\mathbb{M}_{k-2}(\mathcal{K})]^2$.

in [11]. Stricter conformity requirements, as encountered in higher order problems require different conditions within the element interior [99].

This approach solves the difficulty of providing explicit expressions for element basis functions. This implicit definition justifies the terminology *virtual elements* and *virtual spaces*. These bases are numerically evaluated and visualized in Fig. 3.3 for the heptagonal element defined in Fig. 3.2. They are computed through a sub-scale boundary value problem over the element domain with appropriate kinematic constraints.

3.3 Elastostatics

3.3.1 Virtual approximants at the element level

Following the discretization introduced in Eqs. (2.98), the displacement fields is split into its polynomial and non-polynomial components

DoF Type	Location	\mathcal{V}_h^p	
		Number of DoFs	Description
Corner	vertices of \mathcal{K}	$N_C^p = N_v$	$p_h(\mathbf{x}_j)$, $j = 1, \dots, N_v$
Edge	internal boundary points on each edge of \mathcal{K}	$N_E^p = N_v(k-1)$	$p_h(\mathbf{x}_j^e)$, $j = 1, \dots, k-1$ for each edge
Area Moment	point lying in interior of domain \mathcal{K}	$N_A^p = \frac{k(k-1)}{2}$	$\frac{1}{ \mathcal{K} } \int_{\mathcal{K}} p_h \cdot \mathbf{m} \, d\mathcal{K}$ $\forall \mathbf{m} \in \mathbb{M}_{k-2}(\mathcal{K})$

Table 3.3: Degrees of Freedom for $\mathcal{V}_h^p(\mathcal{K})$. For Area moment, the monomials belong to $\mathbb{M}_{k-2}(\mathcal{K})$.

$$\mathbf{u}_h = \mathbf{u}_h^\pi + (\mathbf{u}_h - \mathbf{u}_h^\pi), \quad \delta \mathbf{u}_h = \delta \mathbf{u}_h^\pi + (\delta \mathbf{u}_h - \delta \mathbf{u}_h^\pi). \quad (3.2)$$

This decomposition is illustrated in Fig. 3.4. The index π in Eqs. (3.2) denotes the polynomial component of the respective field. The polynomial components contain the consistent kinematic modes exhibited by the element. These comprise rigid body and deformation modes.

Inserting Eqs. (3.2) into the definition for the local bilinear operator in Eq. (2.97a), the following relation is obtained

$$a_{\mathcal{K}}^\varepsilon(\mathbf{u}_h, \delta \mathbf{u}_h) = P(a_{\mathcal{K}}^\varepsilon) + NP(a_{\mathcal{K}}^\varepsilon), \quad (3.3)$$

where $P(a_{\mathcal{K}}^\varepsilon)$ contains the polynomial and $NP(a_{\mathcal{K}}^\varepsilon)$ the non-polynomial component of the operator, i.e.,

$$P(a_{\mathcal{K}}^\varepsilon) = a_{\mathcal{K}}^\varepsilon \left(\Pi_k^\varepsilon \mathbf{u}_h, \Pi_k^\varepsilon \delta \mathbf{u}_h \right), \quad (3.4)$$

$$NP(a_{\mathcal{K}}^\varepsilon) = a_{\mathcal{K}}^\varepsilon \left((\mathbf{u}_h - \Pi_k^\varepsilon \mathbf{u}_h), (\delta \mathbf{u}_h - \Pi_k^\varepsilon \delta \mathbf{u}_h) \right). \quad (3.5)$$

In Eq. (3.4), $\Pi_k^\varepsilon : \mathcal{V}_k^u(\mathcal{K}) \rightarrow [\mathbb{P}_k(\mathcal{K})]^2$ denotes an unknown projection operator mapping the unknown field \mathbf{u}_h onto the polynomial space $[\mathbb{P}_k(\mathcal{K})]^2$. This projection operator arises from the fact that the operator $\varepsilon_s(\cdot)$ cannot directly interact with the unknown displacement field as the latter is not explicitly defined.

Naturally, this introduces additional error into the formulation. To minimize this error, the projection operators are computed on the basis of the following orthogonality conditions, i.e.,

$$\Pi_k^\varepsilon := a_{\mathcal{K}}^\varepsilon(\mathbf{u}_h - \Pi_k^\varepsilon \mathbf{u}_h, \mathbf{m}) = 0, \in [\mathbb{P}_k(\mathcal{K})]^2. \quad (3.6)$$

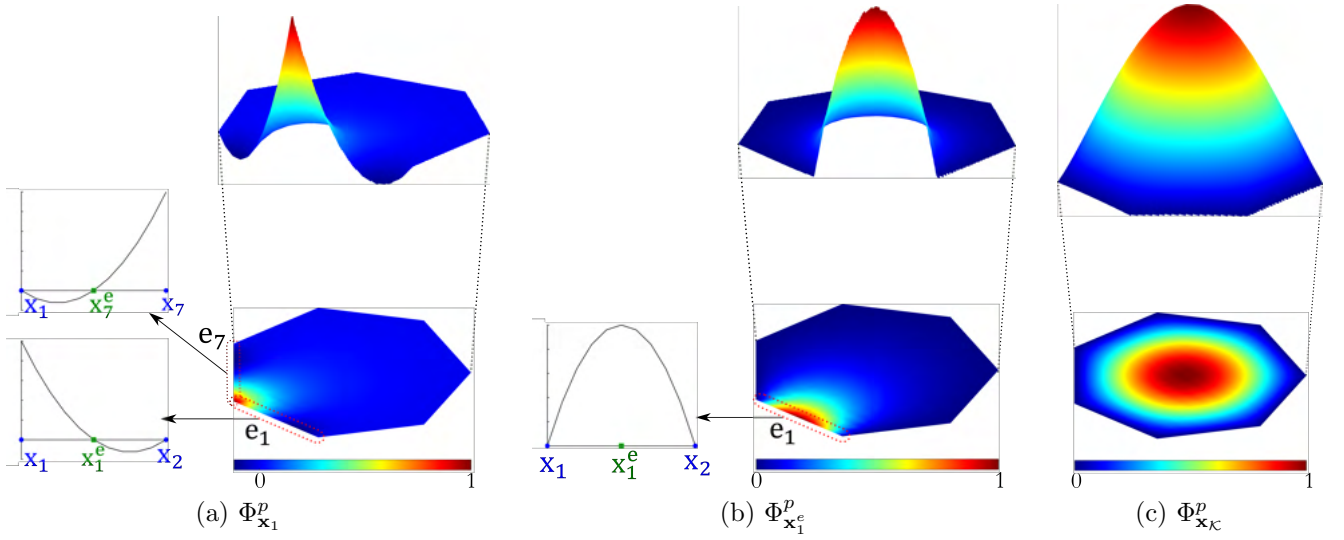


Figure 3.3: Canonical VEM basis functions defined over a heptagonal domain in Fig. 3.2 for (a) a vertex DoF, (b) an edge DoF and (c) an interior DoF. The non-zero quadratic forms recovered on (a) edges e_1 and e_7 for $\Phi_{\mathbf{x}_1}^p$ and (b) edge e_1 for $\Phi_{\mathbf{x}_1^e}^p$ are uniquely defined exclusively through the relevant edge and vertex DoFs.

Operator	Label	Contents	Number of Elements
$a_{\mathcal{K}}^{\varepsilon}(\cdot, \cdot)$	$\mathbb{K}^{\varepsilon}(\mathcal{K})$	$\left\{ \begin{Bmatrix} 1 \\ 0 \end{Bmatrix}, \begin{Bmatrix} 0 \\ 1 \end{Bmatrix}, \begin{Bmatrix} \eta \\ -\xi \end{Bmatrix} \right\}$	3
$a_{\mathcal{K}}^{\nabla}(\cdot, \cdot)$	$\mathbb{K}^{\nabla u}(\mathcal{K})$	$\left\{ \begin{Bmatrix} 1 \\ 0 \end{Bmatrix}, \begin{Bmatrix} 0 \\ 1 \end{Bmatrix} \right\}$	2
$a_{\mathcal{K}}^0(\cdot, \cdot)$	$\mathbb{K}^{0u}(\mathcal{K})$	$\{\emptyset\}$	0
$b_{\mathcal{K}}^{\nabla}(\cdot, \cdot)$	$\mathbb{K}^{\nabla p}(\mathcal{K})$	$\{1\}$	1
$b_{\mathcal{K}}^0(\cdot, \cdot)$	$\mathbb{K}^{0u}(\mathcal{K})$	$\{\emptyset\}$	0

Table 3.4: Definition of operator kernels.

Remark 1 One would expect four terms in the r.h.s of Eqs. (3.3). However, two terms contribute zero energy due to the energetic orthogonality conditions defined in Eqs. (3.6). The polynomial terms in these expressions are called consistency terms as they comprise the consistent kinematic modes defined earlier.

In the monomial spaces involved, there exist members contributing zero energy to $a_{\mathcal{K}}^{\varepsilon}(\cdot, \cdot)$ and $b_{\mathcal{K}}^{\nabla}(\cdot, \cdot)$, e.g., $\varepsilon_s([1, 0]^T) = [0, 0, 0]^T$. $\nabla(1) = [0, 0]^T$. These zero energy modes are operator specific and collected in $\mathbb{K}^{\varepsilon}(\mathcal{K})$ and $\mathbb{K}^{\nabla p}(\mathcal{K})$. They are called the *kernel* of the relevant operator. These operator-specific kernels are provided in Table 3.4. The contents of these kernels can be derived using kinematical decomposition relations mentioned in [124]. The zero-energy modes contained in $\mathbb{K}^{\varepsilon}(\mathcal{K})$ can be understood as rigid body motions, i.e., two translations and one rotation in 2-D physical space.

The projector is computed without the kernel, to avoid spurious results arising from ill conditioned matrices. To this end, Eqs. (3.6) is redefined as

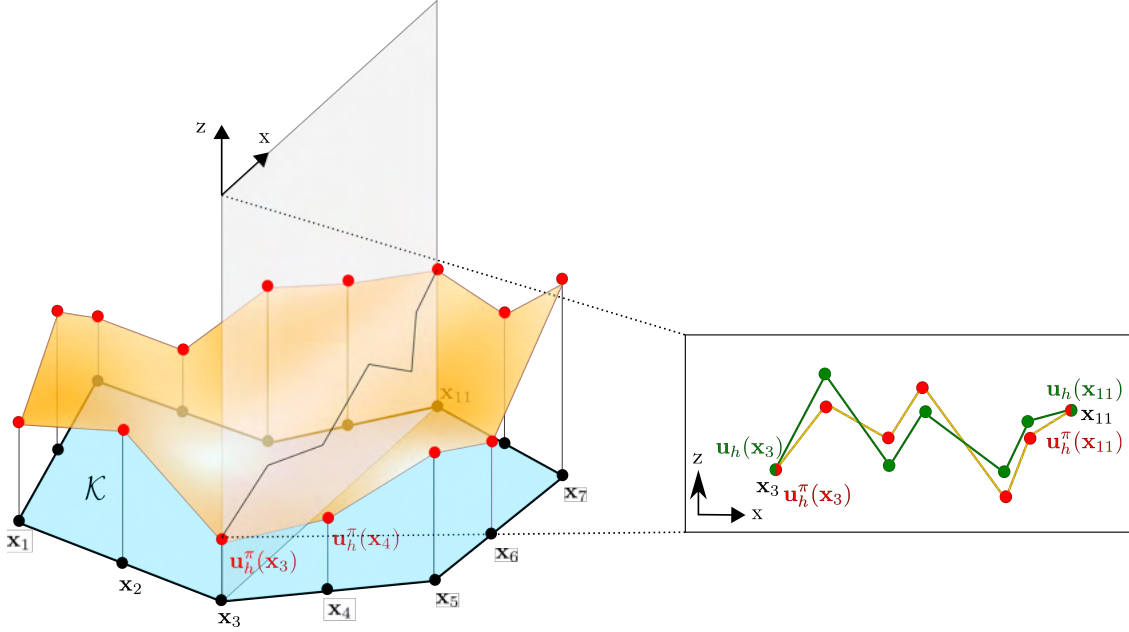


Figure 3.4: A discretized solution field and its polynomial components visualized over a polygonal element. A planar cross-section illustrates that \mathbf{u}_h and \mathbf{u}_h^π vary within the element interior, but coincide at the boundary.

$$\Pi_k^\varepsilon := a_{\mathcal{K}}^\varepsilon(\mathbf{u}_h - \Pi_k^\varepsilon \mathbf{u}_h, \mathbf{m}) = 0, \quad \forall \mathbf{u}_h \in \mathcal{V}_h^u(\mathcal{K}), \quad \mathbf{m} \in [\mathbb{M}_k(\mathcal{K})]^2 \setminus \mathbb{K}^\varepsilon(\mathcal{K}). \quad (3.7)$$

The optimality criteria used above ensure that the energies associated with the bilinear operators $P(\cdot)$ are still computed exactly. This property is called *polynomial k -consistency*, see, e.g., [11].

3.3.2 Computing the projectors

Using the definition in Eq. (3.7), the \mathcal{H}_1 projector, i.e., Π_k^ε is expanded as follows

$$\Pi_k^\varepsilon \mathbf{u}_h = \sum_{i=1}^{n_k^u - 3} \mathbf{m}_{i+3} \zeta_i^\varepsilon, \quad (3.8)$$

where ζ_i^ε is a $(1 \times n_{\text{dof}}^u)$ vector of the unknown expansion coefficients. Each entry in the expansion vector corresponds to a canonical basis function describing \mathbf{u}_h , contained in Φ^u (see Eq. (2.98)).

Eq. (3.8) can be conveniently cast in matrix form as

$$\Pi_k^\varepsilon \mathbf{u}_h = \underbrace{\mathbf{m}^\varepsilon}_{(2 \times n_k^u - 3)} \underbrace{\zeta^\varepsilon}_{(n_k^u - 3 \times n_{\text{dof}}^u)}, \quad (3.9)$$

where the matrix \mathbf{m}^ε holds the appropriate monomial bases and ζ^ε is an arrays whose i_{th} row holds the vectors of expansion coefficients ζ_i^ε .

3.3.3 Computing the projector Π_k^ε

Inserting the expansion of Eq. (3.8) into the orthogonality condition Eq. (3.7) and performing the necessary algebra the following system of equations is established with respect to the unknown expansion coefficients, i.e.,

$$\underbrace{\mathbf{G}^\varepsilon}_{(n_k^u-3 \times n_k^u-3)} \boldsymbol{\zeta}^\varepsilon = \underbrace{\mathbf{B}^\varepsilon}_{(n_k^u-3 \times n_{\text{dof}}^u)}, \quad (3.10)$$

where \mathbf{G}^ε is an array with elements

$$G_{ij}^\varepsilon = \int_{\mathcal{K}} \boldsymbol{\varepsilon}_s(\mathbf{m}_{i+3})^T \boldsymbol{\sigma}_s(\mathbf{m}_{j+3}) \, d\mathcal{K}, \quad (3.11)$$

and \mathbf{B}^ε is an array whose j th row is a vector

$$\mathbf{B}_j^\varepsilon = \int_{\mathcal{K}} \boldsymbol{\varepsilon}_s(\mathbf{u}_h)^T \boldsymbol{\sigma}_s(\mathbf{m}_{j+3}) \, d\mathcal{K}. \quad (3.12)$$

The term G_{ij}^ε in Eqs. (3.11) is computable using numerical integration since $\boldsymbol{\varepsilon}_s(\cdot)$ can be directly performed on the explicitly defined monomials (Table 3.1). A standard Gauss-Legendre quadrature is sufficient as the integrands are composed wholly of polynomial-type terms. For $k = 1$, this is trivial as the integrand is a constant whereas for $k \geq 2$, numerical integration over sub-triangulated domains is required.

Conversely, the term \mathbf{B}_j^ε cannot be evaluated in its current form as explicit definitions for the terms \mathbf{u}_h over the element domain interior do not exist. Performing integration by parts in Eq. (3.12) results in

$$\mathbf{B}_j^\varepsilon = \mathbf{B}_{bj}^\varepsilon + \mathbf{B}_{dj}^\varepsilon, \quad (3.13)$$

where

$$\mathbf{B}_{bj}^\varepsilon = \sum_{e \in \partial\mathcal{K}} \int_e \mathbf{u}_h \cdot (\boldsymbol{\sigma}(\mathbf{m}_{j+3}) \cdot \mathbf{n}^\varepsilon(e)) \, de, \quad (3.14)$$

and

$$\mathbf{B}_{dj}^\varepsilon = - \int_{\mathcal{K} \setminus \partial\mathcal{K}} \mathbf{u}_h \cdot (\text{div}(\boldsymbol{\sigma}_s(\mathbf{m}_{j+3}))) \, d\mathcal{K}, \quad (3.15)$$

respectively, where $\mathbf{n}^\varepsilon(e)$ collects the boundary direction cosines $n_x(e)$ and $n_y(e)$ and is expressed as

$$\mathbf{n}^\varepsilon(e) = \begin{bmatrix} n_x(e) & 0 & n_y(e) \\ 0 & n_y(e) & n_x(e) \end{bmatrix}^T. \quad (3.16)$$

Since \mathbf{u}_h is known over the boundary through the definitions of the corner and edge DoFs (Table 3.2), the boundary integral of Eq. (3.14) can be evaluated with a Gauss-Lobatto quadrature giving rise to the following expression

$$\mathbf{B}_{bj}^{\mathcal{E}} = \left[\overbrace{B_{bj,1}^{\mathcal{E}} \quad \cdots \quad B_{bj,N_B^u}^{\mathcal{E}}}^{N_B^u = N_C^u + N_E^u} \mid \overbrace{0 \quad \cdots \quad 0}^{N_A^u} \right] \quad (3.17)$$

Conversely, the area moment DoFs within the element interior (see Table 3.2, Fig. 3.2) are exploited to evaluate the interior domain integral $\mathbf{B}_{dj}^{\mathcal{E}}$. As there are no interior DoFs for $k = 1$ methods, these integrals vanish. For order $k \geq 2$, the Laplacian condition defined in Eq. (3.1) is exploited. To this end, the term $\text{div}(\boldsymbol{\sigma}_s(\mathbf{m}_{j+3}))$ in Eq. (3.15) is expanded over the $[\mathbb{M}_{k-2}(\mathcal{K})]^2$ basis giving rise to the following expression

$$\text{div}(\boldsymbol{\sigma}_s(\mathbf{m}_{j+3})) = \sum_{\beta=1}^{n_{k-2}^u} d_{j\beta}^{\mathcal{E}} \mathbf{m}_{\beta}, \quad \forall \mathbf{m}_{\beta} \in [\mathbb{M}_{k-2}(\mathcal{K})]^2, \quad (3.18)$$

where the expansion coefficients $d_{j\beta}^{\mathcal{E}}$ are obtained through inspection [186]. Substituting Eq. (3.18) in Eq. (3.15) the following expression is eventually established

$$\mathbf{B}_{dj}^{\mathcal{E}} = -|\mathcal{K}| \sum_{\beta=1}^{n_{k-2}^u} d_{j\beta}^{\mathcal{E}} \text{dof}_{2kN_o+\beta}(\mathbf{u}_h) = -|\mathcal{K}| \mathbf{d}^{\mathcal{E}}, \quad (3.19)$$

where the dof function denotes the evaluation of its argument at the indexed degree of freedom (see Eq. (3.26)), and

$$\mathbf{d}^{\mathcal{E}} = \left[\overbrace{0 \quad \cdots \quad 0}^{N_B^u} \mid \overbrace{d_{j1}^{\mathcal{E}} \quad \cdots \quad d_{j(n_{k-2}^u)}^{\mathcal{E}}}^{N_A^u} \right]. \quad (3.20)$$

Combining Eqs. (3.17) and (3.19) and substituting in Eq. (3.13) provides the computed form of matrix $\mathbf{B}^{\mathcal{E}}$. Hence, Eq. (3.10) can be solved for the array of the expansion coefficients $\boldsymbol{\zeta}^{\mathcal{E}}$. Substituting in Eq. (3.9) the following expression is eventually derived for the projection operator $\Pi_k^{\mathcal{E}} \mathbf{u}_h$

$$\Pi_k^{\mathcal{E}} \mathbf{u}_h = \mathbf{m}^{\mathcal{E}} [\mathbf{G}^{\mathcal{E}}]^{-1} \mathbf{B}^{\mathcal{E}}. \quad (3.21)$$

3.3.4 Consistency terms

Using Eq. (2.97a), the polynomial term in Eq. (3.3) gives rise to an elastic consistency term

$$a_{\mathcal{K}}^{\mathcal{E}}(\mathbf{u}_h, \delta \mathbf{u}_h) = \int_{\mathcal{K}} \boldsymbol{\sigma}_s(\Pi_k^{\mathcal{E}} \mathbf{u}_h) : \boldsymbol{\varepsilon}_s(\Pi_k^{\mathcal{E}} \delta \mathbf{u}_h) \, d\mathcal{K}. \quad (3.22)$$

Substituting the projector approximation from Eq. (3.21) in Eq. (3.22) and performing the necessary algebraic manipulations, the following expression is eventually retrieved for the elastic stiffness consistency term

$$\mathbf{K}_{\mathcal{K}}^C = \boldsymbol{\zeta}^{\mathcal{E}T} [\mathbf{G}^{\mathcal{E}}] \boldsymbol{\zeta}^{\mathcal{E}}, \quad (3.23)$$

where $\mathbf{G}^{\mathcal{E}}$ is provided in Eq. (3.11). The consistency term is not coercive over the complete polynomial space as the monomials from the operator kernel have been omitted.

3.3.5 Stability terms

The second part of the r.h.s. in Eqs. (3.3) cures this rank-deficiency. However, as this contains a non-polynomial integrand without an explicit definition over the element interior, the relevant integral cannot be computed analytically. Further, numerical integration requires higher order quadrature rules to achieve reasonable accuracy. To alleviate this, the non-polynomial contributions are approximated by user defined bilinear forms called *Stability terms*.

These terms are chosen to satisfy basic stability and coercivity properties. They are also designed to reduce to zero over polynomial subspaces as in, e.g., the boundaries of an element. This is necessary as consistency terms exactly account for the entire energy here. These stability terms also provide additional stiffness to higher order modes, thus preventing the entry of spurious higher order hourglass modes. For this reason, the stability terms can also be interpreted as a form of hourglass control [187].

The non-polynomial integrands, \mathbf{u}_h is known only in terms of the canonical bases Φ^u . Conversely, owing to the kinematic decomposition used in Eqs. (3.2), the polynomial projections \mathbf{u}_h^π is also present alongside the non-polynomial term. This quantities is known in terms of the monomial bases $[\mathbb{M}_k(\mathcal{K})]^2$. To facilitate interaction between these two components, as is necessary here, one needs to express \mathbf{u}_h^π in terms of Φ^u . This is done by re-expressing the monomial bases in terms of the canonical bases as follows

$$\Pi_k^\varepsilon \mathbf{u}_h = \mathbf{m}^\varepsilon \zeta^\varepsilon = [\Phi^u]^T \underbrace{\mathbf{D}^\varepsilon}_{(n_{\text{dof}}^u \times n_k^u - 3)} \zeta^\varepsilon, \quad (3.24)$$

where the matrix \mathbf{D}^ε collects the monomials evaluated at the VEM DoFs. It has the form

$$\mathbf{D}^\varepsilon = \begin{bmatrix} \text{dof}_1(\mathbf{m}_1) & \dots & \text{dof}_1(\mathbf{m}_{n_k^u-3}) \\ \vdots & \ddots & \vdots \\ \text{dof}_{n_{\text{dof}}^u}(\mathbf{m}_1) & \dots & \text{dof}_{n_{\text{dof}}^u}(\mathbf{m}_{n_k^u-3}) \end{bmatrix}, \quad (3.25)$$

$$\forall \mathbf{m} \in [\mathbb{M}_k(\mathcal{K})]^2 \setminus \mathbb{K}^\varepsilon(\mathcal{K}),$$

The quantity $\text{dof}_i(\mathbf{m}_j)$ is evaluated according to the following expressions (see Table 3.2)

$$\begin{cases} \text{dof}_i(\mathbf{m}_j) = \mathbf{m}_j(\mathbf{x}_i), & \forall i \leq 2kN_v \\ \text{dof}_i(\mathbf{m}_j) = \frac{1}{|\mathcal{K}|} \int_{\mathcal{K}} \mathbf{m}_j \cdot \mathbf{m}_\beta \, d\mathcal{K} \\ \forall \mathbf{m}_\beta \in [\mathbb{M}_{k-2}(\mathcal{K})]^2, & i > 2kN_v. \end{cases} \quad (3.26)$$

Since the projector has so far been computed only for non-kernel monomials, it is now necessary to have a similar counterpart for the kernel components. This ensures the completeness of the polynomial spaces involved and restores coercivity to the entire formulation. The change-of-basis transformation matrix \mathbf{D}_S^ε contains kernel monomials evaluated at all DoFs, similar to Eq. (3.25)

$$\mathbf{D}_S^\varepsilon = \begin{bmatrix} \text{dof}_1(\mathbf{m}_1) & \dots & \text{dof}_1(\mathbf{m}_3) \\ \vdots & \ddots & \vdots \\ \text{dof}_{n_{\text{dof}}^u}(\mathbf{m}_1) & \dots & \text{dof}_{n_{\text{dof}}^u}(\mathbf{m}_3) \end{bmatrix}, \quad \forall \mathbf{m} \in \mathbb{K}^\varepsilon(\mathcal{K}), \quad (3.27)$$

where $\text{dof}_i(\mathbf{m}_j)$ denotes the j_{th} monomial evaluated at the i_{th} DoF.

The quantity ζ_S^ε is now computed in a straightforward way

$$\zeta_S^\varepsilon = [\mathbf{G}_S^\varepsilon]^{-1} \mathbf{B}_S^\varepsilon, \quad (3.28)$$

where $\mathbf{G}_S^\varepsilon = \mathbf{B}_S^\varepsilon \mathbf{D}_S^\varepsilon$. The term \mathbf{B}_S^ε is specially defined using relations derived in [90, 186]

$$\mathbf{B}_S^\varepsilon = \begin{bmatrix} 1/N_v & 0 & 1/N_v & 0 & \dots \\ 0 & 1/N_v & 0 & 1/N_v & \dots \\ \eta(\mathbf{x}_1) & -\xi(\mathbf{x}_1) & \eta(\mathbf{x}_2) & -\xi(\mathbf{x}_2) & \dots \end{bmatrix}. \quad (3.29)$$

These relations are obtained for \mathbf{B}_S^ε by imposing equality of two mean translations and a single rotation between \mathbf{u}_h and \mathbf{u}_h^π . It is to be noted that since Eq. (3.29) is defined only at vertex DoFs, columns resulting from edge and area DoFs encountered in $k \geq 2$ methods are set to zero.

The complete stability specific projection operators are finally expressed in the canonical bases as follows

$$\mathbf{\Pi}_{\text{tot}}^\varepsilon = \mathbf{D}^\varepsilon \zeta^\varepsilon + \mathbf{D}_S^\varepsilon \zeta_S^\varepsilon. \quad (3.30)$$

Driven by the work of [188] on elastostatics, the following stability term approximants are introduced for the non-polynomial terms

$$\text{NP}(a_{\mathcal{K}}^\varepsilon) \approx \mathcal{S}^{\mathbf{K}}(\mathbf{u}_h, \delta \mathbf{u}_h) = [\Phi^u]^T \tilde{\mathbf{K}}_{\mathcal{K}}^S [\Phi^u]. \quad (3.31)$$

The elastic stability stiffness matrix is now defined

$$\mathbf{K}_{\mathcal{K}}^S = (\mathbb{I}_u - \mathbf{\Pi}_{\text{tot}}^\varepsilon) \beta_{\mathbf{K}} (\mathbb{I}_u - \mathbf{\Pi}_{\text{tot}}^\varepsilon). \quad (3.32)$$

In Eqs. (3.32), \mathbb{I}_u is an identity matrix of size $(n_{\text{dof}}^u \times n_{\text{dof}}^u)$. The stabilization parameters $\beta_{\mathbf{K}}$ is defined using the D-recipe stabilization (originally proposed in [189]) below

$$\beta_{\mathbf{K}} = \gamma_{\mathbf{K}} |\mathcal{K}| \frac{\text{tr}(\mathbb{D})}{\text{tr}(\mathbf{D}^\varepsilon \mathbf{D}^\varepsilon)}. \quad (3.33)$$

In Eq. (3.33), the constant $\gamma_{\mathbf{K}}$, denotes a scaling parameter. In the numerical tests conducted in this work, it is observed that $\gamma_{\mathbf{K}} = 1$ provides accurate and well behaved results in all cases.

3.3.6 State matrices

Employing the consistency and stability term definitions introduced in Eqs. (3.23) and (3.32), respectively, the virtual element state matrices are eventually defined according to the following expressions, i.e.,

$$\boxed{\mathbf{K}_{\mathcal{K}}} \approx \frac{\text{Consistency}}{\mathbf{K}_{\mathcal{K}}^C} + \frac{\text{Stability}}{\mathbf{K}_{\mathcal{K}}^S}. \quad (3.34)$$

This is then assembled into the global elastic stiffness matrix using Eq. (2.105). It is to be noted that as stated in Section 3.2, one recovers from the VEM, a classical Lagrange polynomial based interpolation over the element boundaries. As a result, the boundary terms mentioned in Eq. (2.104) can be computed in a straightforward way without resorting to deriving projectors exclusive to these forms.

Algorithm 1 summarizes the steps taken to evaluate the elastic stiffness matrix using the VEM.

Algorithm 1: Elastic stiffness matrix evaluation schema.

Data: Define mesh and material properties

foreach *micro element i* **do**

Compute: $\mathbf{\Pi}_k^\mathcal{E}, \mathbf{\Pi}_{\text{tot}}^\mathcal{E}$ (see Eqs. (3.21), (3.30)) ;
 Compute: $\mathbf{K}_C, \mathbf{K}_S,$ and $\mathbf{K}_{\mathcal{K}(i)}$ (see Eq. (3.34)) ;
 Assemble to \mathbf{K} (see Eq. (2.105));

3.4 Consolidation

3.4.1 Virtual approximants at the element level

Using the discretization provided in Eq. (2.117), the pressure field is split in a similar manner to Eq. (3.2)

$$p_h = p_h^\pi + (p_h - p_h^\pi), \quad \delta p_h = \delta p_h^\pi + (\delta p_h - \delta p_h^\pi). \quad (3.35)$$

Inserting Eqs. (3.35) into the fluid phase specific operators of Eqs. (2.115a) and (2.115b) results in the following splits

$$b_{\mathcal{K}}^\nabla(p_h, \delta p_h)_{\mathbf{k}/\gamma_f} = P(b_{\mathcal{K}}^\nabla) + NP(b_{\mathcal{K}}^\nabla), \quad (3.36)$$

$$b_{\mathcal{K}}^0(p_h, \delta p_h)_{S_\varepsilon} = P(b_{\mathcal{K}}^0) + NP(b_{\mathcal{K}}^0), \quad (3.37)$$

where the corresponding polynomial and non-polynomial arguments become

$$P(b_{\mathcal{K}}^\nabla) = b_{\mathcal{K}}^\nabla \left(\Pi_k^{\nabla p} p_h, \Pi_k^{\nabla p} \delta p_h \right)_{\mathbf{k}/\gamma_f}, \quad (3.38)$$

$$NP(b_{\mathcal{K}}^\nabla) = b_{\mathcal{K}}^\nabla \left((p_h - \Pi_k^{\nabla p} p_h), (\delta p_h - \Pi_k^{\nabla p} \delta p_h) \right)_{\mathbf{k}/\gamma_f}, \quad (3.39)$$

and

$$P(b_{\mathcal{K}}^0) = b_{\mathcal{K}}^0 \left(\Pi_k^{0p} p_h, \Pi_k^{0p} \delta p_h \right)_{S_\varepsilon}, \quad (3.40)$$

$$\text{NP}(b_{\mathcal{K}}^0) = b_{\mathcal{K}}^0 \left((p_h - \Pi_k^{0p} p_h), (\delta p_h - \Pi_k^{0p} \delta p_h) \right)_{S_\varepsilon}, \quad (3.41)$$

respectively. The projection operators $\Pi_k^{\nabla p} : \mathcal{V}_k^p(\mathcal{K}) \rightarrow \mathbb{P}_k(\mathcal{K})$ and $\Pi_k^{0p} : \mathcal{V}_k^p(\mathcal{K}) \rightarrow \mathbb{P}_k(\mathcal{K})$ arise from the action of $\nabla(\cdot)$ and (\cdot) onto the unknown pressure field.

Similar to Eq. (3.6), the following orthogonality conditions are defined for the fluid phase projection operators

$$\Pi_k^{\nabla p} := b_{\mathcal{K}}^{\nabla} (p_h - \Pi_k^{\nabla p} p_h, m)_{\mathbf{k}/\gamma_f} = 0 \quad (3.42a)$$

$$\Pi_k^{0p} := b_{\mathcal{K}}^0 (p_h - \Pi_k^{0p} p_h, m)_{S_\varepsilon} = 0 \quad (3.42b)$$

$$\forall p_h \in \mathcal{V}_h^p(\mathcal{K}), m \in \mathbb{P}_k(\mathcal{K}),$$

Finally, inserting Eqs. (3.2) and (3.35) into the coupling operator of Eq. (2.116a), the following expressions are derived, i.e.,

$$a_{\mathcal{K}}^{(\varepsilon,0)} = P(a_{\mathcal{K}}^{(\varepsilon,0)}) + \text{NP}(a_{\mathcal{K}}^{(\varepsilon,0)}), \quad (3.43)$$

with

$$P(a_{\mathcal{K}}^{(\varepsilon,0)}) = a_{\mathcal{K}}^{(\varepsilon,0)} \left(\Pi_k^{\nabla p} p_h, \Pi^{0u} \delta \mathbf{u}_h \right)_{\alpha_B \mathbf{m}}, \quad (3.44)$$

$$\text{NP}(a_{\mathcal{K}}^{(\varepsilon,0)}) = a_{\mathcal{K}}^{(\varepsilon,0)} \left((p_h - \Pi_k^{\varepsilon p} p_h), (\delta \mathbf{u}_h - \Pi^{0u} \delta \mathbf{u}_h) \right)_{\alpha_B \mathbf{m}}. \quad (3.45)$$

To avoid poor conditioning, the projectors in Eq. (3.42) are redefined without the kernel members.

$$\begin{cases} \Pi_k^{\nabla p} := b_{\mathcal{K}}^{\nabla} (p_h - \Pi_k^{\nabla p} p_h, m)_{\mathbf{k}/\gamma_f} = 0, \quad \forall p_h \in \mathcal{V}_h^p(\mathcal{K}), m \in \mathbb{M}_k(\mathcal{K}) \setminus \mathbb{K}^{\nabla}(\mathcal{K}) \\ \Pi_k^{0p} := b_{\mathcal{K}}^0 (p_h - \Pi_k^{0p} p_h, m)_{S_\varepsilon} = 0 \quad \forall p_h \in \mathcal{V}_h^p(\mathcal{K}), m \in \mathbb{M}_k(\mathcal{K}) \setminus \mathbb{K}^{0p}(\mathcal{K}). \end{cases} \quad (3.46)$$

It is to be noted that $b_{\mathcal{K}}^0(\cdot, \cdot)$ contains an empty kernel as it has no zero energy modes, i.e., $\mathbb{K}^{0p}(\mathcal{K}) = \emptyset$.

3.4.2 Computing the projectors

Following the revised definition of the projectors in Eq. (3.46), the projected functions are expanded in terms of the appropriate monomial bases. The remaining unknown \mathcal{H}^1 projector, i.e., $\Pi_k^{\nabla p}$ is expanded as

$$\Pi_k^{\nabla p} p_h = \sum_{i=1}^{n_k^p-1} m_{i+1} \zeta_i^{\nabla p}. \quad (3.47)$$

Here, $\zeta_i^{\nabla p}$ is a $(1 \times n_{\text{dof}}^p)$ vector with each entry corresponding to a canonical basis function p_h , contained in Φ^p (see Eq. (2.117)).

Eq. (3.47) is cast in matrix form similar to Eq. (3.8)

$$\Pi_k^{\nabla p} p_h = \underbrace{\mathbf{m}^{\nabla p}}_{(1 \times n_k^p - 1)} \underbrace{\zeta^{\nabla p}}_{(n_k^p - 1 \times n_{\text{dof}}^p)}. \quad (3.48)$$

Similarly, the \mathcal{L}^2 projector, i.e., Π_k^{0p} is expanded as

$$\Pi_k^{0p} p_h = \sum_{i=1}^{n_k^p} m_i \zeta_i^{0p}, \quad (3.49)$$

where ζ_i^{0p} is a $(1 \times n_{\text{dof}}^p)$ vector.

Eq. (3.49) is also cast in its corresponding matrix form, i.e.,

$$\Pi_k^{0p} p_h = \underbrace{\mathbf{m}^{0p}}_{(1 \times n_k^p)} \underbrace{\zeta^{0p}}_{(n_k^p \times n_{\text{dof}}^p)}, \quad (3.50)$$

where the matrices \mathbf{m}^{0p} hold the monomial bases and ζ^{0p} is the corresponding array of the expansion coefficients.

3.4.3 Computing the projector $\Pi_k^{\nabla p}$

The procedure developed in Section 3.3.3 is followed. Inserting Eq. (3.47) into the first of Eqs. (3.46), the following equation is established

$$\underbrace{\mathbf{G}^{\nabla p}}_{(n_k^p - 1 \times n_k^p - 1)} \zeta^{\nabla p} = \underbrace{\mathbf{B}^{\nabla p}}_{(n_k^p - 1 \times n_{\text{dof}}^p)}, \quad (3.51)$$

where

$$\mathbf{G}_{ij}^{\nabla p} = \int_{\mathcal{K}} (\nabla m_{i+1})^T \frac{\mathbf{k}}{\gamma_f} \nabla m_{j+1} d\mathcal{K}, \quad (3.52)$$

and

$$\mathbf{B}_j^{\nabla p} = \int_{\mathcal{K}} (\nabla p_h)^T \frac{\mathbf{k}}{\gamma_f} \nabla m_{j+1} d\mathcal{K}. \quad (3.53)$$

Using quadratures, Eq. (3.53) becomes

$$\mathbf{B}_j^{\nabla p} = \mathbf{B}_{bj}^{\nabla p} + \mathbf{B}_{dj}^{\nabla p}, \quad (3.54)$$

where

$$\mathbf{B}_{bj}^{\nabla p} = \sum_{e \in \partial \mathcal{K}} \int_e p_h \cdot \left(\frac{\mathbf{k}}{\gamma_f} \nabla m_{j+1} \cdot \mathbf{n}^\nabla(e) \right) de, \quad (3.55)$$

and

$$\mathbf{B}_{dj}^{\nabla p} = - \int_{\mathcal{K} \setminus \partial\mathcal{K}} \mathbf{p}_h \cdot \left(\frac{\mathbf{k}}{\gamma_f} \Delta \mathbf{m}_{j+1} \right) d\mathcal{K}, \quad (3.56)$$

respectively, where the array $\mathbf{n}^\nabla(e)$ is defined here as

$$\mathbf{n}^\nabla(e) = [n_x(e) \quad n_y(e)]^T. \quad (3.57)$$

The boundary integral in Eq. (3.54) is evaluated using Gauss-Lobatto quadratures in a similar manner to Eq. (3.17).

To evaluate the corresponding domain integral, the terms $\Delta \mathbf{m}_{j+2}$ in Eq. (3.56) is expanded over the $\mathbb{M}_{k-2}(\mathcal{K})$ basis

$$\frac{\mathbf{k}}{\gamma_f} \Delta \mathbf{m}_{j+1} = \sum_{\beta=1}^{n_{k-2}^p} d_{j\beta}^{\nabla p} \mathbf{m}_\beta, \quad \forall \mathbf{m}_\beta \in \mathbb{M}_{k-2}(\mathcal{K}), \quad (3.58)$$

where the coefficients $d_{j\beta}^{\nabla p}$ are also obtained through inspection and substituting in Eq. (3.56)

$$\mathbf{B}_{dj}^{\nabla p} = -|\mathcal{K}| \sum_{\beta=1}^{n_{k-2}^p} d_{j\beta}^{\nabla p} \text{dof}_{kN_v+\beta}(\mathbf{p}_h) = -|\mathcal{K}| \mathbf{d}^{\nabla p}, \quad (3.59)$$

where

$$\mathbf{d}^{\nabla p} = \left[\overbrace{0 \quad \cdots \quad 0}^{N_B^p} \mid \overbrace{d_{j1}^{\nabla p} \quad \cdots \quad d_{j(n_{k-2}^p)}^{\nabla p}}^{N_A^p} \right]. \quad (3.60)$$

Similar to Eq. (3.21), the projection operator $\Pi_k^{\nabla p} \mathbf{p}_h$ is now evaluated according to the following expression

$$\Pi_k^{\nabla p} \mathbf{p}_h = \mathbf{m}^{\nabla p} [\mathbf{G}^{\nabla p}]^{-1} \mathbf{B}^{\nabla p}. \quad (3.61)$$

3.4.4 Computing the projector Π_k^{0p}

Within this consolidation setting, an \mathcal{L}^2 projector emerges. To evaluate these, Eq. (3.49) is inserted into Eq. (3.46) to obtain

$$\underbrace{\mathbf{G}^{0p}}_{(n_k^p \times n_k^p)} \zeta^{0p} = \underbrace{\mathbf{B}^{0p}}_{(n_k^p \times n_{\text{dof}}^p)}, \quad (3.62)$$

where the term \mathbf{G}^{0p} is an arrays with elements

$$G_{ij}^{0p} = \int_{\mathcal{K}} (\mathbf{m}_i)^T \frac{1}{\tilde{K}_{\text{eq}}} \mathbf{m}_j d\mathcal{K}. \quad (3.63)$$

The quantity \mathbf{B}^{0p} is an array, whose j th row is

$$\mathbf{B}_j^{0p} = \int_{\mathcal{K}} (\mathbf{p}_h)^T \frac{1}{\tilde{K}_{\text{eq}}} \mathbf{m}_j d\mathcal{K}. \quad (3.64)$$

Computing G_{ij}^{0p} in Eq. (3.63) is straightforward. The term \mathbf{B}_j^{0p} in Eq. (3.64) however, is not

computable solely through the DoFs of p_h . This is because the interior DoFs are defined for $m \in \mathbb{M}_{k-2}(\mathcal{K})$. To alleviate this, the procedure shown in [90, 190] is employed.

Hence, this integral is computed through the existing DoFs of $\mathcal{V}_h^p(\mathcal{K})$ when the current monomial has a degree lesser than or equal to $k - 2$. Conversely, the integral is evaluated using $\Pi_k^{\nabla p}$ when the order of the monomial under consideration is larger than $k - 2$.

Following this procedure, \mathbf{B}_j^{0p} assumes the following form

$$\mathbf{B}_j^{0p} = \begin{cases} \mathbf{B}_{1j}^{0p}, & \text{if } 1 \leq j \leq n_{k-2}^p \\ \mathbf{B}_{2j}^{0p}, & \text{if } n_{k-2}^p < j \leq n_k^p. \end{cases} \quad (3.65)$$

A prima-facie notion might be that additional error is introduced through using \mathcal{H}^1 projectors here. However, it is proved in [78, 90] that this is not the case. In fact, it is shown that one can replace p_h here with enhanced stand-in functions $z_h \in \mathcal{Z}_h^p(\mathcal{K})$ where

$$\mathcal{Z}_h^p(\mathcal{K}) = \{z_h \in \mathcal{V}_h^p(\mathcal{K}), \quad b_{\mathcal{K}}^0(z_h - \Pi^{\nabla p} z_h, m_j) \frac{1}{\tilde{K}_{\text{eq}}} = 0, \\ n_{k-2}^p < j \leq n_k^p\}. \quad (3.66)$$

With the additional condition requiring the orthogonality of the \mathcal{H}^1 projection error with respect to the \mathcal{L}^2 bilinear operators, it is seen that no additional error is introduced through this procedure.

Using the definitions for VEM DoFs in Table 3.2, \mathbf{B}_{1j}^{0p} can be evaluated as follows

$$\mathbf{B}_{1j}^{0p} = |\mathcal{K}| \frac{1}{\tilde{K}_{\text{eq}}} \text{dof}(p_h) = |\mathcal{K}| \mathbf{d}_j^{0p}, \quad (3.67)$$

where

$$\mathbf{d}_j^{0p} = \frac{1}{\tilde{K}_{\text{eq}}} \left[\overbrace{0 \quad \dots \quad 0}^{N_B^p} \quad \middle| \quad \underbrace{0 \quad \dots \quad 1 \quad \dots \quad 0}_j \right]. \quad (3.68)$$

Using the monomial expansion for $\Pi_k^{\nabla} p_h$ from Eq. (3.49) with running index β instead of i to avoid confusion, the term \mathbf{B}_{2j}^{0p} is now collected and computed

$$\mathbf{B}_2^{0p} = \underbrace{\mathbf{H}^p}_{(n_k^p - 1 \times n_k^p - 1)} \boldsymbol{\zeta}^{\nabla p}, \quad (3.69)$$

where

$$\mathbf{H}_{\beta j}^p = \int_{\mathcal{K}} (m_{\beta+1})^T \frac{1}{\tilde{K}_{\text{eq}}} m_j \, d\mathcal{K}, \quad \beta = 1, \dots, n_k^p - 1. \quad (3.70)$$

The coefficient arrays $\boldsymbol{\zeta}^{\nabla p}$ has already been derived. The quantity $\mathbf{H}_{\beta j}^p$ can be computed using numerical integration over sub-triangulated domains.

Using Eqs. (3.67) and (3.69), \mathbf{B}^{0p} is eventually expressed as

$$\mathbf{B}^{0p} = [\mathbf{B}_1^{0p} \quad \middle| \quad \mathbf{B}_2^{0p}]^T \quad (3.71)$$

All terms in Eq. (3.62) are now rendered computable.

Solving Eqs. (3.62) for the expansion coefficients and substituting in Eq. (3.50), the following approximations for the \mathcal{L}_2 projection operator is eventually derived, i.e.,

$$\Pi_k^{0p} p_h = \mathbf{m}^{0p} [\mathbf{G}^{0p}]^{-1} \mathbf{B}^{0p}. \quad (3.72)$$

3.4.5 Consistency terms

Substituting Eqs. (2.115a), (2.115b), and (2.116a) in the polynomial terms of Eqs. (3.36), (3.37), and (3.43), respectively results in the following expressions for the fluid kinetic consistency term

$$b^\nabla(p, \delta p_h)_{\mathbf{k}/\gamma_f} = \int_{\mathcal{K}} \frac{\mathbf{k}}{\gamma_f} \nabla \left(\Pi_k^{\nabla p} p_h \right) \cdot \nabla \left(\Pi_k^{\nabla p} \delta p_h \right) d\mathcal{K}, \quad (3.73)$$

the fluid compressibility consistency term

$$b^0(p, \delta p_h)_{S_\varepsilon} = \int_{\mathcal{K}} S_\varepsilon \Pi_k^{0p} p_h \cdot \Pi_k^{0p} \delta p_h d\mathcal{K}, \quad (3.74)$$

and the coupling consistency term

$$a^{(\varepsilon,0)}(p_h, \delta \mathbf{u}_h)_{\alpha_B \mathbf{m}} = \int_{\mathcal{K}} \alpha_B \boldsymbol{\varepsilon} \left(\Pi^\varepsilon \delta \mathbf{u}_h \right) \cdot \mathbf{m} \Pi_k^{0p} p_h d\mathcal{K}, \quad (3.75)$$

respectively.

Hence, the fluid kinetic consistency matrix assumes the following form

$$\mathbf{H}_{\mathcal{K}}^C = \boldsymbol{\zeta}^{\nabla p T} [\mathbf{G}^{\nabla p}] \boldsymbol{\zeta}^{\nabla p}, \quad (3.76)$$

where $\mathbf{G}^{\nabla p}$ is evaluated in Eq. (3.52) and the fluid compressibility matrix becomes

$$\mathbf{S}_{\mathcal{K}}^C = \boldsymbol{\zeta}^{0p T} [\mathbf{G}^{0p}] \boldsymbol{\zeta}^{0p}, \quad (3.77)$$

where \mathbf{G}^{0p} is provided in Eqs. (3.63).

Finally, the phase coupling consistency term assumes the following form

$$\mathbf{Q}_{\mathcal{K}}^C = \boldsymbol{\zeta}^{\varepsilon T} \underbrace{[\mathbf{G}^{\varepsilon 0p}]}_{(n_k^p - 1 \times n_k^u)} \boldsymbol{\zeta}^{0p}, \quad (3.78)$$

where $\mathbf{G}^{\varepsilon 0p}$ is an array with elements

$$\left(\mathbf{G}^{\nabla p 0u} \right)_{ij} = \int_{\mathcal{K}} \alpha_B \boldsymbol{\varepsilon}(\mathbf{m}_{i+1}) \cdot \mathbf{m} \mathbf{m}_j d\mathcal{K}, \quad i = 1, \dots, n_k^u - 3, \quad j = 1, \dots, n_k^p. \quad (3.79)$$

This integral can be computed in a straightforward way using the sub-triangulation approach. The consistency terms are not coercive over the complete polynomial space as the monomials

from the operator kernel have been omitted.

3.4.6 Stability terms

As done in Section 3.3.5, the fluid phase specific projectors, originally defined in the monomial bases, are now re-expressed in the canonical bases

$$\Pi_k^{\nabla p} p_h = \mathbf{m}^{\nabla p} \zeta^{\nabla p} = [\Phi^p]^T \underbrace{\mathbf{D}^{\nabla p}}_{(n_{\text{dof}}^p \times n_k^p - 1)} \zeta^{\nabla p}, \quad (3.80)$$

$$\Pi_k^{0p} p_h = \mathbf{m}^{0p} \zeta^{0p} = [\Phi^p]^T \underbrace{\mathbf{D}^{0p}}_{(n_{\text{dof}}^p \times n_k^p)} \zeta^{0p}, \quad (3.81)$$

where the matrices $\mathbf{D}^{\nabla p}$ and \mathbf{D}^{0p} have the forms

$$\mathbf{D}^{\nabla p} = \begin{bmatrix} \text{dof}_1(\mathbf{m}_1) & \dots & \text{dof}_1(\mathbf{m}_{n_k^p-1}) \\ \vdots & \ddots & \vdots \\ \text{dof}_{n_{\text{dof}}^p}(\mathbf{m}_1) & \dots & \text{dof}_{n_{\text{dof}}^p}(\mathbf{m}_{n_k^p-1}) \end{bmatrix}, \quad (3.82a)$$

$\forall \mathbf{m} \in \mathbb{M}_k(\mathcal{K}) \setminus \mathbb{K}^{\nabla}(\mathcal{K})$

$$\mathbf{D}^{0p} = \begin{bmatrix} \text{dof}_1(\mathbf{m}_1) & \dots & \text{dof}_1(\mathbf{m}_{n_k^p}) \\ \vdots & \ddots & \vdots \\ \text{dof}_{n_{\text{dof}}^p}(\mathbf{m}_1) & \dots & \text{dof}_{n_{\text{dof}}^p}(\mathbf{m}_{n_k^p}) \end{bmatrix}, \quad (3.82b)$$

$\forall \mathbf{m} \in \mathbb{M}_k(\mathcal{K}).$

The quantity and $\text{dof}_i(\mathbf{m}_j)$ is evaluated for the fluid phase

$$\begin{cases} \text{dof}_i(\mathbf{m}_j) = \mathbf{m}_j(\mathbf{x}_i), & \forall i \leq kN_v \\ \text{dof}_i(\mathbf{m}_j) = \frac{1}{|\mathcal{K}|} \int_{\mathcal{K}} \mathbf{m}_j \cdot \mathbf{m}_\beta \, d\mathcal{K}, \\ \forall \mathbf{m}_\beta \in \mathbb{M}_{k-2}(\mathcal{K}), & i > kN_v. \end{cases} \quad (3.83)$$

To ensure coercivity, the fluid-phase projectors need to have kernel specific projectors. It is of interest to note that the \mathcal{L}_2 projector already achieves a complete polynomial projection as the respective operator kernel is empty (see Table 3.4). To this end, it is sufficient to define the kernel-specific projector $\zeta_S^{\nabla p}$ along with the relevant change-of-basis transformation matrix $\mathbf{D}_S^{\nabla p}$

$$\mathbf{D}_S^{\nabla p} = \begin{bmatrix} \text{dof}_1(\mathbf{m}_1) \\ \vdots \\ \text{dof}_{n_{\text{dof}}^p}(\mathbf{m}_1) \end{bmatrix}, \quad \forall \mathbf{m} \in \mathbb{K}^{\nabla p}(\mathcal{K}), \quad (3.84)$$

The quantity $\zeta_S^{\nabla p}$ is now obtained

$$\zeta_S^{\nabla p} = [\mathbf{G}_S^{\nabla p}]^{-1} \mathbf{B}_S^{\nabla p}, \quad (3.85)$$

where $\mathbf{G}_S^{\nabla p} = \mathbf{B}_S^{\nabla p} \mathbf{D}_S^{\nabla p}$. The array $\mathbf{B}_S^{\nabla p}$ is again, specially defined using relations derived in [90,186]

$$\mathbf{B}_S^{\nabla p} = [1/N_v \quad 1/N_v \quad \dots]. \quad (3.86)$$

$\mathbf{B}_S^{\nabla p}$ is obtained through imposing equality of mean pore-fluid pressures between p_h and p_h^π .

The polynomial complete stability projection operators are expressed in the canonical bases as follows

$$\mathbf{\Pi}_{\text{tot}}^{\nabla p} = \mathbf{D}^{\nabla p} \boldsymbol{\zeta}^{\nabla p} + \mathbf{D}_S^{\nabla p} \boldsymbol{\zeta}_S^{\nabla p} \quad (3.87a)$$

$$\mathbf{\Pi}_{\text{tot}}^{0p} = \mathbf{D}^{0p} \boldsymbol{\zeta}^{0p}. \quad (3.87b)$$

Analogous to Section 3.3.5, the follow stability term approximants are used for the fluid phase

$$\text{NP}(b_{\mathcal{K}}^{\nabla}) \approx \mathcal{S}^H(p_h, \delta p_h) = [\boldsymbol{\Phi}^p]^T \tilde{\mathbf{H}}_{\mathcal{K}}^S [\boldsymbol{\Phi}^p], \quad (3.88a)$$

$$\text{NP}(b_{\mathcal{K}}^0) \approx \mathcal{S}^S(p_h, \delta p_h) = [\boldsymbol{\Phi}^p]^T \tilde{\mathbf{Q}}_{\mathcal{K}}^S [\boldsymbol{\Phi}^p], \quad (3.88b)$$

and the coupling term

$$\text{NP}(a_{\mathcal{K}}^{\boldsymbol{\varepsilon},0}) \approx \mathcal{S}^Q(p_h, \delta \mathbf{u}_h) = [\boldsymbol{\Phi}^u]^T \tilde{\mathbf{Q}}_{\mathcal{K}}^S [\boldsymbol{\Phi}^p], \quad (3.89)$$

respectively.

The fluid kinetic, fluid compressibility and coupling stability stiffness matrices, i.e., $\mathbf{H}_{\mathcal{K}}^S$, $\mathbf{S}_{\mathcal{K}}^S$, and $\mathbf{Q}_{\mathcal{K}}^S$ are defined according to the following expressions

$$\mathbf{H}_{\mathcal{K}}^S = (\mathbb{I}_p - \mathbf{\Pi}_{\text{tot}}^{\nabla p}) \beta_H (\mathbb{I}_p - \mathbf{\Pi}_{\text{tot}}^{\nabla p}) \quad (3.90a)$$

$$\mathbf{S}_{\mathcal{K}}^S = (\mathbb{I}_p - \mathbf{\Pi}_{\text{tot}}^{0p}) \beta_S (\mathbb{I}_p - \mathbf{\Pi}_{\text{tot}}^{0p}) \quad (3.90b)$$

$$\mathbf{Q}_{\mathcal{K}}^S = (\mathbb{I}_p - \mathbf{\Pi}_{\text{tot}}^{\boldsymbol{\varepsilon}}) \beta_Q \mathbb{I}_Q (\mathbb{I}_u - \mathbf{\Pi}_{\text{tot}}^{0p}). \quad (3.90c)$$

In Eqs. (3.90), \mathbb{I}_p are identity matrices of sizes $(n_{\text{dof}}^p \times n_{\text{dof}}^p)$. The array $\mathbb{I}_C = [\mathbb{I}_p, \mathbb{I}_p]^T$ is used to ensure compatible matrix multiplication. The stabilization parameters β_H , β_S and β_Q are defined using the D-recipe stabilization adapted to a porous media context in [127] below

$$\beta_H = \gamma_H |\mathcal{K}| \frac{\mathbf{k}/\gamma_f}{\text{tr}(\mathbf{D}^{\nabla p^T} \mathbf{D}^{\nabla p})}, \quad \beta_S = \gamma_S |\mathcal{K}| \frac{S_\varepsilon}{\text{tr}(\mathbf{D}^{0p^T} \mathbf{D}^{0p})}, \quad \beta_Q = \gamma_Q |\mathcal{K}| \frac{\text{tr}(\alpha_B \mathbf{m})}{\text{tr}(\mathbf{D}^{0p^T} \mathbf{D}^{0p})}. \quad (3.91)$$

In Eq. (3.91), the constants $\gamma_H = \gamma_S = \gamma_Q = 1$ yield accurate and well behaved results in all cases.

3.4.7 State matrices

Employing the consistency and stability term definitions introduced in Eqs. (3.76)-(3.78) and Eqs. (3.90), respectively, the virtual element state matrices are eventually defined according to the following expressions, i.e.,

$$\begin{array}{rcc}
& & \begin{array}{c} \textit{Consistency} \\ \hline \end{array} & \begin{array}{c} \textit{Stability} \\ \hline \end{array} \\
\left[\begin{array}{l} \mathbf{H}_{\mathcal{K}} \\ \mathbf{S}_{\mathcal{K}} \\ \mathbf{Q}_{\mathcal{K}} \end{array} \right] \approx & & \begin{array}{l} \mathbf{H}_{\mathcal{K}}^C \\ \mathbf{S}_{\mathcal{K}}^C \\ \mathbf{Q}_{\mathcal{K}}^C \end{array} & + & \begin{array}{l} \mathbf{H}_{\mathcal{K}}^S \\ \mathbf{S}_{\mathcal{K}}^S \\ \mathbf{Q}_{\mathcal{K}}^S \end{array}
\end{array} \quad (3.92)$$

The local state matrices defined in Eq. (3.92) are assembled over the entire domain Ω_h using a direct approach as done in Eq. (2.126). It is to be noted that for reasons stated in Section 3.3.6, the terms mentioned in Eqs. (2.173c) and (2.174b) can be computed using a FEM based approach.

Algorithm 2 summarizes the steps taken to evaluate the consolidation stiffness matrices \mathbf{H} , \mathbf{S} and \mathbf{Q} using the VEM.

Algorithm 2: Consolidation state matrices evaluation schema.

Data: Define mesh and material properties

foreach *micro element* i **do**

Compute: $\mathbf{\Pi}_k^{\nabla p}$, $\mathbf{\Pi}_{\text{tot}}^{\nabla p}$ (see Eqs. (3.61), (3.87a)) ;
: $\mathbf{\Pi}_k^{0p}$, $\mathbf{\Pi}_{\text{tot}}^{0p}$ (see Eqs. (3.72), (3.87b)) ;
 Compute: \mathbf{H}_C , \mathbf{H}_S , and $\mathbf{H}_{\mathcal{K}(i)}$ (see Eq. (3.92)) ;
: \mathbf{S}_C , \mathbf{S}_S , and $\mathbf{S}_{\mathcal{K}(i)}$;
: \mathbf{Q}_C , \mathbf{Q}_S , and $\mathbf{Q}_{\mathcal{K}(i)}$;
 Assemble to \mathbf{H} , \mathbf{S} and \mathbf{Q} (see Eq. (2.126));

3.5 Vibro-acoustics

3.5.1 Virtual approximants at the element level

Observing the abstract weak formulation in Eqs. (2.165), it can be seen that one requires the \mathcal{H}_1 projectors Π_k^ε , $\Pi_k^{\nabla p}$ and the \mathcal{L}_2 operators Π_k^{0u} , Π_k^{0p} .

Eqs. (3.2) are inserted into the solid phase local bilinear operators of Eqs. (2.172a) and (2.172b) to retrieve

$$a_{\mathcal{K}}^\varepsilon(\mathbf{u}_h, \delta \mathbf{u}_h) = P(a_{\mathcal{K}}^\varepsilon) + NP(a_{\mathcal{K}}^\varepsilon), \quad (3.93)$$

$$a_{\mathcal{K}}^0(\mathbf{u}_h, \delta \mathbf{u}_h)_{\bar{p}} = P(a_{\mathcal{K}}^0) + NP(a_{\mathcal{K}}^0), \quad (3.94)$$

where

$$P(a_{\mathcal{K}}^\varepsilon) = a_{\mathcal{K}}^\varepsilon\left(\Pi_k^\varepsilon \mathbf{u}_h, \Pi_k^\varepsilon \delta \mathbf{u}_h\right), \quad (3.95)$$

$$NP(a_{\mathcal{K}}^\varepsilon) = a_{\mathcal{K}}^\varepsilon\left((\mathbf{u}_h - \Pi_k^\varepsilon \mathbf{u}_h), (\delta \mathbf{u}_h - \Pi_k^\varepsilon \delta \mathbf{u}_h)\right), \quad (3.96)$$

and

$$P(a_{\mathcal{K}}^0) = a_{\mathcal{K}}^0 \left(\Pi_k^{0u} \mathbf{u}_h, \Pi_k^{0u} \delta \mathbf{u}_h \right)_{\tilde{\rho}}, \quad (3.97)$$

$$NP(a_{\mathcal{K}}^0) = a_{\mathcal{K}}^0 \left((\mathbf{u}_h - \Pi_k^{0u} \mathbf{u}_h), (\delta \mathbf{u}_h - \Pi_k^{0u} \delta \mathbf{u}_h) \right)_{\tilde{\rho}}, \quad (3.98)$$

respectively.

In Eq. (3.95), the projector Π_k^ε has already been evaluated in Eq. (3.21). However, the \mathcal{L}_2 projector Π_k^{0u} is at present, unknown. As before, this is defined using the following orthogonality criterion

$$\Pi_k^{0u} := a_{\mathcal{K}}^0 (\mathbf{u}_h - \Pi_k^{0u} \mathbf{u}_h, \mathbf{m})_{\tilde{\rho}} = 0, \quad (3.99a)$$

$$\forall \mathbf{u}_h \in \mathcal{V}_h^u(\mathcal{K}), \mathbf{m} \in [\mathbb{P}_k(\mathcal{K})]^2.$$

Similarly, Eqs. (3.35) are inserted into the fluid phase operators of Eqs. (2.173a) and (2.173b) to yield

$$b_{\mathcal{K}}^{\nabla}(\mathfrak{p}_h, \delta \mathfrak{p}_h)_{\frac{1}{\tilde{\rho}_{\text{eq}}}} = P(b_{\mathcal{K}}^{\nabla}) + NP(b_{\mathcal{K}}^{\nabla}), \quad (3.100)$$

$$b_{\mathcal{K}}^0(\mathfrak{p}_h, \delta \mathfrak{p}_h)_{\frac{1}{\tilde{K}_{\text{eq}}}} = P(b_{\mathcal{K}}^0) + NP(b_{\mathcal{K}}^0), \quad (3.101)$$

with the respective arguments

$$P(b_{\mathcal{K}}^{\nabla}) = b_{\mathcal{K}}^{\nabla} \left(\Pi_k^{\nabla p} \mathfrak{p}_h, \Pi_k^{\nabla p} \delta \mathfrak{p}_h \right)_{\frac{1}{\tilde{\rho}_{\text{eq}}}}, \quad (3.102)$$

$$NP(b_{\mathcal{K}}^{\nabla}) = b_{\mathcal{K}}^{\nabla} \left((\mathfrak{p}_h - \Pi_k^{\nabla p} \mathfrak{p}_h), (\delta \mathfrak{p}_h - \Pi_k^{\nabla p} \delta \mathfrak{p}_h) \right)_{\frac{1}{\tilde{\rho}_{\text{eq}}}}, \quad (3.103)$$

and

$$P(b_{\mathcal{K}}^0) = b_{\mathcal{K}}^0 \left(\Pi_k^{0p} \mathfrak{p}_h, \Pi_k^{0p} \delta \mathfrak{p}_h \right)_{\frac{1}{\tilde{K}_{\text{eq}}}}, \quad (3.104)$$

$$NP(b_{\mathcal{K}}^0) = b_{\mathcal{K}}^0 \left((\mathfrak{p}_h - \Pi_k^{0p} \mathfrak{p}_h), (\delta \mathfrak{p}_h - \Pi_k^{0p} \delta \mathfrak{p}_h) \right)_{\frac{1}{\tilde{K}_{\text{eq}}}}, \quad (3.105)$$

respectively.

Both the fluid phase specific projectors $\Pi_k^{\nabla p}$ and Π_k^{0p} have already been evaluated in Eqs. (3.61) and (3.72), respectively.

Eqs. (3.2) and (3.35) are now substituted into the coupling operator in Eq. (2.174a) to derive the expression

$$a_{\mathcal{K}}^{(\nabla,0)} = P(a_{\mathcal{K}}^{(\nabla,0)}) + NP(a_{\mathcal{K}}^{(\nabla,0)}), \quad (3.106)$$

with

$$P(a_{\mathcal{K}}^{(\nabla,0)}) = a_{\mathcal{K}}^{(\nabla,0)} \left(\Pi_k^{\nabla p} p_h, \Pi^{0u} \delta \mathbf{u}_h \right)_{\tilde{\gamma}}, \quad (3.107)$$

$$NP(a_{\mathcal{K}}^{(\nabla,0)}) = a_{\mathcal{K}}^{(\nabla,0)} \left((p_h - \Pi_k^{\nabla p} p_h), (\delta \mathbf{u}_h - \Pi^{0u} \delta \mathbf{u}_h) \right)_{\tilde{\gamma}}, \quad (3.108)$$

To compute the \mathcal{L}_2 projector Π_k^{0u} , an intermediate fifth projector $\Pi_k^{\nabla u} := \mathcal{V}_k^u(\mathcal{K}) \rightarrow [\mathbb{P}_k(\mathcal{K})]^2$ is required [90]. This is a projector specific to the solid phase and is defined here for completeness

$$\Pi_k^{\nabla u} := a_{\mathcal{K}}^{\nabla}(\mathbf{u}_h - \Pi_k^{\nabla u} \mathbf{u}_h, \mathbf{m})_{\delta^*} = 0, \quad \forall \mathbf{u}_h \in \mathcal{V}_h^u(\mathcal{K}), \quad \mathbf{m} \in [\mathbb{M}_k(\mathcal{K})]^2 \setminus \mathbb{K}^{\nabla u}(\mathcal{K}), \quad (3.109)$$

where $\mathbb{K}^{\nabla u}$ denotes the kernel of $a_{\mathcal{K}}^{\nabla}(\cdot, \cdot)$. This operator is defined as follows

$$a_{\mathcal{K}}^{\nabla}(\mathbf{u}_h, \delta \mathbf{u}_h)_{\delta^*} = \int_{\mathcal{K}} \delta^* \nabla \mathbf{u}_h \cdot \nabla \delta \mathbf{u}_h \, d\mathcal{K}, \quad (3.110)$$

where the material parameter δ^* is an arbitrarily chosen scalar real valued number. The need for this additional projector is dealt with in greater detail in Section 3.5.4.

3.5.2 Computing the projectors

As done earlier, the projected functions are expanded in terms of the appropriate monomial bases. The \mathcal{H}^1 projector, i.e., $\Pi_k^{\nabla u}$ is expanded as

$$\Pi_k^{\nabla u} \mathbf{u}_h = \sum_{i=1}^{n_k^u - 2} \mathbf{m}_{i+2} \zeta_i^{\nabla u}, \quad (3.111)$$

where $\zeta_i^{\nabla u}$ is a $(1 \times n_{\text{dof}}^u)$ vector of the unknown expansion coefficients.

Eq. (3.111) is expressed in matrix form as

$$\Pi_k^{\nabla u} \mathbf{u}_h = \underbrace{\mathbf{m}^{\nabla u}}_{(2 \times n_k^u - 2)} \underbrace{\zeta^{\nabla u}}_{(n_k^u - 2 \times n_{\text{dof}}^u)}, \quad (3.112)$$

where the matrix $\mathbf{m}^{\nabla u}$ holds the relevant monomial basis and $\zeta^{\nabla u}$ is an array whose i_{th} row holds the vectors of expansion coefficients $\zeta_i^{\nabla u}$.

The unknown \mathcal{L}^2 projector, Π_k^{0u} is expanded as

$$\Pi_k^{0u} \mathbf{u}_h = \sum_{i=1}^{n_k^u} \mathbf{m}_i \zeta_i^{0u}, \quad (3.113)$$

where ζ_i^{0u} is a $(1 \times n_{\text{dof}}^u)$ vector.

The corresponding matrix for Eq. (3.113) is

$$\Pi_k^{0u} \mathbf{u}_h = \underbrace{\mathbf{m}^{0u}}_{(2 \times n_k^u)} \underbrace{\boldsymbol{\zeta}^{0u}}_{(n_k^u \times n_{\text{dof}}^u)}, \quad (3.114)$$

where the matrix \mathbf{m}^{0u} contains the monomial basis and $\boldsymbol{\zeta}^{0u}$ is the associated array of expansion coefficients.

3.5.3 Computing the projectors $\Pi_k^{\nabla u}$

As done in earlier sections, imposing the orthogonality condition Eq. (3.109) on Eq. (3.111), the following equation is established for the expansion coefficients of the projector $\Pi_k^{\nabla u}$

$$\underbrace{\mathbf{G}^{\nabla u}}_{(n_k^u - 2 \times n_k^u - 2)} \boldsymbol{\zeta}^{\nabla u} = \underbrace{\mathbf{B}^{\nabla u}}_{(n_k^u - 2 \times n_{\text{dof}}^u)}, \quad (3.115)$$

where the matrices $\mathbf{G}^{\nabla u}$, $\mathbf{B}^{\nabla u}$ are defined as

$$\mathbf{G}_{ij}^{\nabla u} = \int_{\mathcal{K}} (\nabla \mathbf{m}_{i+2})^T \delta^* \nabla \mathbf{m}_{j+2} \, d\mathcal{K}, \quad (3.116)$$

and

$$\mathbf{B}_j^{\nabla u} = \int_{\mathcal{K}} (\nabla \mathbf{u}_h)^T \delta^* \nabla \mathbf{m}_{j+2} \, d\mathcal{K}, \quad (3.117)$$

respectively.

The integral $\mathbf{G}_{ij}^{\nabla u}$ in Eq. (3.116) is computable using numerical quadrature rules. On the other hand, $\mathbf{B}_j^{\nabla u}$ cannot be evaluated in its current form as \mathbf{u}_h is not explicitly defined over the element domain interior. Eq. (3.117) is split into its boundary and domain contributions

$$\mathbf{B}_j^{\nabla u} = \mathbf{B}_{bj}^{\nabla u} + \mathbf{B}_{dj}^{\nabla u}, \quad (3.118)$$

where

$$\mathbf{B}_{bj}^{\nabla u} = \sum_{e \in \partial \mathcal{K}} \int_e \mathbf{u}_h \cdot (\delta^* \nabla \mathbf{m}_{j+2} \mathbf{n}_e^\nabla) \, de, \quad (3.119)$$

and

$$\mathbf{B}_{dj}^{\nabla u} = - \int_{\mathcal{K} \setminus \partial \mathcal{K}} \mathbf{u}_h \cdot (\delta^* \Delta \mathbf{m}_{j+2}) \, d\mathcal{K}, \quad (3.120)$$

respectively. The boundary integral in Eq. (3.118) is evaluated with a Gauss-Lobatto quadrature similar to Eqs. (3.17) and (3.54).

To evaluate the corresponding domain integrals, the terms $\Delta \mathbf{m}_{j+2}$ in Eq. (3.120) is expanded over the $[\mathbb{M}_{k-2}(\mathcal{K})]^2$ basis

$$\delta^* \Delta \mathbf{m}_{j+2} = \sum_{\beta=1}^{n_{k-2}^u} d_{j\beta}^{\nabla u} \mathbf{m}_\beta, \quad \forall \mathbf{m}_\beta \in [\mathbb{M}_{k-2}(\mathcal{K})]^2. \quad (3.121)$$

Inserting Eq. (3.121) in Eq. (3.120) the following expression is derived

$$\mathbf{B}_{dj}^{\nabla u} = -|\mathcal{K}| \sum_{\beta=1}^{n_{k-2}^u} d_{j\beta}^{\nabla u} \text{dof}_{kN_v+\beta}(\mathbf{u}_h) = -|\mathcal{K}| \mathbf{d}^{\nabla u}, \quad (3.122)$$

where

$$\mathbf{d}^{\nabla u} = \left[\overbrace{0 \quad \cdots \quad 0}^{N_B^u} \mid \overbrace{d_{j1}^{\nabla u} \quad \cdots \quad d_{j(n_{k-2}^u)}^{\nabla u}}^{N_A^u} \right]. \quad (3.123)$$

The projector $\Pi_k^{\nabla u}$ is now computed

$$\Pi_k^{\nabla u} \mathbf{u}_h = \mathbf{m}^{\nabla u} [\mathbf{G}^{\nabla u}]^{-1} \mathbf{B}^{\nabla u}, \quad (3.124)$$

3.5.4 Computing the projectors Π_k^{0u}

Within this vibroacoustics setting, an additional unknown \mathcal{L}^2 projector, i.e., Π_k^{0u} emerges. This is evaluated in a similar to manner to Π_k^{0p} as done in Section 3.4.4. Eq. (3.113) is substituted into Eq. (3.99) to obtain

$$\underbrace{\mathbf{G}^{0u}}_{(n_k^u \times n_k^u)} \zeta^{0u} = \underbrace{\mathbf{B}^{0u}}_{(n_k^u \times n_{\text{dof}}^u)}, \quad (3.125)$$

where \mathbf{G}^{0u} has the definition

$$G_{ij}^{0u} = \int_{\mathcal{K}} (\mathbf{m}_i)^T \tilde{\rho} \mathbf{m}_j \, d\mathcal{K}, \quad (3.126a)$$

The array \mathbf{B}^{0u} has the j_{th} row

$$\mathbf{B}_j^{0u} = \int_{\mathcal{K}} (\mathbf{u}_h)^T \tilde{\rho} \mathbf{m}_j \, d\mathcal{K}, \quad (3.127)$$

As explained in Section 3.4.4, G_{ij}^{0u} is computable through sub-triangulation, however, B_{ij}^{0u} is not. This integral is computed through the existing DoFs of $\mathcal{V}_h^u(\mathcal{K})$ when the current monomial has a degree lesser than or equal to $k - 2$. Conversely, the integral is evaluated using $\Pi_k^{\nabla u}$ when the order of the monomial under consideration is larger than $k - 2$.

To this end, \mathbf{B}_j^{0u} assumes the following form

$$\mathbf{B}_j^{0u} = \begin{cases} \mathbf{B}_{1j}^{0u}, & \text{if } 1 \leq j \leq n_{k-2}^u \\ \mathbf{B}_{2j}^{0u}, & \text{if } n_{k-2}^u < j \leq n_k^u, \end{cases} \quad (3.128)$$

Using Table 3.2, \mathbf{B}_{1j}^{0u} now reads

$$\mathbf{B}_{1j}^{0u} = |\mathcal{K}| \tilde{\rho} \text{dof}(\mathbf{u}_h) = |\mathcal{K}| \mathbf{d}_j^{0u}, \quad (3.129)$$

where

$$\mathbf{d}_j^{0u} = \tilde{\rho} \left[\overbrace{0 \quad \cdots \quad 0}^{N_B^u} \mid \overbrace{0 \quad \cdots \quad 1 \quad \cdots \quad 0}^{N_A^u} \right]. \quad (3.130)$$

Using the monomial expansion for $\Pi_k^{\nabla u} \mathbf{u}_h$ Eq. (3.113)^j with running index β instead of i to avoid confusion, \mathbf{B}_{2j}^{0u} is now evaluated

$$\mathbf{B}_2^{0u} = \underbrace{\mathbf{H}^u}_{(n_k^u - 2 \times n_k^u - 2)} \boldsymbol{\zeta}^{\nabla u}, \quad (3.131)$$

where

$$\mathbf{H}_{\beta j}^u = \int_{\mathcal{K}} (\mathbf{m}_{\beta+2})^T \tilde{\rho} \mathbf{m}_j \, d\mathcal{K}, \quad \beta = 1, \dots, n_k^u - 2. \quad (3.132)$$

$\mathbf{H}_{\beta j}^u$ and $\mathbf{H}_{\beta j}^p$ is computable using sub-triangulation.

Using Eqs. (3.129) and (3.131), \mathbf{B}^{0u} is cast in the following form

$$\mathbf{B}^{0u} = [\mathbf{B}_1^{0u} \mid \mathbf{B}_2^{0u}]^T. \quad (3.133)$$

Eq. (3.125) is solved for the expansion coefficients and inserted into Eq. (3.114) to yield

$$\Pi_k^{0u} \mathbf{u}_h = \mathbf{m}^{0u} [\mathbf{G}^{0u}]^{-1} \mathbf{B}^{0u}. \quad (3.134)$$

3.5.5 Consistency terms

Using Eqs. (2.172a) and (2.172b), the solid phase polynomial terms in Eq. (3.93) and Eq. (3.94) give rise to an elastic consistency term

$$a_{\mathcal{K}}^{\varepsilon}(\mathbf{u}_h, \delta \mathbf{u}_h) = \int_{\mathcal{K}} \boldsymbol{\sigma}_s(\Pi_k^{\varepsilon} \mathbf{u}_h) : \boldsymbol{\varepsilon}_s(\Pi_k^{\varepsilon} \delta \mathbf{u}_h) \, d\mathcal{K}, \quad (3.135)$$

and a mass consistency term

$$a_{\mathcal{K}}^0(\mathbf{u}_h, \delta \mathbf{u}_h)_{\tilde{\rho}} = \int_{\mathcal{K}} \tilde{\rho} \Pi_k^{0u} \mathbf{u}_h \cdot \Pi_k^{0u} \delta \mathbf{u}_h \, d\mathcal{K}, \quad (3.136)$$

respectively. Similarly, substituting Eqs. (2.173a), (2.173b), and (2.174a) in the polynomial terms of Eqs. (3.100), (3.101), and (3.106), respectively results in the following expressions for the fluid kinetic consistency term

$$b^{\nabla}(\mathbf{p}, \delta \mathbf{p}_h)_{\frac{1}{\tilde{\rho}_{\text{eq}}}} = \int_{\mathcal{K}} \frac{1}{\tilde{\rho}_{\text{eq}}} \nabla \left(\Pi_k^{\nabla p} \mathbf{p}_h \right) \cdot \nabla \left(\Pi_k^{\nabla p} \delta \mathbf{p}_h \right) \, d\mathcal{K}, \quad (3.137)$$

the fluid compressibility consistency term

$$b^0(\mathbf{p}, \delta \mathbf{p}_h)_{\frac{1}{\tilde{K}_{\text{eq}}}} = \int_{\mathcal{K}} \frac{1}{\tilde{K}_{\text{eq}}} \Pi_k^{0p} \mathbf{p}_h \cdot \Pi_k^{0p} \delta \mathbf{p}_h \, d\mathcal{K}, \quad (3.138)$$

and the coupling consistency term

$$a^{\nabla,0}(\mathbf{p}_h, \delta \mathbf{u}_h)_{\tilde{\gamma}} = \int_{\mathcal{K}} \tilde{\gamma} \nabla \left(\Pi^{\nabla p} \mathbf{p}_h \right) \cdot \Pi^{0u} \delta \mathbf{u}_h \, d\mathcal{K}, \quad (3.139)$$

respectively.

Substituting the projector approximation from Eq. (3.21) in Eq. (3.135) and performing the necessary algebraic manipulations, the following expression is eventually retrieved for the elastic stiffness consistency term

$$\tilde{\mathbf{K}}_{\mathcal{K}}^C = \boldsymbol{\zeta}^{\varepsilon T} [\mathbf{G}^{\varepsilon}] \boldsymbol{\zeta}^{\varepsilon}, \quad (3.140)$$

where \mathbf{G}^{ε} is provided in Eq. (3.11).

Similarly, substituting the projector approximation of Eq. (3.134) into Eq. (3.136) the following expression for the mass consistency term is retrieved

$$\tilde{\mathbf{M}}_{\mathcal{K}}^C = \boldsymbol{\zeta}^{0u T} [\mathbf{G}^{0u}] \boldsymbol{\zeta}^{0u}, \quad (3.141)$$

where \mathbf{G}^{0u} is provided in Eq. (3.126a).

The expressions for the fluid phase consistency terms are established by substituting Eqs. (3.61) and (3.72) into Eqs. (3.137) and (3.138), respectively. Hence, the fluid kinetic consistency term assumes the following form

$$\tilde{\mathbf{H}}_{\mathcal{K}}^C = \boldsymbol{\zeta}^{\nabla p T} [\mathbf{G}^{\nabla p}] \boldsymbol{\zeta}^{\nabla p}, \quad (3.142)$$

where $\mathbf{G}^{\nabla p}$ is evaluated in Eq. (3.52) and the fluid compressibility term becomes

$$\tilde{\mathbf{Q}}_{\mathcal{K}}^C = \boldsymbol{\zeta}^{0p T} [\mathbf{G}^{0p}] \boldsymbol{\zeta}^{0p}, \quad (3.143)$$

where \mathbf{G}^{0p} is provided in Eqs. (3.63).

Finally, the phase coupling consistency term in Eq. (3.139) assumes the following form

$$\tilde{\mathbf{C}}_{\mathcal{K}}^C = \boldsymbol{\zeta}^{\nabla p T} \underbrace{[\mathbf{G}^{\nabla p 0u}]}_{(n_k^p - 1 \times n_k^u)} \boldsymbol{\zeta}^{0u}, \quad (3.144)$$

where where $\mathbf{G}^{\nabla p 0u}$ in Eq. (3.144) is an array with elements

$$\left(\mathbf{G}^{\nabla p 0u} \right)_{ij} = \int_{\mathcal{K}} \tilde{\gamma} \nabla (\mathbf{m}_{i+1}) \cdot \mathbf{m}_j \, d\mathcal{K}, \quad i = 1, \dots, n_k^p - 1, \quad j = 1, \dots, n_k^u. \quad (3.145)$$

3.5.6 Stability terms

As done in Eqs. (3.81), the projectors expressed in terms of the monomials are mapped onto a space spanned by the canonical bases

$$\Pi_k^{0u} \mathbf{u}_h = \mathbf{m}^{0u} \boldsymbol{\zeta}^{0u} = [\boldsymbol{\Phi}^u]^T \underbrace{\mathbf{D}^{0u}}_{(n_{\text{dof}}^u \times n_k^u)} \boldsymbol{\zeta}^{0u}, \quad (3.146)$$

where \mathbf{D}^{0u} has the form

$$\mathbf{D}^{0u} = \begin{bmatrix} \text{dof}_1(\mathbf{m}_1) & \dots & \text{dof}_1(\mathbf{m}_{n_k^u}) \\ \vdots & \ddots & \vdots \\ \text{dof}_{n_{\text{dof}}^u}(\mathbf{m}_1) & \dots & \text{dof}_{n_{\text{dof}}^u}(\mathbf{m}_{n_k^u}) \end{bmatrix}, \quad (3.147)$$

$$\forall \mathbf{m} \in [\mathbb{M}_k(\mathcal{K})]^2.$$

The complete stability relevant operator is now provided in the canonical basis

$$\mathbf{\Pi}_{\text{tot}}^{0u} = \mathbf{D}^{0u} \boldsymbol{\zeta}^{0u}. \quad (3.148)$$

The following stability term approximants are introduced for the non-polynomial components of the solid phase

$$\text{NP}(a_{\mathcal{K}}^\varepsilon) \approx \boldsymbol{\mathcal{S}}^K(\mathbf{u}_h, \delta \mathbf{u}_h) = [\boldsymbol{\Phi}^u]^T \tilde{\mathbf{K}}_{\mathcal{K}}^S [\boldsymbol{\Phi}^u] \quad (3.149a)$$

$$\text{NP}(a_{\mathcal{K}}^0) \approx \boldsymbol{\mathcal{S}}^M(\mathbf{u}_h, \delta \mathbf{u}_h) = [\boldsymbol{\Phi}^u]^T \tilde{\mathbf{M}}_{\mathcal{K}}^S [\boldsymbol{\Phi}^u], \quad (3.149b)$$

the fluid phase

$$\text{NP}(b_{\mathcal{K}}^\nabla) \approx \boldsymbol{\mathcal{S}}^H(p_h, \delta p_h) = [\boldsymbol{\Phi}^p]^T \tilde{\mathbf{H}}_{\mathcal{K}}^S [\boldsymbol{\Phi}^p] \quad (3.150a)$$

$$\text{NP}(b_{\mathcal{K}}^0) \approx \boldsymbol{\mathcal{S}}^Q(p_h, \delta p_h) = [\boldsymbol{\Phi}^p]^T \tilde{\mathbf{Q}}_{\mathcal{K}}^S [\boldsymbol{\Phi}^p], \quad (3.150b)$$

and the coupling term

$$\text{NP}(a_{\mathcal{K}}^{(\nabla,0)}) \approx \boldsymbol{\mathcal{S}}^C(p_h, \delta \mathbf{u}_h) = [\boldsymbol{\Phi}^p]^T \tilde{\mathbf{C}}_{\mathcal{K}}^S [\boldsymbol{\Phi}^u], \quad (3.151)$$

respectively.

In Eqs. (3.149a)-(3.151), $\tilde{\mathbf{K}}_{\mathcal{K}}^S$, $\tilde{\mathbf{M}}_{\mathcal{K}}^S$, $\tilde{\mathbf{H}}_{\mathcal{K}}^S$, $\tilde{\mathbf{Q}}_{\mathcal{K}}^S$, and $\tilde{\mathbf{C}}_{\mathcal{K}}^S$ denote the elastic, mass, fluid kinetic, fluid compressibility and coupling stability stiffness matrices, respectively. These are defined according to the following expressions

$$\tilde{\mathbf{K}}_{\mathcal{K}}^S = (\mathbb{I}_u - \mathbf{\Pi}_{\text{tot}}^\varepsilon) \beta_K (\mathbb{I}_u - \mathbf{\Pi}_{\text{tot}}^\varepsilon), \quad (3.152a)$$

$$\tilde{\mathbf{M}}_{\mathcal{K}}^S = (\mathbb{I}_u - \mathbf{\Pi}_{\text{tot}}^{0u}) \beta_M (\mathbb{I}_u - \mathbf{\Pi}_{\text{tot}}^{0u}), \quad (3.152b)$$

$$\tilde{\mathbf{H}}_{\mathcal{K}}^S = (\mathbb{I}_p - \mathbf{\Pi}_{\text{tot}}^{\nabla p}) \beta_H (\mathbb{I}_p - \mathbf{\Pi}_{\text{tot}}^{\nabla p}), \quad (3.152c)$$

$$\tilde{\mathbf{Q}}_{\mathcal{K}}^S = (\mathbb{I}_p - \mathbf{\Pi}_{\text{tot}}^{0p}) \beta_Q (\mathbb{I}_p - \mathbf{\Pi}_{\text{tot}}^{0p}), \quad (3.152d)$$

$$\tilde{\mathbf{C}}_{\mathcal{K}}^S = (\mathbb{I}_p - \mathbf{\Pi}_{\text{tot}}^{\nabla p}) \beta_C \mathbb{I}_C (\mathbb{I}_u - \mathbf{\Pi}_{\text{tot}}^{0u}). \quad (3.152e)$$

where $\mathbb{I}_C = [\mathbb{I}_p, \mathbb{I}_p]$ is used to ensure compatible matrix multiplication. The stabilization parameters β_K , β_M , β_H , β_Q and β_C are defined using the D-recipe stabilization as used earlier for consolidation

$$\begin{aligned}
\beta_{\mathbf{K}}^G &= \gamma_{\mathbf{K}}^G |\mathcal{K}| \frac{\text{tr}(\mathbb{D})}{\text{tr}(\mathbf{D}\boldsymbol{\varepsilon}^T \mathbf{D}\boldsymbol{\varepsilon})} & \beta_{\mathbf{M}}^G &= \gamma_{\mathbf{M}}^G |\mathcal{K}| \frac{\tilde{\rho}}{\text{tr}(\mathbf{D}^{0u^T} \mathbf{D}^{0u})} \\
\beta_{\mathbf{H}}^G &= \gamma_{\mathbf{H}}^G |\mathcal{K}| \frac{1/\tilde{\rho}_{\text{eq}}}{\text{tr}(\mathbf{D}^{\nabla p^T} \mathbf{D}^{\nabla p})} & \beta_{\mathbf{Q}}^G &= \gamma_{\mathbf{Q}}^G |\mathcal{K}| \frac{1/\tilde{K}_{\text{eq}}}{\text{tr}(\mathbf{D}^{0p^T} \mathbf{D}^{0p})} \\
\beta_{\mathbf{C}}^G &= \gamma_{\mathbf{C}}^G |\mathcal{K}| \frac{\tilde{\gamma}}{\text{tr}(\mathbf{D}^{0p^T} \mathbf{D}^{0p})},
\end{aligned} \tag{3.153}$$

where, setting $\gamma_{\mathbf{K}}^G = \gamma_{\mathbf{M}}^G = \gamma_{\mathbf{H}}^G = \gamma_{\mathbf{Q}}^G = \gamma_{\mathbf{C}}^G = 1$ yield good results in all cases.

However, it has been reported in [111], that the stabilization parameter for the elastic stiffness matrix, while stable with regards to uniform/isotropic scaling, is unstable with respect to the aspect ratio of the element. Such unstable ratios can often be encountered, e.g., in the case of non-conforming interfaces. To remedy this, an alternate choice for the elastic stiffness stabilization parameter is proposed in [111]

$$\beta_{\mathbf{K}}^N = \gamma_{\mathbf{K}}^N |\mathcal{K}| \text{tr}(\mathbb{D}) \text{tr}([\mathbf{D}\boldsymbol{\varepsilon}^T \mathbf{D}\boldsymbol{\varepsilon}]^{-1}). \tag{3.154}$$

The value $\gamma_{\mathbf{K}}^N = \frac{1}{9}$ has been suggested in [111]. For a more detailed study on the influence of mesh quality on the VEM, the reader is referred to [191].

3.5.7 State matrices

As before, the virtual element state matrices are now defined according to the expressions below

		<i>Consistency</i>	<i>Stability</i>	
$\tilde{\mathbf{K}}_{\mathcal{K}}$	\approx	$\tilde{\mathbf{K}}_{\mathcal{K}}^C$	+	$\tilde{\mathbf{K}}_{\mathcal{K}}^S$
$\tilde{\mathbf{M}}_{\mathcal{K}}$	\approx	$\tilde{\mathbf{M}}_{\mathcal{K}}^C$	+	$\tilde{\mathbf{M}}_{\mathcal{K}}^S$
$\tilde{\mathbf{H}}_{\mathcal{K}}$	\approx	$\tilde{\mathbf{H}}_{\mathcal{K}}^C$	+	$\tilde{\mathbf{H}}_{\mathcal{K}}^S$
$\tilde{\mathbf{Q}}_{\mathcal{K}}$	\approx	$\tilde{\mathbf{Q}}_{\mathcal{K}}^C$	+	$\tilde{\mathbf{Q}}_{\mathcal{K}}^S$,
$\tilde{\mathbf{C}}_{\mathcal{K}}$	\approx	$\tilde{\mathbf{C}}_{\mathcal{K}}^C$	+	$\tilde{\mathbf{C}}_{\mathcal{K}}^S$.

(3.155)

The local state matrices are then assembled into the relevant global state matrices according to Eqs. (2.180).

It is to be noted that as stated earlier in Section 3.3.6, that the boundary terms mentioned in Eqs. (2.173c) and (2.174b) can be computed in a straightforward way without resorting to deriving projectors exclusive to these forms, as done in Eqs. (2.181).

3.6 Numerical examples

In this section, the accuracy of the VEM through four numerical examples is investigated. A first order method $k = 1$ is used. The accuracy of the displacements and pressures achieved by

the method is measured through relative \mathcal{L}_2 error norms

$$\begin{aligned} & \|\mathbf{u}_h^{\mathcal{Q}}(\omega) - \mathbf{u}_{ref}^{\mathcal{Q}}(\omega)\|_{\mathcal{L}_2} = \\ & \sqrt{\frac{1}{n_{\mathcal{Q}_{el}}} \sum_{i=1}^{n_{\mathcal{Q}_{el}}} \frac{\langle \mathbf{u}_{h(i)}^{\mathcal{Q}}(\omega) - \mathbf{u}_{ref(i)}^{\mathcal{Q}}(\omega), \mathbf{u}_{h(i)}^{\mathcal{Q}}(\omega) - \mathbf{u}_{ref(i)}^{\mathcal{Q}}(\omega) \rangle}{\langle \mathbf{u}_{ref(i)}^{\mathcal{Q}}(\omega), \mathbf{u}_{ref(i)}^{\mathcal{Q}}(\omega) \rangle}}, \end{aligned} \quad (3.156)$$

$$\begin{aligned} & \|\mathbf{p}_h^{\mathcal{Q}}(\omega) - \mathbf{p}_{ref}^{\mathcal{Q}}(\omega)\|_{\mathcal{L}_2} = \\ & \sqrt{\frac{1}{n_{\mathcal{Q}_{el}}} \sum_{i=1}^{n_{\mathcal{Q}_{el}}} \frac{\langle \mathbf{p}_{h(i)}^{\mathcal{Q}}(\omega) - \mathbf{p}_{ref(i)}^{\mathcal{Q}}(\omega), \mathbf{p}_{h(i)}^{\mathcal{Q}}(\omega) - \mathbf{p}_{ref(i)}^{\mathcal{Q}}(\omega) \rangle}{\langle \mathbf{p}_{ref(i)}^{\mathcal{Q}}(\omega), \mathbf{p}_{ref(i)}^{\mathcal{Q}}(\omega) \rangle}}, \end{aligned} \quad (3.157)$$

where $\mathbf{u}_h^{\mathcal{Q}}(\omega)$, $\mathbf{p}_h^{\mathcal{Q}}(\omega)$, where $\mathbf{u}_{ref}^{\mathcal{Q}}(\omega)$, $\mathbf{p}_{ref}^{\mathcal{Q}}(\omega)$ denote numerically computed and reference displacements and pressures at an excitation frequency ω , respectively. The quantities are interpolated over a query mesh \mathcal{Q} with $n_{el}^{\mathcal{Q}}$ elements. The reference solutions $\mathbf{u}_{ref}^{\mathcal{Q}}$ and $\mathbf{p}_{ref}^{\mathcal{Q}}$ are obtained using finely discretized FEM solutions. The stabilization scaling parameters used throughout the examples correspond to Eq. (3.153), unless explicitly stated otherwise.

Useful acoustic indicators like the Sound Absorption Coefficient (SAC) and the Sound Transmission Loss Coefficient (STL) are provided according to Section 2.7.4. For comparisons, a reference SAC or STL curve is generated with the finely discretized post-processed FEM results or the semi-analytical Transfer Matrix Method (TMM) [13].

3.6.1 Square poroelastic domain

The convergence behaviour of the method is investigated herein. A square poroelastic domain with a side $b = 57$ mm is considered. This domain is given impedance tube constraints, i.e. a roller support on the lateral sides and a rigid impervious backing at the rear. It is excited by an acoustic plane wave at normal incidence. This configuration is illustrated in Fig. 3.5.

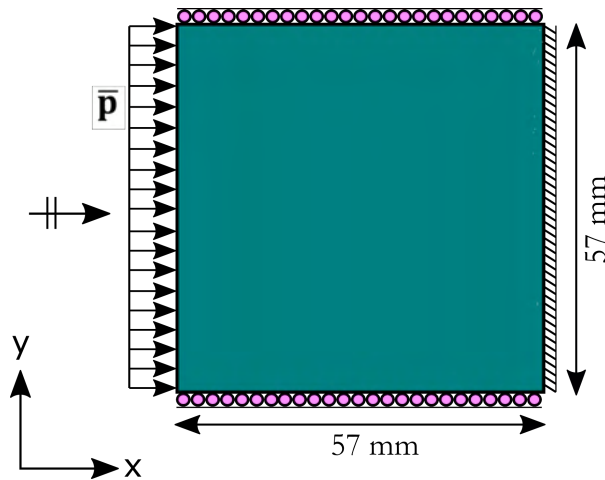


Figure 3.5: A poroelastic domain in impedance tube configuration subject to plane-wave acoustical excitation \bar{p} at normal incidence.

The material used is a poroelastic melamine foam. The macroscopic material parameters are

provided as Material ID III in Table 3.7. Since the governing equations are linear in pressures, the solutions can be appropriately scaled with the excitation. For the sake of brevity, an amplitude of 1 Pa is considered.

The VEM solution procedure is performed using a structured quadrilateral grid (QUAD) and unstructured Centroidal Voronoi Tessellation grid (CVT) over an excitation frequency range $f \in [20\text{Hz}, 5500\text{Hz}]$. Results were found to converge at a discretization of 10×10 QUAD elements and 100 polygonal CVT elements. The converged displacement contours $\|\mathbf{u}\|$ for both meshes are shown in Fig. 3.6 at 20 Hz and 1500 Hz. Similarly, the converged pressure contours p are provided in Fig. 3.7 for the same frequencies.

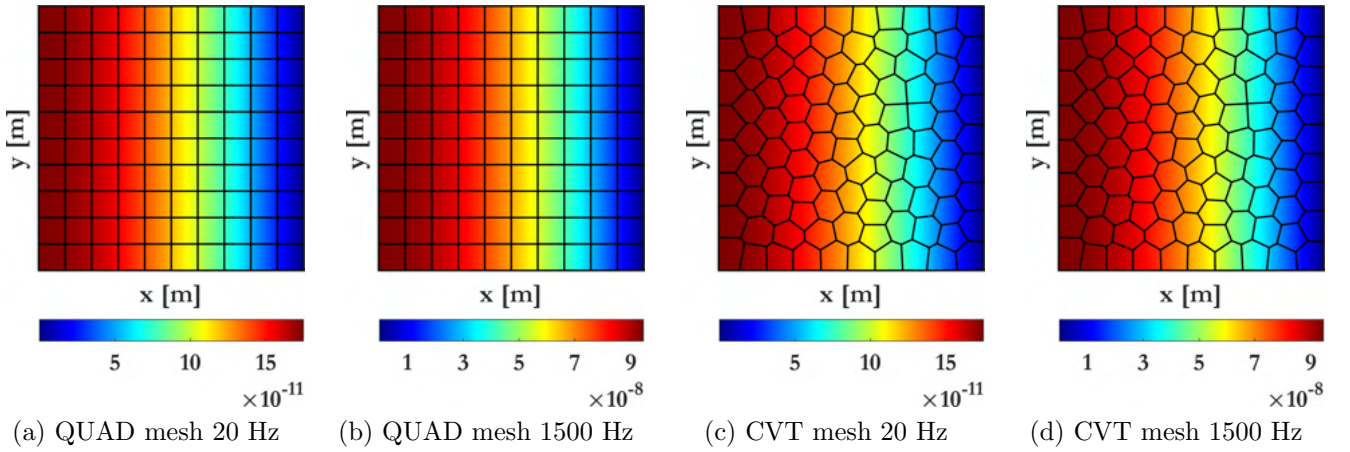


Figure 3.6: Converged $\|\mathbf{u}\|$ displacement contours at excitation frequencies 20 Hz and 1500 Hz for QUAD and CVT type meshes.

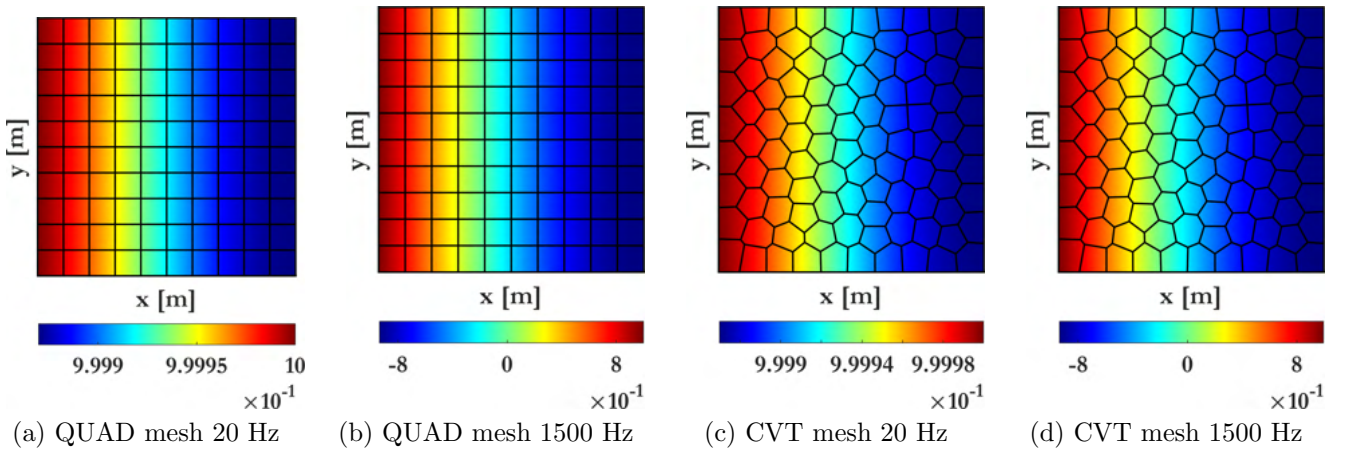


Figure 3.7: Converged p pressure contours at excitation frequencies 20 Hz and 1500 Hz for QUAD and CVT type meshes.

The contours obtained by the VEM for both meshes are practically identical with a linear variation in displacements and a uniform pressure profile across the domain being retrieved. As anticipated, the method converges to a solution that is independent of the type of the underlying discretization.

Next, a convergence study is performed through an a posteriori error- based mesh sensitivity analysis. Five QUAD and five CVT meshes are chosen for this purpose. The details of these

Label	QUAD		CVT	
	Nodes	Elements	Nodes	Elements
I	36	5×5	52	25
II	121	10×10	202	100
III	676	25×25	1251	625
IV	2601	50×50	4993	2500
V	10,201	100×100	19,968	10,000

Table 3.5: Discretization used for the error-based mesh sensitivity analysis.

discretizations are provided in Table 3.5. A finely discretized FEM solution with a structured 250×250 QUAD mesh is used as a reference.

The relative displacement errors in \mathcal{L}_2 norm for both mesh types are shown at frequencies $f = 20$ Hz, $f = 750$ Hz and $f = 1500$ Hz in Fig. 3.8. Variations with respect to the number of degrees of freedom and the average element size are shown on the bottom and top horizontal axes, respectively. Near comparable behaviour is obtained by both meshes. The CVT mesh is shown to achieve smaller errors at higher discretizations than the QUAD mesh. This is expected as the number of nodes and hence degrees of freedom associated with the former practically doubles as shown in Table 3.5 hence resulting in considerably more flexible numerical domains.

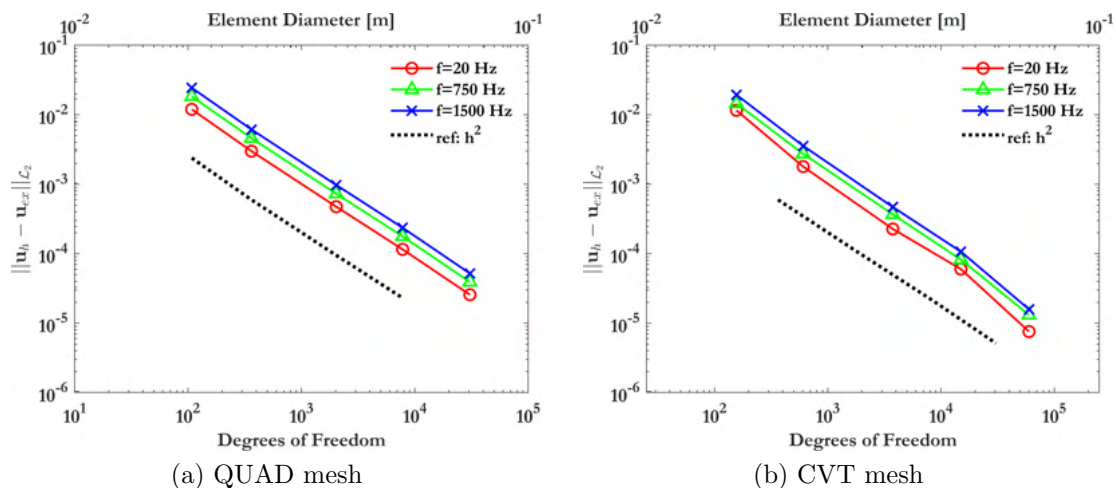


Figure 3.8: Convergence of relative errors in displacements at excitation frequencies 20 Hz, 750 Hz and 1500 Hz.

The relative pressure errors in \mathcal{L}_2 norm are displayed in Fig. 3.9. Once again comparable behaviour is noticed across both meshes. The displacement and pressure fields are approximated in descending accuracy across the excitation frequency spectrum in Figs. 3.8 and 3.9. This is due to the fact that the same spatial resolution is employed across the entire frequency range; yet the higher the frequency becomes the finer mesh discretization is required to accurately resolve the corresponding wave lengths.

First order methods of this nature are expected a priori to converge at h^2 with respect to mesh size in the \mathcal{L}_2 norm. This theoretical slope is provided as "ref: h^2 " in Figs. 3.8 and 3.9. Graphically it can be seen that near optimal convergence rates for errors in displacements and pressures are obtained by the method across both mesh-types. This suggests that the stability

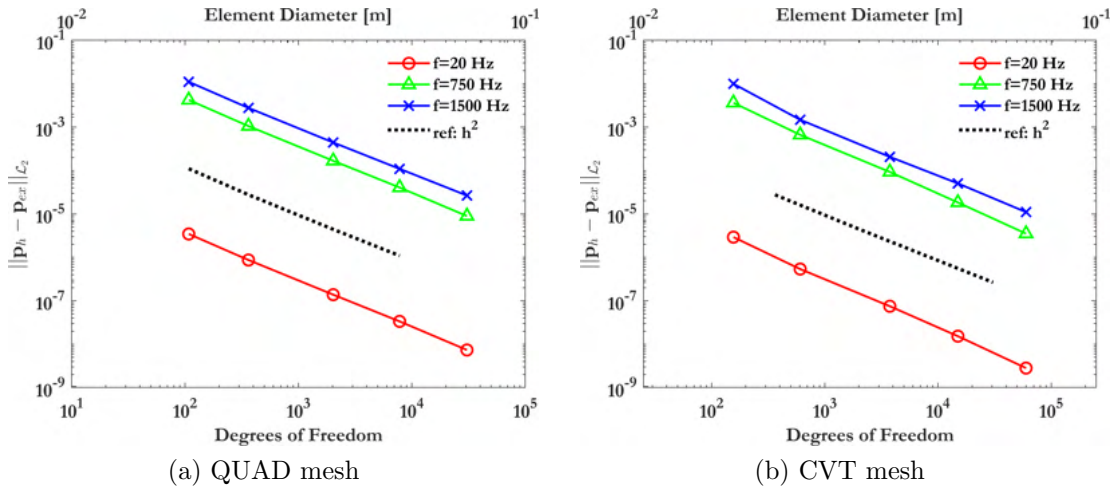


Figure 3.9: Convergence of relative errors in pressures at excitation frequencies 20 Hz, 750 Hz and 1500 Hz.

approximations chosen using the D-recipe stabilization procedure, and the enhancing conditions introduced in computing \mathcal{L}_2 projectors do not generate sub-optimal convergence properties.

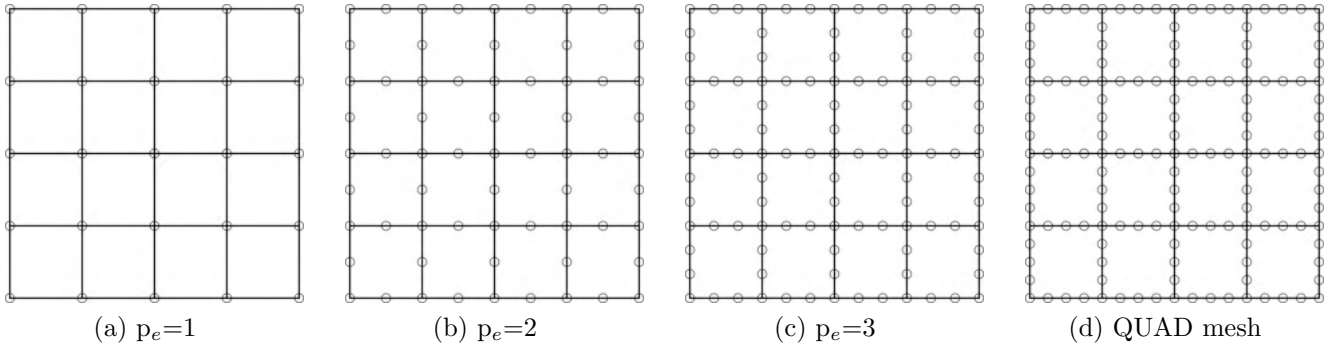
It is of interest to note that a larger spread is observed for errors in pressure in Fig. 3.9 when compared to errors in displacements in Fig. 3.8. This potentially highlights the requirement for a different order of approximation specifically for the pressure field. Such aspects are beyond the scope of this work.

A remark on VEM mesh refinement

To achieve accurate high frequency solutions, several alternatives to standard h-refinement have been proposed in the literature; p refinement or $h - p$ refinement strategies using classical polynomial-driven finite elements do offer a viable route. Alternatives based on enrichment strategies such as generalized finite element methods [192], discontinuity enriched methods [193]. Amongst these, the Spectral Element Method (SEM) [194] has been shown to provide well behaved solutions across the frequency spectrum. These higher order methods are motivated by the creation of more flexible domains without having to decrease element sizes. This criterion can be met using the Virtual Element Method as well.

To examine this, a relatively coarse discretization of 4×4 QUAD elements is shown in Fig. 3.10a. 1, 2 and 3 nodes are inserted per element edge to obtain the 8, 12, and 16 noded element discretizations shown in Figs. 3.10b, 3.10c, and 3.10d, respectively. These elements are parametrised using p_e , which corresponds to the number of subdivisions per edge.

In classical finite element methods, Figs. 3.10b, 3.10c and 3.10d are generally interpreted as serendipity elements and support quadratic, cubic and quartic interpolations, respectively and p_e would correspond to the order of approximation. While these higher order interpolations are certainly achievable through the VEM, an alternate route harnessing the ability of a virtual element to have multiple edges is proposed here. A first order VEM ($k=1$) interprets $p_e=1$, $p_e=2$, $p_e=3$ and $p_e=4$ as 4-sided, 8-sided, 12-sided and 16-sided elements, respectively. Hence, linear polynomials living on each edge can uniquely be defined through adjacent vertex degrees of freedom. This argument is summarized in Table 3.6.

Figure 3.10: p_e refined virtual element meshes.

subdivisions per edge	nodes per element	total nodes	FEM		VEM	
			edges	order	edges	order
$p_e = 1$	4	25	4	1	4	1
$p_e = 2$	8	65	4	2	8	1
$p_e = 3$	12	105	4	3	12	1
$p_e = 4$	16	145	4	4	16	1

Table 3.6: Alternate parametrization of higher order elements using a first order VEM.

Since the elements employed remain linear, an h-refinement based error convergence analysis would continue to yield a relative error convergence rate of h^2 in \mathcal{L}^2 norm. One should not expect the h^{p_e+1} rates more commonly associated with higher order methods.

Remark 2 *It is to be noted that the number of quadrature points required for accurate polynomial integration directly scales with the order of the classical polynomial based higher order methods, such as FEM and SEM. Conversely, on the edge refinement method examined herein, the number of quadrature points will vary only as a function of the sub-triangulation required for integration over the domain interior. It is to be noted that for first order VEM methods, this sub-triangulation is required only for bilinear operators containing \mathcal{L}_2 -type projectors, i.e., $a_{\mathcal{K}}^0, b_{\mathcal{K}}^0$ and $a_{\mathcal{K}}^{(\nabla,0)}$. For the purely \mathcal{H}_1 -type operators, i.e. $a_{\mathcal{K}}^{\mathcal{E}}$ and $b_{\mathcal{K}}^{\nabla}$, numerical integration is moved to the boundary and exactly and uniquely computed through 2 Gauss Lobatto quadrature points per edge, located at the relevant vertex nodes.*

The influence of this procedure on the solution accuracy is illustrated through the SAC. This determines the absorption behaviour of a system and is computed in post-processing (see Section 2.7.4).

The reference SAC is computed through the semi-analytic Transfer Matrix Method (TMM). Although the TMM assumes an infinite lateral dimension, the solution is still valid for the purpose of this example due to the normal plane wave incidence and lateral sliding condition.

The SAC curves computed for the four discretizations described above are compared against the TMM curve in Fig. 3.11. The SAC computed through the VEM agrees with the TMM curve from 20 Hz to ≈ 1500 Hz. Beyond this limit, deviations are noticed, especially for the $p_e=1$ mesh. On the contrary, a near exact correspondence is achieved with $p_e=4$.

To illustrate gains in computational cost, a second-order serendipity finite element method is used to perform the computations over the $p_e=2$ mesh. Total computational times are recorded over 1000 runs to obtain meaningful comparisons. The VEM achieves a time of 0.42 hours, whereas the FEM takes a total time of 0.6 hours. Hence, the order 1 virtual element method achieves in providing accurate results without significantly increasing the computational complexity of the discretized domain.

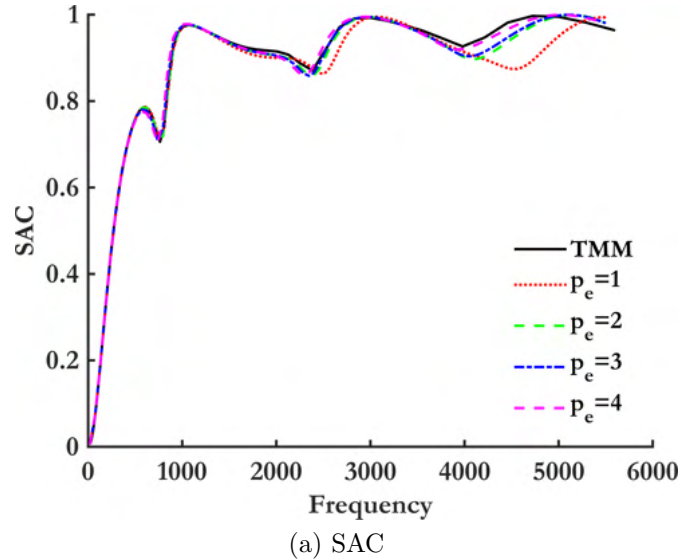


Figure 3.11: Convergence of SAC with p_e refinement.

3.6.2 Multilayer systems

Poroelastic materials generally exhibit reduced sound absorption properties at low excitation frequencies. This is due to a mismatch between the sample thickness and large wavelengths encountered at these frequencies. Multilayer systems are often deployed to improve the low frequency behaviour. Similarly, multilayer configurations are also designed to improve sound transmission properties as well.

This example is chosen to demonstrate the ability of the VEM to account for wave propagation through different types of materials. Varied interface coupling constraints, boundary conditions and acoustic excitation types are considered. A multilayer system comprising three layers, i.e., (I) a melamine foam (poroelastic), (II) an elastic plasterboard (solid) and (III) non-dissipative air (fluid) is taken up for analysis. Each layer is 10 mm thick and has a lateral dimension of 2m. This exaggerated height is used to simulate the infinite diameter assumption used by the Transfer Matrix Method for impedance tube simulations. Contrary to the previous example, here this requirement is necessary owing to the presence of oblique excitations. To avoid spurious reflections at the lateral boundaries due to the fully reflecting zero normal fluid velocity Neumann conditions, Floquet-Bloch type conditions [195] are typically employed to mimic periodic material behaviour in the vertical direction. Alternatively, absorbing/non-reflecting boundaries are also implemented using Infinite Elements [196], Perfectly Matched Layers [197] or doubly asymptotic approximations [198]. Since these possibilities lie outside the scope of our work, we instead choose to model an exaggerated height of 2m to eliminate the possibility of spurious reflections at these lateral boundaries.

The material properties for each layer is summarized in Table 3.7.

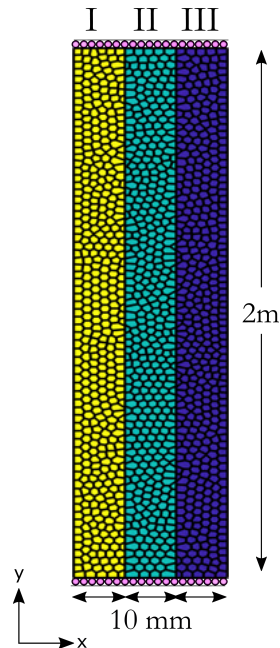


Figure 3.12: Multilayer configuration with roller supports on lateral edges. Material configuration provided in Table 4.1. Each layer is 10 mm thick. Plane wave normal incidence excitation with a fully clamped backing considered for Section 5.5.2. Diffuse field excitation with anechoic termination considered for Section 5.5.2.

Remark 3 *It is to be mentioned that creating multilayer configurations that improve acoustic properties is a matter of engineering judgement and is not our objective here. Our choice of materials for the multilayered system is motivated purely by computational reasons. Layer II is chosen as a solid elastic layer to demonstrate the ability of the VEM to accurately compute the admittance matrix necessary for coupling pressure degrees of freedom of layer I and layer III with the displacement degrees of freedom of layer II at the respective interfaces. This corresponds to $a^{0\Gamma}(p_h, \delta \mathbf{u}_h)_c$ defined in Eq. (2.168b) and Table 2.3.*

The lateral edges are subjected to sliding conditions with roller supports. A polygonal discretization of 30 CVT elements per smallest wavelength is considered to accurately resolve high frequency wave propagation. The smallest wavelength is chosen to be the minimum wavelength of the three Biot waves (P1, P2, S) propagating through a poroelastic media, and the corresponding structural and acoustic waves propagating through elastic and fluid media [57]. The interfaces are appropriately seeded to allow the CVT to accurately capture the geometry. The ability of the VEM to account for potentially non-conforming interfaces is illustrated in Fig. 3.13.

These non-conforming interfaces are converted into conforming ones by exploiting the power of the VEM to accommodate elements with several edges. Nodes that are conventionally treated as "hanging nodes" are detected and added to the relevant interface element to create new corners and edges; it is not necessary to incorporate weak coupling techniques like the Mortar method [199] or the Nitsche method [200] here.

The node-insertion technique may result in elements with non-standard aspect ratios, thereby leading to an unstable aspect ratio as discussed in Section 3.5.6. In this case, the elements may not

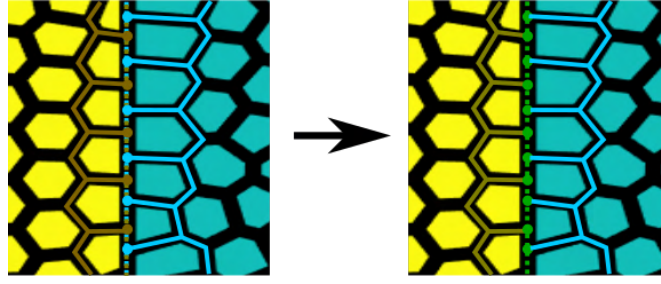


Figure 3.13: Converting a non-conforming interface into a conforming one by adding nodes and edges to each interface element as required.

be amenable to standard isotropic scaling of the elastic stiffness stability terms. To examine this, the alternate elastic stabilization parameter of Eq. (3.154) is also used herein and the stability of the results is examined. A heat map illustrating "diff", i.e., the relative differences between the element-wise elastic stiffness matrix as computed using Eqs. (3.153) and (3.154) is provided in Fig. 3.14. The relative difference is evaluated for the i^{th} element as

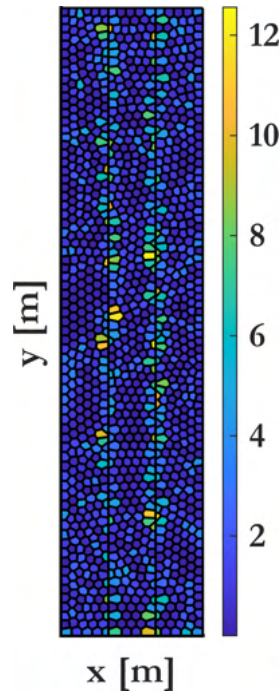


Figure 3.14: Relative differences (in %) in the element-wise elastic stiffness matrix with respect to different stabilization parameter choices (Eqs. (3.153) and (3.154)).

$$\text{diff}_i = \left\| \frac{\tilde{\mathbf{K}}_{\mathcal{K}(i)}^G - \tilde{\mathbf{K}}_{\mathcal{K}(i)}^N}{\tilde{\mathbf{K}}_{\mathcal{K}(i)}^G} \right\|, \quad (3.158)$$

where $\tilde{\mathbf{K}}_{\mathcal{K}(i)}^G$ and $\tilde{\mathbf{K}}_{\mathcal{K}(i)}^N$ indicate the element elastic stiffness matrix as computed using the VEM, with stabilization parameters β_K^G and β_K^N , respectively (see Eqs. (3.153) and (3.154)). The differences are observed to be mostly negligible except from the interface elements where node insertion has taken place.

The behaviour of the method for two problems is examined: (1) an absorption problem subject to plane wave excitation and (2) a transmission problem subject to diffuse field excitation.

ID	Name	σ	ϕ	α_∞	Λ	Λ'	E	ν	η_s	ρ
		$\text{N} \cdot \text{s} \cdot \text{m}^{-4}$	-	-	m	m	$\text{N} \cdot \text{m}^{-2}$	-	-	$\text{kg} \cdot \text{m}^{-3}$
I	Melamine foam	10^4	0.99	1.01	9.8×10^{-5}	1.96×10^{-4}	1.6×10^5	0.44	0.1	8
II	Plaster-board	-	-	-	-	-	3×10^9	0.3	0.08	700
III	Air	-	-	-	-	-	-	-	-	1.197

Table 3.7: Macroscopic material parameters corresponding to the relevant material ID.

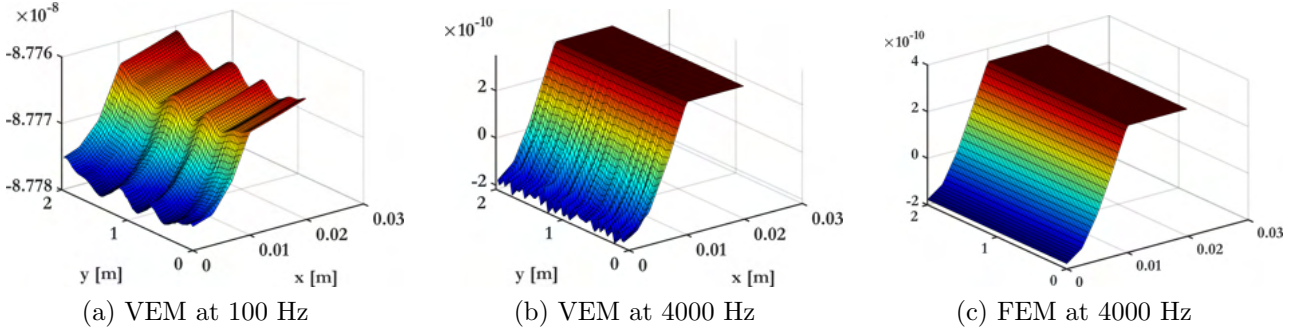


Figure 3.15: u_x (in [m]) contours at low and high frequencies, respectively. High frequency FEM contours are also provided for comparison.

Normal incidence plane wave excitation absorption problem

A plane acoustic wave at normal incidence excites the left face of layer I. The right face of layer III is subject to a rigid backing, i.e., bonded/clamped supports. The response of the system to an excitation frequency spectra of $f = [100, 4000]$ Hz is evaluated. The displacement and pressure contours u_x , u_y and p obtained by the VEM at low and high excitation frequencies 100 Hz and 4000 Hz are shown in Figs. 3.15 and 3.16, respectively. The corresponding contours obtained by the FEM at 4000 Hz is also shown for comparison. All contours are interpolated over a structured query rectangular grid containing 50×50 QUAD elements to make the comparisons fair.

As expected in this normal incidence case, the elastic wave is propagating along the the x-direction as shown in Fig. 3.15 . The high frequency contours obtained by the VEM and FEM are practically identical. It is evident from Figs. 3.15 that the elastic wave does not propagate through the fluid/air layer. The acoustic wave in Fig. 3.16 propagates only through the poroelastic and fluid layers and is fully horizontal. Once again, the high frequency FEM and VEM contours are practically equivalent, and the pressure wave has nearly been damped out in the fluid layer.

The SAC is evaluated by the FEM and the VEM for 30 frequency steps and is shown in Fig. 3.17. The SAC as computed through the semi-analytic Transfer Matrix Method (TMM) is used as a reference. It is clear that all three methods offer coinciding absorption curve results.

The relative differences in the displacement (Eq. (3.156)) and pressure (Eq. (3.157)) values at the interfaces, as obtained by the VEM using the stabilization parameter choices β_K^G and β_K^N are displayed across the frequency spectrum in Figs. 3.18a and Fig. 3.18b, respectively. It can be seen from these figures that the differences have small upper bounds of 1.6×10^{-3} and 1.5×10^{-4} . These are generally prevalent at high frequencies. While they do not affect the quality of the

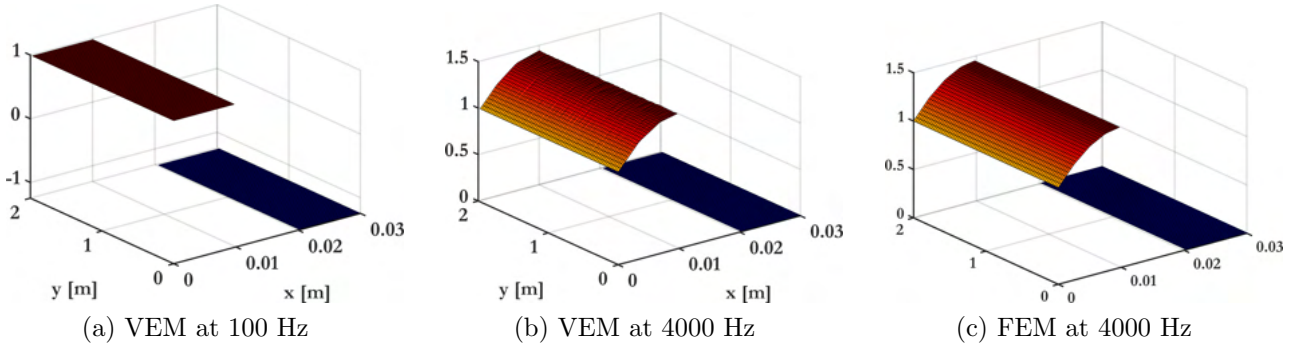


Figure 3.16: p (in [Pa]) contours at low and high frequencies, respectively. High frequency FEM contours are also provided for comparison.

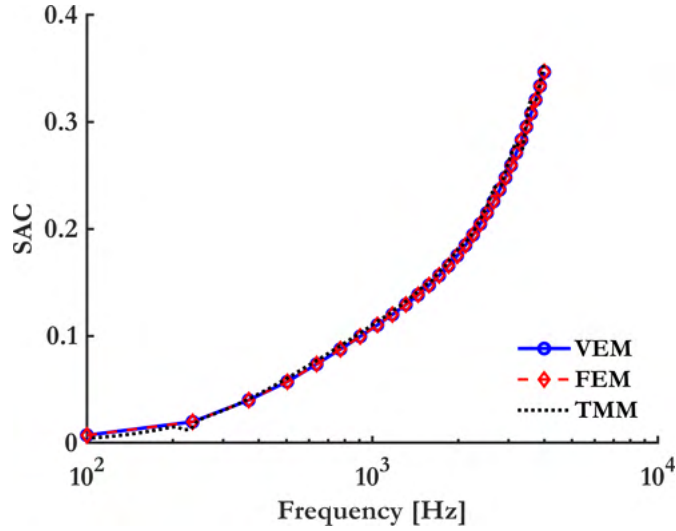


Figure 3.17: SAC computed by VEM, FEM and TMM for the multilayer absorption problem.

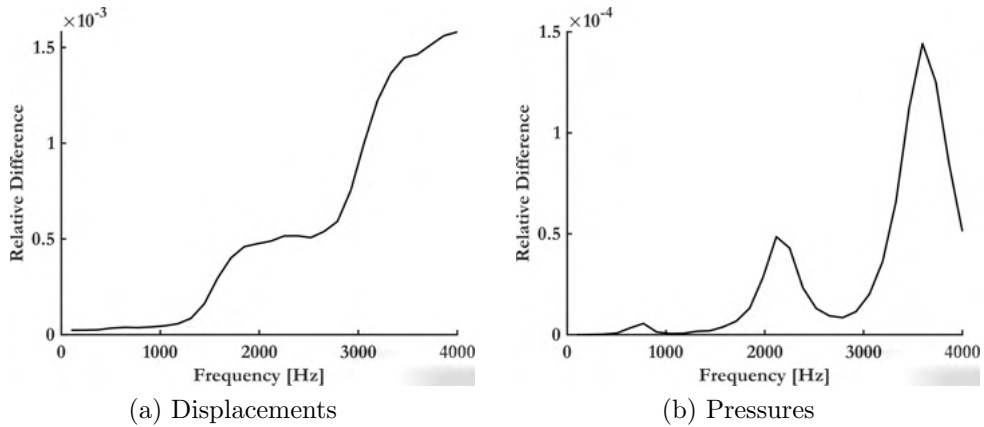


Figure 3.18: Relative differences in spectral solutions generated by the VEM at the interfaces using stabilization parameter choices Eqs. (3.153) and (3.154)

computed SAC in this example, it is still possible that appreciable deviations may be observed in cases where mesh distortion is more severe. Hence, when encountering meshes with potentially non-standard aspect ratios, β_K^N is recommended over β_K^G .

Diffuse field transmission loss

A sound transmission problem is studied here for the same multilayer configuration. The right face has an anechoic termination, i.e., a Robin type impedance boundary condition. This corresponds to the term $b^{0\Gamma}(p_h, \delta p_h)$ defined in Eq. (2.167c) and Table 2.2. A diffuse field acoustic excitation is incident on the left face of the domain. The excitation consists of several oblique incidence plane waves with angles of incidence $\theta \in [0, 75^\circ]$. A total of $N = 20$ samples were computationally determined to be sufficiently representative of the entire diffuse field. The response of the system to an excitation frequency spectra of $f = [100, 4000]$ Hz is evaluated. The associated u_x , u_y and p VEM contours for $\theta = 0^\circ$ and $\theta = 75^\circ$ are shown in Figs. 3.19, 3.20 and 3.21 for 100 Hz and 4000 Hz respectively.

The elastic wave contours u_x and u_y are only computed over the melamine foam and plasterboard domains. Similarly, the acoustic wave contours are evaluated only over the melamine foam and terminating air layers.

There is a good correspondence between the 4000 Hz u_x , u_y and p contours as computed by the FEM and VEM for both the cases of normal and oblique incidence. A fully horizontal contour is observed for the elastic wave in x-direction in Figs. 3.19a, 3.19b, 3.19c. Oblique contours are retrieved in Figs. 3.19c, 3.19d and 3.19e. Contrary to the normal incidence case, waves are propagating along the y direction in the 75° case and are shown in Fig. 3.20a, 3.20b and 3.20c. The high frequency excitations have been almost entirely dissipated by the time they enter the plasterboard layer.

The pressures from the acoustic wave are nearly uniformly distributed over each of the two layers at normal incidence, as seen in Figs. 3.21a, 3.21b and 3.21c. Excepting minor oscillations, the high frequency acoustic wave at oblique incidence has almost died down by the time it has reached the rear air layer in Figs. 3.21e and 3.21f. The oblique excitation contours encountered in Figs. 3.19e, 3.19f, 3.20b, 3.20c, 3.21e and 3.21f are reminiscent of evanescent waves rather than propagating waves.

The sound transmission loss factor (STL) is computed for the diffuse field excitation according to Eq. (3.159)

$$\mathcal{T}_{\text{df}}(\omega) = -10 \log_{10} \left(\frac{\int_{0^\circ}^{75^\circ} \mathcal{T}(\omega, \theta) \sin(\theta) \cos(\theta) d\theta}{\int_{0^\circ}^{75^\circ} \sin(\theta) \cos(\theta) d\theta} \right), \quad (3.159)$$

where $\mathcal{T}(\omega, \theta)$ denotes the STL computed for a single plane wave at incidence θ (see Appendix 2.7.4). The STL evaluated by the FEM, the VEM, and the TMM is shown in Fig. 3.22c. The associated STL curves at normal incidence and oblique incidence $\theta = 75^\circ$ are provided for clarity in Figs. 3.22a and 3.22b, respectively.

The STL curve at normal incidence (Fig. 3.22a) shows good correlations between all methods. Both the FEM and VEM correctly estimate the coincidence frequency at 75° oblique incidence correctly in Fig. 3.22b. Similarly, both methods accurately predict the critical frequency for the diffuse field excitation as well in Fig. 3.22c. However, slight deviations at the peaks of both curves are observed. This is attributed to the following reasoning: the TMM assumes an infinite lateral dimension and as a result does not account for reflections occurring off of the lateral boundaries. This effect is captured by the FEM and VEM and is especially prevalent at large angles of oblique

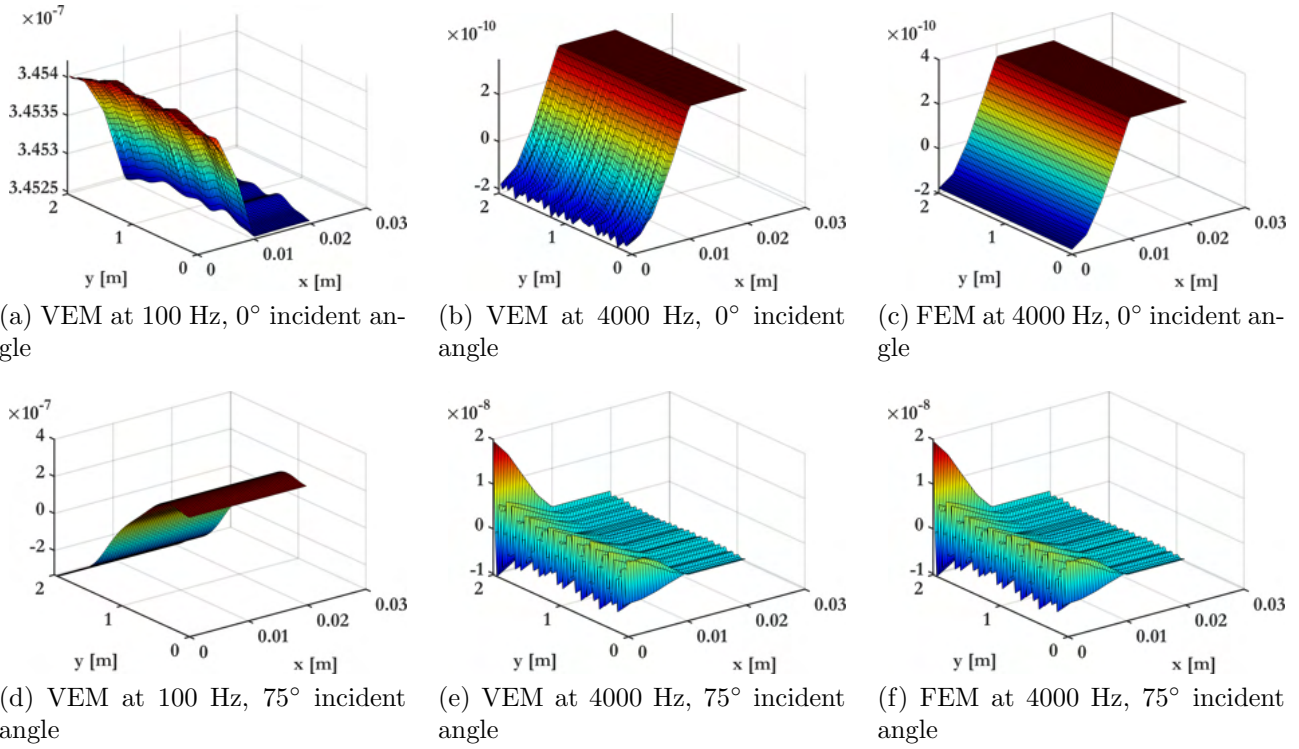


Figure 3.19: u_x (in [m]) contours at low and high frequencies and angles of incidence, respectively. High frequency FEM contours are also provided for comparison.

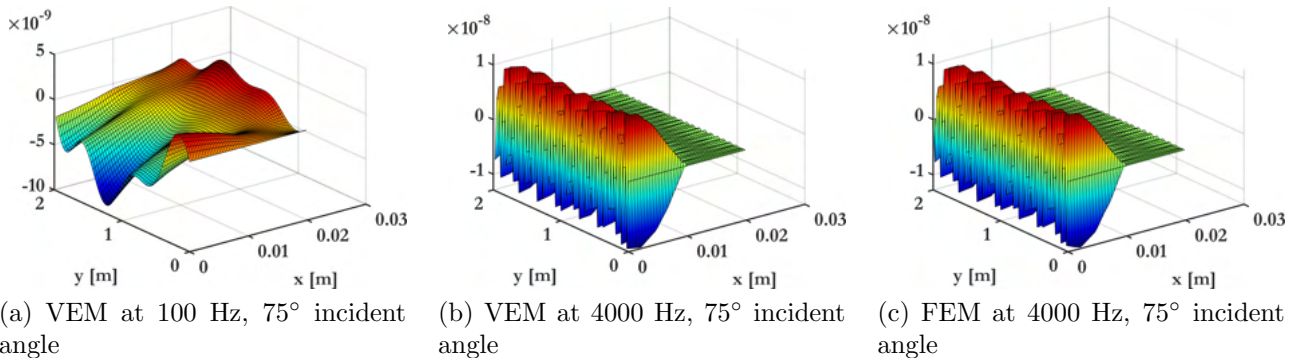


Figure 3.20: u_y (in [m]) contours at low and high frequencies and high angle of incidence, respectively. High frequency FEM contours are also provided for comparison.

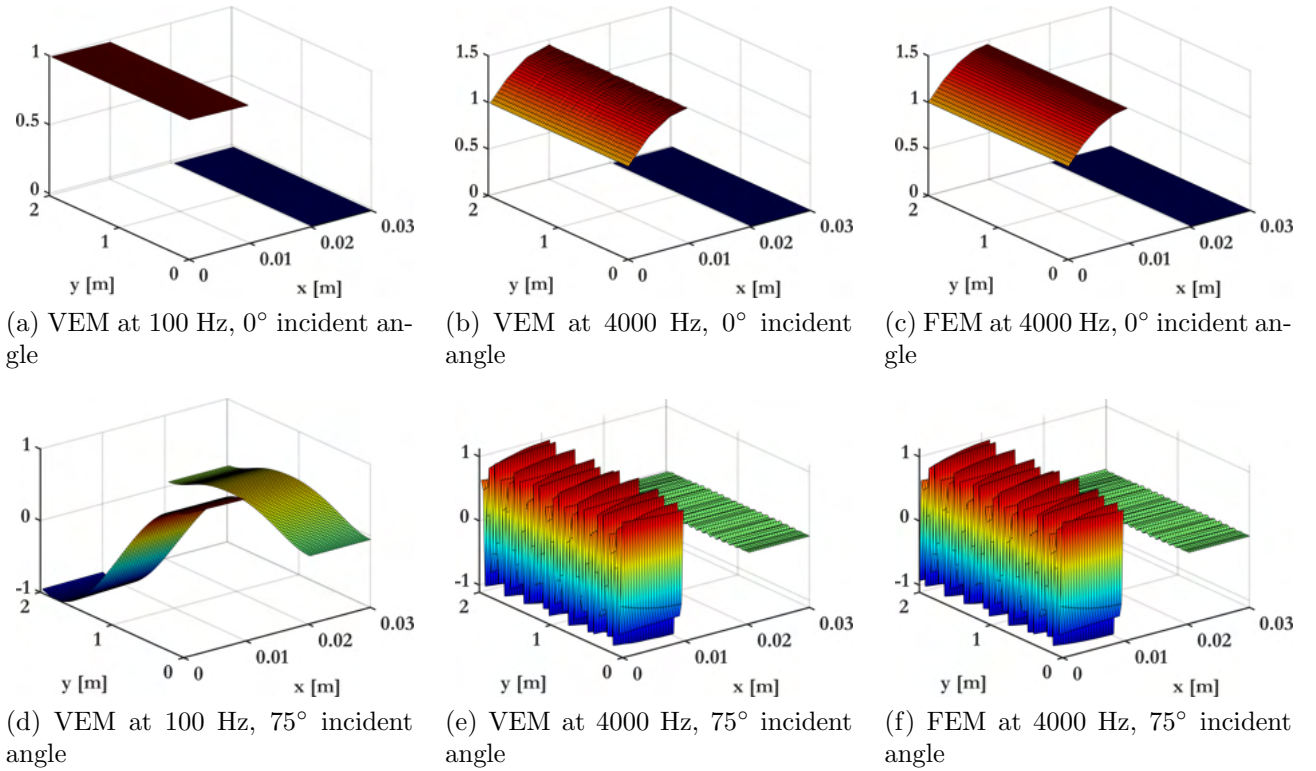


Figure 3.21: p (in [Pa]) contours at low and high frequencies and angles of incidence, respectively. High frequency FEM contours are also provided for comparison.

incidence.

3.6.3 Porous composite with tortuous inclusion

This example is adapted from [48] to demonstrate the ability of the VEM to accurately model the acoustic behaviour of a rigid porous composite material. This medium has a tortuous mesoscale inclusion (material II) embedded within the host material (material I). The client material is more permeable than the host. The macroscopic parameters are summarized in Table 3.8. The configuration is provided with a fully clamped backing (often called rigid backing in acoustical literature) and is subjected to a normal incidence plane wave excitation as shown in Fig. 3.23.

Name	σ	ϕ	α_∞	Λ	Λ'
	$\text{N} \cdot \text{s} \cdot \text{m}^{-4}$	-	-	m	m
I (Host)	10^6	1.00	1	12×10^{-6}	12×10^{-6}
II (Client)	1.15×10^4	0.96	1.01	108×10^{-6}	138×10^{-6}

Table 3.8: Macroscopic material parameters corresponding to the relevant material ID.

Contrary to the previous examples, here the preceding air column contained in the impedance tube also needs to be modeled to account for reflection, scattering, dispersion and edge effects introduced by the heterogeneous interface. The relevant inlet and incident quantities are accordingly computed at the extreme left end. Consequently, along with the 45 mm air column, the entire domain is discretized with 2592 CVT elements - following the 20 elements per minimum wavelength rule. This discretization is illustrated in Fig. 3.24.

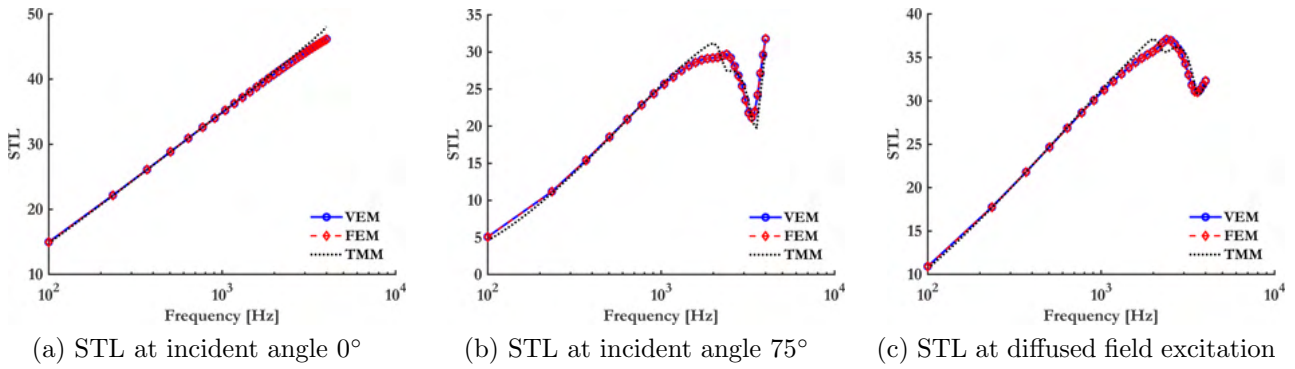


Figure 3.22: Sound Transmission Loss curves computed for the multilayer diffuse field transmission loss problem through the VEM, FEM and TMM.

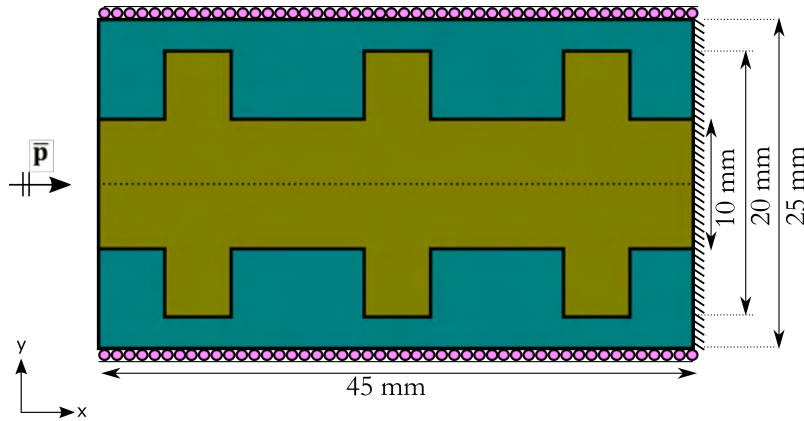


Figure 3.23: Schematic diagram of a 45 mm thick rigid skeleton porous material with a second rigid porous material as a tortuous inclusion. Roller and clamped supports are provided at lateral boundaries and the rear, respectively. The macroscopic parameters of the matrix and inclusion are provided in Table 3.8.

Remark 4 *This is an axisymmetric domain and hence the plane-strain assumption is not expected to hold, especially in high-frequencies. However, this test case is opted for as it provides insight on the capability of the VEM in efficiently treating tortuous geometries. For this purpose, the accuracy of the method is compared against the TMM and also an axisymmetric FEM.*

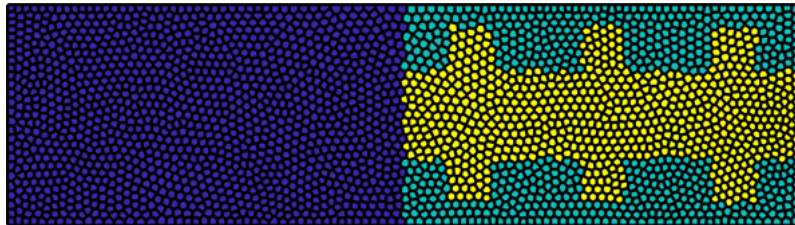


Figure 3.24: The domain along with an equally thick air layer is discretized using 2592 CVT elements, following the 20 elements per minimum wavelength discretization schema.

It is evident from Fig. 3.24 that the interfaces between (a) air and the sample, (b) host and client material are not perfectly enforced. This is deliberately done to investigate the influence of imperfect interfaces on the final result. The problem is solved over equally distributed frequency steps ranging from 20 Hz to 5000 Hz. The pressure contours at low (100 Hz) and high (5000 Hz) as computed by the VEM are displayed in Figs. 3.25a and 3.25c, respectively.

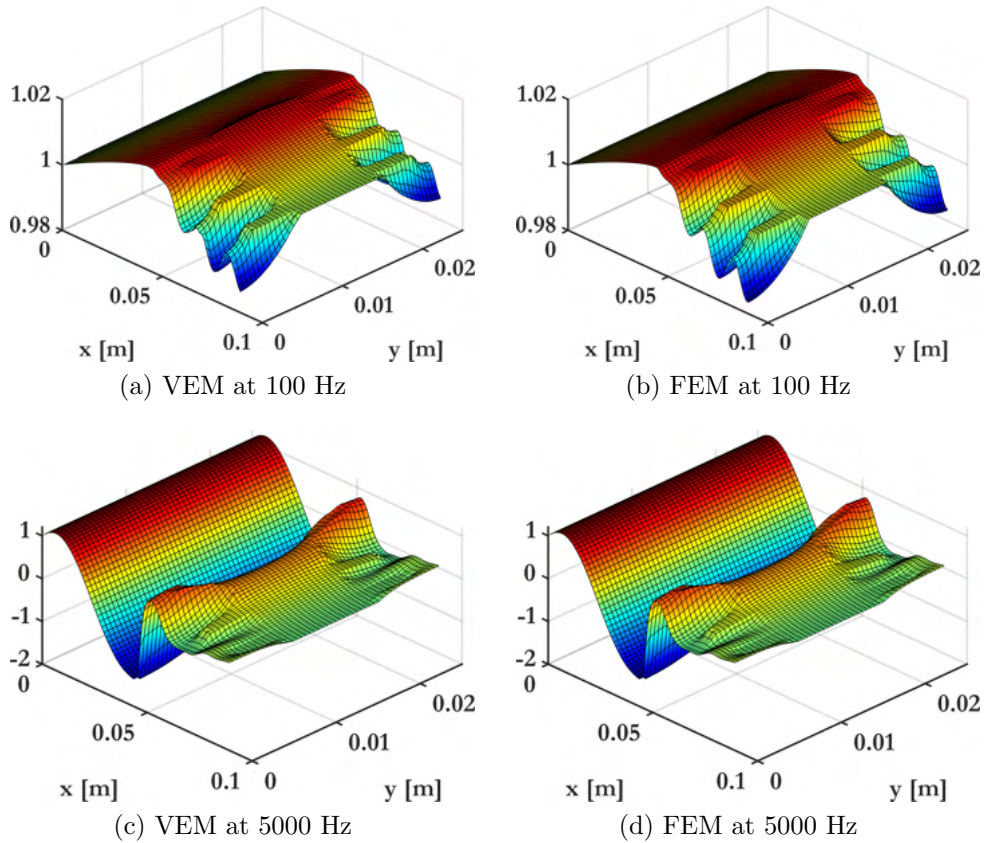


Figure 3.25: p (in [Pa]) FEM and VEM contours at low and high frequencies at normal incidence plane wave excitation.

The corresponding contours as evaluated by the FEM are shown in Figs. 3.25b and 3.25d, respectively. The results are practically identical. The imperfect interfaces does not affect the solutions significantly.

The SACs as computed by the VEM and the axisymmetric FEM are compared with the TMM porous composite model with pressure diffusion effect [48] in Fig. 3.26. Good agreement between the three methods is observed until ≈ 3000 Hz. Beyond this limit, a slight deviation is noticed. This is attributed to two reasons. First, due to the plane strain assumption that cannot account for the domain axisymmetry. Second, the equivalent model theory [48], on which the porous composite model is based, is no longer perfectly valid as scale separation breaks down here. The acoustic wavelength is now smaller than the characteristic mesoscopic size of the inclusion.

3.6.4 Mesoscale inclusions

It has already been mentioned in Section 3.6.2 that porous materials do not offer desirable absorption properties at low frequencies. This is traditionally remedied by deploying multilayered systems, as shown in Section 3.6.4. Alternative solutions are explored in the form of double porosity materials [46], porous composites [48] and embedded inclusions [47]. An example of a tortuous porous composite is provided in Section 3.6.3. In this example, the ability of embedded rigid inclusions to improve absorption at lower frequencies is shown. The cases concerning one and two periodic inclusions per unit cell are directly adapted from [47]. All cases are subjected to plane wave normal incidence excitation and a rigid backing. The porous material involved is a foam

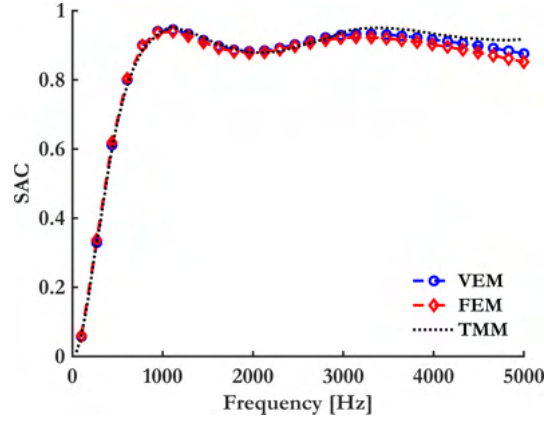


Figure 3.26: SAC computed by the VEM, axisymmetric FEM and TMM for the rigid porous composite material.

with rigid motionless skeleton modelled as an equivalent fluid. The exact material parameters are provided in Table 3.9.

σ	ϕ	α_∞	Λ	Λ'
$\text{N} \cdot \text{s} \cdot \text{m}^{-4}$	-	-	m	m
8900	0.95	1.42	180×10^{-6}	360×10^{-6}

Table 3.9: Macroscopic material parameters corresponding to the relevant material ID.

The inclusions are treated as infinitely rigid cylindrical tubes. This means that the inclusion domain interiors need not be meshed. Additionally, the Neumann boundaries at the inclusion interfaces are zero (zero normal-velocity).

One Inclusion in periodic unit cell

A periodically repeating square unit cell of size 2 cm is taken up. A single cylindrical inclusion centered at (1 cm, 1 cm) of radius 0.75 cm is embedded. The unit cell is repeated ten times in the vertical direction to simulate an infinite lateral dimension. The total vertical dimension is 20 cm. This configuration is illustrated in Fig. 3.27. The domain has been discretized with uniform CVT elements resulting in a polygonal mesh with 7000 elements and 13,961 nodes. The SAC computed over the frequency range 100 Hz-10kHz with the VEM for this configuration is shown in Fig. 3.28. The curve is validated against the analytic mode-matching technique developed in [47]. Additionally, the SAC for the same porous domain without the inclusions is also provided for comparison. It is evident that the configuration with inclusions exhibits an improved absorption behaviour in the 1800 Hz - 3800 Hz frequency range. A near-unity peak is observed at ≈ 3000 Hz. The pressure contours computed by the method at 100 Hz and 10 kHz are shown in Fig. 3.29.

Two Inclusions in periodic unit cell

A second configuration, comprising two cylindrical inclusions of different sizes within the unit cell is shown in Fig. 3.30. The unit cell is rectangular (3.5cm \times 2cm) with a period of 2 cm. The first inclusion is centered at (2.5 cm, 1cm) with radius 0.75 cm. The second inclusion is of radius

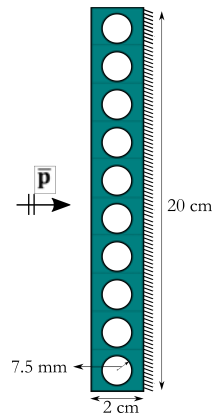


Figure 3.27: A 2 cm thick domain with a single infinitely rigid circular inclusion of radius 7.5 mm, per unit cell. Unit cell repeats periodically in the vertical direction with period 2 cm.

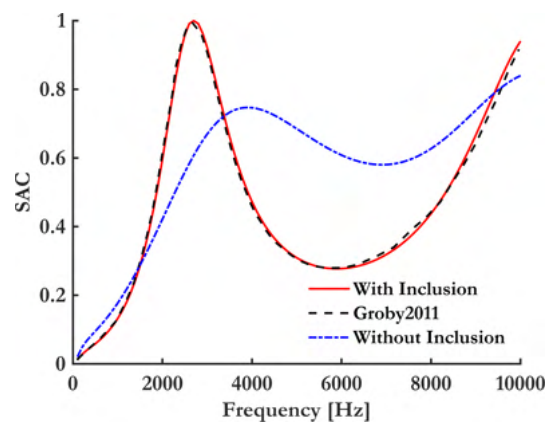


Figure 3.28: SAC computed by the VEM for the domain with and without inclusion. A reference curve using the analytic mode-matching technique from [47] is provided for comparison.

0.5 cm and is centered at $(1.5 \text{ cm}, 2.5 - \sqrt{3})$. The domain is discretized with 7000 uniform CVT elements resulting in 13,990 nodes. The SAC computed over the frequency range 100 Hz-10kHz by the VEM for the configurations with and without inclusions are shown in Fig. 3.31. Improvements in absorption behaviour are exhibited by the configuration with inclusions across two frequency bands: 1600 Hz - 2200 Hz, 3700 Hz - 5000 Hz. These low frequency absorption peaks in both cases are primarily due to the tortuosity added by the solid inclusions.

Complex inclusion geometries

The ability of the VEM to easily model more complex non-periodic inclusions is demonstrated here. The first example is a 5 cm \times 15 cm rectangular domain with irregular infinitely rigid inclusions in the shape of alphabets V-E-M. This domain is discretized with a CVT mesh containing 2500 elements and 5030 nodes. The pressure contours at 100 Hz and 10 kHz are shown in Fig. 3.33. The second example increases the inclusion complexity even further by embedding inclusions in the shape of a bat, spider and pacman in a 6 cm \times 18 cm rectangular domain. The discretization involved contains 5000 CVT elements with 10,054 nodes. The low and high frequency pressure contours are provided in Fig. 3.34. Both examples use the same equivalent fluid porous foam described in Section and 3.6.4 and employ the same boundary conditions.

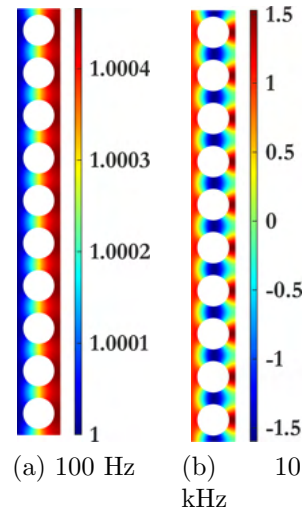


Figure 3.29: p (in [Pa]) contours computed by VEM at low and high frequencies at normal incidence plane wave excitation.

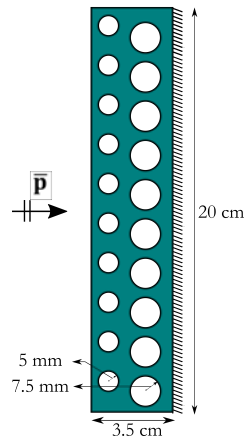


Figure 3.30: A 3.5 cm thick domain with two infinitely rigid circular inclusion of radius 7.5 mm and 5 mm respectively, per unit cell. Unit cell repeats periodically in the vertical direction with period 2 cm.

The discretizations used for these different inclusion-types are summarized in Table 3.10.

3.7 Summary

The VEM is developed for elastostatics and poromechanics. A novel VEM discretization has been proposed for studying the vibroacoustic behaviour of fluid, elastic and poroelastic materials in the frequency domain. The novelty of the method lies in employing the flexible meshing capabilities of the VEM to reduce computational cost and accurately capture complex interfaces. Implicitly defined basis functions are used to evaluate elementary state matrices through employing appropriately defined operator-specific projectors. The final matrix form of equations are non-linear in ω , and are repeatedly solved over the desired frequency spectrum. The solution is post-processed to obtain acoustic indicators like SAC and STL.

The method was shown to exhibit near-optimal convergence rates for different element types

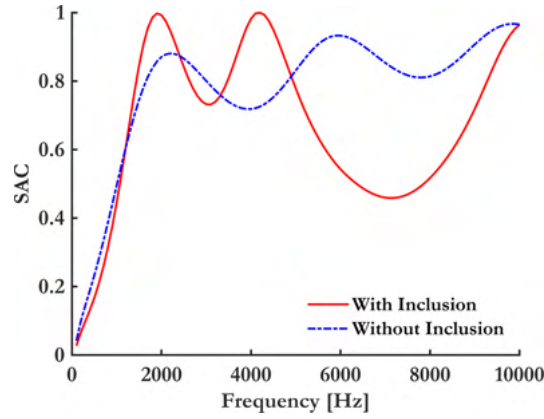


Figure 3.31: SAC computed by the VEM for the domain with and without inclusions.

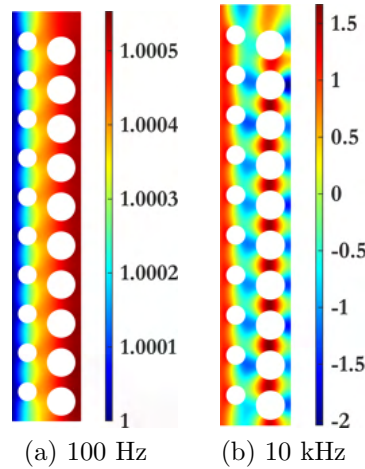


Figure 3.32: p (in [Pa]) contours computed by VEM at low and high frequencies at normal incidence plane wave excitation.

in Example 3.6.1. This illustrates that the VEM can accurately handle versatile mesh configurations at different frequencies. Furthermore, the computational gains achieved are discussed and evidenced by comparisons with the FEM. The ability of the method to handle different types of materials (fluid, elastic, poroelastic) and the resulting interface coupling conditions are provided in Example 3.6.2. This section also shows that the VEM can be used to easily resolve non-conforming interfaces using appropriate node-insertion algorithms. In this context, the accuracy of two different stabilization parameter choices was explored; although the differences were negligible, the non-isotropic stabilisation procedure seems to provide more well-behaved solutions at the higher frequency spectrum. Different excitations (plane waves at normal and oblique incidence, diffuse-fields) and constraints (rigid backing, anechoic termination) were considered and the accuracy of

Mesh	Nodes	Elements
One inclusion	13,961	7000
Two inclusions	13,990	7000
V-E-M	5030	2500
Superhero	10,054	5000

Table 3.10: Discretizations for the four inclusion-types used in Section 3.6.4.

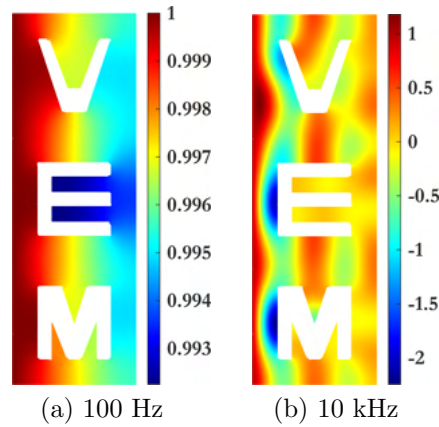


Figure 3.33: p contours computed by the VEM at low and high frequencies at normal incidence plane wave excitation.

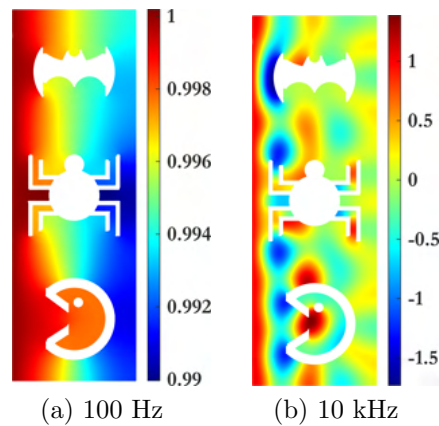


Figure 3.34: p contours computed by the VEM at low and high frequencies at normal incidence plane wave excitation.

the method was verified in each case against the TMM.

Example 3.6.3 concerns tortuous rigid porous composites and shows that the VEM can be used to study the influence of imperfectly defined interfaces. Example 3.6.4 illustrates the power of the VEM in handling complex periodic and non-periodic mesoscale inclusions across a reasonably large frequency bandwidth. Examples 3.6.3 and 3.6.4 show the potential of using the VEM as a simulation tool in investigating the absorption behaviour of porous composites, in contrast to more classical multilayer systems, as shown in Example 3.6.2.

The method is currently limited by its confinement to exclusively 2-D domains. Extending the method to 3-D polyhedral or 2-D axisymmetric discretizations is currently a work in progress.

The next Chapter deals with upscaling methodologies, with a focus on Multiscale Finite Element Methods. The VEM will then be integrated into the MsFEM to obtain a novel Multiscale Virtual Element Method (MsVEM) in Chapter 5.

Part III

Multiscale Methods

Chapter 4

Multiscale Finite Element Methods

In this Chapter, the Multiscale Finite Element Method (MsFEM) is derived for elastostatics and coupled field poromechanical problems, i.e., consolidation and vibro-acoustics. The MsFEM framework is originally applied to the Biot theory of elastic wave propagation in air-saturated porous media. The resulting numerical scheme allows inclusions of air and other potential sources of heterogeneity at the mesoscopic scale. The upscaling procedure and the associated computation of the multiscale basis functions is discussed. Its advantages pertaining to accuracy and computational acceleration are highlighted with industrially relevant benchmark examples.

4.1 Overview on Multiscale Methods

It is often in nature that physics evolve across highly heterogeneous, geometrically complex, and multiscale deformable domains; examples pertain to sound absorption and transmission in foams and fibrous materials [35, 48, 201, 202] and fracture analysis of composite components [203]. Advances in automated manufacturing and in particular additive manufacturing have led to the wide-spread application of components possessing complex and fit-for-purpose material layouts in the construction, aerospace and automotive industries [204]. Additively manufactured functionally graded composites and foams can be tailored to increased mechanical properties when compared to traditional layered composites or metals, e.g., higher strength to weight ratios and higher damping to weight ratios [8]. However, the corresponding manufacturing processes can be extensive, are prone to errors and necessitate several design iterations before a desirable layout is finally produced. This motivates the development of computational methods that can lead to augmenting desirable mechanical traits while reducing undesirable ones while still at the design stage.

Yet, the flexibility provided by manufacturing poses a series of challenges vis-a-vis the numerical simulation of structural components with exotic material layouts. The distribution of material heterogeneities at the micro- or mesoscale significantly affects the overall mechanical response of the component. Hence, both from a physical and a computational perspective, the problem of assessing the mechanical performance of a component becomes a multiscale one. Numerical simulation of physics across multiple length scales can, in principle, be done with the standard finite-element approach [205]. However, this would necessitate the use of extremely fine mesh discretizations to resolve the corresponding heterogeneities, hence leading to high computational

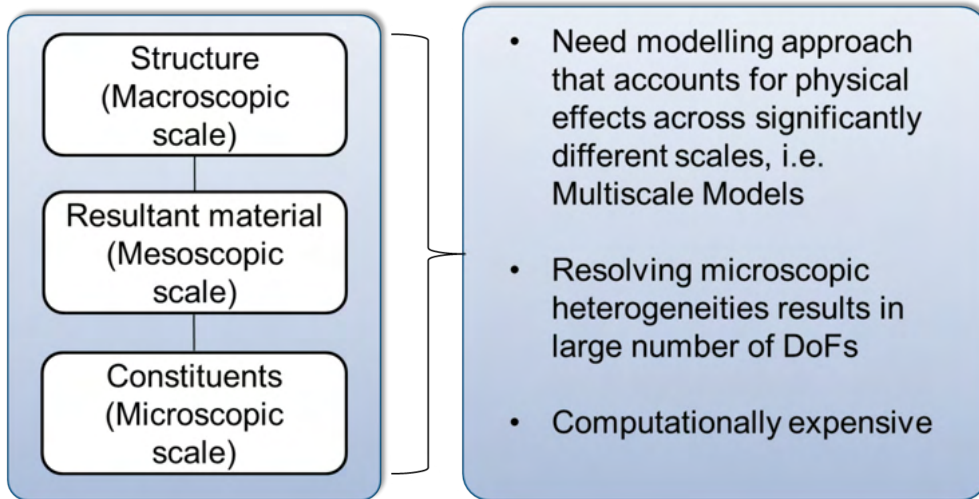


Figure 4.1: Motivation for multiscale approaches.

costs [206].

Multiscale modelling methods [207–209] have been developed over the years to accurately treat heterogeneous material distributions across scales while reducing computational costs using the robust mathematical framework of homogenisation [210–213]. These include volume averaging and analytical homogenization [214–216], computational homogenization approaches [10, 217–220], see, also, FE^2 methods [9, 221–225], variational multiscale methods [226–229], mortar multiscale methods [230–234], heterogeneous multiscale methods [235–238] and other miscellaneous techniques [239–245].

Homogenization theory relies on the assumptions of scale separation and periodicity. However such assumptions do not necessarily hold for the case of highly heterogeneous domains. Hence, alternative methods that do not rely on this assumption have been developed, such as multiscale finite volume [246–249] and multiscale finite element methods (MsFEM) [8, 250]. A comparison between different multiscale approaches in the context of elliptic problems was performed in [251].

The MsFEM relies on the notion of nested computational domains and the evaluation of a numerical basis that maps quantities, i.e., displacements, from the one to the other. Contrary to FE^2 (see, e.g., in [9]) methods where a micro-scale finite element mesh is attached to each coarse scale integration point, in the MsFEM the coarse scale is fully spanned by the fine scale. Hence, the MsFEM is more suited to highly heterogeneous domains where scales cannot be fully separated. The MsFEM was based on the pioneering work of [252] for a single-dimensional case (later extended to multi-dimensional problems in [253]) and was further developed by, e.g., [254] to resolve flows in highly heterogeneous media. Although the method has been widely employed in such flow problems [255, 256], the method does not account for the Poisson effect, i.e., the bulk contraction/expansion of the medium under consideration. This prevents the application of the method to structural engineering problems. The Enhanced/Extended Multiscale Finite Element Method (EMsFEM) has been introduced by [257] to address this shortcoming. This is done through considering additional coupling terms for interpolation at the fine scale level. Since the EMsFEM has now become an accepted standard method; from here on, the labels MsFEM and EMsFEM are used interchangeably to denote the Enhanced/Extended Multiscale Finite Element Method.

The Coupling Multiscale Finite Element Method (CMsFEM) [258] was developed to resolve the coupled field fully saturated porous media consolidation problem using a two-scale (meso-macro) approach. Mesoscale heterogeneities are mapped to the macroscopic scale using numerically computed multiscale basis functions. A thorough discussion on the computational gains of the MsFEM and the CMsFEM is provided in [254, 258, 259]. A more specific comparison of different multiscale finite element approaches for composites and porous media flows was done in [260]. A monograph [261] documents the methods listed above.

In this Chapter, the MsFEM framework is laid out in detail, first for elastostatics in Section 4.2. An illustrative example for constructing multiscale basis functions is provided in Section 4.2.1. The upscaling procedure is detailed in Section 4.2.2. The solution procedure and associated downscaling, to recover fine scale information, is provided in Section 4.2.3. Next, this method is extended to coupled field problems by addressing Consolidation in Section 4.3. This is time-domain problem and the relevant solution and downscaling procedures are given in Section 4.3.3. Finally, we derive, for the first time, the MsFEM framework for the vibroacoustics of poroelastic media in Section 4.4. This is applied to three numerical benchmark examples in Section 4.5; where the accuracy and efficiency of the MsFEM, in relation to the FEM and the TMM are established.

4.2 Elastostatics

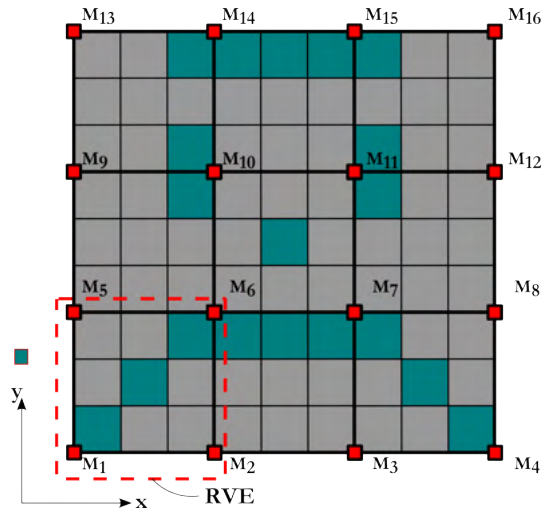


Figure 4.2: Multiscale mesh with 9 coarse quadrilateral elements and 81 quadrilateral fine-elements.

To this point, the MsFEM has been developed to treat regular heterogeneous domains as shown in Fig. 4.2, where each rectangular coarse element clusters its own representative portion of the underlying fine mesh. The fine mesh is designed to resolve all mesoscale heterogeneities. These are upscaled to the coarse level, where the solution is obtained at reduced computational cost.

To achieve this, the FEM is employed to accurately and efficiently resolve the heterogeneities at the fine scale. The heterogeneous domain is coarsely discretized into $\mathcal{K}_{M(\alpha)}$, $\alpha = 1 \dots n_{M_{el}}$, coarse elements, where $n_{M_{el}}$ is the number of coarse elements. Each coarse element clusters its own set of $\mathcal{K}_{m(i)}$, $i = 1 \dots n_{m_{el}}$ micro-elements where $n_{m_{el}}$ is the number of micro-elements in the $\mathcal{K}_{M(\alpha)}$.

For each type of coarse element, a set of multiscale basis functions is evaluated using the standard FEM. These basis functions are then employed to map the fine scale onto the coarse scale where the solution of the governing equations is performed. Since the solution procedure is performed at a coarser discretization, the MsFEM promises to drive down the computational costs pertinent to matrix factorizations and back-substitutions. The accuracy of the method compared to the fine resolution is retained as the information of the micro-scale is propagated to the coarse scale through the mapping. The MsFEM procedure is schematically depicted in Fig. 4.3.

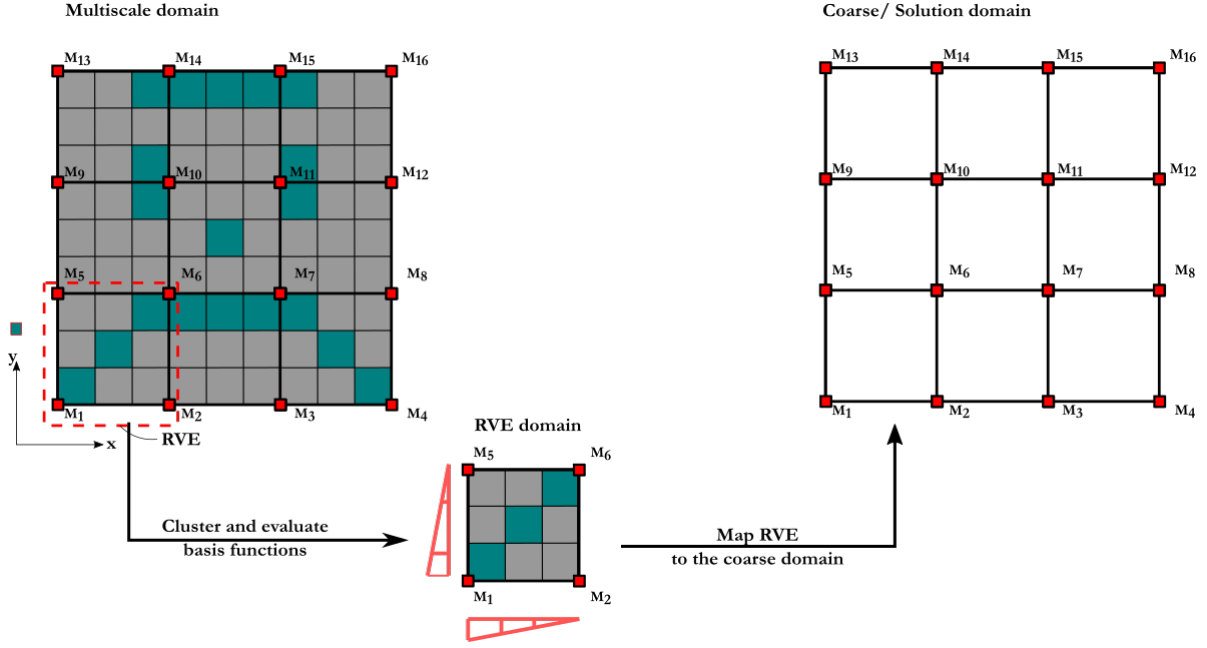


Figure 4.3: Schematic of the MsFEM upscaling procedure. The case of linear boundary conditions for the evaluation of multiscale basis functions is considered.

The terminologies "Coarse-Element" and "Representative Volume Element (RVE)" are used interchangeably here. This is to remain consistent with the literature. A coarse-element, as employed in this work, is not truly representative of the entire domain, and should therefore not be confused with the classical notion of the RVE found in homogenization theory with scale separation.

The multiscale basis functions required for the upscaling procedure are evaluated through the solution of a homogeneous version of Eq. (2.94) over the α^{th} coarse element domain $\mathcal{K}_{M(\alpha)}$, i.e.,

$$\begin{cases} \text{Find } \mathbf{u}_h \in \mathcal{V}_h^u(\mathcal{K}_{M(\alpha)}) \text{ such that} \\ \mathbf{a}^\varepsilon(\mathbf{u}_h, \delta \mathbf{u}_h)_{\mathbb{D}} = 0 \quad \forall \delta \mathbf{u}_h \in \mathcal{V}_h^u(\mathcal{K}_{M(\alpha)}). \end{cases} \quad (4.1)$$

These homogeneous equations are subjected to kinematical constraints that account for heterogeneities and the deformability of the boundary. They are imposed over the RVE in the form of linear or periodic boundaries.

Linear boundaries are the easiest to implement but are less accurate for highly heterogeneous domains when compared with periodic boundaries. This is because linear boundaries produce stiffer elements. Such elements cannot account for oscillatory material coefficients. Periodic boundaries on the other hand, relax this restriction.

Periodic boundaries involve creating periodic pairs on opposite sides of the RVE coarse element and imposing constraints on these pairs. This is normally done employing penalty parameters or Lagrange multipliers. This approach is ideal when considering RVEs that do exhibit some form of periodicity. The procedure for such enforcements are discussed in [8] and will not be detailed here. The choice of the coarse element boundary conditions plays an important role vis-a-vis the accuracy of the method.

Resonance errors may occur when the coarse-element length scale approaches the fine-element scale, i.e., a large number of coarse elements are employed to mesh the domain. This is primarily observed over highly heterogeneous domains. Such errors can be overcome by an oversampling strategy [257].

To give a physical interpretation to these multiscale basis functions, one must compare the features of the multiscale coarse element against the classical finite element. The possible static modes of a four-node plane quadrilateral finite element are the standard bilinear Lagrange polynomials. On the other hand, a multiscale quadrilateral coarse-element can be viewed as a more flexible alternative. Despite having only four nodes, it can exhibit more flexible static modes. This renders such elements an ideal choice for capturing variations in element behaviour driven by underlying heterogeneities. Such variations may be impossible to capture with rigid classical finite elements. For a square domain with an independently, identically distributed random elastic modulus field, sampled from a normal distribution, snapshots of the associated deformation modes are shown in Fig. 4.4. Similar comparisons maybe be drawn up in 3D, between classical

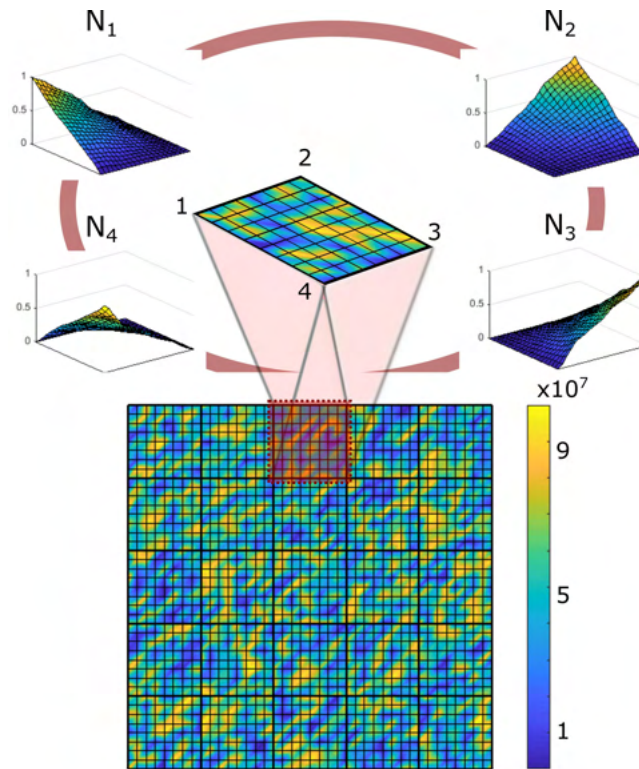


Figure 4.4: Visualizing multiscale basis functions for a heterogeneous domain.

hexahedral finite elements and multiscale hexahedral elements.

The bilinear form defined over the coarse element domain $\mathcal{K}_{M(\alpha)}$ in Eq. (4.1) is evaluated from

individual fine element contributions

$$a^\varepsilon(\mathbf{u}_h, \delta \mathbf{u}_h)_\mathbb{D} = \sum_{i=1}^{n_{m_{el}}^\alpha} a_{\mathcal{K}_m}^\varepsilon(\mathbf{u}_h, \delta \mathbf{u}_h)_\mathbb{D}. \quad (4.2)$$

The fine scale element stiffness matrix $\mathbf{K}_{m(i)}^{\text{el},\alpha}$ is derived from Eq. (2.103) using the finite element method. This is assembled into the RVE stiffness matrix \mathbf{K}_m^α by the same assembly procedure followed in Eqs. (2.105). Similarly, the fine scale element load vector $\mathbf{f}_{m(i)}^{\text{el},\alpha}$ is defined on the basis of Eq. (2.104). This is assembled into the coarse element specific RVE load vector $\mathbf{f}_{M(\alpha)}^{\text{el}}$.

4.2.1 Constructing multiscale basis functions

In the multiscale finite element framework utilized herein, the micro-displacement components of the fine mesh are mapped to the macro-displacement nodal components of the corresponding coarse-element according to Eq. (4.3)

$$\begin{aligned} u_{mx,i} &= \sum_{J=1}^{n_M} N_{iJxx}^u u_{Mx,J} + \sum_{J=1}^{n_M} N_{iJxy}^u u_{My,J} \\ u_{my,i} &= \sum_{J=1}^{n_M} N_{iJyx}^u u_{Mx,J} + \sum_{J=1}^{n_M} N_{iJyy}^u u_{My,J}, \end{aligned} \quad (4.3)$$

where $u_{mx,i}$ and $u_{my,i}$, $i = 1, \dots, n_m$ are the displacement components of the i^{th} micro-node, n_m is the number of micro-nodes within the coarse-element and $n_{M(\alpha)} = 4$ is the number of macro-nodes of the α^{th} coarse-element.

Moreover, $u_{Mx,J}$ and $u_{My,J}$ are the macro-displacement components defined at the J^{th} macro-node of the coarse-element; N_{iJxx} , N_{iJyy} , N_{iJxy} and N_{iJyx} correspond to the micro-basis interpolation functions. Eqs. (4.3) hold if and only if the micro-basis interpolation functions satisfy the following conditions

$$\begin{aligned} \sum_{J=1}^{n_M} N_{IJxx}^u &= 1 & \sum_{J=1}^{n_M} N_{IJxy}^u &= 0 \\ \sum_{J=1}^{n_M} N_{IJyx}^u &= 0 & \sum_{J=1}^{n_M} N_{IJyy}^u &= 1 \end{aligned}, \quad I = 1 \dots n_M \quad (4.4)$$

At the fine-element scale, this mapping assumes the following form

$$\mathbf{u}_{m(i)}^\alpha = \mathbf{N}_{m(i)}^u \mathbf{u}_{M(\alpha)}, \quad (4.5)$$

where $\mathbf{u}_{m(i)}^\alpha$ is the displacement vector for the i^{th} fine-element in the α^{th} RVE. The array $\mathbf{N}_{m(i)}^u$ denotes the multiscale basis functions mapping the associated coarse-nodal displacements in $\mathbf{u}_{M(\alpha)}$ to the current fine-element.

Collecting Eqs. (4.5) for all micro-elements within the coarse-element, the following equation is established

$$\mathbf{u}_m^\alpha = \mathbf{N}_m^u \mathbf{u}_{M(\alpha)}, \quad (4.6)$$

where \mathbf{u}_m^α comprises the nodal displacement of the fine-mesh contained within coarse-element α .

A set of interpolation functions satisfying Eqs. (4.4) (hence Eqs. (4.3) also) can be established

by solving the following boundary value problem derived from Eq. (4.1)

$$\begin{cases} \mathbf{K}_m^\alpha \mathbf{u}_m^\alpha = \{\emptyset\} & \text{on } \mathcal{K}_{M(\alpha)} \\ \mathbf{u}_S = \bar{\mathbf{u}}_{IJ} & \text{on } \partial\mathcal{K}_{M(\alpha)} \end{cases}, I = 1 \dots n_M, J = 1, 2, \quad (4.7)$$

where \mathbf{u}_S is the vector of boundary micro-nodal displacements and $\bar{\mathbf{u}}$ are the prescribed displacements obtained from imposing linear, periodic or oversampling boundary conditions over the coarse-element/RVE boundary [8,257]. Each solution derived for a prescribed set of boundary conditions $\bar{\mathbf{u}}_{IJ}$ corresponds to a column of the multiscale basis function matrix \mathbf{N}_m^u .

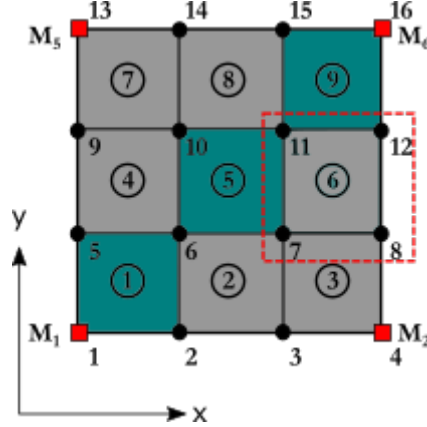


Figure 4.5: RVE with 9 quadrilateral elements. The number of fine-elements and fine-nodes in the RVE are $n_{mel} = 9$ and $n_m = 16$ respectively.

As an example, Eq. (4.5) assumes the following form for the case of the RVE shown in Fig. 4.5 and the micro-element $i = 6$

$$\mathbf{u}_{m(6)}^1 = \mathbf{N}_{m(6)}^u \mathbf{u}_{M(1)}, \quad (4.8)$$

where the vector of nodal displacements for fine-element #6 is

$$\mathbf{u}_{m(6)}^1 = \left[u_{mx,7} \quad u_{my,7} \quad u_{mx,8} \quad u_{my,8} \quad u_{mx,12} \quad u_{my,12} \quad u_{mx,11} \quad u_{my,11} \right]^T, \quad (4.9)$$

the coarse-element nodal displacement vector is

$$\mathbf{u}_{M(1)} = \left[u_{Mx,1} \quad u_{My,1} \quad u_{Mx,2} \quad u_{My,2} \quad u_{Mx,6} \quad u_{My,6} \quad u_{Mx,5} \quad u_{My,5} \right]^T, \quad (4.10)$$

and the corresponding multiscale basis function matrix is expressed as

$$\mathbf{N}_{m(6)}^u = \begin{bmatrix} N_{xx7,1}^u & N_{xy7,1}^u & N_{xx8,1}^u & N_{xy8,1}^u & N_{xx12,1}^u & N_{xy12,1}^u & N_{xx11,1}^u & N_{xy11,1}^u \\ N_{xy7,1}^u & N_{yy7,1}^u & N_{xy8,1}^u & N_{yy8,1}^u & N_{xy12,1}^u & N_{yy12,1}^u & N_{xy11,1}^u & N_{yy11,1}^u \\ N_{xx7,2}^u & N_{xy7,2}^u & N_{xx8,2}^u & N_{xy8,2}^u & N_{xx12,2}^u & N_{xy12,2}^u & N_{xx11,2}^u & N_{xy11,2}^u \\ N_{xy7,2}^u & N_{yy7,2}^u & N_{xy8,2}^u & N_{yy8,2}^u & N_{xy12,2}^u & N_{yy12,2}^u & N_{xy11,2}^u & N_{yy11,2}^u \\ N_{xx7,3}^u & N_{xy7,3}^u & N_{xx8,3}^u & N_{xy8,3}^u & N_{xx12,3}^u & N_{xy12,3}^u & N_{xx11,3}^u & N_{xy11,3}^u \\ N_{xy7,3}^u & N_{yy7,3}^u & N_{xy8,3}^u & N_{yy8,3}^u & N_{xy12,3}^u & N_{yy12,3}^u & N_{xy11,3}^u & N_{yy11,3}^u \\ N_{xx7,4}^u & N_{xy7,4}^u & N_{xx8,4}^u & N_{xy8,4}^u & N_{xx12,4}^u & N_{xy12,4}^u & N_{xx11,4}^u & N_{xy11,4}^u \\ N_{xy7,4}^u & N_{yy7,4}^u & N_{xy8,4}^u & N_{yy8,4}^u & N_{xy12,4}^u & N_{yy12,4}^u & N_{xy11,4}^u & N_{yy11,4}^u \end{bmatrix}, \quad (4.11)$$

respectively.

For the RVE shown in Fig. 4.5, \mathbf{u}_m^α is a 32×1 vector. Furthermore, \mathbf{N}_m^u is the coarse-element matrix of multiscale basis functions; for the case of Fig. 4.5 this is a 32×8 matrix. Each column j of \mathbf{N}_m^u corresponds to the deformed configuration of the RVE when the j^{th} coarse degree of freedom is equal to 1 whereas all other coarse degrees of freedom are equal to zero.

4.2.2 Governing multiscale equilibrium equations

Having evaluated the micro-basis functions, the following procedure is established to upscale the RVE properties at the coarse scale. The element-wise equilibrium equations at the fine-scale of the RVE under consideration are

$$\mathbf{K}_{m(i)}^{\text{el},\alpha} \mathbf{u}_{m(i)}^\alpha = \mathbf{f}_{m(i)}^{\text{u el},\alpha}. \quad (4.12)$$

Substituting Eq. (4.5) into Eq. (4.12) results in the following expression

$$\mathbf{K}_{m(i)}^{\text{el},\alpha} \mathbf{N}_{m(i)}^u \mathbf{u}_{M(\alpha)} = \mathbf{f}_{m(i)}^{\text{u el},\alpha}.$$

Pre-multiplying this by $\mathbf{N}_{m(i)}^{u T}$, the following relation is obtained

$$\mathbf{K}_{M(\alpha),m(i)}^{\text{el}} \mathbf{u}_{M(\alpha)} = \mathbf{f}_{M(\alpha),m(i)}^{\text{u el}}, \quad (4.13)$$

where $\mathbf{K}_{M(\alpha),m(i)}^{\text{el}}$ corresponds to the fine-element stiffness matrix that is however, defined at the coarse nodes

$$\underbrace{\mathbf{K}_{M(\alpha),m(i)}^{\text{el}}}_{2n_{M(\alpha)} \times 2n_{M(\alpha)}} = \mathbf{N}_{m(i)}^{u T} \mathbf{K}_{m(i)}^{\text{el},\alpha} \mathbf{N}_{m(i)}^u, \quad (4.14)$$

and $\mathbf{f}_{M(\alpha),m(i)}^{\text{u el}}$ is the corresponding vector of nodal forces

$$\mathbf{f}_{M(\alpha),m(i)}^{\text{u el}} = \mathbf{N}_{m(i)}^{u T} \mathbf{f}_{m(i)}^{\text{u el},\alpha}, \quad (4.15)$$

respectively.

The reduced order coarse element equilibrium equation can be established in the following form

$$\mathbf{K}_{M(\alpha)}^{\text{el}} \mathbf{u}_{M(\alpha)} = \mathbf{f}_{M(\alpha)}^{\text{u el}}, \quad (4.16)$$

where $\mathbf{K}_{M(\alpha)}^{\text{el}}$ and $\mathbf{f}_{M(\alpha)}^{\text{u el}}$ are the coarse element stiffness matrix and load vector respectively. These quantities are a priori unknown but can be derived on the basis of strain energy equivalence between the coarse element and its underlying fine scale mesh.

The overall strain energy E_{int} of the coarse element can be, in principle, established as

$$E_{\text{int}} = \int_{\mathcal{K}_{M(\alpha)}} \boldsymbol{\varepsilon}_M^T \boldsymbol{\sigma}_M \, d\mathcal{K} = \mathbf{u}_{M(\alpha)}^T \mathbf{K}_{M(\alpha)}^{\text{el}} \mathbf{u}_{M(\alpha)}, \quad (4.17)$$

where $\boldsymbol{\varepsilon}$ and $\boldsymbol{\sigma}$ correspond to the strain and stress fields defined over the RVE.

However, the RVE strain energy can also be considered to be additively decomposed into the

contributions of the associated fine-scale elements, i.e.,

$$\mathbf{E}_{\text{int}} = \sum_{i=1}^{n_{\text{mel}}} \int_{\mathcal{K}_{m(i)}} \boldsymbol{\varepsilon}_{m(i)}^{\alpha T} \boldsymbol{\sigma}_{m(i)}^{\alpha} d\mathcal{K} = \sum_{i=1}^{n_{\text{mel}}} \mathbf{u}_{m(i)}^{\alpha T} \mathbf{K}_{m(i)}^{\text{el},\alpha} \mathbf{u}_{m(i)}^{\alpha}. \quad (4.18)$$

Comparing Eq. (4.17) to Eq. (4.18), the following expression is established

$$\mathbf{u}_{M(\alpha)}^T \mathbf{K}_{M(\alpha)}^{\text{el}} \mathbf{u}_{M(\alpha)} = \sum_{i=1}^{n_{\text{mel}}} \mathbf{u}_{m(i)}^{\alpha T} \mathbf{K}_{m(i)}^{\text{el},\alpha} \mathbf{u}_{m(i)}^{\alpha}. \quad (4.19)$$

Substituting Eq. (4.5) into Eq. (4.19) results in the following expression

$$\mathbf{u}_{M(\alpha)}^T \mathbf{K}_{M(\alpha)}^{\text{el}} \mathbf{u}_{M(\alpha)} = \mathbf{u}_{M(\alpha)}^T \sum_{i=1}^{n_{\text{mel}}} \left(\mathbf{N}_{m(i)}^{\text{u} T} \mathbf{K}_{m(i)}^{\text{el},\alpha} \mathbf{N}_{m(i)}^{\text{u}} \right) \mathbf{u}_{M(\alpha)}. \quad (4.20)$$

Eq. (4.20) holds if and only if

$$\mathbf{K}_{M(\alpha)}^{\text{el}} = \sum_{i=1}^{n_{\text{mel}}} \mathbf{K}_{M(\alpha),m(i)}^{\text{el}}. \quad (4.21)$$

Similarly, the following expression must hold for the RVE reduced order nodal load vector, i.e.,

$$\mathbf{f}_{M(\alpha)}^{\text{u el}} = \sum_{i=1}^{n_{\text{mel}}} \mathbf{f}_{M(\alpha),m(i)}^{\text{u el}}. \quad (4.22)$$

The reduced order RVE stiffness and nodal load matrices defined in Eqs. (4.21) and (4.22) can be assembled using a direct stiffness method to eventually derive the reduced order global equilibrium equation

$$\mathbf{K}_M \mathbf{u}_M = \mathbf{f}_M^{\text{u}}, \quad (4.23)$$

where

$$\mathbf{K}_M = \mathbf{A} \sum_{\alpha=1}^{n_{\text{Mel}}} \mathbf{K}_{M(\alpha)}^{\text{el}}, \quad \mathbf{f}_M^{\text{u}} = \mathbf{A} \sum_{\alpha=1}^{n_{\text{Mel}}} \mathbf{f}_{M(\alpha)}^{\text{u el}}, \quad (4.24)$$

and \mathbf{A} denotes a standard direct stiffness assembly operator.

4.2.3 Solution at the coarse scale and downscaling

Having computed $\mathbf{K}_{m(i)}^{\text{el},\alpha}$, the multiscale basis functions can be evaluated by assembling \mathbf{K}_m^{α} and solving Eq. (4.7). The global system of equations at the coarse-scale has already been established in Eq. (4.23)

$$\mathbf{K}_M \mathbf{u}_M = \mathbf{f}_M^{\text{u}}, \quad (4.25)$$

where \mathbf{K}_M and \mathbf{f}_M denote the $2n_M \times 2n_M$ global coarse stiffness matrix and $2n_M \times 1$ global coarse load vector respectively. The global coarse stiffness is assembled from its local coarse stiffness contributions as shown in Eq. (4.24). The global coarse load vector is evaluated from the local

coarse element load contributions. Finally, the MsFEM solution is performed for the n_M coarse-scale nodes \mathbf{u}_M .

The micro-displacements can be evaluated from the solution of the reduced order solution of Eq. (4.25) using the following down-scaling procedure. The coarse element-wise displacements are first extracted from \mathbf{u}_M and stored in the vector of macro-element nodal displacements $\mathbf{u}_{M(\alpha)}$, $\alpha = 1 \dots n_{M_{el}}$. The displacements associated with the i^{th} fine-element in the α^{th} coarse-element / RVE is computed using Eq. (4.5). The strains and stresses associated with these fine-scale displacements can be computed as follows

$$\boldsymbol{\varepsilon}_{m(i)}^\alpha = \mathbf{B}\mathbf{u}_{m(i)}^\alpha, \quad \boldsymbol{\sigma}_{m(i)}^\alpha = \mathbb{C}\boldsymbol{\varepsilon}_{m(i)}^\alpha, \quad (4.26)$$

where \mathbf{B} is the term provided in Eq. (2.103).

4.3 Consolidation

The standard Coupled Multiscale Finite Element Method (CMsFEM) seeks to compute multiscale basis functions that sufficiently capture all significant static modes of the coarse element under consideration. In coupled porous consolidation problems, this is equivalent to capturing deformation modes of the solid skeleton and pressure gradient modes of the pore-fluid, as elaborated in Chapter 2.

Within this setting, two sets of multiscale basis functions are computed. One set describes the solid skeleton displacements and the other captures the pore-fluid pressure. For these evaluations, both phases are assumed to be decoupled from each other. The basis functions for the displacement field are already evaluated in Eq. (4.1).

Similarly, the fluid phase multiscale basis functions are evaluated as

$$\begin{cases} \text{Find } p_h \in \mathcal{V}_h^p(\mathcal{K}_{M(\alpha)}) \text{ such that} \\ b^\nabla(p_h, \delta p_h)_{k/\gamma_f} = 0 \quad \forall \delta p_h \in \mathcal{V}_h^p(\mathcal{K}_{M(\alpha)}). \end{cases} \quad (4.27)$$

These equations are subjected to Dirichlet constraints, which are imposed at the coarse element boundary, in a manner similar to Section 4.2.

The bilinear form defined over the coarse-element domain $\mathcal{K}_{M(\alpha)}$ in Eq. (4.27), respectively can be assembled from individual fine element contributions as done in Eq. (4.2)

$$b^\nabla(p_h, \delta p_h) = \sum_{i=1}^{n_{mel}^\alpha} b_{\mathcal{K}_m}^\nabla(p_h, \delta p_h). \quad (4.28)$$

The corresponding decompositions for $b^0(p_h, w_h)$ and $a^{(\boldsymbol{\varepsilon}, 0)}(\mathbf{u}_h, w_h)$ are derived in a similar manner and are omitted for brevity.

The element-wise state matrices are now obtained from Eqs. (4.28) using the FEM on the basis of Eqs. (2.121)-(2.125). They are then assembled into their RVE specific counterparts \mathbf{H}_m^α , \mathbf{S}_m^α and \mathbf{Q}_m^α , respectively. Similarly, the relevant fine-element flux vector, $\mathbf{f}_{m(i)}^{p \text{ el}}$ is obtained from Eq. (2.123), and assembled into $\mathbf{f}_{M(\alpha)}^{p \text{ el}}$.

4.3.1 Constructing multiscale basis functions

The micro-nodal field variables \mathbf{u}_m^α and p_m^α are now mapped to the associated coarse-nodes. This has already been done for displacements in Eq. (4.3). The corresponding relations for fluid pressures are

$$p_{m,i}^\alpha = \sum_{J=1}^{n_M} N_{iJ}^P p_{M,J}, \quad (4.29)$$

where $p_{m,i}^\alpha$, $i = 1 \dots n_m^\alpha$ is the pressure component of the i^{th} micro-node, belonging to the α^{th} coarse element. The term $p_{M,J}$ denotes the pressure component at the J^{th} macro-node of the α^{th} coarse-element. The multiscale basis functions N_{iJ}^P interpolate the fine-scale pressures. The relation in Eq. (4.29) holds only if

$$\sum_{J=1}^{n_M} N_{iJ}^P = 1. \quad (4.30)$$

The RVE specific fine-element nodal pressures p_m^α are associated with the corresponding coarse-element field variables through the following equation, i.e.,

$$\mathbf{p}_{m(i)}^\alpha = \mathbf{N}_{m(i)}^P \mathbf{p}_{M(\alpha)}, \quad (4.31)$$

where $\mathbf{p}_{m(i)}^\alpha$ denotes pressure vector for the i^{th} fine-element in the α^{th} element. The array $\mathbf{N}_{m(i)}^P$ represents the multiscale basis functions mapping the α^{th} coarse-element nodal pressures $\mathbf{p}_{M(\alpha)}$ to the fine-scale.

Collecting the contributions from each fine-element, Eq. (4.31) can be expressed over the entire RVE:

$$\mathbf{p}_m^\alpha = \mathbf{N}_m^P \mathbf{p}_{M(\alpha)}, \quad (4.32)$$

where \mathbf{N}_m^P corresponds to the coarse element multi-scale basis functions for the pressure field. Each column of these arrays corresponds to a possible static pressure mode of the RVE. To compute these snapshots of the system in a manner consistent with Eqs. (4.29) and (4.30), the discretized matrix forms of the boundary value sub-problems in Eq. (4.27) are solved over the RVE domain, similar to Eq. (4.7)

$$\begin{cases} \mathbf{H}_m^\alpha \mathbf{p}_m^\alpha = \{\emptyset\} & , \text{ on } \mathcal{K}_{M(\alpha)} \\ \mathbf{p}_S = \bar{\mathbf{p}}_{IJ} & , \text{ on } \partial\mathcal{K}_{M(\alpha)} \end{cases}, I = 1 \dots n_M, J = 1, \quad (4.33)$$

In the CMsFEM, the prescribed pressures \mathbf{p}_S at the RVE boundary are assigned linear or periodic kinematical constraints $\bar{\mathbf{p}}$.

4.3.2 Governing multiscale equilibrium equations

The multiscale basis functions evaluated above are now used to upscale the RVE properties at the coarse scale. The element-wise governing equations introduced in Eq. (2.112) are expressed in

matrix form as

$$\begin{bmatrix} \mathbf{K}_{m(i)}^{\text{el},\alpha} & -\mathbf{Q}_{m(i)}^{\text{el},\alpha} \\ \mathbf{0} & \mathbf{H}_{m(i)}^{\text{el},\alpha} \end{bmatrix} \begin{Bmatrix} \mathbf{u}_{m(i)}^\alpha \\ \mathbf{p}_{m(i)}^\alpha \end{Bmatrix} + \begin{bmatrix} \mathbf{0} & \mathbf{0} \\ \mathbf{Q}_{m(i)}^{\text{el},\alpha T} & \mathbf{S}_{m(i)}^{\text{el},\alpha} \end{bmatrix} \begin{Bmatrix} \dot{\mathbf{u}}_{m(i)}^\alpha \\ \dot{\mathbf{p}}_{m(i)}^\alpha \end{Bmatrix} = \begin{Bmatrix} \mathbf{f}_{m(i)}^{\text{u el},\alpha} \\ \mathbf{f}_{m(i)}^{\text{p el},\alpha} \end{Bmatrix}. \quad (4.34)$$

Substituting the micro to macro mapping Eqs. (4.5) and (4.31) into Eq. (4.34) and pre-multiplying the first row-set of equations by $\mathbf{N}_m^{\text{u} T}$ and the second row-set by $\mathbf{N}_m^{\text{p} T}$ the following equation is obtained

$$\begin{bmatrix} \mathbf{K}_{M(\alpha),m(i)}^{\text{el}} & -\mathbf{Q}_{M(\alpha),m(i)}^{\text{el}} \\ \mathbf{0} & \mathbf{H}_{M(\alpha),m(i)}^{\text{el}} \end{bmatrix} \begin{Bmatrix} \mathbf{u}_{M(\alpha)} \\ \mathbf{p}_{M(\alpha)} \end{Bmatrix} + \begin{bmatrix} \mathbf{0} & \mathbf{0} \\ \mathbf{Q}_{M(\alpha),m(i)}^{\text{el} T} & \mathbf{S}_{M(\alpha),m(i)}^{\text{el}} \end{bmatrix} \begin{Bmatrix} \dot{\mathbf{u}}_{M(\alpha)} \\ \dot{\mathbf{p}}_{M(\alpha)} \end{Bmatrix} = \begin{Bmatrix} \mathbf{f}_{M(\alpha),m(i)}^{\text{u el}} \\ \mathbf{f}_{M(\alpha),m(i)}^{\text{p el}} \end{Bmatrix}, \quad (4.35)$$

where the elastic stiffness matrix and load vector of the i^{th} micro-element mapped at the coarse element nodes, i.e., $\mathbf{K}_{M(\alpha),m(i)}^{\text{el}}$ and $\mathbf{f}_{M(\alpha),m(i)}^{\text{u el}}$ are defined in Eqs. (4.14) -(4.15), respectively. The corresponding coupling, permeability and compressibility matrices are expressed as

$$\mathbf{Q}_{M(\alpha),m(i)}^{\text{el}} = \mathbf{N}_{m(i)}^{\text{u} T} \mathbf{Q}_{m(i)}^{\text{el},\alpha} \mathbf{N}_{m(i)}^{\text{p}}, \quad (4.36)$$

$$\mathbf{H}_{M(\alpha),m(i)}^{\text{el}} = \mathbf{N}_{m(i)}^{\text{p} T} \mathbf{H}_{m(i)}^{\text{el},\alpha} \mathbf{N}_{m(i)}^{\text{p}}, \quad (4.37)$$

$$\mathbf{S}_{M(\alpha),m(i)}^{\text{el}} = \mathbf{N}_{m(i)}^{\text{p} T} \mathbf{S}_{m(i)}^{\text{el},\alpha} \mathbf{N}_{m(i)}^{\text{p}}. \quad (4.38)$$

Finally, the flux term assumes the following form

$$\mathbf{f}_{M(\alpha),m(i)}^{\text{p el}} = \mathbf{N}_{m(i)}^{\text{p} T} \mathbf{f}_{m(i)}^{\text{p el},\alpha}. \quad (4.39)$$

In principle, the coarse-element equilibrium equations could be expressed in a form analogous to Eq. (4.34), i.e.,

$$\begin{bmatrix} \mathbf{K}_{M(\alpha)}^{\text{el}} & -\mathbf{Q}_{M(\alpha)}^{\text{el}} \\ \mathbf{0} & \mathbf{H}_{M(\alpha)}^{\text{el}} \end{bmatrix} \begin{Bmatrix} \mathbf{u}_{M(\alpha)} \\ \mathbf{p}_{M(\alpha)} \end{Bmatrix} + \begin{bmatrix} \mathbf{0} & \mathbf{0} \\ \mathbf{Q}_{M(\alpha)}^{\text{el},T} & \mathbf{S}_{M(\alpha)}^{\text{el}} \end{bmatrix} \begin{Bmatrix} \dot{\mathbf{u}}_{M(\alpha)} \\ \dot{\mathbf{p}}_{M(\alpha)} \end{Bmatrix} = \begin{Bmatrix} \mathbf{f}_{M(\alpha)}^{\text{u el}} \\ \mathbf{f}_{M(\alpha)}^{\text{p el}} \end{Bmatrix}, \quad (4.40)$$

where $\mathbf{K}_{M(\alpha)}^{\text{el}}$, $\mathbf{Q}_{M(\alpha)}^{\text{el}}$, $\mathbf{H}_{M(\alpha)}^{\text{el}}$, $\mathbf{S}_{M(\alpha)}^{\text{el}}$ denote the coarse-element state matrices and $\mathbf{f}_{M(\alpha)}^{\text{u el}}$, $\mathbf{f}_{M(\alpha)}^{\text{p el}}$ denote the coarse-element load vectors, respectively. Due to the heterogeneous material distribution at the fine scale, explicit expressions for these matrices do not exist. Relations for $\mathbf{K}_{M(\alpha)}^{\text{el}}$ and $\mathbf{f}_{M(\alpha)}^{\text{u el}}$ have been derived in Eqs. (4.21)-(4.22). Similarly, the remaining quantities can be evaluated on the basis of energy equivalence between the coarse element domain Eqs. (4.40) and the upscaled fine-element components Eqs. (4.36)-(4.39).

Considering Eq. (4.40), the internal energy associated with each operator is defined as

$$E_{\text{int}}^{\text{Q}} = \int_{\mathcal{K}_{M(\alpha)}} \mathbf{p}_M^T \alpha_B \mathbf{m} \boldsymbol{\varepsilon}_M \, d\mathcal{K} = \mathbf{p}_{M(\alpha)}^T \mathbf{Q}_{M(\alpha)}^{\text{el}} \mathbf{u}_{M(\alpha)} \quad (4.41a)$$

$$E_{\text{int}}^{\text{H}} = \int_{\mathcal{K}_{M(\alpha)}} \nabla \mathbf{p}_M^T \frac{\mathbf{k}}{\gamma_f} \nabla \mathbf{p}_M \, d\mathcal{K} = \mathbf{p}_{M(\alpha)}^T \mathbf{H}_{M(\alpha)}^{\text{el}} \mathbf{p}_{M(\alpha)} \quad (4.41b)$$

$$\mathbf{E}_{\text{int}}^{\text{S}} = \int_{\mathcal{K}_{\text{M}(\alpha)}} \mathbf{p}_{\text{M}}^T \mathbf{S}_{\varepsilon} \mathbf{p}_{\text{M}} \, d\mathcal{K} = \mathbf{p}_{\text{M}(\alpha)}^T \mathbf{S}_{\text{M}(\alpha)}^{\text{el}} \mathbf{p}_{\text{M}(\alpha)} \quad (4.41\text{c})$$

where $\boldsymbol{\varepsilon}_{\text{M}}$ and \mathbf{p}_{M} correspond to the strain and pressure fields defined over the coarse element domain.

The internal energy of the RVE is also additively decomposed into the contributions of its underlying fine-elements, i.e.,

$$\mathbf{E}_{\text{int}}^{\text{Q}} = \sum_{i=1}^{n_{\text{mel}}} \int_{\mathcal{K}_{\text{m}(i)}} \mathbf{p}_{\text{m}(i)}^T \alpha_{\text{B}} \mathbf{m} \boldsymbol{\varepsilon}_{\text{m}(i)} \, d\mathcal{K} = \sum_{i=1}^{n_{\text{mel}}} \mathbf{p}_{\text{m}(i)}^{\alpha T} \mathbf{Q}_{\text{m}(i)}^{\text{el},\alpha} \mathbf{u}_{\text{m}(i)}^{\alpha} \quad (4.42\text{a})$$

$$\mathbf{E}_{\text{int}}^{\text{H}} = \sum_{i=1}^{n_{\text{mel}}} \int_{\mathcal{K}_{\text{m}(i)}} \nabla \mathbf{p}_{\text{m}(i)}^T \frac{\mathbf{k}}{\gamma_{\text{f}}} \nabla \mathbf{p}_{\text{m}(i)} \, d\mathcal{K} = \sum_{i=1}^{n_{\text{mel}}} \mathbf{p}_{\text{m}(i)}^{\alpha T} \mathbf{H}_{\text{m}(i)}^{\text{el},\alpha} \mathbf{p}_{\text{m}(i)}^{\alpha} \quad (4.42\text{b})$$

$$\mathbf{E}_{\text{int}}^{\text{S}} = \sum_{i=1}^{n_{\text{mel}}} \int_{\mathcal{K}_{\text{m}(i)}} \mathbf{p}_{\text{m}(i)}^T \mathbf{S}_{\varepsilon} \mathbf{p}_{\text{m}(i)} \, d\mathcal{K} = \sum_{i=1}^{n_{\text{mel}}} \mathbf{p}_{\text{m}(i)}^{\alpha T} \mathbf{S}_{\text{m}(i)}^{\text{el},\alpha} \mathbf{p}_{\text{m}(i)}^{\alpha}. \quad (4.42\text{c})$$

Equating Eqs. (4.41b) and (4.42b) the following expression is derived

$$\mathbf{p}_{\text{M}(\alpha)}^T \mathbf{H}_{\text{M}(\alpha)}^{\text{el}} \mathbf{p}_{\text{M}(\alpha)} = \mathbf{p}_{\text{M}(\alpha)}^T \sum_{i=1}^{n_{\text{mel}}} \left(\mathbf{N}_{\text{m}(i)}^{\text{p}T} \mathbf{H}_{\text{m}(i)}^{\text{el},\alpha} \mathbf{N}_{\text{m}(i)}^{\text{p}} \right) \mathbf{p}_{\text{M}(\alpha)}, \quad (4.43)$$

that holds if and only if

$$\underbrace{\mathbf{H}_{\text{M}(\alpha)}^{\text{el}}}_{n_{\text{M}(\alpha)} \times n_{\text{M}(\alpha)}} = \sum_{i=1}^{n_{\text{mel}}} \mathbf{H}_{\text{M}(\alpha),\text{m}(i)}^{\text{el}}. \quad (4.44)$$

Hence, Eq. (4.44) provides the reduced order permeability matrix of the coarse element that however comprises stiffness contributions from the underlying micro-elements.

The upscaled expressions for the coupling, and compressibility matrices are derived in a similar manner as

$$\underbrace{\mathbf{Q}_{\text{M}(\alpha)}^{\text{el}}}_{2n_{\text{M}(\alpha)} \times n_{\text{M}(\alpha)}} = \sum_{i=1}^{n_{\text{mel}}} \mathbf{Q}_{\text{M}(\alpha),\text{m}(i)}^{\text{el}}, \quad (4.45)$$

and

$$\underbrace{\mathbf{S}_{\text{M}(\alpha)}^{\text{el}}}_{n_{\text{M}(\alpha)} \times n_{\text{M}(\alpha)}} = \sum_{i=1}^{n_{\text{mel}}} \mathbf{S}_{\text{M}(\alpha),\text{m}(i)}^{\text{el}}, \quad (4.46)$$

respectively.

Finally, the upscaled outflow vector is (see, also, [258]):

$$\mathbf{f}_{\text{M}(\alpha)}^{\text{p el}} = \sum_{i=1}^{n_{\text{mel}}} \mathbf{f}_{\text{M}(\alpha),\text{m}(i)}^{\text{p el}}. \quad (4.47)$$

The coarse element state and load matrices defined in Eqs. (4.44)-(4.47) can then be assembled using a direct assembly approach to derive the reduced order structure matrices and corresponding forcing vectors

$$\mathbf{Q}_M = \mathop{\text{A}}_{\alpha=1}^{n_{M_{el}}} \mathbf{Q}_{M(\alpha)}^{el}, \quad \mathbf{H}_M = \mathop{\text{A}}_{\alpha=1}^{n_{M_{el}}} \mathbf{H}_{M(\alpha)}^{el}, \quad (4.48a)$$

$$\mathbf{S}_M = \mathop{\text{A}}_{\alpha=1}^{n_{M_{el}}} \mathbf{S}_{M(\alpha)}^{el}, \quad \mathbf{f}_M^p = \mathop{\text{A}}_{\alpha=1}^{n_{M_{el}}} \mathbf{f}_{M(\alpha)}^{p,el}. \quad (4.48b)$$

Hence, the upscaled governing equations assume the following form

$$\begin{bmatrix} \mathbf{K}_M & -\mathbf{Q}_M \\ \mathbf{0} & \mathbf{H}_M \end{bmatrix} \begin{Bmatrix} \mathbf{u}_M \\ \mathbf{p}_M \end{Bmatrix} + \begin{bmatrix} \mathbf{0} & \mathbf{0} \\ \mathbf{Q}_M^T & \mathbf{S}_M \end{bmatrix} \begin{Bmatrix} \dot{\mathbf{u}}_M \\ \dot{\mathbf{p}}_M \end{Bmatrix} = \begin{Bmatrix} \mathbf{f}_M^u \\ \mathbf{f}_M^p \end{Bmatrix}. \quad (4.49)$$

The unknown field variables \mathbf{u}_M and \mathbf{p}_M represent the global coarse-nodal displacements and vectors, respectively.

The coarse scale equations in Eq. (4.49) are solved following the procedure detailed in Section 2.7.2.

The algorithmic implementation of the method vis-a-vis the assembly of the discretized governing equations at the coarse scale is summarized in Algorithm 3.

Algorithm 3: Upscaling procedure performed for solid and fluid phases

Result: Global coarse scale stiffness matrices \mathbf{K}_M , \mathbf{H}_M and load vectors \mathbf{f}_M^u , \mathbf{f}_M^p

for $\Omega_{M(\alpha)}$, $1 \leq \alpha \leq n_{M_{el}}$ **do**

1. Compute RVE stiffnesses,

(a) Solid phase: \mathbf{K}_m^α with $\mathbf{K}_m^\alpha = \sum_{i=1}^{n_{m_{el}}} \mathbf{K}_{m(i)}^{el,\alpha}$,

(b) Fluid phase: \mathbf{H}_m^α with $\mathbf{H}_m^\alpha = \sum_{i=1}^{n_{m_{el}}} \mathbf{H}_{m(i)}^{el,\alpha}$;

2. Compute multiscale basis functions using kinematic constraints with

(a) Solid phase: \mathbf{N}_m^u : $\mathbf{K}_m^\alpha \mathbf{u}_m^\alpha = \mathbf{0}$, where $\mathbf{u}_m^\alpha \equiv \mathbf{N}_m^u$,

(b) Fluid phase: \mathbf{N}_m^p : $\mathbf{H}_m^\alpha \mathbf{p}_m^\alpha = \mathbf{0}$, where $\mathbf{p}_m^\alpha \equiv \mathbf{N}_m^p$;

3. Compute multiscale contributions with

(a) Solid phase: $\mathbf{K}_{M(\alpha),m(i)}^{el} = \mathbf{N}_{m(i)}^{uT} \mathbf{K}_{m(i)}^{el,\alpha} \mathbf{N}_{m(i)}^u$ and $\mathbf{f}_{M(\alpha),m(i)}^{u,el} = \mathbf{N}_{m(i)}^{uT} \mathbf{f}_{m(i)}^{u,el,\alpha}$,

(b) Fluid phase: $\mathbf{H}_{M(\alpha),m(i)}^{el} = \mathbf{N}_{m(i)}^{pT} \mathbf{H}_{m(i)}^{el,\alpha} \mathbf{N}_{m(i)}^p$ and $\mathbf{f}_{M(\alpha),m(i)}^{p,el} = \mathbf{N}_{m(i)}^{pT} \mathbf{f}_{m(i)}^{p,el,\alpha}$;

4. Assemble coarse-element stiffnesses with

(a) Solid phase: $\mathbf{K}_{M(\alpha)}^{el} = \sum_{i=1}^{n_{m_{el}}} \mathbf{K}_{M(\alpha),m(i)}^{el}$, and $\mathbf{f}_{M(\alpha)}^{u,el} = \sum_{i=1}^{n_{m_{el}}} \mathbf{f}_{M(\alpha),m(i)}^{u,el}$,

(b) Fluid phase: $\mathbf{H}_{M(\alpha)}^{el} = \sum_{i=1}^{n_{m_{el}}} \mathbf{H}_{M(\alpha),m(i)}^{el}$, and $\mathbf{f}_{M(\alpha)}^{p,el} = \sum_{i=1}^{n_{m_{el}}} \mathbf{f}_{M(\alpha),m(i)}^{p,el}$,

end

Assemble global coarse stiffness matrix and load vector with

(a) Solid phase: $\mathbf{K}_M = \mathop{\text{A}}_{\alpha=1}^{n_{M_{el}}} \mathbf{K}_{M(\alpha)}^{el}$ and $\mathbf{f}_M^u = \mathop{\text{A}}_{\alpha=1}^{n_{M_{el}}} \mathbf{f}_{M(\alpha)}^{u,el}$

(b) Fluid phase: $\mathbf{H}_M = \mathop{\text{A}}_{\alpha=1}^{n_{M_{el}}} \mathbf{H}_{M(\alpha)}^{el}$ and $\mathbf{f}_M^p = \mathop{\text{A}}_{\alpha=1}^{n_{M_{el}}} \mathbf{f}_{M(\alpha)}^{p,el}$

4.3.3 Downscaling

The fine-scale displacements and pressures at each time-step can be evaluated from the solution of Eq. (4.49) by employing the following down-scaling procedure. The coarse element-wise displacements and pressures are first extracted at the desired time steps from $\{\mathbf{u}_M\}_n$ and $\{\mathbf{p}_M\}_n$, respectively. These values are now stored in the vectors of coarse-nodal displacements $\mathbf{u}_{M(\alpha)}$ and pressures $\mathbf{p}_{M(\alpha)}$, $\alpha = 1 \dots n_{M_{el}}$, respectively. The displacements and pressures associated with the i^{th} fine-element in the α^{th} coarse-element / RVE can be evaluated using Eqs. (4.5) and (4.31). Derivative quantities, like strains and stresses associated with the fine-scale elements can now be computed using Eq. (4.26). Similarly, the derivative quantities for the fluid phase, i.e., the pressure flux and specific discharge, can be evaluated

$$\nabla \mathbf{p}_{m(i)}^\alpha = \mathbf{B}^\nabla \mathbf{p}_{m(i)}^\alpha, \quad \mathbf{q}_{m(i)}^\alpha = -\frac{\mathbf{k}}{\gamma_w} \nabla \mathbf{p}_{m(i)}^\alpha. \quad (4.50)$$

An expression for \mathbf{B}^∇ is provided under Eq. (2.121).

4.4 Vibro-acoustics

4.4.1 Evaluation of multiscale basis functions

Similar to the procedure followed in Section 4.3, a set of multiscale basis function are evaluated for the solid and fluid phases. The point of departure here is, they are iteratively evaluated for each frequency step ω_k , $k = 1, \dots, n_{\text{freq}}$, where n_{freq} denotes the number of frequency steps. These are obtained by solving the following set of homogeneous cell problems over each coarse element domain $\Omega_{M(\alpha)}$, $\alpha = 1, \dots, n_{M_{el}}$ for the solid phase

$$\begin{cases} \text{Find } \mathbf{u}_h \in \mathcal{V}_h^u(\mathcal{K}_{M(\alpha)}) \text{ such that} \\ \mathbf{a}^\varepsilon(\mathbf{u}_h, \delta \mathbf{u}_h)_{\mathbb{D}} = \mathbf{0} \quad \forall \delta \mathbf{u}_h \in \mathcal{V}_h^u(\mathcal{K}_{M(\alpha)}), \end{cases} \quad (4.51)$$

and fluid phase

$$\begin{cases} \text{Find } p_h \in \mathcal{V}_h^p(\mathcal{K}_{M(\alpha)}) \text{ such that} \\ \mathbf{b}^\nabla(p_h, \delta p_h)_{\frac{1}{\rho_{\text{eq}}}} = 0 \quad \forall \delta p_h \in \mathcal{V}_h^p(\mathcal{K}_{M(\alpha)}). \end{cases} \quad (4.52)$$

The bilinear forms in Eqs. (4.51)-(4.52) are decomposed into their fine element contributions analogous to Eqs. (4.2) and (4.28). The associated fine element stiffness matrices $\tilde{\mathbf{K}}_{m(i)}^{\text{el},\alpha}$ and $\tilde{\mathbf{H}}_{m(i)}^{\text{el},\alpha}$ are obtained from Eq. (2.175) and (2.177), respectively, and assembled into the RVE state matrices $\tilde{\mathbf{K}}_m^\alpha$ and $\tilde{\mathbf{H}}_m^\alpha$. Consequently, the discretized matrix forms of Eqs. (4.51)-(4.52) are now expressed for the solid phase

$$\begin{cases} \tilde{\mathbf{K}}_m^\alpha(\omega_k) \mathbf{u}_m^\alpha = \{\emptyset\} & , \text{ on } \mathcal{K}_{M(\alpha)} \\ \mathbf{u}_S = \bar{\mathbf{u}}_{IJ} & , \text{ on } \partial \mathcal{K}_{M(\alpha)} \end{cases}, \quad I = 1 \dots n_M, \quad J = 1, \dots, n_{\text{dim}}, \quad k = 1 \dots n_{\text{freq}}, \quad (4.53)$$

and fluid phase

$$\begin{cases} \tilde{\mathbf{H}}_m^\alpha(\omega_k) \mathbf{p}_m^\alpha = \{\emptyset\} & , \text{ on } \mathcal{K}_{M(\alpha)} \\ \mathbf{p}_s = \bar{\mathbf{p}}_{IJ} & , \text{ on } \partial\mathcal{K}_{M(\alpha)} \end{cases}, \quad I = 1 \dots n_M, \quad J = 1, \dots, n_{\text{dim}}, \quad k = 1 \dots n_{\text{freq}}, \quad (4.54)$$

where $n_{\text{dim}} = 2$ or 3 , depending on the dimension of the problem. The remaining element-wise matrices $\tilde{\mathbf{M}}_{m(i)}^{\text{el},\alpha}$, $\tilde{\mathbf{Q}}_{m(i)}^{\text{el},\alpha}$ and $\tilde{\mathbf{C}}_{m(i)}^{\text{el},\alpha}$ are similarly obtained from Eqs. (2.176)-(2.179) and assembled into their RVE specific counterparts, $\tilde{\mathbf{M}}_m^\alpha$, $\tilde{\mathbf{Q}}_m^\alpha$ and $\tilde{\mathbf{C}}_m^\alpha$, respectively.

4.4.2 Upscaling procedure

Using Eq. (2.183), without the boundary and interface coupling matrices, the governing equations at each frequency ω_k are expressed for each micro-element as

$$\begin{bmatrix} \tilde{\mathbf{K}}_{m(i)}^{\text{el},\alpha}(\omega_k) - \omega_k^2 \tilde{\mathbf{M}}_{m(i)}^{\text{el},\alpha}(\omega_k) & -\tilde{\mathbf{C}}_{m(i)}^{\text{el},\alpha}(\omega_k) \\ -\omega_k^2 \tilde{\mathbf{C}}_{m(i)}^{\text{el},\alpha}(\omega_k)^T & \tilde{\mathbf{H}}_{m(i)}^{\text{el},\alpha}(\omega_k) - \omega_k^2 \tilde{\mathbf{Q}}_{m(i)}^{\text{el},\alpha}(\omega_k) \end{bmatrix} \begin{Bmatrix} \mathbf{u}_{m(i)}^\alpha \\ \mathbf{p}_{m(i)}^\alpha \end{Bmatrix} = \begin{Bmatrix} \mathbf{f}_{m(i)}^{\text{u el},\alpha} \\ \mathbf{f}_{m(i)}^{\text{p el},\alpha} \end{Bmatrix}, \quad (4.55)$$

Substituting the micro to macro mapping relations from Eqs. (4.5) and (4.31) into Eq. (4.55), and multiplying the first row-set of equations by $\mathbf{N}^{\text{u}T}$ and second row-set of equations by $\mathbf{N}^{\text{p}T}$, the following equation is obtained

$$\begin{bmatrix} \tilde{\mathbf{K}}_{M(\alpha),m(i)}^{\text{el}} - \omega_k^2 \tilde{\mathbf{M}}_{M(\alpha),m(i)}^{\text{el}} & -\tilde{\mathbf{C}}_{M(\alpha),m(i)}^{\text{el}} \\ -\omega_k^2 \tilde{\mathbf{C}}_{M(\alpha),m(i)}^{\text{el}T} & \tilde{\mathbf{H}}_{M(\alpha),m(i)}^{\text{el}} - \omega_k^2 \tilde{\mathbf{Q}}_{M(\alpha),m(i)}^{\text{el}} \end{bmatrix} \begin{Bmatrix} \mathbf{u}_{M(\alpha),m(i)} \\ \mathbf{p}_{M(\alpha),m(i)} \end{Bmatrix} = \begin{Bmatrix} \mathbf{f}_{M(\alpha),m(i)}^{\text{u el}} \\ \mathbf{f}_{M(\alpha),m(i)}^{\text{p el}} \end{Bmatrix}, \quad (4.56)$$

where $\tilde{\mathbf{K}}_{M(\alpha),m(i)}^{\text{el}}$, $\tilde{\mathbf{M}}_{M(\alpha),m(i)}^{\text{el}}$, $\tilde{\mathbf{H}}_{M(\alpha),m(i)}^{\text{el}}$, $\tilde{\mathbf{Q}}_{M(\alpha),m(i)}^{\text{el}}$, and $\tilde{\mathbf{C}}_{M(\alpha),m(i)}^{\text{el}}$ correspond to the fine-element state matrices mapped onto the coarse element nodes and assume the following form

$$\begin{aligned} \tilde{\mathbf{K}}_{M(\alpha),m(i)}^{\text{el}} &= \mathbf{N}_{m(i)}^{\text{u}T} \tilde{\mathbf{K}}_{m(i)}^{\text{el},\alpha} \mathbf{N}_{m(i)}^{\text{u}} \\ \tilde{\mathbf{M}}_{M(\alpha),m(i)}^{\text{el}} &= \mathbf{N}_{m(i)}^{\text{u}T} \tilde{\mathbf{M}}_{m(i)}^{\text{el},\alpha} \mathbf{N}_{m(i)}^{\text{u}} \\ \tilde{\mathbf{H}}_{M(\alpha),m(i)}^{\text{el}} &= \mathbf{N}_{m(i)}^{\text{p}T} \tilde{\mathbf{H}}_{m(i)}^{\text{el},\alpha} \mathbf{N}_{m(i)}^{\text{p}} \\ \tilde{\mathbf{Q}}_{M(\alpha),m(i)}^{\text{el}} &= \mathbf{N}_{m(i)}^{\text{p}T} \tilde{\mathbf{Q}}_{m(i)}^{\text{el},\alpha} \mathbf{N}_{m(i)}^{\text{p}} \\ \tilde{\mathbf{C}}_{M(\alpha),m(i)}^{\text{el}} &= \mathbf{N}_{m(i)}^{\text{u}T} \tilde{\mathbf{C}}_{m(i)}^{\text{el},\alpha} \mathbf{N}_{m(i)}^{\text{p}}. \end{aligned} \quad (4.57)$$

In Eqs. (4.56) and (4.57) the dependence of the state matrices on (ω_k) is omitted for brevity. Similarly, the forcing terms assume the following form

$$\mathbf{f}_{M(\alpha),m(i)}^{\text{u el}} = \mathbf{N}_{m(i)}^{\text{u}T} \mathbf{f}_{m(i)}^{\text{u el},\alpha}, \quad (4.58)$$

$$\mathbf{f}_{M(\alpha),m(i)}^{\text{p el}} = \mathbf{N}_{m(i)}^{\text{p}T} \mathbf{f}_{m(i)}^{\text{p el},\alpha}, \quad (4.59)$$

for the nodal forces and outflows, respectively.

The equilibrium relation in Eq. (4.55) is re-expressed at the coarse scale for each coarse-element as

$$\begin{bmatrix} \tilde{\mathbf{K}}_{M(\alpha)}^{\text{el}} - \omega_k^2 \tilde{\mathbf{M}}_{M(\alpha)}^{\text{el}} & -\tilde{\mathbf{C}}_{M(\alpha)}^{\text{el}} \\ -\omega_k^2 \tilde{\mathbf{C}}_{M(\alpha)}^{\text{el}T} & \tilde{\mathbf{H}}_{M(\alpha)}^{\text{el}} - \omega_k^2 \tilde{\mathbf{Q}}_{M(\alpha)}^{\text{el}} \end{bmatrix} \begin{Bmatrix} \mathbf{u}_{M(\alpha)} \\ \mathbf{p}_{M(\alpha)} \end{Bmatrix} = \begin{Bmatrix} \mathbf{f}_{M(\alpha)}^{\text{u el}} \\ \mathbf{f}_{M(\alpha)}^{\text{p el}} \end{Bmatrix}. \quad (4.60)$$

Currently, the coarse element state matrices and vectors, i.e., $\tilde{\mathbf{K}}_{M(\alpha)}^{\text{el}}$ - $\mathbf{f}_{M(\alpha)}^{\text{p el}}$ are unknown. These are determined on the basis of the principle of energy equivalence across scales, as done in Sections 4.2.2 and 4.3.2

$$\tilde{\mathbf{K}}_{M(\alpha)}^{\text{el}} = \sum_{i=1}^{n_{\text{mel}}} \tilde{\mathbf{K}}_{M(\alpha),m(i)}^{\text{el}} \quad (4.61a)$$

$$\tilde{\mathbf{M}}_{M(\alpha)}^{\text{el}} = \sum_{i=1}^{n_{\text{mel}}} \tilde{\mathbf{M}}_{M(\alpha),m(i)}^{\text{el}} \quad (4.61b)$$

$$\tilde{\mathbf{H}}_{M(\alpha)}^{\text{el}} = \sum_{i=1}^{n_{\text{mel}}} \tilde{\mathbf{H}}_{M(\alpha),m(i)}^{\text{el}} \quad (4.61c)$$

$$\tilde{\mathbf{Q}}_{M(\alpha)}^{\text{el}} = \sum_{i=1}^{n_{\text{mel}}} \tilde{\mathbf{Q}}_{M(\alpha),m(i)}^{\text{el}} \quad (4.61d)$$

$$\tilde{\mathbf{C}}_{M(\alpha)}^{\text{el}} = \sum_{i=1}^{n_{\text{mel}}} \tilde{\mathbf{C}}_{M(\alpha),m(i)}^{\text{el}} \quad (4.61e)$$

$$\mathbf{f}_{M(\alpha)}^{\text{u el}} = \sum_{i=1}^{n_{\text{mel}}} \mathbf{f}_{M(\alpha),m(i)}^{\text{u el}} \quad (4.61f)$$

$$\mathbf{f}_{M(\alpha)}^{\text{p el}} = \sum_{i=1}^{n_{\text{mel}}} \mathbf{f}_{M(\alpha),m(i)}^{\text{p el}}. \quad (4.61g)$$

The local coarse element state matrices and vectors shown in Eqs. (4.61) can be assembled over the coarse domain using standard assembly operations. Hence, the upscaled global equivalent of Eq. (4.60) assume the following form

$$\underbrace{\begin{bmatrix} \tilde{\mathbf{K}}_M - \omega_k^2 \tilde{\mathbf{M}}_M & -\tilde{\mathbf{C}}_M \\ -\omega_k^2 \tilde{\mathbf{C}}_M^T & \tilde{\mathbf{H}}_M - \omega_k^2 \tilde{\mathbf{Q}}_M \end{bmatrix}}_{\tilde{\mathbf{Z}}_M} \underbrace{\begin{Bmatrix} \mathbf{u}_M \\ \mathbf{p}_M \end{Bmatrix}}_{\mathbf{X}_M} = \underbrace{\begin{Bmatrix} \mathbf{f}_M^{\text{u}} \\ \mathbf{f}_M^{\text{p}} \end{Bmatrix}}_{\mathbf{F}_M}, \quad (4.62)$$

where the unknown field vectors \mathbf{u}_M and \mathbf{p}_M denote the coarse-nodal displacements and pressures, respectively. These quantities can then be downscaled to obtain detailed fine scale contours at all desired frequency steps, using the procedure outlined in Section 4.3.3.

4.5 Numerical examples

Three test cases are provided to examine the validity of the proposed multiscale solution procedure for a) equivalent fluid rigid motionless skeleton models and b) elastically deformable Biot solid skeleton models.

The Sound Absorption Coefficient (SAC) of these configurations are computed through the MsFEM over the frequency range $20\text{Hz} \leq f \leq 5500\text{Hz}$. These results are compared to the corresponding analytical TMM computations [262].

The macroscopic parameters used for all materials in the following examples are summarized in Table 4.1.

ID	σ	ϕ	α_∞	Λ	Λ'	k'_0	E	ν	η_s	ρ_1
	$\text{N} \cdot \text{s} \cdot \text{m}^{-4}$	-	-	m	m	m^2	$\text{N} \cdot \text{m}^{-2}$	-	-	$\text{kg} \cdot \text{m}^{-3}$
I	10^4	0.99	1.01	9.8×10^{-5}	1.96×10^{-4}	4.75×10^{-9}	1.6×10^5	0.44	0.1	8
II	217400	0.98	1.28	6×10^{-6}	2.77×10^{-4}	7.4×10^{-9}	116400	0.43	0.11	26
III	23	1	1	2.5×10^{-3}	2.5×10^{-3}	-	-	-	-	-
IV	10^6	1	1	12×10^{-6}	12×10^{-6}	-	-	-	-	-
V	11500	0.96	1.01	30×10^{-6}	35×10^{-6}	-	-	-	-	-
VI	10	0.68	1.81	4×10^{-3}	4.5×10^{-3}	9.27×10^{-7}	-	-	-	-
VII	20	0.32	1.41	3×10^{-3}	4.5×10^{-3}	15.84×10^{-7}	-	-	-	-

Table 4.1: Macroscopic material parameters corresponding to the relevant material ID.

ID	Name
I	Melamine Foam
II	2437-9B
III	Dissipative Air
IV	Host Material 1
V	Client Material 1
VI	Host Material 2
VII	Client Material 2

Table 4.2: Material names.

The materials associated with the material IDs described in Table 4.1 are mentioned in Table 4.2 for completeness.

All configurations are modelled in 2-D and 3-D. The 2-D geometry is discretized with $[60 \times 12]$ coarse quadrilateral elements with each coarse element clustering an underlying $[2 \times 2]$ fine quadrilateral mesh. The 3-D geometry is discretized with $[60 \times 12 \times 12]$ coarse hexahedral elements with each coarse element clustering an underlying $[2 \times 2 \times 2]$ fine hexahedral mesh.

Unless explicitly stated otherwise, the boundary conditions correspond to standard impedance tube constraints, i.e., the rear (right) side is provided with clamped supports. The lateral boundaries are given roller supports. The Neumann boundaries are all zero valued. This translates to zero tractions and fluid velocities normal to the surface under consideration. The configurations are excited on the incident face (left) by an acoustic plane wave at normal incidence.

Owing to the symmetry of the excitation and the geometrical and material layouts, the lateral boundary conditions, i.e., roller supports and zero normal velocity conditions, are collectively labelled "periodic boundaries". It is to be noted that this is a special case recovered from the more general Floquet-Bloch periodic conditions [195]. These are defined for completeness. Given a pair of faces Γ_1 and Γ_2 respecting y-periodicity, i.e., exhibiting periodically repeating behaviour

along the vertical y-axis, the following relations are observed

$$p|_{\Gamma_1} = p|_{\Gamma_2} e^{-k_y|y|}, \quad (4.63a)$$

$$v_y|_{\Gamma_1} = v_y|_{\Gamma_2} e^{-k_y|y|}, \quad (4.63b)$$

where $p|_{\Gamma_1}$, $p|_{\Gamma_2}$ and $v_y|_{\Gamma_1}$, $v_y|_{\Gamma_2}$ denote acoustic pressures and normal velocities on the two periodic faces, respectively. The distance between both faces is represented by $|y| = |y_{\Gamma_1} - y_{\Gamma_2}|$. The acoustic wave number along the y-direction is contained in k_y . Since the Neumann conditions over these surfaces are zero, Eq. (4.63b) is a tautology. Further, since only normal incidence excitations are dealt with in the following examples, it follows that there are no waves propagating the y-direction, i.e., $k_y = 0$. Inserting this result into Eq. (4.63a) yields the simpler expression $p|_{\Gamma_1} = p|_{\Gamma_2}$. For perfectly symmetric configurations, this condition is naturally achieved, and need not be explicitly imposed.

The efficiency of the MsFEM is measured by comparing its performance against the corresponding FEM. The FEM operates over the associated global fine mesh. Computational times taken to (A) evaluate the multiscale basis functions and (B) perform the solution procedure are recorded and averaged over three runs. Assembly and upscaling of state matrices are included within (A). Similarly, the downscaling operations are included within (B). The acceleration provided by the MsFEM is demonstrated through computing *speedup*

$$speedup = \frac{t_{\text{FEM}}}{t_{\text{MsFEM}}}, \quad (4.64)$$

where t_{FEM} and t_{MsFEM} denote the total times taken by each method, respectively.

4.5.1 Melamine Foam

A standard aero-melamine foam is placed inside an impedance tube of diameter 80 mm in three different configurations. A rigid motionless skeleton assumption is used. This entails using an equivalent fluid constitutive model. The macroscopic material parameters for the melamine foam are provided by Material I in Table 4.1. Non-dissipative air is used in all cases.

Foam with rigid backing

An 80 mm thick foam layer is considered. The full impedance tube geometry is shown here for the sake of completeness by including a 320 mm column of air. A schematic of the 2-D domain with coarse-scale discretization is shown in Fig. 4.6.

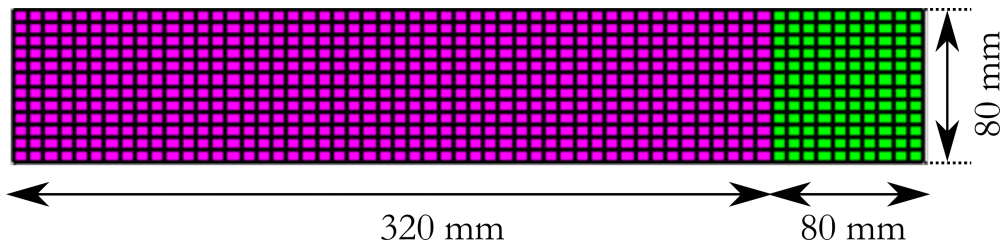


Figure 4.6: Schematic of a melamine foam placed against a rigid backing with coarse mesh.

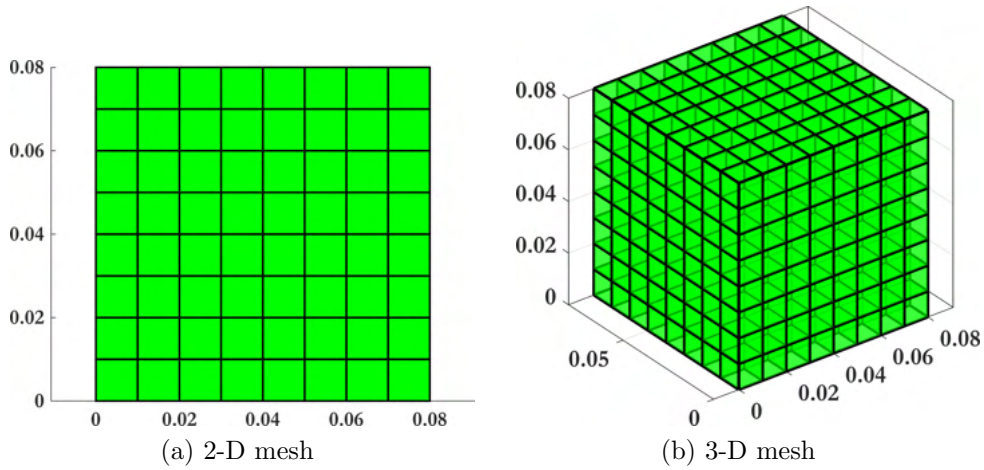


Figure 4.7: Coarse-scale meshes (a) 8×8 quadrilateral coarse-elements with 2×2 quadrilateral fine-elements per coarse-element and (b) $8 \times 8 \times 8$ hexahedral coarse-elements with $2 \times 2 \times 2$ hexahedral fine-elements per coarse-element.

However, as non-dissipative air is being used, it is not necessary to explicitly account for the air column within the MsFEM model. To this, the reduced model are presented in Fig. 4.7 for clarity.

The sound absorption coefficients as evaluated by the MsFEM for the 2-D and 3-D discretizations, and by the TMM are shown in Fig. 4.8.

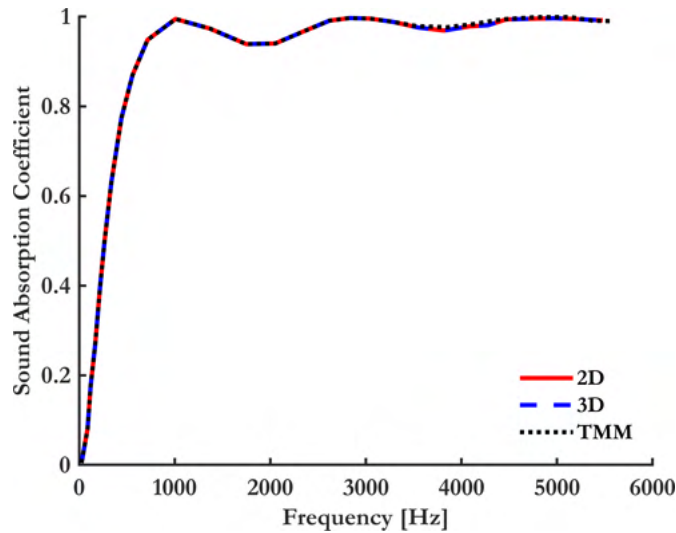


Figure 4.8: Sound absorption coefficient (SAC) curves as a function of the frequency (in Hz) for the geometry of Fig. 4.6.

The curves computed in the three instances appear identical. The averaged computational times and speedup offered by the MsFEM over the FEM in the case of the elastic skeleton assumption is provided in Table 4.3. A significant speedup of 15.66 is obtained for the 3-D discretizations.

		MS Basis	Solving and	Total time	Speedup
		Computation times	Downscaling times		
2-D	FEM	0.20	16.82	17.01	3.19
	MsFEM	0.87	4.45	5.32	
3-D	FEM	4.08	803.67	807.73	15.66
	MsFEM	8.93	42.66	51.59	

Table 4.3: Computation time taken (in seconds) and speedup offered by the MsFEM over FEM for a melamine foam with rigid backing.

Foam with air backing

A 40 mm thick foam layer with an air-column backing of 40 mm is placed inside the impedance tube. This example is provided to examine the accuracy of porous-fluid coupling. A schematic of the 2-D domain with coarse-scale discretization is shown in Fig. 4.9.

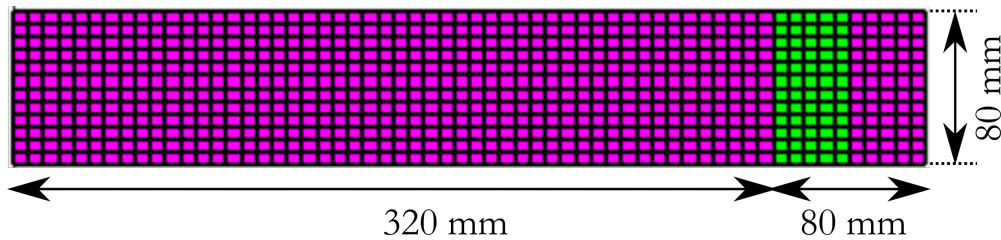


Figure 4.9: Schematic of a melamine foam backed with a 40 mm air activity with coarse mesh.

Once again, accounting for the air column within the MsFEM model is unnecessary, The resultant reduced coarse mesh is provided in Fig. 4.10 for clarity.

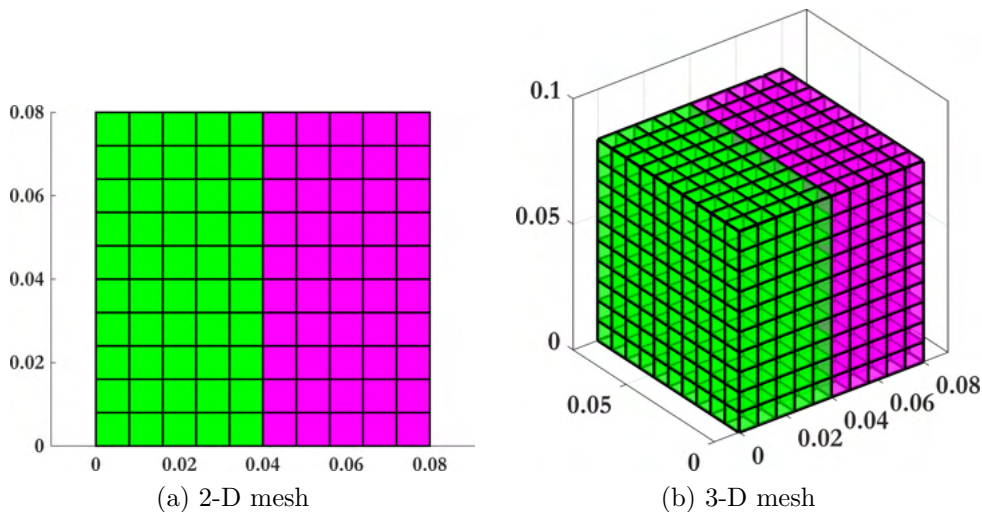


Figure 4.10: Coarse-scale meshes (a) 10×10 quadrilateral coarse-elements with 2×2 quadrilateral fine-elements per coarse-element and (b) $10 \times 10 \times 10$ hexahedral coarse-elements with $2 \times 2 \times 2$ hexahedral fine-elements per coarse-element.

The sound absorption coefficients as evaluated by the MsFEM for the 2-D and 3-D discretizations, and by the TMM are shown in Fig. 4.13.

		MS Basis	Solving and	Total time	Speedup
		Computation times	Downscaling times		
2-D	FEM	0.35	16.53	16.89	2.34
	MsFEM	1.82	5.40	7.23	
3-D	FEM	14.46	1592.07	1606.52	19.04
	MsFEM	27.46	56.89	84.36	

Table 4.4: Computation time taken (in seconds) and speedup offered by the MsFEM over FEM for a melamine foam with air backing.

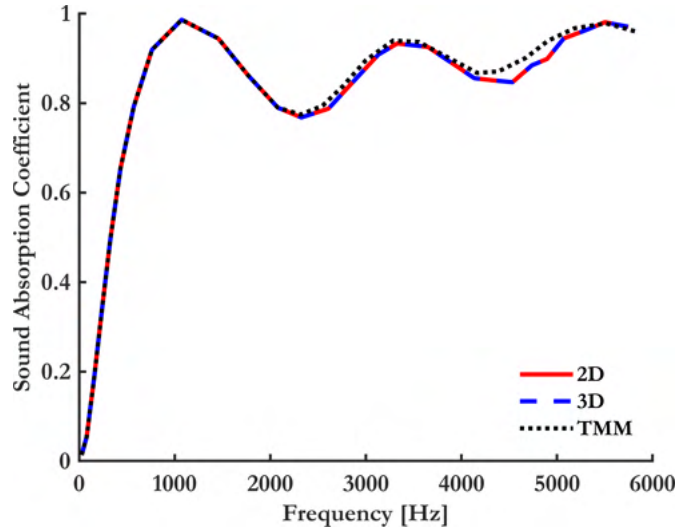


Figure 4.11: Sound absorption coefficient (SAC) curves as a function of the frequency (in Hz) for the geometry of Fig. 4.9.

A near exact correspondence between the MsFEM and TMM results are observed. The averaged computational times and speedup offered by the MsFEM over the FEM in the case of the elastic skeleton assumption is provided in Table 4.4. A significant speedup of 19.04 is obtained for the 3-D discretizations.

Foam with mesoscale perforation

An 80 mm foam layer with a square mesoscale through-perforation of side 40 mm is placed inside the impedance tube. This example is provided to demonstrate the ability of the MsFEM to handle double-porosity materials. Contrary to the previous examples, here the preceding 320 mm air-column is required to account for reflection, scattering, dispersions and edge effects introduced by the the mesoscale perforation. The meshes used for the 2-D and 3-D domain with coarse-scale discretization is shown in Fig. 4.12.

The sound absorption coefficients as evaluated by the MsFEM and TMM are shown in Fig. 4.13.

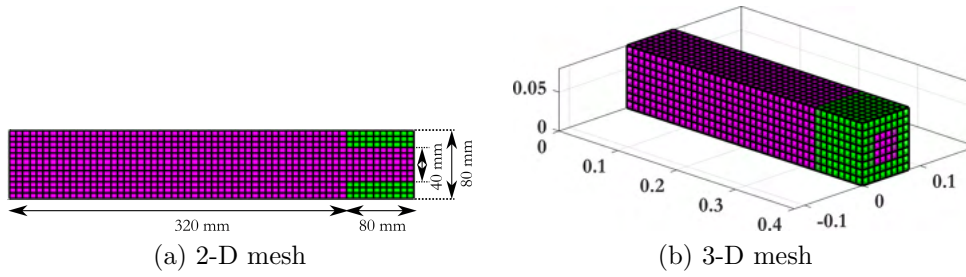


Figure 4.12: Coarse-scale meshes (a) 40×8 quadrilateral coarse-elements with 2×2 quadrilateral fine-elements per coarse-element and (b) $40 \times 8 \times 8$ hexahedral coarse-elements with $2 \times 2 \times 2$ hexahedral fine-elements per coarse-element.

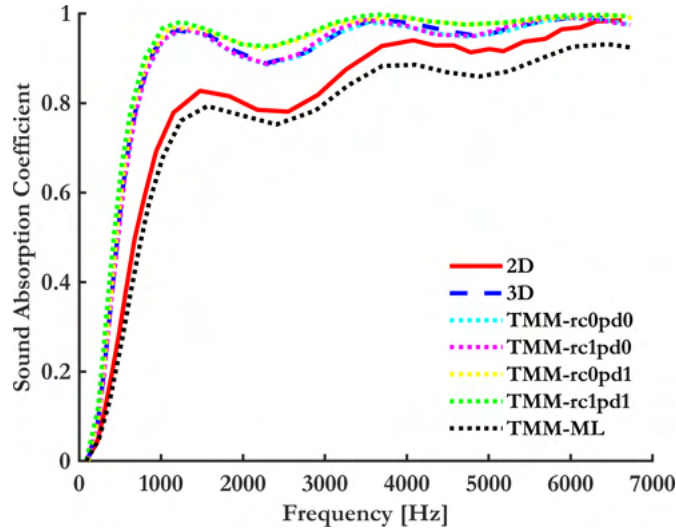


Figure 4.13: Sound absorption coefficient (SAC) curves as a function of the frequency (in Hz) for the geometry of Fig. 4.12.

where the legend labels are summarized in Table 4.5.

Label	ON	OFF
rc - Radiation Correction (Dynamic)	1	0
pd - Pressure Diffusion	1	0
ML - Mixing Law	-	-

Table 4.5: Legend Labels used in Fig. 4.13.

The 3-D MsFEM computation is found to agree with the TMM-rc1pd0 porous composite model [48], accounting for dynamic radiation correction, while neglecting the pressure diffusion effect.

In the context of linear acoustics of porous media, pressure diffusion is a dissipation effect prevalent in porous composites where large permeability contrasts exist between the host and client media. At low frequencies, a duct typically appears longer than it actually is to acoustic waves. Radiation correction is a length correction scheme accounting for this apparent effect [263]

		MS Basis	Solving and	Total time	Speedup
		Computation times	Downscaling times		
2-D	FEM	1.29	51.81	53.10	3.22
	MsFEM	5.20	13.96	19.16	
3-D	FEM	28.28	14,118.37	14,146.65	28.94
	MsFEM	106.88	381.89	488.77	

Table 4.6: Computation time taken (in seconds) and speedup offered by the MsFEM over FEM for a melamine foam with mesoscale perforation.

While the MsFEM naturally accounts for any such effects, these need to be explicitly handled by the TMM-PC to obtain reliable results. The 2-D MsFEM computation is compared against the TMM mixing law (TMM-ML). These represent different volume averaging and analytical homogenization techniques described in [48]. While the trend is replicated correctly, the MsFEM is found to slightly overestimate the SAC. This can be attributed to differences in cross-sectional geometry. The 3-D MsFEM and TMM result can be recovered from the ML procedure when the mesoscale porosity is computed for a 3-D cross-section, i.e., $\phi_m = \frac{40^2}{80^2} = 0.25$. However, to facilitate ML comparisons with the 2-D MsFEM model, a 2-D cross-section is considered, resulting in a mesoscale porosity $\phi_m = \frac{40}{80} = 0.5$.

The averaged computational times and speedup offered by the MsFEM over the FEM is provided in Table 4.6. The FEM procedure in case of 3-D discretizations in the elastic skeleton assumption, proves very expensive, as illustrated by the total times. The MsFEM proves invaluable in accelerating computations here, offering a speedup of 28.94.

4.5.2 Highly dissipative material: 2437-9B

The following set of examples are provided to demonstrated the ability of the MsFEM to handle highly resistive materials. Such materials are expected to be more sensitive to different types of boundary conditions and offer more pronounced instances of the double porosity effect. An example material "2437-9B" is placed inside an impedance tube of diameter 15 mm in three different configurations. The materials parameters for "2437-9B" are provided by Material II in Table 4.1. The same discretization scheme is employed in these examples. Non-dissipative air is used.

Layer with rigid backing

A 15 mm thick layer is placed in side the impedance tube. The full impedance tube geometry is modelled here for completeness by including a 60 mm column of air. The full elastically deformable skeleton assumption is considered. Consequently, the Biot-Helmholtz model is used. A schematic of the 2-D domain with coarse-scale discretization is shown in Fig. 4.14.

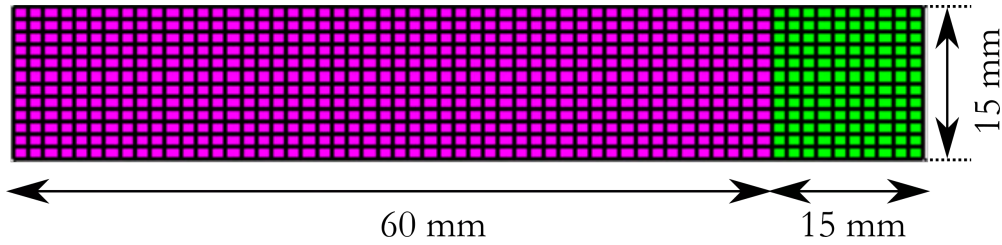


Figure 4.14: Schematic of a dissipative material with rigid backing.

The sound absorption coefficients as evaluated by the MsFEM for the 2-D and 3-D discretizations, and by the TMM are shown in Fig. 4.15.

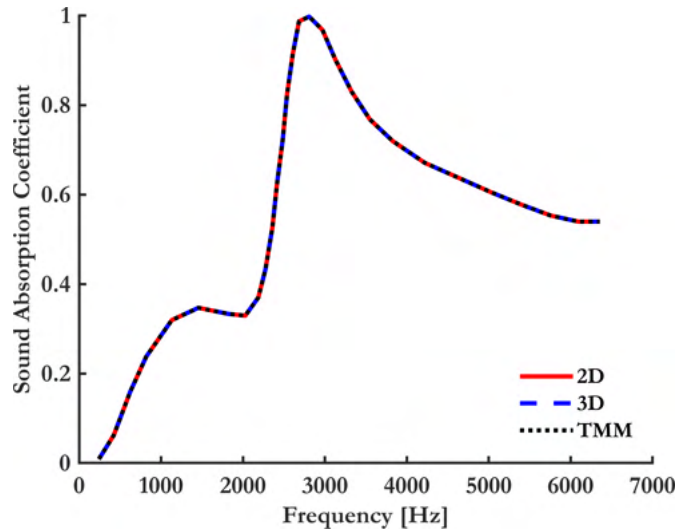


Figure 4.15: Sound absorption coefficient (SAC) curves as a function of the frequency (in Hz) for the geometry of Fig. 4.14.

The SAC curves obtained in all three instances are identical.

Layer with air backing

An 7.5 mm thick foam layer with an air-column backing of 7.5 mm is placed inside the impedance tube. This example is provided to examine the accuracy of porous-fluid coupling in highly resistive materials. Elastically deformable solid skeletons are considered. A schematic of the 2-D domain with coarse-scale discretization is shown in Fig. 4.16.

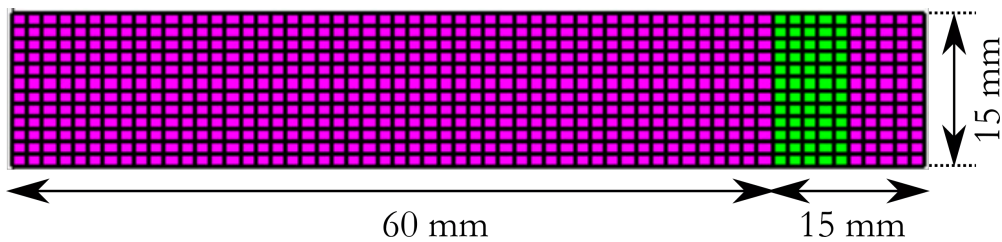


Figure 4.16: Schematic of a dissipative material with air backing.

The sound absorption coefficients as computed by the MsFEM and TMM are shown in Fig. 4.17.

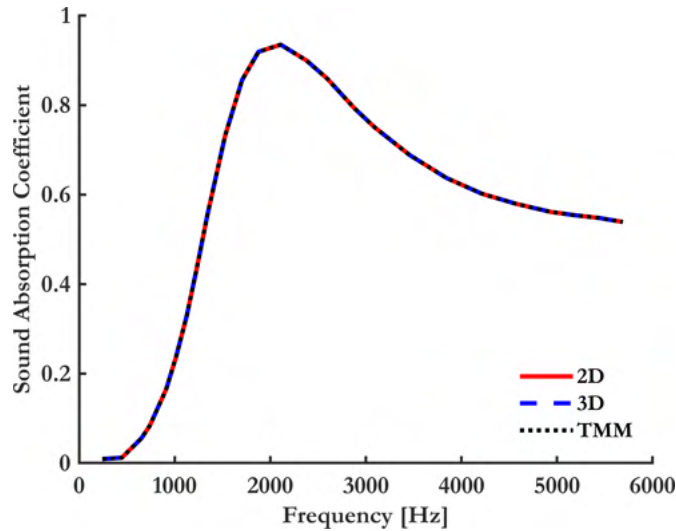


Figure 4.17: Sound absorption coefficient (SAC) curves as a function of the frequency (in Hz) for the geometry of Fig. 4.16.

Once again, the results obtained across all methods are practically identical.

Layer with mesoscale perforation

This example is provided to illustrate the ability of the method to adequately handle mesoscale perforations in highly resistive materials. A 15 mm thick layer with a square perforation of side 7.5 mm is placed inside the impedance tube. An equivalent fluid rigid skeleton assumption is used for this example. A schematic of the 2-D domain with coarse-scale discretization is shown in Fig. 4.18.

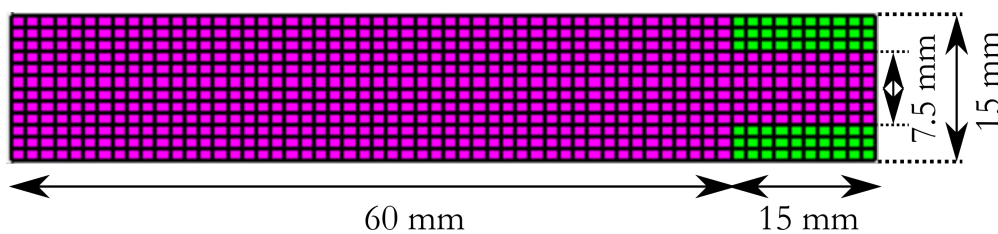


Figure 4.18: Schematic of a dissipative material with mesoscale perforation.

The SAC curves computed through the MsFEM and TMM are provided in Fig. 4.19.

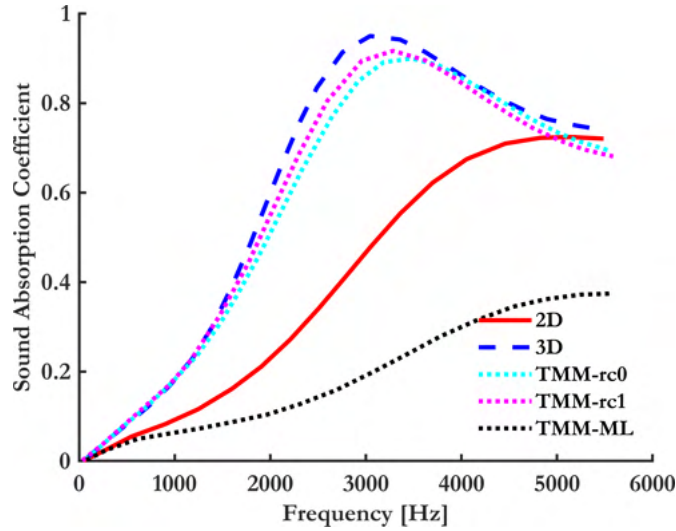


Figure 4.19: Sound absorption coefficient (SAC) curves as a function of the frequency (in Hz) for the geometry of Fig. 4.18.

Following the intuition developed from the results of the double porosity Melamine foam example in Section 4.5.1, the pressure diffusion effect is neglected in the TMM calculations. The 3-D MsFEM result agrees more closely with the TMM with dynamic radiation correction (TMM-rc1), although the SAC is overestimated slightly around the peak.

There is an appreciable deviation between the results offered by the 2-D MsFEM results and the TMM-ML. This can be attributed to the differences in cross-section as before. Moreover, the TMM-ML can only be used to provide reliable comparisons in the case of low-resistive materials.

4.5.3 Porous composites

The following examples are obtained from [48] to directly validate the method's ability to handle alternate materials, porous inclusions and tortuous inclusion paths. The TMM-porous composite (TMM-PC) theory is used to facilitate comparisons. Dissipative air is used in all cases to accurately capture relevant pressure diffusion effects. The material parameters for dissipative air are provided by Material III in Table 4.1.

The FEM validations in [48] were done using an in-house axisymmetric code. Consequently, all mesoscale perforations and inclusions are cylindrical in nature, i.e., they have a circular cross section. Owing to limitations encountered with hexahedral meshing using our own in-house MATLAB multiscale mesher, simplified square cross sections were considered instead.

Rigid frame double porosity medium

A cylindrical perforation of diameter 10 mm is considered in a 20 mm highly resistive porous material with rigid frame. This configuration is placed inside an impedance tube of diameter 20 mm. The macroscopic parameters of this material corresponds to Material IV in Table 4.1. A schematic depicting the 2-D approximation of this domain with coarse-scale discretization is shown in Fig. 4.20.

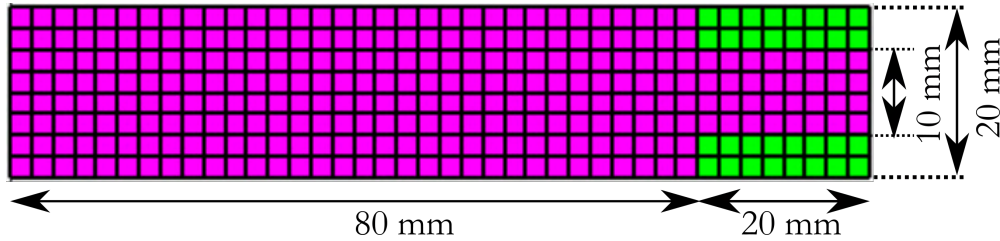


Figure 4.20: Schematic of a rigid frame double porosity medium.

The previous examples considering double porosity media with Melamine Foam and "2437-9B" show that only 3-D discretizations yield meaningful comparisons with the TMM-PC model. Conversely, 2-D comparisons can only be done with TMM-ML results in the case of low-resistive materials. As the host material under consideration in this example is a highly resistive one, the sound absorption curves are only provided for 3-D MsFEM and TMM-PC in Fig. 4.21.

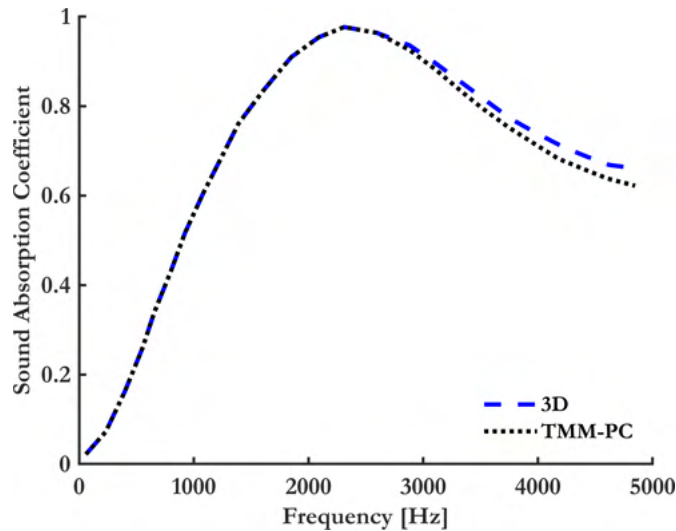


Figure 4.21: Sound absorption coefficient (SAC) curves as a function of the frequency (in Hz) for the geometry of Fig. 4.20.

The TMM-PC considers the pressure diffusion effect here. Near exact correspondence except at high frequencies is observed. These deviations at high frequencies (greater than 3 kHz) may be attributed to differences in perforation cross section and a non-compliance with scale separation [48]. This means that at these frequencies, the acoustic wavelength is no longer significantly larger than the characteristic mesoscopic perforation size. Consequently, the TMM porous composite model loses accuracy at these instances.

Simple rigid porous composite

A rigid composite porous media is examined here. The same configuration from the previous example is used. The perforation is filled with a low-resistive client material, (Material V in Table 4.1). A schematic of the 2-D domain with coarse-scale discretization is shown in Fig. 4.22.

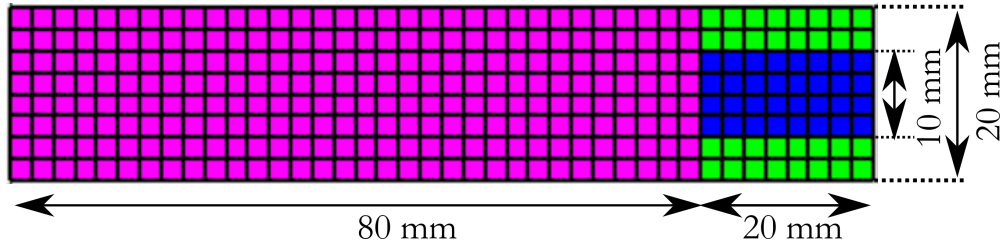


Figure 4.22: Schematic of a rigid frame porous material with porous inclusion.

The sound absorption coefficient evaluated by the 3-D MsFEM and TMM-PC with pressure diffusion effect are shown in Fig. 4.23.

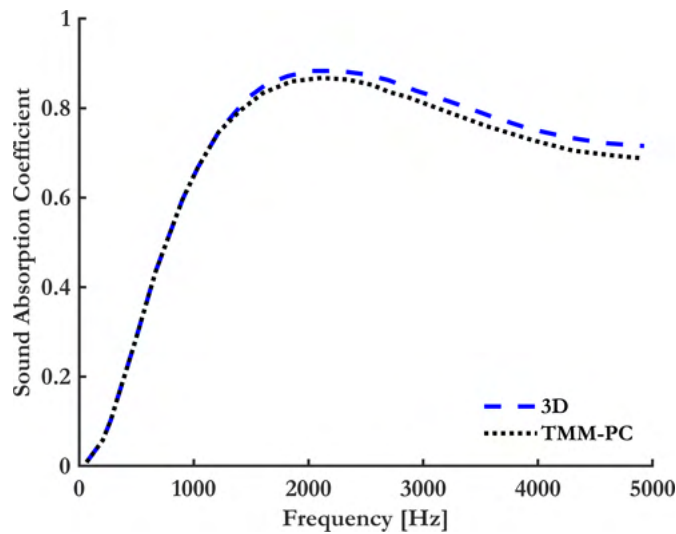


Figure 4.23: Sound absorption coefficient (SAC) curves as a function of the frequency (in Hz) for the geometry of Fig. 4.22.

The results are found to agree well. Once again the deviation from mid to high frequencies are attributed to differences in cross-section considered and the non-compliance with scale separation.

Tortuous rigid frame porous composite

A rigid porous composite with a tortuous inclusion is considered in this example. The host and client materials are provided by Materials VI and VII, respectively in Table 4.1. The 2-D geometry for this configuration is provided in Fig. 4.24.

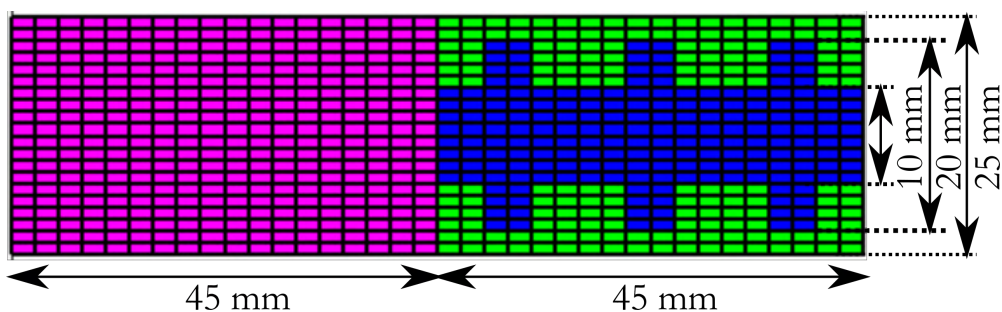


Figure 4.24: Schematic of a rigid frame porous material with tortuous porous inclusion.

The sound absorption coefficients computed through the 3-D MsFEM and TMM-PC with pressure diffusion effect are shown in Fig. 4.25.

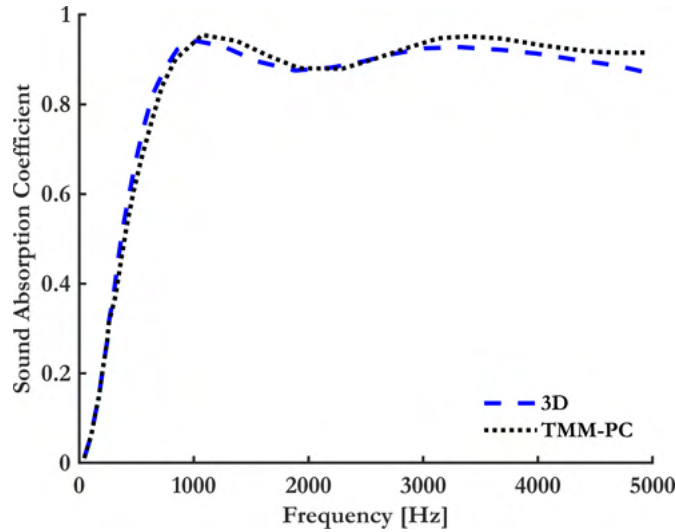


Figure 4.25: Sound absorption coefficient (SAC) curves as a function of the frequency (in Hz) for the geometry of Fig. 4.24.

Good correspondence between both methods is observed till 3000 Hz. Minor deviations beyond this frequency limit is once again, attributed to disagreement in the cross sections used and the non-compliance of scale separation. It is to be reiterated here that this is a shortcoming of the TMM-PC model, and not the MsFEM.

4.6 Summary

In this Chapter, a motivation to investigate the MsFEM as an upscaling tool was established. Other competing upscaling techniques were reviewed in detail. The MsFEM procedure is developed for elastostatics and poromechanics, i.e., consolidation and vibroacoustics. The MsFEM for vibro-acoustics is a novel contribution. Consequently, the method was applied to different industrially relevant acoustical problems and is shown to significantly drive down computational costs while retaining the fidelity of the standard FEM. Three benchmark examples are examined to establish the validity of the proposed methodology in its application to coupled multilayered porous segments and porous composite materials. However, the MsFEM is limited by its inability to efficiently resolve more complex geometric and material layouts. To this end, the VEM as explained in Chapter 3 is integrated into the MsFEM framework in the next Chapter 5 to obtain a new Multiscale Virtual Element Method (MsVEM).

Chapter 5

Multiscale Virtual Element Methods

In this Chapter, the Virtual Element Method (VEM) is originally incorporated into the fine scale of the MsFEM to obtain a novel Multiscale Virtual Element Method (MsVEM). This introduces versatile meshing capabilities at the fine scale. The flexibility offered by the VEM is carried over to the coarse scale, where the MsVEM is generalized to account for polygonal, non-convex coarse elements as well. Oscillatory boundary conditions are developed for the first time in polygonal coarse elements to handle highly heterogeneous material descriptions. The ensuing numerical scheme is successfully applied to elastostatics and coupled poromechanical problems (consolidation and vibroacoustics) to obtain accurate simulations at reduced computational cost. To further accelerate repeated evaluations of multiscale basis functions over a frequency spectrum in porous vibroacoustics problems, a parametric Model Order Reduction technique is originally integrated into the fine scale. Several benchmark examples are provided to demonstrate the validity and efficiency of the proposed method.

5.1 Overview

The standard MsFEM accounts for rectangular elements in the coarse scale and quadrilaterals in the fine scale as shown in Fig. 4.3; this limits the applicability of the method especially for the case of inclusions or voids of an arbitrary and typically non-convex geometry. In principle, one would be able to account for such heterogeneities via a very fine finite element discretization; this would considerably increase the number of elements to be resolved at the micro-scale hence countering the computational advantages of the multiscale procedure. Optimization of the underlying mesh could thus prove critical to improving the performance of the method. Mesh optimization requires, as a prerequisite, numerical methods that allow for more flexible mesh generation capabilities. To achieve this, the VEM is employed to accurately and efficiently resolve the heterogeneities at the fine scale.

In the case of vibroacoustics, repeated evaluation of the multiscale basis functions at each frequency step can still prove expensive, especially when encountering a finely discretized RVE. Other methods such as the mixed multiscale FEM [264], and multiscale finite volume method [256] also suffer from such a limitation. This drawback is addressed in [265] for parametrized elliptic problems through a Multiscale Reduced Basis Method (MsRBM). This is done by introducing RB methods [266–272] at the fine scale to accelerate computations of the multiscale basis functions.

This is a projection based Model Order Reduction (MOR) technique wherein a reduced order basis is generated offline at the RVE level from a collection of high-fidelity solutions (often called snapshots). Next, the Full Order Model (FOM), i.e., the discretized cell problems are projected onto this reduced basis. Finally, the Reduced Order Model (ROM) is simulated online to obtain the multiscale basis functions at a reduced cost. To this point, the MsRBM has been developed exclusively for single phase elliptic problems.

MOR strategies have been successfully applied to structural mechanics problems [273–284], multibody dynamics [285–291], fluid mechanics and aerodynamics [278, 292–297], vibroacoustics [298–300] and coupled field thermal problems [271, 301–307]. These include modal approaches as well [308–312]. The order of non-linear problems were reduced using Proper Orthogonal Decomposition (POD) techniques in [278, 313–317]. A detailed overview of different applications of the method can be found in [318, 319].

There are significant difficulties experienced in applying MOR techniques to poroelastic materials [320]. Owing to the strong coupling between the solid-skeleton and pore-fluid phases, and a low stiffness to weight ratio, a high modal density is experienced in the low frequency range. Consequently, modal-based MOR strategies as applied for the $\mathbf{U} - \mathbf{u}$ formulation in [321, 322] show that a large number of modes are required to retain accuracy. This effectively compromises the efficacy of the method [323]. A second bottleneck involves a treatment of the non-linear eigenvalue problems encountered when computing the reduced basis. A complex modal approach was proposed in [324], using a costly linearization strategy.

The above limitations in applying modal based MOR are addressed using a parametric model order reduction (pMOR) strategy for the $\mathbf{u} - p$ formulation in [325]. This involves the identification of an optimal parametric manifold, wherein the optimal reduced basis varies in relation to the parameter under consideration (in this case, frequency) [326]. A POD scheme is applied offline to extract this basis from the above mentioned snapshot matrix.

The pMOR strategy is originally employed by us in this work, at the fine scale in conjunction with the VEM to obtain a novel Coupled Multiscale Reduced Basis Virtual Method (CMsRB-VEM). This is done with an aim to evaluate multiscale basis functions for the coupled vibroacoustics problem at a reduced computational cost; thereby accelerating the entire procedure.

In this Chapter, the VEM is introduced into the MsFEM in an elastostatics context, to obtain a novel MsVEM for elastostatics in Section 5.2. A set of numerical examples are provided to examine the validity and advantages of the method in Section 5.3. This is extended to the coupled poromechanics consolidation environment in Section 5.4 to obtain a novel CMsVEM. Generalizations to polygonal RVEs and oscillatory boundary conditions are discussed in Section 5.4.1. Numerical examples demonstrating the accuracy and computational gains of the method are illustrated in Section 5.5. Next, this CMsVEM is extended to the frequency regime to describe vibroacoustical problems in Section 5.6. The pMOR technique is introduced at the fine scale to derive a novel CMsRBVEM in Section 5.7. A collection of relevant benchmark examples are provided in Section 5.9.

5.2 Elastostatics

Similar to the MsFEM, the heterogeneous domain is discretized into $\mathcal{K}_{M(\alpha)}$, $\alpha = 1 \dots n_{M_{el}}$, coarse quadrilateral elements, where $n_{M_{el}}$ is the number of coarse elements. Each coarse element clusters its own set of $\mathcal{K}_{m(i)}$, $i = 1 \dots n_{m_{el}}$ micro-elements where $n_{m_{el}}$ is the number of micro-elements in the $\mathcal{K}_{M(\alpha)}$. However, these elements at the fine scale are no longer restricted to quadrilateral shapes; conversely any polygonal (possibly non-convex) shape may be assumed, as illustrated in Fig. 5.1.

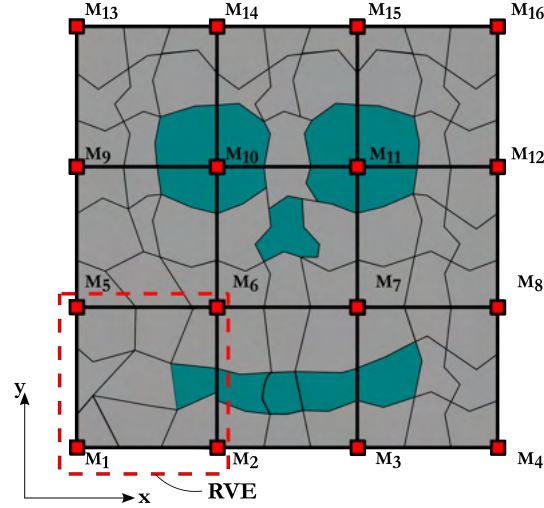


Figure 5.1: Multiscale mesh with 9 coarse quadrilateral elements and 81 polygonal (possibly non-convex) fine-elements.

To evaluate multiscale basis functions for upscaling, the cell boundary value problem in Eq. (4.7) subject to kinematical constraints is solved over an RVE. For the RVE shown in Fig. 5.22a, \mathbf{u}_m^α is a 34×1 vector and \mathbf{N}_m^u is a 34×8 matrix.

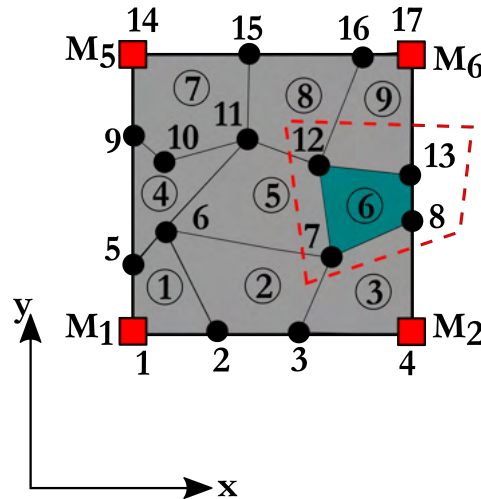


Figure 5.2: RVE with 9 generalized (possibly non-convex) polygonal elements. The number of fine-elements and fine-nodes in the RVE are $n_{m_{el}} = 9$ and $n_m = 17$ respectively.

However, the RVE elastic stiffness matrix \mathbf{K}_m^α is assembled from fine scale element stiffness matrices $\mathbf{K}_{m(i)}^{\text{el},\alpha}$ that are now defined on the basis of the VEM, according to Eq. (3.34). Local projection operators $\Pi_k^{\varepsilon_m}$, specific to the fine element under consideration are derived in accordance

with Section 3.3.3. Algorithm 4 summarizes the procedural steps required for the evaluation of the multiscale basis functions.

Algorithm 4: Multiscale basis function evaluation schema.

Data: Define coarse mesh and fine mesh/micromesh and material properties

foreach coarse element α **do**

foreach micro element i **do**

 Compute: $\mathbf{\Pi}_k^{\varepsilon^m}$ (see Eq. (3.21)) ;

 Compute: \mathbf{K}_C , \mathbf{K}_S , and $\mathbf{K}_{m(i)}^{\text{el},\alpha}$ (see Eq. (3.34)) ;

 Assemble to \mathbf{K}_m^α (see Eq. (2.105)) ;

foreach macro-node $I = 1, \dots, 4$ **do**

foreach macro degree of freedom $J = 1, 2$ **do**

 Define: $\bar{\mathbf{u}}_{IJ}$;

 Solve: $\begin{cases} \mathbf{K}_m^\alpha \mathbf{u}_m^\alpha = \mathbf{0} \\ \mathbf{u}_S = \bar{\mathbf{u}}_{IJ} \end{cases}$ (see Eq. (4.7));

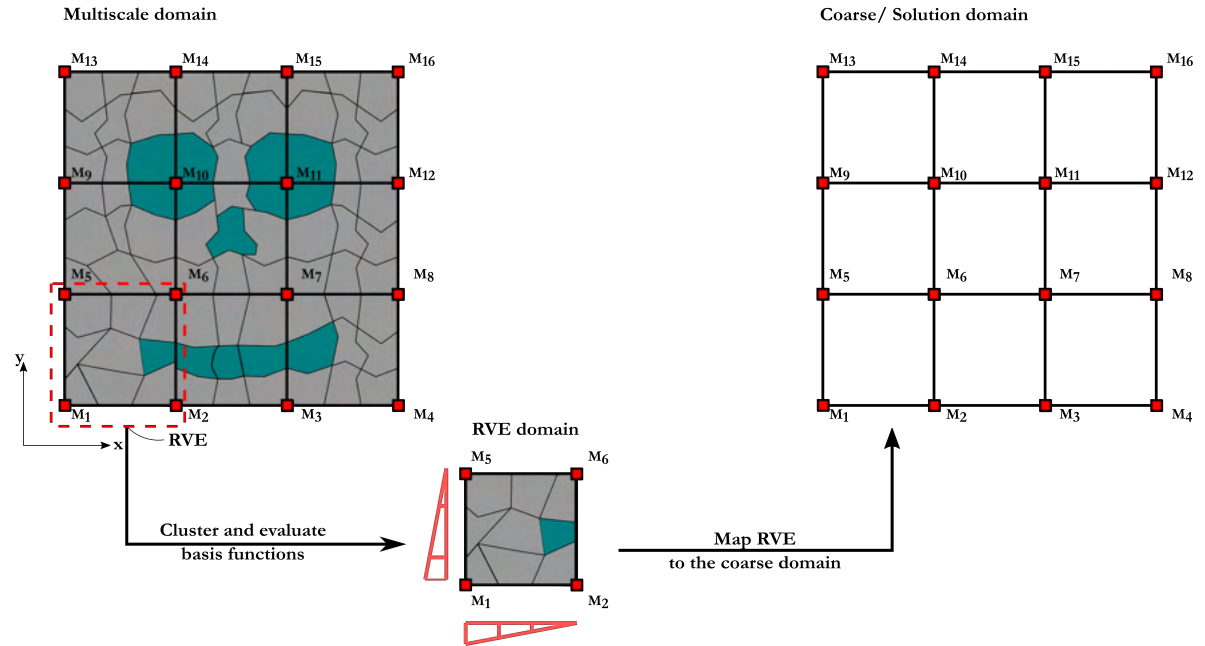


Figure 5.3: Schematic of the MsVEM upscaling procedure. The case of linear boundary conditions for the evaluation of multiscale basis functions is considered.

The solution procedure is then performed at the coarse scale. Fine scale displacements are obtained using Eq. (4.5) as detailed in Section 4.2.3. The strains and stresses associated with these fine-scale displacements can be computed as follows

$$\boldsymbol{\varepsilon}_{m(i)}^\alpha = \mathbf{B}^\varepsilon \mathbf{u}_{m(i)}^\alpha, \quad \boldsymbol{\sigma}_{m(i)}^\alpha = \mathbb{C} \boldsymbol{\varepsilon}_{m(i)}^\alpha, \quad (5.1)$$

where \mathbf{B}^ε is the term provided in Section 3.3.3. These strains and stresses are uniform over the

i^{th} fine-element domain. To allow for compatibility with traditional post-processing routines, the element is decomposed into sub-triangles. The evaluated stresses and strains are then associated with desired quadrature integration points.

The process flow of the EMsVEM is graphically shown in Fig. 5.4.

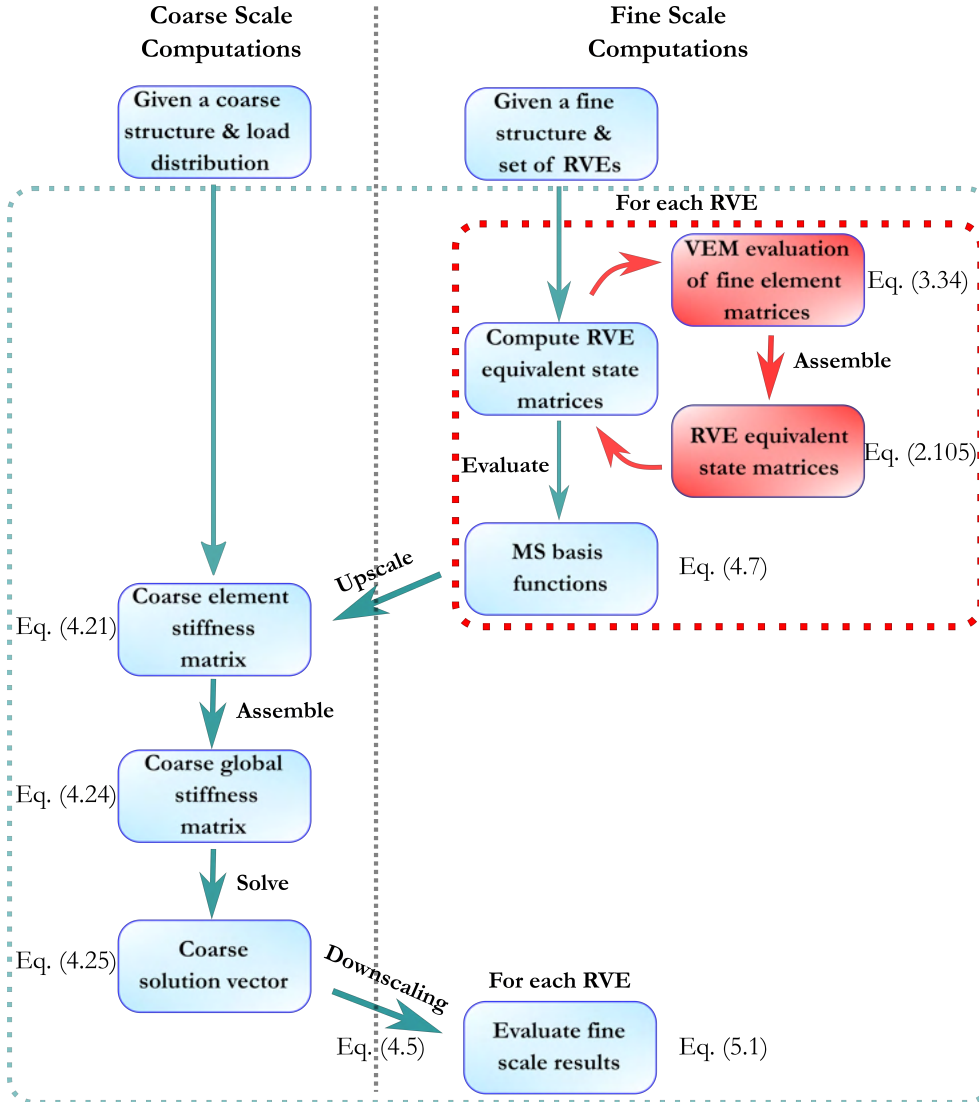


Figure 5.4: Process flow of the Multiscale Virtual Element procedure.

5.3 Numerical examples

The MsVEM is verified by comparing against the standard VEM and analytical solutions. A first order VEM ($k=1$), is used in all cases. In the following, the four different element-types illustrated in Fig. 5.5 are used for the verification. The Centroidal Voronoi Tessellations (CVT) shown in Fig. 5.5b were generated by Lloyd's algorithm [327] with the generated seeds being forced to coincide with the associated centroid of each polygon. The Random Voronoi Elements (RAND) shown in Fig. 5.5d were created by a random set of seeds. The polygonal meshes were generated using PolyMesher [328].

To investigate the fidelity of the proposed method, the \mathcal{L}_2 norm and the \mathcal{H}_1 semi-norm are

employed for the displacement and stress/strain approximations, respectively.

$$\|\mathbf{u}_{h,M} - \mathbf{u}_{ex,M}\|_{\mathcal{L}_2} = \sqrt{\frac{1}{\Omega_{M_{el}}} \sum_{i=1}^{n_{M_{el}}} \frac{\langle \mathbf{u}_{M(i)} - \mathbf{u}_{M(i),ex}, \mathbf{u}_{M(i)} - \mathbf{u}_{M(i),ex} \rangle}{\langle \mathbf{u}_{M(i),ex}, \mathbf{u}_{M(i),ex} \rangle}} \quad (5.2a)$$

$$|\mathbf{u}_{h,M} - \mathbf{u}_{ex,M}|_{\mathcal{H}_1} = \sqrt{\frac{1}{\Omega_{M_{el}}} \sum_{i=1}^{n_{M_{el}}} \frac{\langle \boldsymbol{\varepsilon}(\mathbf{u}_{M(i)} - \mathbf{u}_{M(i),ex}), \boldsymbol{\sigma}(\mathbf{u}_{M(i)} - \mathbf{u}_{M(i),ex}) \rangle}{\langle \boldsymbol{\varepsilon}(\mathbf{u}_{M(i),ex}), \boldsymbol{\sigma}(\mathbf{u}_{M(i),ex}) \rangle}}, \quad (5.2b)$$

where $\langle \cdot, \cdot \rangle$, $\mathbf{u}_{h,M}$ and $\mathbf{u}_{ex,M}$ denotes the scalar product, the numerically evaluated coarse-nodal displacements and the reference solution at the coarse-nodes, respectively.

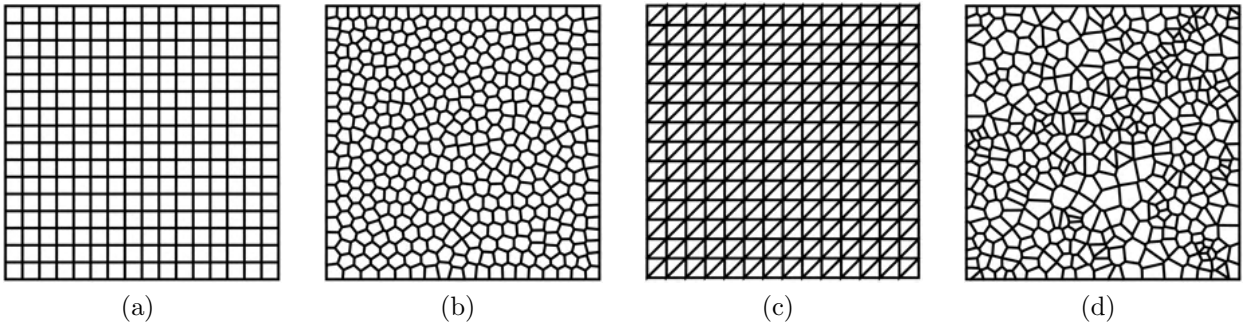


Figure 5.5: Element types (a) Quadrilateral (b) Centroidal Voronoi Tessellations (c) Triangle (d) Random Voronoi.

5.3.1 Square plate under tension

The case of the homogeneous square plate shown in Fig. 5.6a is considered herein. The plate is fully clamped at the bottom and subjected to a traction vector $\mathbf{t} = [0 \ 10]^T$ at the top edge as shown in Fig. 5.6. The vertical sides are left unconstrained. The material has a Young modulus $E = 10^7 \text{ N/m}^2$ and a Poisson's ratio $\nu = 0.3$. A mesh discretization of 40×40 quadrilateral plane

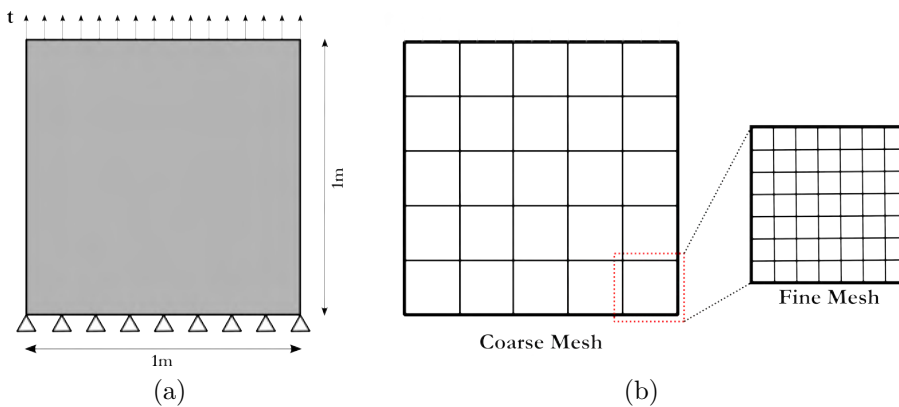


Figure 5.6: (a) Geometry and boundary conditions (b) Multiscale mesh.

stress elements with full integration is employed for the FEM and VEM as shown. The EMsFEM and EMsVEM solutions are derived considering a coarse mesh consisting of 5×5 quadrilateral coarse-elements. This is illustrated by the coarse-grid in Fig. 5.6b. Each coarse-element contains

8×8 quadrilateral fine-elements. The case of rectangular elements only is considered in this case for comparisons between the virtual element and finite element based methods to be meaningful. Linear boundary conditions are used to derive the multiscale basis functions for this example.

The \mathcal{L}_2 -norm of the errors between the FEM and the EMsFEM is 5.7×10^{-3} . The corresponding norm for the VEM to EMsVEM comparison is practically the same, i.e., 5.5×10^{-3} . A convergence study is also performed by retaining the same number of coarse-elements as shown in Fig. 5.6b, and increasing the number of fine-scale elements.

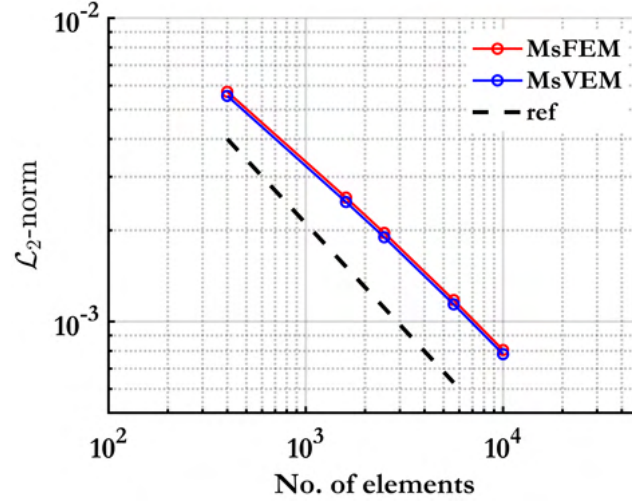


Figure 5.7: Relative error plots: EMsFEM and EMsVEM evaluated displacements compared against FEM and VEM displacements respectively, at coarse-nodes. A reference slope is provided for comparison.

The evolution of the \mathcal{L}_2 -norm as a function of the number of elements is provided in Fig. 5.7, where the EMsFEM and EMsVEM behave in an identical fashion. A reference slope is also shown for comparison of error convergence rates. Near optimal rates are observed for both methods.

5.3.2 Cantilever beam subjected to parabolic traction

The cantilever structure shown in Fig. 5.8 is fully clamped at the left and is subjected to a parabolic traction at its free end. The domain has a length $L = 8$ m, height $D = 4$ m and thickness $t = 1$ m. The material has a Young's modulus $E = 10^7$ N/m² and a Poisson's ratio $\nu = 0.3$. The parabolic traction at the free end assumes the following form

$$t_x = 0, \quad t_y = \frac{p(D^2/4 - y^2)}{2I}, \quad (5.3)$$

where $p = -1000$ N is the total load applied and $I = tD^3/12$.

The displacements are evaluated analytically on the basis of plane strain assumptions [329] according to Eqs. (5.4a) and (5.4b) for the horizontal and vertical component, respectively

$$u_x = -\frac{py}{6EI} \left((6L - 3x)x + (2 + \bar{\nu})y^2 - \frac{3D^2}{2}(1 + \bar{\nu}) \right) \quad (5.4a)$$

$$u_y = \frac{p}{6EI} \left(3\bar{\nu}y^2(L - x) + (3L - x)x^2 \right), \quad (5.4b)$$

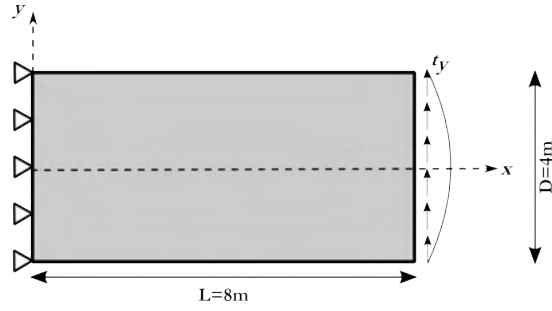


Figure 5.8: Schematic diagram of a cantilever beam subject to parabolic tractions.

where $\bar{E} = \frac{E}{1-\nu^2}$ and $\bar{\nu} = \frac{\nu}{1-\nu}$.

Three different geometries of micro-structure elements are considered; these are summarized in Table 5.1. The problem is also solved with the EMsFEM for the case of quadrilateral micro-elements.

Element Type	Abbreviation	EMsFEM	EMsVEM
Quadrilateral	QUAD	□	□
Centroidal Voronoi Tessellations	CVT	-	★
Random	RAND	-	*

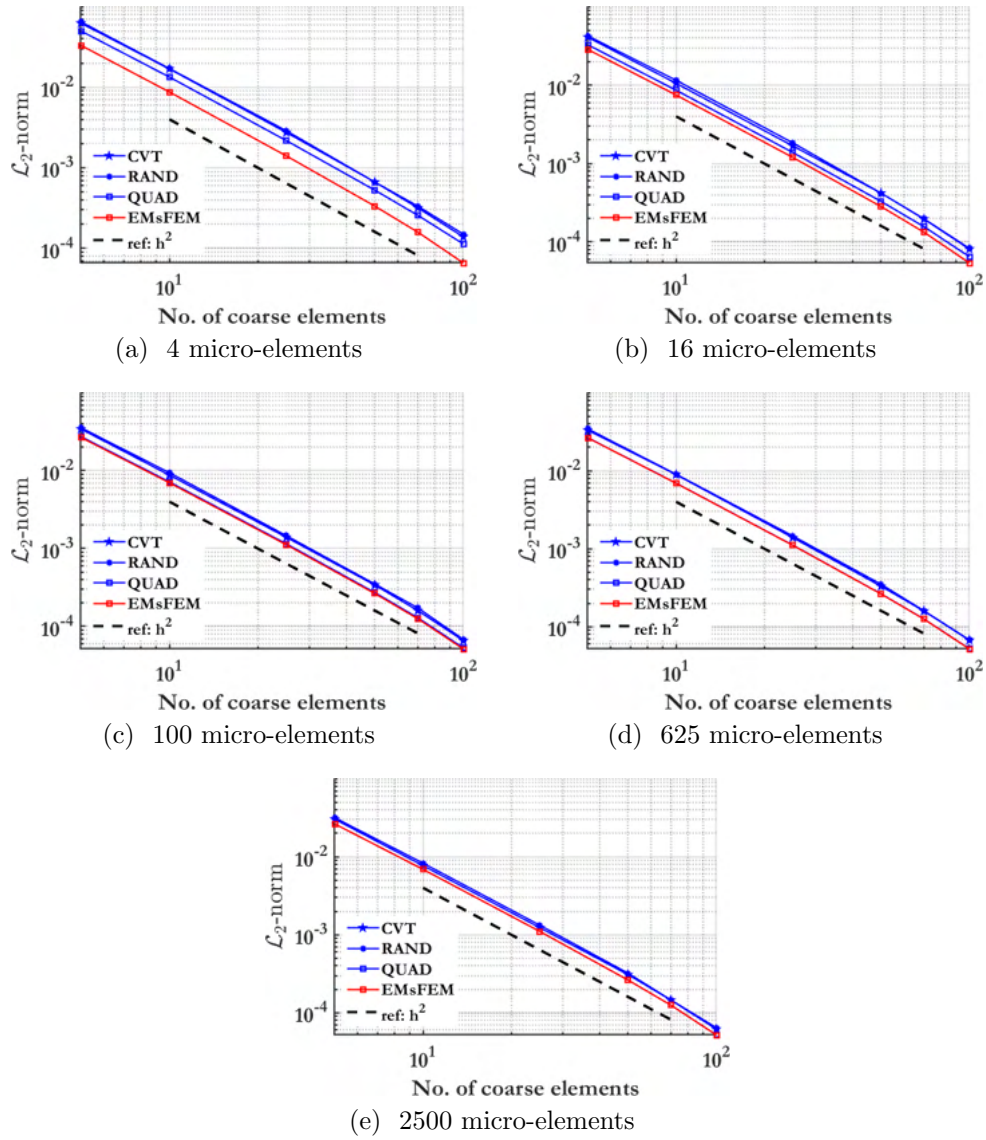
Table 5.1: Convergence behaviour of EMsFEM and EMsVEM are studied with respect to different element types.

The convergence behaviour of the EMsFEM and the EMsVEM with respect to different element-types specified in Table 5.1 is investigated in the form of relative \mathcal{L}_2 and \mathcal{H}_1 error convergence plots shown in Fig. 5.9 and Fig. 5.10. The evolution of the errors are studied as a function of the number of coarse-elements, for 5 micro-structure configurations. At low discretizations (Figs. 5.9 a, 5.9 b, 5.10 a and 5.10 b), the EMsFEM solution provides the best accuracy. However, for finer micro-structure configurations (Figs. 5.9 e and 5.10 e), the CVT, RAND and QUAD element meshes used by the EMsVEM offer accuracies approaching the QUAD EMsFEM method, over all coarse-element mesh discretizations.

The convergence rates are provided in Table 5.2 and Table 5.3. These are found to nearly coincide with the expected theoretical slopes of -2 in the \mathcal{L}_2 and -1 in the \mathcal{H}_1 relative error norms, respectively. The theoretical convergence rates are derived in [330]. One can conclude that near-optimal convergence rates are obtained by the method over all coarse-element discretizations. This suggests that the EMsVEM is a viable alternative to the EMsFEM when a flexible mesh generation is required to account for fine-scale heterogeneities.

The primary advantage offered by the EMsVEM over the EMsFEM lies in its ability to handle any kind of micro-structure configuration. This is illustrated by computing displacements with the EMsVEM for a 10×10 coarse-element discretization with an arbitrarily chosen micro-structure definition described in Table 5.4. The contour plots of the resulting total displacements are shown in Fig. 5.11.

Figs. 5.11a and 5.11b illustrate the method's ability to sufficiently handle widely varying micro-structural configurations within a single problem. The corresponding y-displacements obtained

Figure 5.9: Relative \mathcal{L}_2 error convergence plots for 5 micro-structure configurations.

No. of micro-elements	CVT	RAND	QUAD	EMsFEM
4	-1.8868	-1.9303	-1.9012	-1.9244
16	-1.9547	-1.8829	-1.9255	-1.9325
100	-1.9635	-1.9200	-1.9343	-1.9355
625	-1.8931	-1.9358	-1.9358	-1.9359
2500	-1.9799	-1.9359	-1.9359	-1.9360

Table 5.2: Convergence rates of the \mathcal{L}_2 relative error norm.

for the free end of the neutral axis of the structure are compared against the analytical solution in Table 5.5.

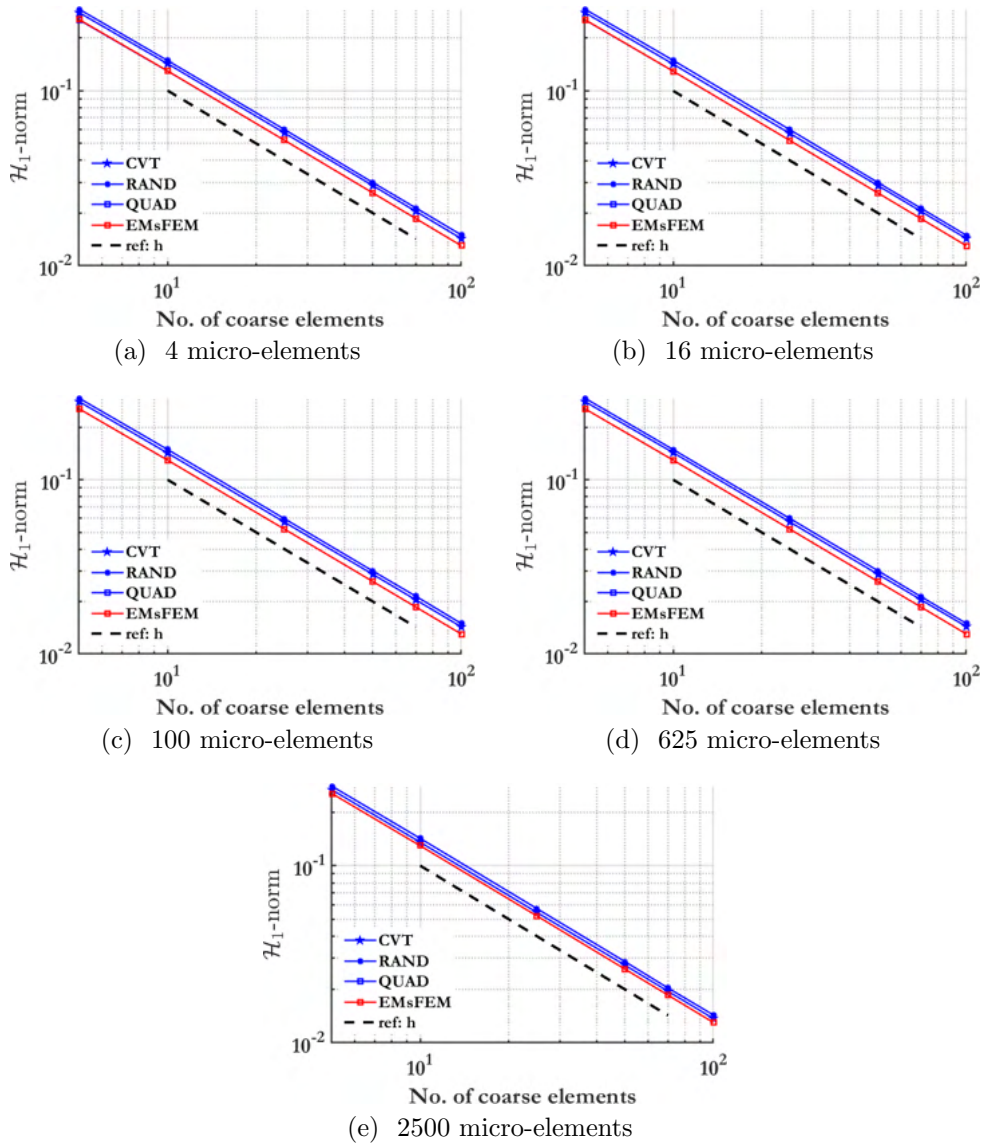


Figure 5.10: Relative \mathcal{H}_1 error convergence plots for 5 micro-structure configurations.

No. of micro-elements	CVT	RAND	QUAD	EMsFEM
4	-0.9681	-0.9724	-0.9695	-0.9750
16	-0.9781	-0.9709	-0.9752	-0.9773
100	-0.9809	-0.9765	-0.9780	-0.9784
625	-0.9742	-0.9785	-0.9785	-0.9786
2500	-0.9829	-0.9786	-0.9786	-0.9786

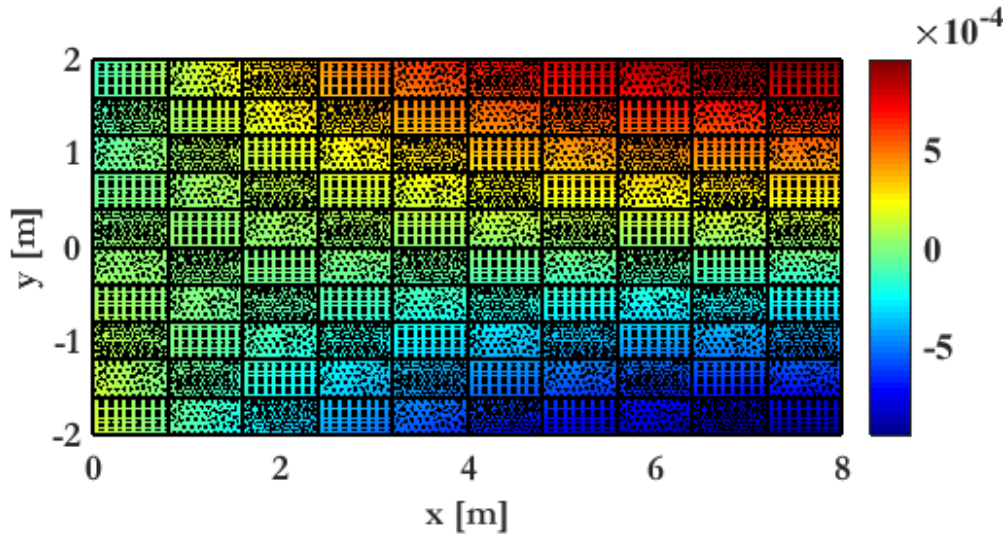
Table 5.3: Convergence rates of the \mathcal{H}_1 relative error norm.

5.3.3 Cantilever beam with a periodic microstructure

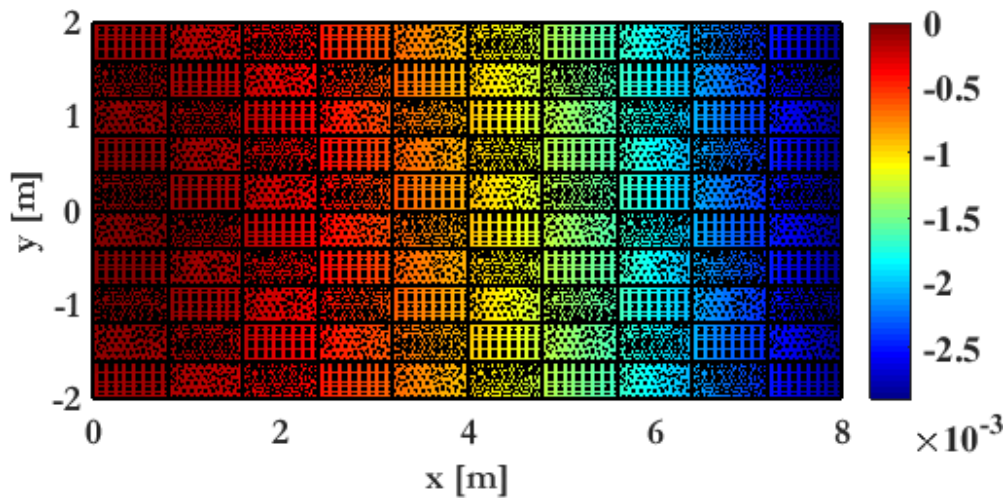
In this example, a cantilever beam with periodically repeating circular inclusions is considered. A 30×6 coarse grid is created over this domain as shown in Fig. 5.12a. The micro-structure enclosed within each coarse element contains a circular inclusion as illustrated in Fig. 5.12b. The material properties considered are $E_m = 1\text{GPa}$, $\nu_m = 0.3$ and $E_i = 10\text{GPa}$, $\nu_i = 0.3$ for the matrix

No.	Element Type	No. of Elements
1	TRI	64
2	QUAD	25
3	RAND	36
4	CVT	100

Table 5.4: Arbitrarily chosen micro-structural definition assigned periodically to each unit-cell.



(a) u_x : Displacements in x-direction



(b) u_y : Displacements in y-direction

Figure 5.11: Total displacement contours for the arbitrarily chosen micro-structure defined in Table 5.4 - Units are in m.

Numerical solution	Analytical solution
$-2.91 \times 10^{-3} \text{ m}$	$-2.96 \times 10^{-3} \text{ m}$

Table 5.5: Neutral axis free end displacements in the y-direction computed using EMsVEM and analytical solution.

m and the inclusion i , respectively.

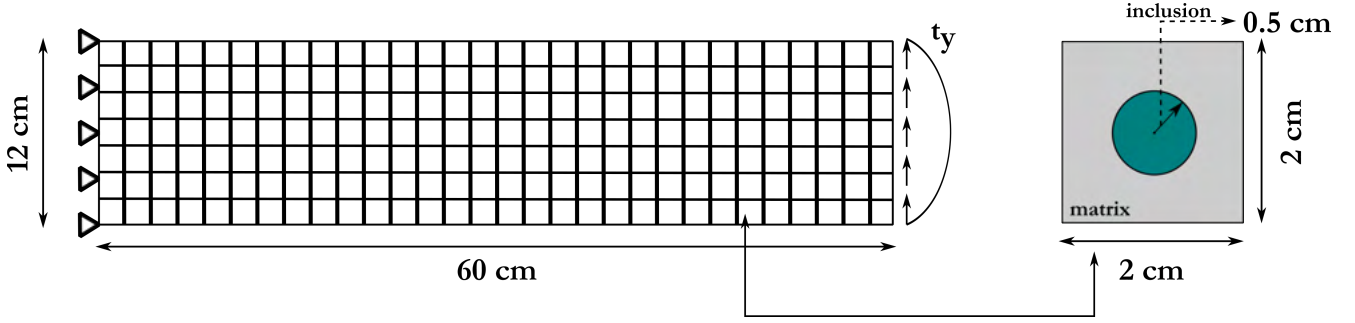


Figure 5.12: Cantilever with a periodic micro-structure: Geometry and boundary conditions.

This example is provided to establish the EMsVEM as a useful tool in the analysis of composites for driving down computational costs. To prove this claim, attention is drawn to the relaxed conformity requirements on polygonal meshes when compared with conventional quadrilateral finite element meshes. This flexibility is exploited to minimize the number of nodes involved in the micro-structural discretization while still retaining satisfactory accuracy. In particular, the microstructure is discretized using three approaches, i.e, uniform quadrilateral elements, uniform polygonal CVT elements, and an adaptively refined mesh as shown in Fig. 5.13. Mesh 1, schematically depicted in Fig. 5.13a, comprises 10,116 uniform quadrilateral elements and is treated as a reference solution. Mesh 2, contains 5000 uniform CVT elements and is shown in Fig. 5.13b. Mesh 3 (Fig. 5.13c) is adapted from [106], wherein efficient polygonal discretizations are exploited for performing a non-linear analysis on fiber composites. The properties of each mesh are summarized in Table 5.6. Periodic boundary conditions are used to derive the multiscale basis functions, for all cases.

Label	Element-Type	No. of Elements	No. of Nodes	Description
Mesh 1	QUAD	10116	10299	Reference Solution
Mesh 2	CVT	5000	7278	Uniform mesh
Mesh 3	POLY	1441	2452	Adaptive mesh

Table 5.6: Meshes used to discretize the micro-structure.

The \mathcal{L}_2 and \mathcal{H}_1 error norms obtained by Mesh 2 and Mesh 3 are summarized in Table 5.7. It is observed that both meshes achieve comparable accuracy despite the fact that Mesh 2 has a considerably larger number of DoFs. The computational time for all cases, averaged over 5 runs is shown in Table 5.7. This result illustrates appreciable benefits attainable through the EMsVEM by using more flexible mesh generation capabilities.

	\mathcal{L}_2 error norm	\mathcal{H}_1 error norm	Analysis time [sec]
Mesh 1	-	-	3870
Mesh 2	0.0062	0.047	1015
Mesh 3	0.0056	0.050	215

Table 5.7: \mathcal{L}_2 and \mathcal{H}_1 error norms for Mesh 2 and Mesh 3 using Mesh 1 as a reference solution and computational times.

Contour plots of the total displacements are shown in Fig. 5.14a and Fig. 5.14b for the EMsVEM-P model with Mesh 3 and the standard VEM, respectively. The corresponding von-Mises stresses σ_{VM} are provided in Fig. 5.15a and Fig. 5.15b for the EMsVEM and the VEM,

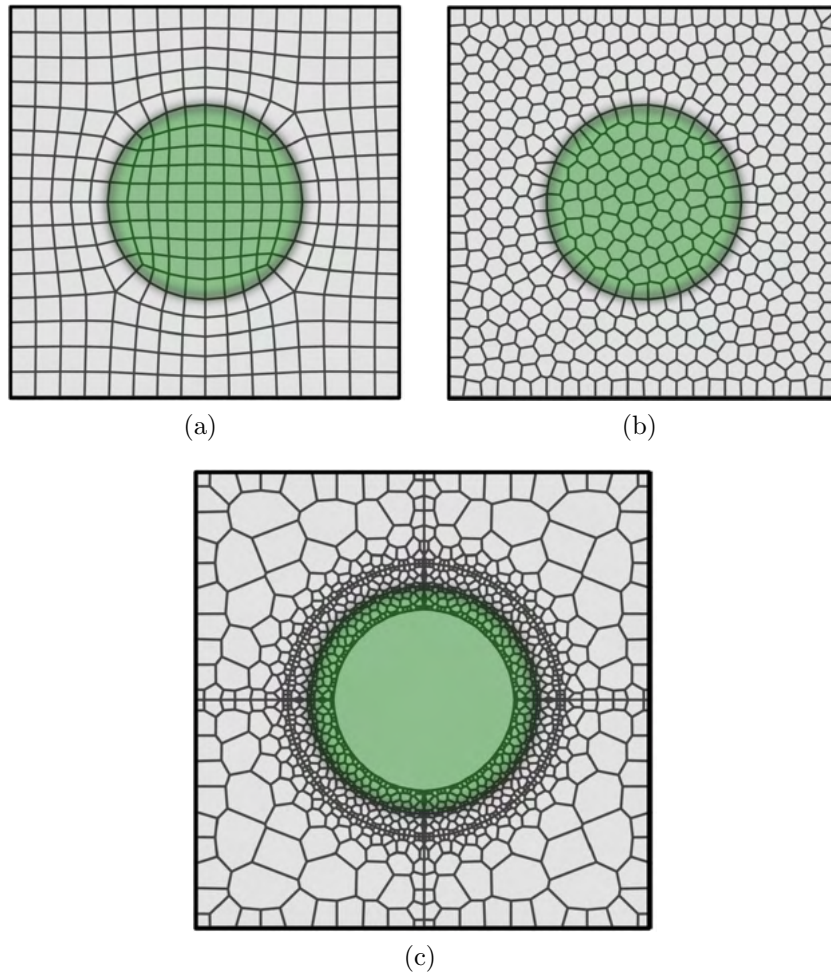


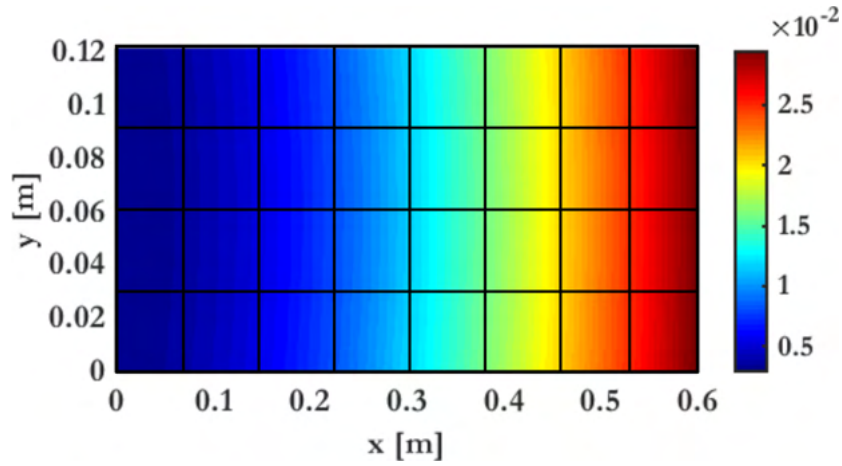
Figure 5.13: Element types (a) Uniform Quadrilateral, (b) Centroidal Voronoi Tessellations (c) Specially designed polygonal mesh.

respectively. Both methods provide practically identical results, as also manifested by the \mathcal{L}_2 and \mathcal{H}_1 norms shown in Table 5.7.

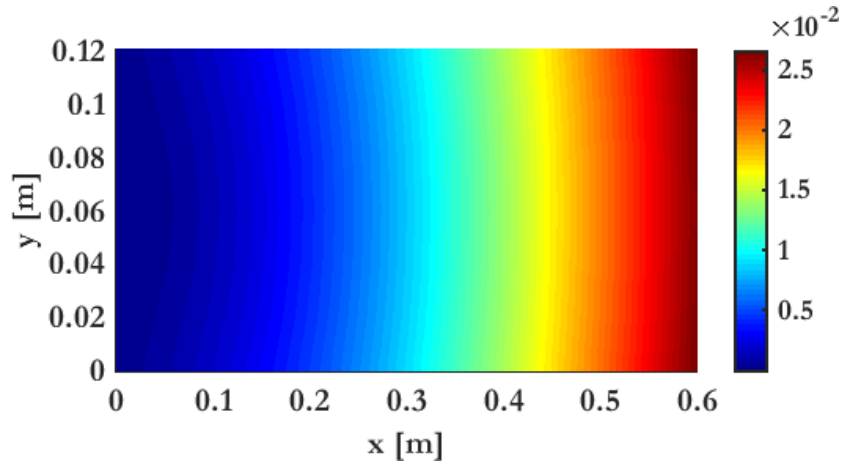
5.3.4 Cantilever beam with a highly heterogeneous material distribution subjected to parabolic traction

The case of the cantilever beam examined in Section 5.3.2 and shown in Fig. 5.8 is considered here also. In this case, the effect of the material heterogeneity on the performance of the proposed EMsVEM is investigated both in terms of accuracy and computational efficiency. The results obtained from the EMsVEM are compared against the standard VEM. Comparisons are also provided against the standard FEM and the EMsFEM for the case of quadrilateral elements. To investigate the effect of the assumed boundary conditions for the evaluation of the multiscale basis functions, two variants are considered, i.e., linear and periodic boundary conditions. The abbreviations of the multiscale methods used in this example are shown in Table 5.8.

Three cases are considered vis-a-vis the geometry of the fine-scale, i.e., with heterogeneities having (a) QUAD, (b) CVT and (c) RAND shapes. Furthermore, two discretizations are examined per case, to assess the effect of the scale separation on the accuracy of the EMsVEM. The mod-



(a) Evaluated using the EMsVEM-P



(b) Evaluated using VEM

Figure 5.14: Total displacement contours - Units are in m.

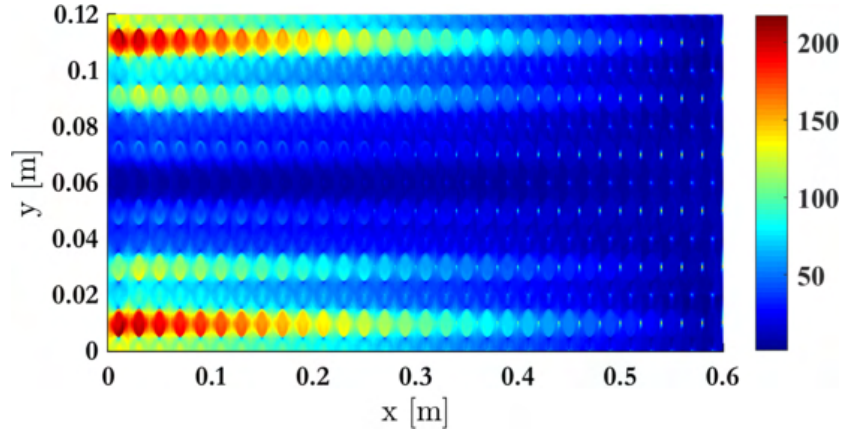
Abbreviation	Method/ Boundary conditions
EMsFEM-L	Multiscale Finite Element Method/ Linear
EMsFEM-P	Multiscale Finite Element Method/ Periodic
EMsVEM-L	Multiscale Virtual Element Method/ Linear
EMsVEM-P	Multiscale Virtual Element Method/ Periodic

Table 5.8: Multiscale method labeling based on the boundary conditions used to evaluate the multiscale basis functions.

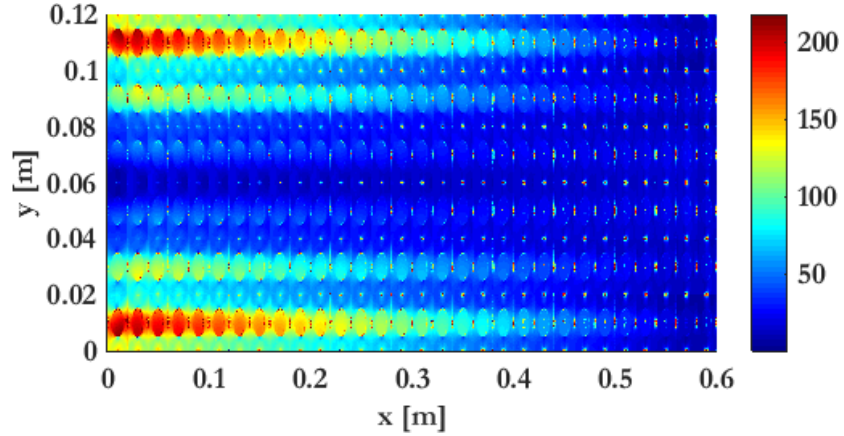
els employed along with their corresponding coarse and fine-scale discretizations are summarized in Table 5.9.

Each micro-element in both discretization schemes is randomly assigned a Young's modulus generated by a uniform distribution. The lower and upper bounds of the Young's modulus are considered to be $E_l = 1$ GPa and $E_u = 100$ GPa, respectively. The material distribution associated with discretization scheme B is illustrated in Fig. 5.16. This material distribution within the coarse-element is assumed to repeat periodically over the entire domain. The Poisson's ratio is 0.3 in all cases.

The profile of the vertical displacements along the neutral axis ($y = 0$) of the structure are



(a) Evaluated using the EMsVEM-P



(b) Evaluated using VEM

Figure 5.15: Von Mises stress contours - Units are in MPa.

shown for all the cases in Fig. 5.17. For discretization scheme A, shown in Figs. 5.17a, 5.17c, and 5.17e, a significant deviation in the displacements obtained through FEM and VEM and the multiscale solutions is observed. The methods using periodic boundaries, i.e., EMsFEM-P and EMsVEM-P are found to approximate the complete solutions better than EMsFEM-L and EMsVEM-L.

On the other hand, in the case of the finer discretization scheme B, as shown in Figs. 5.17b, 5.17d and 5.17f, all methods provide practically identical results. The relative error of the EMsVEM to the VEM solution for linear and periodic boundary conditions is shown in Table 5.10. These are practically identical to the relative errors of the EMsFEM to FEM solution which are also shown in Table 5.10 for completeness.

	Discretization A			Discretization B		
	Full Mesh	Multiscale Mesh		Full Mesh	Multiscale Mesh	
	[-]	Macro	Micro	[-]	Macro	Micro
Quad	720	15x3	16	72000	50x12	144
CVT	720	15x3	16	72000	50x12	144
RAND	720	15x3	16	72000	50x12	144

Table 5.9: Number of elements considered in each run. The discretization scheme B is illustrated in Fig. 5.16.

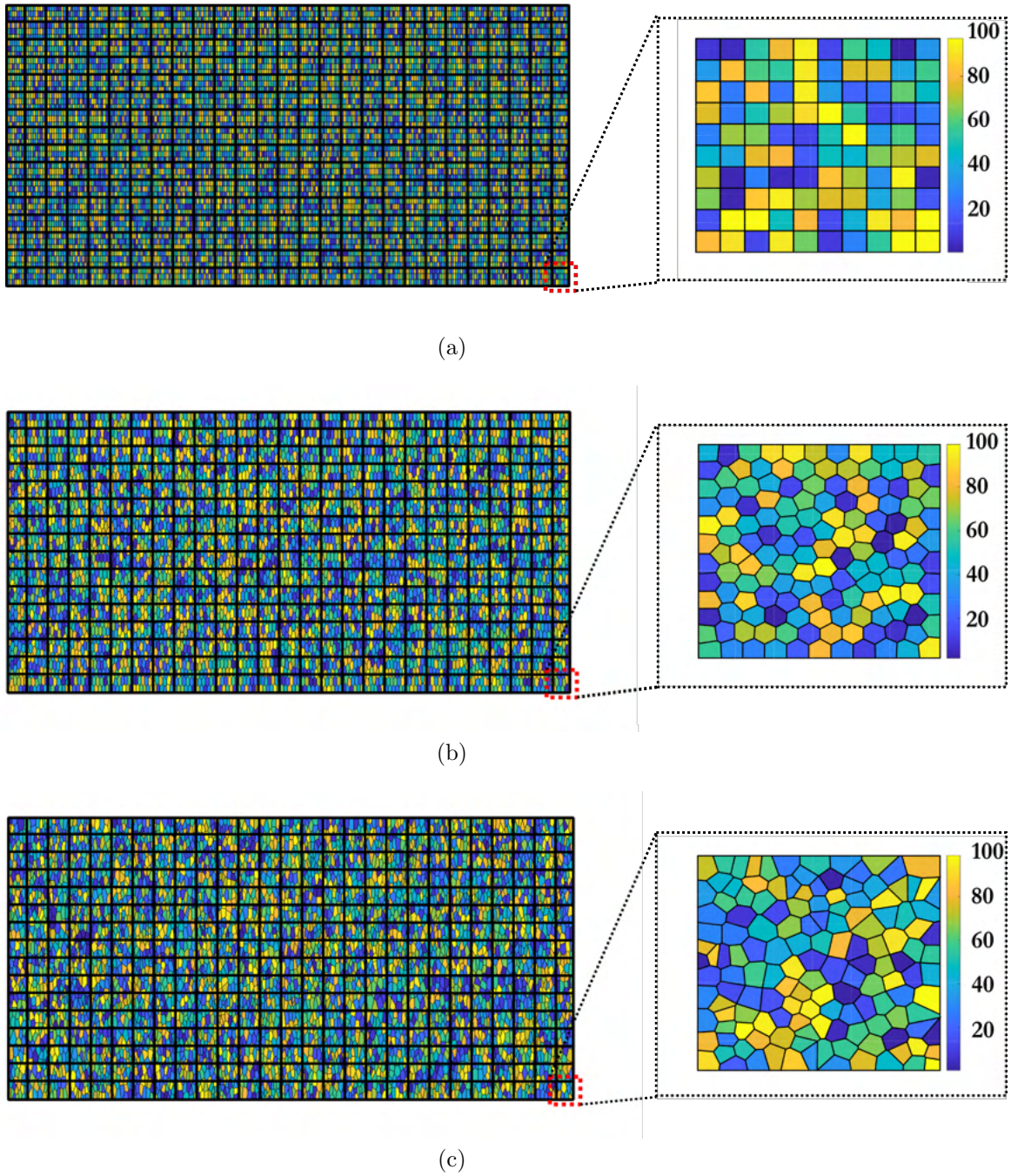
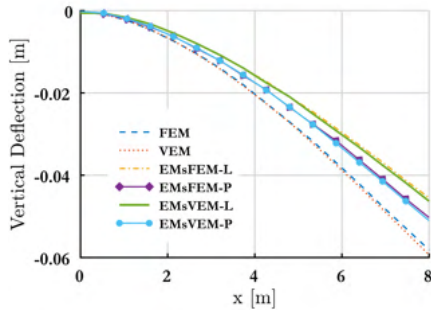
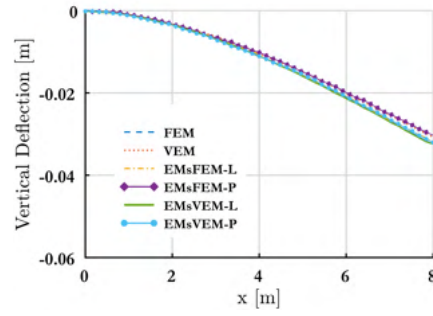


Figure 5.16: Snapshots of randomly distributed Young's modulus in a typical coarse-element with (a) 144 QUAD fine-elements (b) 144 CVT fine-elements (c) 144 RAND fine-elements - Units are in GPa.

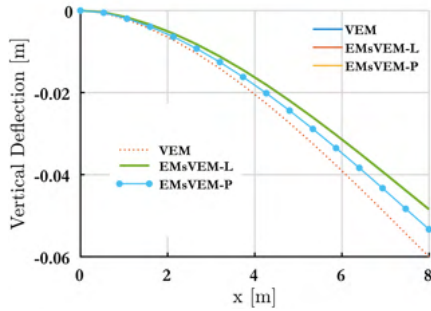
The horizontal displacements (\mathbf{u}_x) obtained for the micro-structure using RAND elements and the discretization scheme B are indicatively shown in Fig. 5.18a and Fig. 5.18b for the VEM and EMsVEM-P, respectively. The Von-Mises stress distribution (σ_{VM}) obtained for all cases using the discretization scheme B, are shown in Fig. 5.19.



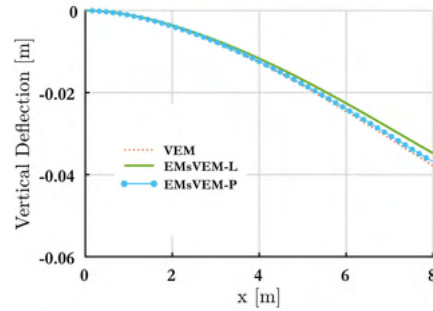
(a) Discretization Scheme A with QUAD elements



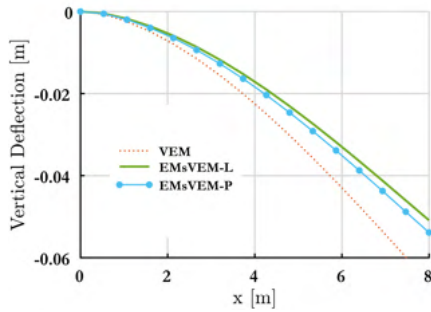
(b) Discretization Scheme B with QUAD elements



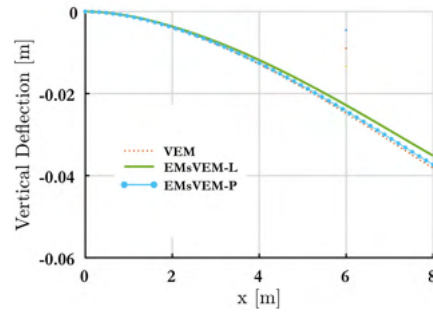
(c) Discretization Scheme A with CVT elements



(d) Discretization Scheme B with CVT elements



(e) Discretization Scheme with RAND elements



(f) Discretization Scheme B with RAND elements

Figure 5.17: Vertical displacement along the neutral axis of the cantilever.

	Discretization A			Discretization B		
	Quad	CVT	RAND	Quad	CVT	RAND
EMsFEM-L	0.2246	-	-	0.0562	-	-
EMsFEM-P	0.1402	-	-	0.0072	-	-
EMsVEM-L	0.2256	0.1953	0.242	0.061	0.0807	0.12
EMsVEM-P	0.1440	0.1111	0.1618	0.0076	0.0144	0.0233

Table 5.10: Relative \mathcal{L}_2 errors between standard solutions and multiscale solutions computed at coarse-nodes.

Discussion on computational gains

To assess the computational effectiveness of the EMsVEM, the time required for the assembly and inversion of the global state matrices is recorded for all the methods employed. The average

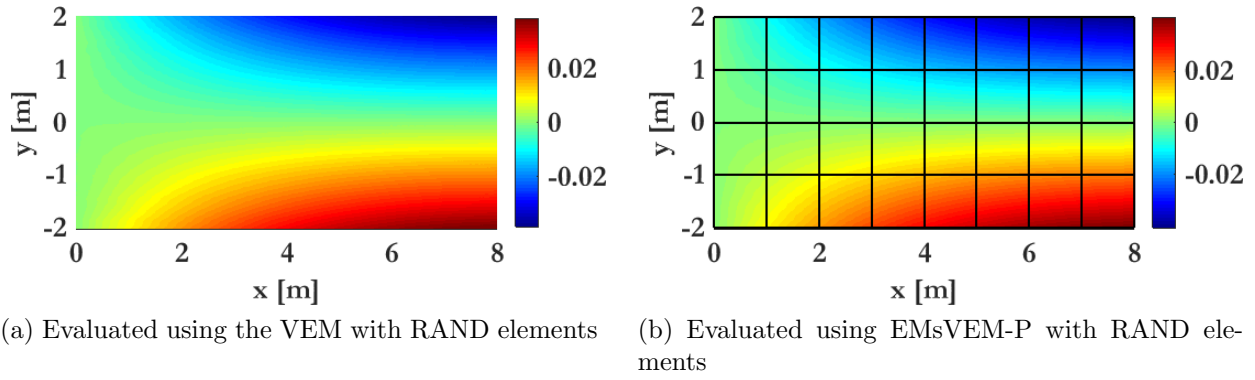


Figure 5.18: Visualization of \mathbf{u}_x (x-displacement) distributions for RAND elements with discretization scheme B.

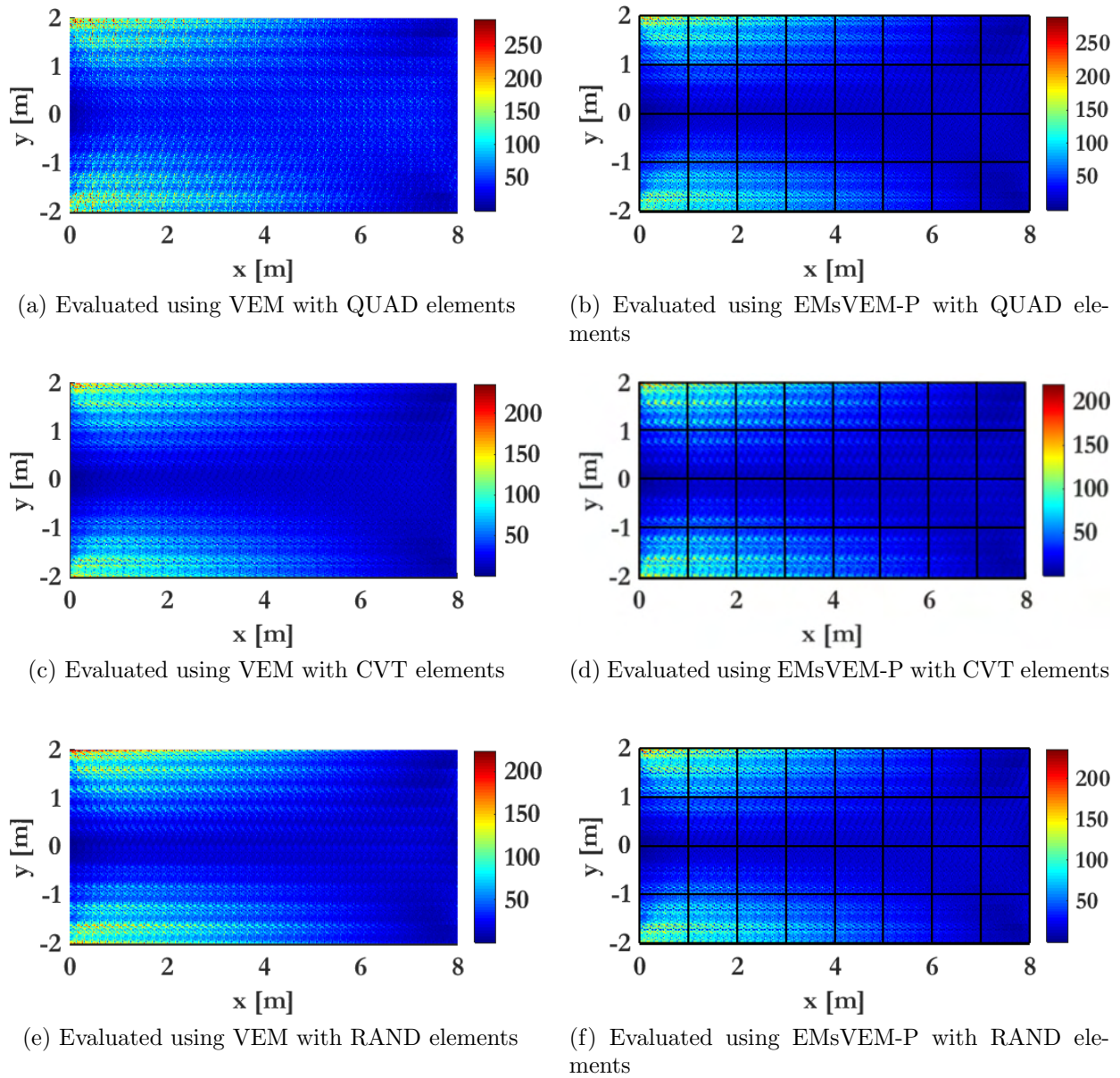
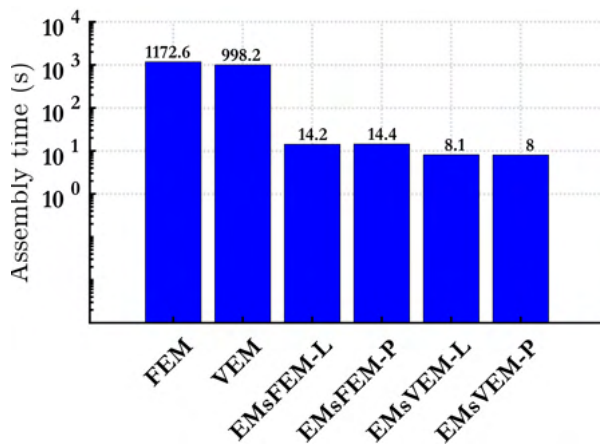


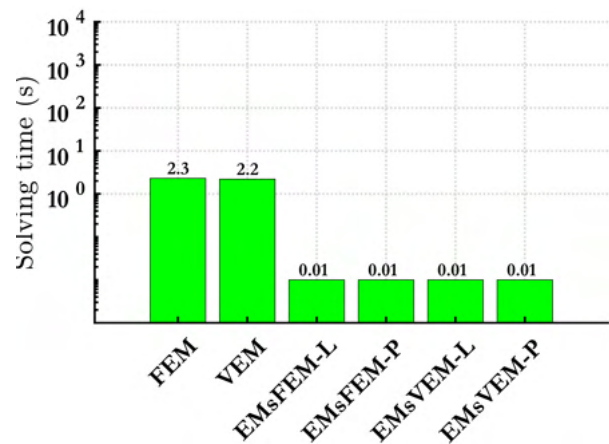
Figure 5.19: Visualization of σ_{VM} (Von-Mises stress) distributions for all element cases with discretization scheme B.

times over five runs are shown in Fig. 5.20. There is an appreciable reduction in the time taken for assembly and matrix inversion when using multiscale methods, as evidenced by Fig. 5.20a and Fig. 5.20b. This is to be expected as the number of nodes involved in the multiscale assembly and solution procedures are significantly reduced when compared to the standard FEM and VEM.

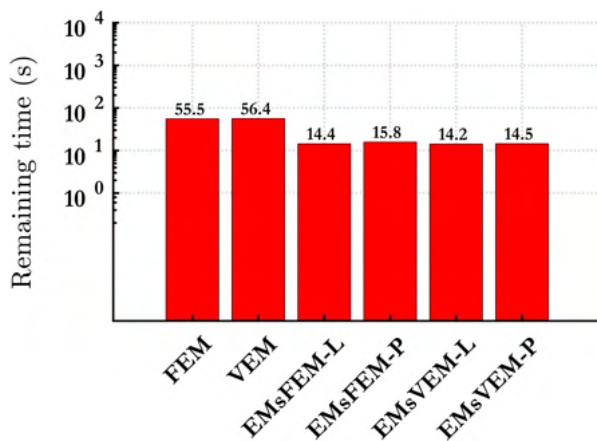
Furthermore, the time required in the EMsVEM is significantly lower when compared to the EMsFEM. This is attributed to the fact that there are no iterative evaluations over quadrature integration points done in the case of first order EMsVEM as opposed to the EMsFEM. In Fig. 5.20c, post-processing times are also compared for all methods. This is to account for the effect potential overheads might have on the computational efficiency of the methods, especially within an incremental/ iterative solution scheme. The time required for the multiscale methods to downscale the coarse-solution is also captured here.



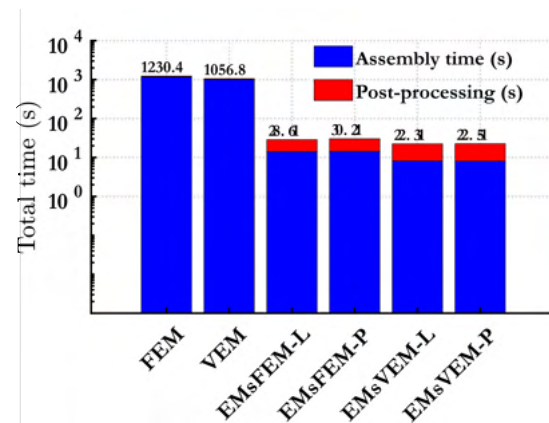
(a) Time required to assemble global stiffness matrix



(b) Time required to solve the linear system of equations



(c) Time required for post-processing



(d) Total analysis time

Figure 5.20: Comparing the time taken at critical points during solving.

While it is clear from Fig. 5.20d that post-processing is a significant factor for the multiscale methods, Fig. 5.20c reveals that this is indeed lower than in the corresponding fine scale implementations. This is due to the fact that down-scaling is performed per coarse element, hence implicitly vectorizing the corresponding strain and stress computation loops.

5.4 Consolidation

The flexibility of the VEM at the fine scale is exploited to generalize the MsVEM to accommodate more complex and arbitrarily shaped domains at the coarse scale as well. To this end, generalize polygonal (possible non-convex) coarse elements are allowed as well. Each polygonal coarse-element $\mathcal{K}_{M(\alpha)}$, $\alpha = 1 \dots n_{M_{el}}$, clusters its own underlying fine-scale virtual element mesh comprising micro-elements $\mathcal{K}_{m(i)}$, $i = 1 \dots n_{m_{el}}^\alpha$, as illustrated in Fig. 5.21.

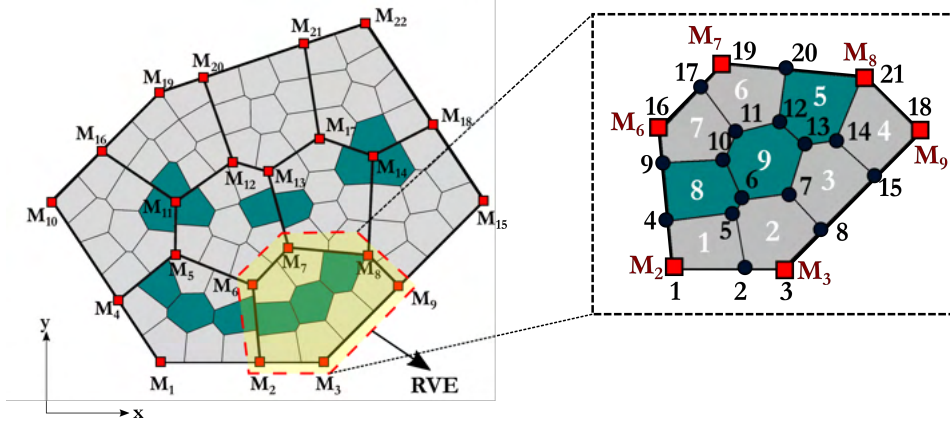


Figure 5.21: Multiscale mesh with $n_M = 22$ coarse nodes and $n_{M_{el}} = 9$ polygonal coarse elements, each clustering its own fine polygonal mesh.

5.4.1 Oscillatory boundary conditions

Two sets of multiscale basis functions, \mathbf{N}_m^u and \mathbf{N}_m^p need to be evaluated for the upscaling procedure, from Eqs. (4.7) and (4.33). These equations are subjected to Dirichlet constraints, which are imposed at the coarse element boundary. The prescribed displacements \mathbf{u}_s and pressures \mathbf{p}_s at the RVE boundary are assigned linear or periodic kinematical constraints $\bar{\mathbf{u}}$ and $\bar{\mathbf{p}}$. For generalized polygonal RVEs (Fig. 5.22b), assigning periodic constraints is not possible. Alternatively, oscillatory boundaries [331] are used, i.e., reduced versions of Eq. (4.7) and Eq. (4.33) are solved over the required edges of the RVE.

In comparison to prescribing linear constraints (Fig. 5.22a), oscillatory conditions allow for a less rigid enforcement of displacement and pressure profiles along the RVE boundaries (Fig. 5.22b). Furthermore, the effect of material heterogeneities along the boundaries naturally emerges in the evaluation of the corresponding displacement profiles hence providing a physically rigorous approach to the evaluation of the multiscale basis functions.

For the RVE ($\alpha = 2$) shown in Fig. 5.22b and the micro-element $i = 9$, Eqs. (4.5) and (4.31) assume the following form

$$\mathbf{u}_{m(9)}^2 = \underbrace{\mathbf{N}_{m(9)}^u}_{12 \times 12} \mathbf{u}_{M(2)} \quad (5.5a)$$

$$\mathbf{p}_{m(9)}^2 = \underbrace{\mathbf{N}_{m(9)}^p}_{6 \times 6} \mathbf{p}_{M(2)}, \quad (5.5b)$$

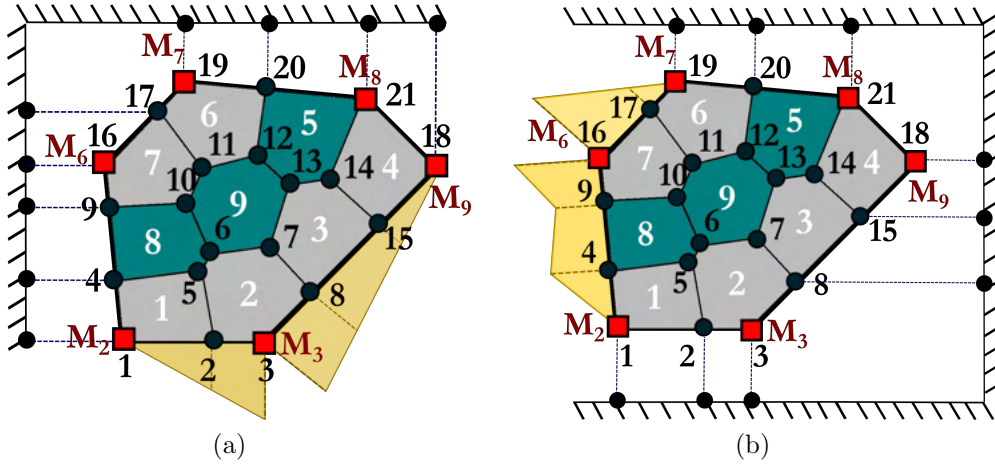


Figure 5.22: An example 6-noded coarse element ($\alpha = 2$) clustering $n_{me1}=9$ fine elements and $n_m = 21$ fine nodes. (a) Linear kinematical constraints are prescribed over edges $\Gamma_{M_2M_3}$ and $\Gamma_{M_3M_9}$, (b) Oscillatory kinematical constraints are prescribed over edges $\Gamma_{M_7M_6}$ and $\Gamma_{M_6M_2}$.

where the fine nodal displacement $\mathbf{u}_{m(9)}^2$ and pressure $\mathbf{p}_{m(9)}^2$ vectors are

$$\mathbf{u}_{m(9)}^2 = \begin{bmatrix} u_{mx,6} & u_{my,6} & u_{mx,7} & u_{my,7} & u_{mx,13} & u_{my,13} \\ & & u_{mx,12} & u_{my,12} & u_{mx,11} & u_{my,11} & u_{mx,10} & u_{my,10} \end{bmatrix}^T, \quad (5.6)$$

and

$$\mathbf{p}_{m(9)}^2 = [p_{m,6} \ p_{m,7} \ p_{m,13} \ p_{m,12} \ p_{m,11} \ p_{m,10}]^T, \quad (5.7)$$

respectively. Similarly, the corresponding nodal vectors at the coarse scale are

$$\mathbf{u}_{M(2)} = \begin{bmatrix} u_{Mx,2} & u_{My,2} & u_{Mx,3} & u_{My,3} & u_{Mx,9} & u_{My,9} \\ & & u_{Mx,8} & u_{My,8} & u_{mx,7} & u_{my,7} & u_{mx,6} & u_{my,6} \end{bmatrix}^T, \quad (5.8)$$

and

$$\mathbf{p}_{M(2)} = [p_{M,2} \ p_{M,3} \ p_{M,9} \ p_{M,8} \ p_{M,7} \ p_{M,6}]^T, \quad (5.9)$$

for the displacements and pressures, respectively.

For the RVE ($\alpha = 2$) shown in Fig. 5.22b, the arrays of multiscale basis function arrays \mathbf{N}_m^u and \mathbf{N}_m^p are 42×12 and 21×6 matrices, respectively. To compute the kinematical constraints for $\mathbf{N}_{M,6}^u$ and $\mathbf{N}_{M,6}^p$ as illustrated in Fig. 5.22b, the edge boundaries are grouped into opposite and adjacent edges as shown in Table 5.11. Kinematical constraints are then assigned to the RVE as follows:

- To compute $\mathbf{N}_{Mx,6}^u$

1. Solve reduced version of Eq. (4.7) for \bar{u}_x over Γ_{Adj} :

$$-\frac{\partial}{\partial \xi} \cdot \left(E \frac{\partial \bar{u}_x}{\partial \xi} \right) = 0 \text{ on } \Gamma_{M_7M_6}, \quad \bar{u}_x(\xi_{M_6}) = 1, \quad \bar{u}_x(\xi_{M_7}) = 0 \quad (5.10a)$$

$$-\frac{\partial}{\partial \xi} \cdot \left(E \frac{\partial \bar{u}_x}{\partial \xi} \right) = 0 \text{ on } \Gamma_{M_6M_2}, \quad \bar{u}_x(\xi_{M_6}) = 1, \quad \bar{u}_x(\xi_{M_2}) = 0. \quad (5.10b)$$

2. Assign \bar{u}_x to x -DoFs on adjacent edges: $\bar{u}_x|_{\Gamma_{\text{adj}}} = \bar{u}_x$.
3. Assign sliding conditions to y -DoFs on adjacent edges: $\bar{u}_y|_{\Gamma_{\text{adj}}} = 0$.
4. Assign fully clamped conditions on opposite edges: $\bar{\mathbf{u}}|_{\Gamma_{\text{opp}}} = \mathbf{0}$.

- To compute $\mathbf{N}_{M_y,6}^u$:

1. Solve reduced version of Eq. (4.7) for \bar{u}_y over Γ_{Adj} :

$$-\frac{\partial}{\partial \xi} \cdot \left(\mathbf{E} \frac{\partial \bar{u}_y}{\partial \xi} \right) = 0 \text{ on } \Gamma_{M_7M_6}, \quad \bar{u}_y(\xi_{M_6}) = 1, \quad \bar{u}_y(\xi_{M_7}) = 0 \quad (5.11a)$$

$$-\frac{\partial}{\partial \xi} \cdot \left(\mathbf{E} \frac{\partial \bar{u}_y}{\partial \xi} \right) = 0 \text{ on } \Gamma_{M_6M_2}, \quad \bar{u}_y(\xi_{M_6}) = 1, \quad \bar{u}_y(\xi_{M_2}) = 0. \quad (5.11b)$$

2. Assign \bar{u}_y to y -DoFs on adjacent edges: $\bar{u}_y|_{\Gamma_{\text{adj}}} = \bar{u}_y$.
3. Assign sliding conditions to x -DoFs on adjacent edges: $\bar{u}_x|_{\Gamma_{\text{adj}}} = 0$.
4. Assign fully clamped conditions on opposite edges: $\bar{\mathbf{u}}|_{\Gamma_{\text{opp}}} = \mathbf{0}$.

- To compute $\mathbf{N}_{M,6}^p$:

1. Solve reduced version of Eq. (4.33) for \bar{p} over Γ_{Adj} :

$$-\frac{\partial}{\partial \xi} \cdot \left(\frac{\mathbf{k}}{\gamma_f} \frac{\partial \bar{p}}{\partial \xi} \right) = 0 \text{ on } \Gamma_{M_7M_6}, \quad \bar{p}(\xi_{M_6}) = 1, \quad \bar{p}(\xi_{M_7}) = 0 \quad (5.12a)$$

$$-\frac{\partial}{\partial \xi} \cdot \left(\frac{\mathbf{k}}{\gamma_f} \frac{\partial \bar{p}}{\partial \xi} \right) = 0 \text{ on } \Gamma_{M_6M_2}, \quad \bar{p}(\xi_{M_6}) = 1, \quad \bar{p}(\xi_{M_2}) = 0 \quad (5.12b)$$

2. Assign \bar{p} on adjacent edges: $\bar{p}|_{\Gamma_{\text{adj}}} = \bar{p}$.
3. Assign zero conditions on opposite edges: $\bar{p}|_{\Gamma_{\text{opp}}} = 0$.

	Edges	Nodes
Opposite (Opp)	$(\Gamma_{M_2M_3}, \Gamma_{M_3M_9}, \Gamma_{M_9M_8}, \Gamma_{M_8M_7})$	$(1, 2, 3, 8, 15, 18, 21, 20, 19)$
Adjacent (Adj)	$(\Gamma_{M_7M_6}, \Gamma_{M_6M_2})$	$(19, 17, 16, 9, 4, 1)$

Table 5.11: Opposite and adjacent boundary edges and nodes used for computing multiscale basis functions

The fine scale pressures are calculated using Eq. (4.31). Derivative quantities for the fluid phase, i.e., the pressure flux and specific discharge, are computed

$$\nabla \mathbf{p}_{m(i)}^\alpha = \mathbf{B}^{\nabla p} \mathbf{p}_{m(i)}^\alpha, \quad \mathbf{q}_{m(i)}^\alpha = -\frac{\mathbf{k}}{\gamma_w} \nabla \mathbf{p}_{m(i)}^\alpha, \quad (5.13)$$

where the VEM based expression for $\mathbf{B}^{\nabla p}$ is provided under Eq. (3.53).

The process flow of the CMsVEM is graphically shown in Fig. 5.23.

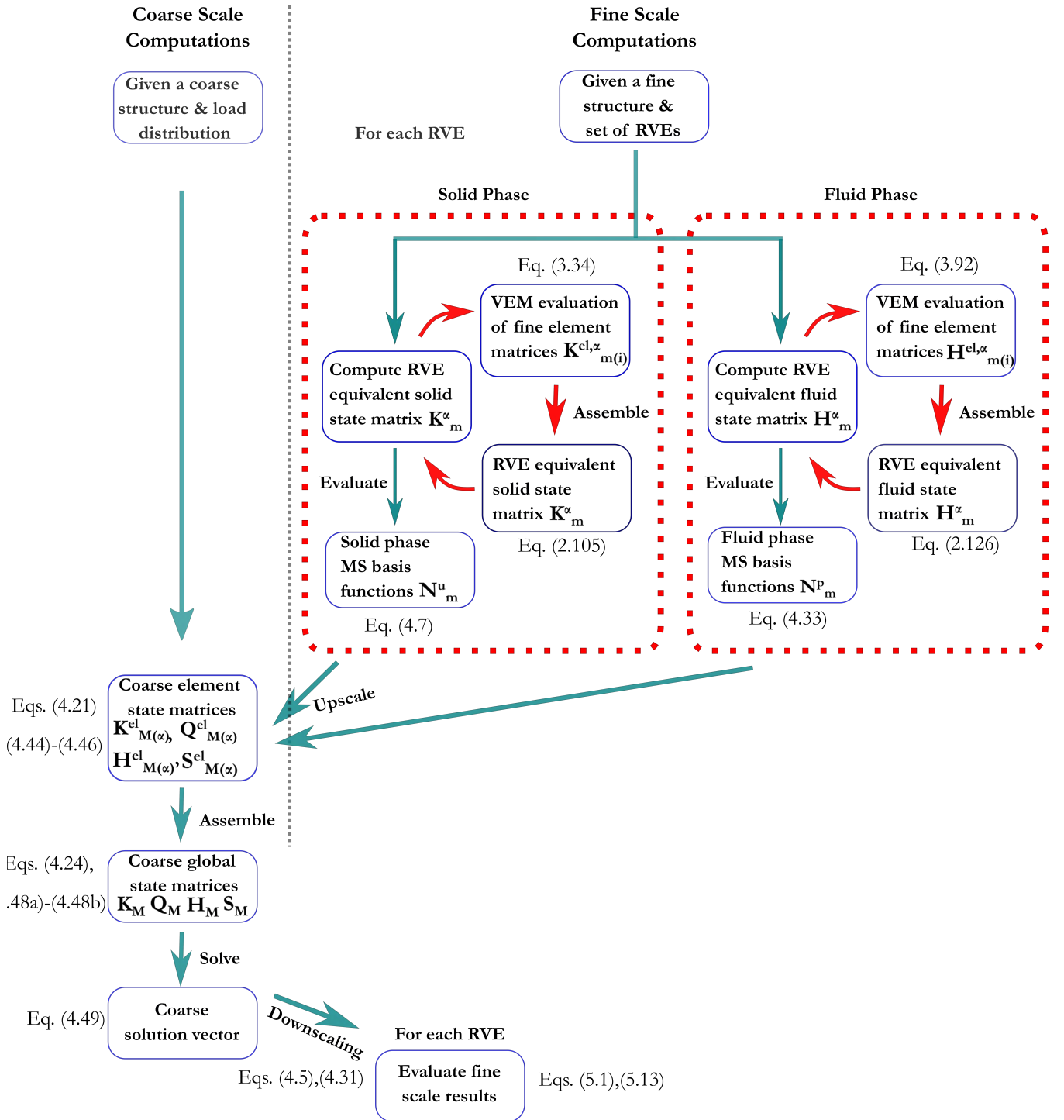


Figure 5.23: Process flow of the Coupled Multiscale Virtual Element procedure.

5.5 Numerical examples

In the following, the performance of the CMsVEM in terms of accuracy and computational efficiency is examined through three numerical examples. A first-order VEM ($k = 1$) is used in all cases. The accuracy of the displacement and stress/strain approximations is quantified through

the relative \mathcal{L}_2 norm and the \mathcal{H}_1 semi-norm, respectively as follows

$$\|\mathbf{u}_h^{\mathcal{Q}} - \mathbf{u}_{ref}^{\mathcal{Q}}\|_{\mathcal{L}_2} = \sqrt{\frac{1}{n_{\mathcal{Q}el}} \sum_{i=1}^{n_{\mathcal{Q}el}} \frac{\langle \mathbf{u}_{h(i)}^{\mathcal{Q}} - \mathbf{u}_{ref(i)}^{\mathcal{Q}}, \mathbf{u}_{h(i)}^{\mathcal{Q}} - \mathbf{u}_{ref(i)}^{\mathcal{Q}} \rangle}{\langle \mathbf{u}_{ref(i)}^{\mathcal{Q}}, \mathbf{u}_{ref(i)}^{\mathcal{Q}} \rangle}} \quad (5.14a)$$

$$\|\mathbf{u}_h^{\mathcal{Q}} - \mathbf{u}_{ref}^{\mathcal{Q}}\|_{\mathcal{H}_1} = \sqrt{\frac{1}{n_{\mathcal{Q}el}} \sum_{i=1}^{n_{\mathcal{Q}el}} \frac{\langle \boldsymbol{\varepsilon}(\mathbf{u}_{h(i)}^{\mathcal{Q}}) - \boldsymbol{\varepsilon}(\mathbf{u}_{ref(i)}^{\mathcal{Q}}), \boldsymbol{\sigma}(\mathbf{u}_{h(i)}^{\mathcal{Q}}) - \boldsymbol{\sigma}(\mathbf{u}_{ref(i)}^{\mathcal{Q}}) \rangle}{\langle \boldsymbol{\varepsilon}(\mathbf{u}_{ref(i)}^{\mathcal{Q}}), \boldsymbol{\sigma}(\mathbf{u}_{ref(i)}^{\mathcal{Q}}) \rangle}}. \quad (5.14b)$$

Similarly, the accuracy of the pressure and the pressure flux/specific discharge approximations is quantified as

$$\|\mathbf{p}_h^{\mathcal{Q}} - \mathbf{p}_{ref}^{\mathcal{Q}}\|_{\mathcal{L}_2} = \sqrt{\frac{1}{n_{\mathcal{Q}el}} \sum_{i=1}^{n_{\mathcal{Q}el}} \frac{\langle \mathbf{p}_{h(i)}^{\mathcal{Q}} - \mathbf{p}_{ref(i)}^{\mathcal{Q}}, \mathbf{p}_{h(i)}^{\mathcal{Q}} - \mathbf{p}_{ref(i)}^{\mathcal{Q}} \rangle}{\langle \mathbf{p}_{ref(i)}^{\mathcal{Q}}, \mathbf{p}_{ref(i)}^{\mathcal{Q}} \rangle}} \quad (5.15a)$$

$$\|\mathbf{p}_h^{\mathcal{Q}} - \mathbf{p}_{ref}^{\mathcal{Q}}\|_{\mathcal{H}_1} = \sqrt{\frac{1}{n_{\mathcal{Q}el}} \sum_{i=1}^{n_{\mathcal{Q}el}} \frac{\langle \nabla \mathbf{p}_{h(i)}^{\mathcal{Q}} - \nabla \mathbf{p}_{ref(i)}^{\mathcal{Q}}, \mathbf{q}(\mathbf{p}_{h(i)}^{\mathcal{Q}}) - \mathbf{q}(\mathbf{p}_{ref(i)}^{\mathcal{Q}}) \rangle}{\langle \nabla \mathbf{p}_{ref(i)}^{\mathcal{Q}}, \mathbf{q}(\mathbf{p}_{ref(i)}^{\mathcal{Q}}) \rangle}}. \quad (5.15b)$$

To enable fair comparisons the relative \mathcal{L}_2 and \mathcal{H}_1 error norms are computed over a query mesh with $n_{\mathcal{Q}el}$ elements unless stated otherwise. The terms $\mathbf{u}_h^{\mathcal{Q}}$, $\mathbf{p}_h^{\mathcal{Q}}$, $\mathbf{u}_{ref}^{\mathcal{Q}}$ and $\mathbf{p}_{ref}^{\mathcal{Q}}$ denote the numerically evaluated and reference displacements and pressures, interpolated at the nodes of the query mesh \mathcal{Q} , respectively. The operator $\langle \cdot, \cdot \rangle$ represents the scalar product. All reference solutions \mathbf{u}_h and \mathbf{p}_h are obtained through finely discretized VEM solutions. All solutions were performed using our in-house source codes developed in Matlab.

5.5.1 Porous domain with cavity

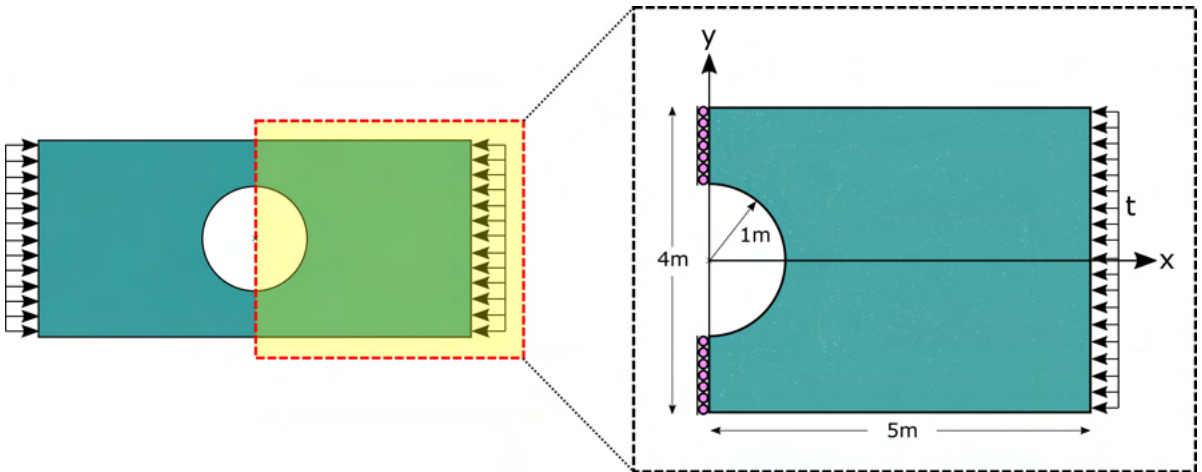


Figure 5.24: Geometry and boundary conditions of a porous domain with circular cavity.

A rectangular porous domain with dimensions $10m \times 4m$ is considered, with a cavity of radius $R = 1m$ as shown in Fig. 5.24. Only half the domain is analysed due to symmetry. The boundary conditions are also shown in Fig. 5.24. The right edge is exposed to air and maintains a pressure $p = 0$. Null flow conditions are imposed at all boundaries, i.e., $\nabla p \cdot \mathbf{n} = 0$. A compressive load denoted by $\mathbf{t} = [t_x, 0]^T$, where $t_x = 75 \text{ kN/m}$ is incrementally applied on the right edge of the

Parameter	E	ν	γ_f	K_s	K_f	\mathbf{g}	ρ_s	ρ_f	n	α_B
	[MPa]	[/]	[Pa · s]	[Pa]	[Pa]	[m · s ⁻²]	kg · m ⁻³	kg · m ⁻³	[/]	[/]
Value	5	0.2	10 ⁻³	3 × 10 ⁴	10 ⁴	0	10 ³	10 ³	0.2	1

Table 5.12: Homogeneous material parameters used

domain. The loading history is shown in Fig. 5.25. A homogeneous material is assumed over the

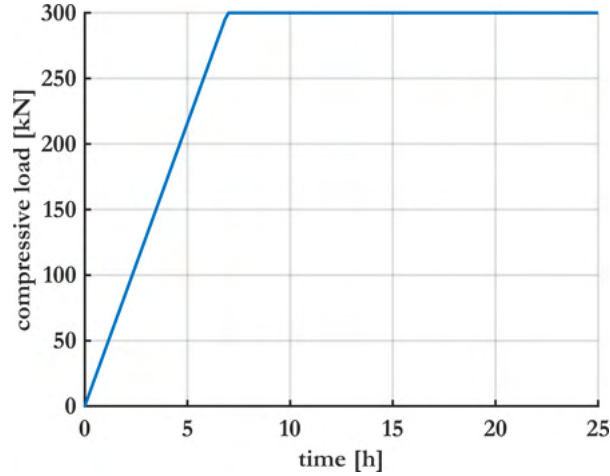


Figure 5.25: Compressive loading history.

entire domain and the corresponding material parameters used are summarized in Table 5.12.

Three discretization schemes are used as shown in Fig. 5.26 and summarized in Table 5.13. Mesh 1 (Fig. 5.26a) is a pure VEM mesh of CVT elements with an average diameter $h = 0.1076m$. Mesh 2 (Fig. 5.26b) is a multiscale mesh comprising 50 coarse CVT elements of average diameter $h = 0.7880m$. Each coarse element clusters 50 fine CVT elements. Mesh 3 (Fig. 5.26c) is also a multiscale mesh consisting of 250 coarse CVT elements of average diameter $h = 0.5543m$. Here, each coarse element clusters 10 fine CVT elements.

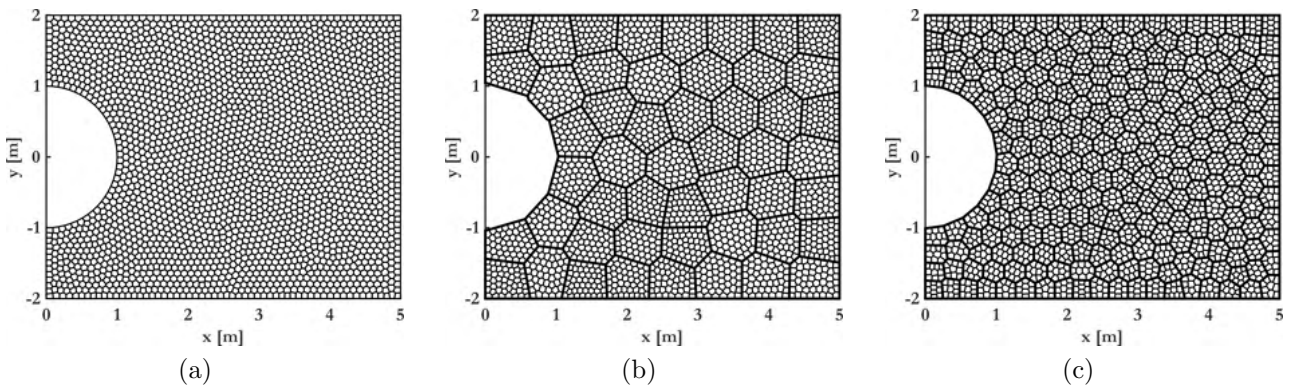


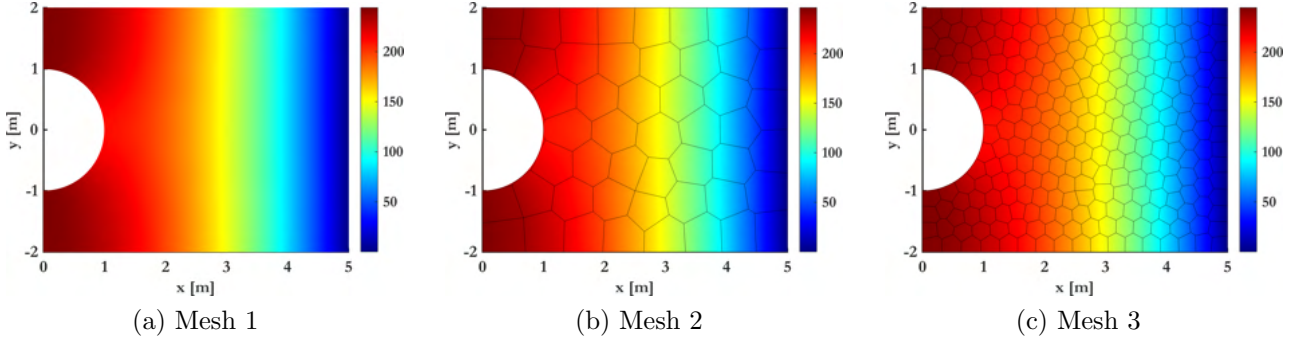
Figure 5.26: (a) Mesh 1, (b) Mesh 2, (c) Mesh 3.

Field contours

In all cases, the maximum pore-fluid pressures occur at $t_i = 6.83$ hours, $i = 42$; these are shown in Fig. 5.27. The corresponding displacement contours u_x and u_y are shown in Figs. 5.28 and 5.29,

Label	Full Mesh	Multiscale Mesh	
		Macro	Micro
Mesh 1	$n_{el} = 2500$	-	-
Mesh 2	$n_{el} = 2500$	$n_{M_{el}} = 50$	$n_{m_{el}} = 50$
Mesh 3	$n_{el} = 2500$	$n_{M_{el}} = 250$	$n_{m_{el}} = 10$

Table 5.13: Discretization scheme specifications.

Figure 5.27: p : pressures of pore fluid at $t_i = 6.83$ hours, $i = 42$.

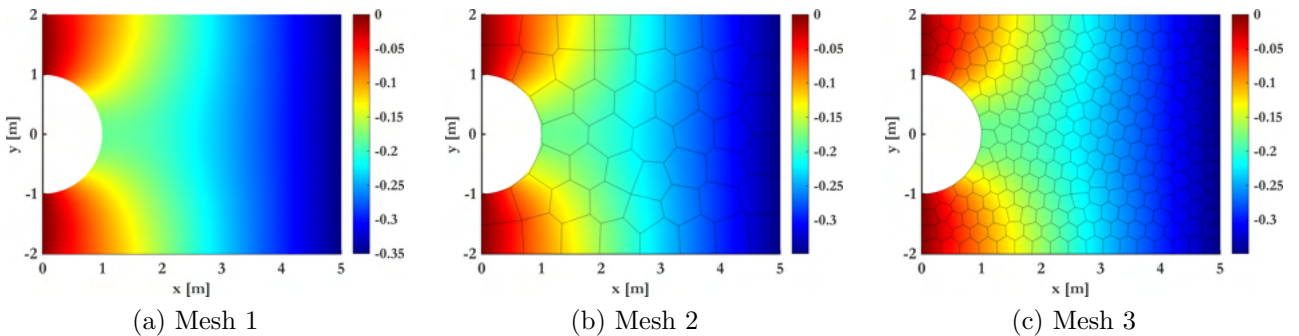
respectively. The pressures computed by the method over Mesh 2 and Mesh 3 are nearly identical to the reference VEM solution, as illustrated in Fig. 5.27. Similarly, the displacements u_x and u_y evaluated over Meshes 2 and 3 are found to be equivalent to the associated Mesh 1 contours. This can be seen from Figs. 5.28 and 5.29, respectively. It can be concluded from this that the CMsVEM procedure over Mesh 2 proves sufficient for computing primary quantities, while offering stark reductions in computational complexity.

The stress contours σ_{xx} , σ_{yy} , σ_{xy} are illustrated in Figs. 5.30 , 5.31 , and 5.32, respectively. The Darcy velocities v_x and v_y are shown in Figs. 5.33 and 5.34, respectively. The Darcy velocity is evaluated through the following expression:

$$\mathbf{v} = \mathbf{q}/n, \quad (5.16)$$

where n denotes the porosity and \mathbf{q} is the Darcy flux computed using Eq. (4.50).

The stresses σ_{xx} , σ_{yy} , σ_{xy} and the Darcy velocities v_x , v_y computed over Mesh 2 show significant deviations from the reference solution i.e., Mesh 1. Conversely, Mesh 3 offers practically equivalent

Figure 5.28: u_x : x-Displacements of solid skeleton at $t_i = 6.83$ hours, $i = 42$.

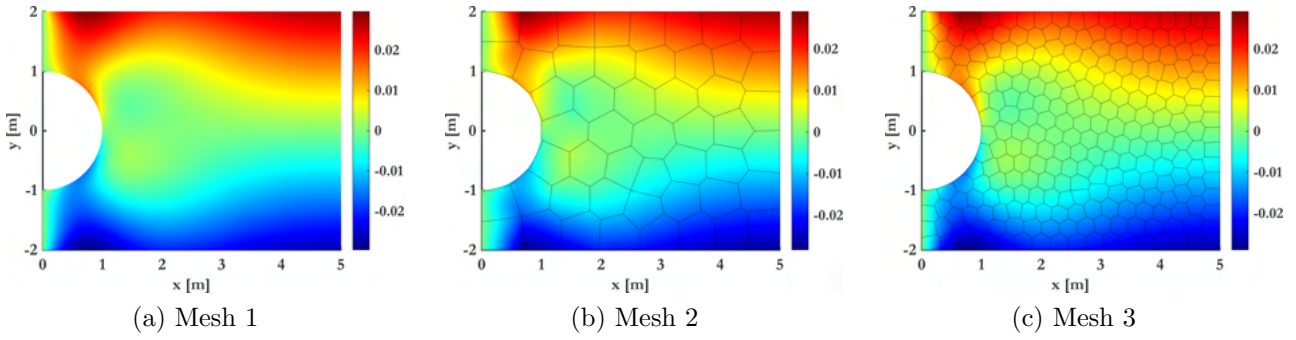


Figure 5.29: u_y : y -Displacements of solid skeleton at $t_i = 6.83$ hours, $i = 42$.

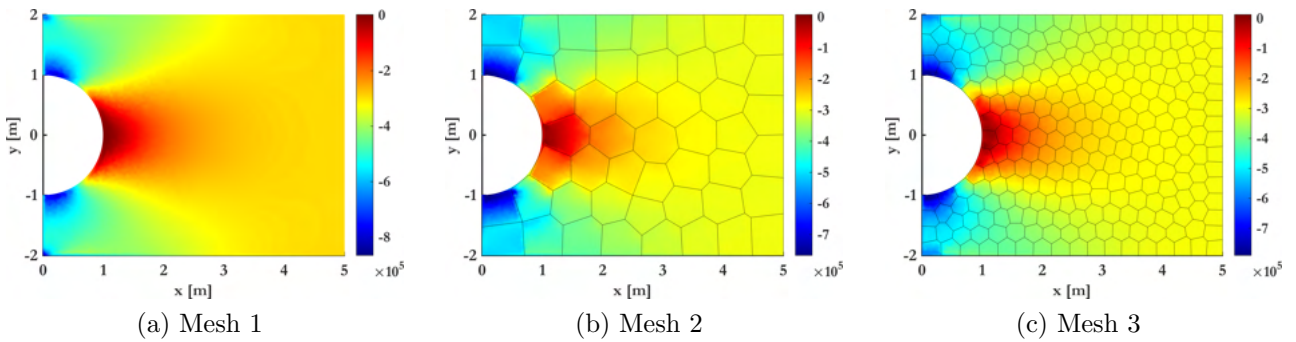


Figure 5.30: σ_{xx} : Stresses of solid skeleton at $t_i = 6.83$ hours, $i = 42$.

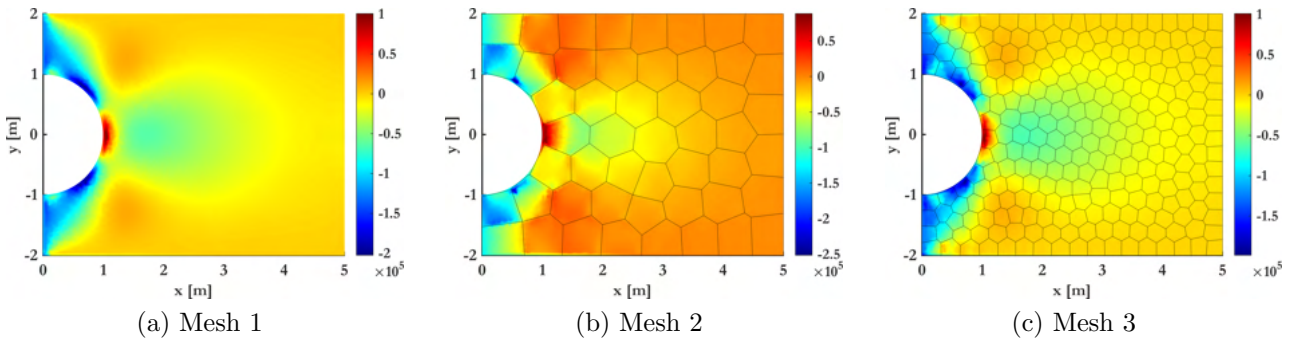


Figure 5.31: σ_{yy} : Stresses of solid skeleton at $t_i = 6.83$ hours, $i = 42$.

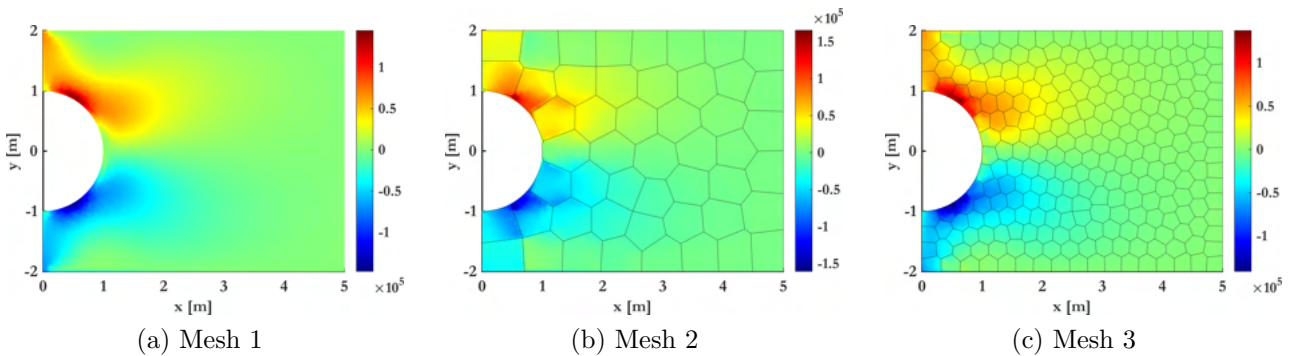


Figure 5.32: σ_{xy} : Stresses of solid skeleton at $t_i = 6.83$ hours, $i = 42$.

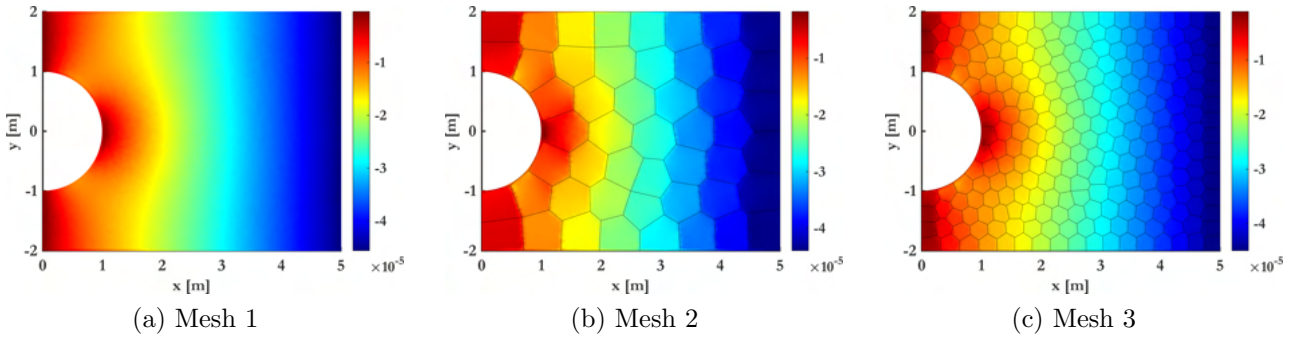


Figure 5.33: v_x : Darcy velocity of pore fluid at $t_i = 6.83$ hours, $i = 42$.

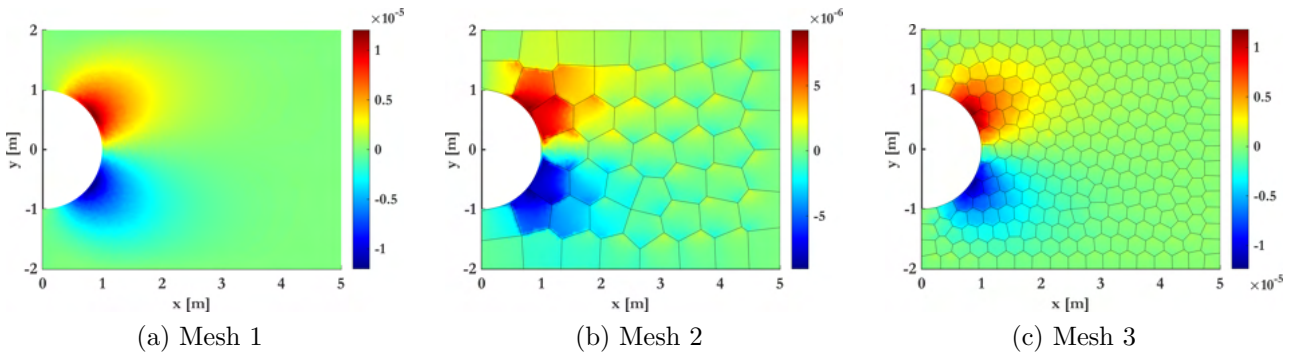


Figure 5.34: v_y : Darcy velocity of pore fluid at $t_i = 6.83$ hours, $i = 42$.

results. Hence, Mesh 2 is insufficient in capturing local variations in secondary or derived fields. A finer coarse discretization, i.e., Mesh 3 is required in such cases. Despite proving more expensive than Mesh 2, it still offers significant reduction in computational effort compared to Mesh 1. This trade-off between accuracy and computational effort is studied more rigorously in Section 5.5.1 and 5.5.1, respectively.

Convergence behaviour

To investigate the convergence behaviour of the proposed CMsVEM, six different discretization schemes are considered at the coarse scale, i.e., with 25, 50, 100, 250, 500 and 1000 polygonal elements. For each case, the five different micro-structure discretizations shown in Fig. 5.35 are employed and the relative \mathcal{L}_2 and \mathcal{H}_1 error norms are evaluated. A standard VEM solution with 5000 CVT elements is used as the reference solution.

Figs. 5.36a and 5.36b summarize the convergence analysis results for the solid skeleton displacements and stresses, respectively. The error in the solid skeleton quantities reduces for finer coarse and micro-element discretizations. The case of 250 coarse elements and 25 micro-elements per coarse element is an upper bound below which all solutions seems to provide identical and well-behaved results. This is not the case for the fluid phase, where the error is primarily controlled by the coarse element size rather than the micro-structure resolution as shown in Figs. 5.36c and 5.36d for the pressures and fluxes, respectively. Although this observation hints at the idea of resolving the two governing equations at different meshes hence further reducing computational costs, it is important to mention that this example involves a homogeneous domain where such a convergence response is to be expected.

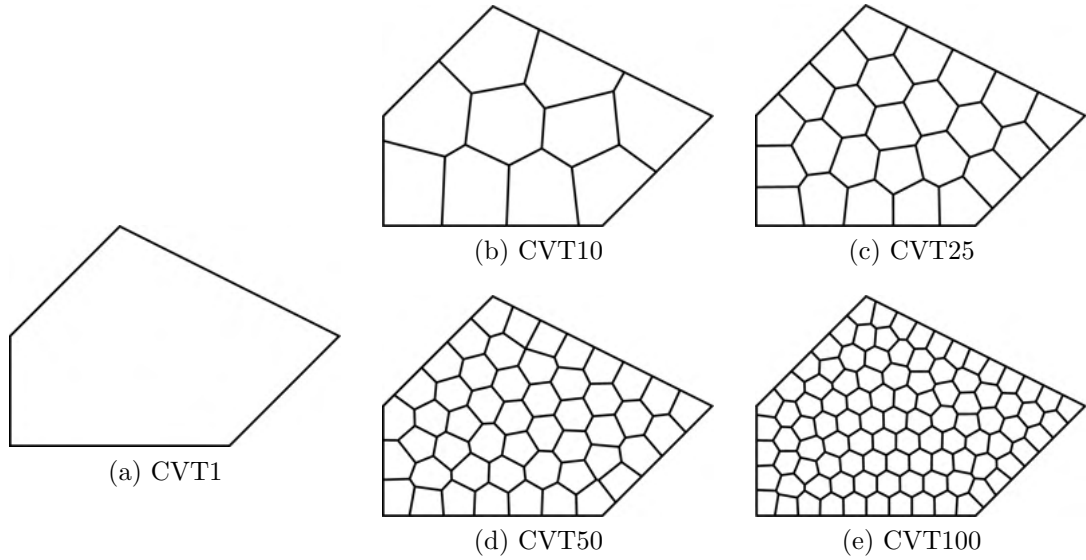


Figure 5.35: 5 microstructures illustrated for an arbitrarily chosen polygonal coarse element.

	$\ \mathbf{u}_h - \mathbf{u}_{ex}\ _{\mathcal{L}_2}$	$\ \mathbf{p}_h - \mathbf{p}_{ex}\ _{\mathcal{L}_2}$	$\ \mathbf{u}_h - \mathbf{u}_{ex}\ _{\mathcal{H}_1}$	$\ \mathbf{p}_h - \mathbf{p}_{ex}\ _{\mathcal{H}_1}$
CVT1	1.6901	1.8265	0.8993	1.0316
CVT10	2.0504	2.0008	0.9279	1.0121
CVT25	1.8949	2.0470	0.9265	1.0141
CVT50	1.7623	1.6956	0.8926	1.0049
CVT100	2.0117	1.7914	1.1331	0.9780

Table 5.14: Rates of error convergence.

The error convergence rates for both phases are summarized in Table 5.14. These are found to nearly coincide with the theoretical convergence rates of 2 in the \mathcal{L}_2 and 1 in the \mathcal{H}_1 relative error norms, respectively. The theoretical convergence rates are provided in [330] for elastostatic problems. Hence, all microstructural configurations result in near optimal error convergence rates. This establishes the CMsVEM as an alternative to the CMsFEM when flexible mesh generation is required.

Discussion on computational effort

To examine the computational toll of the CMsVEM, the time required for preprocessing, analysis, and downscaling is recorded. These times are averaged over five runs and are illustrated as a function of the coarse and fine discretizations used in 5.5.1.

The time required to create the coarse elements is displayed in Fig. 5.37a. This includes the evaluation of the multiscale basis functions and the upscaling procedure used to create coarse element state matrices. A linear front is observed, indicating that the number of operations required depends on both, the number of coarse and fine elements. This is expected as in this case the RVEs are non-periodic and the basis-functions are evaluated for each coarse element individually. In the case of periodically repeated RVEs, basis functions would be evaluated once for each periodic group and the computational time would be independent of the number of coarse elements involved.

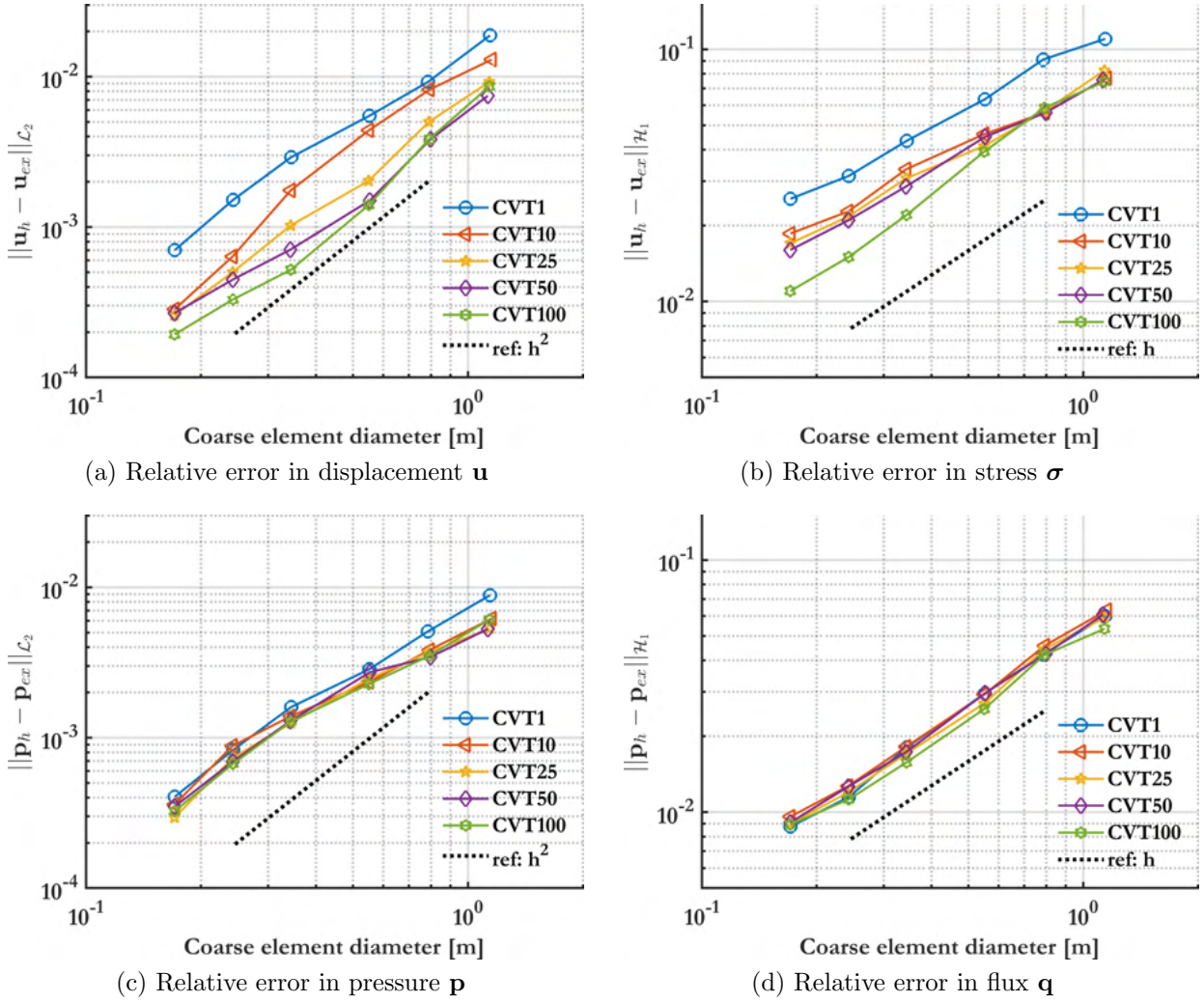


Figure 5.36: Convergence results for 5 microstructure configurations at $t_i = 6.83$ hours, $i = 42$.

The time required for the assembly of the global coarse state matrices \mathbf{K}_M , \mathbf{Q}_M , \mathbf{H}_M , \mathbf{S}_M , and the solution of global system of linear equations at the coarse scale through finite-differences are shown in Figs. 5.37b and 5.37c, respectively. It is evident that these times depend exclusively on the number of coarse elements. The assembly procedure is of the order of magnitude $1E - 02$ seconds and can be considered negligible in comparison to the solve times. This can be accounted for by the fact that the global state matrices are assembled only once.

The time required for downscaling is provided in Fig. 5.37d. This includes the procedure described in Section 4.3.3. The computational effort here is a function of the coarse and fine scale discretizations. Finally, to account for possible overheads in the computation, the total time taken for the entire CMsVEM is provided in Fig. 5.37e.

5.5.2 Heterogeneous Soil Domain

A fully saturated soil domain of $40 \text{ m} \times 25 \text{ m}$ shown in Fig. 5.38 is considered. Two discretizations are examined, which are summarized in Table 5.15. In the first (see also, Fig. 5.38a) a coarse structured grid containing 40 (8×5) quadrilateral elements is considered. Each coarse element comprises a micro-mesh of 5×5 quadrilateral micro-elements. The total number of micro-

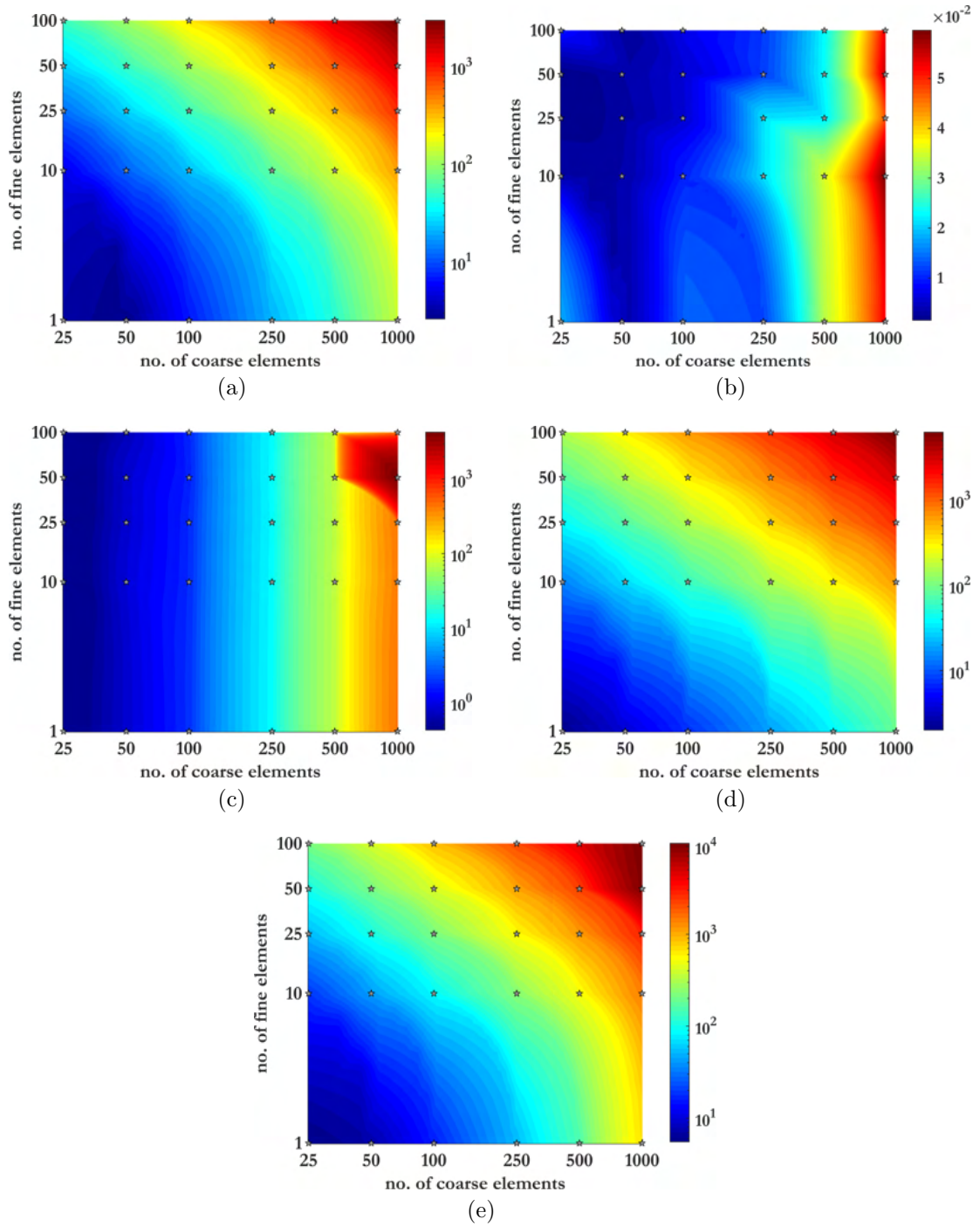


Figure 5.37: Computational time (in seconds) for (a) Coarse elements creation (b) Global coarse element state matrices assembly (c) Solution at the coarse scale (d) Down-scaling (e) Total time.

Label	Full Mesh	Multiscale Mesh	
		Macro	Micro
QUAD	40 x 25	8 x 5	5 x 5
CVT	1000	40	25

Table 5.15: Discretization schemes

elements is 1000. The second discretization, shown in Fig. 5.38b involves an unstructured coarse mesh containing 40 uniform CVT elements. In this case, each coarse element clusters 25 CVT fine elements and the total number of micro-elements is again 1000. A reference discretization of 40×25 quadrilateral elements is considered to facilitate comparisons. The domain is subjected to a compressive load at the top boundary with the loading history shown in Fig. 5.39. The domain is fully supported at its bottom edge. Sliding conditions are considered in the left and right-most edges.

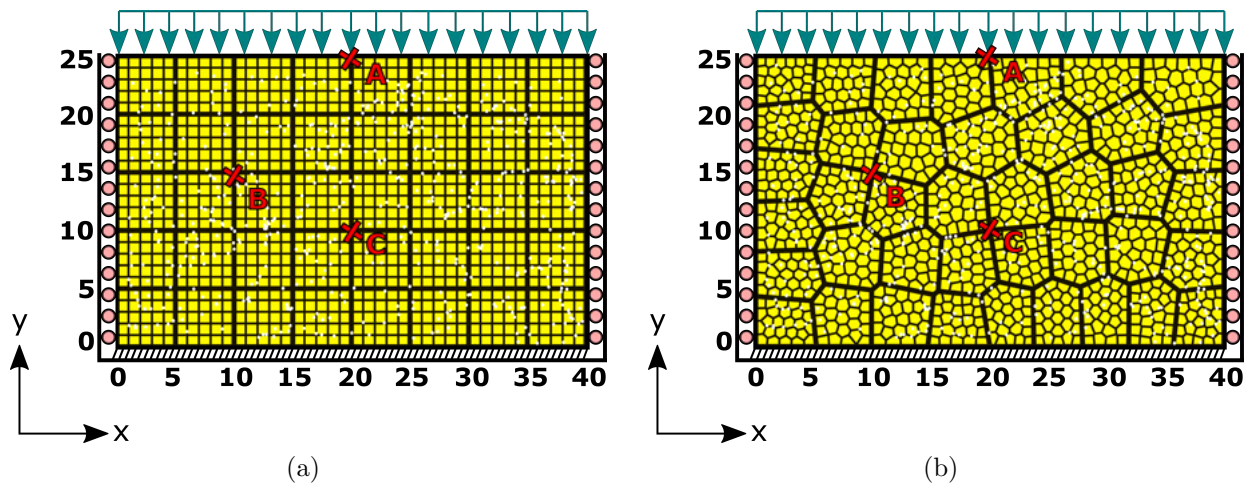


Figure 5.38: Saturated $40 \text{ m} \times 25 \text{ m}$ soil domain with (a) 8×5 coarse structured quadrilateral mesh and 40×25 fine structured quadrilateral mesh, (b) coarse unstructured CVT polygonal mesh with 40 elements and fine unstructured CVT polygonal mesh with 1000 elements.

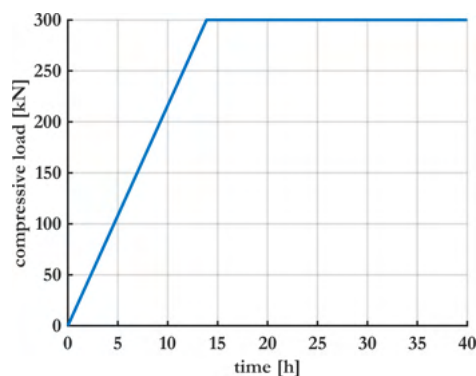


Figure 5.39: Loading history.

To investigate the fidelity of the phase-decoupling hypothesis used in deriving the multiscale basis functions in Section 4.3.1, two heterogeneous descriptions of the domain are examined. To investigate the influence of the assumed boundary conditions at the coarse element boundary for

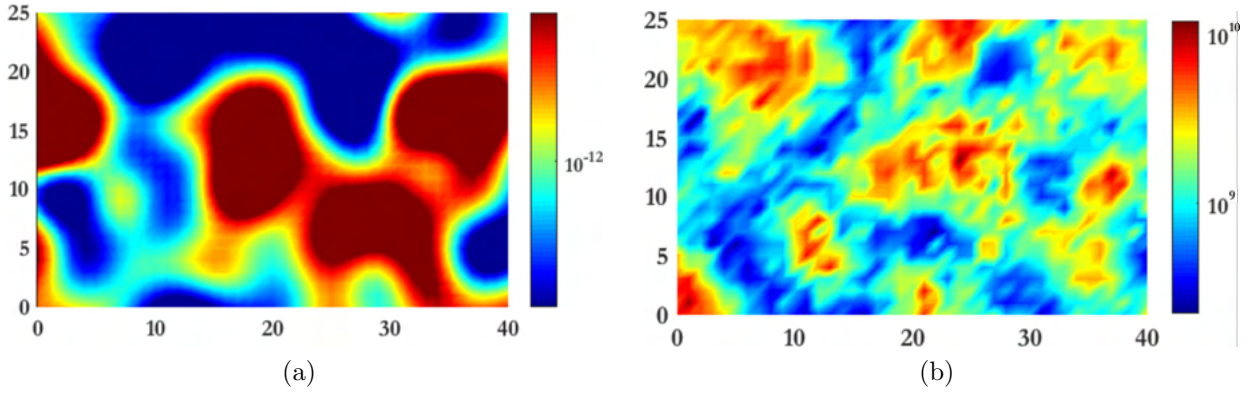


Figure 5.40: (a) Randomly sampled heterogeneous isotropic permeability field, (b) Randomly sampled heterogeneous Young's modulus.

Parameter	ν	γ_f	K_s	K_f	\mathbf{g}	ρ_s	ρ_f	n
		[Pa · s]	[Pa]	[Pa]	[m · s ⁻²]	[kg · m ⁻³]	[kg · m ⁻³]	
Value	0.2	10^{-3}	10^{12}	2×10^9	0	2.8×10^3	10^3	0.2

Table 5.16: Homogeneous material parameters of the soil domain.

the evaluation of the micro-basis functions two cases are run for each heterogeneous description, i.e., the case of linear and oscillatory boundary conditions. The methods used are summarized in Table 5.17.

Case 1 - Heterogeneous permeability \mathbf{k}

In this case, isotropic heterogeneous random permeability fields are considered, sampled from a lognormal distribution of mean $\mu(\log(\mathbf{k})) = -12$ and standard deviation $\sigma(\log(\mathbf{k})) = 1.0$. The field has a maximum and minimum value of $\mathbf{k} = 5 \times 10^{-9} \text{ m}^2$ and $\mathbf{k} = 7 \times 10^{-16} \text{ m}^2$, respectively. A snapshot is provided in Fig. 5.40a. For the solid phase, a homogeneous modulus $E = 5 \times 10^9 \text{ Pa}$ is employed. The remaining material parameters are uniformly distributed over the entire domain and are summarized in Table 5.16. Due to the random distribution of the permeability, multiscale basis functions are evaluated all coarse elements individually.

Three points of interest, i.e., points A(20, 25), B(10,15), and C(20,10) are considered as shown in Fig. 5.38. The time evolution of the expectation values of displacements u_x , u_y , and pressures p obtained over $n_s = 5000$ samples at these points are illustrated in Fig. 5.41.

Due to symmetry the horizontal displacement component u_x at Points A and C is practically

Abbreviation	Method	Mesh-Type	Boundary Conditions
VEM	Virtual Element Method	Quadrilateral	-
MS-QUAD LIN	Multiscale Virtual Element Method	Quadrilateral	Linear
MS-CVT LIN	Multiscale Virtual Element Method	Polygonal	Linear
MS-QUAD OSC	Multiscale Virtual Element Method	Quadrilateral	Oscillatory
MS-CVT OSC	Multiscale Virtual Element Method	Polygonal	Oscillatory

Table 5.17: Methods investigated.

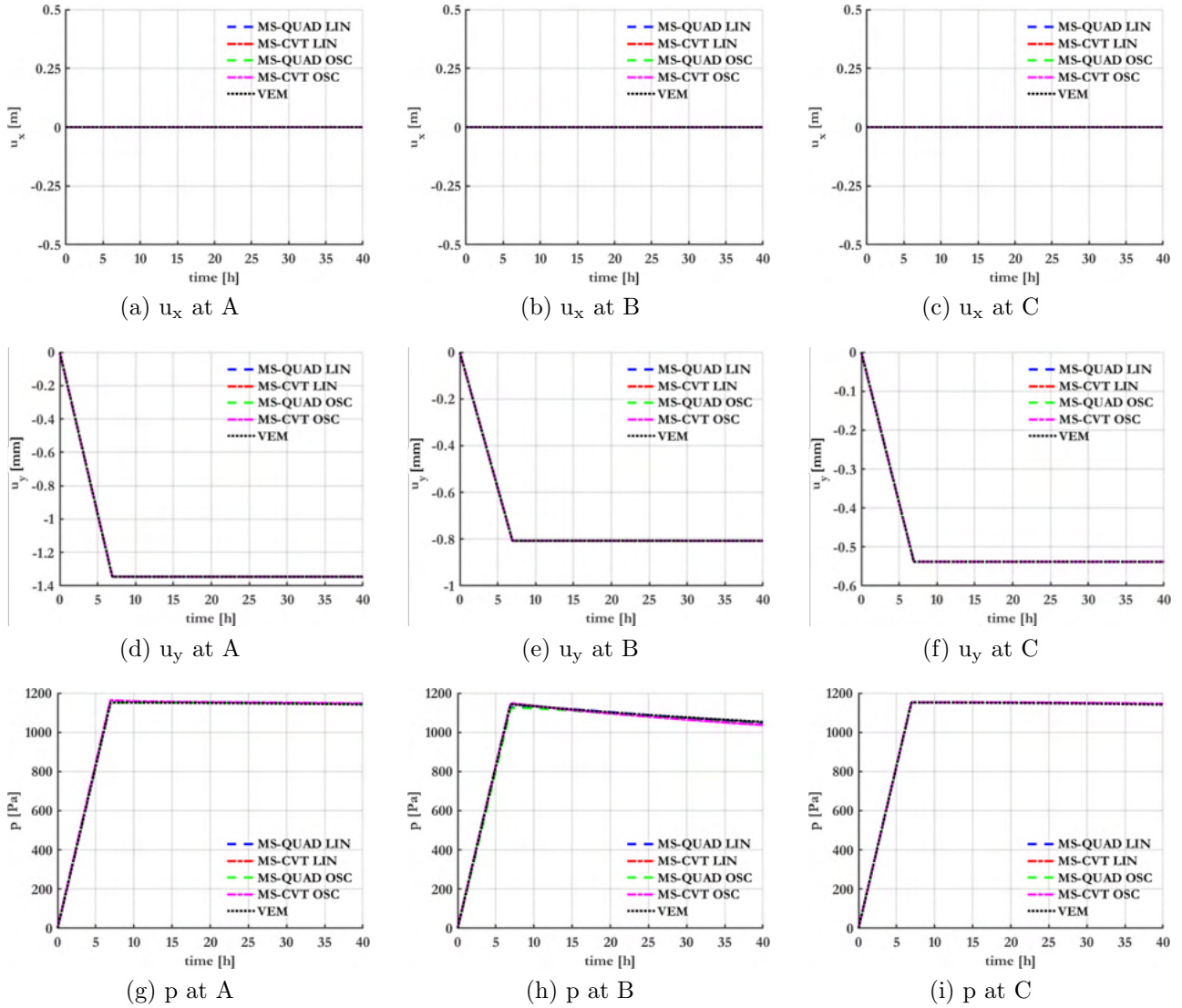


Figure 5.41: Time evolution $t = 40$ h of expectation values of horizontal displacement $E[u_x]$, vertical displacement $E[u_y]$, and pore-fluid pressure $E[p]$ at points A, B, and C, obtained for $n_s = 5000$ samples.

zero as illustrated in Figs. 5.41a and 5.41c, respectively. Minor deviations from zero are attributed to asymmetric permeability fields sampled from the lognormal distribution. As shown in Figs. 5.41 regardless of the boundary conditions employed, all CMsVEM runs match perfectly the standard VEM solutions.

Snapshots of the expectation values of the results obtained at $t = 40$ hours are shown in Figs. 5.42 and 5.43 for the vertical displacement component and the pressures, respectively.

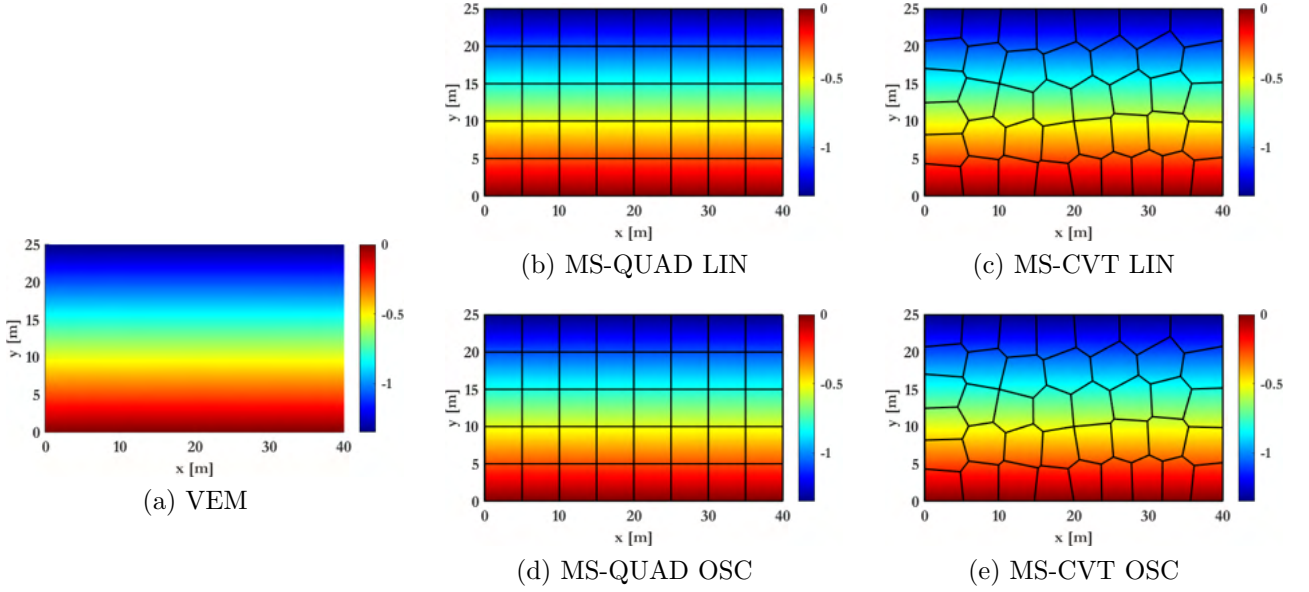


Figure 5.42: $E[u_y]$ displacement contours (in [mm]) at $t = 40$ h obtained for $n_s = 5000$ samples.

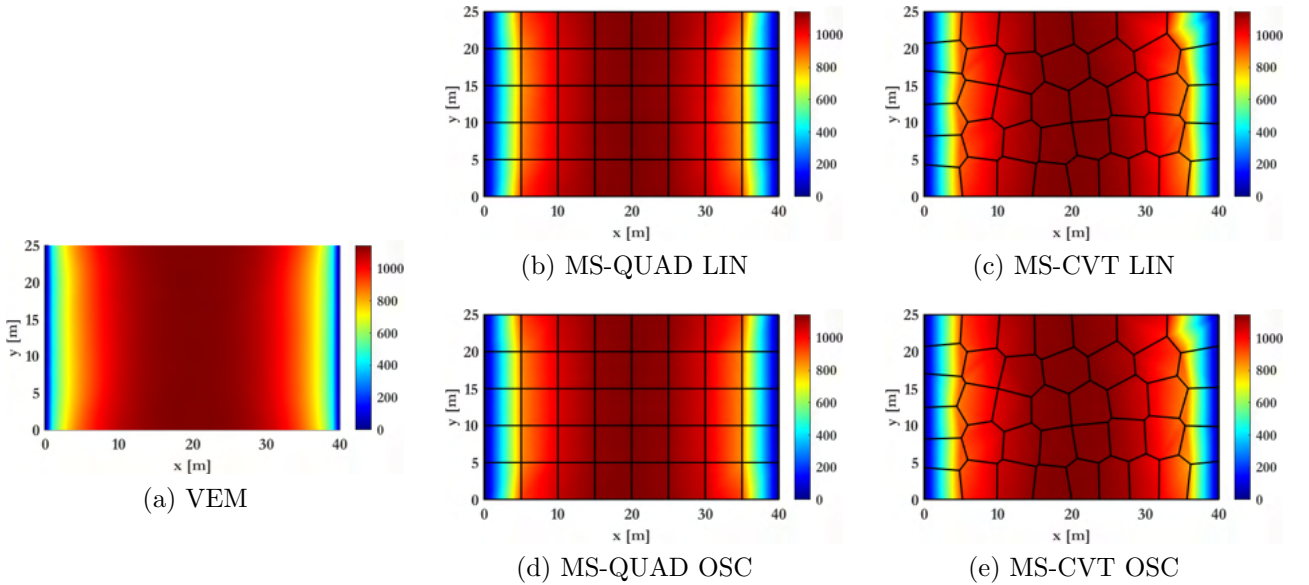


Figure 5.43: $E[p]$ pressure contours (in [Pa]) at $t = 40$ h obtained for $n_s = 5000$ samples.

Case 2 - Heterogeneous permeability k and heterogeneous Young's modulus E

Here, the heterogeneous permeability k field employed in the previous case is considered together with a heterogeneous Young's Modulus E distribution. The heterogeneous random

Young's modulus fields are defined with maximum and minimum values of $E = 1 \times 10^{10}$ Pa and $E = 7 \times 10^8$ Pa, respectively. A snapshot is provided in Fig. 5.40b. The remaining material parameters are uniformly distributed over the entire domain and are summarized in Table 5.16. As in the previous case, the multiscale basis functions are evaluated for all coarse elements individually.

The resulting time evolution of the expectation values of u_x , u_y , and p at points A, B and C as obtained over $n_s = 5000$ samples are shown in Fig. 5.44. Contrary to Case 1, the heterogeneities in the solid domain increase the granularity between the different methods considered. Although the accuracy of the predicted displacements is acceptable, the methods using oscillatory boundary conditions, i.e., MS-QUAD OSC and MS-CVT OSC provide the best match to the standard VEM solution. The differences are more pronounced in the predicted pressure fields Figs. 5.44, where MS-QUAD LIN and MS-CVT LIN consistently under-predict pressures at the three points.

The contours of expectation values for the horizontal and the vertical component of the displacement fields at $t = 40$ hours are shown in Figs. 5.45 and 5.46, respectively. The corresponding pressure field is shown in Fig. 5.47.

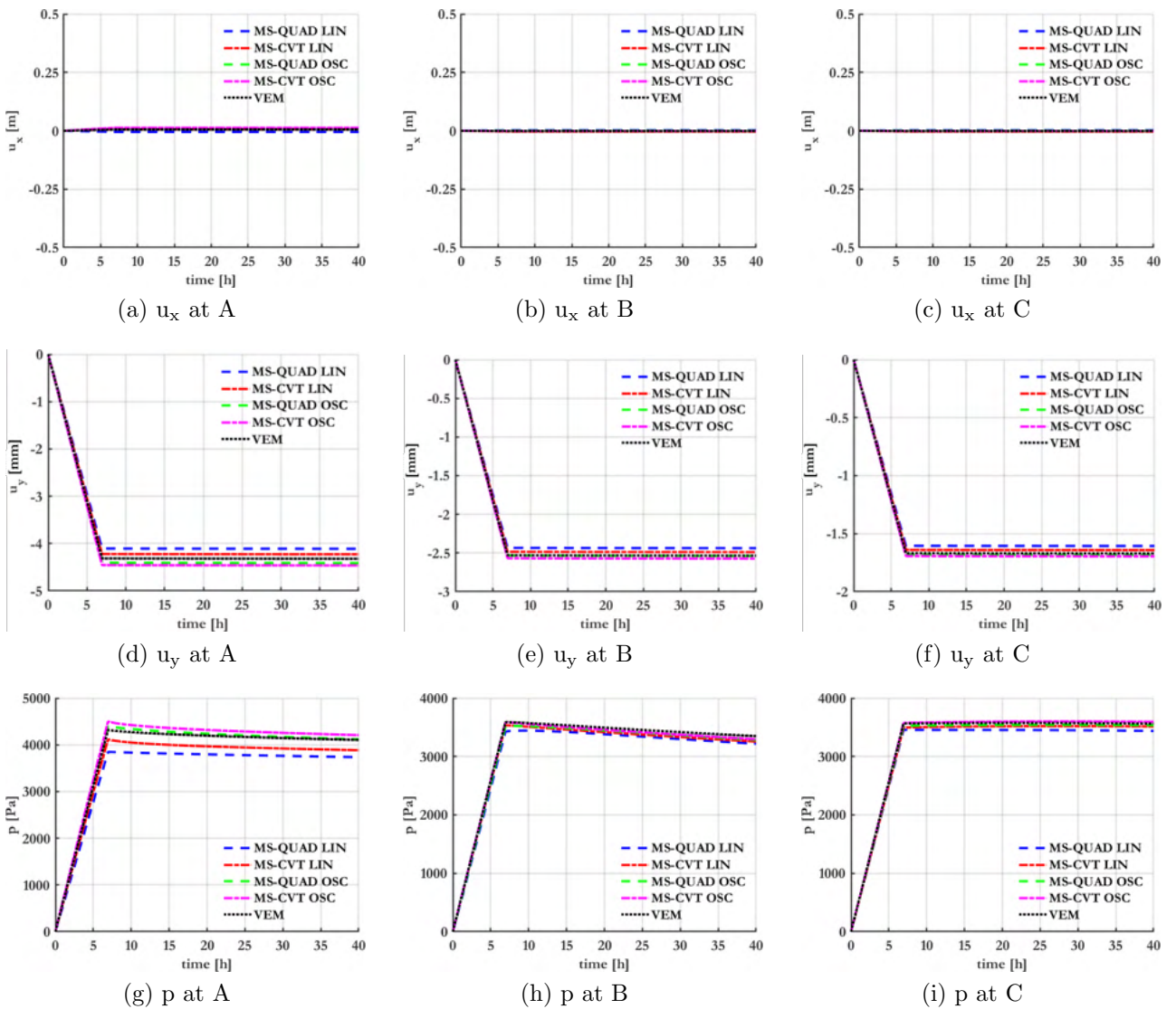


Figure 5.44: Time evolution $t = 40$ h of expectation values of horizontal displacement $E[u_x]$, vertical displacement $E[u_y]$, and pore-fluid pressure $E[p]$ at points A, B, and C, obtained for $n_s = 5000$ samples.

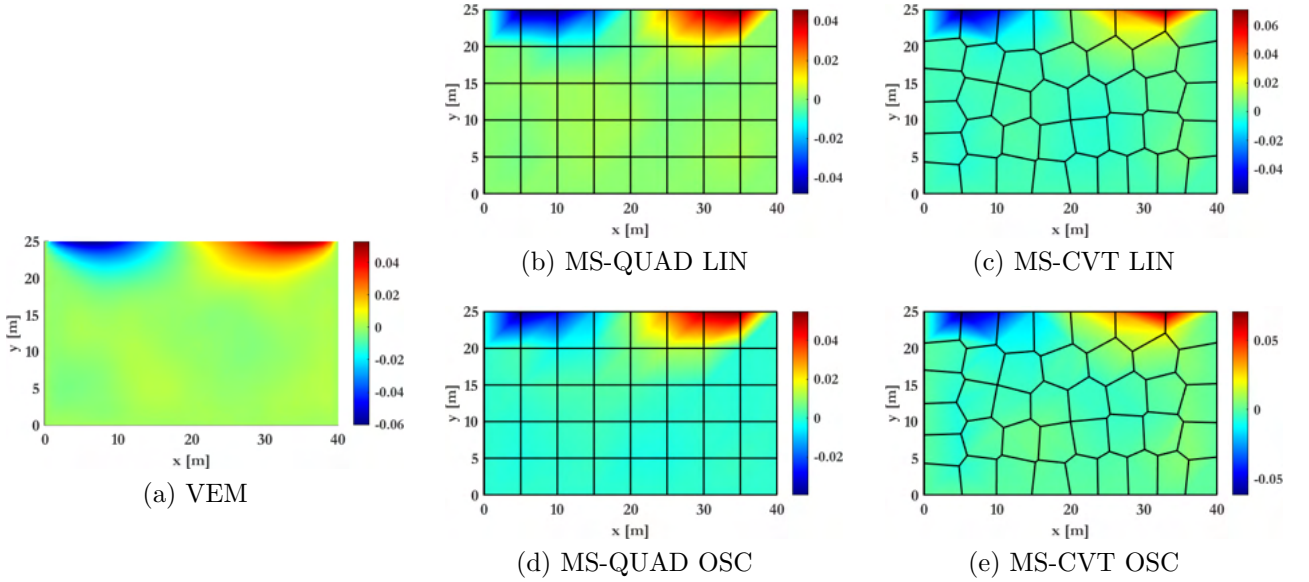


Figure 5.45: $E[u_x]$ displacement contours (in [m]) at $t = 40h$ obtained for $n_s = 5000$ samples.

The linear boundary conditions impose a strict constraint on the deformability of the heterogeneous micro-structure. This is consistent with the physics of the problem where a nonlinear displacement profile is to be expected due to the joined permeability and Young's modulus heterogeneity. The choice on the boundary conditions to be employed for the evaluation of the basis-functions should be driven by the physics. Using a decoupled scheme for the evaluation of the basis-functions on the other hand does not significantly affect the accuracy of the CMsVEM while imposing minimum costs on the evaluation of the basis vector. This observation could prove particularly beneficial in the case of nonlinear problems where a re-evaluation of the basis would be required. However such aspects are beyond the scope of this work.

To examine whether the oscillatory boundary conditions ensure compatibility of the fine scale solution across boundaries, contour plots of the total displacement, pressure, strain component ϵ_{yy} , and stress component σ_{yy} obtained at $t = 40$ hours for a single realization of the heterogeneous Young's modulus and permeability fields using oscillatory boundary conditions are shown in Figs. 5.48. In all cases, the downscaled quantities vary smoothly across the coarse element boundaries, despite the prevalence of significant heterogeneities.

Consistency and continuity properties are investigated in more detail by considering two neighbouring coarse elements, i.e. 16 and 31, as shown in Fig. 5.49. The interface encountered is non-conforming in nature. These elements are chosen as the underlying material description here is highly heterogeneous. Consequently, continuity of field variables at this interface should provide satisfactory guarantees for similar continuous behaviour across other coarse element interfaces as well. The total displacements $\|\mathbf{u}\|$ and strain ϵ_{yy} evaluated at the fine-scale interface nodes belonging to each coarse element are provided in Tables 5.18 and 5.19.

It can be seen from Tables 5.18 and 5.19 that $\|\mathbf{u}\|$ and ϵ_{yy} evaluated at the fine nodes corresponding to coarse node M_{47} , i.e., 1 and 29, and M_{50} , i.e., 15 and 5 are practically identical. Despite non-conformity of intermediate edge interface nodes, the quantities appear continuous here as well.

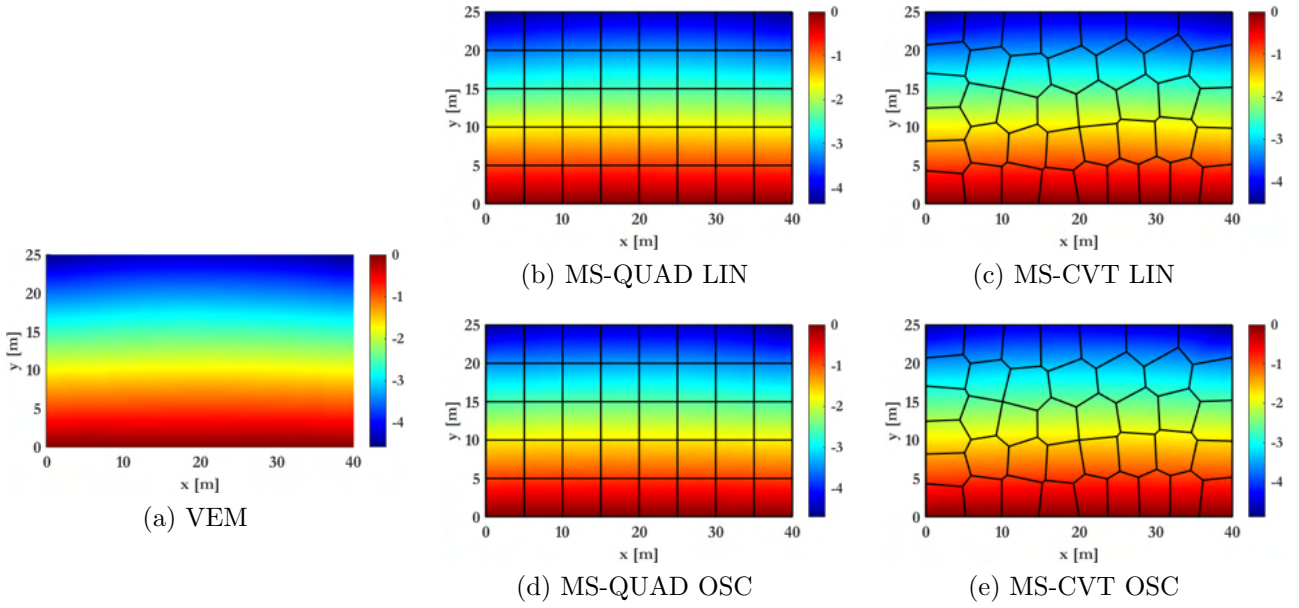


Figure 5.46: $E[u_y]$ displacement contours (in [mm]) at $t = 40h$ obtained for $n_s = 5000$ samples.

Fine Node	15	14	13	5	2	1
$\ \mathbf{u}\ $	3.19442	3.05568	2.98009	2.83392	2.70283	2.65383
ε_{yy}	-0.1645	-0.1645	-0.1646	-0.1647	-0.1647	-0.1648

Table 5.18: Fine-scale $\|\mathbf{u}\|$ (in [mm]) and $\varepsilon_{yy}(\times 10^{-3})$ along interface for coarse element 16.

Discussion on computational gains

The computational efficiency of the CMsVEM is assessed by recording times for critical procedures for all methods. All times displayed are averaged over five runs.

The time taken for assembling global coarse scale state matrices \mathbf{K}_M , \mathbf{Q}_M , \mathbf{H}_M and \mathbf{S}_M is shown in Fig. 5.50a. This includes the computation of multiscale basis functions and upscaling procedures used to create coarse element state matrices. All multiscale methods practically perform equally in this regard and offer a speedup of approximately a factor eight ($\approx 8\times$) when compared to the VEM. As using oscillatory boundary conditions when computing multiscale basis functions does not require more computational effort than the simpler case of linear boundaries, one should always prefer MS-QUAD OSC and MS-CVT OSC over MS-QUAD LIN and MS-CVT LIN in the event of highly heterogeneous material definitions.

The time taken for the solution procedure is illustrated in Fig. 5.50b. All multiscale methods

Fine Node	5	14	15	28	29
$\ \mathbf{u}\ $	3.19442	2.90025	2.82015	2.71886	2.65383
ε_{yy}	-0.165	-0.1649	-0.1648	-0.1649	-0.1649

Table 5.19: Fine-scale $\|\mathbf{u}\|$ (in [mm]) and $\varepsilon_{yy}(\times 10^{-3})$ along interface for coarse element 31.

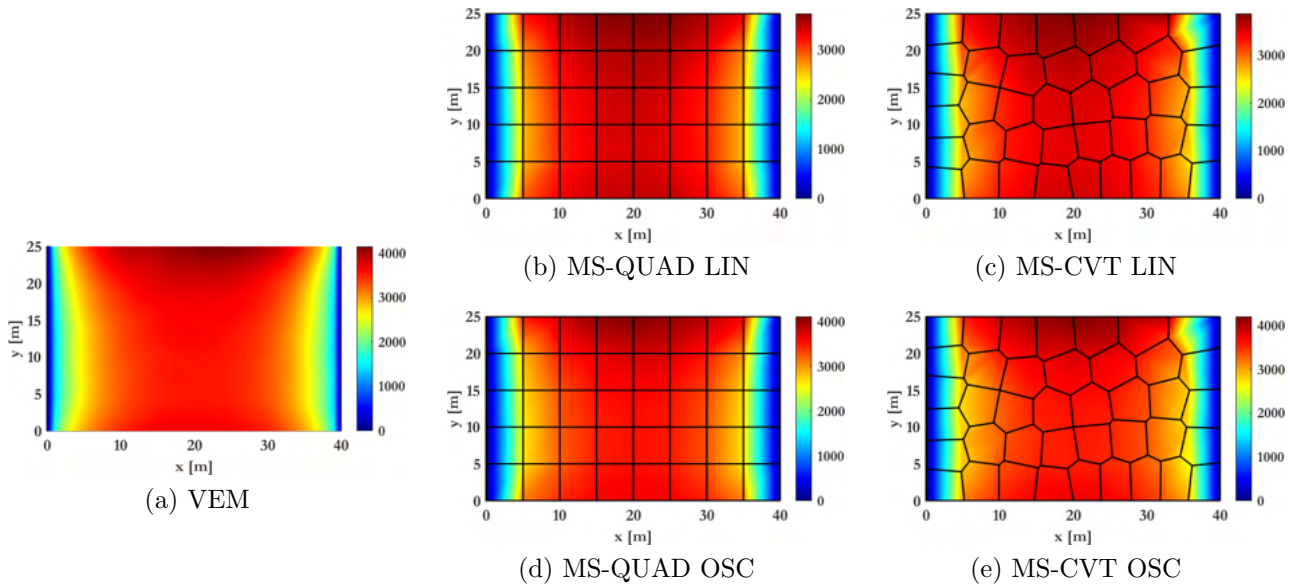


Figure 5.47: $E[p]$ pressure contours (in [Pa]) at $t = 40h$ obtained for $n_s = 5000$ samples.

again perform equally efficiently and offer a speedup of $\approx 200\times$ when compared to the VEM. This enormous reduction in computational effort is to be expected as the number of nodes in the multiscale procedures is significantly reduced in comparison to its VEM counterparts. Repeated matrix inversions in the case of finite-difference time domain solutions further establish the effectiveness of the CMsVEM.

The postprocessing times are displayed in Fig. 5.51a. This involves the downscaling procedure used to recover fine scale information and evaluating derivative quantities like stresses, strains and fluxes over fine element domains. Once again, all multiscale methods perform equivalently and offer a speedup of $\approx 2\times$ in comparison to the VEM. This is attributed to the fact that in the multiscale methods, the downscaling procedure is performed for each coarse element. This implicitly vectorizes the associated stress and flux computation loops. It is of interest to note that since the consolidation problem examined is linear, the multiscale basis functions are computed offline. As a result, no significant overheads are incurred to the overall solution procedure.

It can be seen from Fig. 5.51b that all multiscale methods offer an appreciable total speedup of $\approx 4\times$ when compared with the VEM. Such speedups prove extremely valuable when obtaining statistical moments for random field simulations using for e.g. classical Monte-Carlo approaches. In this example, expectation values for 5000 samples were computed, thus generating an overall speed up of $\approx 20000\times$ when compared to the VEM. A similar comparison between FEM, VEM, MsFEM and MsVEM is provided in Figs. 5.52 and 5.53. The VEM and MsVEM are found to offer quicker assembly and postprocessing computational times than their FEM and MsFEM counterparts.

5.5.3 Honeycomb structure

The honeycomb structure shown in Fig. 5.54 is considered herein. The overall dimensions of the domain are $5m \times 5m$. This domain consists of 25 periodically repeated heterogeneous unit cells. Each unit cell comprises a matrix with a Young's modulus $E = 5$ MPa and a stiffer inclusion

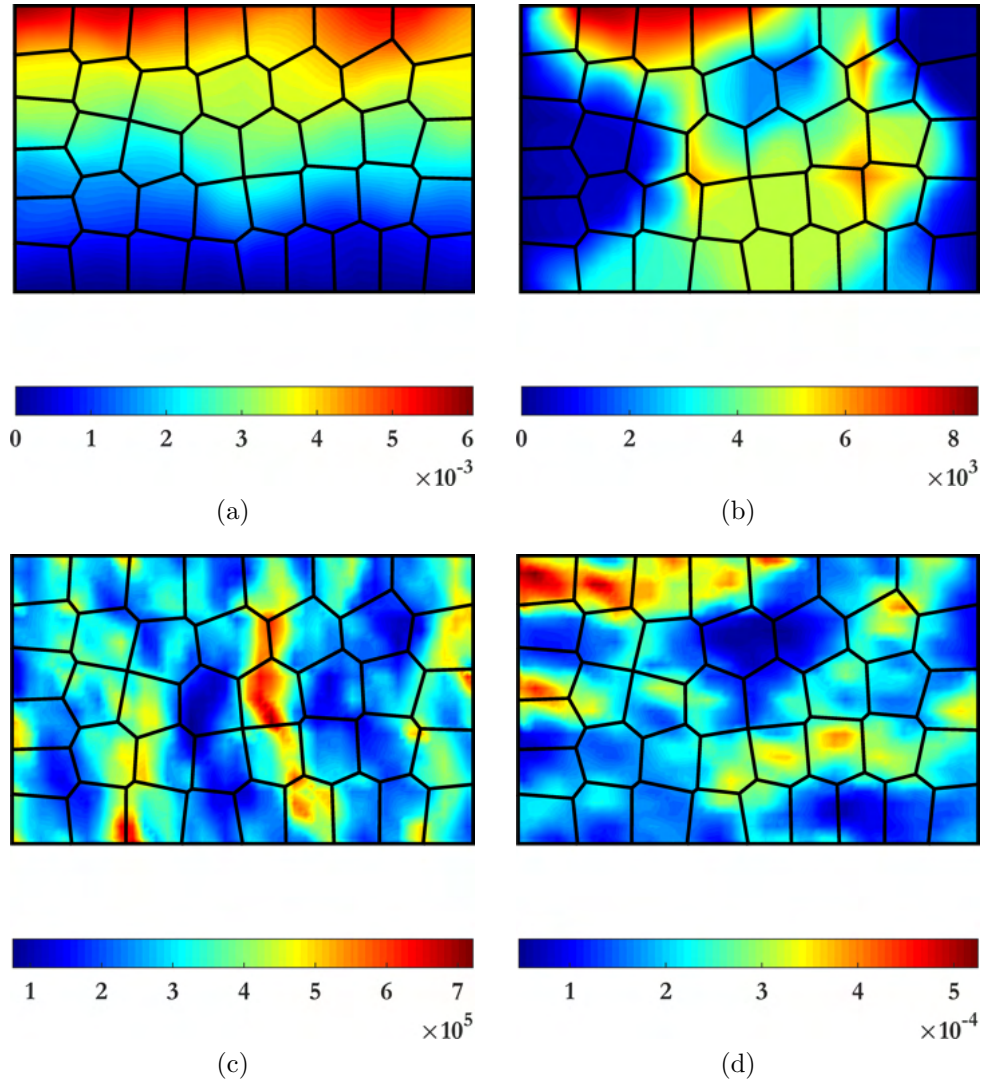


Figure 5.48: (a) $\|\mathbf{u}\|$ (in [m]), (b) p (in [Pa]), (c) $-\sigma_{yy}$ (in [Pa]) and (d) $-\varepsilon_{yy}$ contours at $t = 40$ hours for a single realization of the heterogeneous E and \mathbf{k} field.

with $E = 500$ MPa. The structure is clamped at its bottom. The deflections along the horizontal are restricted on the left and right edges. No-flow conditions are imposed across all boundaries. The top maintains a pressure $p = 0$ and is subject to a progressively applied compressive load $\mathbf{t} = [0, t_y]$. The loading history is shown in Fig. 5.25. The material parameters used are provided in Table 5.20.

A multiscale discretization is considered wherein each of the 25 periodically repeating unit cells comprises 500 CVT elements. This is compared against a reference VEM solution evaluated over 12,500 CVT elements. All multiscale solutions are evaluated using oscillatory boundary conditions. Four multi-node coarse-element configurations, MS_1 to MS_4 , are designed to examine the trade-off between accuracy and speedup. These are illustrated in Fig. 5.55.

All CMsVEM models involve the solution of a significantly reduced system of governing equations when compared to the reference VEM solution. In Fig. 5.56, the order reduction achieved per coarse element is provided as the ratio of the total number of degrees of freedom of the multiscale formulation to the degrees of freedom of the standard VEM implementation. Even in the case of the high-fidelity MS_4 coarse element, the order of the problem is practically halved.

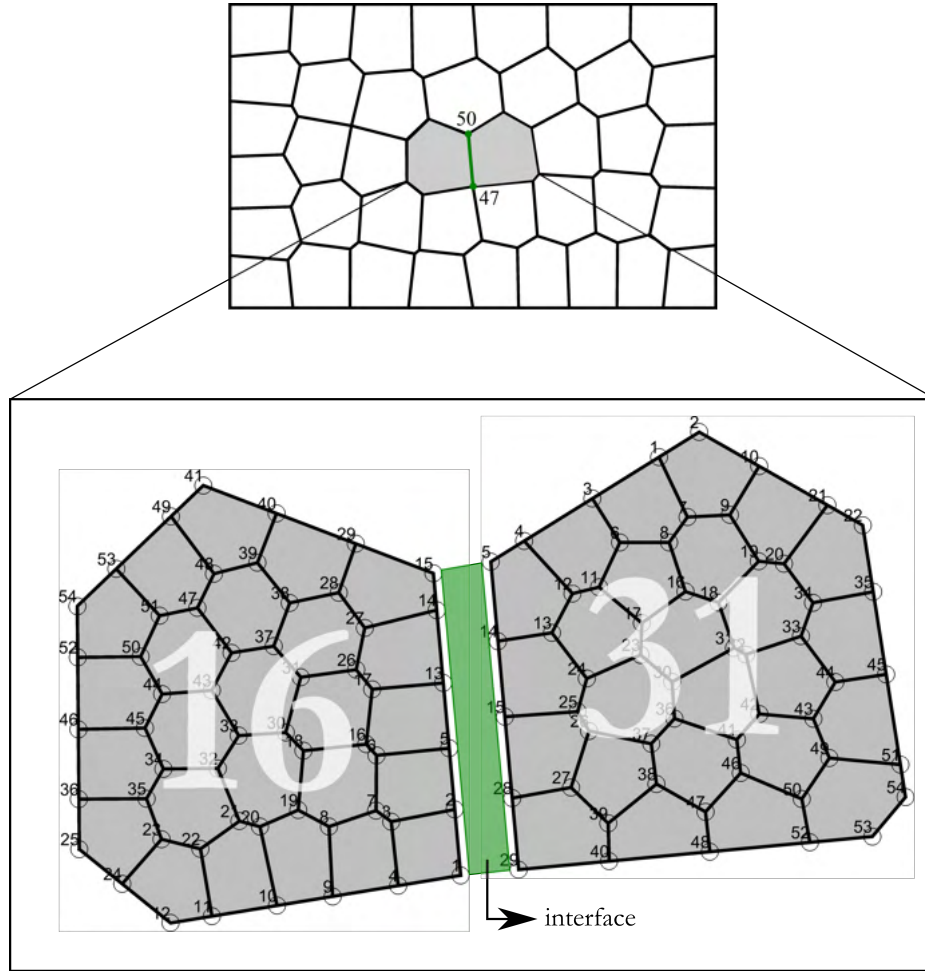


Figure 5.49: Microstructures of adjacent coarse elements 16 and 31. The interface joins coarse nodes M_{47} and M_{50} .

The maximum pore-fluid pressures are found to occur at $t_i = 6.83$ hours, $i = 42$. Displacement, pressure, stress and flux contours are provided at this instant for the VEM and multiscale solutions. The total displacement contours $\|\mathbf{u}\|$ are shown in Fig. 5.57. Pressure contours p are provided in Fig. 5.58.

It can be seen from the Figs. 5.57 and 5.58 that the total displacement $\|\mathbf{u}\|$ and pressure p contours are practically the same for all cases. Von-Mises stress contours σ_{VM} are illustrated in Fig. 5.59. Total Darcy flux contours $\|\mathbf{q}\|$ are displayed in Fig. 5.60.

Fig. 5.60 reveals that the total flux $\|\mathbf{q}\|$ contours is also practically equivalent for all cases. However, significant variations can be observed in the case of the Von-Mises stresses as shown in Fig. 5.59. The contours obtained are increasingly accurate moving from MS_1 to MS_4 when compared against the reference VEM solution. This is to be expected as the coarse element

	E	ν	γ_f	K_s	K_f	ρ_s	ρ_f	n	α_B
	[MPa]	[/]	[Pa · s]	[Pa]	[Pa]	[kg · m ⁻³]	[kg · m ⁻³]	[/]	[/]
Matrix	5								
Inclusion	500	0.2	10^{-3}	3×10^4	10^4	10^3	10^3	0.2	1

Table 5.20: Material parameters used.

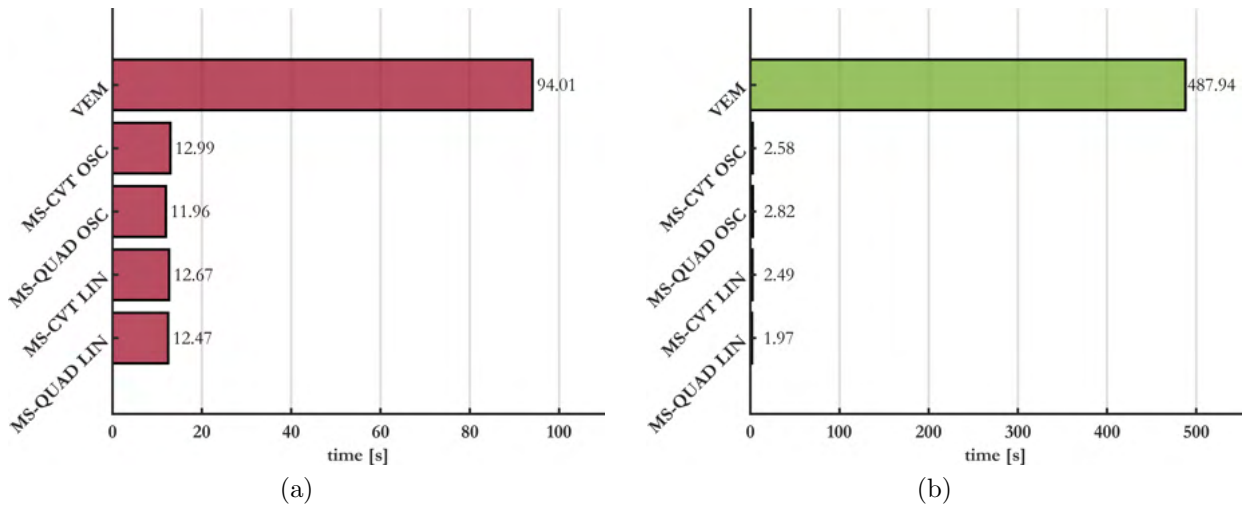


Figure 5.50: (a) Time taken to assemble global coarse element state matrices, (b) Time taken to solve system of linear equations at coarse scale.

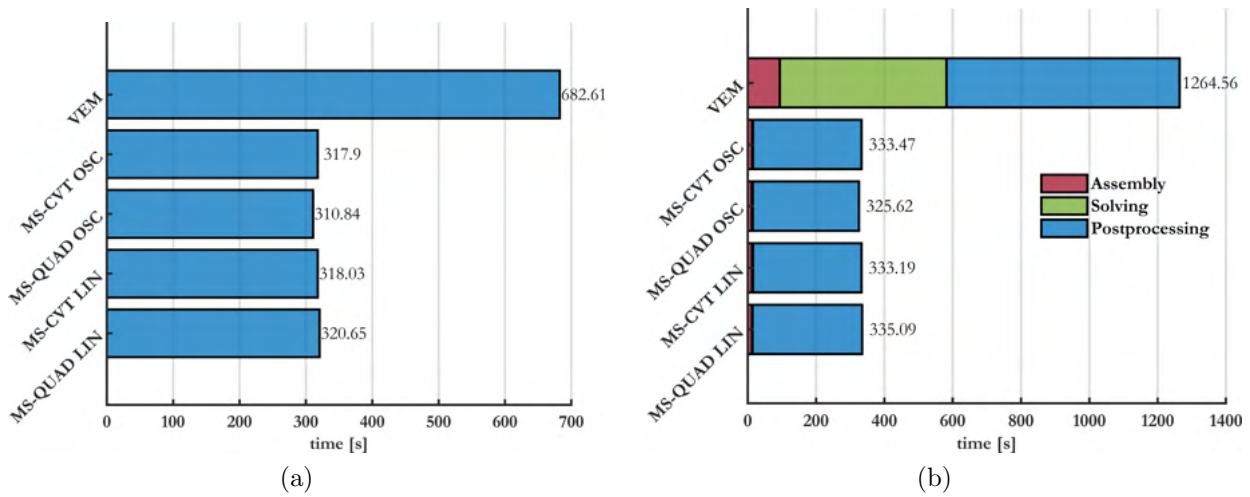


Figure 5.51: (a) Time taken to postprocess the solution, (b) Total time taken for assembly, solving and postprocessing.

described by MS_4 provides a high-fidelity representation of the original curved boundary. This in turn ensures more accurate upscale and downscale mappings performed by the multiscale basis functions.

The time evolution of the relative \mathcal{L}_2 and \mathcal{H}_1 error norms in \mathbf{u} and p are provided in Fig. 5.61. An appreciable reduction in errors is observed in Figs. 5.61a, 5.61b, 5.61c and 5.61d as the number of coarse nodes is increasing. This is to be expected as a more detailed account of the RVE geometry and underlying heterogeneities can prove critical to the fidelity of the upscaling and downscaling procedures.

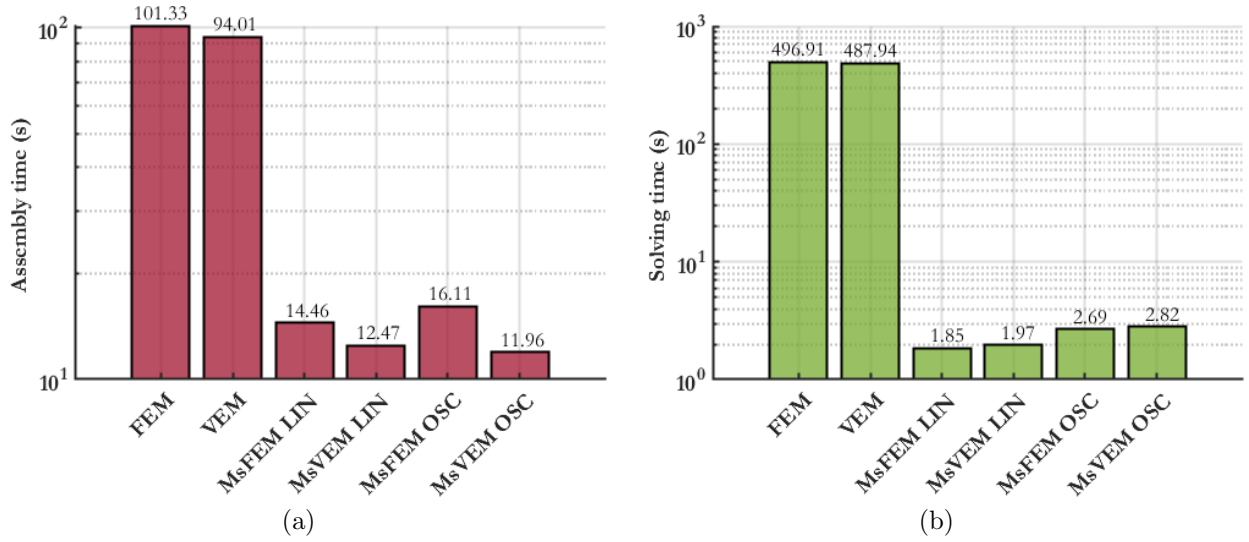


Figure 5.52: (a) Time taken to assemble global coarse element state matrices, (b) Time taken to solve system of linear equations at coarse scale.

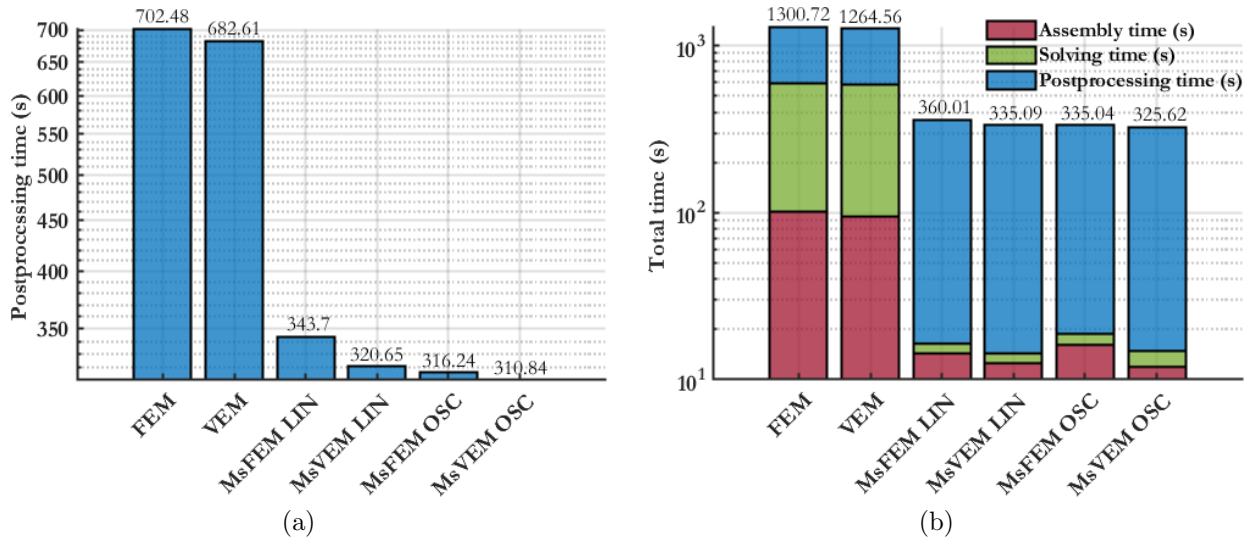


Figure 5.53: (a) Time taken to postprocess the solution, (b) Total time taken.

Discussion on computational gains

The computational cost associated with the MS_1 , MS_2 , MS_3 and MS_4 is studied here in terms of the speedup offered. The speedup metric is defined as follows

$$\text{speedup}(\text{operation}) = \frac{t_{\text{VEM}}(\text{operation})}{t_{\text{MS}_i}(\text{operation})}, \quad i = 1, \dots, 4, \quad (5.17)$$

where $t_{\text{VEM}}(\text{operation})$ and $t_{\text{MS}_i}(\text{operation})$ denote the times taken to complete a certain operation, using the VEM and CMsVEM discretizations, respectively.

The speedup offered by MS_1 through MS_4 for (a) assembly of global coarse element state matrices, (b) solving system of linear equations at the coarse scale, (c) post-processing the solution to obtain fine-scale information, and (d) the complete CMsVEM procedure, are shown in Figs. 5.62a, 5.62b, 5.62c and 5.62d, respectively. These operations are as defined in Section 5.5.2.

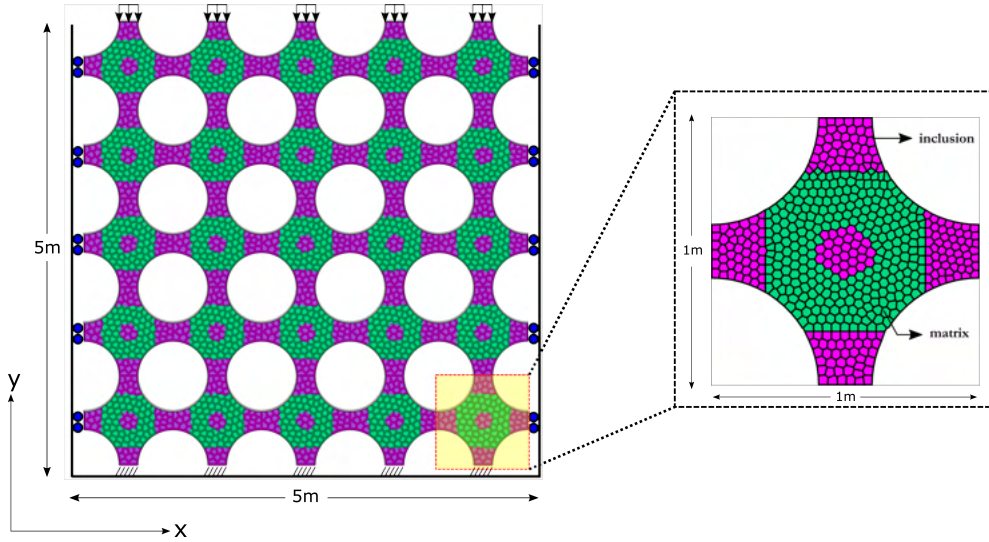


Figure 5.54: Schematic of a honeycomb structure.

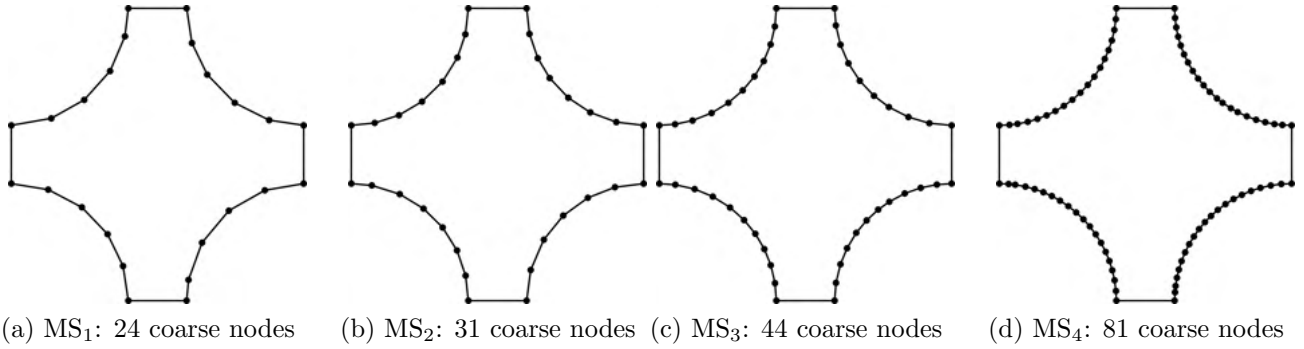


Figure 5.55: The multi-node coarse element configurations.

Near-linear trends in the speedup reduction is observed in Figs. 5.62a, 5.62c and 5.62d. A near-exponential decreasing trend is observed in the case of the solution procedure at the coarse-scale, as shown in Fig. 5.62b. The decreasing trends exhibited at all operations is further evidenced by the decrease in percentage reduction of coarse-scale DoFs, as shown in Fig. 5.56.

5.6 Vibroacoustics

Similar to Section 5.4, the VEM is introduced at the fine scale to compute multiscale basis functions for upscaling. These functions are obtained by solving the cell equations in Eqs. (4.53)-(4.54). The RVE state matrices $\tilde{\mathbf{K}}_m^\alpha$ and $\tilde{\mathbf{H}}_m^\alpha$ are assembled from the fine element contributions $\tilde{\mathbf{K}}_{m(i)}^{\text{el},\alpha}$ and $\tilde{\mathbf{H}}_{m(i)}^{\text{el},\alpha}$. The remaining RVE matrices, i.e., $\tilde{\mathbf{M}}_m^\alpha$, $\tilde{\mathbf{Q}}_m^\alpha$ and $\tilde{\mathbf{C}}_m^\alpha$ are evaluated in the same fashion. The fine element matrices are computed with the VEM using Eqs. (3.155). All subsequent extensions to the MsFEM, including polygonal coarse elements, oscillatory boundary conditions etc. are applicable here as well. The upscaling, solution and downscaling procedures followed are identical to Section 4.4.

The non-linear dependence of all state matrices on the excitation frequency ω necessitates that multiscale basis functions be iteratively evaluated for all frequency steps. This can prove expensive within the context of very finely discretized microstructures, where repeated solutions are required

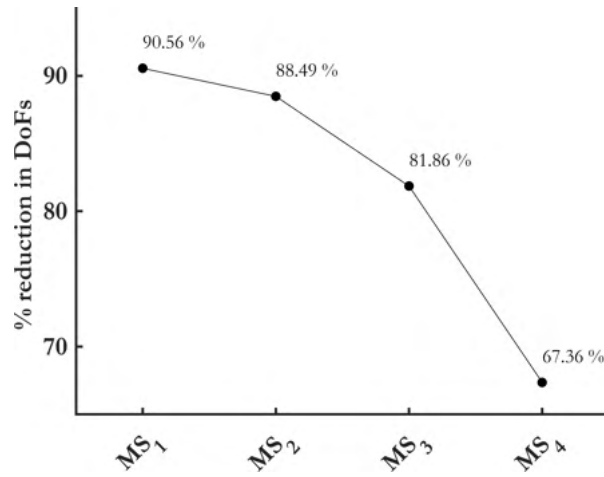


Figure 5.56: Percentage reduction in DoFs offered by each coarse element configuration, in relation to the complete VEM discretization.

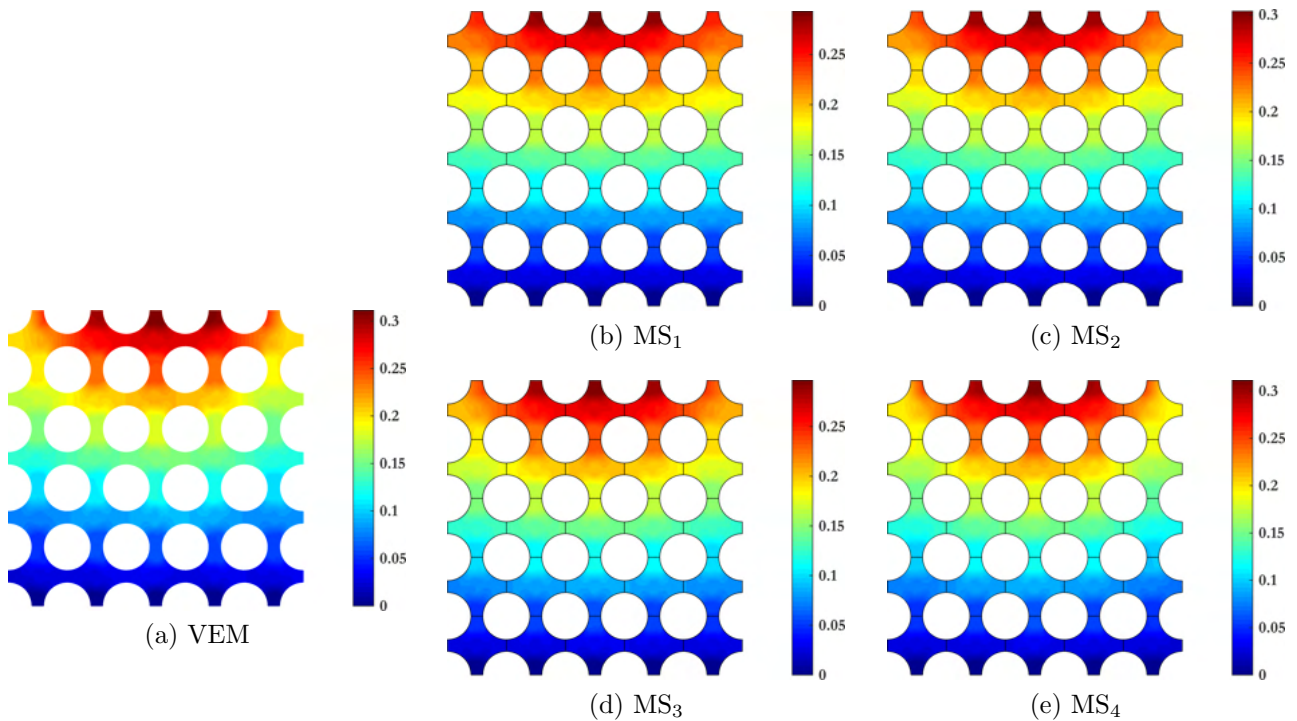


Figure 5.57: $\|\mathbf{u}\|$ total displacement contours at $t_i = 6.83h$, $i = 42$.

for all kinematical constraints and at several frequencies. To this end, a model order reduction scheme is employed at the RVE fine scale to drive down computational costs associated with this procedure.

5.7 Parametric Model Order Reduction

Standard numerical models like the FEM or VEM employ shape functions that exhibit a remarkable degree of versatility and robustness when encountering variations in problem definitions, such as geometries, boundary conditions, excitation, material layouts etc. (it is assumed that all these variations are in principle, parametrizable.) However, this generality results in a basis set

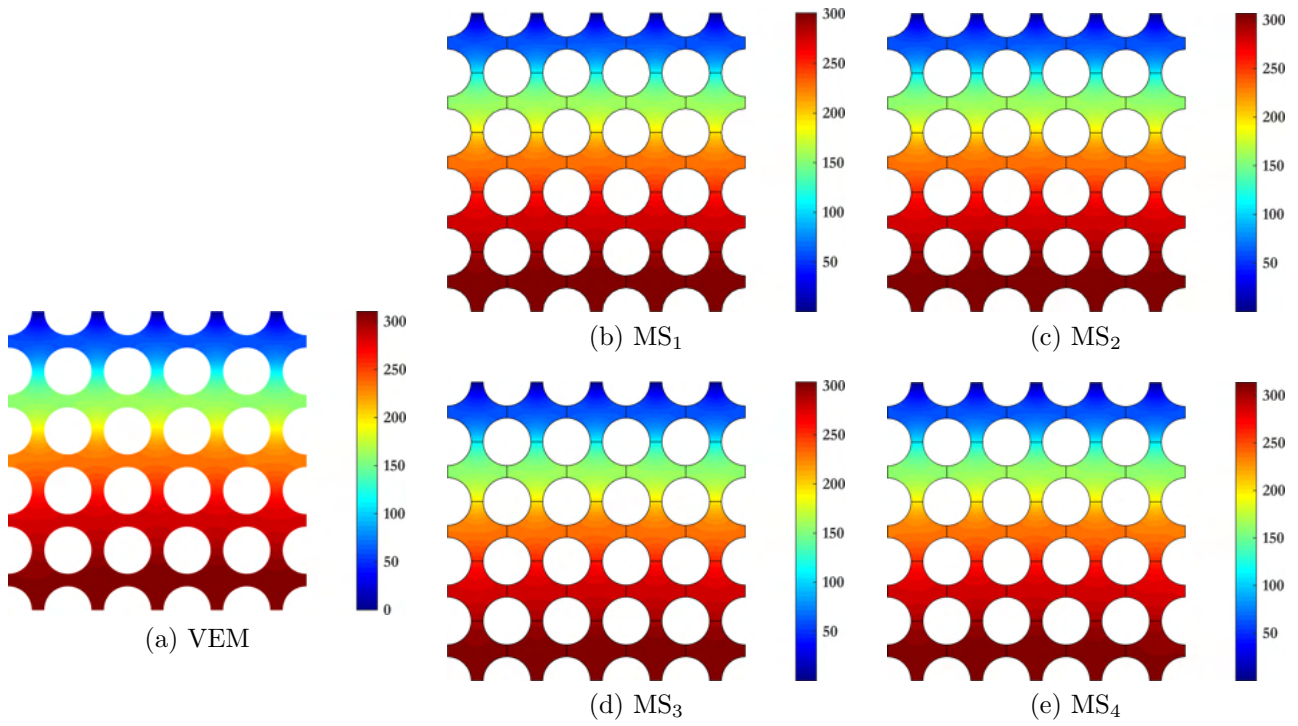


Figure 5.58: p pressure contours at $t_i = 6.83h$, $i = 42$.

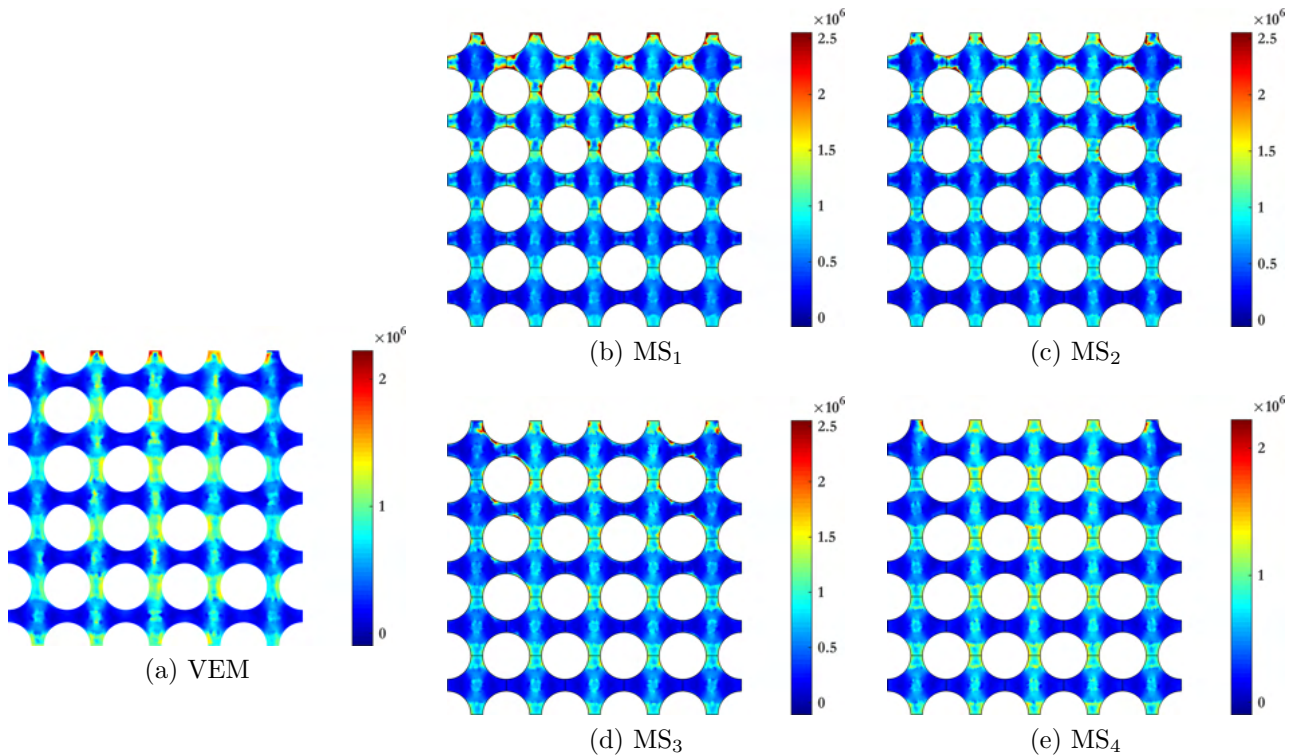


Figure 5.59: σ_{VM} Von-Mises stress contours at $t_i = 6.83h$, $i = 42$.

that is highly non-optimal with regards to characterizing the behaviour of a system in a particular parametric configuration.

Standard Model Order Reduction (MOR) techniques seek to identify an optimal manifold with minimal dimensions, that can accurately describe the behaviour of the system within this

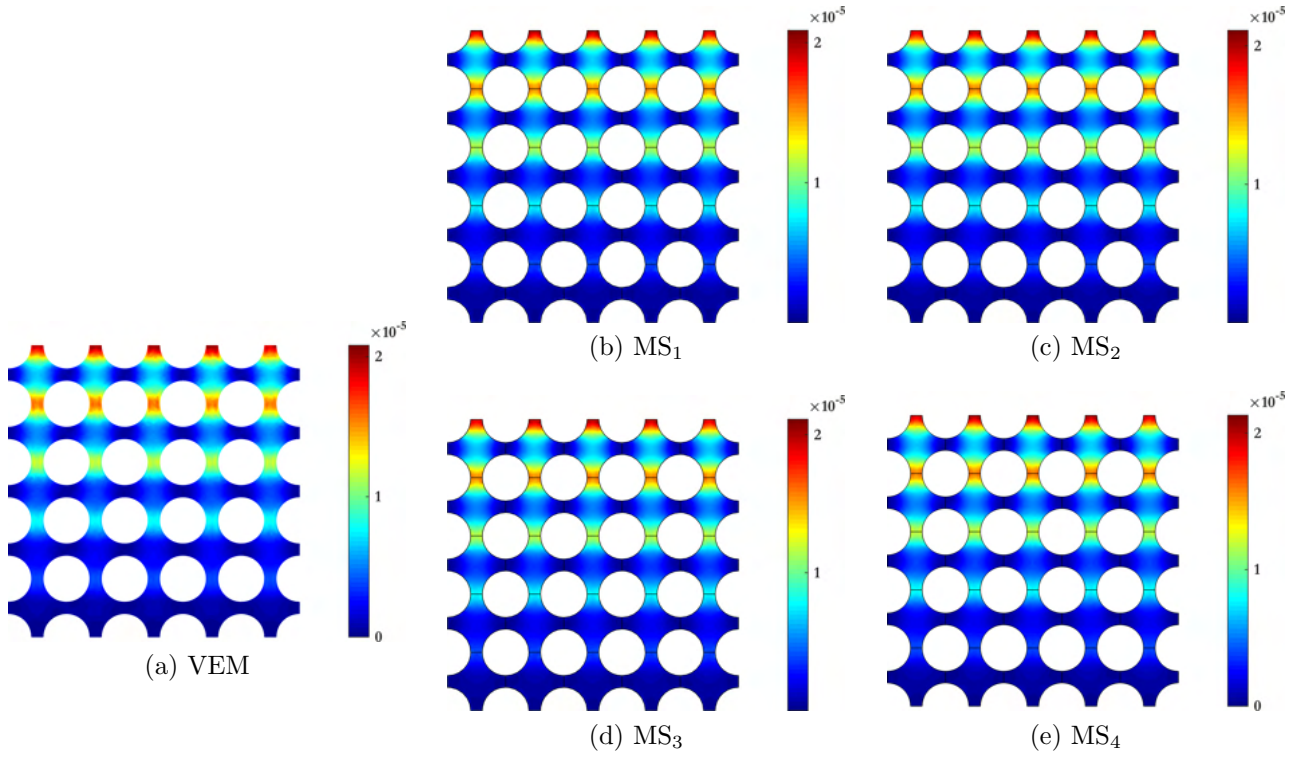


Figure 5.60: $\|\mathbf{q}\|$ total flux contours at $t_i = 6.83h$, $i = 42$.

particular configuration. This reduced manifold is spanned by a locally optimal basis set; hence the term Reduced Basis Methods. Owing to the reduced dimensionality of the system, this method offers significant computational acceleration, without sacrificing the accuracy of the solutions. However, it is to be noted that this reduced basis set is no longer optimal for other configurations, i.e., numerical benefits cannot be guaranteed in a global parameter space.

The complexity of the reduced manifold is quantified by the extent of variation in the underlying parameter configuration. For small variations, a constant reduced basis can span the entire manifold with sufficient accuracy. For larger variations, spatially varying reduced bases need to be constructed [332, 333]. For Eq. (2.183), it has been shown in [321–323], that a single basis set is acceptable for performing the MOR.

5.7.1 Affine representations

The following derivations are a summary of [325]. Examining Eq. (2.183), the frequency-dependent solution vector $\tilde{\mathbf{X}}$ is expanded in terms of an optimal basis set ϕ_i^O , $i = 1, \dots, n_{\text{dof}}$, where $n_{\text{dof}} = n_{\text{dof}}^u + n_{\text{dof}}^p$ denotes the dimension of the manifold under consideration

$$\tilde{\mathbf{X}} = \sum_{i=1}^{n_{\text{dof}}} \tilde{c}_i \phi_i^O = \mathbf{\Phi}^O \tilde{\mathbf{c}}, \quad (5.18)$$

where \tilde{c}_i represents frequency-dependent scalar valued coefficients of the linear expansion. The array $\mathbf{\Phi}^O = [\phi_1^O, \dots, \phi_{n_{\text{dof}}}^O]$ and vector $\tilde{\mathbf{c}} = [\tilde{c}_1, \dots, \tilde{c}_{n_{\text{dof}}}]^T$ collect the optimal basis and expansion coefficients, respectively. The entire algebraic system of equations in Eq. (2.183) is now projected

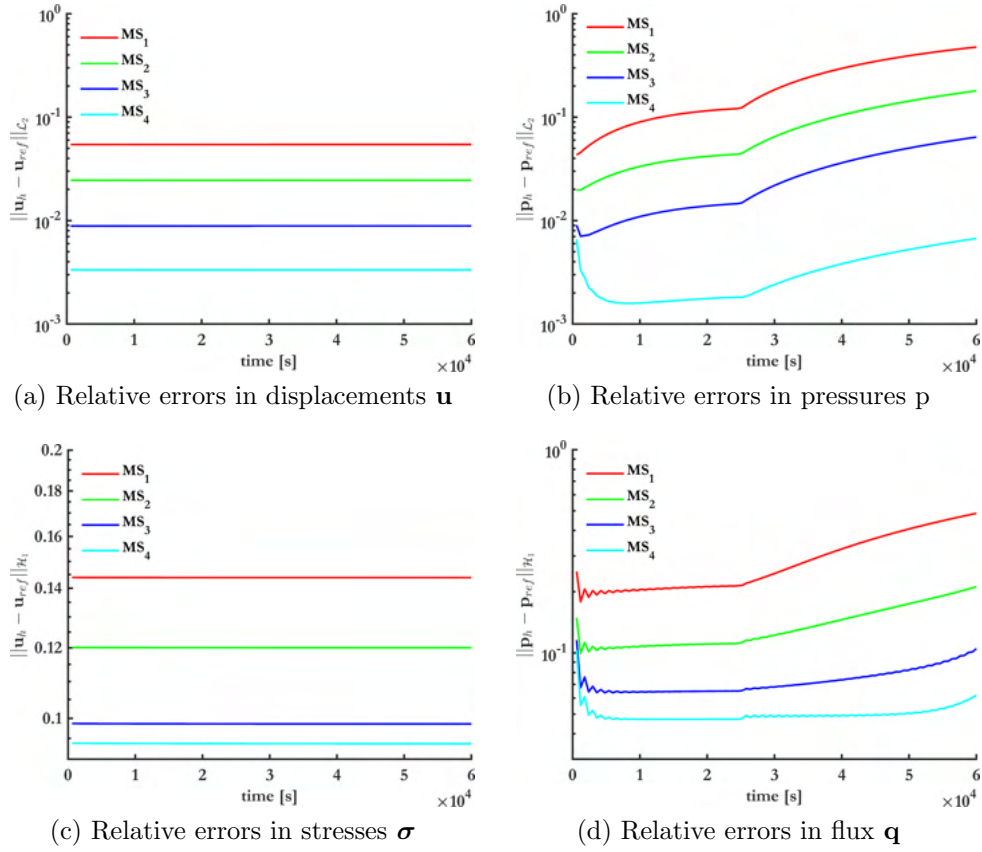


Figure 5.61: Evolution of errors in displacements and pressures for the four coarse-element configurations MS_1 , MS_2 , MS_3 and MS_4 .

onto this basis by pre-multiplying both sides with Φ^{OT} . The resulting system of equations read

$$\underbrace{\left[\Phi^{OT} \tilde{\mathbf{Z}} \Phi^O \right]}_{\tilde{\mathbf{Z}}^O} \tilde{\mathbf{c}} = \underbrace{\Phi^{OT} \tilde{\mathbf{F}}}_{\tilde{\mathbf{F}}^O}. \quad (5.19)$$

Now, the affine nature in Section 2.7.3 is expanded in greater detail, Observing Eqs. (2.175)-(2.179), one can decouple the frequency dependent parameters from the relevant state matrices

$$\tilde{\mathbf{K}} = E(1 + j\eta_s)\mathbf{K}, \quad (5.20a)$$

$$\tilde{\mathbf{M}} = \tilde{\rho}\mathbf{M}, \quad (5.20b)$$

$$\tilde{\mathbf{H}} = \frac{1}{\tilde{\rho}_{eq}}\mathbf{H}, \quad (5.20c)$$

$$\tilde{\mathbf{Q}} = \frac{1}{\tilde{\mathbf{K}}_{eq}}\mathbf{Q}, \quad (5.20d)$$

$$\tilde{\mathbf{C}} = \tilde{\gamma}\mathbf{C}, \quad (5.20e)$$

where $\mathbf{K}, \mathbf{M}, \mathbf{H}, \mathbf{Q}, \mathbf{C}$ denote the associated frequency invariant state matrices. Omitting the

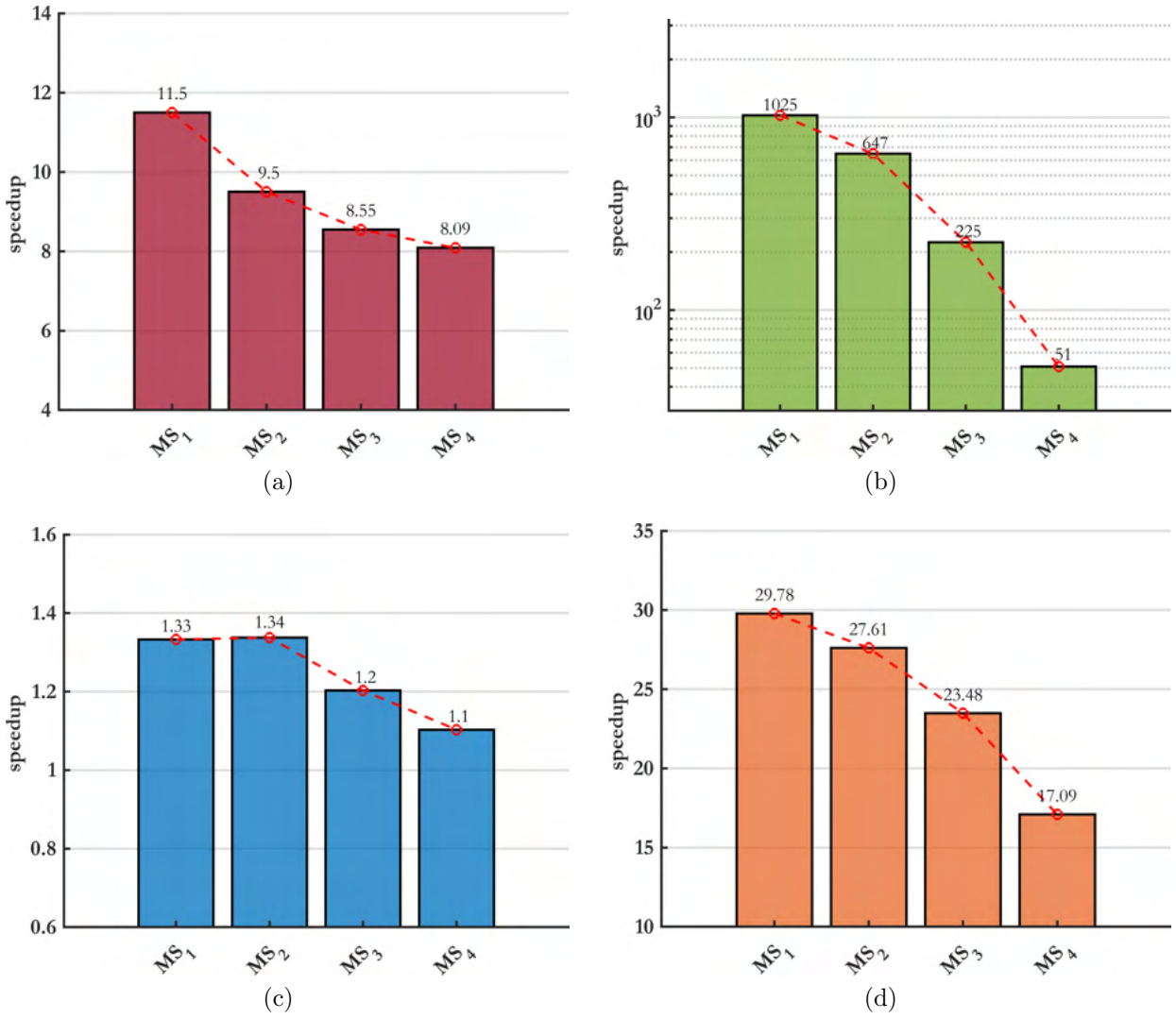


Figure 5.62: Speedup offered during (a) assembly of global coarse element state matrices, (b) solving system of linear equations at the coarse scale, (c) postprocessing the solution, (d) complete CMsVEM procedure.

coupling and robin conditions for brevity

$$\tilde{\mathbf{Z}} = \sum_{k=1}^{n_{\text{param}}} \mathbf{Z}_k f_k(\omega), \quad (5.21)$$

where $n_{\text{param}} = 6$ denotes the number of unique affine parametric terms. The frequency invariant matrices \mathbf{Z}_k have the forms

$$\begin{aligned} \mathbf{Z}_1 &= \begin{bmatrix} \mathbf{K} & 0 \\ 0 & 0 \end{bmatrix}, & \mathbf{Z}_2 &= \begin{bmatrix} \mathbf{M} & 0 \\ 0 & 0 \end{bmatrix}, & \mathbf{Z}_3 &= \begin{bmatrix} 0 & 0 \\ 0 & \mathbf{H} \end{bmatrix}, \\ \mathbf{Z}_4 &= \begin{bmatrix} 0 & 0 \\ 0 & \mathbf{Q} \end{bmatrix}, & \mathbf{Z}_5 &= \begin{bmatrix} 0 & \mathbf{C} \\ 0 & 0 \end{bmatrix}, & \mathbf{Z}_6 &= \begin{bmatrix} 0 & 0 \\ \mathbf{C}^T & 0 \end{bmatrix}. \end{aligned} \quad (5.22)$$

The corresponding frequency dependent scalar quantities $f_k(\omega)$ have the forms

$$\begin{aligned} f_1(\omega) &= E(1 + j\eta_s), & f_2(\omega) &= -\omega^2\tilde{\rho}, & f_3(\omega) &= \frac{1}{\tilde{\rho}_{\text{eq}}}, \\ f_4(\omega) &= -\omega^2\frac{1}{\tilde{K}_{\text{eq}}}, & f_5(\omega) &= -\tilde{\gamma}, & f_6(\omega) &= -\omega^2\tilde{\gamma}, \end{aligned} \quad (5.23)$$

The affine expansion in Eq. (5.21) is applied to the system of equations in Eq. (5.19) to yield

$$\tilde{\mathbf{Z}}^{\text{O}} = \sum_{k=1}^{n_{\text{param}}} \mathbf{Z}_k^{\text{O}} f_k(\omega). \quad (5.24)$$

Eq. (5.24) shows that the projection of $\tilde{\mathbf{Z}}$ onto the optimal bases Φ^{O} is an offline procedure. This is because the projection operation only modifies the frequency invariant matrices \mathbf{Z}_k . The spectral quantities $f_k(\omega)$ remain unaffected. This observation is of vital importance in controlling the computational complexity of the method. This indicates that this projection need be performed only once, through appropriate sub-structuring. The relevant frequency dependent parameters are post-multiplied in when needed.

5.7.2 Computing the reduced optimal basis

The bases set Φ^{O} is currently unknown. There exist multiple ways to evaluate this. Since these bases typically constitute orthogonal vectors, a popular choice is the modal approach, where Φ^{O} are generated with eigenvectors. A reduced order representation requires a selection criterion, based on a modal participation factor. Within the context of linear elastodynamics, this involves eliminating higher frequency modes [334]. However, it has been noted that this approach is not amenable to poroelastic systems [321, 324, 335]. This is because of a higher modal density at low frequency bandwidths, thereby resulting in a reduced basis of high dimension [325]. Further, due to the highly dissipative nature of the lossy medium, the frequency response function does not exhibit clear resonance peaks at these modes [336].

Alternately, the Proper Orthogonal Decomposition (POD) has been successfully used in [325] to generate this bases. The POD is adopted to compute the reduced basis space in this Chapter. To do this, one first constructs a snapshot matrix \mathbf{S} , i.e., a matrix collecting high-fidelity solutions \mathbf{S}_i (also called snapshots), as evaluated by the full order model (FOM) at different frequency steps

$$\underbrace{\mathbf{S}}_{n_{\text{dof}} \times n_s} = [\mathbf{S}_1, \dots, \mathbf{S}_{n_s}], \quad (5.25)$$

where n_s denotes the number of snapshots taken. The POD basis is now obtained from \mathbf{S} using either a) a Principal Component Analysis (PCA), or b) a Singular Value Decomposition (SVD).

Principal Component Analysis

The PCA [337] seeks to identify a system of generalized coordinates $\Phi^{\text{O}} = [\phi_1^{\text{O}}, \dots, \phi_{n_{\text{dof}}}^{\text{O}}]$ such that all significant dynamics in the dataset \mathbf{S} are sufficient captured. To this end, a correlation

matrix \mathbf{C}_S is defined such that

$$\mathbf{C}_S = \mathbf{S}^\dagger \mathbf{S}, \quad (5.26)$$

where $(\cdot)^\dagger$ denotes the complex conjugation transpose operation. Now, the following functional is defined

$$f(\boldsymbol{\xi}_i, \boldsymbol{\xi}_j) = \boldsymbol{\xi}_i^T \mathbf{C}_S \boldsymbol{\xi}_j, \quad (5.27)$$

where $\boldsymbol{\xi}_i$ and $\boldsymbol{\xi}_j$ denote arbitrary trial vectors of appropriate dimensions. This functional indicates a projection of \mathbf{C}_S onto $\boldsymbol{\xi}_i$ and $\boldsymbol{\xi}_j$. An optimization objective can now be defined

$$(\phi_i^O, \phi_j^O) = \operatorname{argmax}(f(\boldsymbol{\xi}_i, \boldsymbol{\xi}_j)), \text{ such that } \boldsymbol{\xi}_i \cdot \boldsymbol{\xi}_j = \delta_{ij}. \quad (5.28)$$

This is a constrained optimization problem with a requirement of orthonormality. A Lagrangian is written out for this problem

$$\mathcal{L}(\boldsymbol{\xi}_i, \boldsymbol{\xi}_j, \lambda_j) = f(\boldsymbol{\xi}_i, \boldsymbol{\xi}_j) + \lambda_j(1 - \boldsymbol{\xi}_i^T \boldsymbol{\xi}_j). \quad (5.29)$$

Eq. (5.29) is extremized with respect to $\boldsymbol{\xi}_i$

$$\frac{\partial \mathcal{L}}{\partial \boldsymbol{\xi}_i} = 0 \implies \mathbf{C}_S \boldsymbol{\xi}_j = \lambda_j \boldsymbol{\xi}_j. \quad (5.30)$$

The above equation is an eigenvalue problem with eigenvalues λ_j and eigenvectors $\boldsymbol{\xi}_j$. Once obtained, these eigenvectors correspond to the optimal proper orthogonal modes ϕ_j^O for the snapshot matrix \mathbf{S} . The POD basis is now reduced using a truncation criterion. This is done by rearranging the eigenvalues in a descending order $\lambda_1 \geq \lambda_2 \geq \dots \lambda_{n_s}$. Depending on the level of accuracy desired, the first n_r reordered basis vectors are chosen to obtain a reduced order model of dimension n_r .

However, this method suffers from a few drawbacks. Constructing the correlation matrix, and subsequently computing eigenvalues and eigenvectors proves expensive. This can compromise computational benefits gained by solving a ROM.

Singular Value Decomposition

Further, it has been shown in [325] that the SVD can be used to generate Φ^O more accurately and efficiently. This decomposition factorizes the snapshot matrix \mathbf{S} into a diagonal matrix $\boldsymbol{\Sigma}$, and two orthogonal matrices \mathbf{L} and \mathbf{R}

$$\mathbf{S} = \underbrace{\mathbf{L}}_{n_{\text{dof}} \times n_{\text{dof}}} \underbrace{\boldsymbol{\Sigma}}_{n_{\text{dof}} \times n_s} \underbrace{\mathbf{R}^T}_{n_s \times n_s}, \quad (5.31)$$

where $\boldsymbol{\Sigma}$ is a rectangular matrix comprising singular values $\sigma_1, \dots, \sigma_{n_s}$ along the main diagonal. The matrices \mathbf{L} and \mathbf{R} comprise left and right singular vectors, respectively. The optimal POD basis corresponds to the left singular matrix, i.e., $\Phi^O = \mathbf{L}$. The reduced order POD basis, Φ^{ROM} , is obtained by selecting $n_r \ll n_s$ left singular vectors from \mathbf{L} .

To do this, the singular values are rearranged in descending order, i.e., $\sigma_1 \geq \sigma_2 \geq \dots \sigma_{n_s}$. The reduced dimension n_r emerges from a truncation tolerance ϵ_σ . This can be defined such that all

the left singular vectors corresponding to the following criterion are eliminated

$$\frac{\sigma_i}{\sigma_1} < \epsilon_\sigma. \quad (5.32)$$

It is critical that ϵ_σ be optimally defined to capture all the necessary dynamics of the data contained in \mathbf{S} ; and at the same time, significantly reduce the dimensionality of the system. This is ensured by considering the singular value decay of the problem. This is analogous to a modal participation factor and indicates the significance of each singular vector, in capturing the dynamics of the data. A good heuristic for tuning ϵ_σ is to set it at a value where a sharp reduction in singular value decay is observed. This indicates that singular vectors from this point contribute negligible information in relation to the existing singular vectors. This procedure is demonstrated in Example 5.9.1.

In the case that there is no such observable changes in the rate of singular value decay, this may indicate that the range of variation in the parameter space is too large to benefit from a POD. In such cases, the reduced basis technique is either inaccurate, or requires too many POD bases to warrant deployment [325, 326].

5.7.3 Reduced order model

The expansion in Eq. (5.18) is now approximated with the reduced basis ϕ^{POD}

$$\tilde{\mathbf{X}} \approx \tilde{\mathbf{X}}^{\text{POD}} = \sum_{i=1}^{n_{\text{dof}}} \tilde{c}_i^{\text{POD}} \phi_i^{\text{POD}} = \mathbf{\Phi}^{\text{POD}} \tilde{\mathbf{c}}^{\text{POD}}, \quad (5.33)$$

Consequently, the basis $\mathbf{\Phi}^O$ in Eq. (5.19) is now replaced with the reduced basis $\mathbf{\Phi}^{\text{POD}}$ to generate a ROM

$$\underbrace{\tilde{\mathbf{Z}}^{\text{POD}}}_{n_r \times n_r} \underbrace{\tilde{\mathbf{c}}^{\text{POD}}}_{n_r \times 1} = \underbrace{\tilde{\mathbf{F}}^{\text{POD}}}_{n_r \times 1}. \quad (5.34)$$

This is solved for $\tilde{\mathbf{c}}^{\text{POD}}$ at the desired frequencies steps at a significantly reduced computational cost. The full fidelity solution $\tilde{\mathbf{X}}^{\text{POD}}$ is recovered from $\tilde{\mathbf{c}}^{\text{POD}}$ using Eq. (5.33).

The accuracy of model order reduction depends largely on the quality of the snapshot matrix \mathbf{S} . Generating FOM snapshots is typically the primary bottleneck in the method, since large high fidelity matrices need to be inverted (or iteratively solved). To this end, sampling strategies play a vital role in determining computational efficiency. Quasi random sampling (Monte-Carlo or Latin Hypercube methods) is recommended over brute force tensorial approaches [326, 338].

The SVD factorization has a complexity of $O(n_{\text{dof}}^2 n_s)$ and can prove expensive for large snapshot matrices, especially when $n_s \approx n_{\text{dof}}$. However, in most cases since $n_s \ll n_{\text{dof}}$, the cost of employing the SVD is justifiable.

5.8 Coupled Reduced Basis Multiscale Methods

The pMOR scheme developed in Section 5.7 is now incorporated at the fine-scale of the multi-scale procedure. For a given set of kinematic constraints over the α^{th} RVE, i.e., \mathbf{u}_S and \mathbf{p}_S , a set of high-fidelity snapshots $\mathbf{u}_m^\alpha(\omega_k)$ and $\mathbf{p}_m^\alpha(\omega_k)$ are obtained at a randomly sampled set of frequencies ω_k , $k = 1, \dots, n_s$ by solving Eqs. (4.53)-(4.54), where the number of snapshots is significantly lesser than the total number of frequency steps, i.e., $n_s \ll n_{\text{freq}}$. Relevant snapshot matrices \mathbf{S}_u^α and \mathbf{S}_p^α are generated.

Truncated POD bases Φ_u^{ROM} and Φ_p^{ROM} are obtained for each phase from \mathbf{S}_u^α and \mathbf{S}_p^α , respectively, using the SVD procedure detailed in Section 5.7.2. Now, the size of the sub-problem is reduced by projecting the system of linear equations onto these reduced manifolds as follows

$$\tilde{\mathbf{K}}_m^{\alpha,ROM} = \Phi_u^{ROMT} \tilde{\mathbf{K}}_m^\alpha \Phi_u^{ROM}, \quad (5.35)$$

and

$$\tilde{\mathbf{H}}_m^{\alpha,ROM} = \Phi_p^{ROMT} \tilde{\mathbf{H}}_m^\alpha \Phi_p^{ROM}. \quad (5.36)$$

The resulting ROM multiscale functions are now evaluated at a reduced cost according to Section 5.7.3. The procedure is summarized in Algorithm 5.

5.9 Numerical examples

5.9.1 Reduced basis pMOR for a poroelastic square domain

This example investigates the accuracy and efficiency of the reduced basis parametric Model Order Reduction technique in vibroacoustic simulations of poroelastic materials as described in Section 5.7. The same physical layout provided in Example 4.5.1 is adopted here, i.e., an 80 mm \times 80 mm Melamine foam with an elastic skeleton description is placed inside an impedance tube with a clamped backing and roller supports on the lateral surfaces. This setup is subject to a plane wave acoustic excitation at normal incidence within the frequency range [20,5000] Hz. This bandwidth is discretized into $n_{\text{freq}} = 100$ equally spaced frequency steps.

The domain is discretized using 25×25 first-order quadrilateral finite elements. This is the minimum discretization necessary to ensure convergence at all frequency steps. The number of free DoFs associated with this system is $n_{\text{dof}}^{\text{FOM}} = 1900$.

A set of high-fidelity snapshots are evaluated at $n_s = 15$ frequency steps and collected in a snapshot matrix \mathbf{S} of size $(n_{\text{dof}}^{\text{FOM}} \times n_s)$. These steps are chosen using a Latin Hypercube (stratified sampling) method, to ensure a good representative sample. This is the most computationally intensive part of the procedure as highlighted in Section 5.7.3 and costs 0.64 seconds. To avoid compromising on the speedup offered by the method, a general heuristic of setting $0.1n_{\text{freq}} \leq n_s \leq 0.2n_{\text{freq}}$ is recommended. However, it is to be noted that this heuristic does not guarantee that the snapshots generated will sufficiently account for all significant system dynamics.

Next, \mathbf{S} is factorized into \mathbf{L} , $\mathbf{\Sigma}$ and \mathbf{R}^T in accordance with the SVD method detailed in Section 5.7.2. If done inefficiently, this factorization can also proved to be a significant bottleneck

Algorithm 5: Multiscale basis function evaluation schema using the pMOR.

Data: Define coarse mesh and fine mesh/micromesh and material properties

foreach *coarse element* α **do**

Assemble \mathbf{K}_m^α ;

foreach *macro-node* $I = 1, \dots, n_M^\alpha$ **do**

foreach *macro degree of freedom* $J = 1, 2$ **do**

Define: $\bar{\mathbf{u}}_{IJ}$;

foreach *sampled frequency* $\omega_k, k = 1, \dots, n_s$ **do**

Solve:
$$\begin{cases} \mathbf{K}_m^\alpha(\omega_k) \mathbf{u}_m^\alpha(\omega_k) = \mathbf{0} \\ \mathbf{u}_s = \bar{\mathbf{u}}_{IJ} \end{cases} ;$$

Assemble to \mathbf{S}_u^α ;

Get Φ_u^{ROM} from \mathbf{S}_u^α (SVD and truncation) ;

foreach *remaining frequency step* $\omega_k, k = 1, \dots, n_{freq} - n_s$ **do**

Solve ROM:
$$\begin{cases} \mathbf{K}_m^{\alpha,ROM}(\omega_k) \mathbf{u}_m^{\alpha,ROM}(\omega_k) = \mathbf{0} \\ \mathbf{u}_s = \bar{\mathbf{u}}_{IJ} \end{cases} ;$$

Get FOM solution: $\mathbf{u}_m^\alpha(\omega_k) = \Phi_u^{ROMT} \mathbf{u}_m^{\alpha,ROM}(\omega_k)$

Assemble \mathbf{H}_m^α ;

foreach *macro-node* $I = 1, \dots, n_M^\alpha$ **do**

foreach *macro degree of freedom* $J = 1$ **do**

Define: $\bar{\mathbf{p}}_{IJ}$;

foreach *sampled frequency* $\omega_k, k = 1, \dots, n_s$ **do**

Solve:
$$\begin{cases} \mathbf{H}_m^\alpha(\omega_k) \mathbf{p}_m^\alpha(\omega_k) = \mathbf{0} \\ \mathbf{p}_s = \bar{\mathbf{p}}_{IJ} \end{cases} ;$$

Assemble to \mathbf{S}_p^α ;

Get Φ_p^{ROM} from \mathbf{S}_p^α (SVD and truncation) ;

foreach *remaining frequency step* $\omega_k, k = 1, \dots, n_{freq} - n_s$ **do**

Solve ROM:
$$\begin{cases} \mathbf{H}_m^{\alpha,ROM}(\omega_k) \mathbf{p}_m^{\alpha,ROM}(\omega_k) = \mathbf{0} \\ \mathbf{p}_s = \bar{\mathbf{p}}_{IJ} \end{cases} ;$$

Get FOM solution: $\mathbf{p}_m^\alpha(\omega_k) = \Phi_p^{ROMT} \mathbf{p}_m^{\alpha,ROM}(\omega_k)$

of the method. In this specific problem instance, since $n_s \ll n_{\text{dof}}^{\text{FOM}}$, this operation is relatively inexpensive and costs 0.28 seconds. Conversely, a more economical approach is desired in situations the full SVD operation can prove costly. When $n_s < n_{\text{dof}}^{\text{FOM}}$, as is the case here, this "economical SVD" computes only the first n_s columns of \mathbf{L} . Furthermore, $\mathbf{\Sigma}$ is a $n_s \times n_s$ diagonal matrix, i.e., only the first n_s singular values are computed. This approach exhibits a reduced cost of 0.018 seconds.

Although this gain in efficiency is not significant here, the resulting speedup of 15.2 promises noticeable accelerations in the SVD procedure when encountering larger problems. The "economical SVD" holds validity in all pMOR applications of this kind. This is because, the singular values $\sigma_{n_s+1}, \dots, \sigma_{n_{\text{dof}}^{\text{FOM}}}$ always remain redundant and irrelevant since only the first $n_r < n_s$ significant left singular vectors are chosen to constitute the reduced POD basis.

To construct the reduced basis, a reducibility analysis is carried out through a singular value decay chart in Fig. 5.63. A sharp change in the decay rate is observed at a singular value ratio

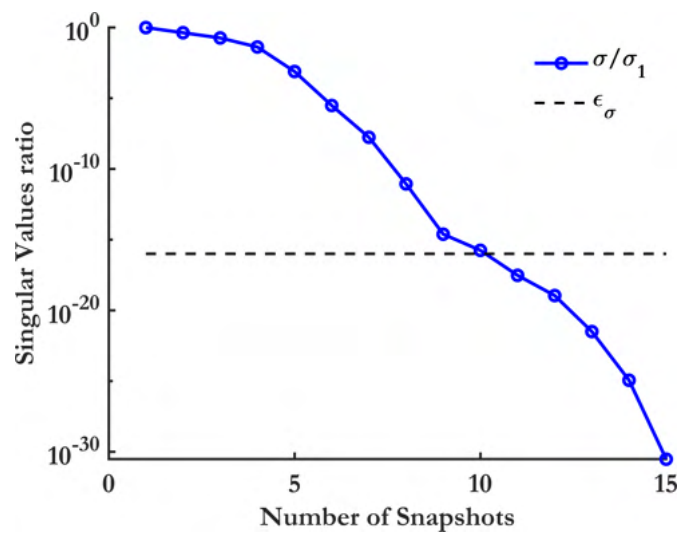


Figure 5.63: Decay of the first $n_s = 15$ singular values computed for the snapshot matrix \mathbf{S} . The horizontal black dashed line indicates the truncation tolerance.

of 10^{-16} . Consequently, the truncation tolerance is set at $\varepsilon_\sigma = 10^{-16}$ in accordance with Section 5.7.2. The resultant POD basis $\mathbf{\Phi}^{\text{POD}}$ is a $n_{\text{dof}}^{\text{FOM}} \times 10$ matrix comprising the first 10 left singular vectors obtained from the SVD factorization. The total time taken for computing the POD basis (including snapshot generation and economical SVD factorization) is 0.67 seconds.

Finally the ROM system is solved according to Section 5.7.3. This procedure takes 0.2096 seconds. It is to be noted that the ROM system need be solved only at the remaining $n_{\text{freq}} - n_s$ frequencies. The FOM solution already exist at the sampled frequency steps in the form of the snapshot matrix \mathbf{S} .

The entire pMOR procedure (including POD basis evaluation and ROM solution procedure) takes a total of 0.88 seconds. Conversely, the FOM procedure takes 3.82 seconds. A speedup of 4.34 is observed.

The accuracy of the ROM solutions are now investigated. To aid with illustration, a low fidelity (Lo-Fi) FE model comprising 12 DoFs is also provided for comparison. This is done to demonstrate the accuracy of the 10 DoF ROM in relation to a FOM of comparable complexity. The x-displacement u_x contours are displayed for the FOM, ROM and Lo-Fi solutions at 20 Hz

in Fig. 5.64 and 5000 Hz in Fig. 5.65, respectively.

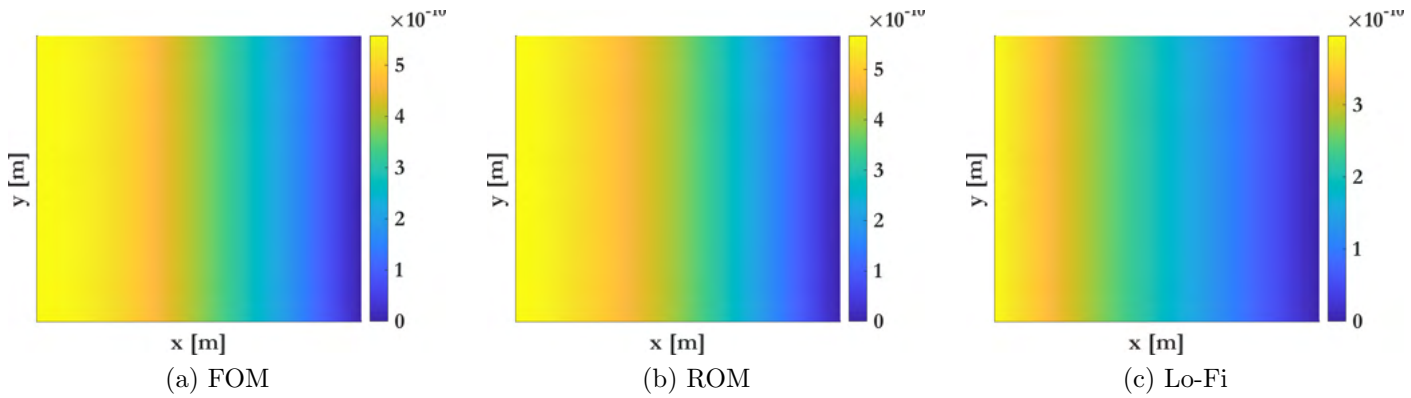


Figure 5.64: u_x x-displacement contours at 20 Hz as computed by (a) the 1900 DoFs FOM, (b) the 10 DoFs ROM, (c) a Lo-Fi 12 DoFs FE model.

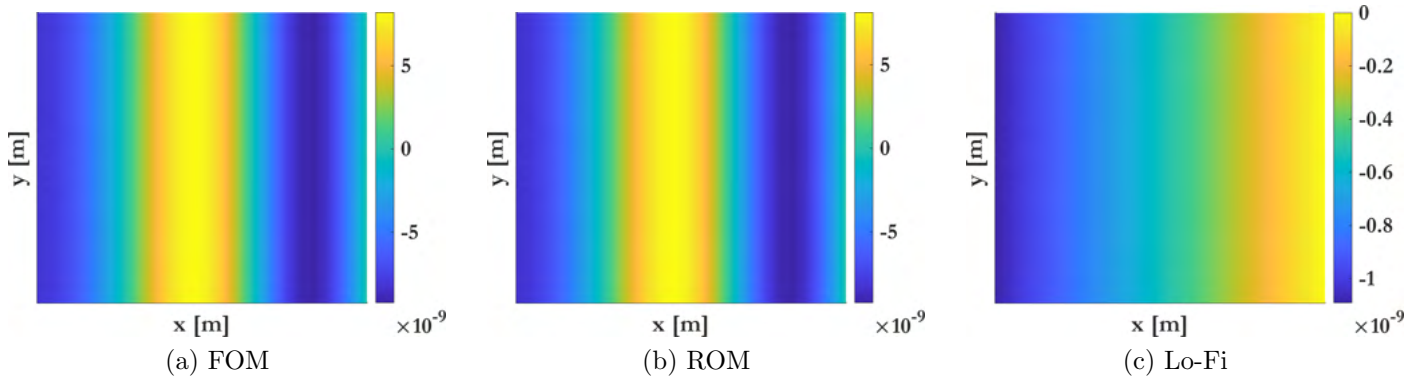


Figure 5.65: u_x x-displacement contours at 5000 Hz as computed by (a) the 1900 DoFs FOM, (b) the 10 DoFs ROM, (c) a lo-Fi 12 DoFs FE model.

The ROM displacement contours at 20 Hz and 5000 Hz appear practically identical to the FOM solutions, as can be seen in Figs. 5.64a-5.64b and Figs. 5.65a-5.65a, respectively. However, the Lo-Fi solution offers a marginally differing contour at 20 Hz in Fig. 5.64c and a significantly different one at 5000 Hz (see Fig. 5.65c).

Similarly, the pressure contours p are displayed for the three cases at 20 Hz in Fig. 5.66, and 5000 Hz in Fig. 5.67, respectively.

Once again, the FOM and ROM are found to offer practically identical pressure contours at both frequencies (see Figs. 5.66a-5.66b and Figs. 5.67a-5.67b). The Lo-Fi model exhibits small deviations at 20 Hz (Fig. 5.66c) and non-negligible ones at 5000 Hz (Fig. 5.67c).

This difference in accuracies between the ROM and Lo-Fi model of comparable complexity illustrates the need for optimizing the choice of basis functions, i.e., a POD basis can capture a fuller range of dynamic behaviour of a particular configuration in comparison to a standard FE basis.

The Sound Absorption Coefficient (SAC) as evaluated by the three scenarios are shown in Fig. 5.68. A reference Transfer Matrix Method (TMM) result is provided for verification.

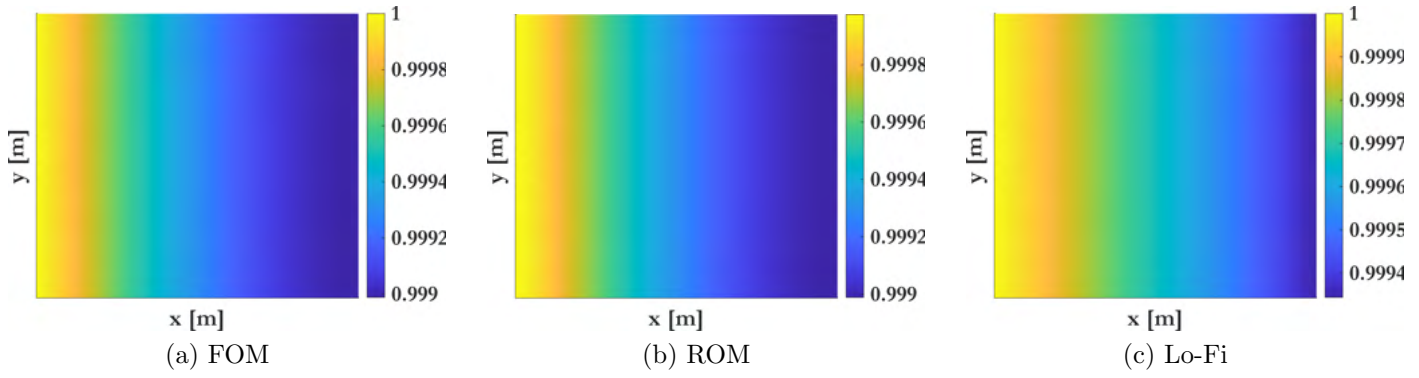


Figure 5.66: p pressure contours at 20 Hz as computed by (a) the 1900 DoFs FOM, (b) the 10 DoFs ROM, (c) a Lo-Fi 12 DoFs FE model.

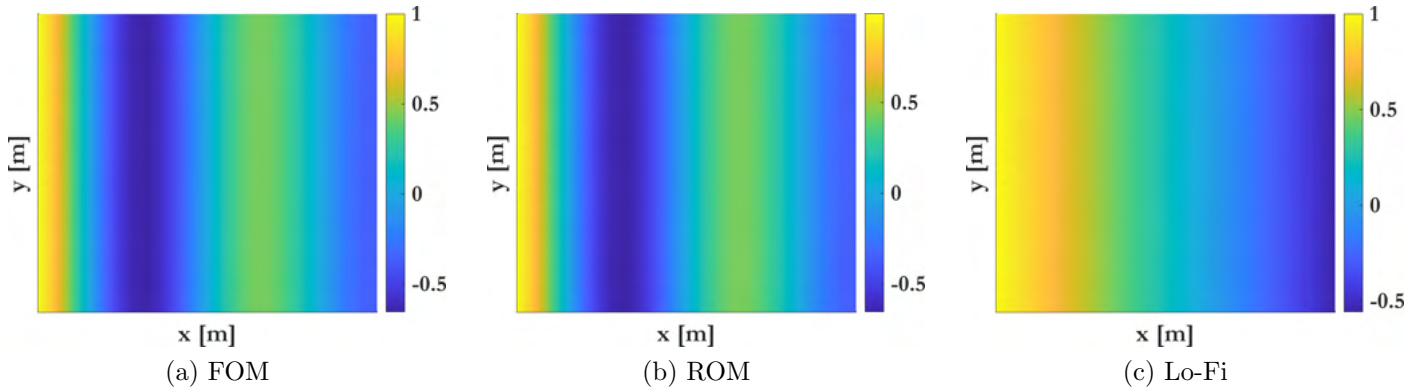


Figure 5.67: p pressure contours at 5000 Hz as computed by (a) the 1900 DoFs FOM, (b) the 10 DoFs ROM, (c) a lo-Fi 12 DoFs FE model.

It is observed that the ROM SAC curve is identical to that of the FOM and TMM. The Lo-Fi model exhibits a reasonable accuracy only upto 1200 Hz. Beyond this, the results offered are unacceptable. This result is consistent with the discussion on displacement and pressure contours mentioned above. Large discrepancies of the Lo-Fi model at higher frequencies is because of the inability of the shape functions to resolve the underlying propagating waves with sufficient clarity.

Now, the ROM solution accuracy is more rigorously quantified with relative \mathcal{L}_2 error norms between the FOM and ROM. The errors in real and imaginary components of the displacements and pressures are given in Fig. 5.69a and Fig. 5.69b, respectively. The discontinuities in the graphs correspond to the randomly sampled snapshot frequencies. The ROM solution need not be evaluated at these frequency steps as the FOM solution is already available in the form of the snapshot matrix \mathbf{S} . Consequently, the error achieved at these points are identically zero. The errors are very small and do not affect the accuracy of the solution, as evidence by the SAC and solution contours.

Hence, the pMOR offers a means to appreciably speed-up spectral computations in poroelastic materials without compromising on accuracy.

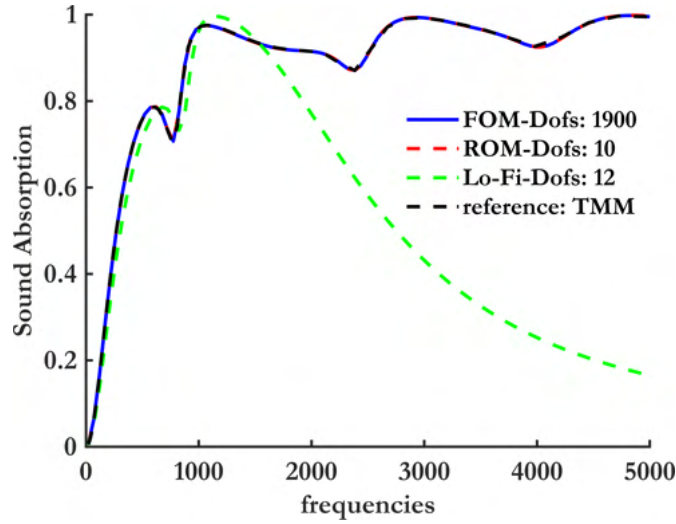


Figure 5.68: Sound Absorption Coefficients as computed by the FOM, ROM and the Lo-Fi model.

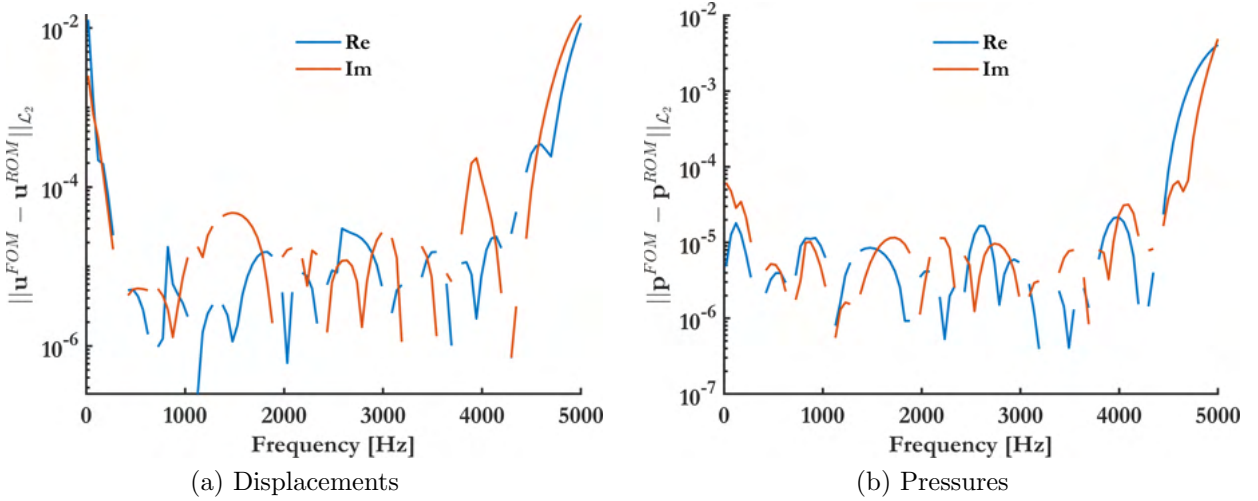


Figure 5.69: Relative errors in \mathcal{L}_2 norm for real (Re) and imaginary (Im) components between the ROM and FOM solutions for (a) displacements and (b) pressures.

5.9.2 Convergence behaviour of the MsVEM for vibroacoustics

The convergence behaviour of the MsVEM in the frequency domain is investigated in this example. Two kinds of coarse-scale meshes are considered, i.e., quadrilateral (QUAD) and polygonal (CVT). Four coarse discretizations are chosen for each type. These are summarized in Table 5.21.

Each coarse-element is subsequently meshed at the fine-scale with the same element type. Four fine-scale discretizations are chosen. These are illustrated in Table 5.22.

Treating a very finely discretized FE solution as a reference (20,000 Nodes), the relative \mathcal{L}_2 error norms in displacements as evaluated by the MsVEM are provided for both mesh types at distinct frequencies in Fig. 5.70. The evolution of these errors is studied as a function of the coarse element discretization. Each figure contains the errors obtained for all microstructural configurations described in Table 5.22. Figs. 5.70a and 5.70d are the QUAD and CVT errors pertaining to a low frequency step, i.e., $f = 775$ Hz. Although an increasing trend can be observed between accuracy and microstructure discretization, this is fairly minimal. The errors achieved by the method over both meshes are comparable in quantity. Similarly, Figs. 5.70b and

Label	No. of Coarse Elements	No. of Coarse Nodes	
		QUAD	CVT
1	120	164	241
2	480	567	959
3	1920	2093	3836
4	7680	8025	9234

Table 5.21: Coarse scale discretizations for QUAD and CVT meshes.

Label	No. of Fine Elements
RVE-1	1
RVE-2	9
RVE-3	100
RVE-4	2500

Table 5.22: Number of QUAD/CVT elements contained in each micro-structure.

5.70e depict the errors at an intermediate frequency step, i.e., $f = 2700$ Hz. Again, while these two figures are practically identical to each other, there is a noticeable decrease in overall accuracy when compared to its low frequency counterparts, i.e., Figs. 5.70a and 5.70d, respectively. This is because the $f = 2700$ Hz excitation contains a larger wave number. There is thus a need for a higher resolution in this case. Finally, Figs. 5.70c and 5.70f show the error convergence for a high frequency step of $f = 5500$ Hz. Once again, excluding insignificant deviations, both figures are nearly equivalent. However, there is a further reduction in accuracy compared to the low and intermediate frequency counterparts, for the same reason described above.

The relative \mathcal{L}_2 error norms in pressures are provided at the same frequency steps for both meshes in Fig. 5.72. Once again, similar behaviour is observed across meshes at the same frequency step. Further, the same reduction in accuracy is seen with increasing excitation frequencies.

The relative \mathcal{L}_2 error norms have a theoretical upper bound

$$\begin{aligned} \|\mathbf{u}_h - \mathbf{u}_{ex}\|_{\mathcal{L}_2} &\leq C_u h^{s_u}, \\ \|p_h - p_{ex}\|_{\mathcal{L}_2} &\leq C_p h^{s_p}, \end{aligned} \quad (5.37)$$

where C_u and C_p denote appropriately chosen arbitrary scalar valued constants; h denotes the coarse-element diameter and s_u , s_p indicate the orders of convergence. In this case the theoretical values are $s_u = s_p = 2$. The h^2 reference line is also provided in all figures for comparing the rates of convergence.

The magnitude of the numerically obtained rates of convergence are illustrated at all three frequencies for displacements in Fig. 5.72a and for pressures in Fig. 5.72b. It is observed in all cases that the choice of microstructure does not significantly affect any convergence rate trends. A slightly reduced average rate of 1.8 is yielded for displacements in the case of QUAD and CVT meshes at $f = 775$ Hz. Optimal or near-optimal rates are noticed in all other cases.

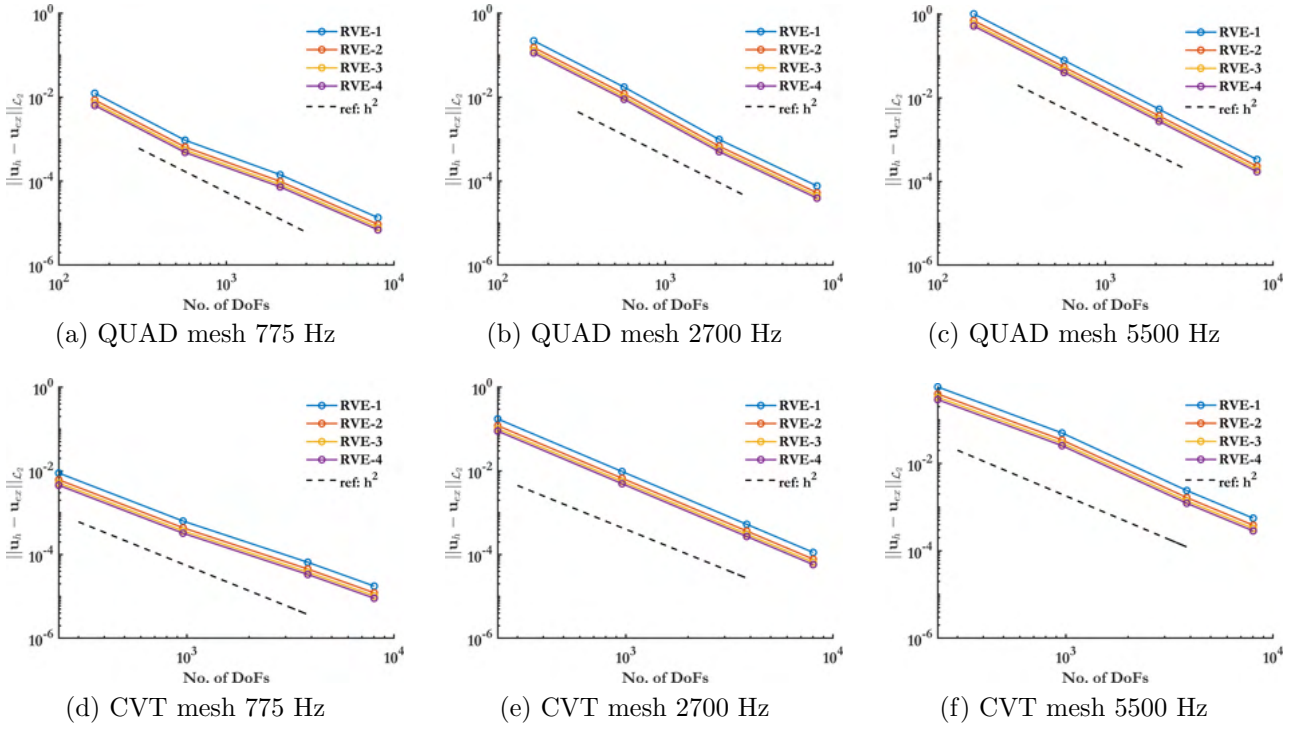


Figure 5.70: Convergence of relative errors in displacements as computed by the MsVEM at excitation frequencies 775 Hz, 2700 Hz and 5500 Hz.

5.9.3 Periodically repeating inclusions

The example provided in Section 3.6.4 is directly adapted here. The MsVEM is applied with the objective of driving down computational costs. A square unit cell, i.e., a $2 \text{ cm} \times 2 \text{ cm}$ domain with a circular mesoscale inclusion of radius 7.5 mm is selected for the upscaling procedure. This is illustrated in Fig. 5.73(I).

This RVE is periodic in the vertical direction with a period of 2 cm. The associated subdomain is discretized with 625 CVT fine elements and the corresponding coarse unit cell comprises 4 coarse nodes. The SAC as computed by the method for multiscale discretization is shown as curve "RVE1-0" in Fig. 5.75a. One can see that while the curve represents the trend of the reference solution "ref" correctly up to 6000 Hz, there are still noticeable deviations. More specifically, the peak at about 3000 Hz is overestimated by "RVE1-0". Moreover, beyond 6000 Hz, the predictions offered are unreliable.

This is expected. It is shown in [104, 127] that the microstructural discretization is critical in capturing fine scale information about heterogeneities and inclusion morphologies. However, the convergence behaviour of the MsVEM is ultimately determined by the coarse scale discretization. The error convergence behaviour of the method is not very sensitive to fine scale discretizations, especially in the case of homogeneous problems such as this. This result is established in Example 5.9.2.

Simulating the behaviour of more classical composites using this unit cell yields more reliable results (see e.g. Example 5.3.3) as the unit cell is periodic in both the horizontal and vertical directions. This results in a sufficiently large number of coarse DoFs. The application of this 4-noded unit cell to this problem on the other hand, only results in 10 coarse elements and 22 coarse

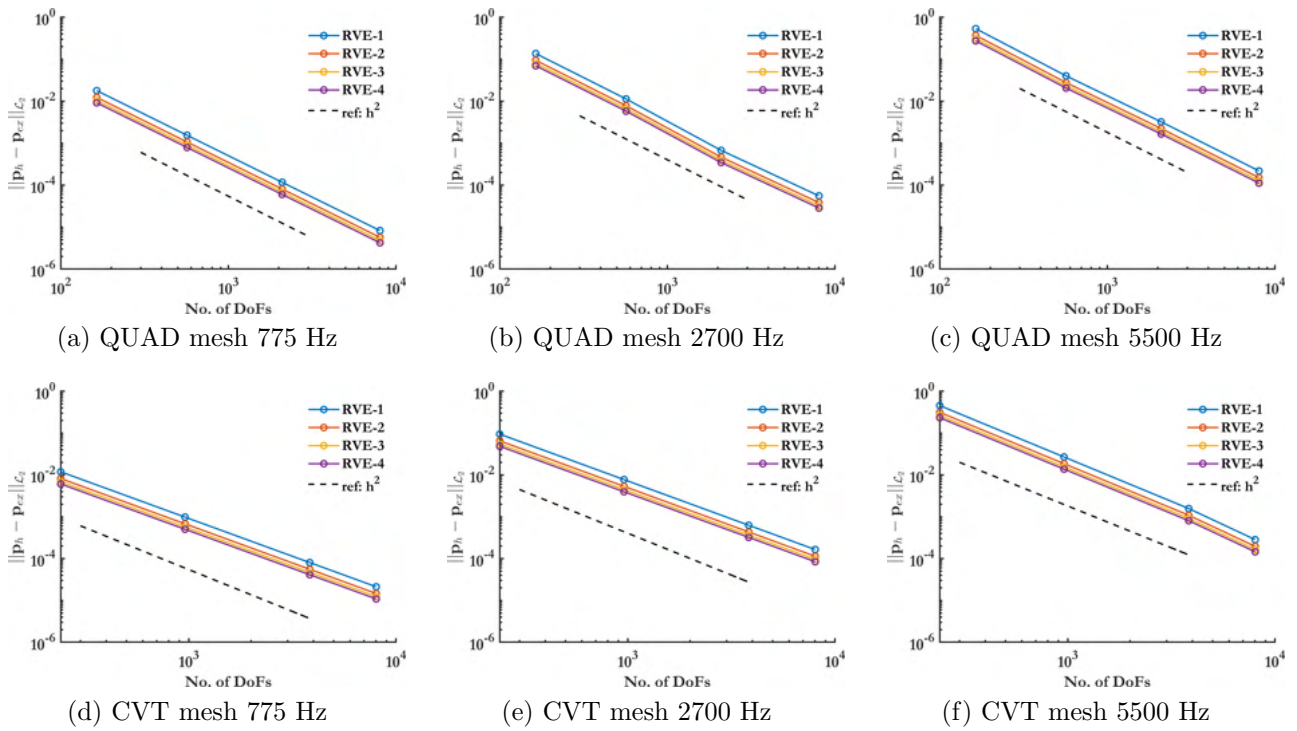


Figure 5.71: Convergence of relative errors in pressures at excitation frequencies 775 Hz, 2700 Hz and 5500 Hz.

DoFs (see "RVE1-0" in Tables 5.23 and 5.24). It is evident that this multiscale discretization only yields reasonably correct results up to 6000 Hz. To improve mid-high frequency predictions, one requires finer coarse scale discretizations.

However, one cannot simply do a classical h-refinement at the coarse scale as is traditionally done. This is because the periodic nature of the underlying domain does not naturally allow for arbitrarily small periodic unit cells. In such cases, one opts for p-refinement inspired strategies instead, analogous to Example 3.6.1. Using the same edge refinement/node insertion strategy proposed there, unit cells of the same geometry are generated, having 2, 5 and 10 subdivisions per edge. These correspond to 8, 20 and 40 coarse nodes per unit cell as summarized in Table 5.23. The SAC curves obtained for the unit cells are represented by curves "RVE1-1", "RVE1-2" and "RVE1-3" in Fig. 5.75a. Appreciable improvement over the "RVE1-0" is noticed, in ascending order of number of subdivisions per edge. The peak at 3000 Hz is progressively represented more accurately and more realistic behaviour at mid-high frequencies > 6000 Hz is seen.

The SACs obtained by "RVE1-2" and "RVE1-3" in Fig. 5.75a are practically equivalent. This reveals that the method has converged for this particular choice of RVE. It is reasonable to assume that no further appreciable improvement in behaviours at frequencies above 6000 Hz can be expected with further edge refinement. The high frequency (10 kHz) downscaled pressure contours associated with "RVE1-3" are shown in Fig. 5.74a. The contours obtained over a single unit cell is also shown here for further clarity. The coarse nodes are denoted in bold. As expected, appreciable deviations are observed when compared with the corresponding reference solution in Fig. 5.74a.

The ability of the method to accommodate flexible, potentially non-convex RVE shapes is now exploited. The current square unit cell is split horizontally into two as shown in Fig. 5.73(II). It

Label	Periodic Unit Cells	Type	Coarse Nodes/ RVE	Fine Elements/ RVE	Unit Cell Description
RVE1-0	1	I	4	2,500	
RVE1-1	1	I	8	2,500	Convex
RVE1-2	1	I	20	2,500	Quadrilateral
RVE1-3	1	I	40	2,500	
RVE2-0	2	II	40	2,500	
RVE2-1	2	II	112	2,500	Non-Convex
RVE2-2	2	II	190	2,500	Polygon
RVE2-3	2	II	272	2,500	
RVE3-0	4	III	60	2,500	
RVE3-1	4	III	212	2,500	Non-Convex
RVE3-2	4	III	295	2,500	Polygon
RVE3-3	4	III	373	2,500	

Table 5.23: Unit cell configurations.

Label	Total Coarse Nodes	Total Coarse Elements	Total Fine Nodes	Total Fine Elements
RVE1-0	22	10	49,644	25,000
RVE1-1	53	10	49,644	25,000
RVE1-2	146	10	49,644	25,000
RVE1-3	301	10	49,644	25,000
RVE2-0	333	20	49,644	25,000
RVE2-1	951	20	49,644	25,000
RVE2-2	1601	20	49,644	25,000
RVE2-3	2381	20	49,644	25,000
RVE3-0	493	40	49,644	25,000
RVE3-1	1695	40	49,644	25,000
RVE3-2	2478	40	49,644	25,000
RVE3-3	3194	40	49,644	25,000

Table 5.24: Global mesh information for the six unit cell configurations.

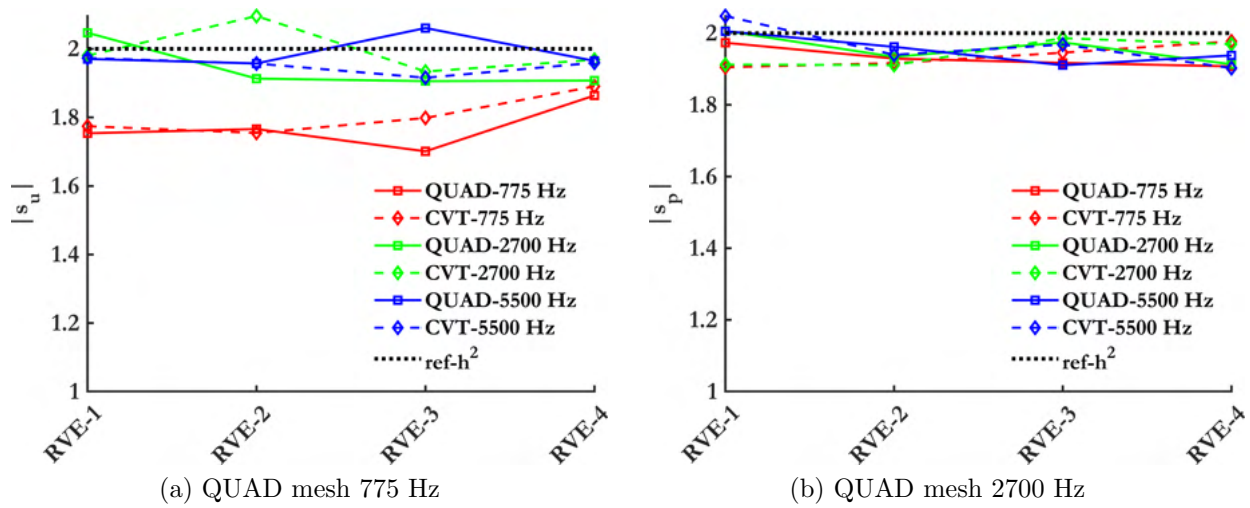


Figure 5.72: Convergence of relative errors in pressures at excitation frequencies 775 Hz, 2700 Hz and 5500 Hz.

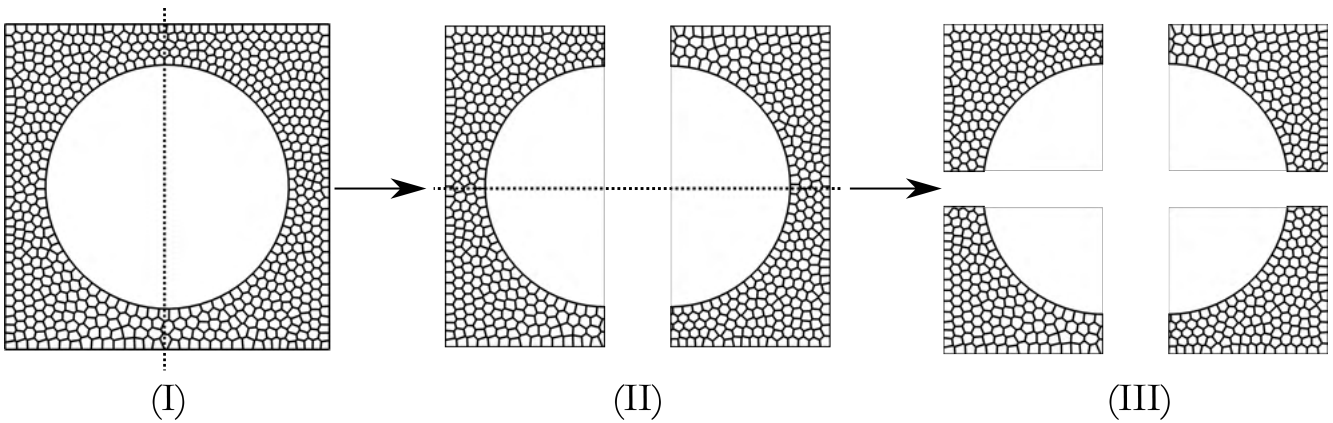


Figure 5.73: Coarse elements chosen and proposed as future extensions.

is to be noted that here the unit cell shape implicitly accounts for the rigid inclusion. Owing to the prevalence of curved boundaries for these elements, one needs multiple coarse nodes per edge even at a low fidelity setting to faithfully capture the coarse element geometry. The number of coarse nodes per unit cell involved are shown in Table 5.23 under Labels "RVE2-0", "RVE2-1", "RVE2-2" and "RVE2-3". The associated SAC contours are provided in Fig. 5.75b.

A significant improvement in the SAC computation is observed here. The peak at 3000 Hz is more accurately captured and the high-frequency responses are predicted more realistically. The curves "RVE2-1", "RVE2-2" and "RVE2-3" correctly capture the peak at 3000 Hz and also replicate the increasing trend beyond 6000 Hz. However, the sound absorption is still under-predicted at higher frequencies. The similarities in "RVE2-2" and "RVE2-3" reveal the solutions have converged for this RVE choice. No further improvements in the solution can be reasonably expected with increasing the number of coarse nodes. The pressure contour offered by "RVE2-3" at 10 kHz is provided in Fig. 5.74c. Once again, the deviations from the reference contour (Fig. 5.74a) is noticeable.

To achieve further improvements in accuracy, one seeks to augment the coarse scale discretization even further by splitting the two unit cells vertically to obtain 4 periodically repeating coarse elements. This is illustrated in Fig. 5.73(III). As before, four fidelity schemes are considered.

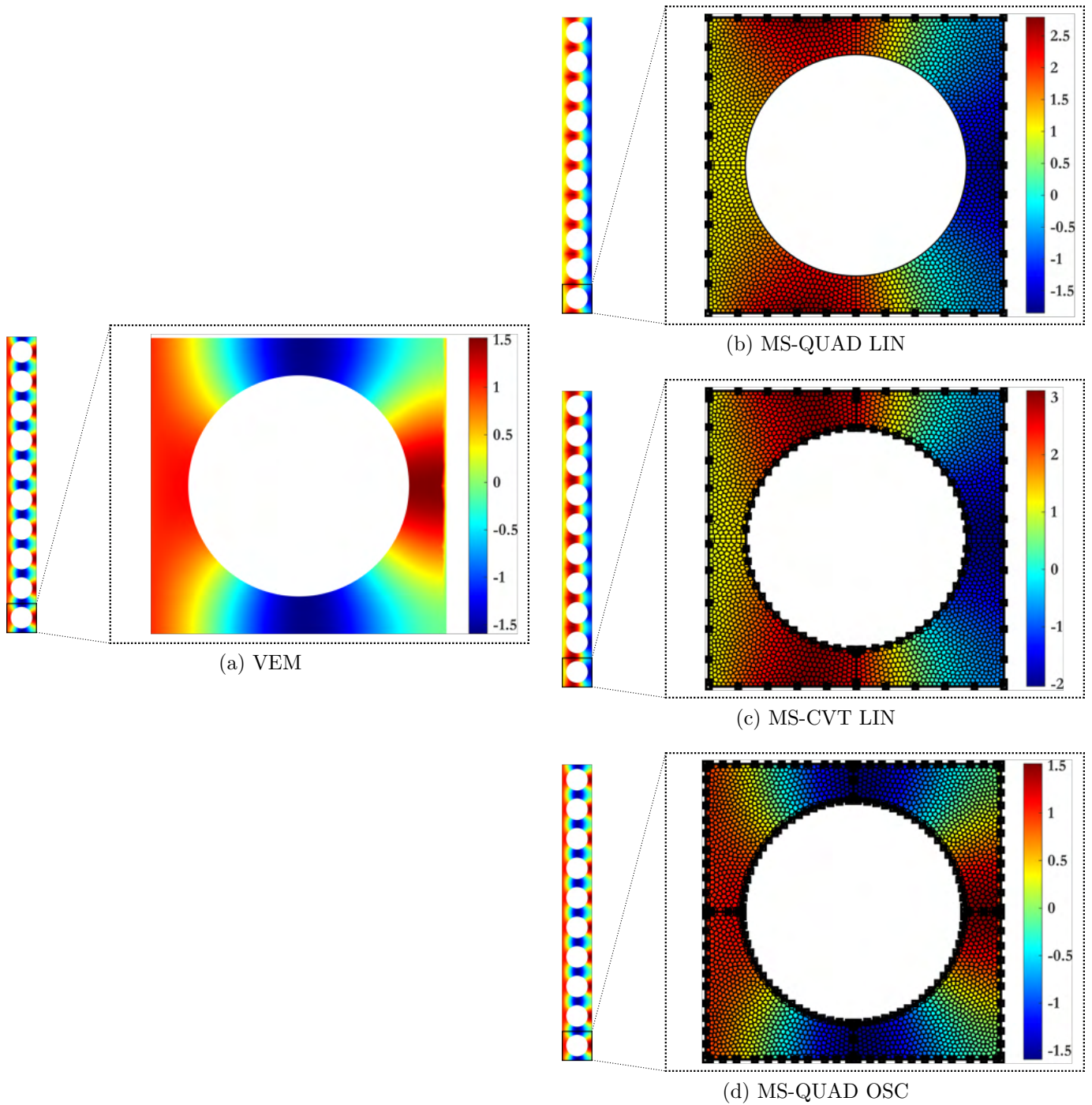


Figure 5.74: Pressure contours at $f = 10$ kHz.

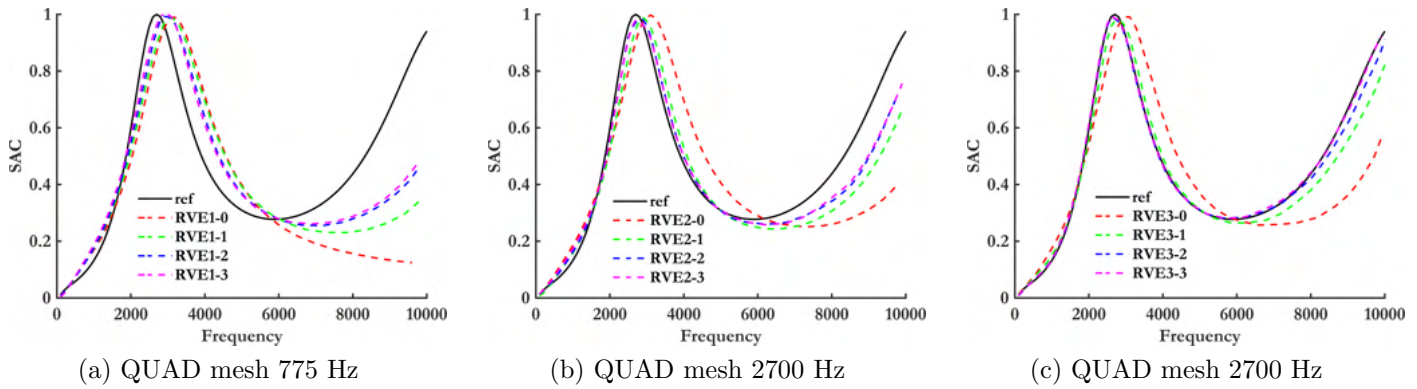


Figure 5.75: Convergence of relative errors in pressures at excitation frequencies 775 Hz, 2700 Hz and 5500 Hz.

These are detailed as "RVE3-0", "RVE3-1", "RVE3-2" and "RVE3-3" in Tables 5.23 and 5.24. The relevant SACs are shown in Fig. 5.75c. Here, a near perfect fit with the reference solution is obtained at all frequencies using "RVE3-3". The pressure contour at 10 kHz as generated using "RVE3-3" is given in Fig. 5.74d. The contour is practically identical to Fig. 5.74a.

5.9.4 Highly heterogeneous poroelastic domain

Manufacturing limitations can introduce uncertainties in the underlying material configuration of a porous material. Such heterogeneities can play a significant role in affecting its absorption or transmission behaviour. This example investigates the ability of the MsVEM and reduced basis MsVEM to provide accurate and efficient simulations of such materials.

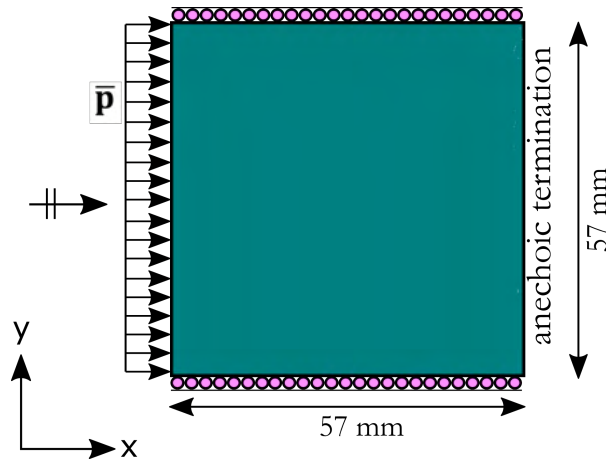


Figure 5.76: A poroelastic domain with an anechoic backing subject to plane-wave acoustical excitation \bar{p} at normal incidence.

A rectangular poroelastic domain of dimensions 57 mm \times 57 mm is subjected to a plane wave acoustic excitation at normal incidence. The lateral edges are given roller supports and an anechoic termination is provided at the rear. This setup is illustrated in Fig. 5.76. 100 equally space frequency steps are considered within the range [20, 5000] Hz for the excitation.

The Young's modulus and static airflow resistivity are treated as random fields. This example illustrates the performance of the above mentioned methods for a single realization. The cor-

responding fields are respectively shown in Fig. 5.77. The remaining material parameters are homogeneously distributed and summarized in Table 5.25.

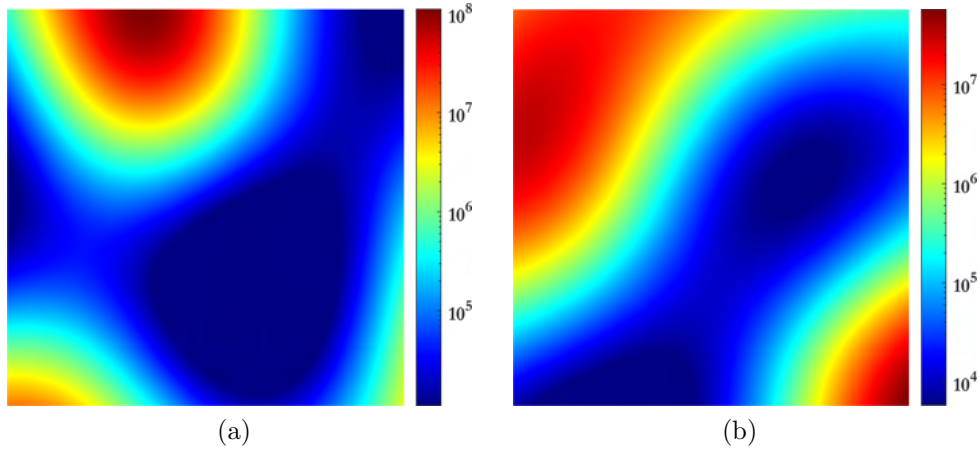


Figure 5.77: (a) Randomly sampled heterogeneous Young's modulus field, (b) Randomly sampled heterogeneous resistivity.

ϕ	α_∞	Λ	Λ'	ν	η_s	ρ
-	-	m	m	-	-	$\text{kg} \cdot \text{m}^{-3}$
0.99	1.01	9.8×10^{-5}	1.96×10^{-4}	0.44	0.1	8

Table 5.25: Homogeneous macroscopic material parameters

The domain is resolved with two meshes, detailed in Table 5.26. Mesh A contains 22,500 CVT elements. The multiscale mesh (Mesh B) comprises 100 coarse CVT elements. Each coarse element subsequently clusters 225 fine CVT elements within its interior.

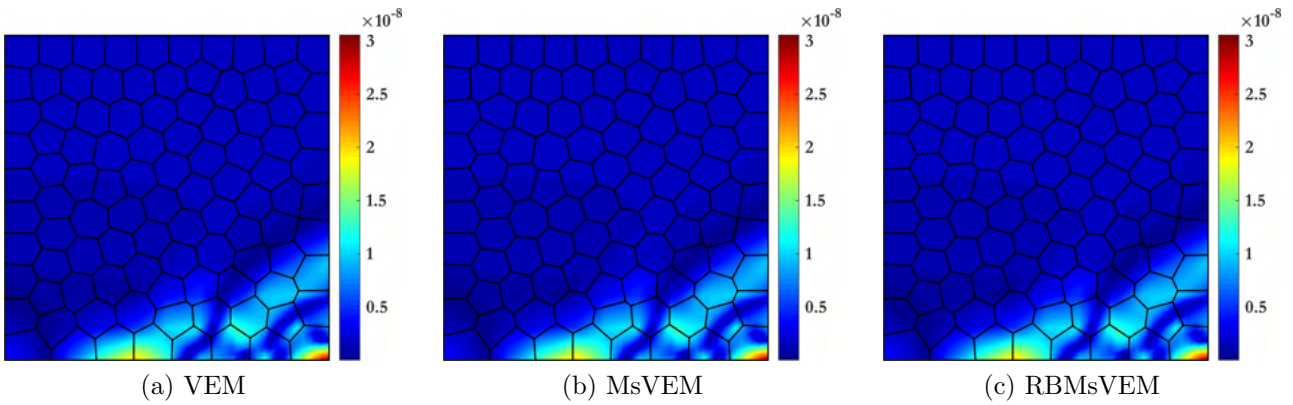
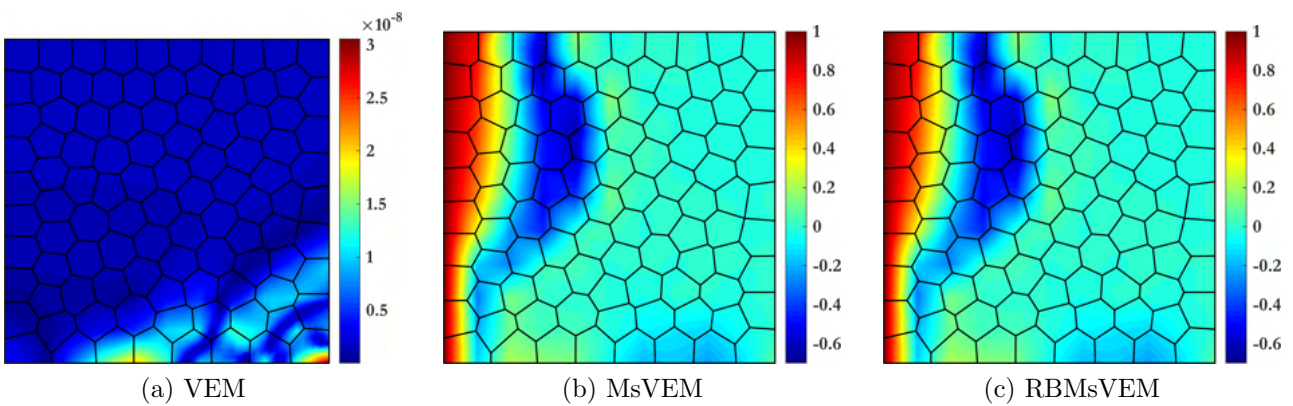
The displacement contours as evaluated by the VEM over Mesh A and the MsVEM (with oscillatory boundary conditions) over Mesh B are displayed in Figs. 5.78a and 5.78b, respectively. The contours as calculated by the Reduced Basis MsVEM (RBMsVEM) are also provided in Fig. 5.78c. Similarly, the corresponding pressure contours are provided in Fig. 5.79. A good agreement is observed between all methods.

The Sound Transmission Loss (STL) coefficient obtained across the spectrum is provided in Fig. 5.80. The STL curve corresponding to the MsVEM and RBMsVEM are observed to be practically identical to the VEM STL curve.

The computational run times incurred at critical bottlenecks by the three methods are provided in Fig. 5.81. The data provided herein has been averaged over three runs. The total time taken by each method is given in Fig. 5.81a. This is divided into preprocessing, solving and postprocessing

Full Mesh (Mesh A)		Multiscale Mesh (Mesh B)			
-	-	Macro		Micro	
Elements	Nodes	Elements	Nodes	Elements	Nodes
22500	44918	100	201	225	449

Table 5.26: Number of elements and nodes contained in each mesh.

Figure 5.78: Net displacement contours $\|\mathbf{u}\|$ at 5000 Hz.Figure 5.79: Pressure contours, i.e., $textp$ at 5000 Hz.

phases. The time taken for different operations in the preprocessing phase is highlighted in Fig. 5.81b. This comprises entirely of assembling operations for the VEM. The multiscale methods consist of an additional operation where multiscale basis functions are evaluated. The upscaling procedure is included within the assembly times here. Finally, the time required by the RBMsVEM to calculate the high-fidelity snapshot matrix, perform the SVD and obtain the POD basis is accounted for in the label "POD Basis".

It can be seen from Fig. 5.81b that the total pre-processing time taken by the MsVEM and RBMsVEM is significantly lower than the VEM. The reduced basis procedure proves to be relatively inexpensive, and noticeably accelerates computation of multiscale bases. The upscaling and assembly procedure costs incurred by both multiscale methods are comparable.

Fig. 5.81a shows that the spectral solution procedure is the primary bottleneck in fine-scale methods. This costs incurred at this phase by the multiscale methods is nearly negligible (1.46 s and 1.59 s for the MsVEM and RBMsVEM, respectively). The downscaling phase, where fine scale information is retrieved, is comparable in both multiscale methods, as evidenced by the postprocessing times. This operation is non-existent in the VEM, where acoustic indicators can directly be computed after solving.

The MsVEM and RBMsVEM offer speedups of 7.75 and 11.97, respectively, over the VEM solution. Further, the RBMsVEM offers a speed of 1.55 over the MsVEM.

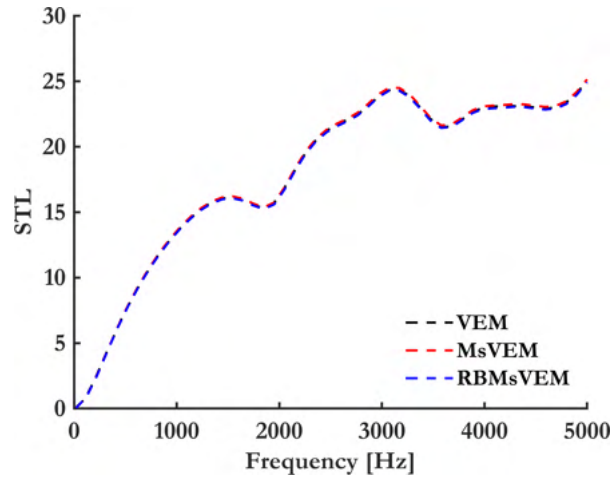


Figure 5.80: Sound Transmission Loss coefficient as calculated with the VEM, MsVEM and RBMsVEM for the heterogeneous realization shown in Fig. 5.77.

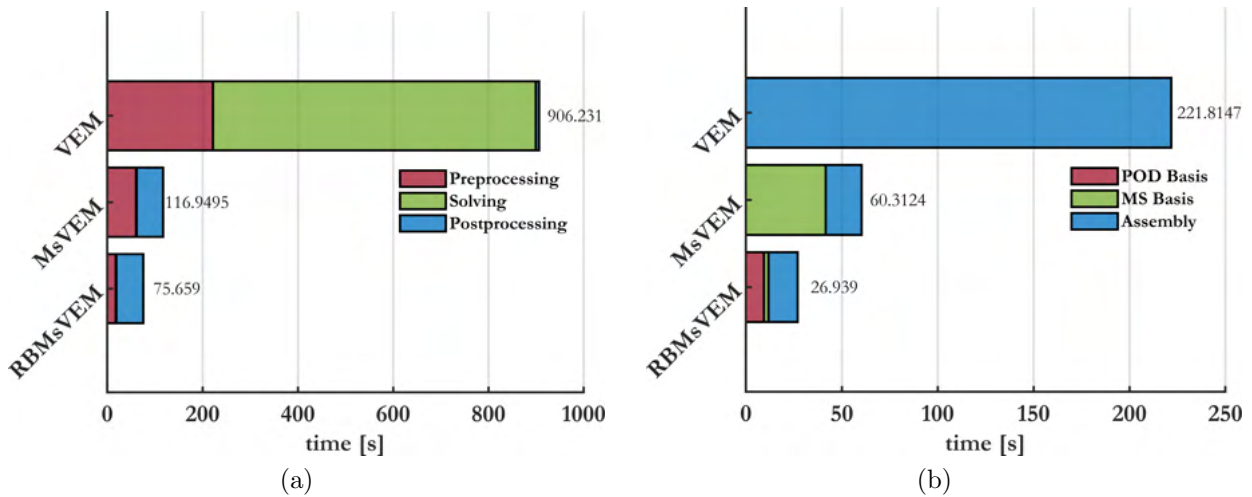


Figure 5.81: (a) Total time taken, (b) Time taken for preprocessing.

5.10 Summary

The MsVEM is introduced as a novel alternative to the MsFEM. The VEM as developed in Chapter 3 is introduced into the fine scale of the MsFEM to allow for flexible meshing opportunities. The optimal convergence behaviour of the method with respect to elastostatic and poromechanical problems is first demonstrated in Examples 5.3.1, 5.5.1 and 5.9.2. The ability of the method to handle different fine scale mesh types for homogeneous and heterogeneous problems are verified in Examples 5.3.2 and 5.3.4. This flexibility is further exploited in Example 5.3.3 to significantly drive down costs in relation to the MsFEM.

Relaxed meshing options are translated across all scales by extending the method in Section 5.4.1 to account for coarse-scale polygonal (non-convex) discretizations as well. The new coarse-scale flexibility is applied to complicated geometries to drive down computational complexity in Examples 5.5.3 and 5.9.3. Oscillatory boundary conditions are introduced as an alternative to linear, periodic and oversampling strategies to compute multiscale basis functions in Section 5.4.1. The accuracy and efficiency of this development over the other standard boundary conditions is demonstrated in Example 5.5.2.

A Parametric Model Order Reduction (pMOR) scheme based on the POD is introduced at the fine scale for the first time in Section 5.8 to develop a novel Reduced Basis Multiscale Virtual Element Method (RBMsVEM). This is used to further accelerate multiscale basis function computations for coupled spectral problems in Examples 5.9.1 and 5.9.4.

The MsVEM is currently restricted to 2-D domains. Extensions to account for 3-D geometries is a work in progress.

Part IV

Summary

Chapter 6

Conclusions and Future Research

6.1 Conclusions

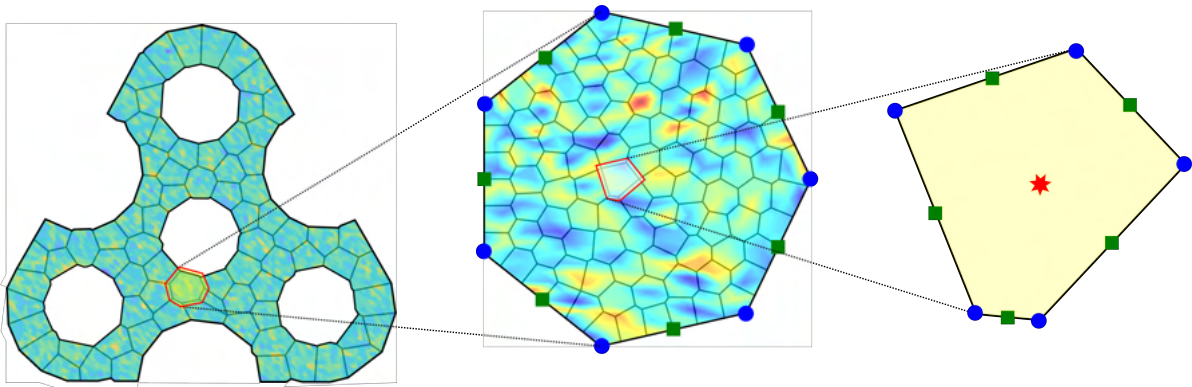


Figure 6.1: A fidget-spinner shaped poroelastic domain with a highly heterogeneous material definition. (a) Coarse-scale CVT mesh, (b) Example coarse-element defining an RVE with a fine-scale CVT mesh, (c) Example fine-element contained within the RVE.

A novel computational method, i.e., the Multiscale Virtual Element Method (MsVEM) is developed in this thesis to describe mechanical and vibroacoustical phenomena in poroelastic media. A schematic of the method is provided in Fig. 6.1.

In this setting, the Virtual Element Method (VEM) is employed at the fine scale as an alternative to classical Finite Element Methods (FEM). The resulting meshing versatility allows for enhanced efficiency with respect to resolving complex inclusions, boundaries, interfaces and waves. Further advantages such as robustness to mesh distortion, ability to naturally accommodate non-conforming domain interfaces and a reduced number of quadrature points, make the VEM a very attractive alternative to conventional discretization approaches.

The proposed method is originally developed initially for elastostatics. Mesh sensitivity analyses show that the method converges at an optimal rate for different fine-mesh types, even in the presence of large heterogeneities. An intelligently chosen fine-scale polygonal discretization is chosen to exploit the power of the VEM to significantly drive down costs associated with computing multiscale basis functions, without affecting the accuracy of the results.

Following this, a mixed-VEM schema was proposed for discretizing the Biot consolidation equa-

tions. The multiscale framework is extended to account for two-phase coupled phenomena. The mixed-VEM is inserted into the fine scale. Fine-scale mesh flexibility induces flexible coarse-scale element geometries as well. The method is generalized to accommodate polygonal (potentially non-convex) elements at all scales, for the first time. Optimal convergence rates are observed for the coupled MsVEM, even in the context of non-standard global geometries. The influence of kinematical constraints on the accuracy of numerically evaluated multiscale basis function is investigated by comparing linear, periodic and oscillatory conditions. Periodic boundaries offer greater accuracies than linear boundary conditions when geometrical periodicity is available. In the case of the unstructured coarse domains, periodic constraints are not possible to implement. In homogeneous cases, oscillatory conditions reduce to linear constraints. In the case of heterogeneous problems, the oscillatory boundaries are shown to provide superior accuracy, at a marginally higher cost.

Next, a mixed-VEM scheme is originally developed to treat wave propagation in poroelastic materials. The method is observed to converge optimally at low, mid and high frequencies. The reduced quadrature requirements mentioned earlier are exploited to mimic p-refinement strategies commonly use in computational acoustics to resolve high frequency waves. The subsequent cost advantages are highlighted. The enhance mesh flexibility is used to resolve non-conforming interfaces through a node-insertion algorithm. The classical isotropic VEM stabilization scheme may not scale appropriately in the presence of elements with non-standard aspect ratios. An alternate non-isotropic VEM stabilisation scheme is investigated and comparisons are made. Although the differences are not highly significant, such deviations may become prevalent in more extreme cases of mesh distortion.

The coupled multiscale framework is now extended to the frequency domain through a Fourier transform, to obtain a novel MsFEM for wave propagation in porous media. Accelerations achieved in comparison to the FEM are given in the context of porous composites. Further, the mixed-VEM for wave propagation is incorporated into the fine scale. The resulting MsVEM is found to converge at optimal rates across the frequency bandwidth. The convergence behaviour is primarily dependent on the coarse scale discretization. Conversely, the fine-scale discretization is found to not play a significant role in affecting absolute errors or error convergence rates in the case of homogeneous problems. The flexibility of the method is exploited in accurately simulating the vibroacoustic response of a porous material with rigid inclusions, at significantly reduced computational run times.

Owing to the non-linear dependence of the governing equations on frequency, the multiscale basis functions need to be repeatedly evaluated at all frequency steps. A Singular Value Decomposition (SVD) based Proper Orthogonal Decomposition (POD) approach is used at the fine scale to speed up this procedure. Computational benefits resulting from the novel Reduced Basis Multiscale Virtual Element Method is shown for a heterogeneous porous material. An economical variant of the SVD is used to control bottlenecks associated with computing the POD bases.

6.2 Limitations and extensions

The following are some research directions that can further improve the work discussed in this thesis:

1. **3-D extensions:** The MsVEM discussed herein is current applicable only to 2-D scenarios. This is because, the state of the art VEM literature primarily deals with employing this method in novel 2-D applications. The 3-D counterparts are relatively sparse [100,189]. The limitation is further augmented by the unavailability of robust polyhedral meshing algorithms. However, such a mesher has been made available very recently in [339]. This will prove invaluable in developing the method to handle more complex problem instances.
2. **Constitutive Modelling**
 - **Pore-fluid:** The Biot $\mathbf{u} - p$ formulations used throughout this thesis for characterizing poromechanics and wave propagation is restricted to a two-phase medium, i.e., an elastic skeleton composed of a single grain, fully saturated by a single pore-fluid. While consolidation problems admit different pore-fluids, e.g., air, water etc., the material models used for acoustic wave propagation currently only admit air. This is reflected in the macroscopic mechanics through a weak coupling, i.e., a one way influence of the skeleton on the pore-fluid. The weak-coupling hypothesis does not necessarily hold when describing other pore-fluids. Relaxing this assumption within the numerical scheme can prove useful in studying wave propagation through water saturated media. Further generalizations to partial saturated materials, multiphase media [22,23] is another interesting future task.
 - **Solid skeleton:** All composite materials discussed in this work are isotropic. This is because of a fundamental limitation of the $\mathbf{u} - p$ coupled framework in accounting for anisotropies. Generalizing the MsVEM to work with alternate formulations, such as the $\mathbf{u} - \mathbf{U}$ or $\mathbf{u} - \mathbf{w}$ will help remedy this shortcoming.
 - **Material and geometric non-linearities:** The materials used in the elastostatics and consolidation problem assume a constant small-strain linear-elastic constitutive law. This is restrictive, and not realistic when considering large deformation problems. Extensions of the MsFEM to non-linear problems have already been done in [8]. Time varying porous material parameters depending on an evolving microstructure has been developed in [340,341]. These developments can be used in the future within an MsVEM framework to widen the scope of applications.
3. **Locking:** Shear and volumetric locking is a well documented phenomena in low order poroelastic finite elements [342]. This thesis does not address these effects as they are not prevalent in the kinds of applications considered herein, as evidenced by the numerous examples presented. However, it is important that the a locking free VEM, as done in [343–345], be integrated into the MsVEM for further extensions.
4. **Boundary Conditions:** The TMM is used throughout this thesis as a verification tool for vibroacoustic applications. It assumes an infinite lateral dimension. This is currently reproduced in a numerical methods context by considering a very large lateral dimension. A more computationally efficient way to do this is a Floquet-Bloch periodic boundary condition [195] (see Section 4.5 for a detailed explanation). Further, all acoustic excitations considered here fall within the regime of plane waves. More general cases such as point excitations and spherical wavefronts cannot be handled at present. This is because, the Robin-type impedance boundary conditions, employed at the rear face in transmission loss problems, can employ only monochromatic angles of incidence (see Eq. (2.144)). This is addressed by

implementing absorbing/non-reflecting boundaries at the rear, such as the Infinite Element Method (IEM) [346–350] or Perfectly Matched Layers (PML) [351–355]. These technologies admit polychromatic angles of incidence and mimic anechoic termination. The IEM achieves this by integrating Sommerfeld far field radiation conditions REF into semi-infinite boundary elements. The PML achieves this by artificially introducing anisotropic dissipation into the absorbing layer. This dissipation is gradually varied so as to not cause numerical wave reflection due to any impedance mismatches (hence the label "Perfectly matched"). The PML has already been implemented. The IEM is currently a work under progress.

5. **Reduced Basis POD:** The POD employed at the fine scale (see Section 5.6) has significant scope for improvement. It is currently limited to material distributions with a low Kolmogorov width, i.e., relatively low parametric manifold complexity. Using the Reduced Basis MsVEM in the case of materials with significantly higher oscillations in the underlying morphology requires more sophisticated approaches, e.g., [332, 333]. This is a useful future avenue for exploration.

6. Methodological Limitations:

- **Virtual Element Methods:** The VEM, while able to accurately resolve singularities and strong discontinuities induced by crack propagation, still requires very fine discretizations to handle asymptotic fields and stress intensity factors generated at crack tips. This is handled more efficiently by XFEM/PUFEM through crack tip enrichment, and by SBFEM through exploiting analytic expressions along the radial direction [356]. Another limitation posed by the method pertains to its reliance on stability approximations. Appropriate scaling and dependence on material and geometric parameters are normally estimated a posteriori through engineering judgment. Establishing rigorous theoretical a priori bounds remains a topic of active research. Consequently, this has become a significant point of debate between the VEM community on the one hand and the PFEM and SBFEM community on the other.
- **Multiscale Finite Element Methods:** The MsFEM does not provide locally conservative solutions [357]. As a result, they cannot be directly applied to solve multiphase porous media transport problems [358]. Alternate methods such as the Mixed Multiscale Finite Element Method [359], the Variational Multiscale Method [227] and the Multiscale Finite Volume Method [360] have been developed to address this shortcoming.

6.3 Future applications

The following contains several interesting future applications of the MsVEM that are not immediately related to the contents of this thesis:

6.3.1 Topology Optimization

Designing optimal shapes and layouts for engineering structures have traditionally been done through informed judgement. This includes expert intuition, trial-error and improvements based

on previous design iterations. The advent of numerical techniques and powerful computational resources have led to more efficient methods, that can yield superior designs. One such method, i.e., structural topology/shape optimization, originally introduced in [361,362], involves searching for a topology that extremizes a desired performance indicator. This is numerically done by identifying an optimal material/void distribution in the underlying finite element structure. However, the complexity of the problem can quickly render most exact optimization techniques prohibitively expensive.

Heuristic approaches address this problem by delivering solutions sufficiently close to the global optima within a reasonable time. It is to be noted that these techniques do not guarantee global optima. Two universally used heuristic approaches in topology optimization are the Solid Isotropic Material with Penalisation (SIMP) [363–366], and Level Set Methods (LSM) [367–369]. The SIMP employs a penalty based interpolation scheme to describe intermediate properties between the chosen materials and void. Further, gradient based strategies such as the Method of Moving Asymptotes (MMA) [370] is used to achieve near-optimal designs. The LSM deploys a scalar valued field describing the design domain. The boundaries of the topology are determined by iso-contours of this field. New topologies are initiated through hole-nucleation techniques. The scalar field is subsequently optimized to yield improved designs. These methods while very powerful, are nevertheless highly dependent on the initial configuration. As these approaches rely on gradient based techniques, it is quite likely that the final converged topology might be constrained to a local optimum. Traditionally, this shortcoming is mitigated by performing the optimization for a large family of randomly sampled initial configurations.

An alternate family of topology optimization techniques, collectively called evolutionary topology optimization, addresses this limitation by using gradient-free methods, e.g., genetic algorithms [371,372], Covariance Matrix Adaptation Evolution Strategies (CMA-ES) [373,374], differential evolution [375,376], tabu search [377,378] etc.

Classical structural topology optimization applications have revolved around compliance minimization problems [379–382]. Extended applications to other relevant engineering problems have been reviewed in [383,384]. Acoustic topology optimization is an emerging field [385–398] and primarily uses the SIMP and LSM. Evolutionary optimization techniques are virtually unexplored in this domain (see e.g., [399]).

Different gradient-based and gradient-free algorithms are novelly applied to a multi-layer acoustic optimization problem in [400] and propose design solutions with regards to maximizing sound absorption. Next, these techniques are applied to an acoustic topology framework in [401], to study the quality and efficiency of the solutions delivered by each method.

There exists a large scope for reducing the size of the problem. The MsFEM with 4-noded quadrilateral and 8-node hexahedral coarse elements have been used to accelerate structural topology optimization problems in [402–404]. The MsFEM with multi-noded coarse-elements has been deployed within a SIMP and LSM framework in [405]. The parallelisability of the MsFEM makes it a highly attractive choice for efficient topology optimization procedures.

The advantages of flexible unstructured meshes over structured quadrilateral meshes has been extensively demonstrated in [62,406,407]. To this end, work is currently being done to apply the multi-node MsVEM to SIMP and LSM frameworks for treated compliance minimisation problems. Extending the method to acoustic topology optimization is a valuable future stake.

6.3.2 Condensed models for vibroacoustics of multi-layered structures

As pointed out in Example 3.6.2, multi-layered systems offer improved weight, stiffness and dissipation properties, thereby augmenting noise and vibration isolation behaviours. A large number of theoretical frameworks have developed to simulate the dynamic response of such materials [408–414, 414–416]. Among these, condensed plate models (alternative called equivalent models) [417–422] replace the entire multilayer system with a single layer comprising equivalent dynamic properties, namely the dynamic bending stiffness $\tilde{D}_{\text{eq}}(\omega)$ and dynamic mass density $\tilde{\rho}_{\text{eq}}(\omega)$. This provides definitive cost related advantages when implemented within a numerical scheme [423].

Up to this point, all condensed plate models employ plate elements to describe the mechanics of the single equivalent layer. These include the Love-Kirchhoff theory [424, 425] for thin plates and Reissner-Mindlin theory [408, 409, 426] for thick plates. Since these theories assume a constant normal displacement, they account only for anti-symmetric modes, i.e., bending and shear. Membrane modes are relatively insignificant in flat structures; although, these modes can, in principle, be captured by deploying shell elements instead of plates. None of these models can describe symmetric motion, i.e., compressional or dilational modes. This is undesirable as such modes can be excited even at low frequencies, especially in double-walled partition windows in building applications. This drawback is addressed in [427] through a novel theoretical condensed model.

A condensed finite element scheme is proposed for the first time in [428], using the equivalent properties developed in [427], to accurately simulate all relevant dynamic modes of symmetric multilayered systems. These include symmetric and antisymmetric modes. The equivalent layer is modelled using two degenerate MITC4+ Reissner-Mindlin shell layers [429, 430]. The two shells are appropriately coupled to each other using Lagrange Multipliers. In addition to accurately forecasting the vibroacoustic behaviour of the system, significant reductions in computational time, when compared with 3-D hexahedral discretizations, are also demonstrated.

The numerical scheme developed by us in [428] is currently applicable only to symmetric, flat multi-layered structures. Extending the approach to account for asymmetric configurations with curved geometries is an important future development. The extension is currently not straightforward as curvature introduces coupling between symmetric and anti-symmetric behaviours.

6.3.3 Random vibroacoustics in porous media

All sound propagation problems addressed in this thesis concern monochromatic stationary excitations. Consequently, solving these problems in the frequency domain proves very simple and efficient. However, there are several applications that are not amenable to a frequency domain treatment. These include polychromatic excitations such as ambient noise [431, 432], random vibroacoustics [433–435], characterisation for medical purposes through inverse problems [436, 437] and scenarios involving transient wave propagation, e.g., earthquake [438, 439], wind [440, 441] and ocean engineering [442, 443]. A time-domain approach is necessary for studying these phenomena in detail.

Mapping the relevant frequency domain equations to the time domain via an inverse Fourier transform poses some interesting challenges. The parameters characterizing the medium of propagation are almost universally known only in the frequency domain [12]. This is attributed to

historical reasons and the relative ease of modelling dissipation with respect to frequencies. Consequently, the ensuing time domain equations also contain frequency dependent content. This is widely encountered in soils, fluids etc. [444–449]. The dissipation models can range from quite simple, e.g. Kelvin Voigt, Maxwell models [450, 451] to highly complicated functions of frequency [12, 17, 452]. Solving time-domain equations containing such frequency-dependent state matrices is not possible.

This limitation is addressed in the signal-processing literature by employing digital filters [453–460]. The response Power Spectral Density (PSD) is approximated by a cascade of linear filters. These filters contain frequency-invariant state-matrices. As a result, the filter approximation can be mapped to the time-domain and readily solved in a straightforward manner. The cascade filter approximation technique is currently being applied to treat the case of rigid skeleton porous media subject to stochastic excitations, e.g., white-noise and solving the resulting frequency-invariant time domain equations with an augmented state-space approach [461].

An alternate powerful approach concerning fractional derivatives [462–465] has been applied to describe the damping behaviour of viscoelastic materials [466, 467] and of transient wave propagation in porous materials [468–472]. The porous media fractional derivative models only address low frequency and high frequency asymptotic limits for ease of presentation. However, this is insufficient for uniform PSD stochastic excitations such as Gaussian white-noise. At present, this knowledge gap is being addressed by developing a generalized fractional calculus model capable of describing transient wave propagation in rigid skeleton porous media. This model is intended to hold validity over the entire excitation spectrum.

Both the filter state space approach and the generalized fractional calculus approach are current restricted only to porous media with rigid skeleton assumptions. Extensions to poroelastic media is an important future area of research. Further, both methods prove very expensive in the case of systems with large number of DoFs. This is because the augmented state space representation drastically increases the number of unknowns by adding additional states. Furthermore, the finite difference scheme used to solve fractional stochastic differential equations is recursive in nature, and proves expensive at fine discretizations [473, 474]. For these reasons, it is currently not possible to quantify the response of materials with more complex layouts, i.e., inclusions, interfaces, heterogeneities etc. to random excitations. The MsVEM developed in this thesis is expected to function as a valuable model order reduction tool to significantly dive down these computational costs.

6.3.4 Fractures in composite materials with mesoscale inclusions

Particle reinforced composite materials are broadly deployed in modern aerospace, automotive, and construction applications [475–477]. This is due to their proven superior mechanical properties over conventional materials. A drawback of composites is their typically complex and in cases tessellated geometry at the mesoscale; this gives rise to combined damage mechanisms, e.g., matrix cracking, particle fracture, debonding that deviate from the typical “high strength and ductile metal” paradigm. However, if harnessed, this complexity can result in components of tailored properties, e.g., of increased fracture toughness and pseudo-ductile post fracture response. Additive manufacturing nowadays provides the means for generating exotic designs. Yet, the flexibility provided by manufacturing also poses a series of challenges vis-à-vis the numerical

simulation of material layouts. Accounting for complex morphologies of the heterogeneities encompassed by a representative volume element (RVE) using traditional element geometries, e.g., quadrilateral and triangular elements, may necessitate quite fine and difficult to generate mesoscopic mesh discretizations, thus driving up the corresponding analysis costs. Allowing for more flexible, even non-convex, element topologies can significantly alleviate this shortcoming.

The application of the VEM to resolve fractures propagating in particle composites with mesoscale inclusions of arbitrary geometries is currently being explored. To this end, a phase field model is employed to robustly model fracture. The accuracy and efficiency of polygonal elements against the standard finite element method is being examined by conducting a series of numerical experiments on randomly generated RVEs. Providing a generic description also accounting for cohesive failure at interfaces is a work in progress. Applying the MsVEM as an acceleration tool is also a useful future avenue of work.

6.3.5 Data driven modelling

Obtaining optimal multilayer configurations and topologies for an absorption problem as done by us [400,401] is an expensive procedure. The complexity of the multilayer problem is significantly reduced by employing our condensed model as proposed in [428]. However, this condensed model is currently restricted to physically symmetric configurations only. To further accelerate such iterative procedures without these restrictive assumptions, one can train a surrogate model to generate near instantaneous solutions.

Training the model is a major bottleneck, as significantly large number of high-fidelity solutions are required as a training set. All model reduction strategies proposed in this thesis, such as the MsVEM and reduced basis methods are currently being investigated as potential solutions to alleviate the costs associated with this operation.

Bibliography

- [1] https://europa.eu/european-union/topics/transport_en.
- [2] <https://www.acare4europe.org/sites/acare4europe.org/files/document/volume1.pdf>.
- [3] Erastus H Lee and Wei H Yang. On waves in composite materials with periodic structure. *SIAM Journal on Applied Mathematics*, 25(3):492–499, 1973.
- [4] Dimitrios Chronopoulos, M Ichchou, B Troclet, and O Bareille. Computing the broadband vibroacoustic response of arbitrarily thick layered panels by a wave finite element approach. *Applied acoustics*, 77:89–98, 2014.
- [5] PJ Shorter. Wave propagation and damping in linear viscoelastic laminates. *The Journal of the Acoustical Society of America*, 115(5):1917–1925, 2004.
- [6] Luc Jaouen, Amélie Renault, and Mickael Deverge. Elastic and damping characterizations of acoustical porous materials: Available experimental methods and applications to a melamine foam. *Applied acoustics*, 69(12):1129–1140, 2008.
- [7] François-Xavier Bécot, Luc Jaouen, and Emmanuel Gourdon. Applications of the dual porosity theory to irregularly shaped porous materials. *Acta acustica united with Acustica*, 94(5):715–724, 2008.
- [8] S. P. Triantafyllou and E. N. Chatzi. A hysteretic multiscale formulation for nonlinear dynamic analysis of composite materials. *Computational Mechanics*, 54:763–787, 2014.
- [9] Jörg Schröder. A numerical two-scale homogenization scheme: the fe 2-method. In *Plasticity and beyond*, pages 1–64. Springer, 2014.
- [10] M Tootkaboni and L Graham-Brady. A multi-scale spectral stochastic method for homogenization of multi-phase periodic composites with random material properties. *International journal for numerical methods in engineering*, 83(1):59–90, 2010.
- [11] L Beirão Da Veiga, F. Brezzi, A. Cangiani, G. Manzini, L.D. Marini, and A. Russo. Basic principles of virtual element methods. *Mathematical Models and Methods in Applied Sciences*, 23(1):199–214, 2013.
- [12] L Jaouen. Acoustical porous material recipes. *Website. URL: http://apmr.matelys.com*, 2019.
- [13] Jean Allard and Noureddine Atalla. *Propagation of sound in porous media: modelling sound absorbing materials 2e*. John Wiley & Sons, 2009.
- [14] Karl Terzaghi. *Erdbaumechanik auf bodenphysikalischer Grundlage*. F. Deuticke, 1925.
- [15] Karl Terzaghi. Liner-plate tunnels on the chicago (il) subway. *Transactions of the American Society of Civil Engineers*, 108(1):970–1007, 1943.
- [16] Maurice A Biot. General theory of three-dimensional consolidation. *Journal of applied physics*, 12(2):155–164, 1941.
- [17] Maurice A Biot. Theory of elasticity and consolidation for a porous anisotropic solid. *Journal of applied physics*, 26(2):182–185, 1955.
- [18] MA Biot. Theory of elastic waves in a fluid-saturated porous solid. 1. low frequency range. *J. Acoust. Soc. Am.*, 28:168–178, 1956.

- [19] Maurice A Biot. Theory of propagation of elastic waves in a fluid-saturated porous solid. ii. higher frequency range. *The Journal of the Acoustical Society of America*, 28(2):179–191, 1956.
- [20] Maurice A Biot. Mechanics of deformation and acoustic propagation in porous media. *Journal of applied physics*, 33(4):1482–1498, 1962.
- [21] Olivier Dazel, Bruno Brouard, Claude Depollier, and Stéphane Griffiths. An alternative biot’s displacement formulation for porous materials. *The Journal of the Acoustical Society of America*, 121(6):3509–3516, 2007.
- [22] David Maria Jacobus Smeulders. *On wave propagation in saturated and partially saturated porous media*. PhD thesis, Citeseer, 1992.
- [23] Reint De Boer. *Theory of porous media: highlights in historical development and current state*. Springer Science & Business Media, 2012.
- [24] Arnold Verruijt. Elastic storage of aquifers. *Flow through porous media*, 1:331–376, 1969.
- [25] James R Rice and Michael P Cleary. Some basic stress diffusion solutions for fluid-saturated elastic porous media with compressible constituents. *Reviews of Geophysics*, 14(2):227–241, 1976.
- [26] OC Zienkiewicz, CT Chang, and P Bettess. Drained, undrained, consolidating and dynamic behaviour assumptions in soils. *Geotechnique*, 30(4):385–395, 1980.
- [27] Jean H Prévost. Mechanics of continuous porous media. *International Journal of Engineering Science*, 18(6):787–800, 1980.
- [28] Jean H Prevost. Nonlinear transient phenomena in saturated porous media. *Computer Methods in Applied Mechanics and Engineering*, 30(1):3–18, 1982.
- [29] Olivier Coussy. *Mécanique des milieux poreux*. Editions Technip, 1991.
- [30] Olivier Coussy. *Poromechanics*. John Wiley & Sons, 2004.
- [31] Yasushi Miki. Acoustical properties of porous materials-modifications of Delany-Bazley models. *Journal of the Acoustical Society of Japan (E)*, 11(1):19–24, 1990.
- [32] D. L. Johnson, J. Koplik, and R. Dashen. Theory of dynamic permeability and tortuosity in fluid-saturated porous media. *J. Fluid Mech.*, 176:379–402, 1987.
- [33] Y. Champoux and J-F. Allard. Dynamic tortuosity and bulk modulus in air-saturated porous media. *J. Appl. Phys.*, 70:1975–1979, 1991.
- [34] D. Lafarge, P. Lemarinié, J-F. Allard, and V. Tarnow. Dynamic compressibility of air in porous structures at audible frequencies. *J. Acoust. Soc. Am.*, 102(4):1995–2006, 1997.
- [35] Francois-Xavier Bécot and Luc Jaouen. An alternative biot’s formulation for dissipative porous media with skeleton deformation. *The Journal of the Acoustical Society of America*, 134(6):4801–4807, 2013.
- [36] Nouredine Atalla, Raymond Panneton, and Patricia Debergue. A mixed displacement-pressure formulation for poroelastic materials. *The Journal of the Acoustical Society of America*, 104(3):1444–1452, 1998.
- [37] OC Zienkiewicz and T Shiomi. Dynamic behaviour of saturated porous media; the generalized biot formulation and its numerical solution. *International journal for numerical and analytical methods in geomechanics*, 8(1):71–96, 1984.
- [38] LM Brekhovskikh. *Waves in layered media* academic press. New York, 1960.
- [39] DL Folds and CD Loggins. Transmission and reflection of ultrasonic waves in layered media. *The Journal of the Acoustical Society of America*, 62(5):1102–1109, 1977.
- [40] Kurt P Scharnhorst. Properties of acoustic and electromagnetic transmission coefficients and transfer matrices of multilayered plates. *The Journal of the Acoustical Society of America*, 74(6):1883–1886, 1983.

- [41] B Brouard, D Lafarge, and J-F Allard. A general method of modelling sound propagation in layered media. *Journal of Sound and Vibration*, 183(1):129–142, 1995.
- [42] TE Vigran. Sound transmission in multilayered structures—introducing finite structural connections in the transfer matrix method. *Applied Acoustics*, 71(1):39–44, 2010.
- [43] Xavier Olny and Claude Boutin. Acoustic wave propagation in double porosity media. *The Journal of the Acoustical Society of America*, 114(1):73–89, 2003.
- [44] Pascale Royer, Jean-Louis Auriault, and Claude Boutin. Macroscopic modeling of double-porosity reservoirs. *Journal of Petroleum Science and Engineering*, 16(4):187–202, 1996.
- [45] Claude Boutin and Pascale Royer. On models of double porosity poroelastic media. *Geophysical Supplements to the Monthly Notices of the Royal Astronomical Society*, 203(3):1694–1725, 2015.
- [46] O Dazel, F-X Bécot, and L Jaouen. Biot effects for sound absorbing double porosity materials. *Acta Acustica united with Acustica*, 98(4):567–576, 2012.
- [47] J-P Groby, O Dazel, A Duclos, L Boeckx, and Luc Kelders. Enhancing the absorption coefficient of a backed rigid frame porous layer by embedding circular periodic inclusions. *The Journal of the Acoustical Society of America*, 130(6):3771–3780, 2011.
- [48] Fabien Chevillotte, Luc Jaouen, and Francois-Xavier Bécot. On the modeling of visco-thermal dissipations in heterogeneous porous media. *The Journal of the Acoustical Society of America*, 138(6):3922–3929, 2015.
- [49] Karel N van Dalen. Governing equations for wave propagation in a fluid-saturated porous medium. In *Multi-Component Acoustic Characterization of Porous Media*, pages 9–28. Springer, 2013.
- [50] Oscar Kelder. *Frequency-dependent wave propagation in water-saturated porous media*. Technische Universiteit Delft, 1997.
- [51] Arnold Verruijt. Theory of consolidation. In *Computational Geomechanics*, pages 8–34. Springer, 1995.
- [52] Andi Merxhani. An introduction to linear poroelasticity. *arXiv preprint arXiv:1607.04274*, 2016.
- [53] Maurice A Biot and D Willis. The elastic coefficients of the theory of consolidation. *J. appl. Mech.*, 24:594–601, 1957.
- [54] Jacob Bear and Arnold Verruijt. *Modeling groundwater flow and pollution (vol. 2)*, 2012.
- [55] Jean-François Sigrist. *Fluid-structure interaction: an introduction to finite element coupling*. John Wiley & Sons, 2015.
- [56] Patricia Debergue, Raymond Panneton, and Noureddine Atalla. Boundary conditions for the weak formulation of the mixed (u, p) poroelasticity problem. *The Journal of the acoustical Society of america*, 106(5):2383–2390, 1999.
- [57] Noureddine Atalla and Franck Sgard. *Finite element and boundary methods in structural acoustics and vibration*. CRC Press, 2015.
- [58] SE Mousavi and N Sukumar. Numerical integration of polynomials and discontinuous functions on irregular convex polygons and polyhedrons. *Computational Mechanics*, 47(5):535–554, 2011.
- [59] Joseph E Bishop. A displacement-based finite element formulation for general polyhedra using harmonic shape functions. *International Journal for Numerical Methods in Engineering*, 97(1):1–31, 2014.
- [60] Gianmarco Manzini, Alessandro Russo, and N Sukumar. New perspectives on polygonal and polyhedral finite element methods. *Mathematical Models and Methods in Applied Sciences*, 24(08):1665–1699, 2014.
- [61] Cameron Talischi, Glaucio H Paulino, Anderson Pereira, and Ivan FM Menezes. Polytop: a matlab implementation of a general topology optimization framework using unstructured polygonal finite element meshes. *Structural and Multidisciplinary Optimization*, 45(3):329–357, 2012.

- [62] Glaucio H Paulino and Arun L Gain. Bridging art and engineering using escher-based virtual elements. *Structural and Multidisciplinary Optimization*, 51(4):867–883, 2015.
- [63] Daniel W Spring, Sofie E Leon, and Glaucio H Paulino. Unstructured polygonal meshes with adaptive refinement for the numerical simulation of dynamic cohesive fracture. *International Journal of Fracture*, 189(1):33–57, 2014.
- [64] N Sukumar and JE Bolander. Voronoi-based interpolants for fracture modelling. *Tessellations in the Sciences*, 2009.
- [65] SE Leon, DW Spring, and GH Paulino. Reduction in mesh bias for dynamic fracture using adaptive splitting of polygonal finite elements. *International Journal for Numerical Methods in Engineering*, 100(8):555–576, 2014.
- [66] SOR Biabanaki, AR Khoei, and P Wriggers. Polygonal finite element methods for contact-impact problems on non-conformal meshes. *Computer Methods in Applied Mechanics and Engineering*, 269:198–221, 2014.
- [67] Cameron Talischi, Anderson Pereira, Glaucio H Paulino, Ivan FM Menezes, and Márcio S Carvalho. Polygonal finite elements for incompressible fluid flow. *International Journal for Numerical Methods in Fluids*, 74(2):134–151, 2014.
- [68] Eugene L Wachspress and WACHSPRESS EL. A rational finite element basis. 1975.
- [69] Joe Warren. Barycentric coordinates for convex polytopes. *Advances in Computational Mathematics*, 6(1):97–108, 1996.
- [70] Robin Sibson. A vector identity for the dirichlet tessellation. In *Mathematical Proceedings of the Cambridge Philosophical Society*, volume 87, pages 151–155. Cambridge University Press, 1980.
- [71] VV Belikov, VD Ivanov, VK Kontorovich, SA Korytnik, and A Yu Semenov. The non-sibsonian interpolation: a new method of interpolation of the values of a function on an arbitrary set of points. *Computational mathematics and mathematical physics*, 37(1):9–15, 1997.
- [72] Michael S Floater. Mean value coordinates. *Computer aided geometric design*, 20(1):19–27, 2003.
- [73] Michael S Floater, Géza Kós, and Martin Reimers. Mean value coordinates in 3d. *Computer Aided Geometric Design*, 22(7):623–631, 2005.
- [74] N Sukumar. Construction of polygonal interpolants: a maximum entropy approach. *International journal for numerical methods in engineering*, 61(12):2159–2181, 2004.
- [75] Marino Arroyo and Michael Ortiz. Local maximum-entropy approximation schemes: a seamless bridge between finite elements and meshfree methods. *International journal for numerical methods in engineering*, 65(13):2167–2202, 2006.
- [76] N Sukumar and EA Malsch. Recent advances in the construction of polygonal finite element interpolants. *Archives of Computational Methods in Engineering*, 13(1):129, 2006.
- [77] Sundararajan Natarajan, Stéphane Bordas, and D Roy Mahapatra. Numerical integration over arbitrary polygonal domains based on Schwarz–Christoffel conformal mapping. *International Journal for Numerical Methods in Engineering*, 80(1):103–134, 2009.
- [78] Bashir Ahmad, Ahmed Alsaedi, Franco Brezzi, L Donatella Marini, and Alessandro Russo. Equivalent projectors for virtual element methods. *Computers & Mathematics with Applications*, 66(3):376–391, 2013.
- [79] Franco Brezzi, Richard S Falk, and L Donatella Marini. Basic principles of mixed virtual element methods. *ESAIM: Mathematical Modelling and Numerical Analysis*, 48(4):1227–1240, 2014.
- [80] Jérôme Bonelle and Alexandre Ern. Analysis of compatible discrete operator schemes for elliptic problems on polyhedral meshes. *ESAIM: Mathematical Modelling and Numerical Analysis*, 48(2):553–581, 2014.
- [81] Giuseppe Vacca and L Beirão da Veiga. Virtual element methods for parabolic problems on polygonal meshes. *Numerical Methods for Partial Differential Equations*, 31(6):2110–2134, 2015.

- [82] Blanca Ayuso de Dios, Konstantin Lipnikov, and Gianmarco Manzini. The nonconforming virtual element method. *ESAIM: Mathematical Modelling and Numerical Analysis*, 50(3):879–904, 2016.
- [83] Konstantin Lipnikov, Gianmarco Manzini, and Mikhail Shashkov. Mimetic finite difference method. *Journal of Computational Physics*, 257:1163–1227, 2014.
- [84] Franco Brezzi, Konstantin Lipnikov, and Valeria Simoncini. A family of mimetic finite difference methods on polygonal and polyhedral meshes. *Mathematical Models and Methods in Applied Sciences*, 15(10):1533–1551, 2005.
- [85] Franco Brezzi, Annalisa Buffa, and Konstantin Lipnikov. Mimetic finite differences for elliptic problems. *ESAIM: Mathematical Modelling and Numerical Analysis-Modélisation Mathématique et Analyse Numérique*, 43(2):277–295, 2009.
- [86] Franco Brezzi, Konstantin Lipnikov, Mikhail Shashkov, and Valeria Simoncini. A new discretization methodology for diffusion problems on generalized polyhedral meshes. *Computer Methods in Applied Mechanics and Engineering*, 196(37-40):3682–3692, 2007.
- [87] F. Brezzi, K. Lipnikov, and V. Simoncini. A family of mimetic finite difference methods on polygonal and polyhedral meshes. *Math. Models Methods Appl. Sci.*, 15:1533–1553, 2005.
- [88] L Beirão Da Veiga. A mimetic finite difference method for linear elasticity. *M2AN: Math. Model. Numer. Anal.*, 44(2):231–250, 2010.
- [89] Pavel B Bochev and James M Hyman. Principles of mimetic discretizations of differential operators. In *Compatible spatial discretizations*, pages 89–119. Springer, 2006.
- [90] L Beirão Da Veiga, F. Brezzi, L.D. Marini, and A. Russo. The hitchhiker’s guide to the virtual element method. *Mathematical Models and Methods in Applied Sciences*, 24(8):1541–1573, 2014.
- [91] L Beirão Da Veiga, Alessandro Russo, and Giuseppe Vacca. The virtual element method with curved edges. *ESAIM: Mathematical Modelling and Numerical Analysis*, 53(2):375–404, 2019.
- [92] E Artioli, L Beirão da Veiga, and M Verani. An adaptive curved virtual element method for the statistical homogenization of random fibre-reinforced composites. *Finite Elements in Analysis and Design*, 177:103418, 2020.
- [93] P Wriggers, B Hudobivnik, and F Aldakheel. A virtual element formulation for general element shapes. *Computational Mechanics*, pages 1–15, 2020.
- [94] Vien Minh Nguyen-Thanh, Xiaoying Zhuang, Hung Nguyen-Xuan, Timon Rabczuk, and Peter Wriggers. A virtual element method for 2d linear elastic fracture analysis. *Computer Methods in Applied Mechanics and Engineering*, 340:366–395, 2018.
- [95] Fadi Aldakheel, Blaž Hudobivnik, and Peter Wriggers. Virtual element formulation for phase-field modeling of ductile fracture. *International Journal for Multiscale Computational Engineering*, 17(2), 2019.
- [96] Ali Hussein, Blaz Hudobivnik, and Peter Wriggers. A combined adaptive phase field and discrete cutting method for the prediction of crack paths.
- [97] L Beirão da Veiga, D Mora, and G Rivera. A virtual element method for Reissner-Mindlin plates. Technical report, CI2MA preprint 2016-14, available from <http://www.ci2ma.udec.cl>.
- [98] Claudia Chinosi. Vem for the Reissner-Mindlin plate based on the mitc approach: The element of degree 2. In *European Conference on Numerical Mathematics and Advanced Applications*, pages 519–527. Springer, 2017.
- [99] Vitaliy Gyrya and Hashem Mohamed Mourad. C1-continuous virtual element method for Poisson-Kirchhoff plate problem. Technical report, Los Alamos National Lab.(LANL), Los Alamos, NM (United States), 2016.
- [100] Arun Gain, Cameron Talischi, and Glaucio H. Paulino. On the virtual element method for three-dimensional elasticity problems on arbitrary polyhedral meshes. *Computer Methods in Applied Mechanics and Engineering*, 282:132–160, 11 2013.
- [101] E Artioli, S De Miranda, C Lovadina, and L Patruno. A stress/displacement virtual element method for plane elasticity problems. *Computer Methods in Applied Mechanics and Engineering*, 325:155–174, 2017.

- [102] Edoardo Artioli, L Beirão Da Veiga, Carlo Lovadina, and Elio Sacco. Arbitrary order 2d virtual elements for polygonal meshes: part i, elastic problem. *Computational Mechanics*, 60(3):355–377, 2017.
- [103] L Beirão Da Veiga, Franco Brezzi, and L Donatella Marini. Virtual elements for linear elasticity problems. *SIAM Journal on Numerical Analysis*, 51(2):794–812, 2013.
- [104] Abhilash Sreekumar, Savvas P Triantafyllou, François-Xavier Bécot, and Fabien Chevillotte. A multiscale virtual element method for the analysis of heterogeneous media. *International Journal for Numerical Methods in Engineering*, 121(8):1791–1821, 2020.
- [105] P Wriggers, WT Rust, and BD Reddy. A virtual element method for contact. *Computational Mechanics*, 58(6):1039–1050, 2016.
- [106] E Artioli, S Marfia, and E Sacco. High-order virtual element method for the homogenization of long fiber nonlinear composites. *Computer Methods in Applied Mechanics and Engineering*, 341:571–585, 2018.
- [107] Marco Pingaro, Maria Laura De Bellis, Patrizia Trovalusci, and Renato Masiani. Statistical homogenization of polycrystal composite materials with thin interfaces using virtual element method. *Composite Structures*, 264:113741, 2021.
- [108] Lourenço Beirao da Veiga, David Mora, Gonzalo Rivera, and Rodolfo Rodríguez. A virtual element method for the acoustic vibration problem. *Numerische Mathematik*, 136(3):725–763, 2017.
- [109] Ilaria Perugia, Paola Pietra, and Alessandro Russo. A plane wave virtual element method for the Helmholtz problem. *ESAIM: Mathematical Modelling and Numerical Analysis*, 50(3):783–808, 2016.
- [110] Christoph Böhm, Blaž Hudobivnik, Michele Marino, and Peter Wriggers. Electro-magneto-mechanically response of polycrystalline materials: Computational homogenization via the virtual element method. *Computer Methods in Applied Mechanics and Engineering*, 380:113775, 2021.
- [111] Odd Andersen, Halvor M Nilsen, and Xavier Raynaud. Virtual element method for geomechanical simulations of reservoir models. *Computational Geosciences*, 21(5-6):877–893, 2017.
- [112] Halvor Møll Nilsen, Idar Larsen, and Xavier Raynaud. Combining the modified discrete element method with the virtual element method for fracturing of porous media. *Computational Geosciences*, 21(5):1059–1073, 2017.
- [113] Giuseppe Vacca. An H1-conforming virtual element for Darcy and Brinkman equations. *Mathematical Models and Methods in Applied Sciences*, 28(01):159–194, 2018.
- [114] Ernesto Cáceres, Gabriel N Gatica, and Filánder A Sequeira. A mixed virtual element method for the brinkman problem. *Mathematical Models and Methods in Applied Sciences*, 27(04):707–743, 2017.
- [115] Kyoungsoo Park, Heng Chi, and Glaucio H Paulino. Numerical recipes for elastodynamic virtual element methods with explicit time integration. *International Journal for Numerical Methods in Engineering*, 121(1):1–31, 2020.
- [116] Paola F Antonietti, Gianmarco Manzini, Ilario Mazzieri, Hashem M Mourad, and Marco Verani. The arbitrary-order virtual element method for linear elastodynamics models: convergence, stability and dispersion-dissipation analysis. *International Journal for Numerical Methods in Engineering*, 122(4):934–971, 2021.
- [117] Edoardo Artioli, Stefano de Miranda, Carlo Lovadina, and Luca Patruno. An equilibrium-based stress recovery procedure for the vem. *International Journal for Numerical Methods in Engineering*, 117(8):885–900, 2019.
- [118] Gang Wang, Ying Wang, and Yinnian He. Least-squares virtual element method for the convection-diffusion-reaction problem. *International Journal for Numerical Methods in Engineering*, 122(11):2672–2693, 2021.
- [119] Antonio Maria D’Altri, Stefano de Miranda, Luca Patruno, Edoardo Artioli, and Carlo Lovadina. Error estimation and mesh adaptivity for the virtual element method based on recovery by compatibility in patches. *International Journal for Numerical Methods in Engineering*, 121(19):4374–4405, 2020.

- [120] Alejandro Ortiz-Bernardin, A Russo, and N Sukumar. Consistent and stable meshfree galerkin methods using the virtual element decomposition. *International Journal for Numerical Methods in Engineering*, 112(7):655–684, 2017.
- [121] Sundararajan Natarajan, Stéphane PA Bordas, and Ean Tat Ooi. Virtual and smoothed finite elements: a connection and its application to polygonal/polyhedral finite element methods. *International Journal for Numerical Methods in Engineering*, 104(13):1173–1199, 2015.
- [122] Rodrigo Silva-Valenzuela, Alejandro Ortiz-Bernardin, N Sukumar, Edoardo Artioli, and Nancy Hitschfeld-Kahler. A nodal integration scheme for meshfree galerkin methods using the virtual element decomposition. *International Journal for Numerical Methods in Engineering*, 121(10):2174–2205, 2020.
- [123] L Beirão Da Veiga, Franco Brezzi, Luisa Donatella Marini, and Alessandro Russo. Mixed virtual element methods for general second order elliptic problems on polygonal meshes. *ESAIM: Mathematical Modelling and Numerical Analysis*, 50(3):727–747, 2016.
- [124] Franco Dassi and Giuseppe Vacca. Bricks for the mixed high-order virtual element method: projectors and differential operators.
- [125] Julien Coulet, Isabelle Faille, Vivette Girault, Nicolas Guy, and Frédéric Nataf. A fully coupled scheme using virtual element method and finite volume for poroelasticity. *Computational Geosciences*, pages 1–23, 2019.
- [126] Raimund Bürger, Sarvesh Kumar, David Mora, Ricardo Ruiz-Baier, and Nitesh Verma. Virtual element methods for the three-field formulation of time-dependent linear poroelasticity. *arXiv preprint arXiv:1912.06029*, 2019.
- [127] Abhilash Sreekumar, Savvas P Triantafyllou, François-Xavier Bécot, and Fabien Chevillotte. Multiscale vem for the Biot consolidation analysis of complex and highly heterogeneous domains. *Computer Methods in Applied Mechanics and Engineering*, 375:113543.
- [128] L Beirão da Veiga, Alexander Pichler, and Giuseppe Vacca. A virtual element method for the miscible displacement of incompressible fluids in porous media. *Computer Methods in Applied Mechanics and Engineering*, 375:113649, 2021.
- [129] Andrea Borio, François P Hamon, Nicola Castelletto, Joshua A White, and Randolph R Settgaest. Hybrid mimetic finite-difference and virtual element formulation for coupled poromechanics. *Computer Methods in Applied Mechanics and Engineering*, 383:113917, 2021.
- [130] John P Wolf and Chongmin Song. Consistent infinitesimal finite-element cell method: in-plane motion. *Computer methods in applied mechanics and engineering*, 123(1-4):355–370, 1995.
- [131] John P Wolf. *The scaled boundary finite element method*. John Wiley & Sons, 2003.
- [132] John P Wolf and Chongmin Song. The scaled boundary finite-element method—a primer: derivations. *Computers & Structures*, 78(1-3):191–210, 2000.
- [133] Chongmin Song. The scaled boundary finite element method in structural dynamics. *International Journal for Numerical Methods in Engineering*, 77(8):1139–1171, 2009.
- [134] Chongmin Song and John P Wolf. The scaled boundary finite-element method. *FLUID MECHANICS AND ITS APPLICATIONS Volume 49*, page 275, 1998.
- [135] Thu Hang Vu and Andrew J Deeks. Use of higher-order shape functions in the scaled boundary finite element method. *International Journal for Numerical Methods in Engineering*, 65(10):1714–1733, 2006.
- [136] Zhenjun Yang. Fully automatic modelling of mixed-mode crack propagation using scaled boundary finite element method. *Engineering Fracture Mechanics*, 73(12):1711–1731, 2006.
- [137] ET Ooi and ZJ Yang. Modelling dynamic crack propagation using the scaled boundary finite element method. *International journal for numerical methods in engineering*, 88(4):329–349, 2011.
- [138] Adrian Egger, Udit Pillai, Konstantinos Agathos, Emmanouil Kakouris, Eleni Chatzi, Ian A Aschroft, and Savvas P Triantafyllou. Discrete and phase field methods for linear elastic fracture mechanics: a comparative study and state-of-the-art review. *Applied Sciences*, 9(12):2436, 2019.

- [139] Chongmin Song, Ean Tat Ooi, and Sundararajan Natarajan. A review of the scaled boundary finite element method for two-dimensional linear elastic fracture mechanics. *Engineering Fracture Mechanics*, 187:45–73, 2018.
- [140] Zhicheng Sun, Ean Tat Ooi, and Chongmin Song. Finite fracture mechanics analysis using the scaled boundary finite element method. *Engineering Fracture Mechanics*, 134:330–353, 2015.
- [141] L Lehmann, S Langer, and D Clasen. Scaled boundary finite element method for acoustics. *Journal of Computational Acoustics*, 14(04):489–506, 2006.
- [142] Sundararajan Natarajan and Chandramouli Padmanabhan. Scaled boundary finite element method for mid-frequency interior acoustics. *The Journal of the Acoustical Society of America*, 146(4):3006–3006, 2019.
- [143] Ivo Babuška, Gabriel Caloz, and John E Osborn. Special finite element methods for a class of second order elliptic problems with rough coefficients. *SIAM Journal on Numerical Analysis*, 31(4):945–981, 1994.
- [144] Ivo Babuška and Jens M Melenk. The partition of unity method. *International journal for numerical methods in engineering*, 40(4):727–758, 1997.
- [145] Jens M Melenk and Ivo Babuška. The partition of unity finite element method: basic theory and applications. *Computer methods in applied mechanics and engineering*, 139(1-4):289–314, 1996.
- [146] Edwin A Munts, Steven J Hulshoff, and R Des Borst. The partition-of-unity method for linear diffusion and convection problems: accuracy, stabilization and multiscale interpretation. *International journal for numerical methods in fluids*, 43(2):199–213, 2003.
- [147] Abdellah El Kacimi and Omar Laghrouche. Numerical modelling of elastic wave scattering in frequency domain by the partition of unity finite element method. *International journal for numerical methods in engineering*, 77(12):1646–1669, 2009.
- [148] Jean-Daniel Chazot, Emmanuel Perrey-Debain, and Benoit Nennig. The partition of unity finite element method for the simulation of waves in air and poroelastic media. *The Journal of the Acoustical Society of America*, 135(2):724–733, 2014.
- [149] Omar Laghrouche, Peter Bettess, Emmanuel Perrey-Debain, and Jon Trevelyan. Wave interpolation finite elements for helmholtz problems with jumps in the wave speed. *Computer methods in applied mechanics and engineering*, 194(2-5):367–381, 2005.
- [150] Omar Laghrouche, P Bettess, and RJ Astley. Modelling of short wave diffraction problems using approximating systems of plane waves. *International Journal for Numerical Methods in Engineering*, 54(10):1501–1533, 2002.
- [151] Nicolas Moës, John Dolbow, and Ted Belytschko. A finite element method for crack growth without remeshing. *International journal for numerical methods in engineering*, 46(1):131–150, 1999.
- [152] Ted Belytschko and Tom Black. Elastic crack growth in finite elements with minimal remeshing. *International journal for numerical methods in engineering*, 45(5):601–620, 1999.
- [153] Anita Hansbo and Peter Hansbo. A finite element method for the simulation of strong and weak discontinuities in solid mechanics. *Computer methods in applied mechanics and engineering*, 193(33-35):3523–3540, 2004.
- [154] Stefano Mariani and Umberto Perego. Extended finite element method for quasi-brittle fracture. *International Journal for Numerical Methods in Engineering*, 58(1):103–126, 2003.
- [155] Kwok Wah Cheng and Thomas-Peter Fries. Higher-order xfem for curved strong and weak discontinuities. *International Journal for Numerical Methods in Engineering*, 82(5):564–590, 2010.
- [156] Konstantinos Agathos, Eleni Chatzi, and Stéphane PA Bordas. A unified enrichment approach addressing blending and conditioning issues in enriched finite elements. *Computer Methods in Applied Mechanics and Engineering*, 349:673–700, 2019.
- [157] Ivo Babuška, Uday Banerjee, and John E Osborn. Survey of meshless and generalized finite element methods: a unified approach. *Acta Numerica*, 12:1–125, 2003.

- [158] C Armando Duarte, LG Reno, and A Simone. A high-order generalized fem for through-the-thickness branched cracks. *International Journal for Numerical Methods in Engineering*, 72(3):325–351, 2007.
- [159] Konstantinos Christodoulou, Omar Laghrouche, M Shadi Mohamed, and Jon Trevelyan. High-order finite elements for the solution of helmholtz problems. *Computers & Structures*, 191:129–139, 2017.
- [160] Yazid Abdelaziz and Abdelmadjid Hamouine. A survey of the extended finite element. *Computers & structures*, 86(11-12):1141–1151, 2008.
- [161] Ted Belytschko, Robert Gracie, and Giulio Ventura. A review of extended/generalized finite element methods for material modeling. *Modelling and Simulation in Materials Science and Engineering*, 17(4):043001, 2009.
- [162] Thomas-Peter Fries and Ted Belytschko. The extended/generalized finite element method: an overview of the method and its applications. *International journal for numerical methods in engineering*, 84(3):253–304, 2010.
- [163] N Sukumar, JE Dolbow, and Nicolas Moës. Extended finite element method in computational fracture mechanics: a retrospective examination. *International Journal of Fracture*, 196(1-2):189–206, 2015.
- [164] Stefan A Sauter and Christoph Schwab. Boundary element methods. In *Boundary Element Methods*, pages 183–287. Springer, 2010.
- [165] Ernian Pan and FG Yuan. Boundary element analysis of three-dimensional cracks in anisotropic solids. *International Journal for Numerical Methods in Engineering*, 48(2):211–237, 2000.
- [166] Alok Sutradhar and Glaucio H Paulino. A simple boundary element method for problems of potential in non-homogeneous media. *International Journal for Numerical Methods in Engineering*, 60(13):2203–2230, 2004.
- [167] Yijun Liu. A new fast multipole boundary element method for solving large-scale two-dimensional elastostatic problems. *International Journal for Numerical Methods in Engineering*, 65(6):863–881, 2006.
- [168] TM van Opstal, EH van Brummelen, R de Borst, and MR Lewis. A finite-element/boundary-element method for large-displacement fluid-structure interaction. *Computational Mechanics*, 50(6):779–788, 2012.
- [169] J Austin Cottrell, Thomas JR Hughes, and Yuri Bazilevs. *Isogeometric analysis: toward integration of CAD and FEA*. John Wiley & Sons, 2009.
- [170] Lin Chen, Bin Li, and René de Borst. Adaptive isogeometric analysis for phase-field modeling of anisotropic brittle fracture. *International Journal for Numerical Methods in Engineering*, 121(20):4630–4648, 2020.
- [171] Faisal Irzal, Joris JC Remmers, Clemens V Verhoosel, and René de Borst. An isogeometric analysis bézier interface element for mechanical and poromechanical fracture problems. *International Journal for Numerical Methods in Engineering*, 97(8):608–628, 2014.
- [172] Antonella Falini, Carlotta Giannelli, Tadej Kanduč, Maria Lucia Sampoli, and Alessandra Sestini. An adaptive iga-bem with hierarchical b-splines based on quasi-interpolation quadrature schemes. *International Journal for Numerical Methods in Engineering*, 117(10):1038–1058, 2019.
- [173] Antonella Falini, Jaka Špeh, and Bert Jüttler. Planar domain parameterization with thb-splines. *Computer Aided Geometric Design*, 35:95–108, 2015.
- [174] Alessandra Aimi, Mauro Diligenti, Maria Lucia Sampoli, and Alessandra Sestini. Isogeometric analysis and symmetric galerkin bem: A 2d numerical study. *Applied Mathematics and Computation*, 272:173–186, 2016.
- [175] Matthias Taus, Gregory J Rodin, and Thomas JR Hughes. Isogeometric analysis of boundary integral equations: High-order collocation methods for the singular and hyper-singular equations. *Mathematical Models and Methods in Applied Sciences*, 26(08):1447–1480, 2016.

- [176] Robert N Simpson, Stéphane PA Bordas, Jon Trevelyan, and Timon Rabczuk. A two-dimensional isogeometric boundary element method for elastostatic analysis. *Computer Methods in Applied Mechanics and Engineering*, 209:87–100, 2012.
- [177] AI Ginnis, KV Kostas, CG Politis, PD Kaklis, KA Belibassakis, Th P Gerostathis, MA Scott, and TJR Hughes. Isogeometric boundary-element analysis for the wave-resistance problem using t-splines. *Computer Methods in Applied Mechanics and Engineering*, 279:425–439, 2014.
- [178] Laurens Coox, Onur Atak, Dirk Vandepitte, and Wim Desmet. An isogeometric indirect boundary element method for solving acoustic problems in open-boundary domains. *Computer Methods in Applied Mechanics and Engineering*, 316:186–208, 2017.
- [179] Robert N Simpson, Michael A Scott, Matthias Taus, Derek C Thomas, and Haojie Lian. Acoustic isogeometric boundary element analysis. *Computer Methods in Applied Mechanics and Engineering*, 269:265–290, 2014.
- [180] CG Politis, A Papagiannopoulos, KA Belibassakis, PD Kaklis, KV Kostas, AI Ginnis, and TP Gerostathis. An isogeometric bem for exterior potential-flow problems around lifting bodies. 2014.
- [181] AA Joneidi, CV Verhoosel, and PD Anderson. Isogeometric boundary integral analysis of drops and inextensible membranes in isoviscous flow. *Computers & Fluids*, 109:49–66, 2015.
- [182] Haojie Lian, Pierre Kerfriden, and Stéphane PA Bordas. Implementation of regularized isogeometric boundary element methods for gradient-based shape optimization in two-dimensional linear elasticity. *International Journal for Numerical Methods in Engineering*, 106(12):972–1017, 2016.
- [183] Ahmed Mostafa Shaaban, Cosmin Anitescu, Elena Atroshchenko, and Timon Rabczuk. 3d isogeometric boundary element analysis and structural shape optimization for helmholtz acoustic scattering problems. *Computer Methods in Applied Mechanics and Engineering*, 384:113950, 2021.
- [184] KV Kostas, MM Fyrrillas, CG Politis, AI Ginnis, and PD Kaklis. Shape optimization of conductive-media interfaces using an iga-bem solver. *Computer Methods in Applied Mechanics and Engineering*, 340:600–614, 2018.
- [185] KV Kostas, AI Ginnis, CG Politis, and PD Kaklis. Ship-hull shape optimization with a t-spline based bem–isogeometric solver. *Computer Methods in Applied Mechanics and Engineering*, 284:611–622, 2015.
- [186] Michael Mengolini, Matias F. Benedetto, and Alejandro M. Aragon. An engineering perspective to the virtual element method and its interplay with the standard finite element method. *Computer Methods in Applied Mechanics and Engineering*, 350(6):995–1023, doi =<https://doi.org/10.1016/j.cma.2019.02.043>, 2019.
- [187] A Cangiani, G Manzini, A Russo, and N Sukumar. Hourglass stabilization and the virtual element method. *International Journal for Numerical Methods in Engineering*, 102(3-4):404–436, 2015.
- [188] Lourenço Beirão da Veiga, Carlo Lovadina, and Alessandro Russo. Stability analysis for the virtual element method. *Mathematical Models and Methods in Applied Sciences*, 27(13):2557–2594, 2017.
- [189] F Dassi and L Mascotto. Exploring high-order three dimensional virtual elements: bases and stabilizations. *Computers & Mathematics with Applications*, 75(9):3379–3401, 2018.
- [190] L Beirão Da Veiga, F Brezzi, LD Marini, and A Russo. Serendipity nodal vem spaces. *Computers & Fluids*, 141:2–12, 2016.
- [191] Tommaso Sorgente, Silvia Biasotti, Gianmarco Manzini, and Michela Spagnuolo. The role of mesh quality and mesh quality indicators in the virtual element method. *arXiv preprint arXiv:2102.04138*, 2021.
- [192] T Strouboulis, K Copps, and Ivo Babuška. The generalized finite element method: an example of its implementation and illustration of its performance. *International Journal for Numerical Methods in Engineering*, 47(8):1401–1417, 2000.
- [193] Charbel Farhat, Isaac Harari, and Leopoldo P Franca. The discontinuous enrichment method. *Computer methods in applied mechanics and engineering*, 190(48):6455–6479, 2001.
- [194] Anthony T Patera. A spectral element method for fluid dynamics: laminar flow in a channel expansion. *Journal of computational Physics*, 54(3):468–488, 1984.

- [195] ED Nobrega, F Gautier, A Pelat, and JMC Dos Santos. Vibration band gaps for elastic metamaterial rods using wave finite element method. *Mechanical Systems and Signal Processing*, 79:192–202, 2016.
- [196] OC Zienkiewicz, C Emson, and P Bettess. A novel boundary infinite element. *International Journal for Numerical Methods in Engineering*, 19(3):393–404, 1983.
- [197] Weng Cho Chew and QH Liu. Perfectly matched layers for elastodynamics: a new absorbing boundary condition. *Journal of Computational Acoustics*, 4(04):341–359, 1996.
- [198] Mohamed Soliman and Frank L DiMaggio. Doubly asymptotic approximations as non-reflecting boundaries in fluid-structure interaction problems. *Computers & Structures*, 17(2):193–204, 1983.
- [199] Barbara I Wohlmuth. A mortar finite element method using dual spaces for the Lagrange multiplier. *SIAM journal on numerical analysis*, 38(3):989–1012, 2000.
- [200] Eddie Wadbro, Sara Zahedi, Gunilla Kreiss, and Martin Berggren. A uniformly well-conditioned, unfitted Nitsche method for interface problems. *BIT Numerical Mathematics*, 53(3):791–820, 2013.
- [201] Fabien Chevillotte, Camille Perrot, and Emmanuel Guillon. A direct link between microstructure and acoustical macro-behavior of real double porosity foams. *The Journal of the Acoustical Society of America*, 134(6):4681–4690, 2013.
- [202] Vu-Hieu Nguyen, Eduard Rohan, and Salah Naili. Multiscale simulation of acoustic waves in homogenized heterogeneous porous media with low and high permeability contrasts. *International Journal of Engineering Science*, 101:92–109, 2016.
- [203] Chandra Veer Singh and Ramesh Talreja. A multiscale approach to modeling of composite damage. In *Modeling Damage, Fatigue and Failure of Composite Materials*, pages 329–345. Elsevier, 2016.
- [204] Carl T Herakovich. Mechanics of composites: a historical review. *Mechanics Research Communications*, 41:1–20, 2012.
- [205] Olek C Zienkiewicz, Robert L Taylor, and Jian Z Zhu. *The finite element method: its basis and fundamentals*. Elsevier, 2005.
- [206] Tarek I Zohdi and Peter Wriggers. *An introduction to computational micromechanics*. Springer Science & Business Media, 2008.
- [207] René De Borst and Ekkehard Ramm. *Multiscale methods in computational mechanics: progress and accomplishments*, volume 55. Springer Science & Business Media, 2010.
- [208] René De Borst. Challenges in computational materials science: multiple scales, multi-physics and evolving discontinuities. *Computational Materials Science*, 43(1):1–15, 2008.
- [209] MV Cid Alfaro, ASJ Suiker, and R De Borst. Multiscale modelling of the failure behaviour of fibre-reinforced laminates. In *Multiscale methods in computational mechanics*, pages 233–259. Springer, 2010.
- [210] YC Chang and KK Mohanty. Scale-up of two-phase flow in heterogeneous porous media. *Journal of Petroleum Science and Engineering*, 18(1-2):21–34, 1997.
- [211] Ulrich Hornung. *Homogenization and porous media*, volume 6. Springer Science & Business Media, 1996.
- [212] Ivo Babuška. Homogenization approach in engineering. In *Computing methods in applied sciences and engineering*, pages 137–153. Springer, 1976.
- [213] Gregori A Chechkin, Andrei L Piatntsi, and Aleksei Shamev. *Homogenization: methods and applications*, volume 234. American Mathematical Soc., 2007.
- [214] Yohan Davit and Michel Quintard. Technical notes on volume averaging in porous media i: how to choose a spatial averaging operator for periodic and quasiperiodic structures. *Transport in Porous Media*, 119(3):555–584, 2017.
- [215] WANG Guannan. An efficient analytical homogenization technique for mechanical-hygrothermal responses of unidirectional composites with applications to optimization and multiscale analyses. *Chinese Journal of Aeronautics*, 32(2):382–395, 2019.

- [216] Nr Talbi, A Batti, R Ayad, and YQ Guo. An analytical homogenization model for finite element modelling of corrugated cardboard. *Composite Structures*, 88(2):280–289, 2009.
- [217] Konstantin Markov and Luigi Preziosi. *Heterogeneous media: micromechanics modeling methods and simulations*. Springer Science & Business Media, 2012.
- [218] Grégoire Allaire. Homogenization and two-scale convergence. *SIAM Journal on Mathematical Analysis*, 23(6):1482–1518, 1992.
- [219] Alexander L Kalamkarov, Igor V Andrianov, and Vladyslav V Danishevs’kyy. Asymptotic homogenization of composite materials and structures. *Applied Mechanics Reviews*, 62(3), 2009.
- [220] Igor V Andrianov, Vladimir I Bolshakov, Vladyslav V Danishevs’kyy, and Dieter Weichert. Higher order asymptotic homogenization and wave propagation in periodic composite materials. *Proceedings of the Royal Society A: Mathematical, Physical and Engineering Sciences*, 464(2093):1181–1201, 2008.
- [221] Frédéric Feyel and Jean-Louis Chaboche. Fe2 multiscale approach for modelling the elastoviscoplastic behaviour of long fibre sic/ti composite materials. *Computer methods in applied mechanics and engineering*, 183(3-4):309–330, 2000.
- [222] Frédéric Feyel. Multiscale fe2 elastoviscoplastic analysis of composite structures. *Computational Materials Science*, 16(1-4):344–354, 1999.
- [223] Marcelo Raschi, Oriol Lloberas-Valls, Alfredo Huespe, and Javier Oliver. High performance reduction technique for multiscale finite element modeling (hpr-fe2): Towards industrial multiscale fe software. *Computer Methods in Applied Mechanics and Engineering*, 375:113580, 2021.
- [224] Rui Xu, Yanchuan Hui, Heng Hu, Qun Huang, Hamid Zahrouni, Tarak Ben Zineb, and Michel Potier-Ferry. A fourier-related fe2 multiscale model for instability phenomena of long fiber reinforced materials. *Composite Structures*, 211:530–539, 2019.
- [225] I Özdemir, WAM Brekelmans, and Marc GD Geers. Fe2 computational homogenization for the thermo-mechanical analysis of heterogeneous solids. *Computer Methods in Applied Mechanics and Engineering*, 198(3-4):602–613, 2008.
- [226] Thomas JR Hughes. Multiscale phenomena: Green’s functions, the dirichlet-to-neumann formulation, subgrid scale models, bubbles and the origins of stabilized methods. *Computer methods in applied mechanics and engineering*, 127(1-4):387–401, 1995.
- [227] Thomas JR Hughes, Gonzalo R Feijóo, Luca Mazzei, and Jean-Baptiste Quinicy. The variational multiscale method—a paradigm for computational mechanics. *Computer methods in applied mechanics and engineering*, 166(1-2):3–24, 1998.
- [228] Ruben Juanes. A variational multiscale finite element method for multiphase flow in porous media. *Finite elements in analysis and design*, 41(7-8):763–777, 2005.
- [229] James Nolen, George Papanicolaou, and Olivier Pironneau. A framework for adaptive multiscale methods for elliptic problems. *Multiscale Modeling & Simulation*, 7(1):171–196, 2008.
- [230] Todd Arbogast, Gergina Pencheva, Mary F Wheeler, and Ivan Yotov. A multiscale mortar mixed finite element method. *Multiscale Modeling & Simulation*, 6(1):319–346, 2007.
- [231] Malgorzata Peszynska. Mortar adaptivity in mixed methods for flow in porous media. *Int. J. Numer. Anal. Model*, 2(3):241–282, 2005.
- [232] Malgorzata Peszyńska, Mary F Wheeler, and Ivan Yotov. Mortar upscaling for multiphase flow in porous media. *Computational Geosciences*, 6(1):73–100, 2002.
- [233] Mi-Young Kim, Eun-Jae Park, Sunil G Thomas, and Mary F Wheeler. A multiscale mortar mixed finite element method for slightly compressible flows in porous media. *Journal of the Korean Mathematical Society*, 44(5):1103–1119, 2007.
- [234] Todd Arbogast and Hailong Xiao. A multiscale mortar mixed space based on homogenization for heterogeneous elliptic problems. *SIAM Journal on Numerical Analysis*, 51(1):377–399, 2013.

- [235] Assyr Abdulle, E Weinan, Björn Engquist, and Eric Vanden-Eijnden. The heterogeneous multiscale method. *Acta Numerica*, 21:1–87, 2012.
- [236] Björn Engquist, Xiantao Li, Weiqing Ren, Eric Vanden-Eijnden, et al. Heterogeneous multiscale methods: a review. *Communications in Computational Physics*, 2(3):367–450, 2007.
- [237] Eric Vanden-Eijnden. Heterogeneous multiscale methods: a review. *Communications in Computational Physics2 (3)*, pages 367–450, 2007.
- [238] E Weinan, Bjorn Engquist, Xiantao Li, Weiqing Ren, and Eric Vanden-Eijnden. The heterogeneous multiscale method: A review. In *Commun. Comput. Phys.* Citeseer, 2007.
- [239] Li-Qun Cao. Multiscale asymptotic expansion and finite element methods for the mixed boundary value problems of second order elliptic equation in perforated domains. *Numerische Mathematik*, 103(1):11–45, 2006.
- [240] Li-qun Cao, Jun-zhi Cui, De-chao Zhu, and Jian-lan Luo. Multiscale finite element method for subdivided periodic elastic structures of composite materials. *Journal of Computational Mathematics*, pages 205–212, 2001.
- [241] Ludovic Chamoin, J Tinsley Oden, and Serge Prudhomme. A stochastic coupling method for atomic-to-continuum monte-carlo simulations. *Computer Methods in Applied Mechanics and Engineering*, 197(43-44):3530–3546, 2008.
- [242] Leopoldo P Franca, Alexandre L Madureira, and Frederic Valentin. Towards multiscale functions: enriching finite element spaces with local but not bubble-like functions. *Computer Methods in Applied Mechanics and Engineering*, 194(27-29):3006–3021, 2005.
- [243] Wing Kam Liu, Yan Zhang, and Martin R Ramirez. Multiple scale finite element methods. *International Journal for Numerical Methods in Engineering*, 32(5):969–990, 1991.
- [244] Alexandre Madureira. A multiscale finite element method for partial differential equations posed in domains with rough boundaries. *Mathematics of Computation*, 78(265):25–34, 2009.
- [245] Harold S Park and Wing Kam Liu. An introduction and tutorial on multiple-scale analysis in solids. *Computer methods in applied mechanics and engineering*, 193(17-20):1733–1772, 2004.
- [246] Irina Sokolova, Muhammad Gusti Bastisya, and Hadi Hajibeygi. Multiscale finite volume method for finite-volume-based simulation of poroelasticity. *Journal of Computational Physics*, 379:309–324, 2019.
- [247] Hadi Hajibeygi, Giuseppe Bonfigli, Marc Andre Hesse, and Patrick Jenny. Iterative multiscale finite-volume method. *Journal of Computational Physics*, 227(19):8604–8621, 2008.
- [248] Ivan Lunati and Patrick Jenny. Multiscale finite-volume method for compressible multiphase flow in porous media. *Journal of Computational Physics*, 216(2):616–636, 2006.
- [249] Hadi Hajibeygi and Patrick Jenny. Multiscale finite-volume method for parabolic problems arising from compressible multiphase flow in porous media. *Journal of Computational Physics*, 228(14):5129–5147, 2009.
- [250] Thomas Hou and Yalchin Efendiev. *Multiscale Finite Element Methods*. 2009.
- [251] James G Berryman. Comparison of upscaling methods in poroelasticity and its generalizations. *Journal of Engineering Mechanics*, 131(9):928–936, 2005.
- [252] Ivo Babuška and John E Osborn. Generalized finite element methods: their performance and their relation to mixed methods. *SIAM Journal on Numerical Analysis*, 20(3):510–536, 1983.
- [253] Ivo Babuška and Uday Banerjee. Stable generalized finite element method (sgfem). *Computer methods in applied mechanics and engineering*, 201:91–111, 2012.
- [254] Thomas Y Hou and Xiao-Hui Wu. A multiscale finite element method for elliptic problems in composite materials and porous media. *Journal of computational physics*, 134(1):169–189, 1997.
- [255] Yalchin R Efendiev and Louis J Durlofsky. Accurate subgrid models for two-phase flow in heterogeneous reservoirs. In *SPE Reservoir Simulation Symposium*. OnePetro, 2003.

- [256] Xinguang He and Li Ren. Finite volume multiscale finite element method for solving the groundwater flow problems in heterogeneous porous media. *Water resources research*, 41(10), 2005.
- [257] Hong-Wu Zhang, Jing-Kai Wu, Jun Lü, and Zhen-Dong Fu. Extended multiscale finite element method for mechanical analysis of heterogeneous materials. *Acta Mechanica Sinica/Lixue Xuebao*, 26(6):899–920, 12 2010.
- [258] HW Zhang, ZD Fu, and JK Wu. Coupling multiscale finite element method for consolidation analysis of heterogeneous saturated porous media. *Advances in water resources*, 32(2):268–279, 2009.
- [259] Hong-Wu Zhang, Jing-Kai Wu, Jun Lü, and Zhen-Dong Fu. Extended multiscale finite element method for mechanical analysis of heterogeneous materials. *Acta mechanica sinica*, 26(6):899–920, 2010.
- [260] Vegard Kippe, Jørg E Aarnes, and Knut-Andreas Lie. A comparison of multiscale methods for elliptic problems in porous media flow. *Computational Geosciences*, 12(3):377–398, 2008.
- [261] Yalchin Efendiev and Thomas Y Hou. *Multiscale finite element methods: theory and applications*, volume 4. Springer Science & Business Media, 2009.
- [262] J-F Allard and Gilles Daigle. Propagation of sound in porous media: Modeling sound absorbing materials, 1994.
- [263] Luc Jaouen and Fabien Chevillotte. Length correction of 2d discontinuities or perforations at large wavelengths and for linear acoustics. *Acta Acustica united with Acustica*, 104(2):243–250, 2018.
- [264] Jørg E Aarnes, Vegard Kippe, and Knut-Andreas Lie. Mixed multiscale finite elements and streamline methods for reservoir simulation of large geomodels. *Advances in Water Resources*, 28(3):257–271, 2005.
- [265] Ngoc Cuong Nguyen. A multiscale reduced-basis method for parametrized elliptic partial differential equations with multiple scales. *Journal of Computational Physics*, 227(23):9807–9822, 2008.
- [266] Maxime Barrault, Yvon Maday, Ngoc Cuong Nguyen, and Anthony T Patera. An ‘empirical interpolation’ method: application to efficient reduced-basis discretization of partial differential equations. *Comptes Rendus Mathematique*, 339(9):667–672, 2004.
- [267] MA Grepl, NC Nguyen, K Veroy, AT Patera, and GR Liu. Certified rapid solution of parametrized partial differential equations for real-time applications. In *Proceedings of the 2nd Sandia Workshop of PDE-Constrained Optimization: Towards Real-Time and On-Line PDE-Constrained Optimization*, SIAM Computational Science and Engineering Book Series. Citeseer, 2004.
- [268] Nguyen Ngoc Cuong, Karen Veroy, and Anthony T Patera. Certified real-time solution of parametrized partial differential equations. In *Handbook of materials modeling*, pages 1529–1564. Springer, 2005.
- [269] Ngoc Cuong Nguyen. A posteriori error estimation and basis adaptivity for reduced-basis approximation of nonaffine-parametrized linear elliptic partial differential equations. *Journal of Computational Physics*, 227(2):983–1006, 2007.
- [270] Christophe Prud’Homme, Dimitrios V Rovas, Karen Veroy, Luc Machiels, Yvon Maday, Anthony T Patera, and Gabriel Turinici. Reliable real-time solution of parametrized partial differential equations: Reduced-basis output bound methods. *J. Fluids Eng.*, 124(1):70–80, 2002.
- [271] Gianluigi Rozza, Dinh Bao Phuong Huynh, and Anthony T Patera. Reduced basis approximation and a posteriori error estimation for affinely parametrized elliptic coercive partial differential equations. *Archives of Computational Methods in Engineering*, 15(3):1, 2007.
- [272] Sugata Sen, Karen Veroy, Dinh Bao Phuong Huynh, Simone Deparis, Ngoc Cuong Nguyen, and Anthony T Patera. “natural norm” a posteriori error estimators for reduced basis approximations. *Journal of Computational Physics*, 217(1):37–62, 2006.
- [273] Bart Besselink, Umut Tabak, Agnieszka Lutowska, Nathan Van de Wouw, H Nijmeijer, Daniel J Rixen, ME Hochstenbach, and WHA Schilders. A comparison of model reduction techniques from structural dynamics, numerical mathematics and systems and control. *Journal of Sound and Vibration*, 332(19):4403–4422, 2013.

- [274] Peter Benner and Jens Saak. Efficient balancing-based mor for large-scale second-order systems. *Mathematical and Computer Modelling of Dynamical Systems*, 17(2):123–143, 2011.
- [275] Younes Chahlaoui, Kyle A Gallivan, Antoine Vandendorpe, and Paul Van Dooren. Model reduction of second-order systems. In *Dimension Reduction of Large-Scale Systems*, pages 149–172. Springer, 2005.
- [276] Philip Holzwarth, Nadine Walker, and Peter Eberhard. Interface reduction of linear mechanical systems with a modular setup. *Multibody System Dynamics*, 43(1):1–19, 2018.
- [277] David Amsallem, Matthew Zahr, Youngsoo Choi, and Charbel Farhat. Design optimization using hyper-reduced-order models. *Structural and Multidisciplinary Optimization*, 51(4):919–940, 2015.
- [278] Charbel Farhat, Todd Chapman, and Philip Avery. Structure-preserving, stability, and accuracy properties of the energy-conserving sampling and weighting method for the hyper reduction of nonlinear finite element dynamic models. *International journal for numerical methods in engineering*, 102(5):1077–1110, 2015.
- [279] Igor Pontes Duff Pereira, Pierre Vuillemin, Charles Poussot-Vassal, Corentin Briat, and Cédric Seren. Stability and performance analysis of large-scale aircraft vibration delay model using model reduction techniques. In *EuroGNC 2015*. Institut Supérieur de l’Aéronautique et de l’Espace ISAE, 2015.
- [280] C Bach, I Cuevas Salazar, L Song, J Fender, and F Duddeck. Nonlinear model order reduction of explicit finite element simulations for crash analysis. In *14th Int. Conf. on Comput. Plast*, pages 1692–1709, 2017.
- [281] D Scheffold, C Bach, F Duddeck, G Müller, and M Buchschmid. Vibration frequency optimization of jointed structures with contact nonlinearities using hyper-reduction. *IFAC-PapersOnLine*, 51(2):843–848, 2018.
- [282] Bart Blockmans, Tommaso Tamarozzi, Frank Naets, and Wim Desmet. A nonlinear parametric model reduction method for efficient gear contact simulations. *International Journal for Numerical Methods in Engineering*, 102(5):1162–1191, 2015.
- [283] Paramita Guha and Mashuq Un Nabi. Reduced order modeling of a microgripper using svd-second-order krylov method. *International Journal for Computational Methods in Engineering Science and Mechanics*, 16(2):65–70, 2015.
- [284] SN Voormeeren, PLC Van Der Valk, BP Nortier, D-P Molenaar, and DJ Rixen. Accurate and efficient modeling of complex offshore wind turbine support structures using augmented superelements. *Wind Energy*, 17(7):1035–1054, 2014.
- [285] Norman Lang, Jens Saak, and Peter Benner. Model order reduction for systems with moving loads. *at-Automatisierungstechnik*, 62(7):512–522, 2014.
- [286] Michael Lehner and Peter Eberhard. A two-step approach for model reduction in flexible multibody dynamics. *Multibody System Dynamics*, 17(2):157–176, 2007.
- [287] Jörg Fehr and Peter Eberhard. Simulation process of flexible multibody systems with non-modal model order reduction techniques. *Multibody System Dynamics*, 25(3):313–334, 2011.
- [288] Jörg Fehr and Peter Eberhard. Error-controlled model reduction in flexible multibody dynamics. *Journal of Computational and Nonlinear Dynamics*, 5(3), 2010.
- [289] Charles Poussot-Vassal and Clement Roos. Generation of a reduced-order lpv/lft model from a set of large-scale mimo lti flexible aircraft models. *Control Engineering Practice*, 20(9):919–930, 2012.
- [290] Gert HK Heirman, Frank Naets, and Wim Desmet. A system-level model reduction technique for the efficient simulation of flexible multibody systems. *International journal for numerical methods in engineering*, 85(3):330–354, 2011.
- [291] Daniel J Rixen. A dual craig–bampton method for dynamic substructuring. *Journal of Computational and applied mathematics*, 168(1-2):383–391, 2004.
- [292] Alfio Quarteroni and Gianluigi Rozza. Numerical solution of parametrized navier–stokes equations by reduced basis methods. *Numerical Methods for Partial Differential Equations: An International Journal*, 23(4):923–948, 2007.

- [293] Simone Deparis and Gianluigi Rozza. Reduced basis method for multi-parameter-dependent steady navier–stokes equations: applications to natural convection in a cavity. *Journal of Computational Physics*, 228(12):4359–4378, 2009.
- [294] Giuseppe Pitton and Gianluigi Rozza. On the application of reduced basis methods to bifurcation problems in incompressible fluid dynamics. *Journal of Scientific Computing*, 73(1):157–177, 2017.
- [295] Giuseppe Pitton, Annalisa Quaini, and Gianluigi Rozza. Computational reduction strategies for the detection of steady bifurcations in incompressible fluid-dynamics: Applications to coanda effect in cardiology. *Journal of Computational Physics*, 344:534–557, 2017.
- [296] VB Nguyen, M Buffoni, K Willcox, and BC Khoo. Model reduction for reacting flow applications. *International Journal of Computational Fluid Dynamics*, 28(3-4):91–105, 2014.
- [297] David Amsallem and Charbel Farhat. Interpolation method for adapting reduced-order models and application to aeroelasticity. *AIAA journal*, 46(7):1803–1813, 2008.
- [298] John William Strutt and John William Strutt Baron Rayleigh. *The theory of sound*, volume 1. Macmillan, 1894.
- [299] Walter C Hurty. Dynamic analysis of structural systems using component modes. *AIAA journal*, 3(4):678–685, 1965.
- [300] Walter C Hurty. Vibrations of structural systems by component mode synthesis. *Journal of the Engineering Mechanics Division*, 86(4):51–69, 1960.
- [301] Norman Lang, Jens Saak, and Peter Benner. Model order reduction for thermo-elastic assembly group models. In *Thermo-energetic Design of Machine Tools*, pages 85–93. Springer, 2015.
- [302] Tamara Bechtold, Evgenii B Rudnyi, and Jan G Korvink. Automatic generation of compact electro-thermal models for semiconductor devices. *IEICE Transactions on Electronics*, 86(3):459–465, 2003.
- [303] Tamara Bechtold, Evgenii B Rudnyi, and Jan G Korvink. *Fast simulation of electro-thermal MEMS: efficient dynamic compact models*. Springer Science & Business Media, 2006.
- [304] Tamara Bechtold, Dennis Hohlfeld, Evgenii B Rudnyi, and Jan G Korvink. Moment-matching-based linear model order reduction for nonparametric and parametric electrothermal mems models. *Syst. Model. MEMS*, 10:211–235, 2013.
- [305] Max Meindl, Maria Cruz Varona, Alessandro Castagnotto, Felix Thomann, Wolfgang Polifke, and Boris Lohmann. Model order reduction in thermoacoustic stability analysis. In *9th Vienna International Conference on Mathematical Modelling*, 2018.
- [306] S Hu, Chengdong Yuan, Alessandro Castagnotto, Boris Lohmann, Sofiane Bouhedma, Dennis Hohlfeld, and Tamara Bechtold. Stable reduced order modeling of piezoelectric energy harvesting modules using implicit schur complement. *Microelectronics Reliability*, 85:148–155, 2018.
- [307] Paramita Guha and Mashuq un Nabi. Optimal control of a nonlinear induction heating system using a proper orthogonal decomposition based reduced order model. *Journal of Process Control*, 22(9):1681–1687, 2012.
- [308] Robert J Guyan. Reduction of stiffness and mass matrices. *AIAA journal*, 3(2):380–380, 1965.
- [309] Roy R Craig Jr and Mervyn CC Bampton. Coupling of substructures for dynamic analyses. *AIAA journal*, 6(7):1313–1319, 1968.
- [310] Om P Agrawal and Ahmed A Shabana. Dynamic analysis of multibody systems using component modes. *Computers & Structures*, 21(6):1303–1312, 1985.
- [311] Christine Nowakowski, Jörg Fehr, Michael Fischer, and Peter Eberhard. Model order reduction in elastic multibody systems using the floating frame of reference formulation. *IFAC Proceedings Volumes*, 45(2):40–48, 2012.
- [312] Christine Nowakowski, Patrick Kürschner, Peter Eberhard, and Peter Benner. Model reduction of an elastic crankshaft for elastic multibody simulations, 2013.

- [313] Karl Kunisch and Stefan Volkwein. Control of the burgers equation by a reduced-order approach using proper orthogonal decomposition. *Journal of optimization theory and applications*, 102(2):345–371, 1999.
- [314] YC Liang, HP Lee, SP Lim, WZ Lin, KH Lee, and CG Wu. Proper orthogonal decomposition and its applications—part i: Theory. *Journal of Sound and vibration*, 252(3):527–544, 2002.
- [315] Gaetan Kerschen, Jean-claude Golinval, Alexander F Vakakis, and Lawrence A Bergman. The method of proper orthogonal decomposition for dynamical characterization and order reduction of mechanical systems: an overview. *Nonlinear dynamics*, 41(1):147–169, 2005.
- [316] Saifon Chaturantabut and Danny C Sorensen. Nonlinear model reduction via discrete empirical interpolation. *SIAM Journal on Scientific Computing*, 32(5):2737–2764, 2010.
- [317] Charbel Farhat, Philip Avery, Todd Chapman, and Julien Cortial. Dimensional reduction of nonlinear finite element dynamic models with finite rotations and energy-based mesh sampling and weighting for computational efficiency. *International Journal for Numerical Methods in Engineering*, 98(9):625–662, 2014.
- [318] B Lohmann, T Bechtold, P Eberhard, J Fehr, DJ Rixen, M Cruz Varona, C Lerch, CD Yuan, EB Rudnyi, B Frohlich, et al. Model order reduction in mechanical engineering. 2020.
- [319] Peter Benner and Lihong Feng. Model order reduction for coupled problems. *Appl Comput Math Int J*, 14(1):3–22, 2015.
- [320] Franck C Sgard, Nouredine Atalla, and Raymond Panneton. A modal reduction technique for the finite element formulation of biot’s poroelasticity equations in acoustics applied to multilayered structures. *The Journal of the Acoustical Society of America*, 103(5):2882–2882, 1998.
- [321] Romain Rumpler, Jean-François Deü, and Peter Göransson. A modal-based reduction method for sound absorbing porous materials in poro-acoustic finite element models. *The Journal of the Acoustical Society of America*, 132(5):3162–3179, 2012.
- [322] Olivier Dazel, B Brouard, J-P Groby, and Peter Göransson. A normal modes technique to reduce the order of poroelastic models: application to 2d and coupled 3d models. *International journal for numerical methods in engineering*, 96(2):110–128, 2013.
- [323] Romain Rumpler, Peter Göransson, and J-F Deü. A finite element approach combining a reduced-order system, padé approximants, and an adaptive frequency windowing for fast multi-frequency solution of poro-acoustic problems. *International Journal for Numerical Methods in Engineering*, 97(10):759–784, 2014.
- [324] Olivier Dazel, F Sgard, and C-H Lamarque. Application of generalized complex modes to the calculation of the forced response of three-dimensional poroelastic materials. *Journal of Sound and Vibration*, 268(3):555–580, 2003.
- [325] Ettore Lappano, Markus Polanz, Wim Desmet, and Domenico Mundo. A parametric model order reduction technique for poroelastic finite element models. *The Journal of the Acoustical Society of America*, 142(4):2376–2385, 2017.
- [326] Alfio Quarteroni, Andrea Manzoni, and Federico Negri. *Reduced basis methods for partial differential equations: an introduction*, volume 92. Springer, 2015.
- [327] Qiang Du, Maria Emelianenko, and Lili Ju. Convergence of the lloyd algorithm for computing centroidal voronoi tessellations. *SIAM journal on numerical analysis*, 44(1):102–119, 2006.
- [328] Cameron Talischi, Glaucio H. Paulino, Anderson Pereira, and Ivan F. M. Menezes. Polymesh: a general-purpose mesh generator for polygonal elements written in matlab. *Structural and Multidisciplinary Optimization*, 45(3):309–328, Mar 2012.
- [329] Charles E. Augarde and Andrew J. Deeks. The use of timoshenko’s exact solution for a cantilever beam in adaptive analysis. *Finite Elements in Analysis and Design*, 44(9):595 – 601, jun 2008.
- [330] L Beirão da Veiga, Franco Dassi, and Alessandro Russo. High-order virtual element method on polyhedral meshes. *Computers & Mathematics with Applications*, 74(5):1110–1122, 2017.

- [331] Marco Buck, Oleg Iliev, and Heiko Andrä. Multiscale finite elements for linear elasticity: oscillatory boundary conditions. In *Domain Decomposition Methods in Science and Engineering XXI*, pages 237–245. Springer, 2014.
- [332] David Amsallem and Bernard Haasdonk. Pebl-rom: Projection-error based local reduced-order models. *Advanced Modeling and Simulation in Engineering Sciences*, 3(1):1–25, 2016.
- [333] David Amsallem and Charbel Farhat. An online method for interpolating linear parametric reduced-order models. *SIAM Journal on Scientific Computing*, 33(5):2169–2198, 2011.
- [334] Ettore Lappano, Frank Naets, Martijn Vermaut, Wim Desmet, and Domenico Mundo. Development of a parametric model order reduction technique for beam-based structures. In *9th International Styrian Noise, Vibration and Harshness Congress*, 2016.
- [335] Olivier Dazel, F Sgard, C-H Lamarque, and Noureddine Atalla. An extension of complex modes for the resolution of finite-element poroelastic problems. *Journal of Sound and Vibration*, 253(2):421–445, 2002.
- [336] Romain Rumpler, Peter Göransson, and Jean-François Deü. A residue-based mode selection and sorting procedure for efficient poroelastic modeling in acoustic finite element applications. *The Journal of the Acoustical Society of America*, 134(6):4730–4741, 2013.
- [337] Svante Wold, Kim Esbensen, and Paul Geladi. Principal component analysis. *Chemometrics and intelligent laboratory systems*, 2(1-3):37–52, 1987.
- [338] Morris H Hansen, William N Hurwitz, and William G Madow. Sample survey methods and theory. vol. i. methods and applications. 1953.
- [339] Heng Chi, Anderson Pereira, Ivan FM Menezes, and Glaucio H Paulino. Virtual element method (vem)-based topology optimization: an integrated framework. *Structural and Multidisciplinary Optimization*, 62(3):1089–1114, 2020.
- [340] P Ponte Castañeda and M Zaidman. Constitutive models for porous materials with evolving microstructure. *Journal of the Mechanics and Physics of Solids*, 42(9):1459–1497, 1994.
- [341] K Lee and S Ghosh. A microstructure based numerical method for constitutive modeling of composite and porous materials. *Materials Science and Engineering: A*, 272(1):120–133, 1999.
- [342] Son-Young Yi. A study of two modes of locking in poroelasticity. *SIAM Journal on Numerical Analysis*, 55(4):1915–1936, 2017.
- [343] Xialan Tang, Zhibin Liu, Baiju Zhang, and Minfu Feng. On the locking-free three-field virtual element methods for biot’s consolidation model in poroelasticity. *ESAIM: Mathematical Modelling & Numerical Analysis*, 55, 2021.
- [344] L Beirao da Veiga, F Brezzi, and LD Marini. A locking free virtual element method for linear elasticity.
- [345] Xialan Tang, Zhibin Liu, Baiju Zhang, and Minfu Feng. A low-order locking-free virtual element for linear elasticity problems. *Computers & Mathematics with Applications*, 80(5):1260–1274, 2020.
- [346] Klaus Gerdes. A review of infinite element methods for exterior helmholtz problems. *Journal of Computational Acoustics*, 8(01):43–62, 2000.
- [347] L Cremers, KR Fyfe, and JP Coyette. A variable order infinite acoustic wave envelope element. *Journal of Sound and Vibration*, 171(4):483–508, 1994.
- [348] Luc Cremers and Ken R Fyfe. On the use of variable order infinite wave envelope elements for acoustic radiation and scattering. *The Journal of the Acoustical Society of America*, 97(4):2028–2040, 1995.
- [349] GR Buchanan and M Sallah. Some simplified methods for infinite elements. *Computational mechanics*, 6(3):167–172, 1990.
- [350] Jean-Christophe Autrique and Frédéric Magoulès. Studies of an infinite element method for acoustic radiation. *Applied Mathematical Modelling*, 30(7):641–655, 2006.

- [351] Eli Turkel and A Yefet. Absorbing pml boundary layers for wave-like equations. *Applied Numerical Mathematics*, 27(4):533–557, 1998.
- [352] Isaac Harari, Michael Slavutin, and Eli Turkel. Analytical and numerical studies of a finite element pml for the helmholtz equation. *Journal of Computational Acoustics*, 8(01):121–137, 2000.
- [353] Quan Qi and Thomas L Geers. Evaluation of the perfectly matched layer for computational acoustics. *Journal of Computational Physics*, 139(1):166–183, 1998.
- [354] Steven G Johnson. Notes on perfectly matched layers (pmls). *Lecture notes, Massachusetts Institute of Technology, Massachusetts*, 29:2008, 2008.
- [355] Yanbin He, Tianning Chen, and Jinghuai Gao. Perfectly matched absorbing layer for modelling transient wave propagation in heterogeneous poroelastic media. *Journal of Geophysics and Engineering*, 17(1):18–34, 2020.
- [356] Dibyendu Adak, ALN Pramod, Ean Tat Ooi, and Sundararajan Natarajan. A combined virtual element method and the scaled boundary finite element method for linear elastic fracture mechanics. *Engineering Analysis with Boundary Elements*, 113:9–16, 2020.
- [357] Hui Zhou. *Algebraic multiscale finite-volume methods for reservoir simulation*. PhD thesis, Stanford University, 2010.
- [358] Zhiming Chen and Thomas Hou. A mixed multiscale finite element method for elliptic problems with oscillating coefficients. *Mathematics of Computation*, 72(242):541–576, 2003.
- [359] Jorg E Aarnes. On the use of a mixed multiscale finite element method for greater flexibility and increased speed or improved accuracy in reservoir simulation. *Multiscale Modeling & Simulation*, 2(3):421–439, 2004.
- [360] Patrick Jenny, SH Lee, and Hamdi A Tchelepi. Multi-scale finite-volume method for elliptic problems in subsurface flow simulation. *Journal of computational physics*, 187(1):47–67, 2003.
- [361] Martin Philip Bendsøe and Noboru Kikuchi. Generating optimal topologies in structural design using a homogenization method. *Computer methods in applied mechanics and engineering*, 71(2):197–224, 1988.
- [362] Mathias Stolpe and Martin P Bendsøe. Global optima for the zhou–rozvany problem. *Structural and Multidisciplinary Optimization*, 43(2):151–164, 2011.
- [363] Martin P Bendsøe. Optimal shape design as a material distribution problem. *Structural optimization*, 1(4):193–202, 1989.
- [364] M Zhou and GIN Rozvany. The coc algorithm, part ii: Topological, geometrical and generalized shape optimization. *Computer methods in applied mechanics and engineering*, 89(1-3):309–336, 1991.
- [365] Ole Sigmund. A 99 line topology optimization code written in matlab. *Structural and multidisciplinary optimization*, 21(2):120–127, 2001.
- [366] Martin P Bendsøe and Ole Sigmund. *Optimization of structural topology, shape, and material*, volume 414. Springer, 1995.
- [367] Michael Yu Wang, Xiaoming Wang, and Dongming Guo. A level set method for structural topology optimization. *Computer methods in applied mechanics and engineering*, 192(1-2):227–246, 2003.
- [368] Grégoire Allaire, François Jouve, and Anca-Maria Toader. Structural optimization using sensitivity analysis and a level-set method. *Journal of computational physics*, 194(1):363–393, 2004.
- [369] Martin Burger, Benjamin Hackl, and Wolfgang Ring. Incorporating topological derivatives into level set methods. *Journal of computational physics*, 194(1):344–362, 2004.
- [370] Krister Svanberg. The method of moving asymptotes—a new method for structural optimization. *International journal for numerical methods in engineering*, 24(2):359–373, 1987.
- [371] John H Holland. Genetic algorithms. *Scientific american*, 267(1):66–73, 1992.
- [372] Lawrence Davis. Handbook of genetic algorithms. 1991.

- [373] Grahame A Jastrebski and Dirk V Arnold. Improving evolution strategies through active covariance matrix adaptation. In *2006 IEEE international conference on evolutionary computation*, pages 2814–2821. IEEE, 2006.
- [374] Nikolaus Hansen and Andreas Ostermeier. Convergence properties of evolution strategies with the derandomized covariance matrix adaptation: The (/i,)-es. *Eufit*, 97:650–654, 1997.
- [375] Kelly Fleetwood. An introduction to differential evolution. In *Proceedings of Mathematics and Statistics of Complex Systems (MASCOS) One Day Symposium, 26th November, Brisbane, Australia*, pages 785–791, 2004.
- [376] Kenneth V Price. Differential evolution. In *Handbook of optimization*, pages 187–214. Springer, 2013.
- [377] Fred Glover and Manuel Laguna. Tabu search. In *Handbook of combinatorial optimization*, pages 2093–2229. Springer, 1998.
- [378] Fred Glover. Tabu search—part i. *ORSA Journal on computing*, 1(3):190–206, 1989.
- [379] Pooya Rostami and Javad Marzbanrad. Identification of optimal topologies for continuum structures using metaheuristics: A comparative study. *Archives of Computational Methods in Engineering*, pages 1–28, 2021.
- [380] Ole Sigmund and Kurt Maute. Topology optimization approaches. *Structural and Multidisciplinary Optimization*, 48(6):1031–1055, 2013.
- [381] Martin Philip Bendsoe and Ole Sigmund. *Topology optimization: theory, methods, and applications*. Springer Science & Business Media, 2013.
- [382] David Guirguis, Nikola Aulig, Renato Picelli, Bo Zhu, Yuqing Zhou, William Vicente, Francesco Iorio, Markus Olhofer, Wojciech Matusik, Carlos Artemio Coello Coello, et al. Evolutionary black-box topology optimization: challenges and promises. *IEEE Transactions on Evolutionary Computation*, 24(4):613–633, 2019.
- [383] George IN Rozvany. Aims, scope, methods, history and unified terminology of computer-aided topology optimization in structural mechanics. *Structural and Multidisciplinary optimization*, 21(2):90–108, 2001.
- [384] Joshua D Deaton and Ramana V Grandhi. A survey of structural and multidisciplinary continuum topology optimization: post 2000. *Structural and Multidisciplinary Optimization*, 49(1):1–38, 2014.
- [385] Eddie Wadbro and Martin Berggren. Topology optimization of an acoustic horn. *Computer methods in applied mechanics and engineering*, 196(1-3):420–436, 2006.
- [386] Maria B Dühring, Jakob S Jensen, and Ole Sigmund. Acoustic design by topology optimization. *Journal of sound and vibration*, 317(3-5):557–575, 2008.
- [387] Joong Seok Lee, Yoon Young Kim, Jung Soo Kim, and Yeon June Kang. Two-dimensional poroelastic acoustical foam shape design for absorption coefficient maximization by topology optimization method. *The Journal of the Acoustical Society of America*, 123(4):2094–2106, 2008.
- [388] Jin Woo Lee and Yoon Young Kim. Topology optimization of muffler internal partitions for improving acoustical attenuation performance. *International journal for numerical methods in engineering*, 80(4):455–477, 2009.
- [389] Junghwan Kook, Kunmo Koo, Jaeyub Hyun, Jakob S Jensen, and Semyung Wang. Acoustical topology optimization for zwicker’s loudness model—application to noise barriers. *Computer methods in applied mechanics and engineering*, 237:130–151, 2012.
- [390] Gil Ho Yoon. Acoustic topology optimization of fibrous material with delany–bazley empirical material formulation. *Journal of Sound and Vibration*, 332(5):1172–1187, 2013.
- [391] Joong Seok Lee, Peter Göransson, and Yoon Young Kim. Topology optimization for three-phase materials distribution in a dissipative expansion chamber by unified multiphase modeling approach. *Computer Methods in Applied Mechanics and Engineering*, 287:191–211, 2015.
- [392] Ki Hyun Kim and Gil Ho Yoon. Optimal rigid and porous material distributions for noise barrier by acoustic topology optimization. *Journal of Sound and Vibration*, 339:123–142, 2015.

- [393] Esubalewe Lakie Yedeg, Eddie Wadbro, and Martin Berggren. Interior layout topology optimization of a reactive muffler. *Structural and Multidisciplinary Optimization*, 53(4):645–656, 2016.
- [394] Leilei Chen, Cheng Liu, Wenchang Zhao, and Linchao Liu. An isogeometric approach of two dimensional acoustic design sensitivity analysis and topology optimization analysis for absorbing material distribution. *Computer Methods in Applied Mechanics and Engineering*, 336:507–532, 2018.
- [395] Won Uk Yoon, Jun Hyeong Park, Joong Seok Lee, and Yoon Young Kim. Topology optimization design for total sound absorption in porous media. *Computer Methods in Applied Mechanics and Engineering*, 360:112723, 2020.
- [396] Yanming Xu, Wenchang Zhao, Leilei Chen, and Haibo Chen. Distribution optimization for acoustic design of porous layer by the boundary element method. *Acoustics Australia*, 48(1), 2020.
- [397] Leilei Chen, Chuang Lu, Haojie Lian, Zhaowei Liu, Wenchang Zhao, Shengze Li, Haibo Chen, and Stéphane PA Bordas. Acoustic topology optimization of sound absorbing materials directly from subdivision surfaces with isogeometric boundary element methods. *Computer Methods in Applied Mechanics and Engineering*, 362:112806, 2020.
- [398] Zi-xiang Xu, Hao Gao, Yu-jiang Ding, Jing Yang, Bin Liang, and Jian-chun Cheng. Topology-optimized omnidirectional broadband acoustic ventilation barrier. *Physical Review Applied*, 14(5):054016, 2020.
- [399] Junghwan Kook. Evolutionary topology optimization for acoustic-structure interaction problems using a mixed u/p formulation. *Mechanics Based Design of Structures and Machines*, 47(3):356–374, 2019.
- [400] Vivek T Ramamoorthy, Ender Özcan, Andrew J Parkes, Jaouen Luc, and François-Xavier Bécot. Metaheuristic optimisation of sound absorption performance of multilayered porous materials. 2019.
- [401] Comparison of heuristics and metaheuristics for topology optimisation in acoustic porous materials.
- [402] Jun Yan, Suxia Yang, Zunyi Duan, and Chunqiu Yang. Minimum compliance optimization of a thermoelastic lattice structure with size-coupled effects. *Journal of Thermal Stresses*, 38(3):338–357, 2015.
- [403] Jun Yan, Xu Guo, and Gengdong Cheng. Multi-scale concurrent material and structural design under mechanical and thermal loads. *Computational Mechanics*, 57(3):437–446, 2016.
- [404] Boyan S Lazarov. Topology optimization using multiscale finite element method for high-contrast media. In *International Conference on Large-Scale Scientific Computing*, pages 339–346. Springer, 2013.
- [405] Hui Liu, Yiqiang Wang, Hongming Zong, and Michael Yu Wang. Efficient structure topology optimization by using the multiscale finite element method. *Structural and Multidisciplinary Optimization*, 58(4):1411–1430, 2018.
- [406] Cameron Talischi, Glaucio H Paulino, Anderson Pereira, and Ivan FM Menezes. Polygonal finite elements for topology optimization: A unifying paradigm. *International journal for numerical methods in engineering*, 82(6):671–698, 2010.
- [407] Emily D Sanders, Anderson Pereira, Miguel A Aguiló, and Glaucio H Paulino. Polymat: an efficient matlab code for multi-material topology optimization. *Structural and Multidisciplinary Optimization*, 58(6):2727–2759, 2018.
- [408] Raymond D Mindlin. Influence of rotatory inertia and shear on flexural motions of isotropic, elastic plates. 1951.
- [409] Eric Reissner. The effect of transverse shear deformation on the bending of elastic plates. 1945.
- [410] H Hencky. Über die berücksichtigung der schubverzerrung in ebenen platten. *ingenieur-archiv*, 16(1):72–76, 1947.
- [411] X Lu and D Liu. Interlayer shear slip theory for cross-ply laminates with nonrigid interfaces. *AIAA journal*, 30(4):1063–1073, 1992.

- [412] Chin-Teh Sun and JM Whitney. Theories for the dynamic response of laminated plates. *AIAA journal*, 11(2):178–183, 1973.
- [413] RD Ford, P Lord, and AW Walker. Sound transmission through sandwich constructions. *Journal of sound and vibration*, 5(1):9–21, 1967.
- [414] Jean-Loui Guyader and Claude Lesueur. Acoustic transmission through orthotropic multilayered plates, part i: Plate vibration modes. *Journal of Sound and Vibration*, 58(1):51–68, 1978.
- [415] JL Guyader and C Lesueur. Acoustic transmission through orthotropic multilayered plates, part ii: transmission loss. *Journal of Sound and Vibration*, 58(1):69–86, 1978.
- [416] CY Lee and D Liu. Layer reduction technique for composite laminate analysis. *Computers & structures*, 44(6):1305–1315, 1992.
- [417] Jean-Louis Guyader and Christian Cacciolati. Viscoelastic properties of single layer plate material equivalent to multi-layer composites plate. In *INTER-NOISE and NOISE-CON Congress and Conference Proceedings*, volume 2007, pages 4190–4199. Institute of Noise Control Engineering, 2007.
- [418] Donald Ross. Damping of plate flexural vibrations by means of viscoelastic laminae. *Structural damping*, pages 49–97, 1959.
- [419] Edward M Kerwin Jr. Damping of flexural waves by a constrained viscoelastic layer. *The Journal of the Acoustical society of America*, 31(7):952–962, 1959.
- [420] Eric E Ungar and Edward M Kerwin Jr. Loss factors of viscoelastic systems in terms of energy concepts. *The Journal of the acoustical Society of America*, 34(7):954–957, 1962.
- [421] Ondiz Zarraga, Imanol Sarriá, Jon García-Barruetabeña, and Fernando Cortés. Dynamic analysis of plates with thick unconstrained layer damping. *Engineering Structures*, 201:109809, 2019.
- [422] U Arasan, F Marchetti, F Chevillotte, L Jaouen, D Chronopoulos, and E Gourdon. A simple equivalent plate model for dynamic bending stiffness of three-layer sandwich panels with shearing core. *Journal of Sound and Vibration*, 500:116025, 2021.
- [423] Ondiz Zarraga, Imanol Sarriá, Jon García-Barruetabeña, and Fernando Cortés. Homogenised formulation for plates with thick constrained viscoelastic core. *Computers & Structures*, 229:106185, 2020.
- [424] Augustus Edward Hough Love. Xvi. the small free vibrations and deformation of a thin elastic shell. *Philosophical Transactions of the Royal Society of London.(A.)*, (179):491–546, 1888.
- [425] Gustav Kirchhoff. "U about the balance and movement of an elastic disc. *Journal for pure and applied mathematics (Crelles Journal)*, 1850(40):51–88, 1850.
- [426] H Hencky. "U about taking into account ü consideration of shear distortion in flat plates. *engineer-archive*, 16(1):72–76, 1947.
- [427] Fabien Marchetti, Uthayasuriyan Arasan, Fabien Chevillotte, and Kerem Ege. On the condensation of thick symmetric multilayer panels including dilatational motion. *Journal of Sound and Vibration*, 502:116078, 2021.
- [428] Arasan Uthayasuriyan, Abhilash Sreekumar, Fabien Chevillotte, Savvas P. Triantafyllou, Dimitrios Chronopoulos, and Gourdon Emmanuel. Condensed finite element scheme for symmetric multi-layer structures including dilatational motion. *Journal of Sound and Vibration*, In review.
- [429] Yeongbin Ko, Phill-Seung Lee, and Klaus-Jürgen Bathe. A new mitc4+ shell element. *Computers & Structures*, 182:404–418, 2017.
- [430] Udit Pillai, Savvas P Triantafyllou, Ian Ashcroft, Yasser Essa, and Federico Martin de la Escalera. Phase-field modelling of brittle fracture in thin shell elements based on the mitc4+ approach. *Computational Mechanics*, 65, 2020.
- [431] Robert Urick and WA Kuperman. Ambient noise in the sea, 1989.
- [432] Daniel E McNamara and Raymond P Buland. Ambient noise levels in the continental united states. *Bulletin of the seismological society of America*, 94(4):1517–1527, 2004.

- [433] PD Spanos and BA Zeldin. Pitfalls of deterministic and random analyses of systems with hysteresis. *Journal of engineering mechanics*, 126(10):1108–1110, 2000.
- [434] David Edward Newland. *An introduction to random vibrations, spectral & wavelet analysis*. Courier Corporation, 2012.
- [435] TK Caughey. Nonlinear theory of random vibrations. In *Advances in applied mechanics*, volume 11, pages 209–253. Elsevier, 1971.
- [436] Denis Lafarge. *Propagation of sound in porous materials – a rigid structure saturated by a viscothermic fluid: Definition of parameters g et ω é triques, electromagnetic analogy, relaxation time*. PhD thesis, Le Mans, 1993.
- [437] Lassi Päiväranta and Erkki Somersalo. Inverse problems in mathematical physics. *Inverse Problems in Mathematical Physics*, 422, 1993.
- [438] Muneo Hori. *Introduction to computational earthquake engineering*. World Scientific, 2011.
- [439] Yu-Xian Hu, Shih-Chi Liu, and Weimin Dong. *Earthquake engineering*. CRC Press, 1996.
- [440] Ahsan Kareem, Kyle Butler, and Dae Kwon. Modeling and simulation of transient wind load effects. In *Proc. of the 4th UJNR Panel on Wind and Seismic Effects Workshop on Wind Engineering, Tsukuba, Tokyo*, 2006.
- [441] Dae-Kun Kwon and Ahsan Kareem. Gust-front factor: New framework for wind load effects on structures. *Journal of structural engineering*, 135(6):717–732, 2009.
- [442] Kurtis Gurley and Ahsan Kareem. Applications of wavelet transforms in earthquake, wind and ocean engineering. *Engineering structures*, 21(2):149–167, 1999.
- [443] Jan Erik Weber and Arne Melsom. Transient ocean currents induced by wind and growing waves. *Journal of physical oceanography*, 23(2):193–206, 1993.
- [444] TH Richards and Y Tan Leung. An accurate method in structural vibration analysis. *Journal of Sound Vibration*, 55(3):363–376, 1977.
- [445] Bingen Yang and CA Tan. Transfer functions of one-dimensional distributed parameter systems. 1992.
- [446] Artur Pais and Eduardo Kausel. Approximate formulas for dynamic stiffnesses of rigid foundations. *Soil Dynamics and Earthquake Engineering*, 7(4):213–227, 1988.
- [447] John P Wolf. Soil-structure-interaction analysis in time domain. In *Structural mechanics in reactor technology*. 1987.
- [448] John P Wolf. *Foundation vibration analysis using simple physical models*. Pearson Education, 1994.
- [449] SS Chen, MW t Wambsganss, and JA Jendrzejczyk. Added mass and damping of a vibrating rod in confined viscous fluids. *American Society of Mechanical Engineers*, 1976.
- [450] RM Christensen. Theory of viscoelasticity: an introduction. academic, new york. 1971.
- [451] Stephen H Crandall. The role of damping in vibration theory. *Journal of sound and vibration*, 11(1):3–IN1, 1970.
- [452] David Frank Golla and Peter C Hughes. Dynamics of viscoelastic structures—a time-domain, finite element formulation. 1985.
- [453] P-TD Spanos. Filter approaches to wave kinematics approximation. In *Studies in Applied Mechanics*, volume 14, pages 459–473. Elsevier, 1986.
- [454] PD Spanos and BA Zeldin. Random vibration of systems with frequency-dependent parameters or fractional derivatives. *Journal of Engineering Mechanics*, 123(3):290–292, 1997.
- [455] Leon Emry Borgman. Ocean wave simulation for engineering design. *Journal of the Waterways and Harbors Division*, 95(4):557–583, 1969.
- [456] Ben G Burke and James T Tighe. A time series model for dynamic behavior of offshore structures. In *Offshore technology conference*. OnePetro, 1971.

- [457] P-TD Spanos and JE Hansen. Linear prediction theory for digital simulation of sea waves. 1981.
- [458] PT D Spanos. Arma algorithms for ocean wave modeling. 1983.
- [459] NK Lin and WH Hartt. Time series simulations of wide-band spectra for fatigue tests of offshore structures. 1984.
- [460] K Samii and JK Vandiver. A numerically efficient technique for the simulation of random wave forces on offshore structures. In *Offshore Technology Conference*. OnePetro, 1984.
- [461] John Brian Roberts and Pol D Spanos. *Random vibration and statistical linearization*. Courier Corporation, 2003.
- [462] Igor Podlubny. *Fractional differential equations: an introduction to fractional derivatives, fractional differential equations, to methods of their solution and some of their applications*. Elsevier, 1998.
- [463] Fred Riewe. Mechanics with fractional derivatives. *Physical Review E*, 55(3):3581, 1997.
- [464] JL Lovoie, Thomas J Osler, and R Tremblay. Fractional derivatives and special functions. *SIAM review*, 18(2):240–268, 1976.
- [465] Changpin Li and Weihua Deng. Remarks on fractional derivatives. *Applied Mathematics and Computation*, 187(2):777–784, 2007.
- [466] Michele Caputo. Vibrations of an infinite plate with a frequency independent q . *The Journal of the Acoustical Society of America*, 60(3):634–639, 1976.
- [467] Ronald L Bagley and Peter J Torvik. On the fractional calculus model of viscoelastic behavior. *Journal of Rheology*, 30(1):133–155, 1986.
- [468] ZEA Fella and C Depollier. Transient acoustic wave propagation in rigid porous media: A time-domain approach. *The Journal of the Acoustical Society of America*, 107(2):683–688, 2000.
- [469] M Hodaei, V Rabbani, and P Maghoul. Transient acoustic wave propagation in bone-like porous materials using the theory of poroelasticity and fractional derivative: a sensitivity analysis. *Acta Mechanica*, 231(1):179–203, 2020.
- [470] ZEA Fella and C Depollier. On the propagation of acoustic pulses in porous rigid media: A time-domain approach. *Journal of Computational Acoustics*, 9(03):1163–1173, 2001.
- [471] Zine El Abidine Fella, M Fella, Walter Lauriks, and Claude Depollier. Direct and inverse scattering of transient acoustic waves by a slab of rigid porous material. *The Journal of the Acoustical Society of America*, 113(1):61–72, 2003.
- [472] ZEA Fella, C Depollier, and M Fella. Application of fractional calculus to the sound waves propagation in rigid porous materials: validation via ultrasonic measurements. *Acta Acustica united with Acustica*, 88(1):34–39, 2002.
- [473] Chan Ghee Koh and James M Kelly. Application of fractional derivatives to seismic analysis of base-isolated models. *Earthquake engineering & structural dynamics*, 19(2):229–241, 1990.
- [474] Mario Di Paola, Francesco P Pinnola, and Pol D Spanos. Analysis of multi-degree-of-freedom systems with fractional derivative elements of rational order. In *ICFDA'14 International Conference on Fractional Differentiation and Its Applications 2014*, pages 1–6. IEEE, 2014.
- [475] Elias Ghossein and Martin Lévesque. A fully automated numerical tool for a comprehensive validation of homogenization models and its application to spherical particles reinforced composites. *International Journal of Solids and Structures*, 49(11-12):1387–1398, 2012.
- [476] Nikhilesh Chawla, RS Sidhu, and VV Ganesh. Three-dimensional visualization and microstructure-based modeling of deformation in particle-reinforced composites. *Acta materialia*, 54(6):1541–1548, 2006.
- [477] YP Qiu and GJ Weng. A theory of plasticity for porous materials and particle-reinforced composites. 1992.